Proceedings of the

18th Annual Conference on Fossil Energy Materials

June 2-4 2004

Published by:
Oak Ridge National Laboratory
Fossil Energy Program
Oak Ridge, TN 37831-6084

DISCLAIMER

Available to DOE and DOE contractors from the Office of Scientific and Technical Information, P.O. Box 62, Oak Ridge, TN 37831; prices available at 865-576-8401.

Available to the public from the National Technical Information Service, U.S. Department of Commerce, 5285 Port Royal Road, Springfield, VA 22161; prices available at 703-487-4650.

ORNL/R04-1203.5

U.S. Department of Energy
Fossil Energy
Advanced Research and Technology Development

PROCEEDINGS
OF THE
EIGHTEENTH ANNUAL CONFERENCE
ON FOSSIL ENERGY MATERIALS

June 2-4, 2004
Knoxville, Tennessee

Fossil Energy AR&TD Materials Program

OAK RIDGE NATIONAL LABORATORY
MANAGED BY
UT-BATTELLE, LLC
FOR THE
U.S. DEPARTMENT OF ENERGY
UNDER CONTRACT DE-AC05-00OR22725

ORNL/R04-1203.5

PROCEEDINGS OF THE EIGHTEENTH ANNUAL CONFERENCE ON FOSSIL ENERGY MATERIALS

June 2-4, 2004
Knoxville, Tennessee

Compiled by
R. R. Judkins and L.S. Mack

Date Published: October 2004

Prepared by
OAK RIDGE NATIONAL LABORATORY
P.O. Box 2008
Oak Ridge, Tennessee 37831-6285
Managed by
UT-Battelle, LLC
for the
U.S. DEPARTMENT OF ENERGY
Under contract DE-AC05-00OR22725

CONTENTS

PREFACE

The 18th Annual conference on Fossil Energy Materials was held in Knoxville, Tennessee, on June 2 through June 4, 2004. The meeting was sponsored by the U.S. Department of Energy's (DOE) Office of Fossil Energy through the Advanced Research Materials Program (ARM). The objective of the ARM Program is to conduct research and development on materials for longer-term fossil energy applications, as well as for generic needs of various fossil fuel technologies. The management of the program has been decentralized to the DOE Oak Ridge Operations Office and Oak Ridge National Laboratory (ORNL). The research is performed by staff members at ORNL and by researchers at other national laboratories, universities, and in private industry. The work is divided into the following categories: (1) structural, ceramics, (2) new alloys and coatings, (3) functional materials, and (4) technology development and transfer.

These proceedings were produced primarily from electronic files provided by the authors. They have been neither refereed nor extensively edited. However, most of the papers have already undergone technical review within the individual organizations before submission to the Program Office. The proceedings are available on the Fossil Energy home page at http://www.ornl.gov/fossil (Workshops and Conferences).

The successful completion of the conference and publication of the proceedings has required help from several people. The organizers wish to thank Angela Beach of the ORNL Conference Office for her help in the many arrangements and the numerous staff and support personnel associated with the conference. Finally we express our sincere appreciation to the authors whose efforts are the very basis of the conference.

Conference Chairmen

ORNL
Roddie R. Judkins
Ian G. Wright
Timothy R. Armstrong

DOE
Robert R. Romanosky, Jr.

Conference Coordinator
LaRonda Mack/ORNL

SESSION I

FUNCTIONAL MATERIALS

DEVELOPMENT OF INORGANIC MEMBRANES FOR HYDROGEN SEPARATION

Brian L. Bischoff, Roddie R. Judkins, K. Dale Adcock, and Lawrence E. Powell
Oak Ridge National Laboratory
P.O. Box 2008
Oak Ridge, TN 37831-7271

ABSTRACT

This paper presents information and data relative to recent advances in the development at Oak Ridge National Laboratory of microporous inorganic membranes for high-temperature hydrogen separation. These membranes incorporate a metal tubular support with a thin ceramic layer applied to the inside of the support tube. Research emphasis during the last year has been directed toward the development of these high-permeance (high-flux) and high-separation-factor sub 2nm pore-size metal-supported membranes. In addition, improvements were made to our test systems to both increase their operating temperatures and qualify them to work with flammable gases such as hydrogen and propane. Lastly, we have submitted a prototype to DOE for a classification and nonproliferation review (NPR) and received approval for the testing and evaluation of the physical properties and performance characteristics at national labs, universities, and industrial facilities. Performance data for recent membranes are presented and new insights into diffusion mechanisms are included in the discussion.

INTRODUCTION

The U. S. is committed to a future hydrogen economy[1] but hydrogen is not available as an elemental resource. Coal gasification offers one of the most versatile and cleanest ways to convert the energy content of coal into hydrogen. Rather than burning coal directly, gasification breaks down coal or virtually any carbon based feedstock into its basic chemical constituents. Effective recovery of hydrogen from gas mixtures then becomes a central issue.

Inorganic membranes have been employed for well over half a century for separating uranium isotopes. In the early 1980's inorganic membranes began to be applied to the separation of particles from fluids and to the separation of mixtures of fluids, both liquids and gases[2-5]. The smallest pore diameters available in commercial inorganic membranes are about 4 nm.

ORNL has been engaged in the development of microporous membranes for hydrogen separation for several years. Prior to 1999, this effort was directed to very high temperature (i.e., ≥600°C) all-ceramic membranes. As a result of changing system requirements in, for example, coal gasification, the temperature at which hydrogen separation may be conducted is decreased to about 250 to 350°C. The lower temperature operation negates the need for all-ceramic structures and suggests that metal-supported membranes would be an option. Certain advantages accrue from the use of metal-supported membranes. The metal supports provide much greater flexibility in fabrication and in system integration. The support tubes may be equipped with metal end fittings and welded or brazed into the system support structure, usually a tubesheet type arrangement. Ceramic support tubes are, of course, usually much more brittle than metal support tubes and thus are more prone to catastrophic failure. Should a tube fail catastrophically, broken shards and pieces could result in a cascading effect, causing other elements to break. The ORNL membranes are composite structures consisting of a macroporous support tube (pore diameter > 50.0 nm, usually about 2.0–5.0 μm) coated with one or more membrane layers. The layers are thin, about 2.0 μm thick, and, for hydrogen separation, the separative layer pore size is typically < 1.0 nm.

*This research was sponsored by the U.S. Department of Energy, Office of Fossil Energy Advanced Research Materials Program, DOE/FE AA1510100, and Work Breakdown Structure Element IMTL-3 (B). Oak Ridge National Laboratory is managed by UT Battelle, LLC, for the U. S. Department of Energy under contract DE-AC05-00OR22725. Accordingly, the U.S. Government retains a nonexclusive, royalty-free license to publish or reproduce the published form of this contribution, or allow others to do so, for U.S. Government purposes.

A microporous membrane is defined by the International Union of Pure and Applied Chemistry (IUPAC) as a membrane with a pore diameter ≤ 2.0 nm. Molecular diffusion, the mode of transport in these membranes, is distinct from the ionic transport in ion-transport membranes and from solution-diffusion transport in palladium membranes. Ion-transport and palladium membranes are fully dense structures, whereas microporous membranes have significant void fractions with open porosity.

For microporous hydrogen-separation membranes, separation occurs by a combination of mechanisms. For gas mixtures containing molecules with significantly different molecular diameters, separation may occur via molecular sieving as is depicted in Fig. 1. Other diffusion mechanisms include Knudsen diffusion, surface diffusion or surface flow, and viscous flow (which has no separation function). Membranes are designed to offer the best combination of flux or volumetric flow rate and selectivity for hydrogen. These designs may differ for different gas mixtures. The focus of the ORNL activity has been toward designing membranes with a pore diameter of less than 1 nm (i.e., approaching a molecular sieve concept).

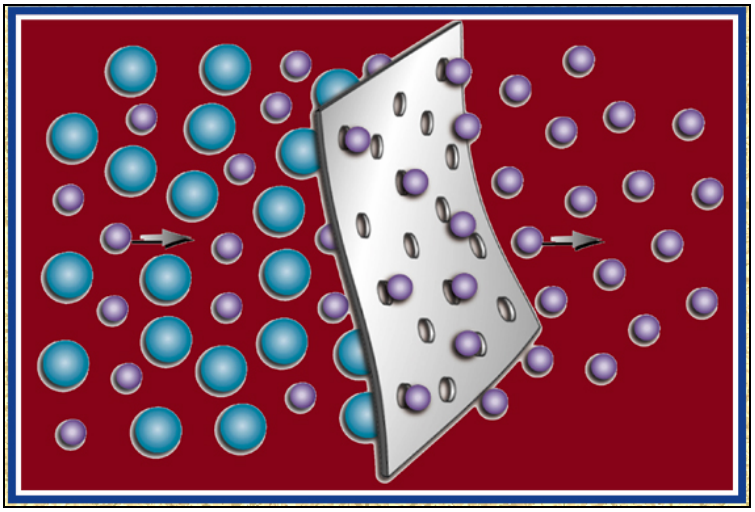

Figure 1 Simplified graphical depiction of a microporous membrane functioning as a molecular sieve.

Recently there has been concerted work to decrease the pore sizes of inorganic membranes to 2 nm or less. Although they are the most well-understood gas separation processes, Knudsen diffusion[6] and surface diffusion fail to describe permeation of gases in membranes having pore sizes below 2 nm, where potentially high separation factors can be achieved.

Inorganic membranes with pore sizes less than 1 nm offer many advantages over thin-film palladium membranes and ion-transport membranes for the separation of hydrogen from mixed-gas streams such as reformed natural gas, coal-derived synthesis gas, and refinery purge gases. In microporous membranes, flux is directly proportional to transmembrane pressure, whereas in palladium membranes, for example, flux is proportional to the square root of transmembrane pressure. Thus, microporous membranes become the preferred option for systems that operate at high pressure (see Fig. 2). The permeance of microporous membranes also increases dramatically as the temperature is increased. Consequently, inorganic membranes have the potential to produce very high fluxes at elevated temperatures and pressures. Because the separation process and transport mechanism are purely physical and thus do not involve ion transport or solution diffusion, the ORNL membranes can be fabricated of almost any combination of materials, such as a ceramic membrane on a metallic support or a ceramic membrane on a ceramic support. Proper material selection is usually based on environmental compatibility, which can ensure that the membrane will have a long lifetime while maintaining high flux and selectivity. The ORNL microporous membranes are low-cost in large measure because their fabrication does not require the use of strategic materials or precious metals, such as palladium.

One disadvantage of microporous iorganic membranes is that they are porous and have a distribution of pore sizes as opposed to having a discrete pore size as is found in zeolites. They can never produce 100% pure gas streams as can thin-film-palladium or ion-transport membranes. In those instances where pure hydrogen is the desired product, that apparent disadvantage can be overcome by coupling microporous membranes with pressure swing adsorption (PSA) to produce pure hydrogen. In such a scenario, PSA would only be required to separate the final 1% of the impurities, which implies a very compact and efficient separation system. Another approach to obtaining very high purity, but not 100% pure, hydrogen is to use two microporous membrane systems in stages or cascades. The impact of staging membranes in this way may be illustrated by considering that a membrane with a relatively low separation factor of 10 will in a single stage enrich a 50:50 mixture of hydrogen with a second gas to ~91% hydrogen. A two-stage system results in an effective separation factor of 100 (i.e., 10^2) and will enrich the initial 50:50 mixture to ~99% hydrogen. Many power generation systems, even hybrid systems using fuel cells, can accommodate less than that purity of hydrogen.

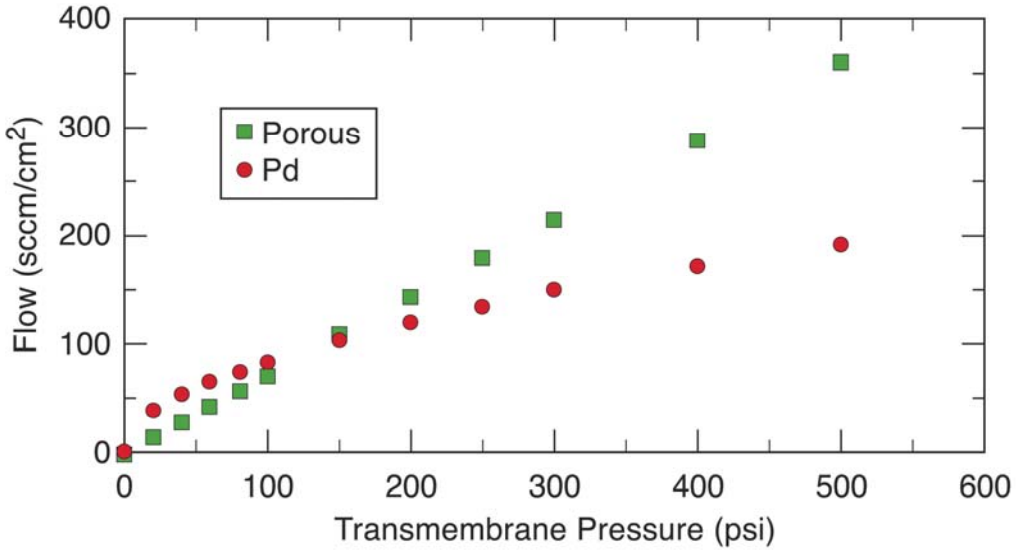

Figure 2 Hydrogen flows as a function of transmembrane pressure (ΔP) for an ORNL microporous membrane and a palladium membrane.

MEMBRANE FABRICATION

The permeance of a homogeneous membrane is inversely proportional to the membrane thickness. To be effective for gas separations, the mean pore diameter should be 2 nm or less. With such small pores, the membrane must be very thin, preferably less than 2 μm, in order to have the highest flux at the lowest transmembrane pressure. Such a thin membrane is too weak to support itself and must be applied as a layer onto a strong, porous support material, either metal or ceramic. It is preferable that the separative layer be applied to the inside of the tube. This provides for protection of the membrane from damage incidental to handling. Metal was chosen for the support tube for the reasons discussed earlier.

The primary or separative membrane layer can be applied directly to the support tube or to an intermediate layer. A layer having an intermediate pore size applied to the support tube first can provide a better surface for the primary separative layer, resulting in a thinner and more uniform membrane. The intermediate layer should be as thin as possible (usually less than 5 μm thick) and have a mean effective pore diameter of 10 nm or less and preferably as small as 2 nm. Once the primary layer is in place, various chemical treatments can be used to reduce the effective pore diameter to the desired value (as low as 0.5 nm). A photomicrograph of a microfilter (Fig. 3) shows the typical intermediate layer thickness, in this case an approximately 3-μm-thick layer of zirconia on a stainless steel support.

It is extremely difficult to fabricate a membrane with absolutely no defects. Fabricated membranes are evaluated by combining measurements made on them with a model[3] to estimate the percentage of flow through the defects and to

estimate the amount that the separation factor would be lowered by their presence. Because a defect can allow the unimpeded flow of both the desired product gas and the undesired gases, the number of defects must be minimized in order to achieve a high separation factor. Several methods have been developed to reduce the effective pore diameter of a defect or to eliminate the defect altogether. These defect repair methods do not significantly reduce the number of small pores and thus do not lower the flux rate of hydrogen through the membrane.

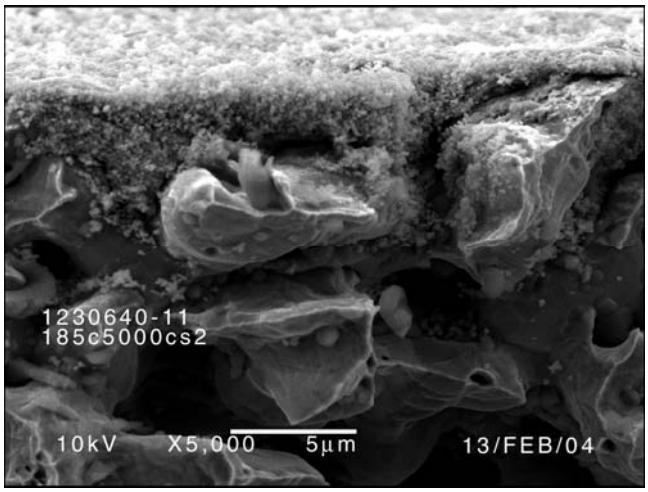

Figure 3 Photomicrograph of a porous zirconia membrane on a porous stainless steel support tube.

TECHNICAL APPROACH

In order to evaluate the separation of H_2 from a gas mixture relevant to applications where various hydrocarbons and combustion products may be present, a number of test gases were selected including propane (C_3H_8) and carbon dioxide (CO_2) which were chosen because of their relevance to needed separation applications. Helium was included also, both for benchmarking with previous work and because it is of interest in itself in connection with our membranes having potential for improved recovery of helium from gas mixtures. Initially, SF_6 was also included for benchmarking with earlier work. However, tests at higher temperatures indicated that SF_6 could be interacting with and modifying the properties of the membranes, so measurements using this gas were discontinued. Two existing gas permeation test systems were modified for use with the flammable gases H_2 and C_3H_8. The required safety documentation was completed and approved.

In order to help determine the fundamental operating mechanisms of gas separation, it is essential that data be obtained over a wide range of temperatures, with the maximum temperature as high as possible. Therefore, the membrane sealing mechanism for one of these systems was modified for operation up to and above 400 °C. Previous membrane seals using this system limited testing to temperatures below 275 °C. Most of the work was carried out on this system and consisted of sequential permeation measurements on individual gases. The ratios of permeances of the individual gases give the selectivity or ideal separation factor for the membrane in question. In addition, however, this system provides the capability to measure the actual separation of hydrogen from mixtures of two or more gases. Mixed gas measurements, using hydrogen and propane, were carried out for one membrane during the research reported here. This capability will be utilized in future work.

The test system, capable of operating at 400 °C and above, consisted of a stainless steel membrane holder, surrounded by a clamshell furnace connected to gas feed, permeate, and retentate lines. Tubular separation membranes were sealed into the holder using graphite ferrules. Each membrane was tested using the gases H_2, He, CO_2, and C_3H_8 for each temperature from 100 to 400 ºC (see Fig. 4). Tests at room temperature were also carried out for H_2 and He. Most of the work consisted of permeation measurements on individual gases. The ratios of permeances of the individual gases give the selectivity or ideal separation factor. In addition, the system provides

the capability to measure the actual separation of hydrogen from mixtures of two or more gases.

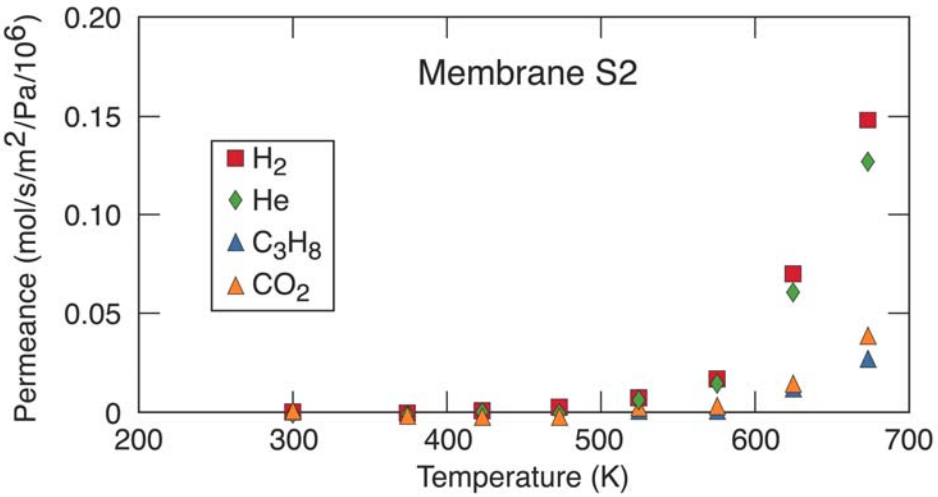

Figure 4. Measured permeance with respect to temperature. At room temperature, only He and H_2 were measured. At other temperatures all four gases were measured.

RESULTS AND ACCOMPLISHMENTS

Measurements were carried out on eight different membranes, here designated as S1 through S8 (see Table 1). The membranes tested consisted of stainless steel tubes supporting various ceramic membrane separation layers. The tube holder was also constructed of stainless steel. Each membrane had different permeance and separation properties based on different processing parameters during membrane fabrication.

Table 1

	H_2/C_3H_8 Ideal Separation Factor*						
Membrane	**100 °C**	**150 °C**	**200 °C**	**250 °C**	**300 °C**	**350 °C**	**400 °C**
S1	***2.55***	***4.10***	**5.70**	**6.79**	**6.74**	**6.48**	***3.37***
S2	**18.26**	**19.87**	**31.39**	**22.71**	**10.59**	**6.69**	**5.45**
S3	**6.59**	**8.86**	**9.30**	**11.88**	**8.14**	**6.22**	**4.85**
S4	***4.42***	***3.82***	**5.78**	**5.63**	**6.02**	**4.93**	**4.70**
S5	**5.34**	No Data	**5.14**	**5.07**	**5.49**	**5.65**	No Data
S6	**7.73**	No Data	**9.20**	**12.41**	**11.58**	**6.08**	No Data
S7	***1.87***	***3.63***	**4.94**	**5.69**	No Data	No Data	No Data
S8	***2.73***	***2.65***	***3.43***	***4.00***	***4.46***	No Data	No Data

* Values in Blue/Bold indicate an ideal separation factor higher than expected for Knudsen diffusion and values in Red/Italics indicate an ideal separation factor less than expected for Knudsen diffusion. Ideal separation factors for membrane S7 were determined at 100, 150, 175, 225, and 275 °C. The highest temperature data for membrane S8 were obtained at 275 °C.

Figures 5 and 6 show the permeance and selectivity, respectively, for membrane S2. This is the membrane that showed the highest product of selectivity and permeance for H_2 with respect to C_3H_8. This product is generally accepted as a figure of merit to assess membrane performance. At 200 ºC the measured selectivity of hydrogen with respect to propane was 31.39. The corresponding number for helium with respect to propane was 32.69. These numbers are 6.71 and 9.85 times the Knudsen selectivity, respectively, and indicate that the pore diameters in this membrane are on the order of one nanometer. The corresponding permeance at the highest temperature of 673 K was approximately 1.5 x 10^{-7} mol/s/m^2/Pa.

There was some variation in the properties of the membranes with time at temperature. This is illustrated in Figure 5. Here the results of repeated permeation measurements of H_2 on membrane S2 are shown. It is evident that the permeation of hydrogen increased by about 30 %between the first and the last measurement at 400 ºC.

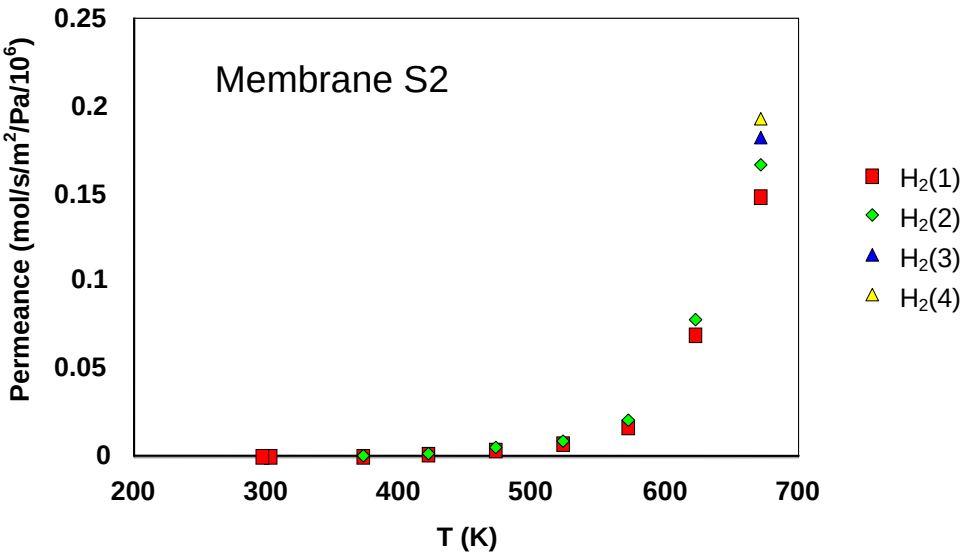

Figure 5. Results of repeated measurements of H_2 permeance for Membrane S2 at each temperature. H_2 permeance was first measured at a given temperature and then again after the permeance measurement for each of the other gases, for a total of four H_2 measurements at each temperature.

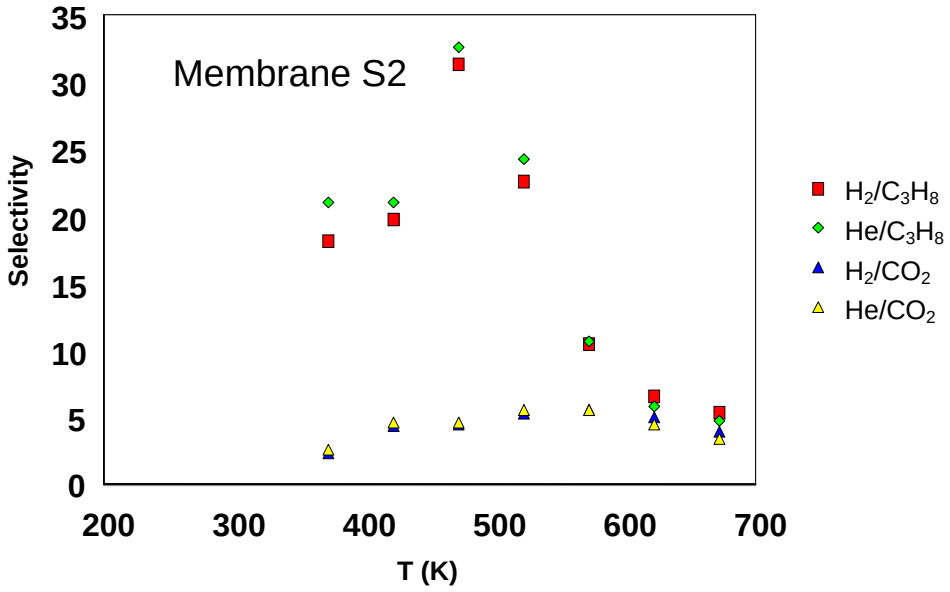

Figure 6. Measured selectivity for Membrane S2 with respect to temperature of the four gas combinations indicated.

Generally, for pore diameters > 2nm, the dominant permeation mechanisms in operation are Knudsen diffusion and surface transport, together with molecular diffusion and viscous flow (Poiseuille or laminar flow) at larger pore diameters. For pore diameters of about 1nm and smaller, other mechanisms, which are covered by the term "nanopore diffusion," become operative. Several mechanisms of gas transport through a membrane are summarized

in Table 2. Key parameters include temperature (T), pressure (P), molecular mass (m), kinetic molecular diameter (d_m), pore diameter (d_p), molecular collision free path (λ), and several thermal activation energies. The latter are H_a, the heat of gas adsorption, E_s, the activation energy for surface diffusion, and E_d, the activation energy for nanopore diffusion. Expressions for selectivity and permeance also are given in the table for those cases where the dependencies on important variables can be expressed in simple form.

Figures 4 and 5 indicate an increase in permeance with increasing temperature. If Knudsen diffusion were dominant the permeances would decrease with temperature. The increase with temperature of the permeances indicates the possibility of thermally activated behavior. This characteristic is similar to the diffusion of defects or atoms in the solid state in the presence of traps[7], with activation energy E_d. Physically this is plausible, because delay time and activation energy have a one-to-one correspondence in a trapping model. Here the jump distance is determined by the pore diameter rather than the crystal lattice dimension, however, the lower limit on size of a pore must correspond to interatomic spacing in the solid state.

Table 2 Expressions for key membrane gas-transport mechanisms.

Mechanism	Pore	Selectivity	Permeance
Viscous Flow	$\lambda < d_p$	None	$d_p^2\ P\ T^{-1}$
Molecular Diffusion	$\lambda < d_p$	None	
Knudsen diffusion	$\lambda > d_p$	$m^{-1/2}$	$m^{-1/2}\ d_p\ T^{-1/2}$
Surface Transport	All d_p	Variable	$d_p^{-1}\ P\ \exp[(H_a - E_s)/RT]$
Capillary Condensation	f(P)	Variable	
Nanopore Diffusion	$3\ d_m > d_p$	Highest	$m^{-1/2}\ d_p\ T^{-1/2}\ \exp[-E_d/RT]$

STATUS OF APPROVAL OF MEMBRANES FOR COMMERCIALIZATION AND USE

Legacy classified technology issues impose the requirements for classification and nonproliferation reviews of membranes fabricated by ORNL's Inorganic Membrane Technology Laboratory. A hydrogen membrane classification and nonproliferation review package was submitted for review on January 16, 2004. These membranes were determined to be unclassified and ORNL obtained approval from DOE on July 9, 2004. The implications of this approval are that the membranes may be distributed to outside laboratories for characterization and testing, and scale-up, pilot testing, and demonstration of the membranes may be accomplished. Hydrogen membranes approved as unclassified are those with any type 300 or 400 stainless steel, Hastelloy X, or iron aluminide support tube; a membrane layer of alumina; and a final separative layer of any oxide of aluminum, zirconium, titanium, or silicon.

SUMMARY AND CONCLUSIONS

Much of the work during the past year has been directed toward modifying test systems and membrane sealing mechanisms so that evaluations with flammable gases, such as hydrogen and propane, could be accomplished at temperatures of 400 °C and higher. Eight membranes were examined, six of which demonstrated selectivity higher than for Knudsen diffusion. Selectivities of hydrogen and helium with respect to propane and carbon dioxide were demonstrated as high as 30. Membranes of this type have excellent potential for application to separation of hydrogen from hydrocarbons and combustion products. It is also apparent that the best membranes showed an increase of permeance with increasing temperature, of a form that is consistent with a thermally activated gas transport mechanism.

Also, membrane prototypes were designed, fabricated, and submitted for a Classification and Nonproliferation Review on January 16, 2004. These membranes were determined to be unclassified and ORNL obtained approval from DOE on July 9, 2004 so that the physical properties and performance characteristics of the ORNL membranes could be tested and evaluated at other national labs, universities, and industrial facilities.

Future work will include characterizing the membranes using high resolution electron microscopy at the High Temperature Materials Laboratory (HTML) and comparing the physical characteristics with flow data. Also, we will continue to expand the temperature range of our permeance and separations tests and perform a more

comprehensive thermal stability study of the membranes. Data over a wider range of temperatures will help us to better understand thermally activated diffusion so that we can develop a model which will predict the performance of the membranes and how the thermally activated diffusion can be taken advantage of to improve the overall membrane performance.

ACKNOWLEDGMENTS

This research was sponsored by the U.S. Department of Energy, Office of Fossil Energy Advanced Research Materials Program, DOE/FE AA1510100, and Work Breakdown Structure Element IMTL-3 (B). Oak Ridge National Laboratory is managed by UT Battelle, LLC, for the U. S. Department of Energy under contract DE-AC05-00OR22725. Accordingly, the U.S. Government retains a nonexclusive, royalty-free license to publish or reproduce the published form of this contribution, or allow others to do so, for U.S. Government purposes.

REFERENCES

1. National Hydrogen Energy Roadmap (2002): November 2002, Report released by Secretary of Energy Spencer Abraham, November 12, 2002
2. R. S. A. de Lange, K. Keizer, A. J. Burggraaf, J. Membrane Sci. 104 (1995) 81-100
3. D. E. Fain, Membrane Tech. 120 (2000) 9-13
4. A. F. Ismail, L. I. B. David, J. Membrane Sci. 193 (2001) 1-18
5. D. L. Meixner, P. N. Dyer, J. Membrane Sci. 140 (1998) 81-95
6. M. Knudsen, Ann. Phys. 28 (1909) 75-130
7. L. K. Mansur, Acta Met. 29 (1981) 375-381

INFLUENCE OF SURFACE COATING ON THE PERFORMANCE OF V–Cu, V–Ti, AND Ta MEMBRANES FOR HYDROGEN SEPARATION

Stephen N. Paglieri[1], David R. Pesiri[2], Robert C. Dye[1], Craig R. Tewell[1], Stephen A. Birdsell[1], Ronny C. Snow[1]

[1]Los Alamos National Laboratory; P.O. Box 1663, MS-C348; Los Alamos, NM, 87545, USA

[2]Essex Technology Group, LLC; P.O. Box 17034; Irvine, CA 92623, USA

ABSTRACT

Hydrogen-separating membranes have the potential to facilitate the generation of pure hydrogen for use in fuel cells. Foils of VTi_5, $VCu_{1\text{-}10}$ (atomic %) and Ta coated with thin films of Pd or Pd alloys (Pd–Cu or Pd–Ag), and other metal interlayers were fabricated and tested for hydrogen permeability and stability during operation at temperatures from 320-450ºC. Vanadium-alloy or Ta foils were ion-milled and coatings between 30 and 250 nm thick were applied to both sides *in-situ*, via electron beam evaporation PVD. Membranes were between 40 and 120 microns thick and were completely permselective for hydrogen. Pt or Ni surface coatings on VTi_5 foils reduced the permeability by at least an order of magnitude while a membrane coated with the thinnest Pd layer (30 nm) exhibited the fastest hydrogen flux decline at 450ºC. Foils of Ta were coated with layers of Ti or Mo and then Pd in order to increase the hydrogen flux stability during operation above 400ºC. Although the hydrogen flux through the coated Ta foils was generally an order of magnitude less than through the V-alloy membranes, the hydrogen flux stability was greater. Composite membranes comprised of porous stainless steel tubes coated with V-Cu alloy and Pd were also fabricated and tested.

The hydrogen flux through a 75 micron thick Pd/$VCu_{1.1}$/Pd composite membrane with 100 nm Pd per side was 0.66 mol (STP)/m^2·s at 350ºC and a transmembrane pressure differential (ΔP) of 3.5 atm compared to 0.44 mol (STP)/m^2·s for a 71 micron thick Pd/VCu_{10}/Pd membrane at the same conditions. A 50% decrease in hydrogen flux was observed through the Pd/VCu_{10}/Pd membrane after 75 hours at 450ºC. Metallic interdiffusion between various surface coatings and foils tested at different temperatures was characterized with AES depth profiles. One mechanism of hydrogen flux decline at 450ºC was diffusion of V to the surface of the Pd coating.

INTRODUCTION

With increasing pressure on energy supplies and the threat of global climate change, more efficient and less polluting ways of utilizing fossil fuels are being explored. Near-zero emission coal power plants of the future could use hydrogen separating membranes to facilitate the recovery and utilization of pure hydrogen[1-3]. Metals such as vanadium, niobium, and tantalum have been considered since the 1960's as cheaper alternatives to palladium alloys for hydrogen separating membranes[4]. A catalytic coating is necessary on these metals to facilitate hydrogen entry and exit from the metal[5]. Metallic interdiffusion between Pd coatings and membrane supports has been recognized to cause a decrease in the hydrogen permeability of composite membranes around 400ºC[6-9], while hydrogen embrittlement is known to cause premature failure of metal membranes[10]. Addition of alloying elements to reduce the solubility of hydrogen and prevent the formation of brittle hydrides can increase membrane strength[11]. Therefore, alloys of V with Ti or Cu were investigated for hydrogen permeability and increased resilience, while

various surface coatings were studied for resistance to metallic interdiffusion. For comparison, Ta foils with various surface coatings were also tested.

EXPERIMENTAL PROCEDURES

High purity (99.9%) metals were electron beam (*e*-beam) melted into buttons in a vacuum furnace. The buttons were flipped and re-melted several times to ensure compositional uniformity. Buttons of roughly 250 g were sliced and cold rolled into ~5×15 cm strips with nominal thicknesses of 40-75 ±5 μm. Ta foil was obtained commercially. The foils were washed with warm soap and water, rinsed with methanol, blown dry with nitrogen, mounted by clamping the ends of the foil strip, and loaded into the physical vapor deposition (PVD) chamber. After evacuation, argon was bled into the chamber to a pressure of $1.5 \cdot 10^{-4}$ torr and the ion-gun was used to ion-mill each side of the foil for 60-90 min. The foil was visually inspected through a window during ion-milling to ensure removal of all remaining macroscopic contaminants. After ion-milling, the chamber was evacuated again to $1 \cdot 10^{-7}$ torr and palladium was *e*-beam evaporated onto the foil to the desired thickness at 3-5 Å/s. A quartz crystal was used to monitor the thickness of metal deposited. The Pd–Ag films were deposited by sputtering from a $Pd_{0.50}Ag_{0.50}$ target. In all cases, the same metal coating was deposited onto both sides of each foil.

Samples were handled using gloves and forceps. Discs (2 cm diameter) were laser cut from the foil or cut by hand from larger foil samples using clean scissors. The membrane foil was sandwiched between two Ni VCR gaskets (12.7 mm OD) and positioned in the fixture, a stainless steel VCR fitting adapted with an impinging flow design. A final helium pressurization test was performed to confirm the absence of leaks. The membrane module was placed in a heater and connected to a gas plumbing and measurement system. Mass flow controllers metered the gas while 0-10,000 or 0-100 torr pressure transducers measured upstream and downstream pressures, respectively. All gases used were at least 99.999% pure and used without further purification. The membrane module was heated in the absence of hydrogen (vacuum at the feed and permeate sides). The inlet flow was 200 sccm of hydrogen during all tests. The feed pressure was set at 760 torr and the retentate pressure ranged from 700 to 750 torr. The permeate pressure was typically between 10 and 25 torr. Sweep gas was not used during the permeation experiments.

Auger Electron spectroscopy (AES) results were obtained with a PHI 5600 System. Electron energy analysis was accomplished using a CHA with an OMNI Focus IV input lens system. AES results were obtained with a 5 keV electron beam. Background pressure was essentially 1×10^{-10} torr. Elemental analysis should be considered to be semi-quantitative (± 20%). The built in SEM was used for sample imaging.

RESULTS & DISCUSSION

The hydrogen flux vs. time at 1 atm pressure differential through 40 μm thick $V_{0.95}Ti_{0.05}$ membranes with 30, 100, or 250 nm Pd coatings is shown in Fig. 1a. The fluxes through membranes coated with 30 or 100 nm of Pd were comparable at 400°C, while the flux through the membrane with a 30 nm Pd coating declined at a faster rate. In all cases the flux dropped much more quickly at 450°C. In the case of the membranes coated with 250 nm of Pd, one was tested for hydrogen flux at 320°C before testing at 450°C, while the other was heated directly to 450°C before introducing hydrogen. The formation of hydride at 320°C appeared to increase the hydrogen flux subsequently observed at 450°C (Fig. 1a).

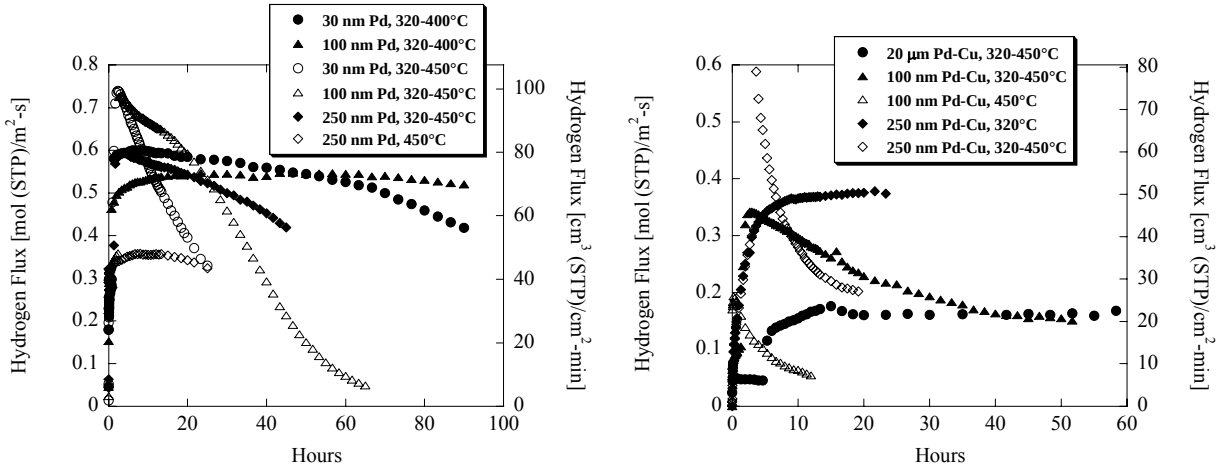

(a) (b)

Figure 1: Influence of surface coating thickness and composition on hydrogen flux through 40 µm thick $V_{0.95}Ti_{0.05}$ membranes (a) coated with 30, 100 or 250 nm of Pd (b) coated with 100 or 250 nm of $Pd_{0.47}Cu_{0.53}$, plus results for a 20 µm thick $Pd_{0.47}Cu_{0.53}$ foil.

Hydrogen flux vs. time data for 40 µm thick $V_{0.95}Ti_{0.05}$ membranes coated with 100 or 250 nm of $Pd_{0.47}Cu_{0.53}$ are shown in Fig. 1b. While the fluxes were similar to the Pd coated membranes, the flux declined more quickly at 450°C. The flux was stable for a membrane tested at 320°C. Once again, a membrane first exposed to hydrogen at 320°C exhibited higher initial hydrogen flux at 450°C. The flux through a 20 µm thick $Pd_{0.47}Cu_{0.53}$ foil was constant at 450°C suggesting that the flux decline was related to interaction of the V–Ti foil with the surface coating. Coating the V–Ti foil with $Pd_{0.50}Ag_{0.50}$ resulted in higher initial flux than for the Pd–Cu coated membranes, however, similar flux decline with time at 450°C was observed (not shown). Interlayers of 30 or 90 nm of Ni or Pt between the $V_{0.95}Ti_{0.05}$ foil and the 100 nm Pd coating reduced the hydrogen flux to ≤0.5 $cm^3(STP)/cm^2 \cdot min$ with no discernable increase in flux stability. The low flux may be attributed to the low hydrogen permeability of both Ni and Pt.

Hydrogen flux results for V–Cu membranes with 100 nm Pd coatings are displayed in Fig. 2a. After testing at 450°C for 75 hours, the hydrogen flux through the $V_{0.88}Cu_{0.12}$was reduced by 50%. SEM revealed the formation of light and dark regions on the membrane surface and AES indicated that Cu had segregated into Cu-rich regions, likely due to the low solubility of Cu in V. An AES depth profile revealed that V and Cu had diffused to the surface while Pd had diffused into the membrane (Fig. 1b). Tubular membrane modules have been fabricated by *e*-beam welding the Pd coated foil to itself in a special fixture and then to 6 mm VCR fittings.

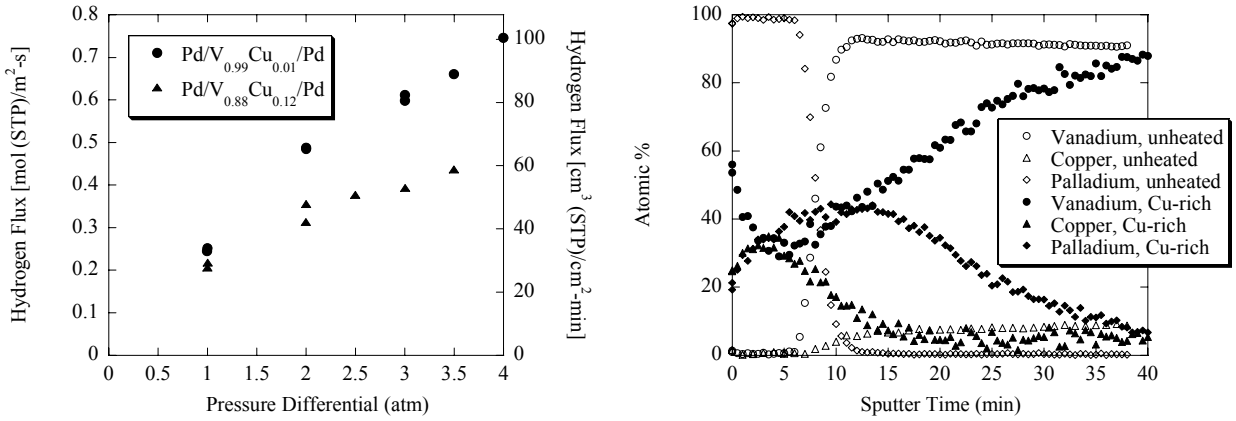

(a) (b)

Figure 2: (a) Hydrogen flux at 350°C through V–Cu membranes coated with 100 nm of Pd (b) AES depth profile of $V_{0.88}Cu_{0.12}$ membrane before heating and of a Cu-rich region on the upstream side after testing at 450°C for 75 hours.

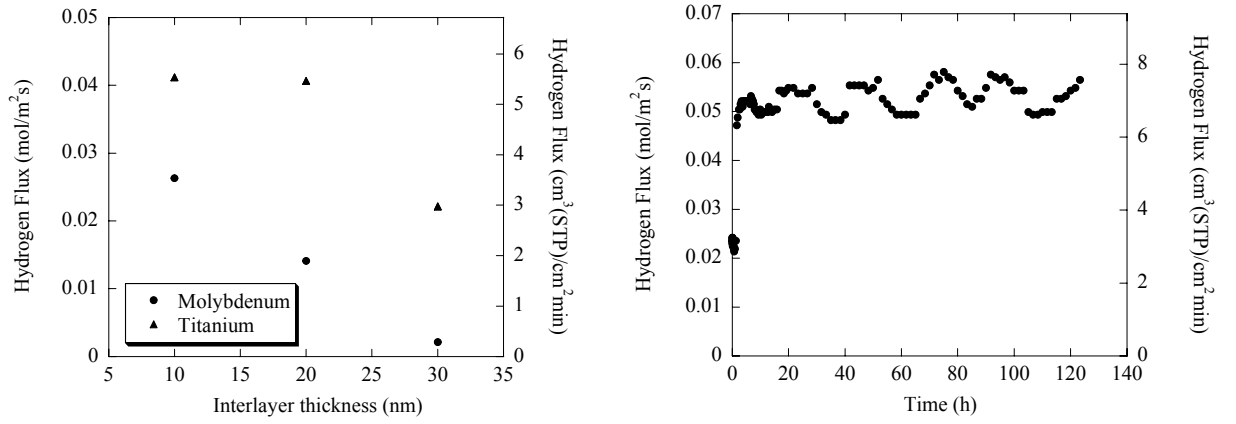

(a) (b)

Figure 3: (a) Hydrogen flux at 400°C through 50 μm thick Ta vs. interlayer composition and thickness (coated with 200 nm Pd per side) (b) Hydrogen flux vs. time through 40 μm thick Ta at 400°C (coated with 100 nm Pd per side).

Ta has a much higher melting point than V (3014°C vs. 1902°C) although the hydrogen permeability is lower[12; 13]. Fig. 3a presents hydrogen permeability vs. interlayer composition and thickness for 50 μm thick Ta foils coated on both sides with either Mo or Ti and then 200 nm of Pd. As expected, the hydrogen permeability was less than through the V-alloy membranes, and the hydrogen flux decreased with increasing interlayer thickness. Ti also appeared to have less of an impact on hydrogen flux through the membrane than Mo. The hydrogen flux was fairly stable through all of the Ta membranes tested, even for those without Ti or Mo interlayers. Hydrogen

flux vs. time at 400°C through a 40 μm thick Ta membrane coated with 100 nm Pd is shown in Fig. 3b. The flux was essentially constant, with some drift, over a period of over 125 hours.

CONCLUSIONS

The hydrogen flux and flux stability through $V_{0.95}Ti_{0.05}$, $V_{1-x}Cu_x$ (x = 0.01-0.12), and Ta foils coated with various thicknesses and compositions of surface coating was determined at 320-450°C. Based on AES depth profiles of a $Pd/V_{0.88}Cu_{0.12}/Pd$ composite membrane, the decline in hydrogen flux with time at 450°C was the result of metallic interdiffusion and Cu segregation. Interlayers deposited between the metal foil and Pd coating reduced hydrogen flux without increasing flux stability.

ACKNOWLEDGEMENTS

The authors are indebted to D. Hammon and S. Quintana for preparation of the vanadium-alloy foils, R. Schulze for assistance with AES, and Prof. D. Chandra for helpful discussions. Thanks also to B. Espinoza, M. Katalinich, V. Hesch, C. Grastataro, J. Moya, B. Bennett, S. Cole, G. Schobert, J. Valdez, and B. Smith for help with the experiments. The authors gratefully acknowledge financial support from Ford Motor Co. and the Advanced Materials Research Program, Office of Fossil Energy, U.S. Department of Energy.

REFERENCES

1. L.A. Ruth, "Advanced clean coal technology in the USA," *Mater. High Temp.*, **20**(1) (2003), 7.
2. M. Rutkowski, M. DeLallo, M. Klett, J. Badin, and J. Temchin, "Coal Processing Plants For Hydrogen Production With CO_2 Capture," *J. Franklin Institute*, **8** (2002), 149.
3. S. Paglieri, and J.D. Way, "Innovations in Palladium Membrane Research," *Sep. Purif. Meth.*, **31**(1) (2002), 1.
4. A.C. Makrides, M.A. Wright, and D.N. Jewett, (1967). "Separation of hydrogen by permeation." *US Patent* 3,350,846.
5. N. Boes, and H. Züchner, "Secondary ion mass spectrometry and Auger electron spectroscopy investigations of Vb metal foils prepared for hydrogen permeation measurements," *Surf. Tech.*, **7** (1978), 401.
6. D.J. Edlund, and J. McCarthy, "The relationship between intermetallic diffusion and flux decline in composite-metal membranes: implications for achieving long membrane lifetime," *J. Membr. Sci.*, **107** (1995), 147.
7. N.M. Peachey, R.C. Snow, and R.C. Dye, "Composite Pd/Ta metal membranes for hydrogen separation," *J. Membr. Sci.*, **111** (1996), 123.
8. T.S. Moss, N.M. Peachey, R.C. Snow, and R.C. Dye, "Multilayer metal membranes for hydrogen separation," *Int. J. Hydrogen Energy*, **23**(2) (1998), 99.
9. P.P. Mardilovich, Y. She, Y.H. Ma, and M.-H. Rei, "Defect-Free Palladium Membranes on Porous Stainless-Steel Support," *AIChE J.*, **44**(2) (1998), 310.
10. R.E. Buxbaum, R. Subramanian, J.H. Park, and D.L. Smith, "Hydrogen transport and embrittlement for palladium coated vanadium–chromium–titanium alloys," *J. Nucl. Mater.*, **233-237** (1996), 510.

11. C. Nishimura, T. Ozaki, M. Komaki, and Y. Zhang, "Hydrogen permeation and transmission electron microscope observations of V−Al alloys," *J. Alloys Compd.*, **356-357** (2003), 295.
12. S.A. Steward, "Review of Hydrogen Isotope Permeability Through Materials," *US National Laboratory Report*, UCRL-53441 (1983).
13. K.S. Rothenberger, B.H. Howard, R.P. Killmeyer, A.V. Cugini, R.M. Enick, F. Bustamante, M.V. Ciocco, B.D. Morreale, and R.E. Buxbaum, "Evaluation of tantalum-based materials for hydrogen separation at elevated temperatures and pressures," *J. Membr. Sci.*, **218** (2003), 19.

Economic Fabrication of Membrane Materials

Glen H. Kirby
Oak Ridge National Laboratory
1 Bethel Valley Road, P. O. Box 2008, Oak Ridge, Tennessee 37831-6063
Phone: (865) 576-6545, E-mail: kirbygh@ornl.gov

Timothy R. Armstrong
Oak Ridge National Laboratory
1 Bethel Valley Road, P. O. Box 2008, Oak Ridge, Tennessee 37831-6186
Phone: (865) 574-7996, E-mail: armstrongt@ornl.gov

Beth L. Armstrong,
Oak Ridge National Laboratory
1 Bethel Valley Road, P. O. Box 2008, Oak Ridge, Tennessee 37831-6063
Phone: (865) 241-5862, E-mail: armstrongbl@ornl.gov

ABSTRACT

Ceramic membranes provide superior thermal and chemical stability when compared to commercially available organic membranes and may find widespread use in fossil energy systems to improve the efficiency and performance of a wide range of processes including hydrogen and oxygen production, natural gas and syngas cleanup and production, wastewater and oil purification, chemical sensing, chemical synthesis, and energy production. The goal of this project is to develop low-cost fabrication methods for ceramic membranes which can be used for gas separation (oxygen or hydrogen) or catalytic oxidation processes. Thin ceramic layers are required because the gas flux efficiency increases inversely with membrane thickness; however, the mechanical integrity of the membrane must also be maintained. In our approach, thick films of $Ca_2Al_xFe_{2-x}O_5$ were deposited, onto porous stainless steel supports using a dip coating process. Concentrated, aqueous $Ca_2Al_xFe_{2-x}O_5$ suspension precursors were developed with the appropriate rheological behavior for dip-coating using a colloidal processing approach. Zeta potential experiments were carried out to understand the behavior of $Ca_2Al_xFe_{2-x}O_5$ particle surfaces in aqueous suspension. Chemical additives, including citric acid and a poly(acrylic acid)-poly(ethylene oxide) copolymer dispersant were used to tailor the chemical and colloidal stability of the suspensions, respectively. Rheological measurements were carried out on suspensions of varying copolymer and $Ca_2Al_xFe_{2-x}O_5$ particle concentration to determine the appropriate behavior for dipping. Dense coatings were obtained after drying in ambient conditions and sintering in flowing argon.

INTRODUCTION

Inorganic, asymmetric membranes have many potential applications in fossil energy systems in hydrogen and oxygen separation processes such as H_2 recovery from mixed gas streams, H_2S removal, efficient O_2 combustion, aromatic upgrading, fuel reforming, and conversion of natural gas to syngas. The current class of ceramic monolithic membranes have relatively low flux due to high membrane thickness (> 100 μm). In order to reduce the number footprint of the separation device thinner membranes are required. Thin membranes, however, maybe too fragile to function as self-supported structures in high pressure, fossil environments. As a result, porous supports are used to impart the necessary mechanical behavior, while also allowing for fluid flow through the pore network to the membrane. Typically, the membrane and support are manufactured from the same material (i.e., a rare-earth based ceramic), in order to assure that they have the same coefficient of thermal expansion (CTE) and thus, eliminate complications that

may arise when cofiring. However, the expense associated with using larger quantities of the rare-earth based material, coupled with the need for glass or glass-ceramic seals, eliminates the long-term commercial viability of such devices.

In order to utilize inorganic membranes in a wide array of energy applications, low-cost fabrication methods must be developed that utilize inexpensive membrane and support materials. Calcium ferrite-based ceramics with brownmillerite structure have been recently identified as excellent candidates for dense, asymmetric membranes. The base composition ($Ca_2Fe_2O_5$) elicits strong, mixed conducting behavior and is easily doped, e.g., with Ga, Al, Cr, Co, Ti, and Ni, to improve the conductivity via an oxygen vacancy diffusion mechanism and mechanical stability. Furthermore, metallic supports with high temperature capabilities (1300 ^oC) have great potential for improving the mechanical strength and reducing the material costs. The use of metallic membranes also facilitates the use of simple seals, such as brazes, thus avoiding the need for glass or glass-ceramic seals.

Aqueous colloidal processing of ceramic suspension precursors offers a low cost approach for producing uniform, ceramic membranes on porous metallic supports via a simple dip coating process. This approach has been demonstrated in many multi-disciplinary areas such as coatings (paints, glazes), fabrication of monolithic components (casting, deposition), and emulsions (gels, food additives, cosmetics). Control of the suspension rheological behavior is paramount to produce quality coatings and can be accomplished by tailoring interparticle (or surface) forces. In aqueous-based suspensions, long-range attractive van der Waals forces are ubiquitous and must be balanced by repulsive forces to tailor the desired degree of colloidal stability. For example, ionizable polymeric dispersants, a.k.a. polyelectrolytes, are commonly used to modify the surface of particles to impart repulsive electrosteric interparticle forces.[1, 2] In aqueous colloidal processing of calcium ferrite suspensions, however, additional complications arise due to particle hydrolysis and hydration (cementitious) reactions. Hydrolysis occurs as the particles undergo partial dissolution and the release of multivalent ions, e.g. Ca^{2+}, Al^{3+}, and Fe^{3+}, into solution. The rising ionic strength and the presence of multivalent ions in solution mitigate repulsive forces imparted by adsorbed (pure) polyelectrolyte layers.[3] Calcium ferrite also elicits strong cementitious behavior in aqueous suspension (note, it is one of the four primary phases in Portland cement).[4] Hydration reactions occur when hydrolyzed ions react to form new solid phases. These phases typically form at the particle-particle contacts resulting in irreversible hardening and ultimately, set of concentrated suspensions.

In the current study, aqueous calcium ferrite suspensions are developed for use as precursors in a dip-coating process with select chemical additions to impart stability to the system. Additions of oxalic acid and citric acid are studied based on claims that they retard hydrolysis[5] and hydration,[4] respectively. Addition of a novel, polyelectrolyte-based dispersant with comb polymer architecture is also studied based on success in other suspensions where hydrolysis is observed, including barium titanate[3] and Portland cement.[6] Zeta potential experiments are carried out to characterize the surface of calcium ferrite particles in dilute aqueous suspension. Furthermore, the set time and rheological behavior are characterized for concentrated suspensions (45-55 vol% solids) formulated with a wide range of oxalic acid, citric acid, and comb polymer addition. Concentrated calcium ferrite suspensions suitable for a dip-coating process are identified and used to form membranes on porous metallic supports. The coated supports are sintered in a flowing argon atmosphere over a wide temperature range. Results show that the suspension structure and rheology can be carefully controlled to govern the quality of green and ultimately, dense membranes.

EXPERIMENTAL PROCEDURE

$Ca_2Fe_2O_5$ (Praxair) with an average particle size of 1.0 μm determined using dynamic light scattering (LA-700, Horiba Instruments Incorporated, Irvine, CA) and a surface area of 1.47 m^2/g, determined using

nitrogen adsorption BET (Autosorb-1, Quantachrome Instruments, Boynton Beach, FL), was the ceramic powder used in this study. Oxalic acid and citric acid were obtained and used to modify the reactivity of the $Ca_2Fe_2O_5$ powder in water. Note, these molecules are very similar in chemical structure, i.e., citric acid differs from oxalic acid by only one hydroxycarboxylic acid group located between the two carboxylic acid groups (see Fig. 1). The dispersant in this study was a poly(acrylic acid)-poly(ethylene oxide) copolymer with comb-like molecular architecture, i.e., it has an anionic, poly(acrylic acid) (PAA) backbone and charge-neutral, poly(ethylene oxide) (PEO) teeth (see Fig. 1). The PAA/PEO copolymer had a number and weight average molecular weight of 23,400 g/mole and 8,330 g/mole, respectively, as determined by GPC analysis.

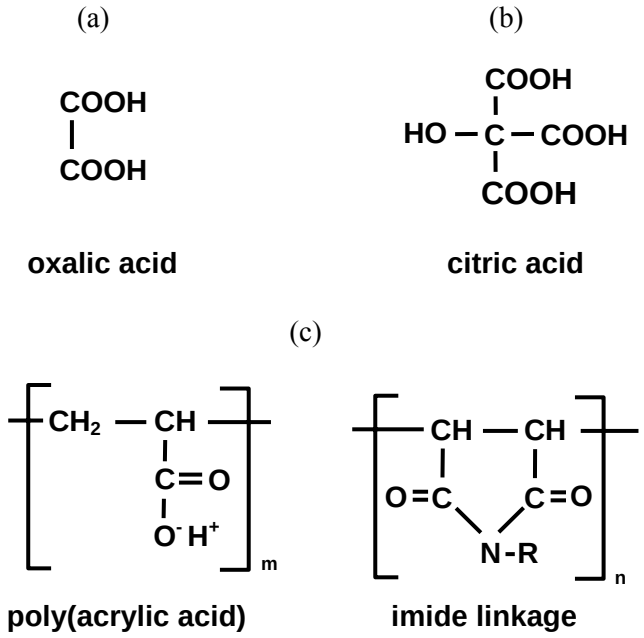

Fig. 1. The chemical structure of (a) oxalic acid, (b) citric acid, and (c) PAA/PEO. Note, in (c) R = $(CH_2CH_2O)_x$-CH_3, i.e., poly(ethylene oxide), which is grafted onto the poly(acrylic acid) backbone at random intervals through the imide linkages (m = 59, n = 8, x = 45).

Zeta potential measurements were carried out on the $Ca_2Fe_2O_5$ particles in dilute aqueous suspension using capillary electrophoresis (Zetasizer 3000HS, Malvern Instruments Ltd., Worcestershire, UK). Dilute suspensions (10^{-3} vol% solids) were prepared by adding the appropriate amount of powder to aqueous, KNO_3 solutions (0.01 *M*) of varying pH ranging from 2 – 11. The solutions were adjusted to the appropriate pH using stock solutions of nitric acid or ammonium hydroxide. The suspensions were ultrasonically treated for 2 min. to break up soft agglomerates prior to measurement.
Concentrated $Ca_2Fe_2O_5$ suspensions (45-55 vol% solids) were fabricated by combining an appropriate amount of $Ca_2Fe_2O_5$ powder with aqueous solutions of varying oxalic acid, citric acid, and PAA/PEO concentration. The suspensions were ultrasonically treated for 5 min (60 Hz) to break up soft agglomerates, then mixed on a shaker table to achieve equilibrium. A needle penetration test was utilized to determine the set time for these suspensions after initial water contact.

Rheological measurements were carried out on concentrated suspensions using a controlled-stress rheometer (Rheometric Scientific SR5, TA Instruments, New Castle, DE) fitted with concentric cylinder geometry. Prior to measurement, the suspensions were presheared at a rate of 200 s^{-1} for 5 min and then

allowed to equilibrate for 15 min. Furthermore, a specially designed solvent trap was used to minimize the evaporation of water. In this way, variations in sample handling were minimized to ensure reproducibility of the data. Stress viscometry measurements were carried out by ramping an applied shear stress (logarithmically) from 0.025 to 200 Pa. A delay time (i.e., the time between two consecutive data acquisition events) of 1 min was used in this study. After repeating the preshear procedure mentioned above, storage modulus (G') measurements were carried out by ramping an oscillatory shear stress (logarithmically) from 0.025 to 200 Pa at a constant frequency of 1 Hz. All rheological measurements were performed at a constant temperature of 25°C.

Porous, stainless steel tubular supports were obtained (9.78 mm ID, 11.05 mm OD) and sectioned into ~ 6.5 mm lengths. The sectioned tubes were ultrasonically cleaned in ethanol for 10 min and dried in ambient conditions. Rubber stoppers were inserted before dipping to prevent the suspension from coating the inner diameter of the support. The tubes were dipped into 45, 50, and 55 vol% $Ca_2Fe_2O_5$ suspensions with 10 mg citric acid and 2 mg PAA/PEO per m^2 $Ca_2Fe_2O_5$. The substrates were dipped at a rate of 85.7 mm/min, submerged for 10 sec, and withdrawn at a rate of 85.7 mm/min. Coated tubes were dried under ambient conditions and sintered at varying temperature in 300 cm^3/min flowing argon.

RESULTS AND DISCUSSION

ZETA POTENTIAL

Zeta potential measurements were carried out as a function of pH for dilute $Ca_2Fe_2O_5$ suspensions (10^{-3} vol%) using capillary electrophoresis (Zetasizer 3500HS, Malvern Instruments Ltd.) and the results are shown in Fig. 2. The isoelectric point (IEP) was observed at pH 8, which is within the range of literature values for Fe_2O_3 (pH 6-9).[7] This result is consistent with the surface behavior of inorganic particles that undergo hydrolysis, i.e., Ca^{2+} dissolves into solution leaving behind an Fe-rich surface. The particle surface has a positive zeta potential over a broad pH range and thus, is effectively modified with anionic, poly(acrylic acid)-based dispersants ($pK_a = 5.5 \pm 0.5$).

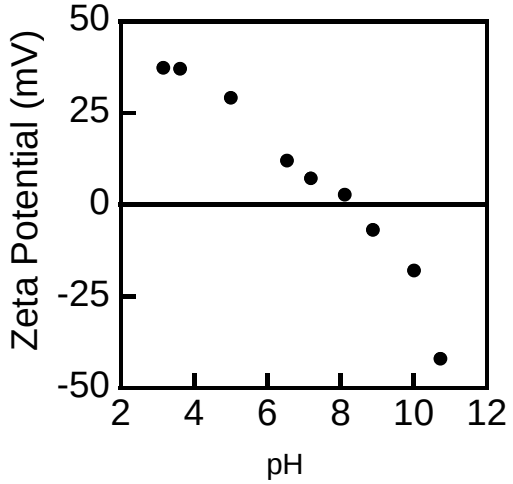

Fig. 2. Zeta potential as a function of pH for $Ca_2Fe_2O_5$ particles in dilute, aqueous suspension (10-3 vol% solids).

SETTING BEHAVIOR

Concentrated $Ca_2Fe_2O_5$ suspensions (45 vol% solids) were observed for their setting behavior after initial $Ca_2Fe_2O_5$ powder contact with pure water, aqueous oxalic acid solution (10 mg per m^2 $Ca_2Fe_2O_5$), and aqueous citric acid solution (10 mg per m^2 $Ca_2Fe_2O_5$). In pure water and aqueous oxalic acid solution,

setting occurred 5-10 min after initial $Ca_2Fe_2O_5$/water contact; however, setting did not occur until 17 days after $Ca_2Fe_2O_5$ contact with aqueous citric acid solution. Strong set retardation imparted by citric acid can be attributed to its additional hydroxycarboxylic acid group as compared with oxalic acid. It has been demonstrated that hydroxycarboxylic acid and carboxylic acid groups form strong and weak complexes, respectively, with multivalent cations in solution.[8] Strong hydroxycarboxylic acid-Ca^{2+} complexes are highly stable and thus, prevent Ca^{2+} ions from participating in hydration reactions to form hydrated solid phases. As a result, setting behavior is delayed until enough free Ca^{2+} ions become available from slow, continuous $Ca_2Fe_2O_5$ dissolution.

RHEOLOGICAL BEHAVIOR

Rheological measurements were carried out on concentrated $Ca_2Fe_2O_5$ suspensions of constant citric acid addition (10 mg/m^2 $Ca_2Fe_2O_5$) and the results are shown in Figs. 3-4. The apparent viscosity is plotted as a function of applied shear stress in Fig. 3 for suspensions of varying PAA/PEO addition (constant solids loading, 45 vol%) and varying solids loading (constant PAA/PEO addition, 2 mg per m^2 $Ca_2Fe_2O_5$). The degree of shear-thinning decreased with increasing PAA/PEO concentration until it was minimized at 2 mg PAA/PEO per $Ca_2Fe_2O_5$. However, it was not possible to eliminate shear-thinning behavior, which is indicative of net attractive interparticle interactions. By increasing the solids loading, i.e., the number of attractive particles, shear-thinning behavior increased as expected.

The elastic modulus is plotted as a function of applied shear stress in Fig. 4 for suspensions of varying PAA/PEO addition (constant solids loading, 45 vol%) and varying solids loading (constant PAA/PEO addition, 2 mg per m^2 $Ca_2Fe_2O_5$). Solid-like behavior, indicative of colloidal gels, was always observed. The linear elastic modulus and yield stress increased with decreasing PAA/PEO concentration (i.e., increasing net interparticle attraction) and increasing solids loading (i.e., increasing concentration of attractive particles). These parameters can be adjusted over several orders of magnitude to fabricate $Ca_2Fe_2O_5$ suspensions with a wide-range of dip-coating behavior.

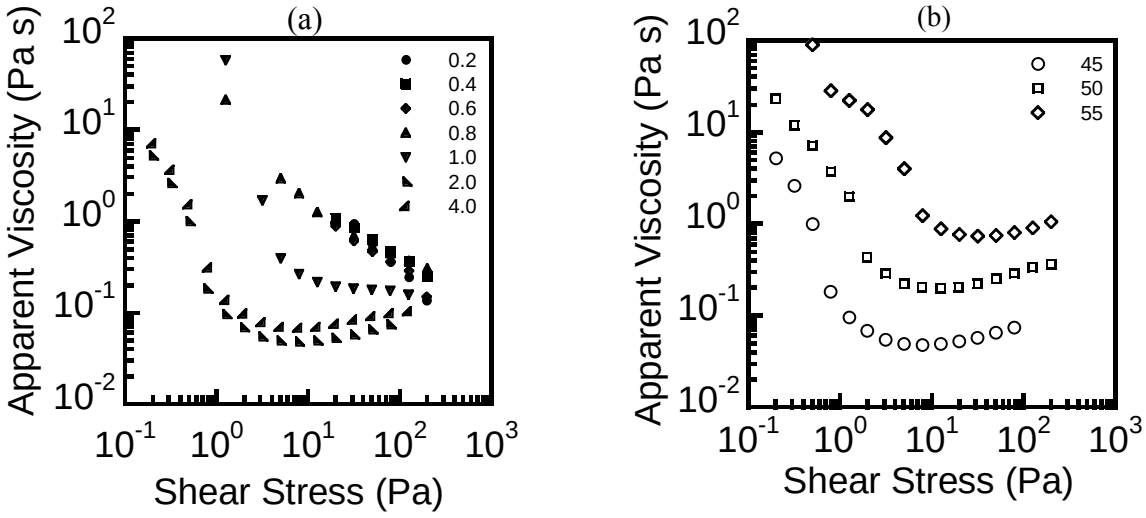

Fig. 3. Apparent viscosity as a function of shear stress for (a) 45 vol% $Ca_2Fe_2O_5$ suspensions with 10 mg citric acid per m^2 $Ca_2Fe_2O_5$ and varying PAA/PEO concentration (0.2 – 4.0 mg per m^2 $Ca_2Fe_2O_5$) and (b) $Ca_2Fe_2O_5$ suspensions with 10 mg citric acid and 2 mg PAA/PEO per m^2 $Ca_2Fe_2O_5$ and varying solids loading (45 – 55 vol% solids).

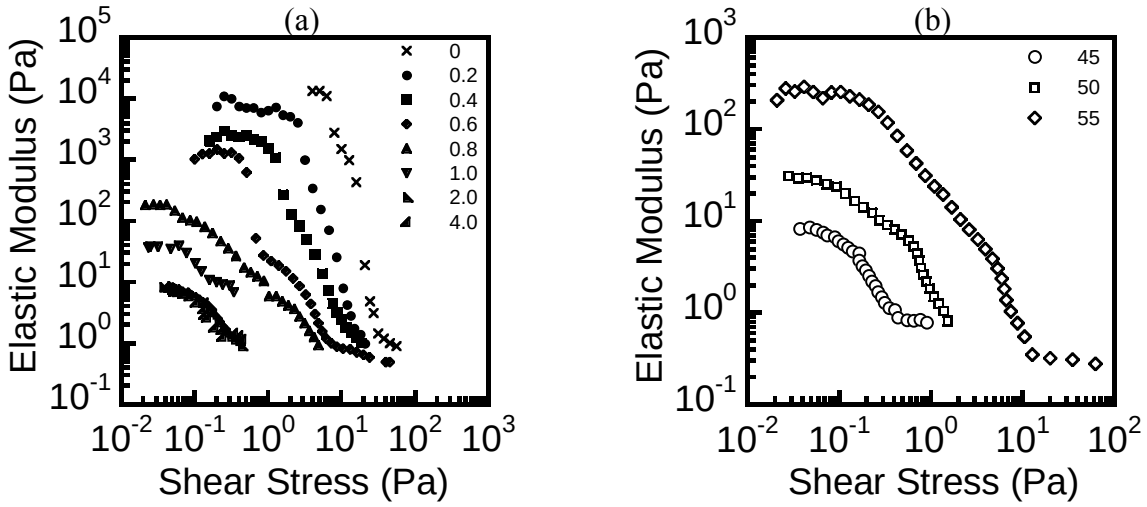

Fig. 4. Elastic modulus as a function of shear stress for (a) 45 vol% $Ca_2Fe_2O_5$ suspensions with 10 mg citric acid per m^2 $Ca_2Fe_2O_5$ and varying PAA/PEO concentration (0.2 – 4.0 mg per m^2 $Ca_2Fe_2O_5$) and (b) $Ca_2Fe_2O_5$ suspensions with 10 mg citric acid and 2 mg PAA/PEO per m^2 $Ca_2Fe_2O_5$ and varying solids loading (45 – 55 vol% solids).

MEMBRANE FORMATION

Stainless steel supports were dipped into $Ca_2Fe_2O_5$ suspensions (2 mg PAA/PEO per m^2 $Ca_2Fe_2O_5$) of varying solids loading and the resulting membranes are displayed in Fig. 5. The rheological behavior of each suspension had strong impact on the resulting membrane quality. Uniform membranes were obtained from suspensions with solids loading ranging between 45 – 50 vol% (linear elastic moduli (G'_0) between 10 - 30 Pa), although the membrane thickness increased with solids loading because of the increase in G'_0. Non-uniform membranes, with thick sections that cracked during drying, were obtained from suspensions of 55 vol% solids that had G'_0 of 300 Pa.

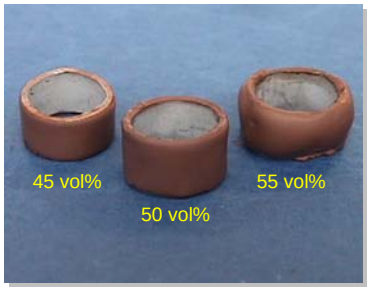

Fig. 5. $Ca_2Fe_2O_5$ membranes on the outer diameter of stainless steel, tubular supports.

The $Ca_2Fe_2O_5$ membranes (from 45 and 50 vol% suspension precursors) and stainless steel supports were co-sintered over a wide range of temperatures in a flowing argon atmosphere. A reducing environment was required to prevent oxidation of the metallic support. At 1200°C and above, the membrane and metallic support reacted and a liquid phase formed. $Ca_2Fe_2O_5$ membranes densified between 900 and 1100°C, although cracking was observed that increased with increasing sintering temperature and membrane thickness. These parameters are proportional to residual stresses generated within the

membrane due to shrinkage against the metallic support. At 800°C, cracking was eliminated from the thinnest $Ca_2Fe_2O_5$ membrane (from 45 vol% suspension), although it is not know if complete densification occurred. In future work, we will minimize the thickness to obtain dense, crack-free membranes.

CONCLUSIONS

Aqueous colloidal processing of ceramic suspensions offers a low-cost approach of forming inorganic membranes on porous, metallic supports. It has been demonstrated that this approach is feasible even for membrane materials that undergo deleterious reactions with water by the use of key additives such as citric acid and PAA/PEO comb polymer dispersants to promote long-term suspension stability. Furthermore, it has been demonstrated that it is possible to co-sinter $Ca_2Fe_2O_5$ membranes on stainless steel supports, although more work is required to fine tune the temperature and coating thickness required to obtain dense, crack free coatings.

REFERENCES

1. Cesarano III, J., I.A. Aksay, and A. Bleier, "Stability of Aqueous α-Al_2O_3 Suspensions with Poly(methacrylic acid) Polyelectrolyte," *J. Am. Ceram. Soc.*, **71** [4] 250-55 (1988).
2. Cesarano III, J. and I.A. Aksay, "Processing of Highly Concentrated Aqueous α-Alumina Suspensions Stabilized with Polyelectrolyte," *J. Am. Ceram. Soc.*, **71** [12] (1988).
3. Kirby, G.H., D.J. Harris, Q. Li, and J.A. Lewis, "Poly(acrylic acid)-Poly(ethylene oxide) Comb Polymer Effects on $BaTiO_3$ Nanoparticle Suspension Stability," *J. Am. Ceram. Soc.*, **87** [2] 181-86 (2004).
4. Taylor, H.F.W., *Cement Chemistry*. 2 ed. 1997, London: Thomas Telford Publishing.
5. Mandanas, M.M., W. Shaffer, and J.H. Adair, "Aqueous Processing and Stabilization of Manganese Zinc Ferrite Powders via a Passivation-Dispersion Approach," *J. Am. Ceram. Soc.*, **85** [9] 2156-60 (2002).
6. Lewis, J.A., H. Matsuyama, G. Kirby, S. Morissette, and J.F. Young, "Polyelectrolyte Effects on the Rheological Properties of Concentrated Cement Suspensions," *J. Am. Ceram. Soc.*, **83** [8] 1905-13 (2000).
7. Reed, J.S., *Principles of Ceramics Processing*. second ed. 1995: John Wiley & Sons, Inc.
8. Hewlett, P.C., "Physico-Chemical Interactions Between Chemical Admixtures and Portland Cement," *Journal of Materials Education*, **9** [4] 395-435 (1983).

Advances in Air Brazing for Use in Joining and Sealing High-Temperature Gas Separation Membranes

K. Scott Weil,[*] Jens T. Darsell,[**] John S. Hardy,[*] and Jin Yong Kim[*]

[*]Pacific Northwest National Laboratory, 902 Battelle Blvd, P.O. Box 999, Richland, WA 99352
[**]Washington State University, P.O. Box 642920, Pullman, WA 99164-2920

ABSTRACT

One of the enabling technologies required for high efficiency, low emissions fossil energy conversion is the development of sealing materials for hermetically joining the inorganic membranes used in high temperature gas separation to the underlying support structure of the separation device. The sealing materials must not only be compatible with both the membrane and support materials, but must also be physically and chemically stable at the temperatures, pressures, gas atmospheres, and thermal cycling conditions typical of the electrochemical separation processes employed with gasified coal and air. The types of membrane materials that are being considered and developed by the Office of Fossil Energy (FE) include microporous alumina and mixed ionic/electronic conducting oxides (MIECs) for the separation of hydrogen from coal gas and syngas and perovskite and brownmillerite MIECs for the separation of oxygen from air.

We have recently developed a method of ceramic-to-metal brazing specifically for these types of membrane materials. Referred to as air brazing, the technique differs from traditional active metal brazing in two important ways: (1) it utilizes a liquid-phase oxide-noble metal melt as the basis for joining and therefore exhibits high-temperature oxidation resistance and (2) the process is conducted directly in air without the use of fluxes and/or inert cover gases. In fact, the strength of the bond formed during air brazing relies on the formation of a thin, adherent oxide scale on the metal substrate. The technique employs a molten oxide that is at least partially soluble in a noble metal solvent to pre-wet the oxide faying surfaces, forming a new surface that the remaining molten filler material easily wets. To date, we have focused our efforts on proof-of-principle development and testing of the Ag-CuO system, for example demonstrating the use of air brazing in joining a variety of ceramic membranes and heat resistant alloys of interest to the FE program, as well as examining the resulting strengths and microstructures of these joints in the as-joined condition; after long-term, high-temperature exposure testing; and upon thermal cycling. Until recently however, little emphasis has been placed on fundamentally understanding the wetting and adhesion characteristics of the braze as a function of composition. Specifically, we want to consider what effect ternary phases may have on the thermodynamic and joining properties of the Ag-CuO system and whether can we use this knowledge to engineer the braze and enhance its performance properties, such as resistance to corrosion in the coal-gas environment.

INTRODUCTION

The development of high-temperature electrochemical devices such as oxygen and hydrogen separators, fuel gas reformers, solid oxide fuel cells, and chemical sensors is part of a rapidly expanding segment of the solid state technology market. These devices employ an ionic conducting ceramic as the active membrane that establishes the electrochemical potential of the device, either under voltage (i.e. to carry out gas separation) or under chemical gradient (to develop an electrical potential and thereby generate electrical power). Because the device operates under an ionic gradient that develops across the electrolyte, hermiticity across this layer is paramount. That is, not only must this thin ceramic membrane be dense with no interconnected porosity, but it must be connected to the rest of the device, typically constructed from a heat resistant alloy, with a high-temperature, gas-tight seal. A significant engineering challenge in fabricating these devices is how to effectively join the thin electrochemically active membrane to the metallic body of the device such that the resulting seal is hermetic, rugged, and stable during continuous high temperature operation.

A new brazing technique, referred to as air brazing, has recently been developed specifically for use in joining and sealing the ceramic and metallic components in high temperature electrochemical devices.[1-3] Employing silver as the filler material and CuO as a wetting agent, joining can be readily conducted in air and acceptable wetting obtained on a

number of ceramic surfaces with as little as 1mol% CuO added to the filler.[4] Select ratios of silver to copper oxide have been shown to offer both excellent joint strength and high temperature oxidation resistance[5] and we are currently investigating how the Ag-CuO system can be compositionally modified to achieve greater wettability, better gap filling characteristics, and higher use temperature. In this paper, we will present initial results obtained on alumina substrates when either palladium or titanium dioxide was added as a ternary component to our standard Ag-CuO braze formulation.

Ag-CuO-Pd BRAZE COMPOSITIONS

EXPERIMENTAL

Materials

Sessile drop experiments were performed on polycrystalline alumina discs (Al-23, Alpha Aesar, Ward Hill, MA 01835, 98% dense, 99.7 % pure) that contained a small amount of silicate as an impurity. These discs were 50mm in diameter and 6mm thick. One surface of the disc, on which a braze pellet was placed for the contact angle measurement, was polished to a 1μm finish using water-based diamond suspensions. The discs were then cleaned with acetone, and rinsed with propanol, air dried, and finally heated in static air to 600°C for 4 hours to burn off any residual organic species. Alumina crucibles (Netzsch, Burlington MA) used in the differential scanning calorimetry (DSC) experiments were also preheated to remove organic contamination.

As listed in Table I, various braze compositions were selected. These compositions were formulated by dry mixing the appropriate amounts of silver powder (99.9%, 0.75μm average particle size, Alpha Aesar), copper powder (99%, 1.25μm average particle size, Alpha Aesar) and palladium powder (submicron, 99.9+%, Aldrich). These mixed powders were then cold-pressed into pellets measuring approximately 7mm in diameter and 10mm tall for sessile drop experiments. For DSC experiments, 2mm diameter pellets were prepared from approximately 5-10mg of braze powder in the same manner.

Characterization

DSC analysis was conducted using a Netzsch system (model STA 449C Jupiter) equipped with a high temperature furnace and a Type-S sample carrier. All the experiments were performed in flowing dry air at a flow rate of 10ml/min. A heating rate of 10°C/min was employed in each run, and the maximum temperature for the experiment was determined based on the Pd content of the sample. Sessile drop experiments were conducted in a static air muffle furnace, furnished with a quartz window through which the contact angle of heated specimen could be observed. The braze pellets were placed on the polished face of the substrate and heated in the furnace. The heating cycle employed for each sample was dependent on the braze composition. For example in samples containing no palladium, the furnace was heated at 30°C/min to an initial temperature of 900°C and held for 15min then subsequently heated at 10°C/min to soak temperatures of 950 °C, 1000 °C, 1050 °C, and 1100°C, at each of which the furnace was held for a period of 15min. For samples containing 25 mol% palladium in silver, the furnace was heated at 30°C/min to an initial temperature of 1100 °C, followed by a heating at 10°C/min, with 15min soaks at 1150°C, 1200°C, and 1250°C. For samples containing 50 mol % Pd in Ag, the same heating cycle was used with the addition of 15min holds at 1300°C, and 1350°C. A video camera with a zoom lens recorded the profile of the specimens during the heating cycle. Selected frames from the videotape were converted using Ulead™ software to digital images from which the contact angle between the braze and alumina substrate could be measured. Microstructural analysis was performed on polished cross sections of the wetting samples, using a scanning electron microscope (SEM, JEOL, JSM-5900 LV) equipped with an energy dispersive X-ray (EDX) detector and analysis system. To avoid electrical charging of the samples in the SEM, they were carbon coated and grounded.

RESULTS AND DISCUSSION

Melting Behavior

Figure 1 shows DSC curves exhibiting endothermic peaks corresponding to melting of pure Ag, Ag with 1 mol % CuO, the 1:3 Pd:Ag alloy with 1 mol % CuO, and the 1:1 Pd:Ag alloy with 1 mol% CuO. To obtain the onset of melting, the first derivative of each DSC curve was calculated by differentiating the DSC curve with respect to temperature. The onset was identified as a temperature at which the derivative of the DSC curve revealed deviation from the baseline. The liquidus temperature was defined by the temperature at which the endothermic peak re-joins the baseline. Some samples such as the Ag-1 mol% CuO exhibited an endotherm with double peaks. For these samples, the solidus temperature was

defined as the temperature where the derivative of the first peak deviated from baseline, while the liquidus temperature was defined as the point at which the derivative of the second peak returned to baseline.

Table I. Braze compositions employed in this study

Braze I.D.	Ag Content (mol%)	Pd Content (mol%)	CuO Content (mol%)
Ag-1Cu	99	0	1
1Pd:3Ag-1Cu	74.2	24.8	1
1Pd:1Ag-1Cu	49.4	49.6	1
Ag-1.4Cu	98.6	0	1.4
1Pd:3Ag-1.4Cu	73.9	24.7	1.4
1Pd:1Ag-1.4Cu	49.2	49.4	1.4
Ag-2Cu	98	0	2
1Pd:3Ag-2Cu	73.4	24.6	2
1Pd:1Ag-2Cu	48.9	49.1	2
Ag-4Cu	96	0	4
1Pd:3Ag-4Cu	71.9	24.1	4
1Pd:1Ag-4Cu	47.9	48.1	4
Ag-8Cu	92	0	8
1Pd:3Ag-8Cu	68.9	23.1	8
1Pd:1Ag-8Cu	45.9	46.1	8
90Ag10Cu	90	0	10
1Pd:3Ag-10Cu	67.4	22.6	10
1Pd:1Ag-10Cu	44.9	45.1	10
Ag-20Cu	80	0	20
1Pd:1Ag-20Cu	39.9	40.1	20
Ag-30Cu	70	0	30
1Pd:3Ag-34Cu	49.4	16.5	34.1
1Pd:1Ag-34Cu	32.9	33.1	34
Ag-40Cu	60	0	40
Ag-50Cu	50	0	50
Ag-60Cu	40	0	60
Ag-69Cu	30.65	0	69.35
Ag-80Cu	20	0	80

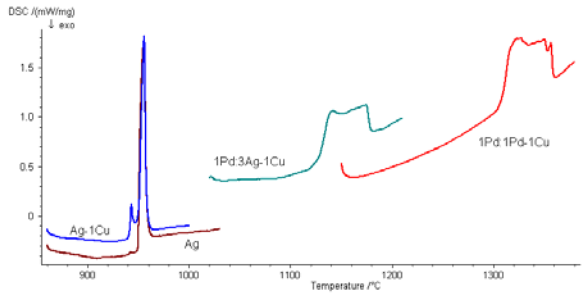

Figure 1 DSC curves obtained from pure Ag, Ag with 1 mol% CuO, the 1:3 Pd:Ag alloy with 1 mol% CuO, and the 1:1 Pd:Ag alloy with 1 mol% CuO.

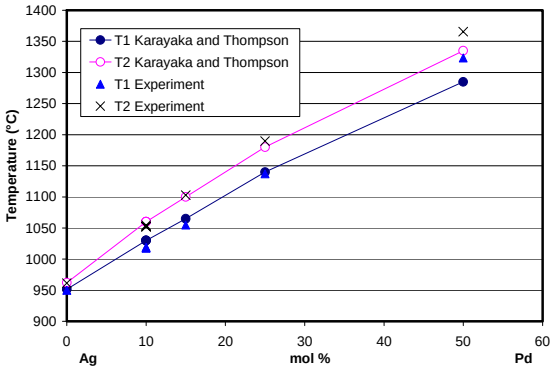

Figure 2 Solidus (T1) and liquidus (T2) temperatures of Ag-Pd obtained in the DSC analysis. For comparison, values reported by Karyaka and Thomson[6] are also plotted along with our experimental values.

Solidus and liquidus temperatures of Pd-Ag compositions obtained in this study are plotted as a function of Ag content in the range of 50 ~ 100 mol%, and also compared with values reported by Karayaka and Thompson[6] in Figure 2. The solidus temperature obtained for pure Ag was 950°C, which agrees well with values regularly obtained on the Netzsch instrument of 951°C. A liquidus temperature for pure Ag was found to be 961°C which agrees with literature values[7]. Shown in Figure 3 are the solidus (T1) and liquidus (T2) temperatures obtained for the Ag-CuO samples containing 90, 96, 98, and 100 mol% Ag. The figure indicates that the onset of melting occurs at approximately 945 ± 5°C and the liquidus temperature is approximately 972 ± 2°C for the samples with Ag contents of 90-98 mol%, while the liquidus temperature for the 99 mol% Ag sample is reduced to 961°C. This result agrees well with the data reported by Nishiura et al.[8] This result validates the accuracy of our method for obtaining the solidus and liquidus temperatures in this study. The solidus and liquidus temperatures of the two series of Pd-Ag-CuO compositions are shown as a function of noble metal

content (Ag + Pd) in Figure 4. A significant increase in the solidus and liquidus temperatures is observed as the Pd to Ag ratio increases. The increase is less dramatic at higher CuO contents (low metal contents).

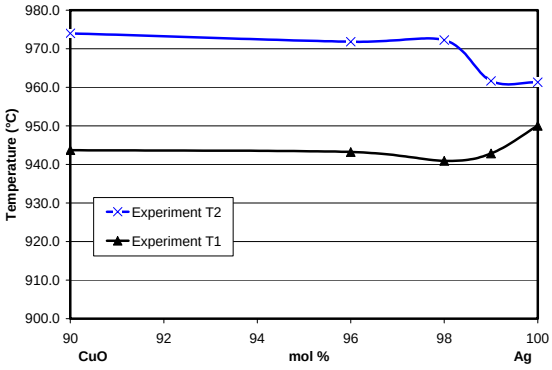

Figure 3 Solidus (T1) and Liquidus (T2) temperatures of the Ag-CuO system obtained in the DSC analysis.

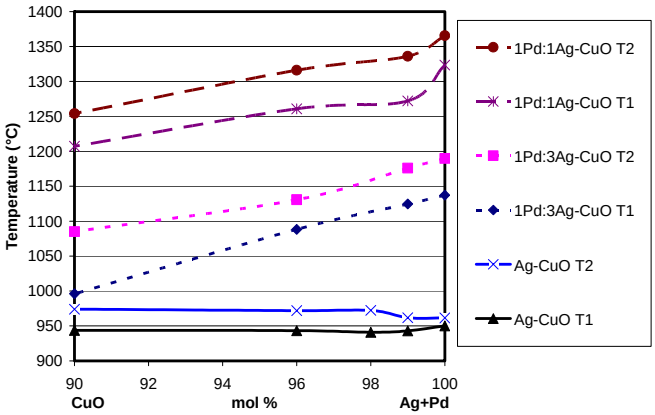

Figure 4 Experimental solidus (T1) and Liquidus (T2) temperatures for Pd-Ag-CuO containing varying metal (Ag + Pd) compositions and Pd:Ag ratios

Wetting Properties

Results from the sessile drop experiments are plotted as a function of metal contents in Figure 5. An increase in contact angle is observed with increasing Pd content in the braze. All of the samples with a Pd:Ag ratio of 1:3 revealed a wetting condition (contact angle < 90°), although the contact angle is approximately 5-20° larger than the comparable Ag-CuO braze in the metal content between 66 and 96 mol%. In the case of samples containing 98 and 99 mol% metals, the contact angle obtained from the Pd:Ag specimens with a 1:3 ratio is almost identical to that of the Ag-CuO system. On the other hand, the samples with a higher Pd content (Pd:Ag = 1:1) exhibited a significant increase in the contact angle, which was on average 10-60°larger than that of the Ag-CuO system. This effect was especially severe at low CuO contents, displaying non-wetting (contact angle > 90°) when the CuO content is less than 10 mol%.

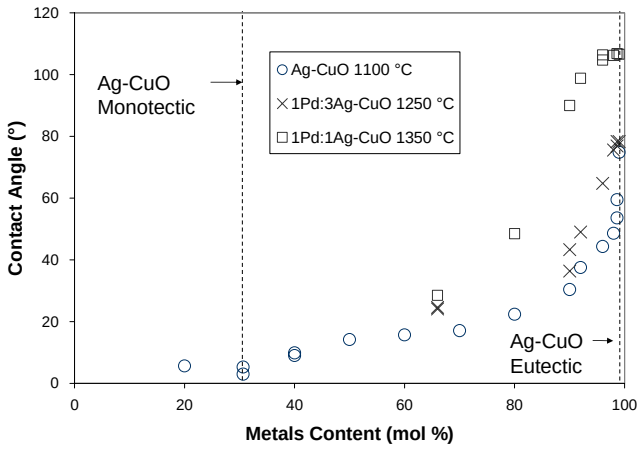

Figure 5 Contact angle of the Pd-Ag-CuO braze with various Pd/Ag ratios as a function of total metal contents. Samples held at final temperatures (1100°C for Ag-CuO, 1250°C for 1Pd:3Ag-CuO and 1350°C for 1Pd:3Ag-CuO) for 15min.

Microstructure

Figure 6 shows SEM images collected on the braze/alumina interfaces with brazes containing 4 mol% CuO. The Ag-4CuO sample exhibits no porosity at the interface indicating good bonding between the braze and substrate as see in Figure 6(a). The CuO phase in the braze exists in two forms; precipitates along the alumina-braze interface and inclusions in the Ag phase. A trace amount of copper was also observed within the alumina substrate along the grain boundaries, indicating possible migration of the CuO along the grain boundaries of alumina.

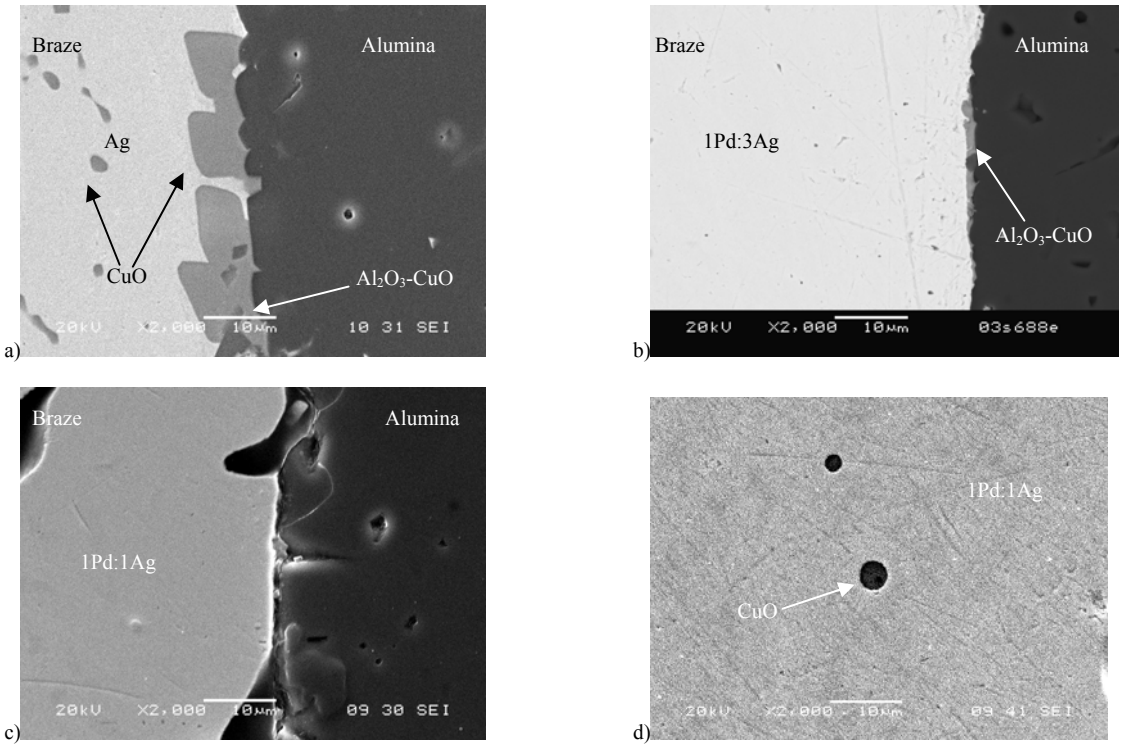

Figure 6 Scanning electron micrographs at 2000x of the braze/alumina interface of sessile drop samples containing 4 mol% of CuO and a) Ag, b) 1Pd:3Ag, and c) 1Pd:1Ag as well as d) the precipitates containing Cu in the 1Pd:1Ag-Cu sample.

The 1Pd:3Ag sample also exhibits excellent bonding of the braze to the substrate as indicated by the lack of porosity [refer to Figure 6(b)]. EDX analysis shows a metal matrix containing approximately 25 mol% Pd and 70 mol% Ag. There are also inclusions in the metal matrix, which contain Cu and O in a ratio of approximately 2 to 1 possibly indicating the presence of Cu_2O. In addition, two different interfacial products were observed: (1) a lighter gray layer containing Cu, Al, and O and (2) darker precipitates also containing Cu, Al, and O but with a larger amount of O and the addition of a trace of Mg.

On the other hand, the 1Pd:1Ag-4CuO sample shows poor bonding between the braze and substrate [Figure 6(c)]. This result was expected since this sample exhibited poor wettability in comparison with the other brazes with no Pd or a lower Pd content (refer to Figure 5). EDX analysis shows that the braze matrix (a light gray region) contains Ag and Pd in a ratio of 1 Pd to 1 Ag. The particles at the interface between the braze and alumina contain mostly Al and O with a trace of Si, but no Cu is observed at this site. Cu was mostly observed in a form of precipitates within the braze matrix as can be seen in Figure 6(d). These precipitates contain Cu and O, and a trace of Si.

Ag-CuO-TiO_2 BRAZE COMPOSITIONS

EXPERIMENTAL

Materials

Sessile drop experiments were again performed on polycrystalline alumina substrates of the type and preparation used in the experiments with palladium modified air brazing. Braze pellets were fabricated by dry mixing powders of silver (spherical, 0.5-1μm average particle size, 99.9% pure by metals basis, Alpha Aesar, Ward Hill, MA 01835), copper (1-1.5μm average particle size, 99% pure by metals basis, Alpha Aesar, Ward Hill, MA 01835) and titanium hydride (-325 mesh, 98% pure, Aldrich, Milwaukee, WI). For sessile drop experiments 0.84g of powders were pressed into approximately 7mm diameter by 10mm tall pellets. Titanium hydride decomposes at approximately 450°C to form titanium which oxidizes to form TiO_2 during the experiment. Sessile drop experiments and subsequent microstructural analyses were conducted as above.

Table I. Braze compositions employed in this study

Braze I.D.	Ag Content (mol %)	CuO Content (mol %)	TiO_2 Content (mol %)
Ag0.5Ti	99.5	0	0.5
Ag1Ti	99	0	1
99Ag1Cu	99	1	0
99Ag1Cu0.5Ti	98.5	1	0.5
99Ag1Cu1Ti	98	1	1
99Ag1Cu2Ti	97	1	2
98.6Ag1.4Cu	98.6	1.4	0
98Ag2Cu	98	2	0
98Ag2Cu0.5Ti	97.5	2	0.5
98Ag2Cu1Ti	97	2	1
96Ag4Cu	96	4	0
96Ag4Cu0.5Ti	95.5	4	0.5
96Ag4Cu1Ti	95	4	1
96Ag4Cu2Ti	94	4	2
92Ag8Cu	92	8	0
92Ag8Cu0.5Ti	91.5	8	0.5
92Ag8Cu1Ti	91	8	1
90Ag10Cu	90	10	0
84Ag16Cu0.5Ti	83.5	16	0.5
84Ag16Cu1Ti	83	16	1
84Ag16Cu2Ti	82	16	2
80Ag20Cu	80	20	0
70Ag30Cu	70	30	0
66Ag34Cu0.5Ti	65.5	34	0.5
66Ag34Cu2Ti	64	34	2
60Ag40Cu	60	40	0
50Ag50Cu	50	50	0
40Ag60Cu	40	60	0
40Ag60Cu	40	60	0
31Ag69Cu	30.65	69.35	0
31Ag69Cu0.5Ti	30.15	69.35	0.5
31Ag69Cu2Ti	28.65	69.35	2
20Ag80Cu	20	80	0

RESULTS AND DISCUSSION

Wetting

Shown in Figure 7 is a comparison of the wetting behavior for 96 mol%-Ag 4 mol% CuO with additions of 0, 0.5, 1, and 2 mol% TiO_2. The data indicate that the contact angle of Ag-CuO decreases significantly with the addition of TiO_2. However, the difference in contact angle for brazes with 0.5, 1, and 2 mol% TiO_2 is within the experimental error of ±3°. Apparently 0.5 mol% TiO_2 is sufficient to improve wetting and further additions do not increase the effect. Figure 8 displays contact angle as a function of copper oxide content for both the binary and ternary compositions at 1100°C. It can be seen that the addition of TiO_2 lowers the contact angle from the baseline of Ag-CuO in the range of approximately 66-99 mol% Ag. The contact angle decreased by approximately 25° for the 99Ag1Cu0.5Ti sample over the 99Ag1Cu sample. However, this difference in wetting behavior is reduced to within experimental error for braze compositions containing less than 66 mol% Ag; i.e. with respect to wetting, at CuO contents of $\geq$ 34 mol%, the addition of TiO_2 offers no benefit over the corresponding binary braze. Alternatively, at low CuO-content, a detrimental effect is observed. For example, the 99Ag1Cu0.5Ti sample displays a relatively low contact angle of 33°, while the 99Ag1Cu1Ti sample exhibits a much higher contact angel of 66°, and the 99Ag1Cu2Ti composition displays a still higher contact angle of 70°, which is almost identical to that of the analogous binary, 99Ag1Cu. This data suggests that in addition to CuO-content, the ratio of TiO_2 to CuO is an important variable defining the wetting behavior of the ternary braze.

Microstructure

Shown in Figures 9(a) – (d) are cross-sectional SEM images of the braze/alumina interfaces in sessile drop specimens produced with 96Ag4Cu, 96Ag4Cu2Ti, 70Ag30Cu, and 66Ag34Cu2Ti. As seen in Figure 9(a), away from this interface the solidified 96Ag4Cu sessile drop displays a silver rich region containing copper oxide precipitates measuring on average ~1 – 3μm in size. At the interface with alumina, the copper oxide forms a 10μm thick semi-continuous layer that appears to be in direct contact with the substrate. Quantitative EDX analysis indicates that the precipitates and interfacial oxide layer contain oxygen and copper. Traces of copper are also found within the alumina substrate along grain

boundaries, indicating possible diffusional migration of copper into the alumina. The effect of 2 mol% TiO_2 addition on this Ag-CuO composition is shown in Figure 9(b). Some grain boundary dissolution is apparent by the infiltration of the braze filler into the sub-surface of the alumina. EDX analysis indicates that this intergranular phase is composed of Al, Cu, and O. Interestingly, titanium was not found in this region or at the original braze/substrate interface, but rather within precipitates in the bulk and at the top surface of the solidified drop, as shown in Figure 10.

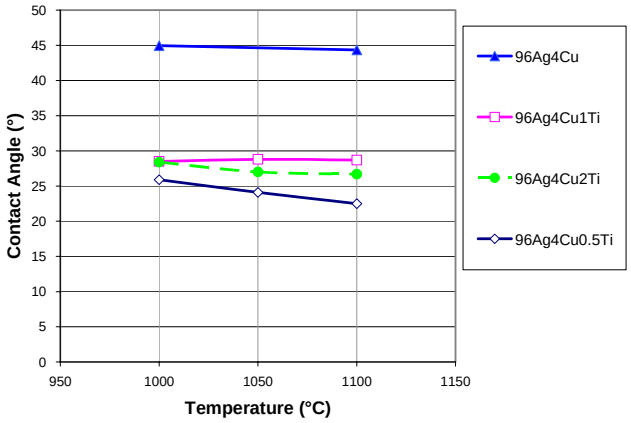

Figure 7 Contact angle as a function of temperature for samples with 96 mol % Ag-4 mol % CuO with additions of 0.5, 1.0, and 2.0 mol % TiO_2. Samples were held at given temperatures for 15 minutes.

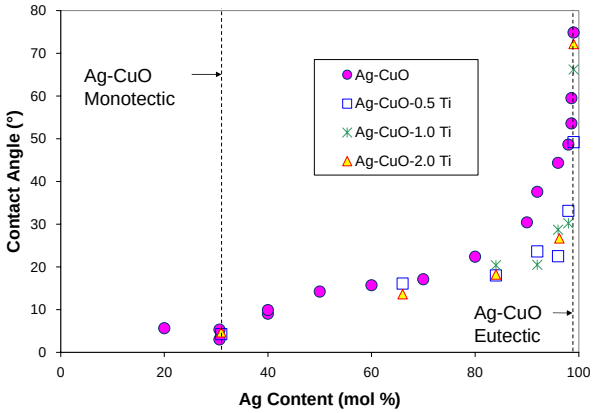

Figure 8 Contact angle as a function of Ag content for Ag-CuO with additions of 0.5, 1.0, and 2.0 mol % TiO_2 after a final hold temperature of 1100 °C for 15 minutes.

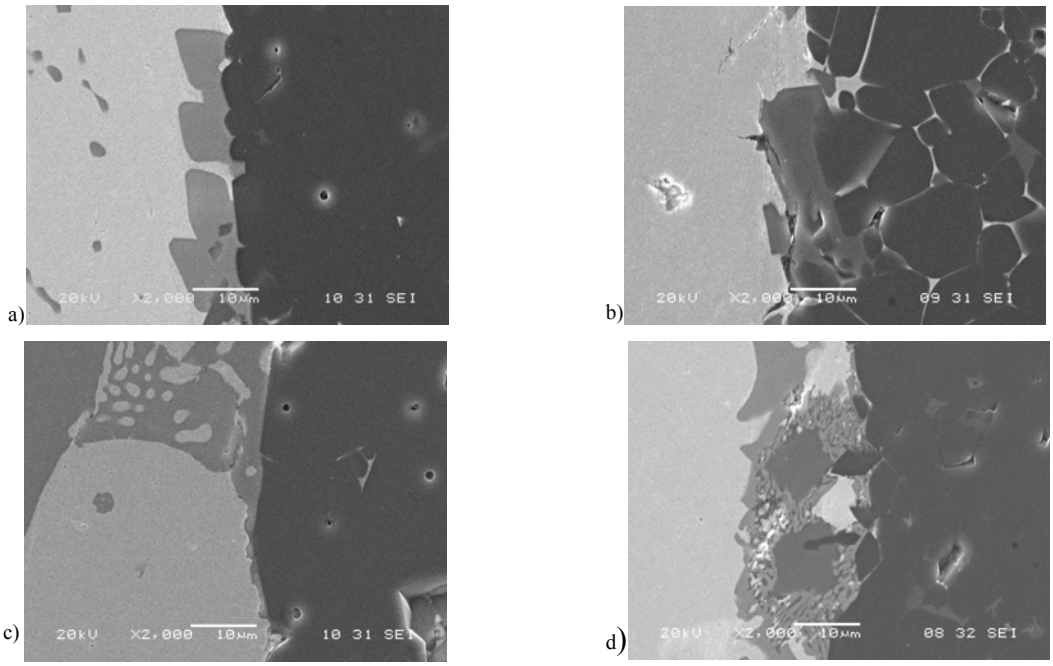

Figure 9 Scanning electron micrograph at 2000x, comparison of the braze/alumina interface formed with a) 96Ag4Cu, b) 96Ag4Cu2Ti, c) 70Ag30Cu, and d) 66Ag34Cu2Ti. All samples were held at 1100°C for 15 minutes.

In the 70Ag30Cu/alumina sample, a fully continuous layer of copper oxide forms in contact with the alumina substrate and measures on average approximately 50μm thick. As shown in the high magnification image in Figure 9(c), a substantial amount of silver is found within this oxide band. Based on the phase diagram for Ag-CuO[9,10], at the composition for this braze two immiscible liquids are expected to form at 1100°C, one rich in CuO and the other rich in silver. We propose that when segregation takes place, the oxide-rich liquid will preferentially wet the substrate because of its higher CuO content and, therefore, lower expected interfacial energy with Al_2O_3. As the specimen is further cooled, copper oxide will first precipitate out on the surface, then below the eutectic point, both silver and additional copper oxide will precipitate onto this proeutectic layer. This possibly explains not only the prevalence of CuO at the

droplet/substrate interface, but also the occurrence of silver within. The effect of adding TiO_2 to a sample containing a large amount of copper oxide can be seen in Figure 9(d). A silver rich region with light gray particles containing Cu and O can be found in the Ag matrix as well as at the interface. Darker gray particles containing Al, Cu, and O, as well as a mixed phase containing Cu, Ti, Al, and O are also found at the interface.

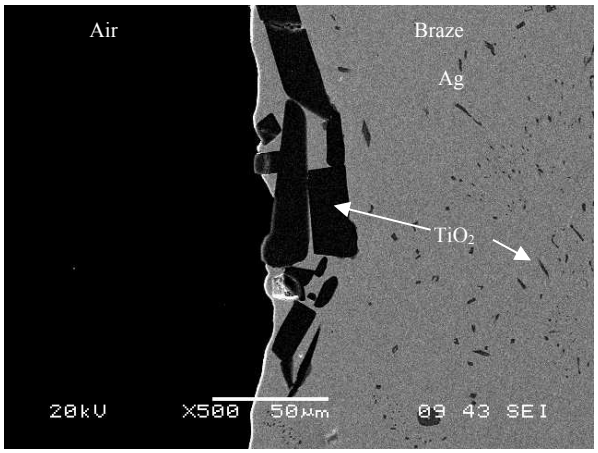

Figure 10 Scanning electron micrograph at 500x, of the 96Ag4Cu2Ti/alumina sessile drop sample shows precipitates containing Ti at the top of the braze surface of solidified drop (air/braze interface).

CONCLUSIONS

This addition of palladium significantly influenced melting behavior, wetting properties and microstructure of the braze. A significant increase in the solidus and liquidus temperatures was observed as the Pd to Ag ratio increased but this increase was less dramatic at higher CuO contents (low metal contents). In the case of samples containing a Pd:Ag ratio of 1:1, the contact angle was 10-60°larger than that of the Ag-CuO or 1Pd:3Ag-CuO. This effect was especially severe at low CuO contents, displaying non-wetting (contact angle > 90°) when the CuO content was less than 10 mol %. Microstructural analysis revealed that this decrease in wettability also caused significant interfacial porosity in the high Pd content (1Pd:1Ag) braze. Similarly, it was found that the addition of amounts as small as 0.5 mol % of TiO_2 could significantly decrease the contact angle for the Ag-CuO system on alumina in the range of 66-99 mol % Ag. This effect is most apparent in the brazes with large amounts of Ag and not apparent bellow 34 mol % Ag. No benefit was seen by adding 1 or 2 mol % TiO_2 over 0.5 mol % on the wetting behavior, although the ratio of CuO to TiO_2 may be an important factor. Microscopy shows that all of the samples wet the alumina substrate well. The addition of TiO_2 causes increased grain boundary dissolution of the alumina. Particles containing Ti were found in the bulk of the braze and at the braze/air interface for sample containing small amounts of CuO. Samples containing large amounts of CuO formed a mixed Cu, Ti, Al, and O phase at the braze/alumina interface in addition to CuO precipitates and a Cu, Al, and O phase.

ACKNOWLEDGEMENTS

The authors would like to thank Nat Saenz, Shelly Carlson, and Jim Coleman for their assistance in polishing a portion of the wetting samples and conducting the metallographic and SEM analysis work. This work was supported by the U.S. Department of Energy, Office of Fossil Energy, Advanced Research and Technology Development Program. The Pacific Northwest National Laboratory is operated by Battelle Memorial Institute for the United States Department of Energy (U.S. DOE) under Contract DE-AC06-76RLO 1830.

REFERENCES

[1] C.C. Shüler, A. Stuck, N. Beck, H. Keser, and U. Täck, "Direct Silver Bonding - An Alternative for Substrates in Power Semiconductor Packaging," *Journal of Materials Science: Materials in Electronics*, **11** [3] 389-96 (2000).

[2] K.M. Erskine, A.M. Meier, and S.M. Pilgrim, "Brazing Perovskite Ceramics with Silver/Copper Oxide Braze Alloys," *Journal of Materials Science*, **37** [8] 1705-9 (2002).

[3] J.S. Hardy, J.Y. Kim, and K.S. Weil, "Joining Mixed Conducting Oxides Using an Air-Fired Electrically Conductive Braze," *Journal of the Electrochemical Society*, in press.

[4] K.S. Weil, J.S. Hardy, and J.Y. Kim, "A New Technique for Joining Ceramic and Metal Components in High Temperature Electrochemical Devices," *Journal of Advanced Materials*, in press.

[5] J.Y. Kim, J.S. Hardy, and K.S.Weil, "Effects of CuO Content on the Wetting Behavior and Mechanical Properties of a Ag-CuO Braze for Ceramic Joining," *Journal of the American Ceramic Society*, in review.

[6] I. Karayaka and W.T. Thompson, *Bull. Alloy Phase Diagrams*, **9** [3] 237-243 (1988).

[7] Smithell's Metals Reference Book, 6th edition, E. A. Brandes, ed., Butterworths London (1983).

[8] H. Nishiura, R.O. Suzuki, K. Ono, L.J. Gauckler, "Experimental Phase Diagram in the Ag-Cu_2O-Cuo System," *Journal of the American Ceramic Society*, **81** [8] 2181-87 (1998).

[9] Z.B. Shao, K.R. Liu, and L.Q. Liu, "Equilibrium Phase Diagrams in the Systems PbO-Ag and CuO-Ag," *Journal of the American Ceramic Society*, **76** [10] 2663-64 (1993)

[10] H. Nishiura, R.O. Suzuki, K. Ono, and L.J. Gauckler, "Experimental Phase Diagram in the Ag-Cu_2O-CuO System," *Journal of the American Ceramic Society*, **81** [8] 2181-87 (1998)

ADVANCED PROCESSING OF METALLIC POWDERS

Iver E. Anderson
222 Metals Development, Ames Lab. (USDOE), Iowa State University, Ames, IA 50011
E-mail: andersoni@ameslab.gov; Telephone: (515) 294-9719; Fax: (515) 294-8727

Robert L. Terpstra
109 Metals Development, Ames Lab. (USDOE), Iowa State University, Ames, IA 50011
E-mail: terpstra@ameslab.gov; Telephone: (515) 294-5747; Fax: (515) 294-8727

Brian Gleeson
124 Metals Development, Ames Lab. (USDOE), Iowa State University, Ames, IA 50011
E-mail: gleeson@ameslab.gov; Telephone: (515) 294-4446; Fax: (515) 294-8727

ABSTRACT

This project seeks to enhance the control of metal powder production by gas atomization methods to benefit the implementation of several emerging Fossil Energy technologies that utilize metal powders of specific size ranges and types, which are not efficiently produced by industrial powder makers. Further improvements in fundamental understanding and design of high efficiency gas atomization nozzles will be directed toward maximizing powder yields in special size classes, including ultrafine (dia. < 10 μm) powders, for example. Efficient production of such powders can eliminate a major technological barrier to the use of new concepts for fabrication, for example, of hydrogen membranes. To provide a direct route for rapid transfer of the atomization technology improvements, powder production tests will be performed in a laboratory atomization system that will be adapted to a level consistent with an advanced industrial operation in terms of steady state operation and controls systems. Some benchmark trials on the complex alloys involved with Fossil Energy applications will be performed initially to provide assurance that significant improvements will be achieved. It is also important to note that laboratory hot gas corrosion test results and coal-fired combustion system exposure tests will be reported in this manuscript that dealt with previous work involving gas atomization and controlled sintering (into porous sheets) of materials suitable for hot gas filtration, as a summary of these results.

INTRODUCTION

The powder making process that is most suitable for the complex, high melting alloys of current interest in Fossil Energy technologies is gas atomization, especially by the use of a close-coupled nozzle. While close-coupled gas atomization nozzles have the most potential for improvements

in efficiency[1] and process control, most industrial gas atomization practitioners have not pursued the developments needed to push beyond a fairly simple level of control needed to ensure stable, reliable powder production. Thus, the typical method of providing special particle size fractions of specific alloys is to produce a powder batch of the "natural" size distribution that results from normal operation parameters and, then, to size classify the resulting size distribution with sieves and pneumatic separators into the desired fraction. Especially for complex alloy compositions without additional markets, this conventional practice is quite costly, because of the expense of extensive particle size classification operations and the need to inventory or to scrap the remaining powder that is not desired.

A better approach is to gain improved control of the energy transfer process involved with liquid metal disintegration by supersonic gas flows to generate liquid droplets only of the desired size range in the atomization spray, which will solidify to powders of the proper size for a specific application. As stated above, a close coupled atomization nozzle is the most suitable for these performance improvements, but experiments have indicated that the specific design of the gas flow passages should be changed from the conventional continuous annular slit[2] to a linked series of discrete axi-symmetric gas jets to provide the most experimental latitude for nozzle design improvements[3]. One example of increased latitude is the ability to provide a segmented gas flow curtain that can be aligned with a series of melt flow rivelets from a novel melt feed tube to provide highly efficient coupling of the kinetic energy of the gas flow to the melt[4]. These improved nozzle performance characteristics were demonstrated by a significant shift of the resulting particle size distributions from a bimodal to a single mode distribution and by detection of enhanced spray uniformity with high-speed (10,000 frame/sec) cinematography at a temporal resolution of 30 nsec (ref. 5). If additional improvements can succeed in forcing the domination of primary disintegration, i.e., in the near-field of the initial gas/melt impact, it is quite possible to gain enhanced control of the droplet disintegration process, resulting in significant reductions of particle size variance of the resulting powder[5]. Recent progress on comparisons of our experimental particle size results to melt disintegration theories suggest that fully-expanded gas jet velocity can be used for direct control of particle size[6]. However, much further work is needed to verify the operation of the acceleration wave theory[7] that dictates this particle size trend in a highly controlled gas atomization process and to exploit the obvious advantages for production of special powders.

The enhanced production of ultra-fine powders of high temperature alloys with dia. ≤ 10 μm was chosen for an initial objective of the new research thrust involving improved powder processing for various fossil energy applications. Such powders can be used for development of porous sintered metallic support structures (in a laminated type of composite) for inorganic (ceramic) hydrogen separation membranes, that are used in coal-fired IGCC applications. Since a physical separation principle is the primary mechanism for this type of composite membrane, it is critical to promote permeability in the metallic support structure (through pore contiguity and reduced wall thickness), while reducing pore size to provide sufficient mechanical support for the thin (less than 2 μm), porous (less than 2 nm pore dia.) ceramic membrane layer[8]. With a properly designed porous ceramic layer coupled to the metallic support structure, the composite membrane can exhibit a maximum permeance for hydrogen with a maximum separation factor[8] for other contaminating gases, e.g., COx, NOx, and SOx. A conceptual sketch of a tubular design of the laminated physical separation membrane is given in Figure 1, which shows an

external porous tube (intended to be partially sintered spherical alloy powders for this project) to provide mechanical protection for the fragile interior ceramic membrane. The other important characteristics of the porous metallic support tube include high strength at high temperatures, sufficient ductility, and joining compatibility to permit integration into the synthesis gas separation system[8].

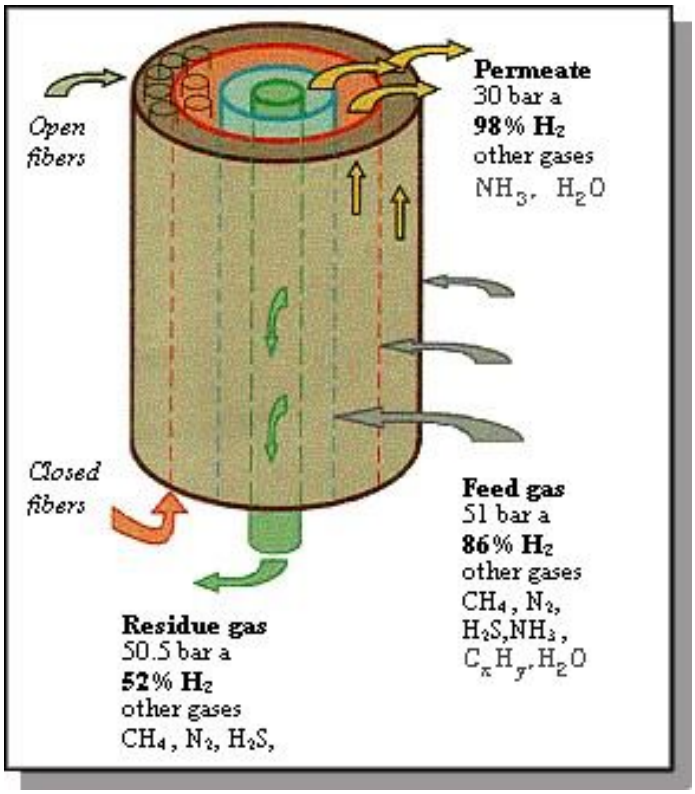

Figure 1. Schematic of a multilayer gas separation membrane (USDOE-FE website).

The requirements for such a porous metallic support layer indicate that spherical ultra-fine metallic powders of high temperature, corrosion resistant alloys would be preferred, but this type of powder is a commercial rarity. One alloy family of current interest for production as ultrafine powder is a simplified iron aluminide composition, Fe-Al-Cr, because of its resistance to integrated gassification-combined cycles (IGCC) environments[9] and compatibility with current ceramic membrane choices. Thus, an Fe-Al-Cr alloy was targeted for the initial trial of our laboratory gas atomization system for these project goals. A schematic of the laboratory gas atomization system is given in Figure 2 to provide a summary of the features of the system, where several publications can be consulted for details on the operation and its development[3, 4, 5, 6]. To establish a baseline for laboratory gas atomization practice, a prototypical discrete-jet gas atomization nozzle was utilized with high pressure He gas, employing the well-accepted advantage (for He relative to Ar or N_2) of a high gas velocity for fine powder production[10]. In the interest of baseline simplification, a standard melt pour tube shape also was utilized, without the slotted internal design that was developed for improved melt filming and atomization

uniformity[5]. Preliminary test samples of porous metallic sheets were fabricated by controlled partial sintering of ultra-fine (<10μm) spherical Fe-Al-Cr alloy powders in close size fractions, following the methods previously developed in this project[11].

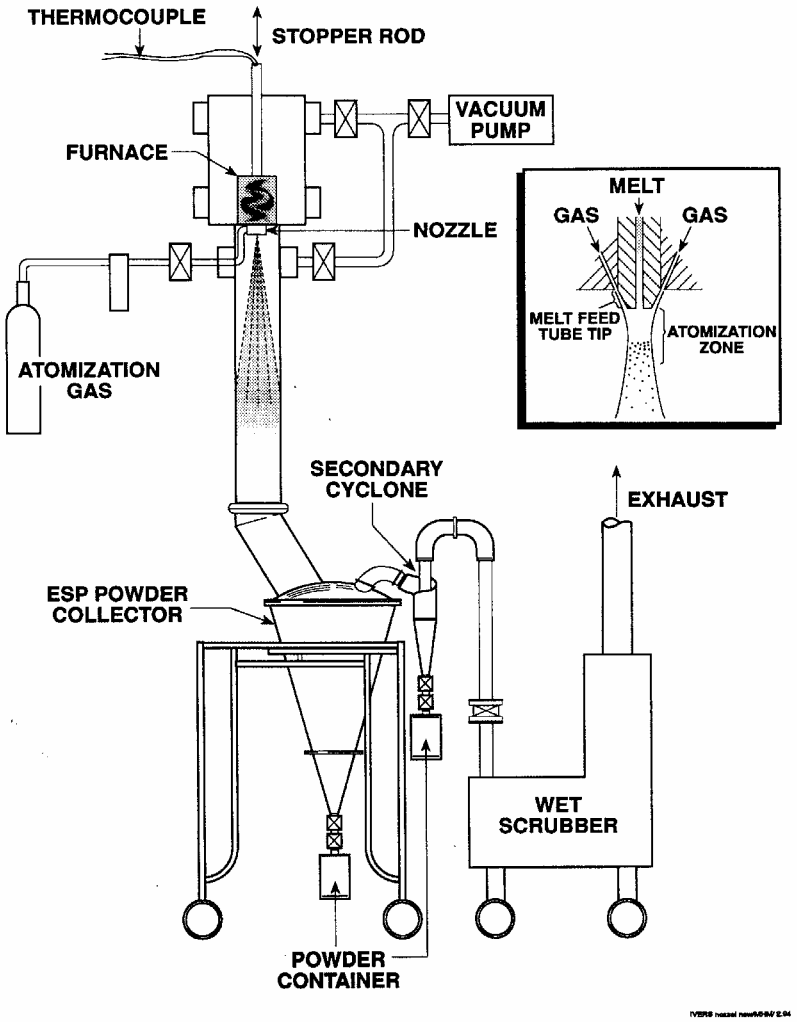

Figure 2. Schematic of the high pressure gas atomization system utilized for powder production in this project. The inset illustrates the essential elements of design and operation of a discrete-jet close-coupled atomization nozzle (in central cross-section), as employed in the system.

Also in this report are contained the results that represent final completion of the milestones for the hot gas filter work, the previous emphasis of our project. For this purpose, a set of alloys for IGCC applications were selected after highly sulfidizing corrosion testing at 650˚C. Also, the selected alloys and other alloy designs were tested in the considerably harsher conditions of simulated downtime corrosion with the same highly sulfidizing gas environment at 650˚C. The results will also be reported of exposure tests conducted on porous o-ring samples in a realistic coal-fired combustion environment at the Energy and Environmental Research Center. These exposure tests allowed assessment of one of the most promising alloys from this project in a thin

porous sheet form that had been rolled and welded, according to the processing methods developed in this project, for both IGCC and pressurized fluidized bed combustion (PFBC) applications[11].

EXPERIMENTAL PROCEDURE

To provide a baseline for testing the future nozzle developments, a typical atomization nozzle in use in our laboratory, HPGA-I (45-30) with cylindrical jets, a 45˚ jet apex angle, and 30 jets, was employed for high pressure He gas atomization of a simplified iron aluminide alloy. A laboratory gas atomization system, similar to that shown in Fig. 2, was utilized, where the full atomization vessel was evacuated to less than 100 milli-torr before backfilling with a full atmosphere of Ar gas to begin melting of the pre-cast (3.8 kg) Fe-16Al-2Cr (wt.%) ingot. The molten alloy was poured at 1750˚C and atomized with He gas at a supply pressure of 5.5MPa into a fine droplet spray (see Figure 2) that cooled during free-fall in the spray chamber and solidified into powder which was collected from the powder containers.

After screening of the complete process yield at 106μm (ASTM 140 mesh) to eliminate a small amount of atomization debris (splats and irregular agglomerates), the resulting powder was riffled to obtain a representative sample for size distribution analysis in an automated laser scattering size analyzer, a Microtrac (from Leeds & Northrup). Screening at 20μm (ASTM 635 mesh) generated a finer size distribution that was suitable for pneumatic size classification runs in an AccuCut (from Donaldson) at intended cut sizes of 10μm and 5μm. The powders from screening and air classification were used for preliminary vacuum sintering experiments at a series of temperatures and times, using a shallow (0.5mm) alumina (99.7%) mold cavity, consistent with the earlier method of hot gas filter fabrication[11].

For the corrosion testing of hot gas filter materials to simulate more closely the expected sulfidizing/oxidizing atmosphere in an IGCC system, laboratory hot (650˚C) corrosion testing was initiated with an enriched H_2S concentration (2,000 ppm, compared to the previous 20 ppm). As a preliminary measure during this test, one of the specimens experienced 4 cycles of simulated downtime corrosion (due to acidic condensation) in a total of 500 hours of exposure by application of an HCl-water solution (pH=2) spray after every 100 hour hot exposure interval, during ambient temperature handling (for weighing). The hot gas exposure was conducted in the simulated IGCC atmosphere (N_2 – 24 CO – 5 CO_2 – 5 H_2O – 14 H_2 – 1.3 CH_4 – 2000 ppm H_2S). Four different chill cast bulk alloys were included in the test: Ni-16Cr-4.5Al-3Fe (Ni-Cr-Al-Fe), Fe-15.8Al-2.2Cr-0.2Zr (Fe_3Al), Ni-16Cr-9Al-3Fe (Ni-Cr-2xAl-Fe), and Ni-16Cr-9Al-3Fe-20Mo (Ni-Cr-2xAl-Fe-Mo), with the composition listed in wt.% (along with each alloy designation). The Ni-16Cr-4.5Al-3Fe alloy, equivalent to Haynes alloy 214, was tested both with and without (untreated) the HCl spray exposure. All samples were characterized by weight change and cross-section microstructure analysis with SEM.

The final round of laboratory hot (650˚C) corrosion testing also was designed to simulate 4 cycles of downtime corrosion (due to acidic condensation) in a total of 500 hours of exposure by application of an HCl-water solution (pH=2) spray after every 100 hour hot exposure interval,

during ambient temperature handling (for weighing). The hot exposure was conducted in the same simulated IGCC atmosphere with an enriched (2000 ppm) H_2S content. However, this corrosion test involved 6 different alloys with each alloy tested with (-HCl) and without the acidic spray exposure. The 6 chill cast bulk alloys (in wt.%) included: (1) Ni-16Cr-4.5Al-3Fe, (2) Fe-15.8Al-2.2Cr-0.2Zr, (3) Ni-16Cr-9.0Al-3Fe, (4) Ni-16Cr-9Al, (5) Ni-16Cr-7.9Al, and (6) Ni-16Cr-7.9Al-10Mo. All samples were characterized by weight change and cross-section microstructure analysis with SEM.

One alloy, Ni-16Cr-9Al-3Fe, also was tested as a set of rolled and resistance spot-welded porous (approx. 70% dense) hanging "o-ring" samples (60 mm OD x 25 mm long x 0.5 mm thick) in an oxygen-blown coal-fired combustion chamber exhaust that was loaded with fly-ash, as a method to investigate the combined effects of corrosive gas composition and fly-ash deposition. The test was intended for 200 hour exposure and was conducted in the Slagging Furnace System (SFS) at the Energy and Environmental Research Center at the University of North Dakota. This 2.6 x 10^6 kJ/hr solid-fuel down–fired combustor system is capable of achieving furnace exit temperatures of 1480 - 1590˚ C to ensure that the ash in the main combustor is molten and flowing. Within this system there are 2 locations/temperatures at which sample coupons can be subjected to the exhaust gas environment of the SFS combustor. The high temperature location is in a convective air heater zone which is capable of maintaining temperatures of approximately 980˚ C. The cooler temperature zone is downstream of the convective air heater zone in the exhaust elbow of the high pressure air pre-heater, which is typically at approximately 750˚ C. Both regions were employed to simulate operation in a PFBC environment and an IGCC environment, respectively. A sample from each exposure temperature was characterized by cross-section microstructure analysis with SEM.

RESULTS

The gas atomization experiment was completed in a total time of 82.6 seconds, with a gas (He) mass flow rate of 3.2 kg/min. and a molten metal mass flow rate of 2.8 kg/min., producing a gas/metal mass flow ratio of 1.2. The gas volumetric flow rate was 19.5 m^3/min., which is important to consider for atomization systems with He gas recycling. Size distribution analysis of the resulting powder revealed that the d(50) or average particle dia. (by wt.) was 14.4 µm. The geometric standard deviation was 2.3, as calculated by d(84)/d(50), which is consistent with other experiments with this type of nozzle without the use of a slotted pour tube[5]. Commercial yields of dia. < 15µm powders of such alloys are often far less than 10% by wt., for comparison, typically using either Ar or N_2 atomization gas. As described above, several close size fractions of ultrafine powders were obtained from the yield for subsequent experiments on partial sintering of porous samples, e.g., 1-5µm and 3-10µm, and these are shown in Figure 3, along with the as-atomized size distribution. The typical spherical appearance of the powder from the finest size fraction is illustrated in Figure 4.

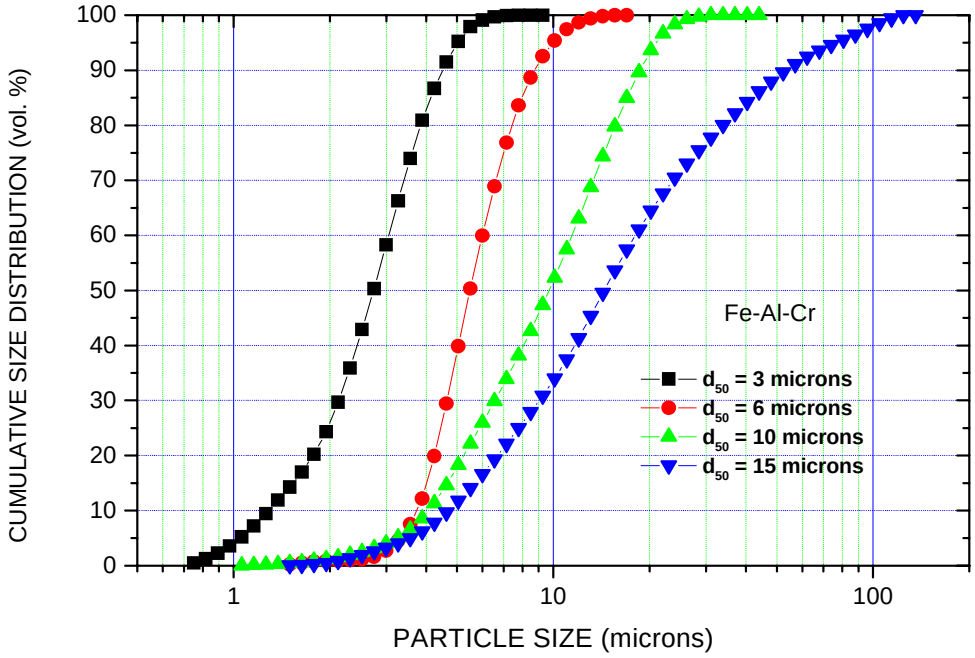

Figure 3. Summary of as-atomized and size classified cumulative size distribution results for He-atomized Fe-16Al-2Cr.

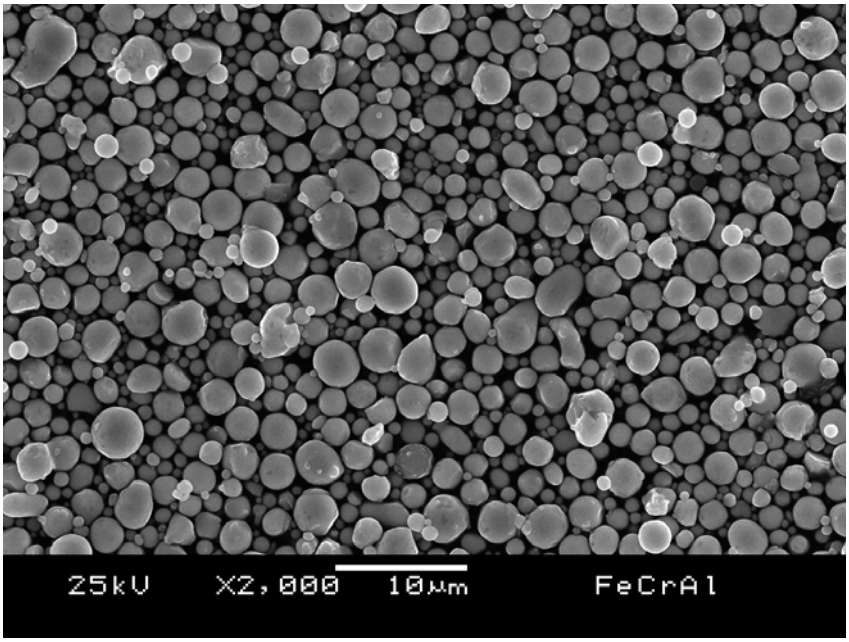

Figure 4. Example of He-atomized Fe-16Al-2Cr powder that was size classified to 1-5 µm, with a d_{50} of 3µm.

As part of the preliminary experiments on generation of porous sheets from the Fe-16Al-2Cr powder, several powder size classes were vacuum sintered at various temperatures from loose

powder contained in a 0.5 mm deep alumina mold cavity. The 1-5 μm powder of Figure 4 appears to be over-sintered in the micrograph of Figure 5a, which shows the sintered surface appearance after 1 hr. at 1100˚C. In other words, previous work[12] has shown that the porous network in such a sample would be partially blocked by the excessive sintered neck growth and particle agglomeration that is evident in Figure 5a. The influence of ultrafine particle size on acceleration of the sintering kinetics is evident when Figure 5a is compared to Figure 5b, which shows powder of a 20-45 μm size fraction that was vacuum sintered for the same time at a temperature of 1200˚C.

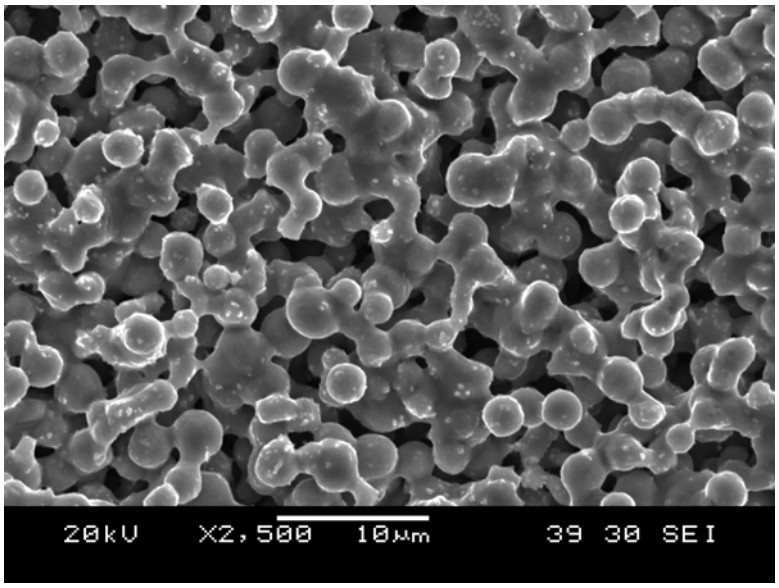

a)

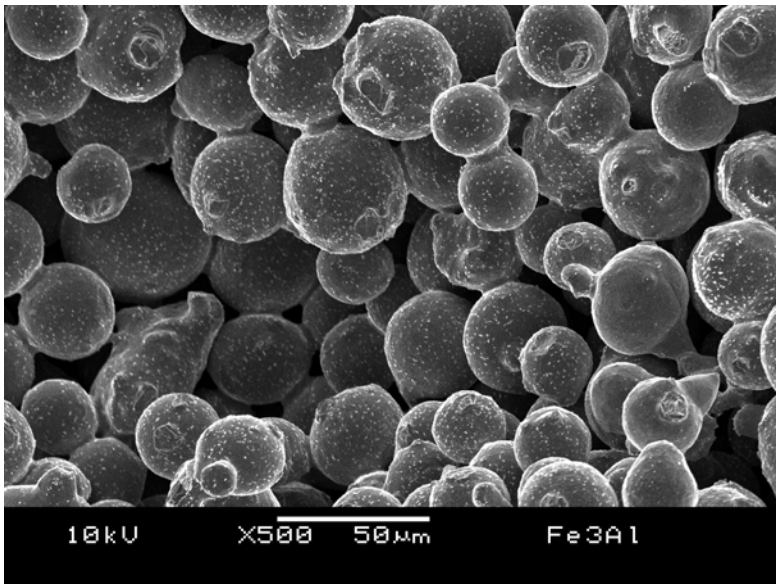

b)

Figure 5. SEM micrographs of sintered Fe-16Al-2Cr powder morphologies from a) a 1-5 μm powder size fraction, vacuum sintered at 1100˚C for 1 h, and b) a 20-45 μm powder size fraction, vacuum sintered at 1200˚C for 1 h.

Results from the initial IGCC hot gas corrosion test with enhanced sulfidation potential (H_2S) are summarized in Figure 6, with the alloys designated as given in the Experimental Procedure. The Ni-Cr-Al-Fe-20Mo and Fe_3Al were both obvious in their susceptibility to attack with weight changes of about +45 mg/cm^2 and –50 mg/cm^2, respectively. Both the Ni-Cr-Al-Fe (untreated) and Ni-Cr-2xAl-Fe had negligible weight gain (<1.5mg/cm^2), while the Ni-Cr-Al-Fe (with HCl spray) exhibited a moderate weight gain of about 13mg/cm^2. These results were very encouraging for the final round of corrosion testing, involving three additional alloys and several of these baseline alloys. This new data also allowed the IGCC gas environment corrosion data for one alloy, Ni-Cr-Al-Fe, to be compared for three cases, i.e., for H_2S = 20 ppm (ref. 11), for H_2S = 2,000 ppm, and for H_2S = 2,000 ppm with HCl exposure, as shown in Fig. 6b. This comparison indicates that the alloy is fairly tolerant of an increase in H_2S concentration, but that the addition of HCl, simulating downtime corrosion, can increase oxide scale weight gain by more than 10 times.

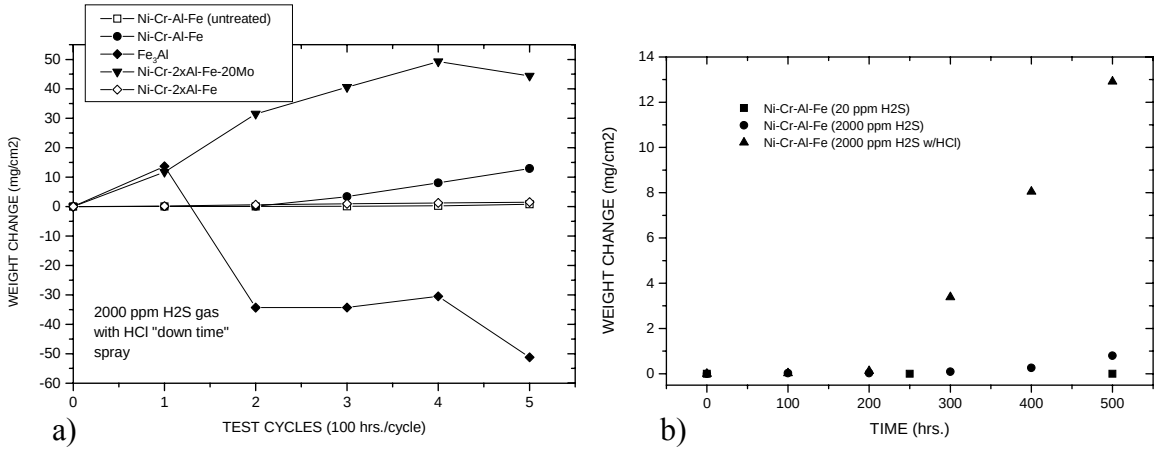

Figure 6. Summary of results of initial hot gas corrosion testing with IGCC conditions with enhanced sulfidation, showing a) the overall results, and b) a comparison of the results for one alloy, Ni-Cr-Al-Fe, at three different conditions.

In general, all alloy samples from the final IGCC gas corrosion test gained weight (see Figure 7), with samples exposed to HCl spray gaining more weight than their unsprayed alloy partners. The alloys 1, 4, and 5 gained the most weight (>30 mg/cm^2) in the HCl spray after 500 h, compared to alloys 2,3, and 6, which gained <10 mg/cm^2. In the baseline sample, alloy 1 (Ni-Cr-Al-Fe), which was included in the initial round of testing, exhibited a weight gain of about 3X the previous test in the HCl sprayed condition. This observation suggests that the additional sprayed samples in the final test may accentuate the corrosion effects, in spite of attempts to randomize replacement in the sample tray after each spray, and illustrates the importance of relative measurements within one test. Without HCl spray, the alloys 4, 5, and 6 gained the most weight (>6 mg/cm^2) after 500 h, compared to alloys 1, 2, and 3, which gained <1 mg/cm^2. Of the best, the alloys 2 and 3 seem to be essentially equivalent in superior resistance to highly sulfidizing attack and to HCl spray (downtime) corrosion resistance, while the alloy 6 is clearly reduced in resistance, but has some promise.

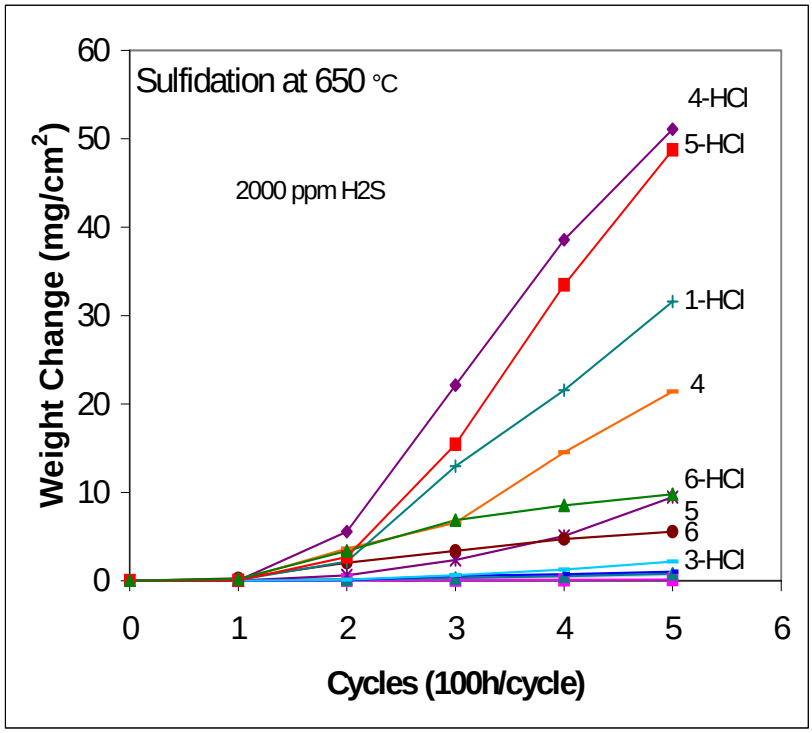

a)

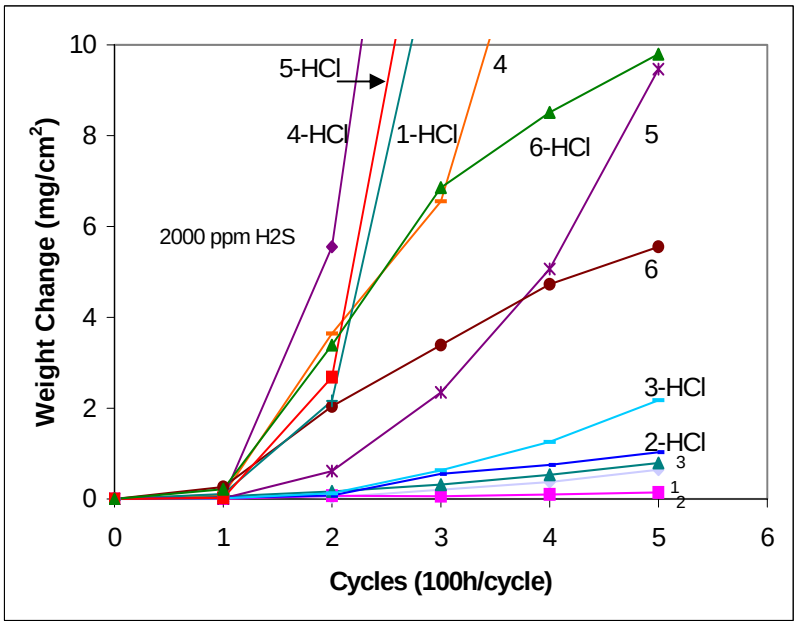

b)

Figure 7. Summary of results of final hot gas corrosion testing with IGCC conditions with enhanced sulfidation, showing a) the overall results, and b) a enlarged vertical scale for the results that allows the best alloys to be distinguished.

In the actual combustion exhaust hot corrosion tests, the SFS combustor gas environment test conditions were established by exposure for 100 hours under natural gas-firing conditions with a

gas composition of 5% O_2 - 29% CO_2 - 45% H_2O – 43 ppm NO_x - 0 ppm SO_2, followed by 8.75 hours of coal firing. Under the coal-fired portion of the test, the test samples were exposed to a gas environment containing 5% O_2 – 22% CO_2 – 22% H_2O – 260 ppm NO_X - 1840 ppm SO_2. During the full run of 108.75 hours, the O-ring samples were maintained at measured temperatures of 921˚C at the convective zone and 604˚C at the exhaust elbow of the air pre-heater. From Fig. 8, the difference in ash buildup on the samples can be observed, with the heavier ash accumulation found at the 921˚C location, closer to the combustor exit. It can be observed from the cross-section SEM micrographs given in Fig. 9 that the porous o-ring samples underwent minimal surface degradation after exposure at both temperatures, with the samples exposed to 604˚C incurring the least attack, as expected.

a)  b) 

Figure 8. Photographs taken of the o-ring samples immediately after SFS combustor gas environment testing for a total of 109 hours under enhanced sulfidizing conditions, showing the difference in fly ash deposition at a) 921˚C and b) 604˚C.

a) 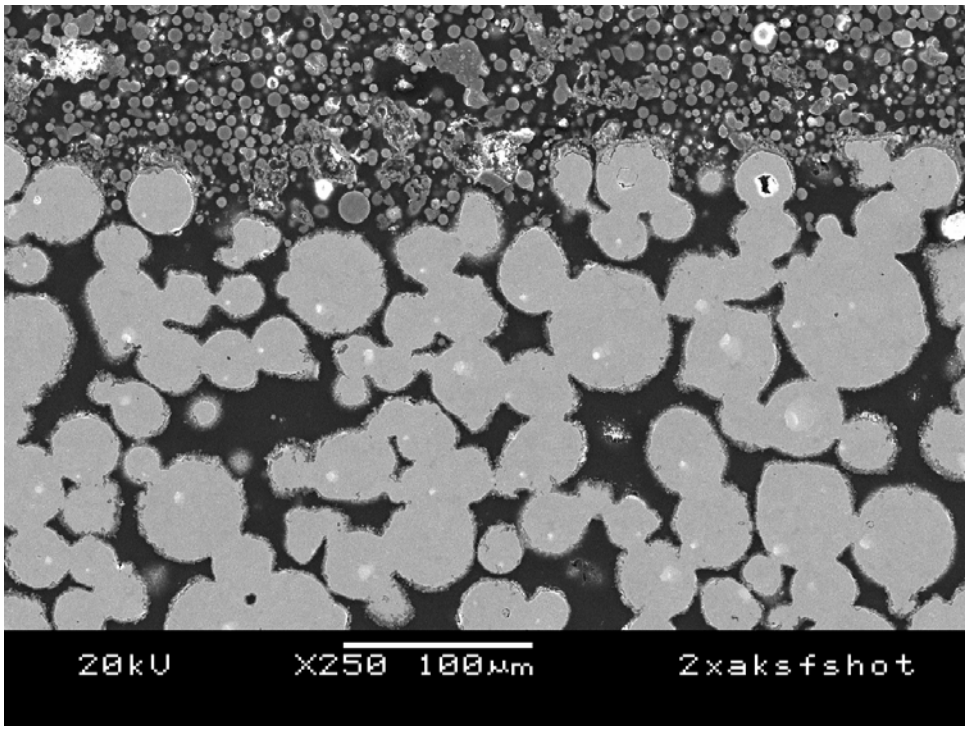

b) 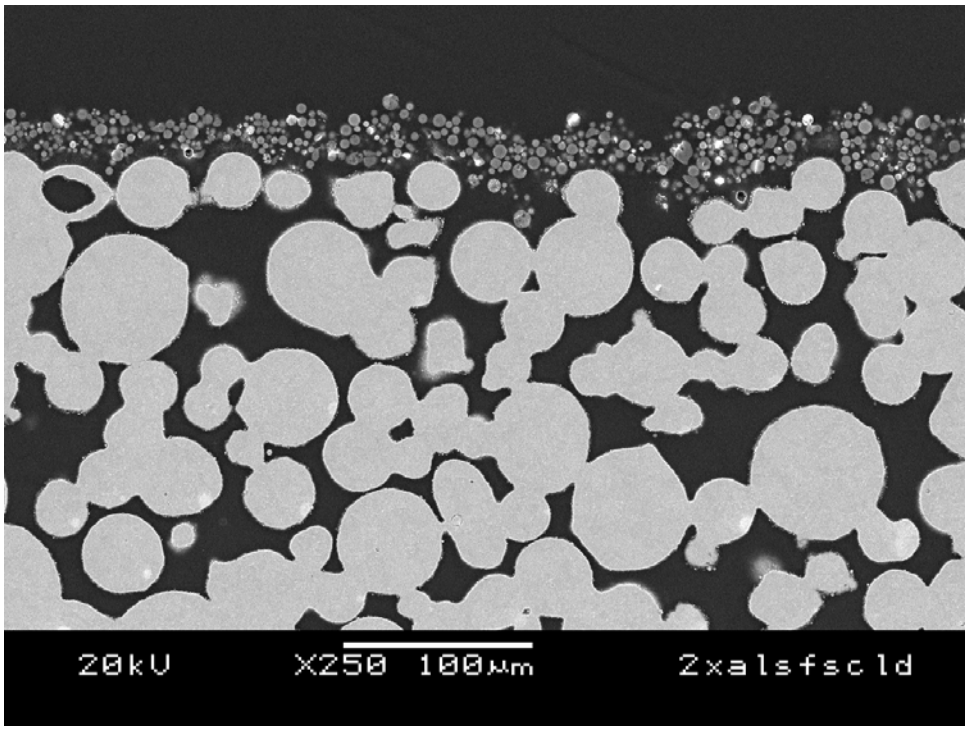

Figure 9. SEM micrographs of as-polished cross-sections of the o-ring samples immediately after SFS combustor gas environment testing for a total of 109 hours under enhanced sulfidizing conditions, showing the difference in corrosive attack at a) 921˚C and b) 604˚C.

DISCUSSION

The high yield, almost 35 wt.%, of ultra-fine (dia. <10 µm) spherical Fe-16Al-2Cr powder, that was generated by discrete-jet, close-coupled gas atomization with He is an indication of the baseline yield of this type of powder production process. One major reason for the high yield of ultrafine powder is the increased gas velocity of the He, nearly 3 times that of N_2, for example, for the same manifold pressure. According to the acceleration wave model of gas atomization, an increased gas velocity should produce a significant refinement of the average particle size, since the gas velocity (relative to the melt) is a squared factor[7]. While it is true that He is a more expensive gas than, e.g., N_2 or Ar, to utilize for gas atomization, commercial He gas atomization facilities typically employ gas recycling to reduce costs. Moreover, several improvements in the gas atomization process, including modifications in both the gas jets and the melt pour tube design, perhaps with alternative inert atomization gas choices, should enable further increases in the ultrafine powder yield for similar alloys. These improvements in powder availability should be useful for gas separation membrane supports and other significant fossil energy applications.

Initial powder yield was classified distinct powder size fractions to permit preliminary sintering trials for gas membrane support materials. Additional powders generated from atomization experiments will be used to support research collaborations with other groups in gas membranes and other FE projects. While some small quantities of the initial powder and sintered porous

samples can be provided to other laboratories for preliminary testing, larger runs (e.g., 25 kg/batch) under similar conditions are planned to provide more useful trial quantities of size classified powder and porous materials.

In the work on hot gas filters, recent reports[11] on development of the thin porous sheet fabrication process, using vacuum sintering of spherical powders, have described characterization methods to gain control of the sintered state to ensure reproducibility. Both tensile and permeability testing have provided useful quantitative criteria, along with microstructure, for assessing suitable sintering conditions for filter samples. Moreover, microstructural analysis of tensile samples of porous Ni-16Cr-9Al-3Fe materials have suggested that second phase coarsening from excessive sintering temperature or time could degrade ductility and corrosion resistance, showing the need for maintaining a close sintering tolerance range or an alloy redesign[13]. This type of alloy redesign may involve a small reduction of the Al content to eliminate Al-rich β-phase formation during sintering, without a significant decrease in Al available to maintain the protective oxide scale[13].

The collected results from aggressive IGCC corrosion tests (enhanced H_2S levels and simulated downtime corrosion) showed that Ni-16Cr-9Al-3Fe had very similar corrosion resistance to a typical iron aluminide composition, Fe-15.8Al-2.2Cr-0.2Zr, after two rounds of testing for 500 hours at 650˚C. Both lower Al levels and Mo additions to this Ni-Cr-Al-Fe alloy appear to degrade its desirable corrosion resistance, but small alloy adjustments and minor alloying additions could prove useful for further increases in performance for IGCC applications, both at conventional operating temperatures, 600-700˚C, and during off-normal temperature excursions into the 900˚C range. The combustion environment exposure results substantiate the laboratory-scale gas exposure tests by showing the exceptional high-temperature robustness and degradation resistance of the Ni-Cr-Al-Fe filter alloy and porous material processing developed in this study. These hot gas corrosion and combustion environment results, along with previous work[11], indicate that the combination of ambient temperature (sheet deformation) ductility and high temperature strength, along with weldability, make the Ni-Cr-Al-Fe alloys highly competitive with iron aluminides for hot gas filtration in advanced combustion applications.

CONCLUSIONS

High yields (35%) of ultra-fine (dia. <10 μm) spherical powder of high temperature alloy (Fe_3Al) can be generated by high pressure gas atomization with He. The atomization gas (He) was selected to provide baseline data on the expected powder size distribution for the use of a typical close-coupled discrete jet nozzle with high gas velocity.

The initial powder yield was classified into two distinct powder size fractions to permit preliminary sintering trials for gas membrane support materials. Subsequent atomization experiments will be conducted with advanced nozzle designs to explore use of alternative atomization parameters for improved ultra-fine powder yields. Powders generated from atomization experiments will be used to support research collaborations with other groups in gas membranes and other FE projects.

The Ni-16Cr-9Al-3Fe and Fe-15.8Al-2.2Cr-0.2Zr alloys (or minor variants) can be recommended for future hot gas filtration trials for IGCC applications (<650˚C) with significant downtime corrosion problems, but Ni-16Cr-9Al-3Fe would be preferred (due to high temperature strength) if higher temperature excursions may be encountered. The robust performance of the rolled and welded thin sheets of porous Ni-16Cr-9Al-3Fe in actual combustion environment exposure tests is strong support for the hot gas filter material fabrication approach that was developed in this project, as well as for the alloy design.

ACKNOWLEDGEMENTS

Support from: USDOE-FE(ARM) and USDOE-BES (Materials Sciences) through contract No. W-7405-ENG-82.

REFERENCES

1. A. Lawley, "Atomization: The Production of Metal Powders," MPIF, Princeton, NJ, 1992, pp. 102-107.

2. A. J. Yule and J. J. Dunkley, "Atomization of Melts for Powder Production and Spray Deposition," Oxford University Press, New York, NY, 1994, pp. 30-38.

3. I. E. Anderson, R. S. Figliola, and H. Morton, "Flow Mechanisms in High Pressure Gas Atomization", *Materials Science and Engineering* **A148**, 1991, pp.101-114.

4. I. E. Anderson, R. L. Terpstra, and S. Rau, "Enhanced Understanding of High Pressure Gas Atomization Processing, Powder Materials: Current Research and Industrial Practices", compiled by F. D. S. Marquis, N. N. Thadhani, and E. V. Barrera, The Minerals, Metals, and Materials Society, Warrendale, PA, 2001, pp. 3-18.

5. I. E. Anderson, R. S. Figiola, R. L. Terpstra, S. Rau and B. Rauscher, "Progress in Experimental Analysis of Gas Atomization Process Physics", *Advances in Powder Metallurgy and Particulate Materials*, compiled by V. Arnhold, C.-L. Chu, W.F. Jandeska, and H. I. Sanderow, Metal Powder Industries Federation, Princeton, NJ, 2002, part 3, pp. 150-162.

6. I. E. Anderson and R. L. Terpstra, "Progress Toward Gas Atomization Processing with Increased Uniformity and Control," *Materials Science and Engineering*, **A326**, (2002), p. 101.

7. R. D. Ingebo, "Capillary and Acceleration Wave Breakup of Liquid Jets in Axial-Flow Airstreams", NASA Technical Paper 1791, National Aeronautics and Space Administration, Scientific Technical Information Branch, 1981, pp. 1-10.

8. B. L. Bishoff, R. R. Judkins, K. D. Alcock, and L. E. Powell, "Development of Inorganic Membranes for Hydrogen Separation," in Conference Proceedings of 17th Annual Conference on Fossil Energy Materials, 2003, available at the USDOE website: www.netl.doe.gov.

9. P. F. Tortorelli, E. Lara-Curzio, D. McCleary, J. Sawyer, and R. R. Judkins, "Characterization of Field-Exposed Iron Aluminide Hot Gas Filters," in Proceedings of the 5th International Symposium on Gas Cleaning at High Temperatures, USDOE/NETL, Morgantown, WV, DOE/NETL-2003/1185, paper no. 4.3, 15 pages, available at the USDOE website: www.netl.doe.gov.

10. A. Unal, "Effects of Processing Variables on Particle Size in Gas Atomization of Rapidly Solidified Aluminum Powders," *Materials Science and Technology*, **3** (1987), pp. 1029-1039.

11. R. L. Terpstra, I. E. Anderson, and B. Gleeson, "Development of Metallic Hot Gas Filters," in Advances in Powder Metallurgy and Particulate Materials-2001, MPIF-APMI, Princeton, NJ, Vol.8, 2001 pp. 84-97.

12. I. E. Anderson, B. Gleeson, and R. L. Terpstra, "Development of Metallic Hot Gas Filters," in Conference Proceedings of 16th Annual Conference on Fossil Energy Materials, 2002, available at the ORNL (USDOE) website: www.ornl.gov/fossil/.

13. R. L. Terpstra, I. E. Anderson, and B. Gleeson, "Alloy Development for Hot Gas Filters," in *Advances in Powder Metallurgy and Particulate Materials — 2002*, compiled by V. Arnhold, C.-L. Chu, W. F. Jandeska, Jr., H. I. Sanderow (Metal Powder Industries Federation, Princeton, NJ), (2002) pp. 1-92 to 1-102 (2002).

NOVEL ACTIVATED CARBON COMPOSITES FOR AIR SEPARATION

Tim Burchell, Omats Omatete, Nidia Gallego, and Fred Baker
Carbon Materials Technology Group
Oak Ridge National Laboratory

ABSTRACT

The adsorption behavior of oxygen and nitrogen on a novel carbon fiber composite material was investigated using static and dynamic techniques. The kinetic studies revealed that oxygen was more rapidly adsorbed on the carbon composite than nitrogen, and at higher uptake under equilibrium conditions. Preliminary dynamic separation experiments indicated that the carbon composite is capable of separating oxygen and nitrogen from air on the basis of the markedly different diffusion rates of the respective molecules in the narrow micropore network of the adsorbent. The dependence on the degree of activation of micropore size distribution in the carbon composite is discussed, and related to molecular sieving effects. A gas separation process is proposed which would exploit the unique electrical properties of the novel carbon composite material.

INTRODUCTION

A novel adsorbent material, carbon fiber composite molecular sieve (CFCMS), has been developed by the Oak Ridge National Laboratory (ORNL) [1-3]. Upon thermal activation, usually in CO_2 or steam, the carbon fiber-based material develops a large micropore volume (0.5-1.0 cm^3/g) and high BET surface area (1000-2200 m^2/g). A typical nitrogen adsorption isotherm for a sample of CFCMS is shown in Figure 1. The isotherm exhibits the classic type-I shape under the BDDT classification [4], indicating that CFCMS is microporous.

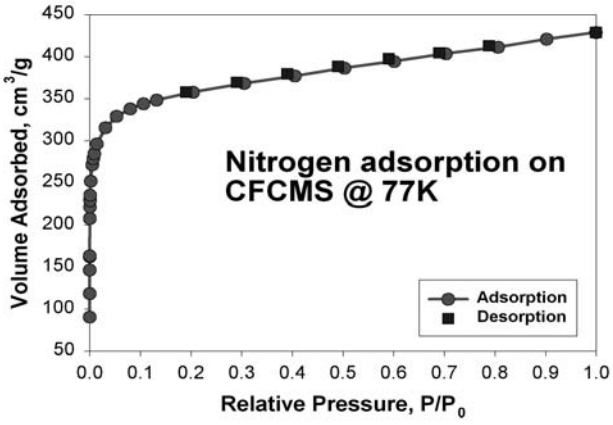

Figure 1 - A typical type-I N_2 adsorption isotherm for CFCMS material

Confirmation of the highly microporous nature of CFCMS material was obtained through small angle neutron scattering (SANS) studies. SANS data reproduced in Figure 2 for high pressure adsorption of deuterated methane (CD_4) on CFCMS material shows that the bulk of CD_4 adsorption occurs in micropores; i.e., at high Q (A-1) values.

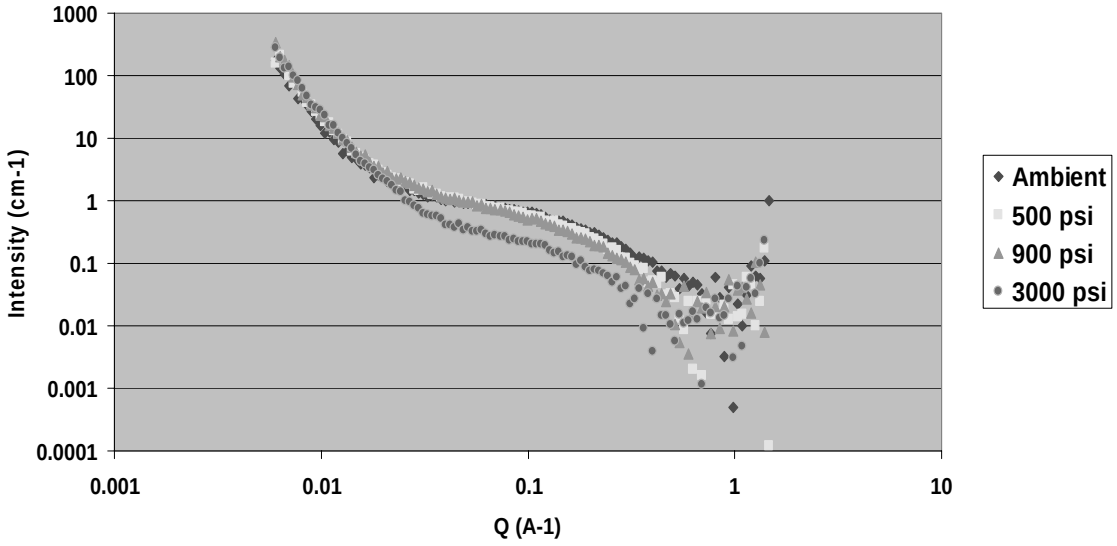

Figure 2 - SANS data showing CD_4 filling micropores of CFCMS material

As shown in the scanning electron microscopy (SEM) image in Figure 3, the structure of CFCMS consists of ~12 μm diameter carbon fibers bonded at their contact points to provide a continuous carbon skeleton that is electrically conductive. The structure is open and permeable, which allows fluids to readily flow through the material with minimal pressure drop. The unique combination of the open structure, microporosity, and electrical conductivity allows the material to be used in a regenerative, electrical swing adsorption (ESA) system [5-7].

In essence, ESA is an electrical analog of pressure swing adsorption (PSA), whereby desorption of the adsorbate is facilitated by the passage of an electric current through the adsorbent to obtain resistive heating. In this context, CFCMS represents an enabling technology for an ESA process in which efficient desorption could be achieved in the absence of pressure swings. The bottom line is that significant energy savings could be realized because the adsorption beds do not, in principle, require repressurization after each desorption step. This is consistent with the viewpoint of Jasra et al. [8], who in a review of the separation of gases by PSA noted that "although there is some room for improvement in the PSA process, the potential gains in process economics in the future are likely to come from the development of new and improved adsorbents."

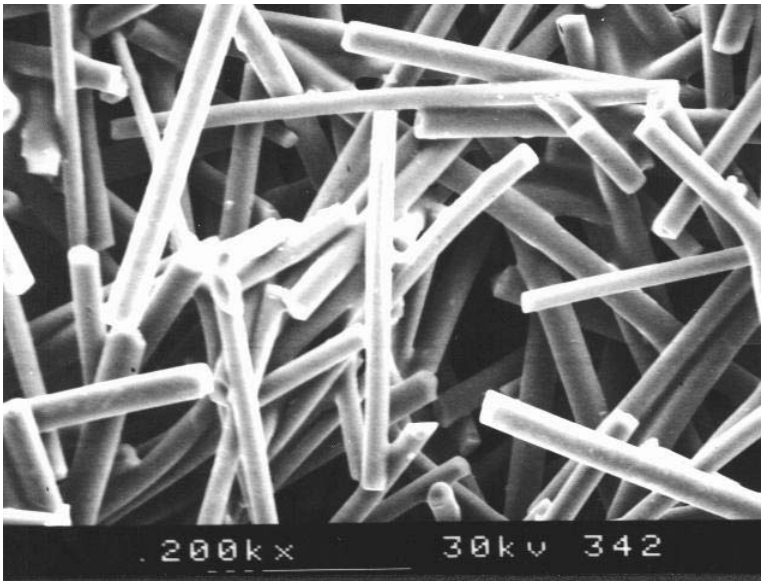

Figure 3 - SEM image showing the macrostructure of CFCMS material

The nanoscale structure of CFCMS is shown in the transmission electron microscope (TEM) image in Figure 4. The structure of the carbon is essentially amorphous but individual graphene layers can be discerned. Micropores of <2 nm in width are evident, and it appears that they are neither cylindrical nor slit-shaped.

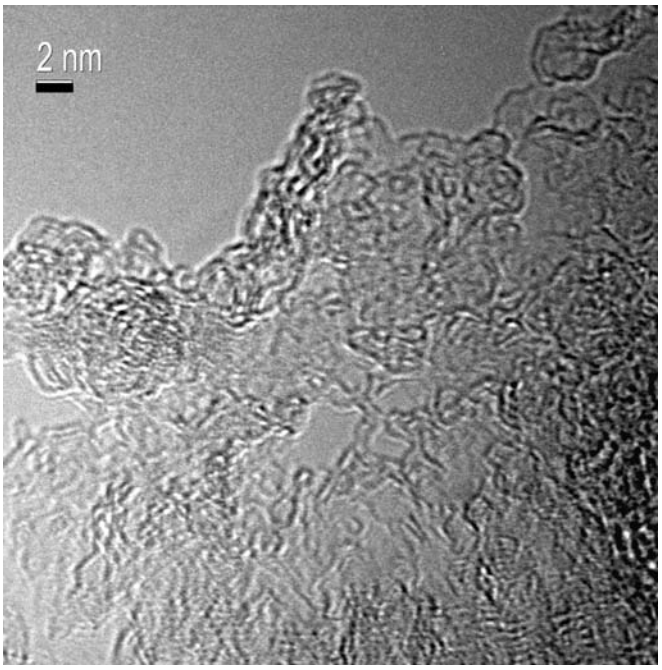

Figure 4 - TEM image of the nanoscale structure of CFCMS material

In this paper, a preliminary evaluation of the potential for the separation of air using CFCMS material coupled with ESA is described.

EXPERIMENTAL

CFCMS FABRICATION PROCESS

CFCMS billets were produced using the slurry molding process illustrated in Figure 5. The billets were manufactured from an isotropic pitch fiber developed by Ashland Petroleum, and a powdered phenolic resin from Occidental Chemicals. Using a purpose-built vacuum slurry molding apparatus at ORNL (Figure 6), the fibers and resin were combined at a ratio of four parts fiber to one part resin powder (by weight) in water to form a dilute slurry, and molded in a process somewhat similar to the forming of a pulp fiber mat in a papermaking process.

After molding, the green CFCMS billets were dried at ~60°C for 24 hours and then heated to 150°C for a further 24 hours to cure the phenolic resin. The billets were carbonized in a nitrogen atmosphere at 650°C for 4 hours, followed by thermal activation in a CO_2 atmosphere at 850°C until the desired level of carbon burn-off, i.e., activation, was attained (as measured by weight-loss). The two billets were designated CFCMS-1 and CFCMS-2. The carbon burn-off levels were 10 and 26%, respectively.

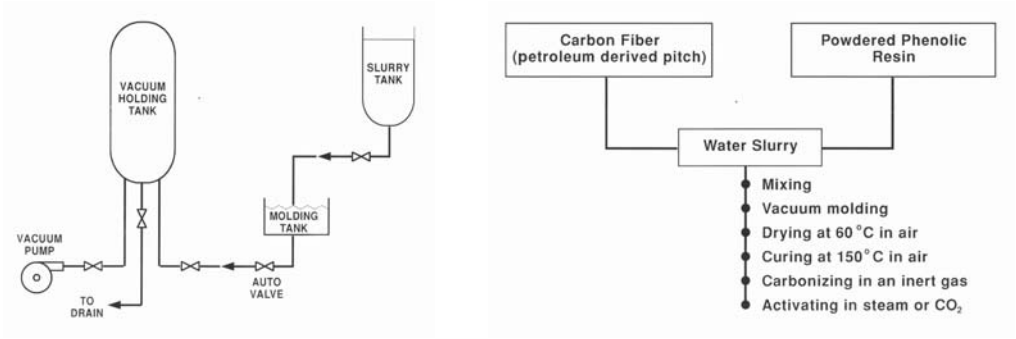

Figure 5 - Schematic of CFCMS slurry molding equipment and major processing

Figure 6 - The CFCMS slurry molding equipment at ORNL

MATERIALS CHARACTERIZATION

The surface area and pore size distribution of representative samples of the activated CFCMS billets were characterized via nitrogen adsorption at -196°C (77K) and CO_2 adsorption at 0°C (273K) using a Quantachrome Autosorb-1 instrument. Apparent surface areas were derived from the N_2 and CO_2 adsorption isotherms using the standard BET method [9, 10]. Micropore volume and mean micropore width were estimated using the Dubinin-Radushkevich (D-R) equation [10, 11]. The microstructure of the adsorbent carbon composites was investigated using a Hitachi S4700 Field Emission Scanning Electron Microscope (SEM) at a working distance of 5 mm. The accelerating voltage was 5 kV and the emission current was 15 μA.

HIGH PRESSURE GAS ADSORPTION EXPERIMENTS

Samples of the CFCMS materials (100-200 mg) were placed on a Hidden IGA high-pressure thermo-gravimetric analyzer (Figure 7) and outgassed under high vacuum ($< 10^{-6}$ mbar) at a temperature of 300°C. Adsorption isotherms of pure O_2 and N_2, respectively, were determined at room temperature over the pressure range 0-2 MPa (0-20 bar) at pressure intervals of 0.1 MPa (1 bar). The sample mass was constantly monitored as the pressure was progressively ramped to 2 MPa to obtain adsorption kinetics data, in addition to the equilibrium uptake data at each incremental pressure.

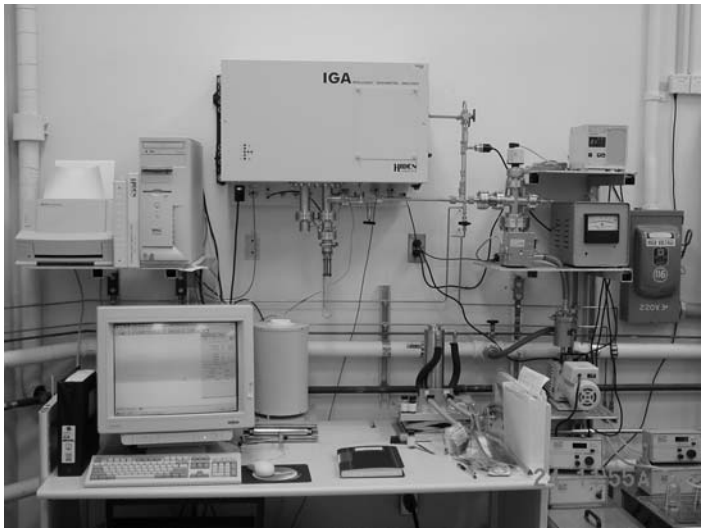

Figure 7 - Hidden IGA high pressure microbalance (IGA)

2.4. Dynamic Air Separation Experiments

Preliminary dynamic air separation experiments were conducted in a breakthrough apparatus shown schematically in Figure 8. The separation experiments were conducted at room temperature and ambient pressure using bottled compressed air. Air separation studies were conducted on CFCMS-1 assembled into the ESA cell pictured in Figure 20.

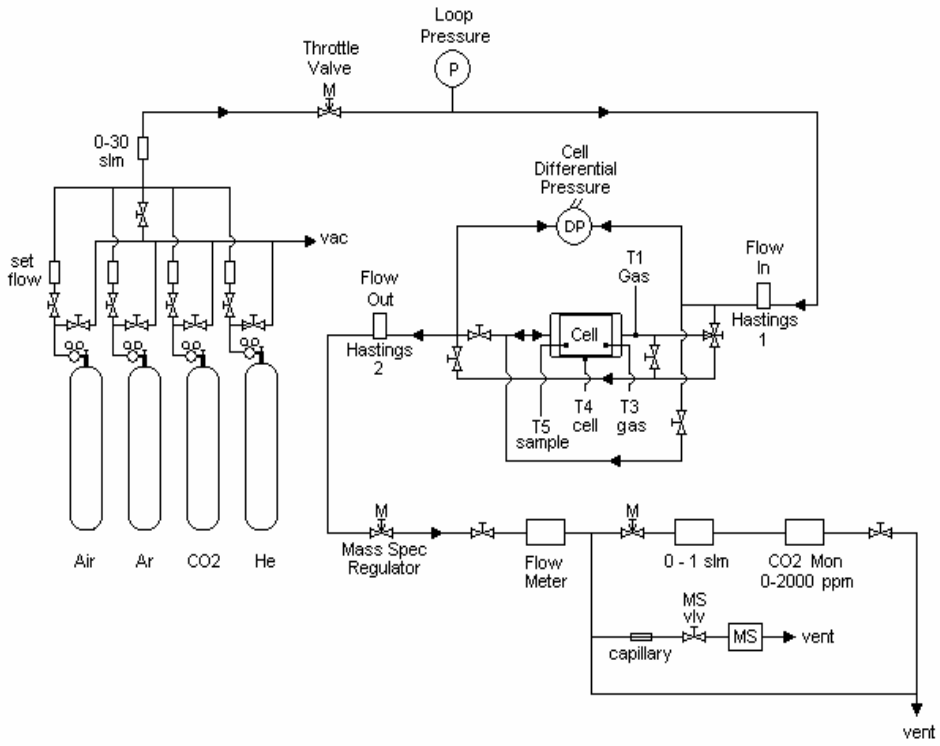

Figure 8 - Schematic diagram of breakthrough apparatus

Breakthrough experiments were conducted at an air flow rate of 1.0 standard liters per minute (slpm) and at a temperature of 21°C. Prior to conducting breakthrough runs, the CFCMS/ESA cell was conditioned by flowing dry He through the cell at a rate of 1.4 slpm to purge the lines and cell. The exhaust gas composition was monitored using an Aero Vac Odyssey magnetic sector mass spectrometer (Vacuum Technology, Inc.).

RESULTS AND DISCUSSION

CFCMS MATERIAL CHARACTERIZATION

The macrostructure of CFCMS as revealed by SEM examination is shown in Figures 3 and 9, from which it is apparent that the individual carbon fibers were bonded at their contact points with carbon derived from the phenolic resin binder. The resultant structure is rigid, fairly strong, and provides a continuous, electrically-conductive carbon skeleton.

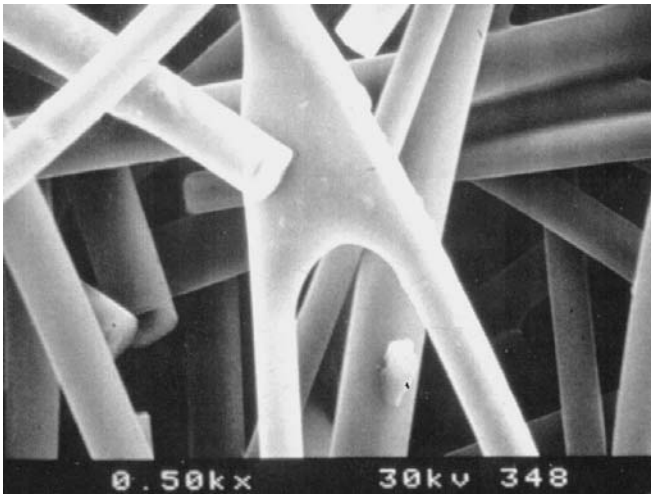

Figure 9 - SEM image of the macrostructure of CFCMS

Nitrogen adsorption isotherms for the two CFCMS materials are shown in Figure 10. Both are type-I, characteristic of a microporous adsorbent [4, 10]. A small degree of hysteresis is apparent over the pressure range of $0.1 < P/Po < 1.0$ for CFCMS-2, which is consistent with its larger mesopore volume (Figure 11).

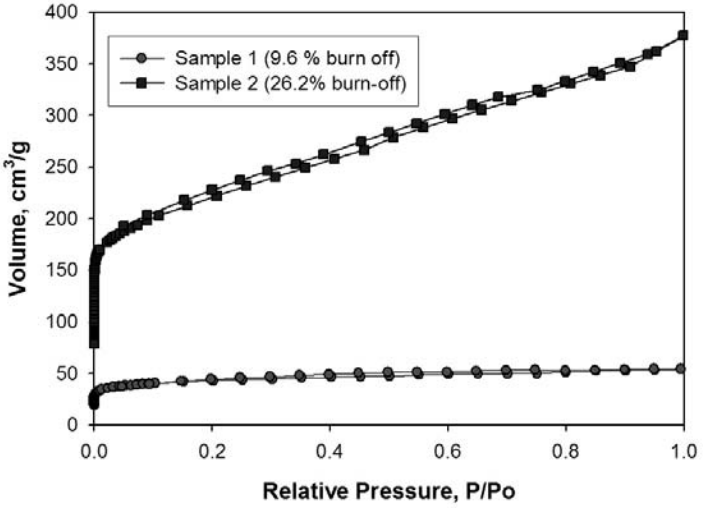

Figure 10 - N_2 adsorption isotherms at 77K for CFCMS-1 and CFCMS-2

Surface area and micropore volume data derived from the N_2 adsorption isotherms at 77K are reported in Table 1. CFCMS-2 exhibited significantly larger BET surface area and micropore volume than CFCMS-1, which is consistent with the higher burn-off of the former. Both samples had similar mean micropore widths (nominal) as calculated using the Dubinin-Radushkevich (D-R) approach [10-12]. However, as shown by the Dubinin-Astakov (D-A) plots [10] in Figure 11, the distribution of pore sizes was different between the two composites. CFCMS-1, which had the apparently much smaller micropore volume, exhibited a narrower pore size distribution.

Table 1 - Nitrogen surface area and micropore volume data for CFCMS materials

Property	Billet	
	CFCMS-1	CFCMS-2
Burn-off, %	9.6	26.2
BET Surface Area, m^2/g	158	637
D-A Micropore Surface Area, m^2/g	175	671
D-R Micropore Volume, cm^3/g	0.06	0.24
D-R Micropore Avg. Width, nm	2.1	1.9

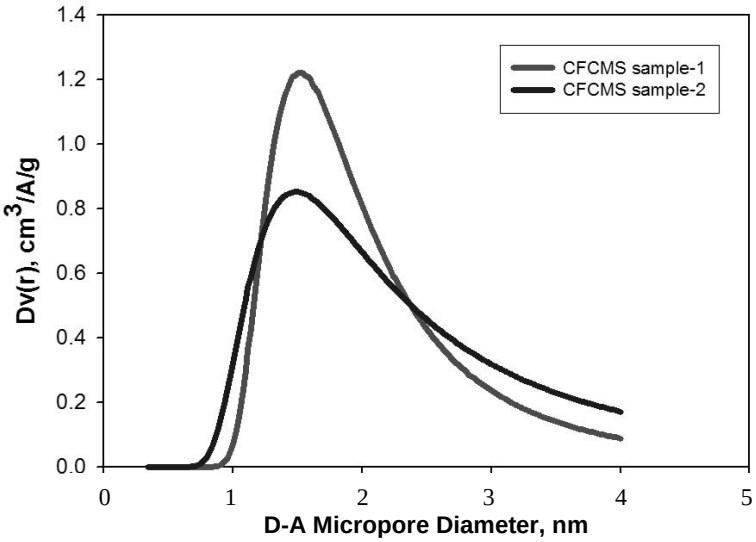

Figure 11 - DA micropore diameter distribution for CFCMS-1 and CFCMS-2,

To better differentiate between the micropore size distributions of the two CFCMS composites, CO_2 adsorption isotherms were measured at 273K (Figure 12). The flat molecular shape of CO_2 allows it to penetrate narrower pores than N_2, thus revealing details of the smallest micropores. The use of CO_2 adsorption for the characterization of microporous carbons has been advocated [13] to overcome the slow diffusion or possible exclusion of N_2 molecules from the smallest pores at 77K.

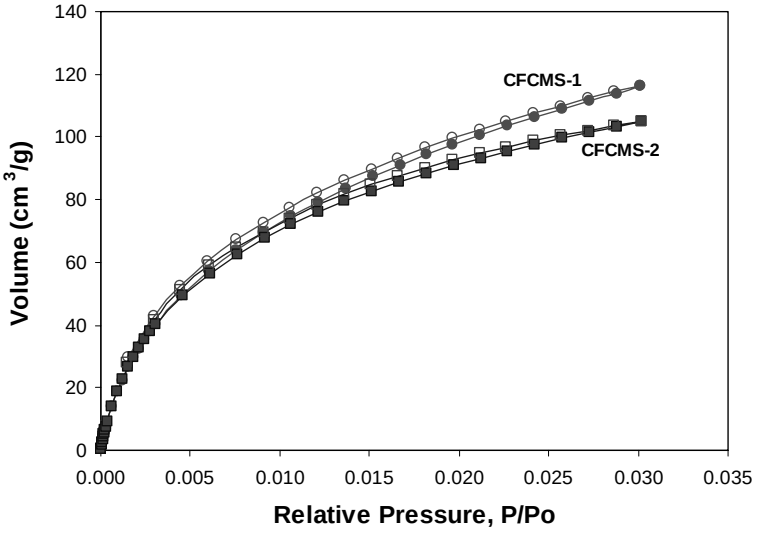

Figure 12 - CO_2 adsorption isotherms at 273K for CFCMS-1 and CFCMS-2

Both isotherms in Figure 12 are type-I, but, in very marked contrast to the case for nitrogen adsorption, CFCMS-1 adsorbed significantly more CO_2 than CFCMS-2. From the CO_2 adsorption data shown in Table 2, it is apparent that the BET surface area and D-R micropore volume were greater, by about 25%, for the CFCMS-1 composite. It should also be noted that the BET surface area and micropore volume of the CFCMS-1 composite as calculated from the CO_2 adsorption data were very much greater than those obtained from the nitrogen adsorption data, clearly indicating a molecular sieve effect.

Although there was no significant difference between the D-R micropore widths of the two composites, the higher CO_2 micropore volume of CFCMS-1 indicated that this material (10% burn-off) almost certainly contained a greater proportion of very small micropores compared to the CFCMS-2 material (26% burn-off). This observation is significant since the separation of O_2 and N_2 is a kinetic phenomenon, relying on the differences in the diffusion rates of the two molecules in narrow pore networks. The closer the pore width is to the molecular dimensions of the gasses the more significant the kinetic effects will be. Lower carbon burn-off appears to be advantageous in this respect.

Table 2 - CO_2 surface area and micropore volume data for CFCMS materials

Property	Billet	
	CFCMS-1	CFCMS-2
Burn-off, %	9.6	26.2
BET Surface Area, m^2/g	1003	805
D-R Micropore Surface Area, m^2/g	1258	1044
D-R Micropore Volume, cm^3/g	0.54	0.45
D-R Micropore Avg. Width, nm	1.6	1.5

High Pressure, Single Gas Equilibrium Adsorption Studies

Using the Hidden IGA instrument shown in Figure 7, adsorption isotherms of pure O_2 and N_2, respectively, were determined on the CFCMS materials over a pressure range 0-2 MPa, each at temperatures of 294 and 338K. The equilibrium uptakes of O_2 and N_2 at each of these temperatures are shown in Figures 13 and 14 for the CFCMS-1 material, the product with the narrower pore size distribution. In both Figures, adsorption points are depicted as closed symbols and desorption points as open symbols.

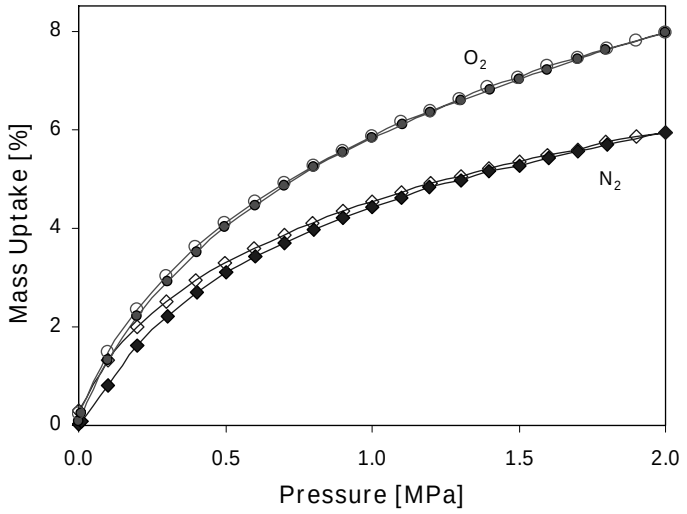

Figure 13 - High pressure O_2 and N_2 adsorption isotherms on CFCMS-1 at 294K

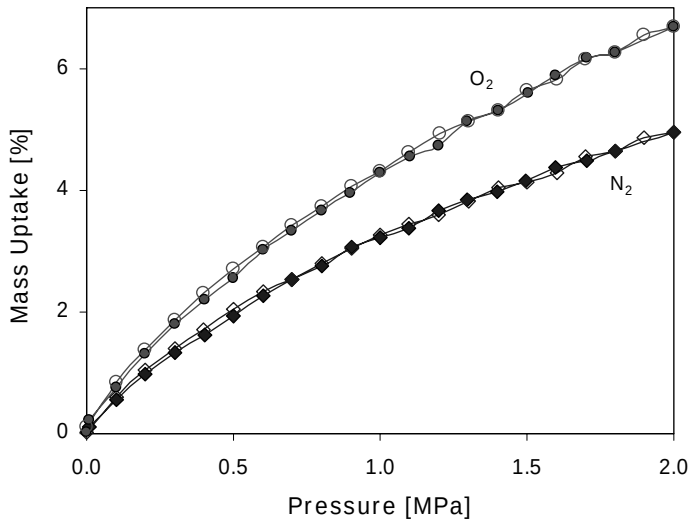

Figure 14 - High pressure O_2 and N_2 adsorption isotherms on CFCMS-1 at 338K

In keeping with adsorption thermodynamics, equilibrium uptake of each gas decreased with increasing temperature. At each temperature, the equilibrium uptake of O_2 on the CFCMS material exceeded that of N_2. However, the differences between the equilibrium uptakes of N_2 and O_2 on the CFCMS material were small, and insufficient to indicate that the two molecules could be efficiently separated purely on the basis of their equilibrium adsorption behavior. For example, at 2 MPa pressure and 294K, the uptakes of O_2 and N_2 on the CFCMS material were ~8 and ~6 wt%, respectively.

Single Gas Dynamic Adsorption Studies

Work by many researchers on molecular sieving carbons has shown that the separation of N_2 and O_2 must be based on the differences in the diffusions rates through narrow pores; i.e., kinetic, not equilibrium selectivity [8, 14]. Therefore, dynamic gas adsorption measurements were made on the CFCMS composites, in which the adsorption of N_2 and O_2 at 294K was measured as a function of time to examine the approach to equilibrium (during and after a constant rate pressure rise from 0.0001 to 0.1 MPa). This pressure range was selected because the isotherms shown in Figures 13 and 14 are steepest at low pressure, and therefore kinetic effects should be more easily observed.

The kinetic plots for O_2 and N_2 adsorption on the CFCMS-1 material are shown in Figures 15 and 16, respectively. Each figure includes the sample temperature (upper pane), the pressure change (center pane), and the mass gain (lower pane), each as a function of time. The corresponding plots for O_2 and N_2 adsorption on the CFCMS-2 material are shown in Figures 17 and 18, respectively.

It is apparent from Figure 15 that the rate of O_2 adsorption on the CFCMS-1 material was rapid, followed the pressure change closely, and ended very shortly after the set pressure limit of 0.1 MPa was reached. Thus, equilibrium was established very quickly for oxygen adsorption on the CFCMS-1. In marked contrast, N_2 adsorption on the same material (Figure 16) occurred extremely slowly, with no mass gain observed until well after the pressure increase was initiated. Moreover, approximately 50% of the mass gain occurred after the pressure step was completed at 0.1 MPa. Saturation of the sample mass was very slow, taking ~10 minutes to approach equilibrium. For both gases, the expected increase in sample temperature during the adsorption process was observed.

From Figures 17 and 18, it is apparent that the difference in rates of O_2 and N_2 adsorption was much less marked for the CFCMS-2 material, however. Although O_2 adsorption equilibrated more rapidly than N_2 adsorption, equilibrium for both O_2 and N_2 adsorption on the CFCMS-2 material was reached relatively soon after the pressurization step ended at 0.1 MPa. Thus, the N_2 adsorption behavior of CFCMS-1 and CFCMS-2 were significantly different, with the former exhibiting slow adsorption and the latter relatively fast adsorption. The N_2 molecule is larger in size than the O_2 molecule (critical diameters of 0.30 and 0.28 nm, respectively), and consequently kinetic effects will be more noticeable when pore sizes are very small and comparable with adsorbate molecular size. In this context, the kinetic data for O_2 and N_2

adsorption on the two CFCMS materials are consistent with the fact that the micropore volume of CFCMS-1 (10% burn-off) was significantly greater than that of CFCMS-2 (26% burn-off); i.e., as determined via CO_2 adsorption (Table 2).

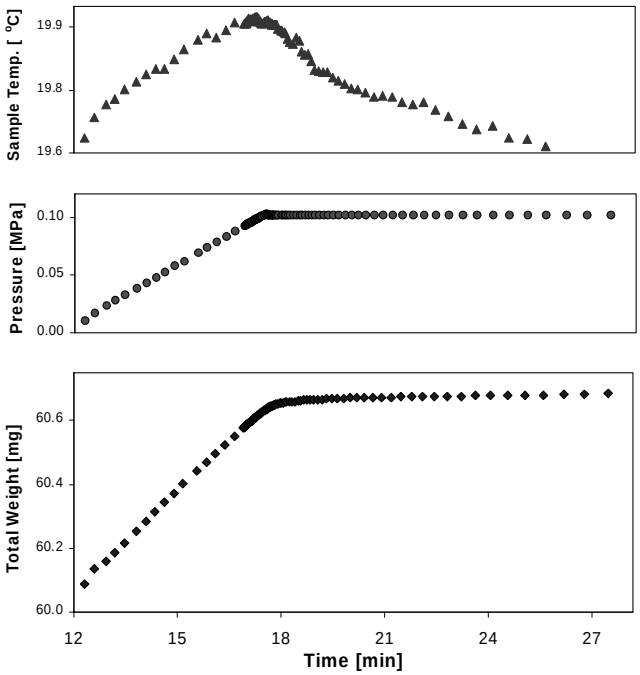

Figure 15 - O_2 adsorption kinetics data for CFCMS-1 at 294K

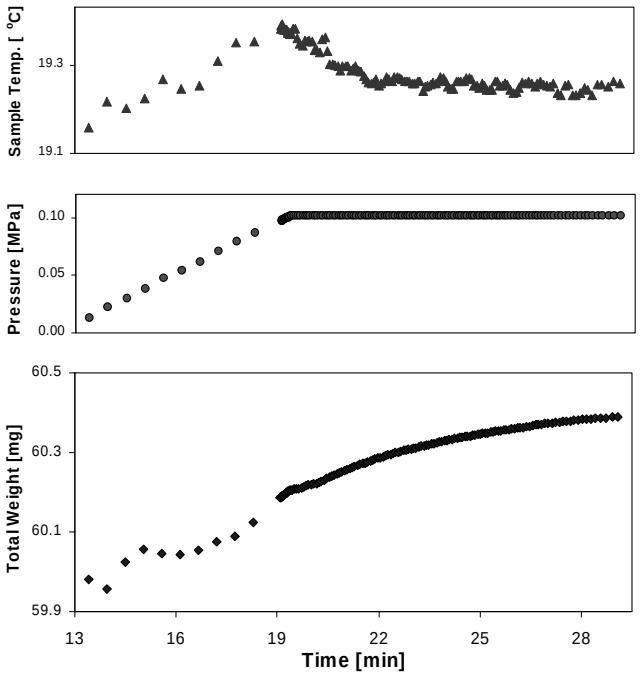

Figure 16 - N_2 adsorption kinetics data for CFCMS-1 at 294K

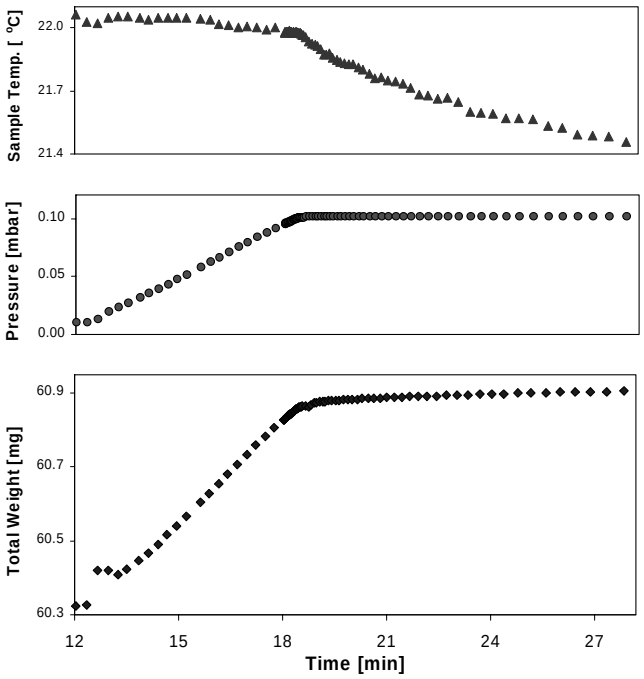

Figure 17 - O_2 adsorption kinetics data for CFCMS-2 at 294K

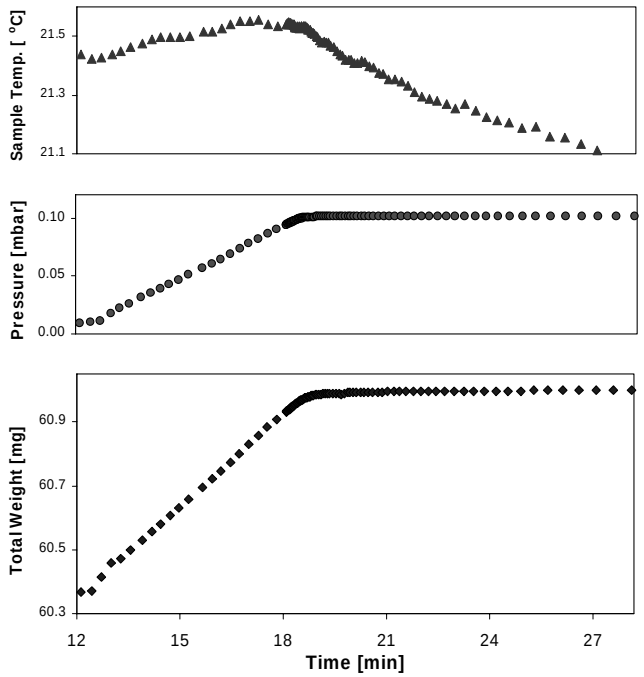

Figure 18 - N_2 adsorption kinetics data for CFCMS-2 at 294K

GENERAL DISCUSSION

Potential nanostructures of molecular sieving carbons that contribute to air separation are illustrated in Figure 19 (I and II). The third illustration (III) in Figure 19 depicts a possible modification to a microporous carbon that would potentially enhance its molecular sieving capability and adsorption capacity for kinetically-separated gases.

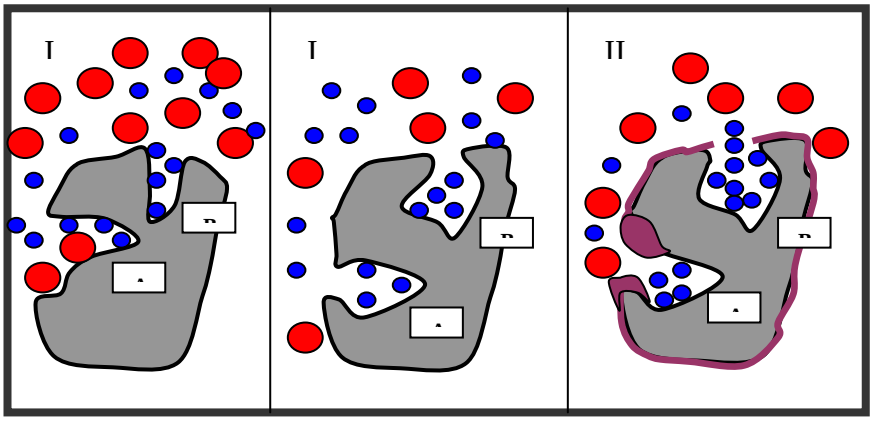

Figure 19 - Illustration of the gas separation mechanisms of carbon molecular sieves

I. Narrow pores in which kinetic separation ("A") or size exclusion occur ("B")
II. Kinetic separation ("A") and size exclusion enhanced by nano-pore shape ("B")
III. Modification of a non-sieving carbon by deposition of a carbon layer to alter pore shape ("A") or to create a nano-porous membrane ("B")

Gas separation in pore "A" in Figure 19-I occurs by virtue of the difference in diffusion rates of different size gas molecules in narrow pores (kinetic separation), whereas in pore "B" of the same Figure gas separation is solely by size exclusion; i.e., the larger molecule cannot penetrate the nano-dimension pore. In Figure 19-II, however, the "ink-bottle" shape of the micropore ("A" and "B") allow kinetic separation and size exclusion mechanisms to both operate. As depicted in Figure 19-III, molecular-sieving properties can be imparted to a porous carbon, which is not inherently a molecular sieve material, by the subsequent deposition of a carbon layer. The sieving layer, which may be deposited by carbon vapor deposition (CVD), can be in the form of a semi-permeable membrane (pore "B") or as a thick deposit around the pore opening, which in essence creates an "ink bottle" type pore shape (pore "A").

It is postulated that the CFCMS-1 material exhibits the molecular-sieving mechanisms illustrated in Figure 19 (I & II). The formation of a molecular sieving layer or modification of pore shape, illustrated in Figure 26 (III), offers the potential of converting a high capacity, but non-sieving adsorbent, such as CFCMS-2, into a sieving adsorbent carbon capable of kinetically separating O_2 and N_2 in air. Although the difference in the critical molecular diameters of O_2 and N_2 is small (0.02 nm), the difference in their diffusion rates is, by comparison, quite large [8]; namely

$D/r^2 = 1.7 \times 10^{-4}$ s^{-1} for O_2 compared to 7×10^{-6} s^{-1} for N_2. Thus, it is further postulated that the diffusion mechanism illustrated by pore "A" in Figure 26 (I, II, III) is more favorable than the size exclusion mechanism represented by pore "B" in the same Figures.

In summary, the work described here indicates that an air separation system based upon CFCMS/ESA could be developed. The dynamic separation experiments revealed that the difference in breakthrough times between O_2 and N_2 is very small, indicating that short cycle times would be sufficient; i.e., on the order of one minute. Moreover, the shape of the high pressure isotherms for O_2 and N_2 adsorption on the CFCMS samples indicates that air pressurization above about 0.5 MPa would be unproductive (and uneconomical).

An experimental ESA cell used in the work reported here is shown in Figure 20, and a simple schematic of its set-up is illustrated in Figure 21.

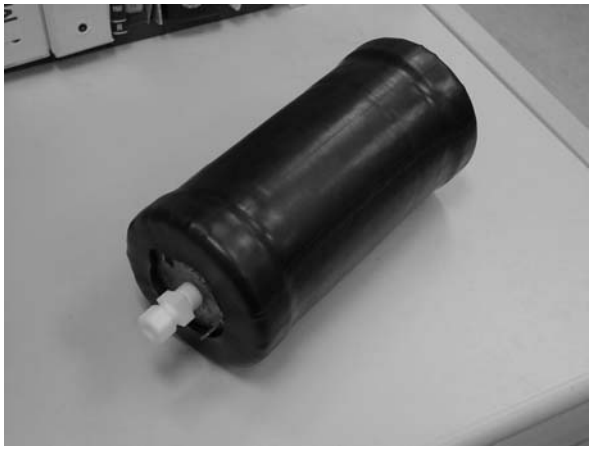

Figure 20 - Experimental ESA cell containing a block of CFCMS material

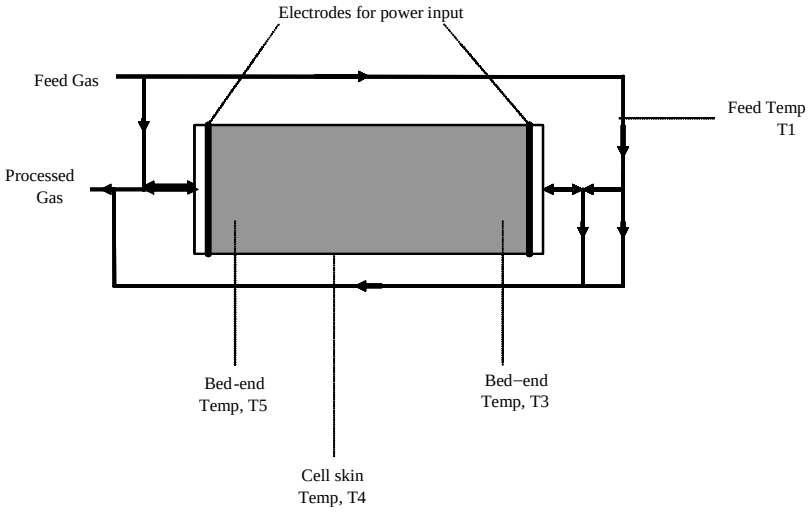

Figure 21 - Schematic of experimental ESA cell

It is envisaged that several CFCMS/ESA cells, appropriately sized for the required O_2 (and N_2) production rate, would be incorporated into a separation system with all necessary piping, valves, and control systems for switching gas flows from cell to cell (based on cycle times for the separation, regeneration, and re-equilibration steps). A moderate pressure (< 0.5 MPa) air stream would be directed into the first ESA cell. Oxygen would be preferentially adsorbed and the high-pressure effluent stream would be enriched in N_2. If desired for nitrogen production, further enrichment in nitrogen content could be obtained by cascading the effluent stream through another adsorption cell. After a short duration (~1 minute) the air flow would be directed to a second CFCMS/ESA cell, allowing the first cell to be regenerated electrically (and possibly depressurized). The product gas from Cell 1, enriched in O_2 desorbed from the CFCMS adsorbent, would be piped to a storage reservoir for use, for example, in a fuel cell (as the oxidant gas), and/or cascaded through another CFCMS/ESA cell for further enrichment.

When regeneration (O_2 desorption) of Cell 1 is complete, it would be allowed to thermally equilibrate and placed in standby mode, ready to accept the moderate pressure air feed. Temperature excursions during electrical regeneration of the CFCMS adsorbent could be minimized, perhaps avoided, by applying only that amount of electrical power required to compensate for the energy of gas desorption. A small gas purge could be used to accelerate gas desorption and cell regeneration, which could be drawn from the nitrogen-rich effluent stream from cells during the adsorbing cycles. When Cell 2 becomes saturated, the high pressure air stream would be switched to a third cell, and Cell 2 regenerated. The moderate pressure feed gas, switching sequentially through the cells, would be returned to the first cell when thermal equilibration was (reasonably) established.

Depending on product demand, cell size, O_2 (and N_2) capacity, and equilibration times required, the overall system could consist of many CFCMS/ESA cells. Ideally, regeneration of the CFCMS/ESA cells would be achieved entirely with electrical stimulation; i.e., process economics would be greatly improved if depressurization was avoided, certainly minimized.

SUMMARY AND CONCLUSIONS

- ORNL has developed a novel monolithic adsorbent carbon composite material, designated CFCMS.
- CFCMS material has an open, permeable structure, yet is reasonably strong.
- When activated, the carbon fibers in CFCMS become highly microporous.
- Gas adsorption on the CFCMS is associated with micropores in the carbon fibers.
- Characterization of CFCMS materials by classical adsorption techniques revealed a molecular sieving effect between N_2 and CO_2, indicating that the selection of the adsorptive for characterizing micropore size distribution is very important.
- The amounts of O_2 & N_2 adsorbed increased with increasing pressure and micropore volume, and decreased with increasing temperature.
- For the two CFCMS materials produced with different burn-off levels (10 and 26%), the equilibrium uptake of O_2 was greater than that of N_2.

- Kinetics of adsorption data clearly showed that the adsorption of O_2 was significantly faster than that of N_2 in the small pore (10% burn-off) CFCMS material. This was not observed with the more mesoporous (26% burn-off) CFCMS material.
- For maximum separation efficiency, the pore size distribution of CFCMS material should be commensurate with the molecular diameters of gas species to be separated. In this instance, separation was favored by low carbon burn-off.
- A separation mechanism was postulated based upon size exclusion or diffusion rate differences (molecular size effects).
- It is proposed that a kinetic air separation system based upon a narrow pore size CFCMS material coupled with electrical swing adsorption (ESA) could be developed.

REFERENCES

1. T. D. Burchell, R. R. Judkins, M. R. Rogers, and A. M. Williams, "A Novel Process for the Separation of Carbon Dioxide and Hydrogen Sulfide for Gas Mixtures," *CARBON*, **35 (**9), pp. 1279-1294 (1997).
2. T. D. Burchell, C. E. Weaver, B. R. Chilcoat, F. Derbyshire, and M. Jagtoyen, "Activated Carbon Fiber Composite Material and Method of Making," United States Patent Number 6,030,698, February 29, 2000, Assigned to Lockheed Martin Energy Research Corporation.
3. T. D. Burchell, C. E. Weaver, B. R. Chilcoat, F. Derbyshire, and M. Jagtoyen, "Activated Carbon Fiber Composite Material and Method of Making," United States Patent Number 6,258,300, July 10, 2001, Assigned to UT-Battelle, LLC.
4. S. Brunauer, L. S. Deming, W. E. Deming, and E. Teller, "On a Theory of the van der Waals Adsorption of Gases," *J. Amer. Chem. Soc*., **62**, 1723- (1940).
5. T. D. Burchell and R. R. Judkins, "A Novel Carbon Fiber Based Material and Separation Technology," *Energy Conservation and Managemen*t, **38** Supplement, pp. S99-S104 (1997).
6. R. R. Judkins and T. D. Burchell, "Gas Separation Device Based on Electrical Swing Adsorption," United States Patent Number 5,972,077, October 26, 1999, Assigned to Lockheed Martin Energy Research Corporation.
7. K. A. Wilson, T. D. Burchell, and R. R. Judkins, "Carbon Fiber Composite Molecular Sieve Electrically Regenerable Air Filter Media," United States Patent Number 5,827,355, October 27, 1998, Assigned to Lockheed Martin Energy Research Corporation.
8. R. V. Jasra, N. V. Choudary, and S. G. T. Bhat, "Review: Separation of Gases by Pressure Swing Adsorption," *Separation and Science Technology*, **26**, pp. 885-930 (1991).
9. S. Brunauer, P. H. Emmett, and E. Teller, "Adsorption of Gases in Multimolecular Layers," *J. Am. Chem. Soc*., **60**, pp. 309-319 (1938).
10. S. J. Gregg and K. S. W. Sing, *Adsorption, Surface Area and Porosity*, 2nd Edition, Academic Press, London, 1982.
11. M. M. Dubinin, *Russ. J. Phys. Chem*., **39**, 697 (1965).
12. M. M. Dubinin and L. V. Radushkevich, *Proc. Acad. Sci. USSR*, **55**, 331 (1947).
13. F. Rodriquez-Reinoso and A. Linares-Solano, "Microporous Structure of Activated Carbons as Revealed by Adsorption Methods," in *Chemistry and Physics of Carbon*, Edited by P. A. Thrower, Volume 21, pp.1-146, Marcel Dekker, New York (1988).

14. B. McEnaney, E. Alain, Y-F Yin, and T. J. Mays, “Porous Carbons for Gas Storage and Separation: Characterization and Performance,” in Design and Control of Structure of Advanced Carbon Materials for Enhanced Energy Performance, B. Rand, S. P. Appleyard, and M. F. Yardim (Editors), pp. 295-318, NATO Science Series, Volume E374, Kluwer Academic Publishers, The Netherlands (2001).

ACKNOWLEDGEMENTS

Research sponsored by Office of Fossil Energy, U.S. Department of Energy, National Energy Technology Laboratory, under the Fossil Energy Advanced Research Materials Program, contract number DE-AC05-00OR22725 with UT-Battelle, LLC.

SESSION II

POSTERS

UNDERSTANDING DAMAGE MECHANISMS IN FERRITIC STEELS

Robert W. Swindeman, Michael L. Santella, John Shingledecker, and Philip J. Maziasz

Oak Ridge National Laboratory, P.O. Box 2008, Oak Ridge, TN 37831-6155
E-mail: swindemanrw@ornl.gov: Telephone: (865) 574-5108; Fax (865) 574-0641

Douglas L. Marriott and Michael J. Swindeman

Stress Engineering Services, Inc.
5380 Courseview Drive, Mason, OH, 45040
E-mail: mswindeman@ses-oh.com: Telephone: (513) 336-6701; Fax (513) 336-6817

ABSTRACT

A considerable effort is underway on an international level to better understand the performance of advanced ferritic/martensitic steels under service conditions typical of power boilers. These 9-12% Chromium alloys have been modified by means of Mo, W, V, Nb, N, B, Cu, Cu, and other additions that influence the critical transformation temperatures, corrosion resistance, strength, or long-time stability. Without exception the strength of the steels degrades during service at temperatures above 600°C, so the understanding of damage mechanisms that lead to this degradation is of vital concern in the selection and optimization of the steels for specific boiler components. In the work reported here, a number of damage mechanisms were explored for the advanced 9-12% Cr-Mo steels. The mechanisms included fireside and steamside corrosion of tubes, long-term aging effects, strain-induced dynamic recovery, and microstructural modifications introduced by excursions above the A_1 temperature. In most of the work 9Cr-1Mo-V steel was selected as the reference material but use was made of damage models developed for other advanced steels. Creep-rupture testing was undertaken on material aged for times up to 75,000 hours, exposed to creep stress for times up to 82,000 hours, and service-exposed for times to 143,000 hours. Damage models that were examined included the life-fraction, the Monkman-Grant, the MPC Omega function, and the Dyson Continuum Damage Mechanics model. Because of the importance of weldment behavior to damage models, special efforts were made to develop the capability to predict the critical temperatures as a function of base metal and weld metal compositions. Both experimental and computational methods were used to explore equilibrium and non-equilibrium microconstituents. The rate of evolution of these microconstitutents was found to be an important consideration in the development of "more advanced" damage models but was not needed in the simple damage approximation provided by life fraction and Monkman-Grant.

INTRODUCTION

Advanced ferritic/martensitic steels such as 9Cr-Mo-V, 9Cr-W-V, and 12Cr-W-V are experiencing increased usage for construction of boilers and heat recovery steam generator components. Also, they are being used to replace stainless steels and lower strength Cr-Mo steel in both subcritical and supercritical steam plants. There is concern about the high-temperature performance of the advanced steels for several reasons. First, they exhibit a higher sensitivity to temperature than the 300 series stainless tubing steels that they often replace. Second, they tend to be metallurgically unstable and undergo significant degradation at service temperatures in the creep range. Third, the experience base is limited in regard to duration. Fourth, they will be used for thick-section, high-pressure components that require high levels of integrity. To better understand the potential limitations of these steels, damage models are being developed by a number of investigators. These models vary greatly in complexity from simple concepts such as summation of life-fractions to continuum damage mechanics (CDM) formulations that consider both the metallurgical and mechanical factors that effect component life under constant and variable loadings. In the evaluation of pressure-bearing components, the concerns usually relate to long-time service. The activities described below outline some of the research directed toward resolving some of the issues that are linked to the usage of these steels. Most of the effort involves 9Cr-1Mo-V steel which has experienced service since 1980.

DAMAGE MODELS

Of the many life prediction and damage models that have been proposed over the years, only a few were selected for examination. The models include the Life Fraction, which is time-based and often identified as Robinson's rule (1), the iso-stress method which was used in the 1980s and 1990s (2), the Monkman-Grant method, which makes use of the observed correlation between rupture life and creep rate (3), constitutive creep law models that include tertiary creep (4, 5), the recently developed API-MPC Omega method, which is based on tertiary creep behavior (6) and is often used for fitness-for-service evaluations (7), and Continuum Damage Mechanics models, that incorporate specific damage mechanisms into a creep deformation model (8, 9). Several of these models were reviewed and evaluated recently by Holdsworth and Merckling (10). More details regarding the application of the models to 9Cr-1Mo-V steel are available elsewhere (11,12).

CREEP BEHAVIOR AFTER LONG-TIME EXPOSURE

In the past year, creep tests were undertaken of 9Cr-1Mo-V steel samples exposed to prior creep for times from 40,000 hours to 83,000 hours. In most instances the new testing conditions were 600°C and 100 MPa which would correspond to a life of approximately 60,000 hours for an unexposed sample. The tests condition was maintained for 10,000 hours then new conditions were imposed by changing the temperature, stress, or both. Creep rates for all conditions were observed and the response

compared to expectations from different damage models. Results to date indicate that well-established phenomenological models are suitable for representing the long-term performance under creep conditions providing that the thermal aging effects are incorporated into the models either explicitly or implicitly. The rate of evolution of microconstitutents was found to be an important consideration in the development of "more advanced" damage models but was not needed in the simple damage approximation provided by life fraction and Monkman-Grant.

WELDING ISSUES

The performance of weldments in the advanced ferritics/martensitic steels is of a major concern. Issues regarding weldments that were addressed in the past year included the effect of filler metal composition on the critical temperatures, subsequent microstructures, and creep performance. A model was developed for determining the A_1 transformation temperature base on the composition of the base metal or filler metal. Here, 1300 compositions within the chemical specification of 9Cr-1Mo-V were used to estimate the variability of the A_1 temperature using the Thermocalc® program. These values were served as input into a routine for rapid calculation of the A_l. The program was made available to vessel fabricators seeking to optimize fabrication schedules. Creep-rupture testing of weldments was continued to establish the influence of Ni and Mn content of the filler metal. A series of experiments on flux-core arc weldments was completed (13), and test were started to examine the effect of post weld heat treatments near the A_1 temperature.

SUMMARY

In the past year the focus of work on advanced ferritic/martensitic steels has been on a better understanding of factors that contribute to damage accumulation. A number of damage models has been examined with respect to there ability to represent variable loads after long-time creep exposure. The preliminary evaluation of results suggests that phenomenological models are adequate representations of behavior.

Further work on weldments was undertaken and models were developed to provided guidelines for tempering on post-weld heat treatment of weldments that are linked to alloy composition.

ACKNOWLEDGEMENTS

The work was sponsored by the U.S. Department of Energy, Office of Fossil Energy under contract DE-AC05-00OR22725 with Oak Ridge National Laboratory, managed by UT-Battelle, LLC.

REFERENCES

1. E. L. Robinson, "Effect of Temperature on the Creep Strength of Steel," *Trans., ASME*, 1938, vol. 60, 253-259.
2. R. Viswanathan and J. Foulds, "Accelerated Stress Rupture Testing for Creep Life Prediction – Its Value and Limitations," *J. Pressure Vessel Technology*, 1998, vol. 120, 105-115.
3. F. C. Monkman and N. J. Grant, Proc. ASTM, 1956, vol 56, 593.
4. F. V. Ellis and R. W. Swindeman, "Creep Constitutive Equations for Grade 91 Steel," *High-Temperature Service and Time-Dependent Failure*, PVP-Vol. 262, American Society of Mechanical Engineers, New York, NY, 1983, 157-166.
5. D. I. G. Jones, R. M. French, and R. L. Bagley, "Renewal Inelastic Theory With a Damage Function," *Proceedings of the 2nd International Conference on Heat-Resistant Materials*, ASM International, Materials Park, OH, 1995, 303-310
6. M. Prager, "The Omega Method-An Engineering Approach to Life Assessment," *J. Pressure Vessel Technology*, 2000, Vol. 122, No. 3, 273-280.
7. Anon., *Recommended Practice for Fitness-for-Service*, API 579, American Petroleum Institute, 1220 L Street, N.W., Washington, D.C., USA, 1997.
8. R. K. Penny, "The Use of Damage Concepts in Component Life Assessment," Int. *J. Pressure Vessels & Piping*, Vol 66, 1966, 263-280.
9. B. Dyson, "The Use of CDM in Materials Modeling and Component Creep Life Prediction," *J. Pressure Vessel Technology,* 2000, Vol. 122, No. 3, 281-296.
10. S. R. Holdsworth and G. Merckling, "ECCC Developments in the Assessment of Creep-Rupture Properties," *Proceedings of the Sixth International Charles Parsons Turbine Conference*, Inst. Materials, Minerals, & Mining, Carlton House Terrace, London, UK, 2003, 411-426.
11. R. W. Swindeman, M. L. Santella, P. J. Maziasz, B. W. Roberts, and K. Coleman, "Issues in Replacing Cr-Mo Steels and Stainless Steels with 9Cr-1Mo-V Steel," paper to be published in the International Journal of Pressure Vessels and Piping.
12. R. W. Swindeman, P. J. Masiasz, and M. J. Swindeman, "comparative Damage Models for Martensitic Steels," paper presented at the EPRI International Conference on Materials and Corrosion Experience for Fossil Power Plants, November 18-21, 2003, Wild Dunes Resort, Isle of Palms, South Carolina
13. R. Menon, J. Wallen, M. L. Santella, R. W. Swindeman, and W. Layo, "Recent Welding Experiences with Grade 91 Flux and Metal Cored Wires," paper presented at the Sixth International EPRI Conference on Welding and Repair Technology for Power Plants, June 16-18, 2004, Sandestin, Florida

HIGH CREEP-STRENGTH ALLOYS

P.J. Maziasz, J.P Shingledecker, R.W. Swindeman, R.L. Klueh and N.D. Evans

Oak Ridge National Laboratory
P.O. Box 2008
Oak Ridge, TN 37831-6115

ABSTRACT

Current coal-fired supercritical-steam power plants currently operate with steam boiler and turbine inlet temperatures at about or slightly above 600^{o}C. New ultra supercritical (USC) steam power plants will require boiler tubing and turbines capable of reliable operation at steam temperatures up to 760^{o}C. ORNL has been involved in alloy development of a wide range of steels, stainless steels and alloys, and various superalloys with more creep-strength and temperature capability based on careful design and control of microstructures. This paper highlights recent processes in three areas relevant to USC steam conditions, including modifications of wrought and cast stainless steels that correspond to grade 347 stainless steels, modifications of bainitic 3Cr and martensitic 9Cr steels, and studies of processing effects on the new 740 alloy (introduced by Special Metals).

INTRODUCTION

Alloys with high creep strength at 650-750^{o}C are essential for new, highly efficient, ultrasupercritical (USC) steam power plants [1-3]. While such alloys for boiler application must also be construction-code approved materials which resist both creep deformation and the severe fire-side corrosion environment, those constraints are relaxed somewhat for USC steam turbines [4]. This effort highlights and summarizes some of the latest work going on at ORNL to characterize and develop alloys with significantly better creep-resistance relative to standard, commercially available materials in the alloy classes of martensitic/ferritic steels, austenitic stainless steels and nickel-based superalloys. One fundamental premis here is that better properties performance is achieved by careful control of alloy composition and processing conditions to produce materials that develop appropriate and stable microstructures for prolonged high-temperature creep-strength and rupture resistance. This paper highlights the following: a.) wrought and cast lean austenitic stainless steels based on modifications of type 347 stainless steel (cast grade is CF8C); b.) bainitic 3Cr and martensitic 9Cr steels with modified compositions and processing; and c.) collaboration with Special Metals on processing to improve the creep-resistance of the new 740 alloy, which is stronger than alloy 617. The steels and stainless steels are most relevant to turbine casing or steam supply hardware applications, while the alloy 740 originally designed for superheater tubing and headers may also be applicable to turbine bolting or blading component applications.

DISCUSSION OF CURRENT ACTIVITIES

WROUGHT AND CAST AUSTENITIC STAINLESS STEELS

Wrought stainless steels have been developed at ORNL for better creep rupture strength at 700-750°C. Using the "engineered microstructures" approach, these alloys are designed to have stable nano-scale carbide dispersions within the grains for strength without the coarse intermetallic phases (i.e., Laves or sigma) that cause embrittlement. Modified steels based on type 347 stainless steel, but containing judicious additions of Mn, N and other elements, have been developed as foils for other applications [5].

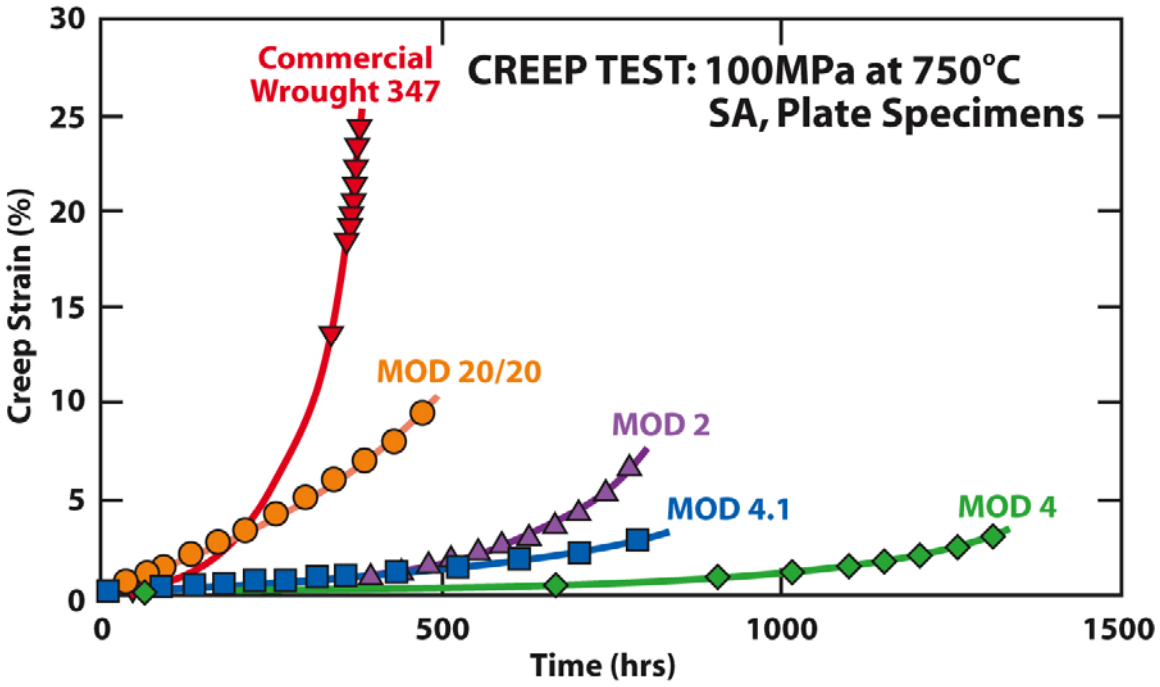

Figure 1 – Creep curves of annealed plate specimens of commercial 347 stainless steel and lab-scale heats of ORNL developmental alloys, including a Fe-20Cr-20Ni alloy and several modified 347 steels.

Plate of these new steels have been creep tested here at 750°C and 100 MPa, and creep-rupture data are shown in Fig. 1. Clearly, the modified 347-4 and 347-4.1 steels show significantly better creep resistance than standard, commercial 347 stainless steel at 750°C.

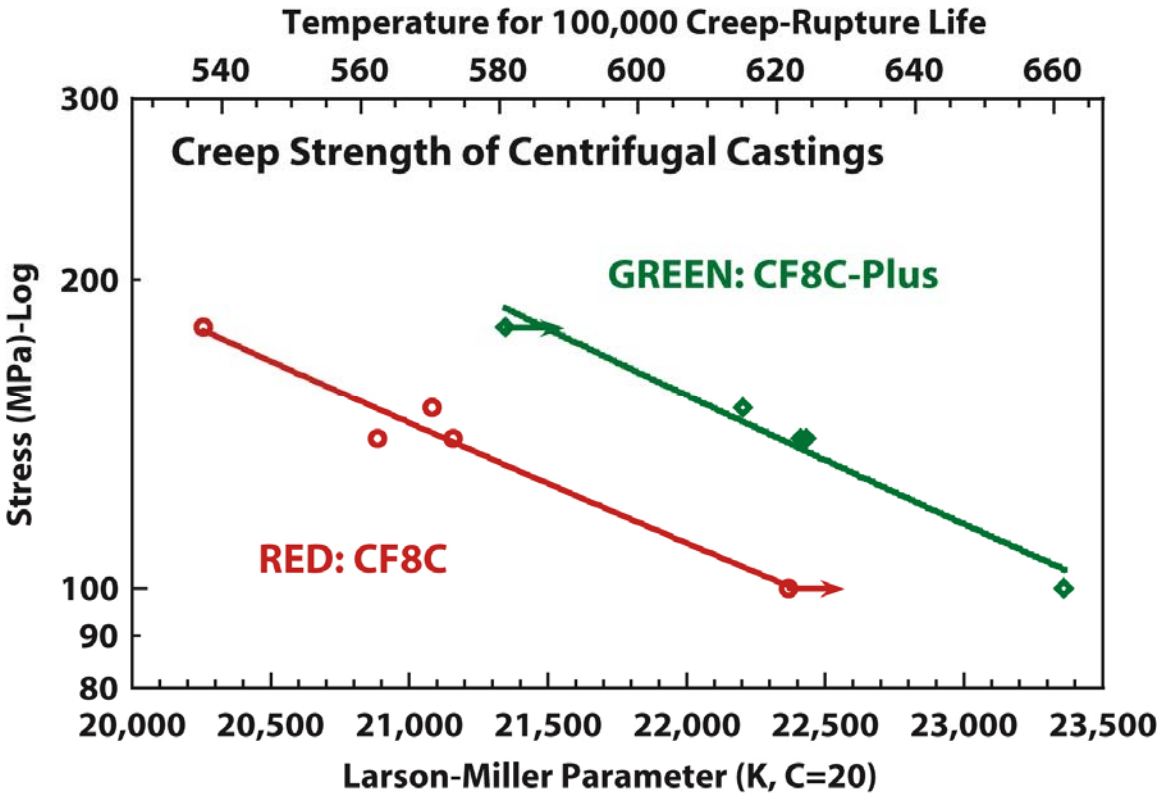

Figure 2 – Comparison of commercial centrifugal castings of standard CF8C and the new CF8C-Plus cast austenitic stainless steels creep rupture tested in air at 700-800°C. The upper axis is an extrapolation of shorter term data to temperatures that would allow the material to have a 100,000 h rupture life at the given stress level.

ORNL has also been working with Caterpillar for the last several years to develop a modified CF8C cast stainless steel with better creep-rupture resistance at 700-850°C for heavy-duty truck diesel exhaust component applications [6]. Cast CF8C steel is similar to wrought 347 steel. The modified version, CF8C-Plus, has additions of Mn and N and was designed to have an "engineered microstructure" for better creep, fatigue, thermal fatigue and aging resistance relative to the standard steel. The new cast CF8C-Plus stainless steel has significantly better creep-rupture strength than standard CF8C steel for testing at 700-800°C, as shown in Fig. 2. This material is a candidate for turbine casings with better heat-resistance and temperature capability than standard bainitic or martensitic steels used for steam- or combustion gas-turbines today.

The new ORNL modified 347 and the new cast CF8C-Plus steels have creep resistance comparable to NF709 steel developed by Nippon Steel in Japan, and better creep resistance than either Esshete 1250 steel or the European Union (EU) modified (Cr, N, Cu and W) versions of that steel (Fig. 3) [3]. The CF8C-Plus steel appears to have a clear advantage above 700°C over the other steels and alloys.

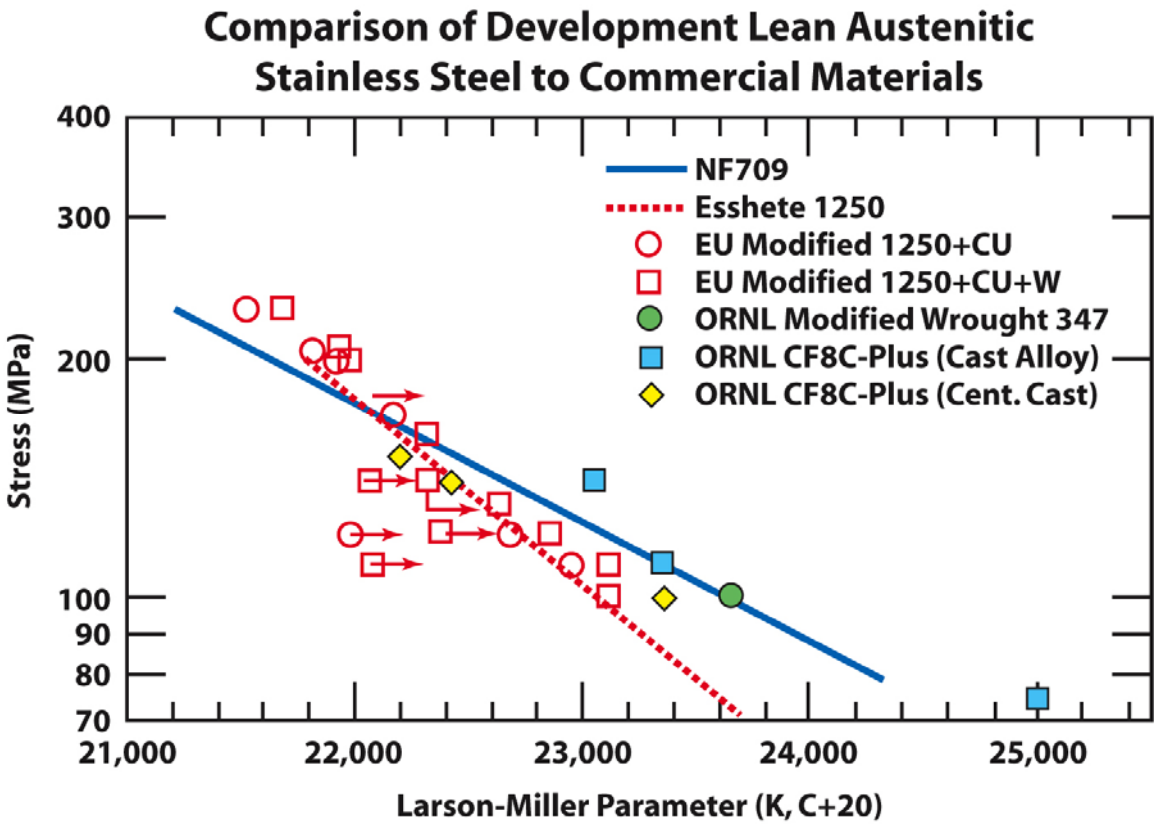

Figure – 3 Plots of Larson-Miller Parameter (LMP) versus test stress for new wrought ORNL modified 347 steels and cast CF8C-Plus steel together with comparable creep data on European developmental steels to improve on Esshete 1250 or the NF709 (Fe-20Cr-25Ni-Nb,N) stainless alloy developed in Japan. The new ORNL steels compare well with NF709, which is one of the strongest stainless alloys.

WROUGHT BAINITIC AND MARTENSITIC STEELS

While there has been considerable work over the last several decades aimed at improving the high-temperature strength and use temperatures of bainitic and martensitic steels [1-4,7,8], recent work at ORNL has produced new 3Cr-3WV and 3Cr-3WVTa bainitic steels and new 9Cr steels with much better strength at 550-700^{o}C [9-12]. Again, as found for the austenitic stainless steels describe above, the improved high temperature strength is directly attributable to unique, nanoscale carbide or other phase structures that are very resistant to dissolution or coarsening. Creep properties of the bainitic steels are shown in Fig. 4, and properties of the new 9 Cr steels are shown in Fig. 5. For the new 9Cr steel, there is an additional processing benefit, in that this steel shows even higher strength in the untempered condition. The strength of the untempered 9Cr steels is comparable to the very high strength of oxide-dispersion-strengthened (ODS) alloys, which is extraordinary.

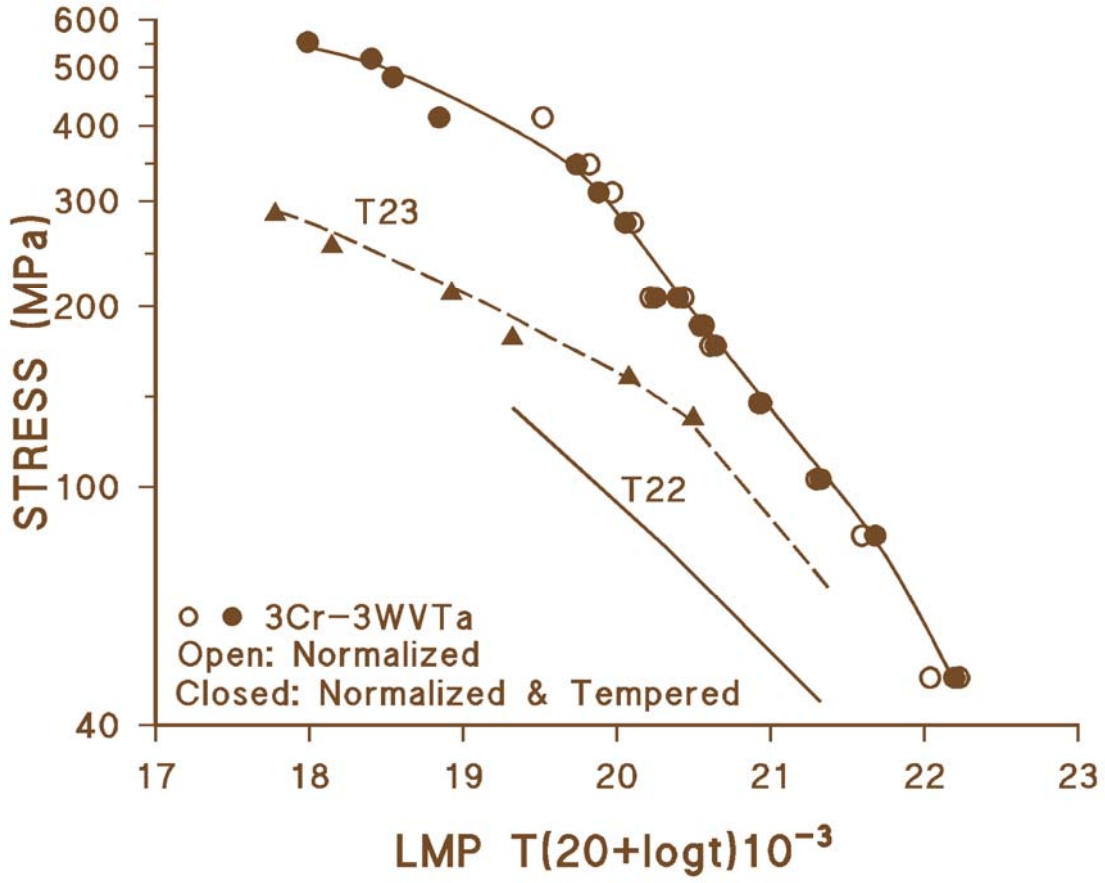

Figure 4 – A plot of Larson-Miller Parameter (LMP) versus stress for creep data on the new wrought ORNL 3Cr-3WVTa bainitic steel developed recently, with commercial bainitic steels T22 and T23 for comparison. The new ORNL steel has significantly better creep-strength when tested at 550-650°C.

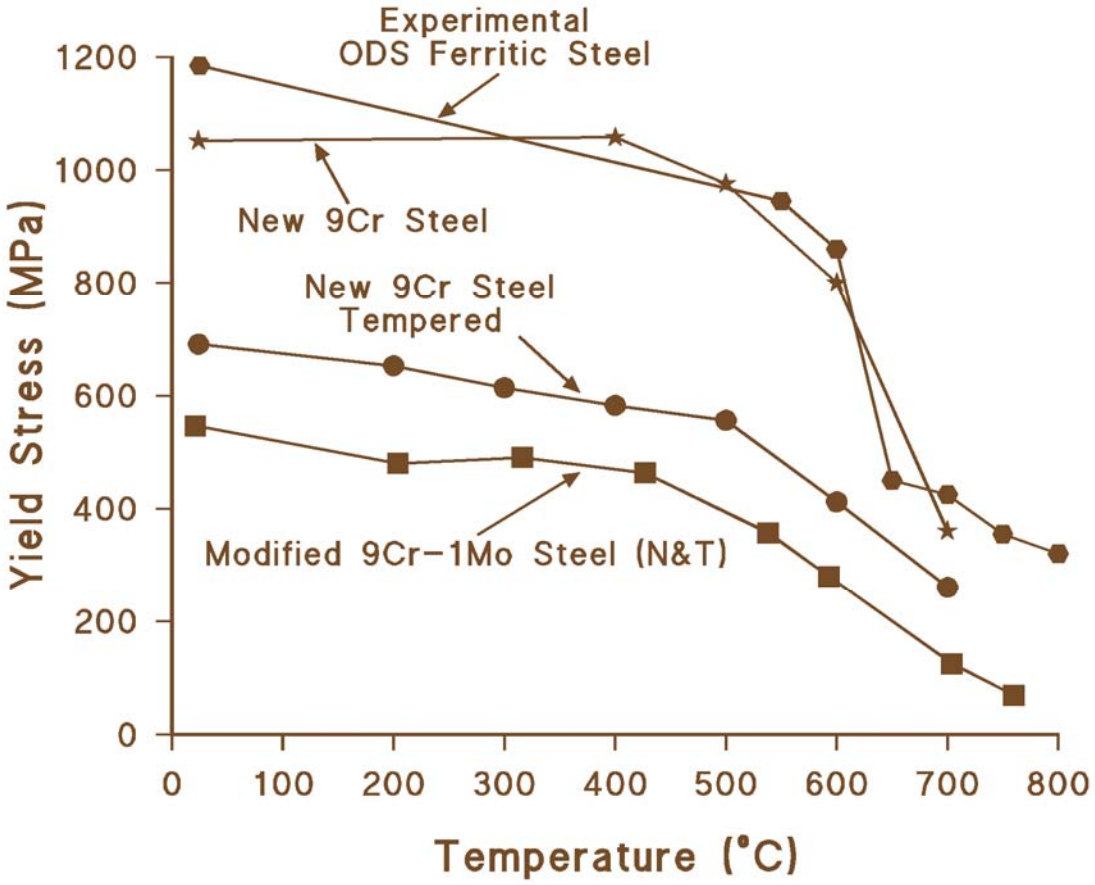

Figure 5 – Comparison of yield strength versus test temperature for new ORNL 9Cr steel which has significantly better strength than standard normalized and tempered 9Cr-1Mo-VNb steel, but is as strong as an ODS Fe-14Cr steel in the untempered condition.

NEW WROUGHT INCONEL@ 740 ALLOY

INCONEL@ 740 alloy is a new Ni- and Co-based superalloy developed by Special Metals to have high creep resistance and fire-side corrosion resistance in ultra-supercritical (USC) boiler conditions at 700°C and above [1,2]. This new alloy is also one of the candidate alloys being studied by the U.S. USC Boiler Consortium for steam temperatures approaching or exceeding 760°C [2,13]. It may also be applicable to some of the components in the corresponding USC steam turbine program [4]. Work at ORNL examined processing variables for alloy 740, and showed the obvious benefits of higher solution-annealing temperatures on creep-rupture resistance, as shown for creep-testing at 816°C in air in Fig. 6. As with the other classes of materials, microcharacterization work at ORNL has shown that improvements in creep resistance are related to clear changes in microstructural evolution caused by the difference in heat-treatment conditions.

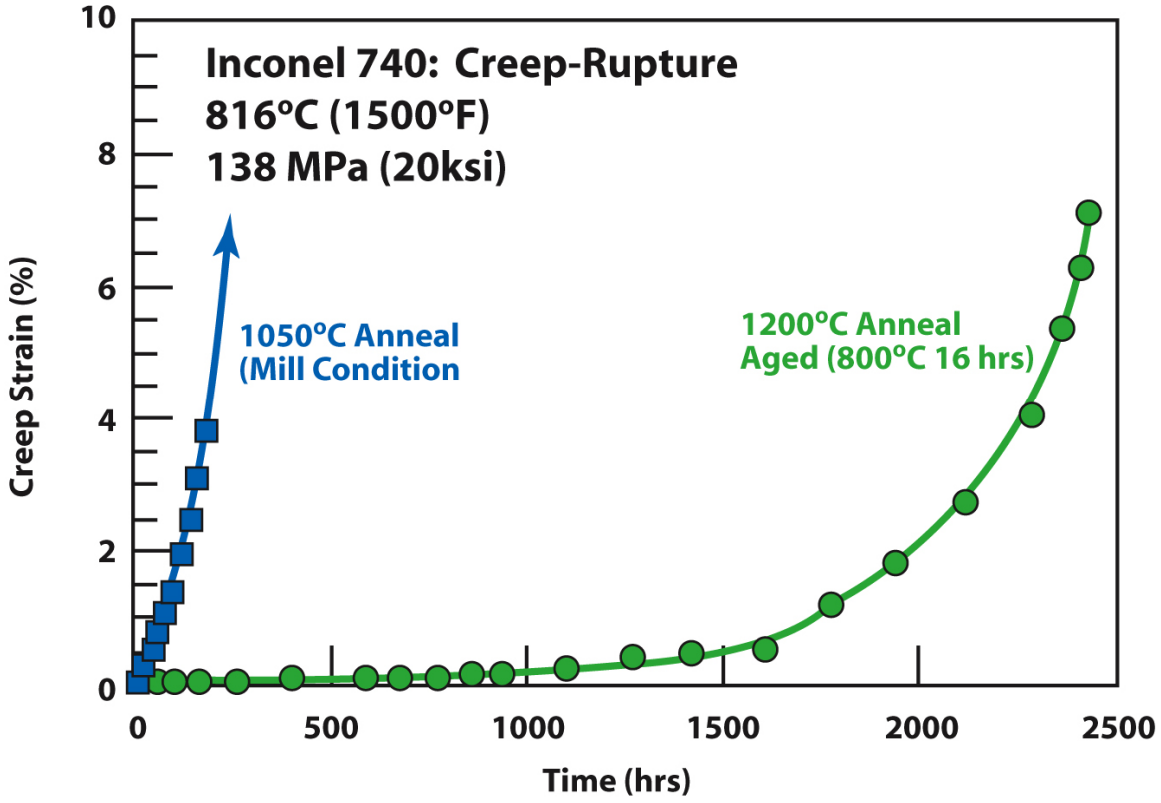

Figure 6 – Comparison of creep strain versus time for specimens of new Inconel 740 (Ni-Cr-Co alloy) tested with different solution-annealing temperatures.

ACKNOWLEDGEMENTS

Thanks to Fred Glaser at the Department of Energy, Robert Romanosky at NETL/DOE for their management, support and funding of this research. This research was supported by the U.S. Department of Energy, Office of Fossil Energy, Advanced Research Materials Program under Contract DE-AC05-00OR22725 with UT-Battelle, LLC.

REFERENCES

1.) R. Viswanathan, R. Purgert and U. Rao, "Materials for Ultra-Supercritical Coal-Fired Power Plant Boilers," *Materials for Advanced Power Engineering 2002*, Proceedings Part II, Forschungszentrum Julich GmbH, 2002, p. 1109-1129.

2.) R. Viswanathan, J.F. Henry, J. Tanzosh, G. Stanko, J.P. Shingledecker, and B. Vitalis, "Materials for Ultrasupercritical Coal Fired Power Plant Boilers," *Proceedings of the 29th Internat. Conf. on Coal Utilization and Fuel Systems*, held April 18-23, 2004 in Clearwater, FL, Coal Technology Association, Gaithersburg, MD 20878.

3.) R. Blum and R.W. Vanstone, "Materials Development for Boilers and Steam Turbines Operating at 700°C," in *Parsons 2003 – Engineering Issues in Turbine Machinery, Power Plant*

and Renewables, Institute for Materials, Minerals and Mining, Maney Publishing, London, England, 2003, p. 489-510.

4.) I.G. Wright, P.J. Maziasz, F.V. Ellis, T.B. Gibbons, and D.A. Woodford, "Materials Issues for Turbines for Operations in Ultra-Supercritical Steam," *Proceedings of the 29th Internat. Conf. on Coal Utilization and Fuel Systems*, held April 18-23, 2004 in Clearwater, FL, Coal Technology Association, Gaithersburg, MD 20878.

5.) P.J. Maziasz, R.W. Swindeman, J.P. Shingledecker, K.L. More, B.A. Pint, E. Lara-Curzio, and N.D. Evans, "Improving High Temperature Performance of Austenitic Stainless Steels for Advanced Microturbine Recuperators," in *Parsons 2003 – Engineering Issues in Turbine Machinery, Power Plant and Renewables*, Institute for Materials, Minerals and Mining, Maney Publishing, London, England, 2003, p. 1057-1073.

6.) P.J. Maziasz and M. Pollard, "High-Temperature Cast Stainless Steel," *Advanced Materials and Processes*, ASM-International, Materials Park, OH, vol. 161, 2003, p. 57-59.

7.) M. Staubli, B. Scarlin, K.H. Mayer, T.U. Kern, W. Bendick, P. Morris, A. DiGainfrancesco, and H. Cerjak, "Materials for Advanced Steam Power Plants: The European COST522 Action," in *Parsons 2003 – Engineering Issues in Turbine Machinery, Power Plant and Renewables*, Institute for Materials, Minerals and Mining, Maney Publishing, London, England, 2003, p. 306-324.

8.) G. Scheffknecht, Q. Chen and G. Weissinger, "Design and Materials Aspects of Advanced Boilers," in *Parsons 2003 – Engineering Issues in Turbine Machinery, Power Plant and Renewables*, Institute for Materials, Minerals and Mining, Maney Publishing, London, England, 2003, p. 114-128.

9.) R.L. Klueh, D.J. Alexander, and E.A. Kenik, "Development of Low-Chromium Chromium-Tungsten Steels for Fusion, *Journal of Nuclear Materials*, vol. 227, 1995, p. 11.

10.) R.L. Klueh, D.J. Alexander, and P.J. Maziasz, "Bainitic Chromium-Tungsten Steels With 3 Percent Chromium," *Metallurgical Transactions A*, vol. 28A, 1997, p. 335.

11.) V.K. Sikka, R.L. Klueh, P.J. Maziasz, S. Babu, M.J. Santella, J.R. Paules, M.H. Jawad, K.E. Orie, "Mechanical Properties of New Grades of Fe-3Cr-W Alloys," *Proc. ASME/JSME Conf. on Pressure Vessel and Piping*, ASME International, New York, NY, 2004.

12.) R.L. Klueh, unpublished data, Oak Ridge National Laboratory, 2004.

13.) J.P. Shingledecker, R.W. Swindeman, R.L. Klueh, and P.J. Maziasz, "Mechanical Properties and Analysis of Ultra-Supercritical Steam Boiler Materials, "*Proceedings of the 29th Internat. Conf. on Coal Utilization and Fuel Systems*, held April 18-23, 2004 in Clearwater, FL, Coal Technology Association, Gaithersburg, MD 20878

Ultra Supercritical Turbines—Steam Oxidation

Gordon R. Holcomb, Bernard S. Covino, Jr., Sophie J. Bullard, Stephen D. Cramer,
Malgorzata Ziomek-Moroz, and David E. Alman
Albany Research Center, U.S. Dept. of Energy, 1450 Queen Ave SW, Albany OR 97321
E-mail: Holcomb@alrc.doe.gov; Telephone: (541) 967-5874; Fax: (541) 967-5914
E-mail: Covino@alrc.doe.gov; Telephone: (541) 967-5828; Fax: (541) 967-5914
E-mail: Bullard@alrc.doe.gov; Telephone: (541) 967-5989; Fax: (541) 967-5914
E-mail: Cramer@alrc.doe.gov; Telephone: (541) 967-5924; Fax: (541) 967-5914
E-mail: Moroz@alrc.doe.gov; Telephone: (541) 967-5943; Fax: (541) 967-5914
E-mail: Alman@alrc.doe.gov; Telephone: (541) 967-5885; Fax: (541) 967-5914

ABSTRACT

Ultra supercritical (USC) power plants offer the promise of higher efficiencies and lower emissions, which are goals of the U.S. Department of Energy's Advanced Power Systems Initiatives. Most current coal power plants in the U.S. operate at a maximum steam temperature of 538°C. However, new supercritical plants worldwide are being brought into service with steam temperatures of up to 620°C. Current Advanced Power Systems goals include coal generation at 60% efficiency, which would require steam temperatures of up to 760°C. This research examines the steamside oxidation of advanced alloys for use in USC systems, with emphasis placed on alloys for high- and intermediate-pressure turbine sections. Initial results of this research are presented.

INTRODUCTION

For many years the temperatures and pressures of steam boilers and turbines were intentionally increased. These increases allowed for greater efficiencies in steam and power production, and were enabled by improvements in materials properties such as high temperature strength, creep resistance, and oxidation resistance. From 1910 to 1960, there was an average increase in steam temperature of 10°C per year, with a corresponding increase in plant thermal efficiency from less than 10% to 40%.[1] The first commercial boiler with a steam pressure above the critical value of 22.1 MPa (3208 psi) was the 125 MW Babcock & Wilcox (B&W) Universal Pressure steam generator in 1957—located at the Ohio Power Company's Philo 6 plant.[2] Since 1960, the overall trend of increasing temperatures and pressures has stopped and stabilized in the United States at about 538°C and 24.1 MPa.[3] In Europe and Japan, where fuel costs are a higher fraction of the cost of electricity, temperatures and pressures continued to rise. An example of a state of the art power plant in Europe is the Westfalen (2004) plant, with steam conditions of 31.0 MPa/593°C/621°C.[4] It has a net plant efficiency of 43.5%, compared to 37% for a subcritical 16.5 MPa/538°C/ 538°C plant.[4] Today there is again interest in the United States for advanced supercritical power plants. Large increases in the cost of natural gas have led to the reexamination of coal power plants, and advanced supercritical plants offer advantages in lower fuel costs and lower emissions of SO_X, NO_X, and CO_2.[5] Current U.S. Department of Energy research programs are aimed at 60% efficiency from coal generation, which would require increasing the operating conditions to as high as 760°C and 37.9 MPa. In general terms, plants operating above 24 MPa/593°C are regarded as ultra supercritical (USC), those operating below 24 MPa as subcritical, and those at or above 24 MPa as supercritical (SC).[3]

In the past thirty years, advances in the high temperature strength of ferritic steels have allowed for the increase of operating temperatures and pressures, but without the thermal fatigue issues of the austenitic steels that had to be used to obtain the required high temperature strengths in the early 1960s. Ferritic steels, as used here, refers to the equilibrium structure. In practice, a martensitic or partially martensitic structure is obtained from heat-treating. The temperature limit for use of ferritic steels appears to be limited to about 620 to 630°C. For temperatures above 630°C, the most promising candidate alloys are nickel-base superalloys.

The purpose of this paper is to report on research that examines the steamside oxidation of advanced alloys for use in supercritical systems. Emphasis is placed on alloys for high- and intermediate-pressure turbine sections. Initial results are presented.

BENEFITS

The driving force for increased operating temperatures and pressures has been increased efficiency in power generation. Recently, an additional recognized benefit has been decreased CO_2 emissions. Estimates of the cost effectiveness of various ways to improve the efficiency of power plants are shown in Table 1. Table 1 shows that increasing the steam temperature is one of the more cost effective ways of increasing efficiency, while increasing the steam pressure is less effective.

For reduced CO_2 emissions, calculations by Booras *et al.*[6] indicate that a subcritical 37% efficient plant 500 MW plant burning Pittsburgh #8 coal would produce about 850 tons of CO_2 per kWh. Ultra supercritical plants at 43% and 48% efficiency would respectively produce about 750 and 650 tons of CO_2 per kWh.

TABLE 1. Cost Effectiveness of Methods to Improve Fossil Fuel Power Plant Efficiency.[3] Cost is in terms of millions of U.S. Dollars per net percent increase in LHV efficiency.

Rank	Method	Cost
1	Reducing condenser back pressure	3.1
2	Increase to 8th extraction point feed water heater, raising feed water temperature	3.8
3	Raising live steam and reheat temperatures	8.3
4	Raising live steam temperature	8.6
5	Using separate boiler feed pump turbine (BFPT) instead of main turbine driven pump	9.6
6	Raising live steam pressure	25.1
7	Change from single to double reheat	38.2
8	Using separate BFPT condenser	41

RESEARCH APPROACH

The research presented here aims to bridge the gap in information between the various steam conditions to study the steamside oxidation resistance of target alloys. To be examined are the effects from steam temperature, steam pressure, and, to a limited extent, the effect of sample curvature. The importance of steam chemistry is also recognized, and will be controlled during the experiments.

The primary alloys to be tested are the ferritic alloy SAVE12, the austenitic alloy SUPER 304H, the high Cr and high Ni alloy HR6W, and three nickel-base superalloys Inconel 617, Haynes 230, and Inconel 740. All represent the highest high-temperature strength alloys in their respective alloy classes. The nominal compositions of these target alloys are given in Table 2.

TABLE 2. Nominal compositions of target alloys for USC applications.[7-9]

	Fe	Cr	Ni	Co	Mo	W	V	Nb	C	Si	Mn	Other
SAVE12[7]	Bal	11		3		3	0.2	0.07	0.10	0.3	0.2	0.04 Nd 0.04 N
Super 304H[7]	Bal	18	9					0.40	0.10	0.2	0.8	3 Cu 0.1 N
HR6W[7]		23	43			6		0.18	0.08	0.4	1.2	0.08 Ti 0.003 B
Inconel 617[8]		22.0	55.0	12.5	9.0				0.07			1.0 Al
Haynes 230[8]	<3.0	22.0	55.0	<5.0	2.0	14.0			0.10			0.35 Al <0.015B 0.02 La
Inconel 740[9]		24	Bal	20				2				2 Ti Al

There are two versions of the SAVE12 alloy (nominally 11Cr) that will be examined: a more corrosion resistant version (10.5Cr), and a higher strength version (9.5Cr). A limited number of tests will be done on SAVE12 samples that have been surface treated on one side to increase oxidation resistance.

Curvature effects will be examined on HR6W and on the two SAVE12 alloys (without surface treatment) by machining samples from thick walled pipe. Each of these curvature samples will have one curved surface, representing either the inside (concave) or outside (convex) of the pipe. The curvature can modify the spallation behavior of oxides by changing the stress fields that are the driving force to detach part or all of the scale.

The research approach consists of three types of tests:

- **Supercritical Steam Tests:** Long-term tests at the supercritical steam temperatures and pressures. The test durations of 1000 and 3000 hours.

- **Cyclic Oxidation:** Experiments using cyclic oxidation tests in air in the presence of steam. This will test the adhesion and spallation behavior of the protective oxides that form on the test alloys.

- **TGA in Steam:** Experiments using thermogravimetric analysis (TGA) with steam at atmospheric pressure. This will test alloys for susceptibility to steam oxidation using relatively short (300 hr) test durations.

Supercritical Steam Tests: Experiments will be carried out using a commercially procured René 41 autoclave (rated at 760°C and 5500 psig) and an Albany Research Center (ARC) built steam generator. These experiments will allow data to be gathered in a flowing supercritical steam environment. The present design of the system is shown in Fig. 1. The test apparatus system is currently in the process of being assembled.

Typical experiments will be 1000-hour and 3000-hour exposures run in the autoclave at temperatures up to 760°C with steam pressures of 3300, 4000, and 5000 psi. Deaerated water (with measured dissolved oxygen (DO) levels and conductivity values) will be used to generate steam at a flow rate of 2 mm/sec, a target DO of 150-200 ppb, and a target pH of 9.2-9.6. Steam will be delivered to the pressure vessel from a high-pressure steam generator and the flow rate through the sample region will be controlled.

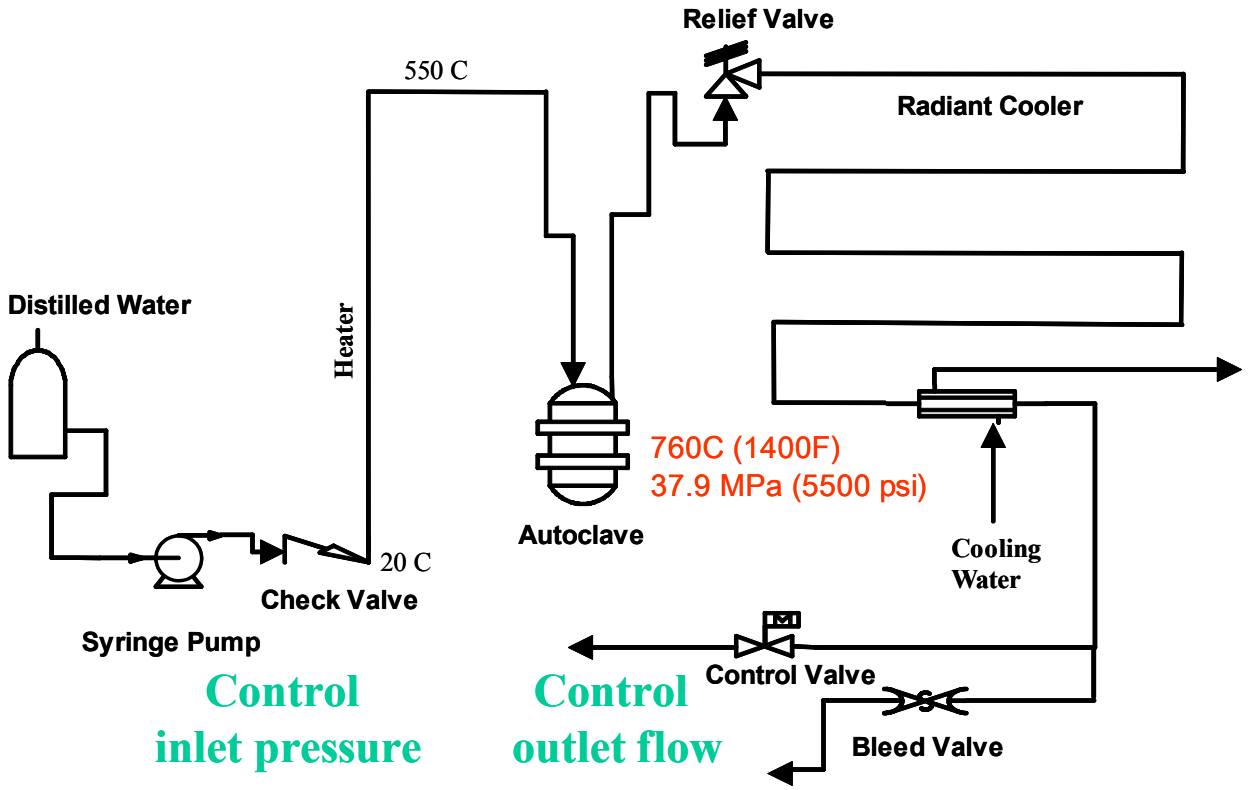

Fig. 1: Supercritical steam loop with inlet pressure control and outlet flow control.

Cyclic Oxidation: Tests with cyclic heating and cooling (1 hour cycles) have been initiated in a tube furnace equipped with a programmable slide to raise and lower the samples, Fig. 2. Water is metered into heated tubing and fed into the tube furnace. The exposures are in steam/air mixtures at up to 800°C. Both flat and curvature samples will be examined.

TGA in Steam: Experiments with thermogravimetric analysis (TGA) have been initiated to examine alloys for susceptibility to steam oxidation using relatively short test durations, Fig. 3. The TGA tests consist of suspending a sample from a Cahn D-101 microbalance in flowing steam for 300 hours at a constant elevated temperature (650-800°C). Steam is generated by injecting a metered amount of water into heated tubing to supply a minimum flow rate of 2 mm/sec of steam in the reaction chamber. Initial experiments have used either N_2- or O_2-saturated water as inputs. Current tests use a carrier gas of 50% Ar along with the steam. Even though the presence of Ar is further removed from the actual steam conditions of a power plant, it has been reported[9] that the resulting scale morphologies more closely match industrial conditions than with pure steam alone (for tests conducted at atmospheric pressure).

Fig. 2: Cyclic oxidation apparatus for testing in atmospheric pressure steam/air mixtures at up to 800°C.

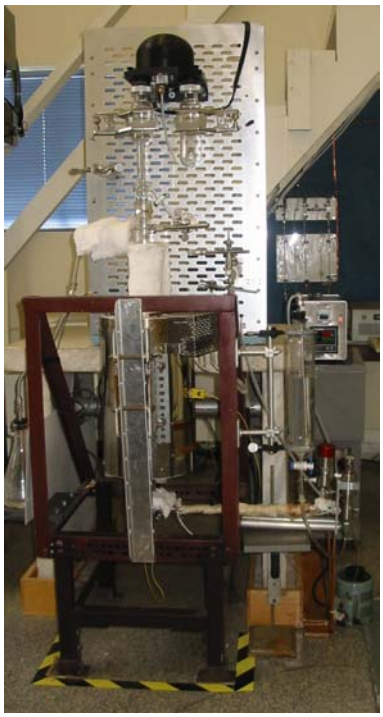

Fig. 3: TGA apparatus for testing in atmospheric pressure steam at up to 800°C.

INITIAL RESULTS

Samples of five of the six target alloys have been obtained for study. The remaining alloy to be obtained is the austenitic alloy Super 304H. While obtaining the target alloys, most of the tests using the TGA apparatus have principally been done on alloys other than the target alloys. The other alloys of interest that were tested were AISI 304, AISI 347, René 41 (the high pressure autoclave material with a nominal composition[8] of Ni-19Cr-11Co-10Mo-3.1Ti-1.5Al-<0.3Fe-0.09C-0.01B), and ARC research alloys[10-12] X3, X8, J1, and J5 (compositions of Fe-16Cr-16Ni-2Mn-1Mo-2Si, Fe-16Cr-16Ni-2Mn-1Mo-2Si-1Al, Ni-12.1Cr-18Mo-1Ti-0.8Al and Ni-12.5Cr-22Mo-1Ti-0.5Mn-0.04Y respectively). Alloy J1 is an equivalent composition to Mitsubishi alloy LTES700, a low coefficient of thermal expansion nickel-base alloy developed for use as fasteners and blades in both current and USC steam turbines.[13]

Figure 4 shows the TGA results from the longest running test on AISI 347 at 760°C in O_2 saturated steam. Figure 4A shows a relatively large mass increase with time, with little noise in the data. In Fig. 4B, the slope is the parabolic rate constant, and is relatively constant after 25 hr.

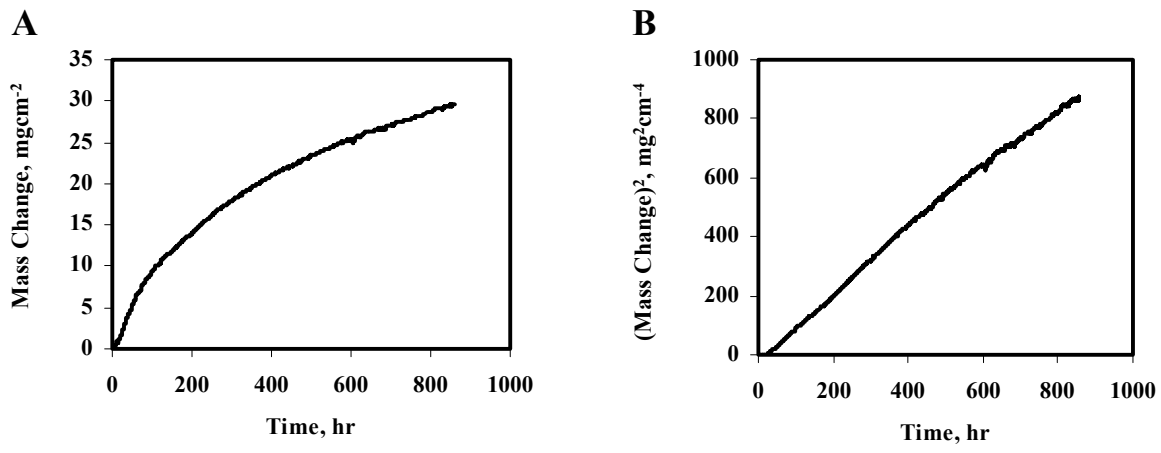

Fig. 4: TGA results from AISI 347 at 760°C with O_2 saturated feed water. The slope in B is the parabolic rate constant (with conversion from $mg^2cm^{-4}hr^{-1}$ to $mg^2cm^{-4}sec^{-1}$).

Table 3 summarizes the conditions and results to date. The parabolic rate constant has varied from fast kinetics for AISI 347 (2.1×10^{-4} $mg^2cm^{-4}sec^{-1}$) to very slow kinetics for Haynes 230 (4.9×10^{-9} $mg^2cm^{-4}sec^{-1}$). The columns "Log-Log Slope" and "Parabolic R^2" are measures of how well parabolic kinetics describes the results. The "Log-Log Slope" is the slope of the log(mass change) versus log(time), and should be 0.5 for parabolic kinetics. The parabolic R^2 values are how well the data correlate with parabolic behavior using the calculated k_p (with 1 being exact correlation and 0 being no correlation).

TABLE 3. Results from TGA experiments.

Alloy	Temp, °C	Feed Water Saturated with	60% Ar Carrier Gas?	Log-Log Slope	Parabolic Rate Constant, $mg^2cm^{-4}sec^{-1}$	Parabolic R^2
AISI 304	700	N_2	No	0.50	1.2×10^{-8}	0.882
AISI 347	760	O_2	No	0.88	2.1×10^{-4}	0.988
AISI 347	760	O_2	No	0.72	2.9×10^{-4}	0.997
X3	760	O_2	No	0.56	3.5×10^{-8}	0.863
X8	760	O_2	No	0.45	3.2×10^{-8}	0.773
Haynes 230	760	O_2	No	0.31	4.9×10^{-9}	0.451
Haynes 230	800	O_2	Yes	0.56	6.9×10^{-8}	0.878
René 41	800	O_2	No	0.58	7.2×10^{-7}	0.983
Inconel 617	800	O_2	Yes	0.29	1.9×10^{-8}	0.330
J1	800	O_2	Yes	0.58	3.8×10^{-7}	0.990
J5	800	O_2	Yes	0.52	1.7×10^{-7}	0.990

The morphologies of two of the corroded samples are shown in Figs. 5-6. Even taking into account the longer exposure time for the AISI 347, the scale is much thicker for the AISI 347 (~ 80 μm, Fig. 6) than for the Haynes 230 (~1.4 μm Fig. 5). The scale on the AISI 347 consisted of two layers—a wide inner layer of Cr-Fe oxide (Cr:Fe of 1:1) and a thin outer layer of iron oxide. The scale on the Haynes 230 was a Cr-Ni oxide (Cr:Ni of 3:1).

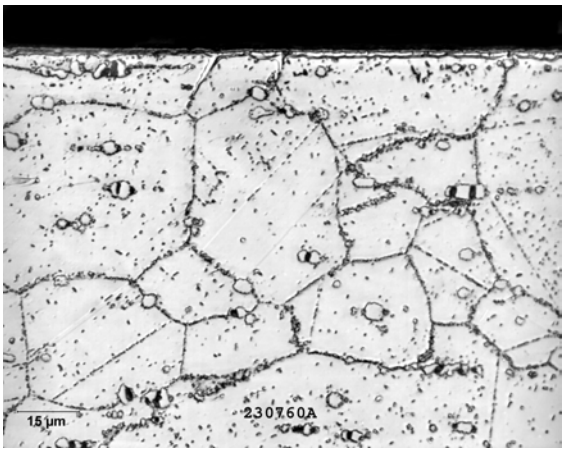

Fig. 5: Haynes 230 after exposure in O_2 saturated steam at 760°C for 150 hr. Above is the sample after exposure; below is a cross section using light microscopy.

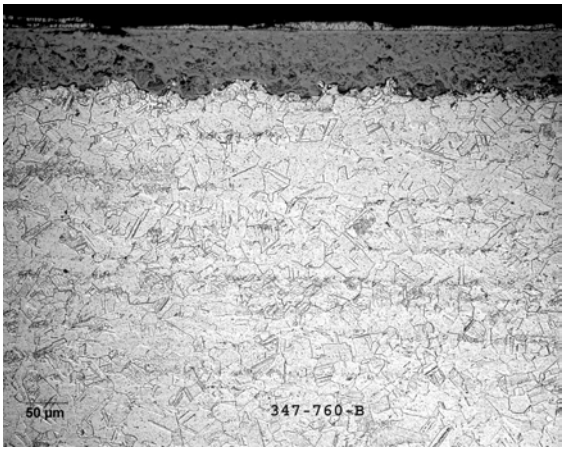

Fig. 6: AISI 347 after exposure in O_2 saturated steam at 760°C for 850 hr. Above is the sample after exposure; below is a cross section using light microscopy.

Initial results for cyclic oxidation testing at 760°C are shown in Figs. 7 and 8 for the three nickel-base superalloys and for the SAVE12 alloys, respectively. The nickel-base superalloys had an initial mass increase followed by a slow decrease in mass. The SAVE12 alloys are at higher temperatures then they were designed for and show large increases in mass with time. These tests are ongoing and so scale analyses have not been performed.

SUMMARY

An outline for examining steamside corrosion in USC power generation plants was presented to aid in increasing operating temperatures of steam boilers and turbines for increased efficiencies and lower emissions. Three basic types of experimentation are planned: high temperature-high pressure exposures in steam, cyclic oxidation at atmospheric pressures in air plus steam, and shorter duration thermogravimetric analysis (TGA) in steam and steam plus argon. Initial results for cyclic oxidation and TGA tests were presented.

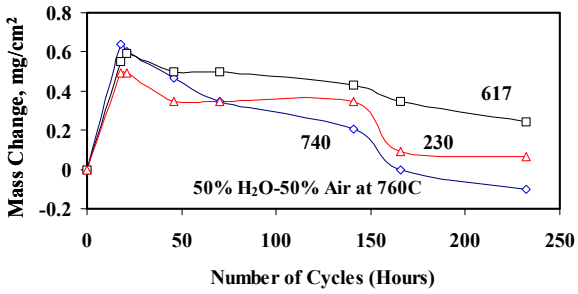

Fig. 7: Cyclic oxidation results for nickel-based superalloys at 760°C in 50% H_2O-50% air with hourly cycles.

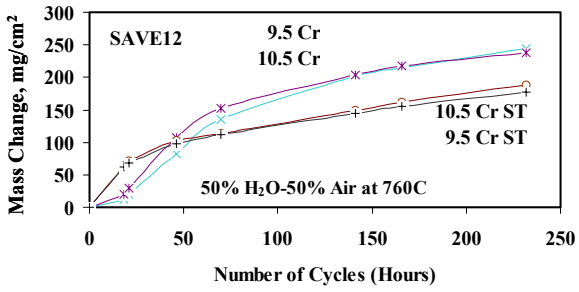

Fig. 8: Cyclic oxidation results for The 9.5Cr and 10.5Cr versions of SAVE12 at 760°C in 50% H_2O-50% air with hourly cycles. The curves marked as ST had a proprietary surface treatment on one side of each sample.

REFERENCES

1. B.B. Seth, "US Developments in Advanced Steam Turbine Materials," *Advanced Heat Resistance Steels for Power Generation*, EPRI, 1999, pp. 519-542.
2. S.C. Stultz, J.B. Kitto, *Steam*, 40th ed., Babcock & Wilcox, 1992, p. 9.
3. R. Viswanathan, A.F. Armor, G. Booras, "Supercritical Steam Power Plants—An Overview," *Best Practices and Future Technologies*, October 2003, Proceedings (New Delhi, India), National Thermal Power Corporation's Center for Power Efficiency and Environmental Protection and the US Agency for International Development (USAID), 2003.
4. R. Swanekamp, *Power*, 146 (4), 2002, pp. 32-40.
5. R. Viswanathan, A.F. Armor, and G. Booras, *Power*, 148 (4), 2004, pp. 42-49.
6. G.S. Booras, R. Viswanathan, P. Weitzel, A. Bennett, "Economic Analysis of Ultra Supercritical PC Plants," *Pittsburgh Coal Conference*, September 2003, Proceedings, (Pittsburgh, PA), University of Pittsburgh, 2003, paper 55.1.
7. R. Viswanathan, W. Bakker, *J. of Materials Eng. and Performance*, 10, 2001, pp. 81-95.
8. M.J. Donachie, S.J. Donachie, *Superalloys: A Technical Guide,* ASM International, Materials Park, OH, 2002, p. 4.
9. J. Sarver, R. Viswanathan, S. Mohamed, "Boiler Materials for Ultra Supercritical Coal Power Plants—Task 3, Steamside Oxidation of Materials—A Review of Literature," Topical Report, U.S. Department of Energy Grant Number DE-FG26-01NT41174 and Ohio Coal Development Office Grant Agreement D-0020, 2003.
10. J.S. Dunning, D.E. Alman, J.C. Rawers, *Oxidation of Metals*, 54 (5-6), 2002, pp. 409-425.
11. J.S. Dunning, D.E. Alman, "Improvements in the High Temperature (>700°C) Performance of Lean Chromium Stainless Steels for Power Plant Efficiency," *27th International* Conference *on Coal Utilization and Fuel Systems*, Coal Technology Association, Gaithersburg, MD 2002, pp. 1131-1141.
12. D.E. Alman and P.D. Jablonski, Proc. 10th International Symposium on Superalloys, TMS, in press.
13. R. Yamamoto, Y. Kadoya, H. Kawai, R. Magoshi, T. Noda, S. Hamano, S. Ueta, and S. Isobe, "New Wrought Ni-Based Superalloys with Low Thermal Expansion for 700C Steam Turbines," *Materials of Advanced Power Engineering—2002,* Proc. 7th Liege Conf., Sept 30-Oct 3, 2002, Energy and Technology Vol. 21, Forschungszentium Julich Gmbh Inst. Fur Wekstoffe und Verfahren der Energietechnik.

OPTIMIZATION OF HOOP CREEP RESPONSE IN ODS-FE_3AL TUBES

Bimal K. Kad[1], Ian Wright[2], Vinod Sikka[2] and Rod Judkins[2]
[1]University of California - San Diego, La Jolla, CA 92093
[2]Oak Ridge National Laboratory, Oak Ridge, TN 37830

ABSTRACT

Oxide dispersion strengthened (ODS) Fe_3Al alloys are currently being developed for heat-exchanger tubes for eventual use at operating temperatures of up to 1100°C in the power generation industry. The development challenges include a) efforts to produce thin walled ODS-Fe_3Al tubes, employing powder extrusion methodologies, with b) adequate increased strength for service at operating temperatures to c) mitigate creep failures by enhancing the as-processed grain size. A detailed and comprehensive research and development methodology is prescribed to produce ODS-Fe_3Al thin walled tubes. Current single step extrusion consolidation methodologies typically yield 8ft. lengths of 1-3/8" diameter, 1/8" wall thickness ODS-Fe_3Al tubes. The process parameters for such consolidation methodologies have been prescribed and evaluated as being routinely reproducible. Recrystallization treatments at 1200°C produce elongated grains (with their long axis parallel to the extrusion axis), typically 200-2000μm in diameter, and several millimeters long. The dispersion distribution is unaltered on a micro scale by recrystallization, but the high aspect ratio grain shape typically obtained limits grain spacing and consequently the hoop creep response. Improving hoop creep in ODS-alloys requires an understanding and manipulating the factors that control grain alignment and recrystallization behavior. In this report we examine the mechanisms of hoop creep failure and describe our efforts to improve creep performance via variations in thermal-mechanical treatments. Current results indicate a 100% improvement in creep stress threshold for improvised heat-treatments and thermal-mechanical treatments.

Research Sponsored by the U.S. Department of Energy, Office of Fossil Energy, Advanced Research Materials Program, under contract DE-ACOR-96OR22464 with UT-Batelle subcontract to the University of California-San Diego.

INTRODUCTION

Oxide dispersion strengthened ferritic FeCrAl (MA956, PM2000, ODM751) and the intermetallic Fe_3Al-based alloys are promising materials for high temperature, high pressure, tubing applications, due to their superior corrosion resistance in oxidizing, oxidizing/ sulphidizing, sulphidizing, and oxidizing/chlorinating environments[1-4]. Such high temperature corroding environments are nominally present in the coal or gas fired boilers and turbines in use in the power generation industry. Currently, hot or warm working of as-cast ingots by rolling, forging or extrusion in the 650-1150^{o}C temperature range is being pursued to produce rod, wire, sheet and tube products[5-7]. *A particular 'in service application' anomaly of ferritic and Fe_3Al-based alloys is that the environmental resistance is maintained up to 1200^{o}C, well beyond where such alloys retain sufficient mechanical strength.* Thus, powder metallurgy routes, incorporating oxide dispersions, are required to provide adequate strength at the higher service temperatures.

The target applications for ODS-Fe_3Al base alloys in the power generation industry are thin walled (0.1" thick) tubes, about 1 to 3 inches in diameter, intended to sustain internal pressures (P) of up to 1000psi at service temperatures of 1000-1100^{o}C. Within the framework of this intended target application, the development of suitable materials containing Y_2O_3 oxide dispersoids must strive to deliver a combination of high mechanical strength at temperature, as well as prolonged creep-life (hoop creep in particular) in service. Such design requirements are at odds with each other, as strengthening measures severely limit the as-processed grain size, resulting in decreased creep life. Thus post-deformation recrystallization processes are essential to increase the grain size, and possibly modify the grain shape for the anticipated use. This paper describes our microstructure and property optimization of ODS-Fe_3Al alloy tubes, with a view to improving the high temperature creep response. In particular, we examine thermal-mechanical processing steps to affect and enhance secondary recrystallization kinetics and abnormal grain growth during post-extrusion processing to create large grains. Such procedures are particularly targeted to improve hoop creep performance at service temperatures and pressure.

EXPERIMENTAL DETAILS

Three separate powder batches (labeled as A, B, C) of the Fe_3Al+0.5wt%Y_2O_3 composition were milled. Table 1 lists the alloy powder chemistry before and after three separate milling conditions[9]. Two separate analyses (labeled as HM, PM) were performed for the starting powders as listed in the table. The powders are labeled as A, B and C in the order of decreasing total interstitial (C+N+O) impurity. Process control agents were used for all milled batches and batch C was milled for a short period. As shown later this interstitial impurity plays a crucial role in the recrystallization kinetics and the resulting microstructures. The milled powders were encapsulated and vacuum-sealed in annular cans at about 400^{o}C. Sealed cans were then soaked over the 1000-1100^{o}C temperature range for 2 hours and directly extruded into tubes via the single step extrusion consolidation over a mandrel.

Figure 1 shows a set of tubes in the as extruded and surface finished condition. Further extrusion processing parameters are available elsewhere[7,8]. The tubes (6-8 ft. long, 1-3/8" diameter, 1/8" wall thickness) are of sound quality and exhibit no cracking after routine machining operations.

Table 1: Chemical analyses of the as-received and milled powder batches[9]

Element	As-Received HM	As-Received PM	Batch A	Batch B	Batch C
Fe	Bal.	79.6			
Al	16.3	18.20			
Cr	2.4	2.18			
Zr	20 ppm	26 ppm			
O (total)	60 ppm	110 ppm	1800 *ppm*	1900 *ppm*	1400 ppm
O (in Y_2O_3)			1025 *ppm*	1053 *ppm*	1080 ppm
O balance			775 *ppm*	847 *ppm*	320 ppm
O *pickup*			**665 *ppm***	**737 *ppm***	**210 ppm**
N	18 ppm	7 ppm	1264 *ppm*	145 *ppm*	88 *ppm*
N *pickup*			**1257 *ppm***	**138 *ppm***	**81 *ppm***
C		24 ppm	667 *ppm*	360 *ppm*	303 *ppm*
C *pickup*			**643 *ppm***	**336 *ppm***	**279 *ppm***
H		16 ppm	115 *ppm*	40 *ppm*	29 *ppm*
C+N+O *pickup*			**2565 *ppm***	**1211 *ppm***	**570 *ppm***

(Bulk compositions are identified in wt%) HM and PM are two separate analyses of atomized Fe_3Al powder

Recrystallization heat treatments for the extruded tubes are performed in the 1000-1300°C temperature range in air. Microstructures are examined using optical, SEM and TEM techniques. High temperature mechanical testing is performed on ASTM E-8 miniature samples extracted from the longitudinal and transverse orientations of the tubes. All further testing details are described in the relevant sections below.

Figure 1. Assorted ODS-Fe_3Al alloy tubes in the as extruded and surface finished condition produced via an annular can (top left) consolidation methodology.

MATERIALS CHARACTERIZATION

Figure 2 shows the optical micrographs of polished and etched transverse section microstructures for the A (top) and the C (bottom) chemistry. We note that for tubes of batch A chemistry, Figure 2a, only a 25% section of the wall thickness (in the interior) exhibits primary recrystallization. As shown earlier via transmission electron microscopy studies[8], this primary recrystallized grain size remains small of the order of 1-2μm. However, tubes of batch C chemistry, Figure 2b, exhibit secondary recrystallization. The recrystallized grains are elongated, typically 200-2000μm in diameter, and several millimeters long.

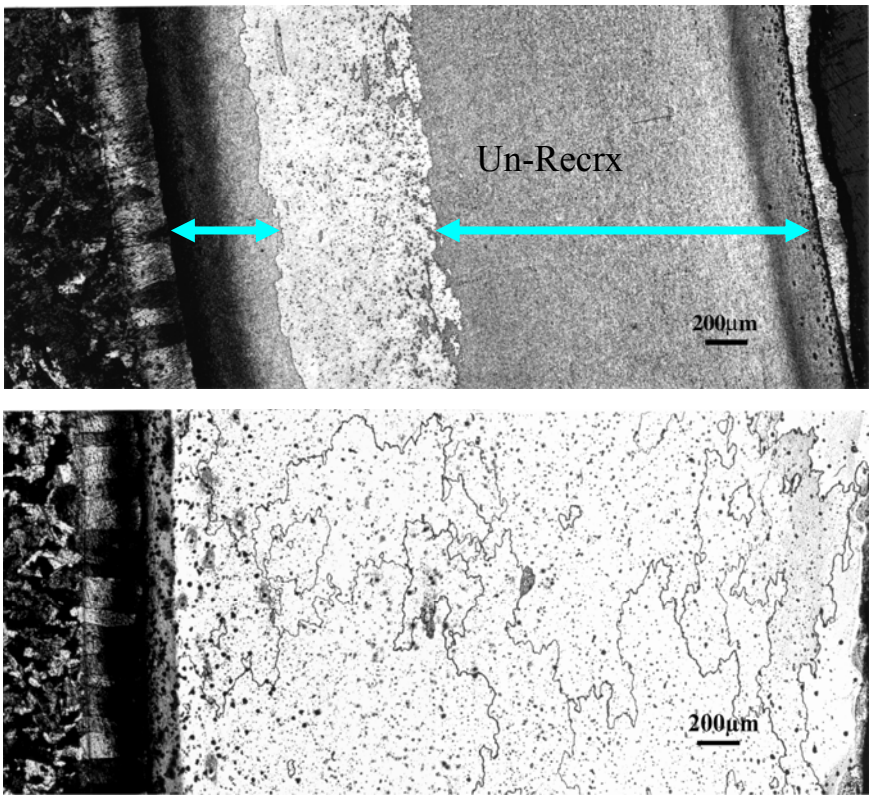

Figure 2. Recrystallized tube sections of ODS-Fe_3Al alloys (a) high impurity batch A (top) and (b) low impurity batch C (bottom).

TEM Microstructures

Figure 3 shows TEM micrographs of specimens extracted from recrystallized tube (batchC). The transverse and longitudinal views exhibit a coarse grain structure with a {111} recrystallized texture[10] in the extruded direction, Figure 3a, 3b. The precipitate distribution in batch C is rather uniform but also exhibits a cell-type structure on the scale of 1 μm. This cell dimension is consistent with the as-extruded grain size of 1-2μm and it is suggested that this particle distribution is originally present on the surface of the milled powders, which is incorporated at the as-extruded grain boundaries upon consolidation. The Y_2O_3 precipitates are about 10-20nm in diameter with an aggregate of 80-90nm spacing. The intra-granular dispersion distribution is separate from the milling induced impurity that coats the prior particle boundaries. The extent of such impurity pickup is milling process-dependent.

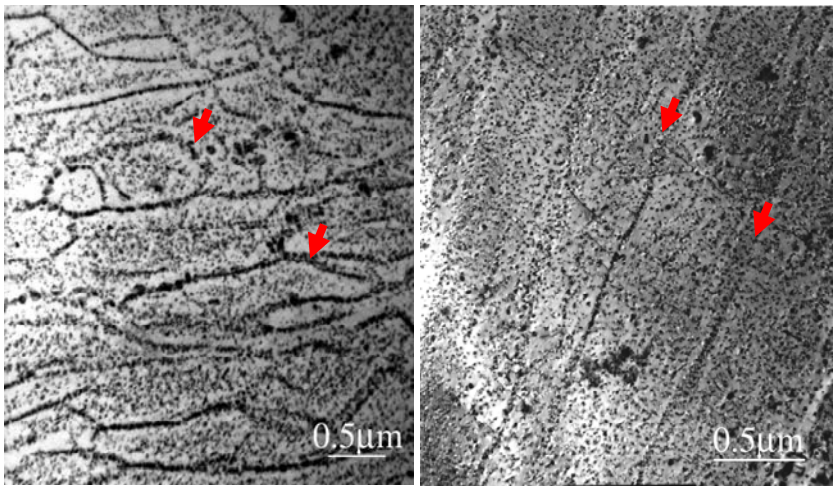

Figure 3. TEM micrographs of recrystallized ODS alloy batch C. a) transverse, and b) longitudinal view as extracted from the heat-treated tubes. Red arrows indicate prior particle boundaries.

HIGH TEMPERATURE CREEP PROPERTIES

High temperature creep testing is limited to the 800 - 1100°C range (i.e., in the creep regime) for all the three tubes. ASTM E-8 miniature creep specimens are spark machined from tube sections. Longitudinal samples are cut from as-extruded tubes and transverse sections are cut from flattened (hot pressed at 900°C) tubes. The hot pressing temperature is limited to 900°C to prevent any recrystallization at this step. Samples are initially heat-treated at 1200°C for 1 hour.

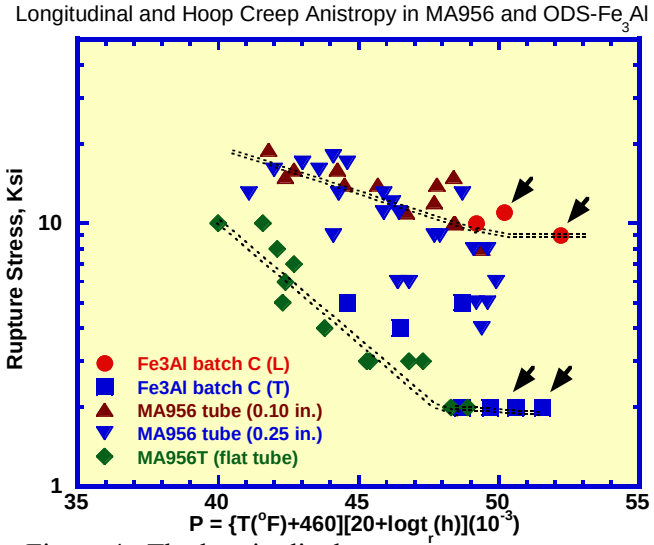

Figure 4. The longitudinal vs. transverse creep anisotropy for the ODS-Fe_3Al and MA956 alloys.

Longitudinal vs. Transverse Anisotropy

Preliminary creep tests were carried out for the ODS-Fe_3Al as well as the commercially available MA956 alloy tubes, Figure 4. The Fe_3Al samples were subjected to a uniform recrystallization heat treatment at 1200°C for 1 hour. Commercial MA956 tubes were recrystallized at 1350°C for

1 hour. Figure 4 shows the longitudinal (L) vs. transverse (T) creep anisotropy for both the Fe_3Al and the commercial MA956 (FeCrAl) alloys. The ODS-Fe_3Al tests were conducted at 1000°C in air and the MA956 test were conducted in the 900-1000°C temperature range in air. We note the improved creep response (see black arrows) of the Fe_3Al batch C chemistry over the commercial MA956 alloy in both the L and T orientations. The longitudinal and transverse creep response of ODS-Fe_3Al powder batches A and B (not shown here) is much inferior to that of batch C. This poor performance stems directly from the milling induced impurities that inhibit primary and secondary recrystallization. Thus, batch C is selected as the most promising alloy chemistry for further development based on the large processed grain size and superior hoop creep responses.

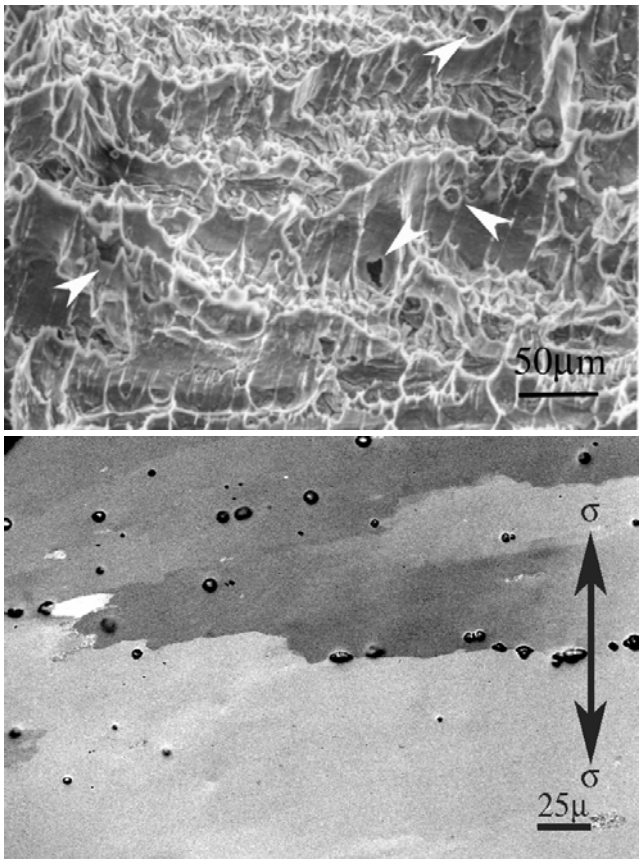

Figure 5. Transverse creep failure by void formation and coalescence in ODS-Fe_3Al crept at 3ksi at 1000°C. a) fracture surface (top) and b) specimen surface just below the fracture surface (bottom).

Transverse Creep Failures In ODS-Fe_3Al Alloys

A mechanistic understanding of hoop creep failures is an important prerequisite to aid any subsequent microstructural modifications and/or redesign efforts at the system, sub-system or component level. Figure 5a shows a typical transverse creep failure as observed in fully recrystallized ODS-Fe_3Al alloy (batch C) tested at 1000°C. Significant ductile lobes and voids are observed and it is presumed that failure is preceded by void formation and coalescence. A better insight into the origin of voids is obtained by examining the specimen surface immediately below the creep failure. Figure 5b shows void formation in crept ODS-Fe_3Al and the origin of such voids is predominantly at the grain boundary. The tensile creep loading direction as

indicated in Figure 5b is vertical. Similar results (not reported here) are also obtained for the MA956 transverse creep tests. Our program efforts are directed towards exploring metallurgical and microstructural means to enhancing and optimizing hoop creep response. Presently variations in recrystallization heat-treatments and thermal-mechanical processing schemes are being explored for the ODS-Fe_3Al alloys. We surmise that a 1000hour exposure is sufficient for predicting long-term survivability at a specific test condition on account of the high stress exponent. This is observed in ODS-alloy creep tests particularly in the transverse orientation.

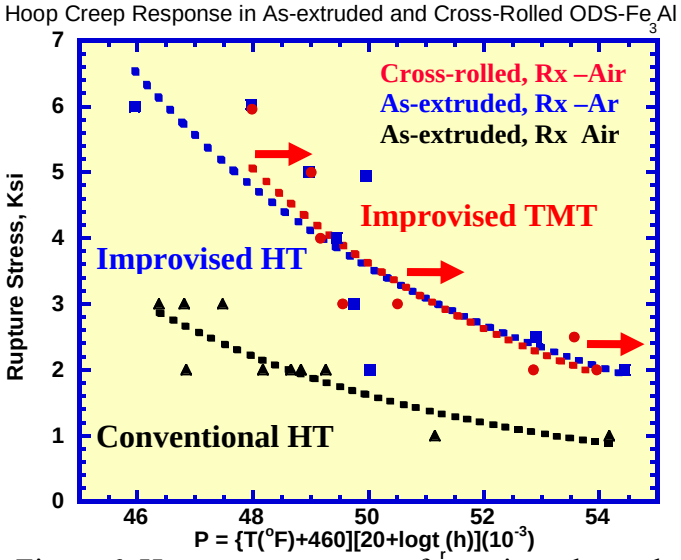

Figure 6. Hoop creep response for various thermal -mechanical treatments of ODS-Fe_3Al alloys.

Variations In Thermal-Mechanical Processing

Two separate approaches for improving transverse hoop creep strength are reported here. Initial attempts were aimed at heat-treating ODS tubes in an inert argon environment for the nominal 1hour soak at 1200°C. The intent is to avoid air exposure at the higher recrystallization temperatures (about 1200°C) that are in excess of the service temperature of about 1000°C. Figure 6 shows a direct comparison of creep response of high purity (batch C) alloys heat-treated in air (conventional HT) and in argon (improvised HT). Results indicate a 100% improvement in the creep stress at equivalent exposure life times. An alternate perspective is an order of magnitude improvement in creep life is observed at equivalent stress. For example, conventional heat treatment yields a Larsen-Parameter of 48 at 2Ksi stress, which is improved to 54 for the inert heat treatment. Within the context of aggressive thermal treatments it is important to note that commercial ODS-FeCrAl alloys are recrystallized in the 1300-1400°C range in air. Looking back to Figure 4, we note the improved creep response (see arrows) of the Fe_3Al batch C chemistry over the commercial MA956 alloy in both the L and T orientations. This trend of poor creep response in MA956 is consistent with the higher recrystallization temperatures employed. This aggressive temperature is in part necessary to overcome the Zener pinning as the Y_2O_3 dispersion volume fraction is about 15% higher in MA956 alloys. Prior studies[12,13] indicate the formation of subsurface voids when samples are exposed to aggressive environments, and it is surmised that similar effects might be operative here. This effect may be particularly detrimental to transverse creep response – which in fact fails via grain boundary void formation and coalescence. Efforts to decrease the recrystallization temperature in commercial ODS-ferritic and intermetallic Fe_3Al alloys may be a promising avenue of further ODS-alloy development.

Thermal-mechanical processing efforts have been prompted by the extreme longitudinal vs. transverse (hoop) creep anisotropy in ODS-Fe_3Al and MA956 alloys, Figure 4. Longitudinal creep limit is dictated by ODS strengthening of the matrix while transverse creep strength is limited by the grain boundary void formation and coalescence, Figure 5. Such boundary void formation is further enhanced by the presence of large impurity oxides and unrecrystallized stringers aligned along the primary extrusion axis (i.e., normal to the hoop loading axis). Thus the strength anisotropy is linked with the underlying grain structure of the processed tubes. With respect to the end-use application of internally pressurized tubes, the hoop stress required is twice the longitudinal stress. This application specific requirement is at odds with (and inverse of) the intrinsic material anisotropy illustrated in Figure 4. What is clearly desired is an exploration of likely thermo-mechanical methodologies to alter the underlying grain structure. Such a process is routine in plates and sheets, which are cross-rolled to effect isotropic in-plane response. Cross rolling of tubes is a technical challenge and as a first step flattened tube segments (of as-extruded tubes) were cross-rolled at 900°C in multiple passes to a total of 25% thickness reduction. Samples in the transverse orientation (to the original tube) were spark machined from the rolled plate and pre-oxidized at 900°C for 30 minutes prior to the recrystallization heat-treatment of 1200°C for 1 hour in air. Preliminary results of hoop creep tests in such cross-rolled materials are also plotted in Figure 6. The creep performance of thermal-mechanical treatment (TMT) samples is comparable, and is expected to surpass, the inert treated alloys. Efforts to perform recrystallization of TMT processed materials under inert atmospheres are underway and will be evaluated for hoop creep performance in the near future.

Summary and Conclusions

High temperature creep response in ODS-Fe_3Al tubes is reported for the longitudinal and transverse orientations. The kinetics of grain growth is affected by interstitial impurity content, which limit the extent of recrystallized regions observed in the tube wall. Consequently, the microstructure exhibiting the best creep response is one of high purity that undergoes complete primary and secondary recrystallization.

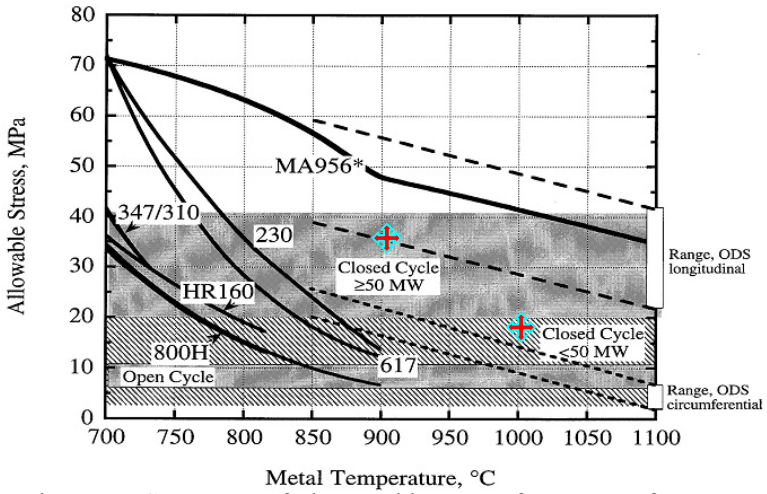

Figure 7. Summary of observed hoop performance of ODS-Fe_3Al alloys in 900°C and 1000°C tests, viewed against the desired performance metrics for ODS alloys.

Figure 7 provides a concise summary of the overall hoop creep enhancement as measured in 900°C and 1000°C tests (red crosses as indicated). In each case the results are better than the projected performance of ODS alloys for the power generation system requirements. Hoop creep evaluation at 1100°C will be reported later. The results of optimization efforts to date are summarized as follows:

- Powder milling appears to be the most pervasive processing component dominating microstructural and material response. It is suggested that coarse nitrides and oxides of aluminum (formed during milling) inhibit recrystallization grain growth in high impurity alloys.

- Creep response of the respective powder batches is proportional to the underlying grain structure produced via heat-treatments. Thus, ODS Fe_3Al powder batch C with its completely recrystallized tube wall section offers the best creep response.

- Recrystallization processing in inert atmospheres exhibits a significant and reproducible improvement in hoop creep response.

- Thermo-mechanical processing to alter the underlying grain shape via cross rolling has a similar beneficial effect on improving hoop creep response.

ACKNOWLEDGEMENTS

Electron microscopy studies are conducted in part at the DOE-BES funded SHaRE facility at the Oak Ridge National Laboratory with the assistance of Dr. Ed Kenik, Dr. Neal Evans and Dr. Jim Bentley. The assistance of Ken Blakely of the Materials Processing Group at ORNL with the cross rolling trials in ODS alloys is gratefully acknowledged.

REFERENCES

1 C. Capdevila and H.K. Bhadeshia, 'Manufacturing and Microstructural Evolution of Mechanically Alloyed Oxide Dispersion Strengthened Superalloys', *Advanced Engineering Materials*, 2001, **3**(9), 647.
2. R.F. Singer and E. Arzt, *High Temperature Alloys for Gas Turbine and Other Applications*, D. Reidel Publishing Co., Liege, 1986.
3. F. Starr, 'Emerging Power Technologies and Oxide Scale Spallation', *Mater. High. Temp*., 1995, **13**(4), 185-192.
4 B.A. Pint and I.G. Wright, 'Long Term High Temperature Oxidation Behavior of ODS Ferritics', *Journal of Nuclear Materials*, 2002, **307-311**, 763-768.
5. V.K. Sikka, S. Viswanathan, C.G. McKamey, *Structural Intermetallics*, 1993, TMS Publication, Warrendale PA, 483.
6. P.G. Sanders, V.K. Sikka, C.R. Howell, R.H. Baldwin, 'A Processing Method to Reduce the Environmental Effect in Fe_3Al-Based Alloys', *Scripta Met*., 1991, **25**(10), 2365-2369.

7. B.K. Kad, 'Oxide Dispersion Strengthened Fe_3Al Bases Alloy Tubes', *Advanced Research Materials Report*, ORNL/Sub/97-SY009/02, October 2001.
8. B.K. Kad, V.K. Sikka and I.G. Wright, 'Oxide Dispersion Strengthened Fe_3Al-Based Alloy Tubes', *14th Ann. Conf. Fossil Energy Materials*, Knoxville, TN, May 2000; *ibid*. 'High Temperature Performance of ODS Fe_3Al-Based Alloy Tubes' *15th Ann. Conf. Fossil Energy Materials*, Knoxville, TN, April 2001; *ibid*. 'Optimization of High Temperature Hoop Creep Response in ODS-Fe3Al Tubes' *17th Ann. Conf. Fossil Energy Materials*, Knoxville, TN, April 2003
9. I.G. Wright, B.A. Pint, E.K. Ohriner and P.F. Tortorelli, 'Development of ODS- Fe_3Al Alloys', *Proc. 11th Ann. Conf. on Fossil Energy Materials*, 1996, ORNL Report ORNL/FMP-96/1, CONF-9605167, p. 359.
10. B.K. Kad, S.E. Schoenfeld, R.J. Asaro, C.G. McKamey, V.K. Sikka, 'Deformation Textures in Fe_3Al Alloys: An Assessment of Dominant Slip System Activity in the 900-1325K Temperature Range of Hot Working', *Acta Metallurgica*, 1997, **45**(4), 1333-1350.
11. M. Mujahid, C.A. Carter and J.W. Martin, 'Microstructural Study of a Mechanically Alloyed ODS Superalloy', *J. Mater. Eng. Performance*, 1998, **7**(4), 524.
12. Y. Iino, 'Effects of High Temperature Air and Vacuum Exposure on Tensile Properties and Fracture of ODS Alloy MA6000', *Mater. Sci. Eng*., 1997, **A234-236**, 802-805.
13. A. Czyrska-Filemonowicz, D.Clemens and W.J. Quadakkers, 'The Effect of High Temperature Exposure on the Structure and Oxidation Behavior of Mechanically Alloyed Ferritic ODS Alloys', *J. of Mater. Proc. Tech*., 1995, **53**, 93-100.

REDUCTION IN DEFECT CONTENT IN ODS ALLOYS

Justin Ritherdon
University of Liverpool, Department of Engineering, Liverpool, L69 3GH, UK
E-mail: j.ritherdon@liv.ac.uk; Telephone: (0044) 151 794 5396; Fax: (0044) 151 794 4675

Andy R Jones
University of Liverpool, Department of Engineering, Liverpool, L69 3GH, UK
E-mail: andy.jones@liv.ac.uk; Telephone: (0044) 151 794 8026; Fax: (0044) 151 794 8344

ABSTRACT

In applications where creep resistance is paramount, the coarse, high aspect ratio grains attainable in mechanically alloyed (MA) oxide dispersion strengthened (ODS) FeCrAl alloys are extremely desirable where appropriately aligned. It is generally accepted that the formation and growth of such grain structures owes much to the presence and distribution of the different oxide dispersions in ODS alloys. In particular, it has been shown that nucleation of recrystallisation can occur much more readily in regions characterised by low number densities of oxide particles e.g. where there are powder processing defects. To study such effects further, deliberate inhomogeneities have been introduced through controlled addition of ODS-free Fe powder to PM2000 alloy prior to powder batch consolidation, to produce an alloy that is a mixed ODS/ODS-free variant of the standard commercial alloy PM2000.

This work describes studies on the specially produced ODS/ODS-free variant ranging from its condition in the as-extruded state through to full alloy recrystallisation. It is found that the ODS-free stringers are already essentially recrystallised in the as-extruded condition. Further annealing at higher temperatures leads to limited growth of these incipient recrystallisation nuclei into surrounding PM2000 alloy; but there is little general impact on final grain size and morphology: in effect, the ODS-free and PM2000 regions virtually recrystallise separately. Methods to facilitate greater recrystallisation interaction between the ODS-free and the bulk PM2000 are detailed and the interaction processes observed through scanning and transmission electron microscopy and electron backscattering diffraction techniques are described. Also considered are the changes that occur in the microstructure in the neighbourhood of the interface between the original mild steel containment can and the fully consolidated ODS/ODS-free FeCrAl alloy during subsequent recrystallisation annealing.

INTRODUCTION

Commercial Fe-based mechanically alloyed (MA) ODS alloys such as PM2000, have a composition and microstructure designed to impart creep and oxidation resistance in components operating at temperatures from ~1050ºC to 1200ºC and above. These alloys achieve their creep resistance from a combination of factors including: the dispersion of fine scale (20-50nm diameter) Y_2O_3 particles introduced during MA which, despite formation of complex oxides involving Al from solid solution, is highly stable to Ostwald ripening; and the presence of a very coarse, highly textured, high grain aspect ratio (GAR) structure which results from and is sensitive to the alloy thermomechanical processing history.[1-3]

Alloys are, typically, hot consolidated to full density using techniques such as Hot Isostatic Pressing (HIP), extrusion, upsetting or forging following which further hot and cold working (e.g. rolling, drawing etc) is used to produce the final alloy form.[4] Subsequently Fe-based ODS alloys are given a secondary recrystallisation anneal to produce very coarse grain structures for creep resistance. A wide variety of product forms can be achieved, including bar, sheet, wire, tube and foil etc.

Despite the benefits offered by the currently processed range of Fe-based ODS alloys they suffer from a number of performance shortfalls. In particular, the high GAR structures induced for creep resistance lead to anisotropic creep properties, which exhibit maximum creep resistance when the principal creep stress is aligned with the major axis of the grain structures.[5,6] But the grain structures evolved during secondary recrystallisation of currently available Fe-based ODS alloys strongly align with the principal product forming direction, which means that in a product such as conventionally HIP'd and hot extruded tube the high GAR direction is along the tube axis.[1,2,5,7] Moreover, in the Fe-based ODS alloys this alignment cannot be altered by directional thermal treatments such as zone annealing.[7] So, for Fe-based ODS alloy tubing currently available for high temperature internally pressurised applications, the direction of maximum creep strength is orthogonal to the direction of maximum principal creep stress (the hoop stress). As a result, creep life in the hoop orientation in Fe-based ODS alloy tube may be no better than 20% of that in uniaxially loaded and crept tube.[8] Moreover, pressurised tube burst data for material with current microstructures indicates a creep life (~ 14,500h / 1100ºC / 5.9MPa pressure) that is ~ 10% of that likely to be required for tube for application in high temperature heat exchangers (100,000h life) for power generation applications.[9]

Much work has been undertaken and is still in progress to optimise this grain size and to steer it so that it is favourably orientated with respect to the principal stresses in a particular system by means of techniques such as flow-forming and torsional deformation.[10,11] However, the idea of an optimised microstructure is subjective and depends upon the intended application of the FeCrAl alloy. In some situations, it may be advantageous for the FeCrAl component to have an increased level of ductility and impact resistance, or more isotropic mechanical properties. In such situations a refined grain structure may be preferable, with finer, more equiaxed grains. It has been shown that recrystallisation occurs much more readily at gaps in the dispersoid distribution, notably at stringers found in some ODS-Fe_3Al alloys, and it is hoped that this effect can be understood and utilised to more successfully manipulate nucleation of recrystallisation, offering not only better control of evolution of coarse grained microstructures but also the option for more refined microstructures in ODS FeCrAl alloys.[10] In the present study, such gaps in the oxide distribution have been made by the deliberate addition of non-ODS powder to a PM2000 ODS alloy prior to consolidation.

RECRYSTALLISATION IN AS-EXTRUDED PM2000/ODS-FREE VARIANT

The PM2000/ODS-free variant was manufactured by Plansee GmbH by mixing 1wt% of pure Fe (ODS-free) powder (MPD 127μm) with standard PM2000 MA powder and then consolidating at an extrusion ratio of 9:1 in a mild steel can. The resulting rod comprised a solid core of PM2000, containing elongated, Fe-rich, ODS-free regions of ~25μm diameter and up to 2mm long, surrounded by an integral mild steel sleeve.

Immediately after extrusion, the microstructure of the PM2000/ODS-free variant was as shown in Figs 1a-b. It appears that the elongated regions of ODS-free material (arrowed in Fig. 1a) have recrystallised at the extrusion temperature to a fairly coarse grain size of ~20μm, while the ODS material has the typical deformed, as-extruded microstructure of standard PM2000. A region surrounding the stringers of more deeply polished material is also visible, particularly in Fig. 1a. The high polishing rate is believed to be due to chemical inhomogeneity between the PM2000 and the Fe-rich ODS-free material as measured by TEM-EDS analysis. The effect disappeared on further annealing as inter-diffusion caused the composition to homogenise. The TEM micrograph in Fig. 2 does not show any microstructural changes coincident with the softening effect.

At this stage, no recrystallisation interaction was seen between the ODS-free and the PM2000 and the larger grains were confined to the ODS-free regions as can be seen in Fig. 3.

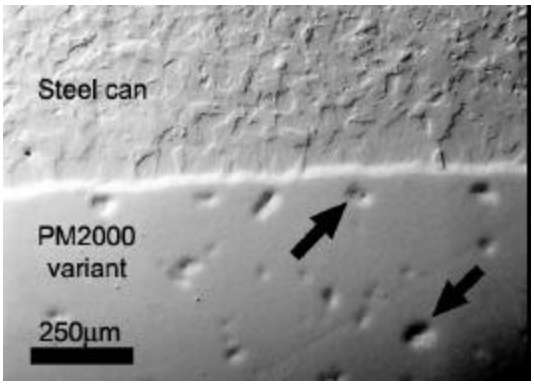

Figure 1a

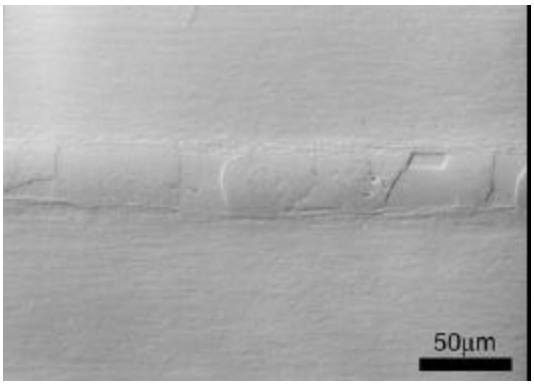

Figure 1b

a) Transverse and b) longitudinal (higher magnification) sections of as-extruded PM2000 variant.

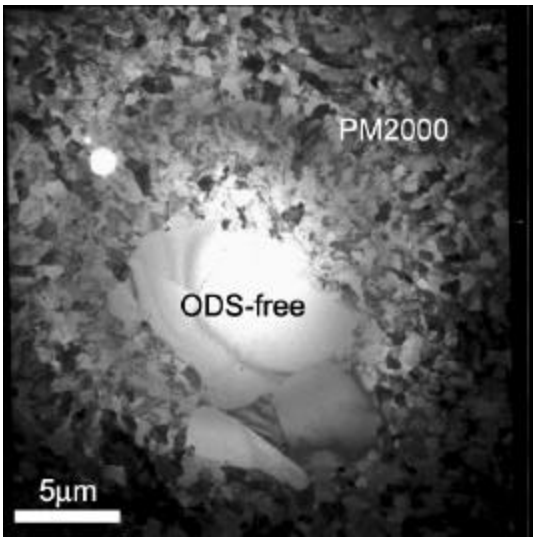

Figure 2
TEM micrograph of a transverse section though an ODS-free region.

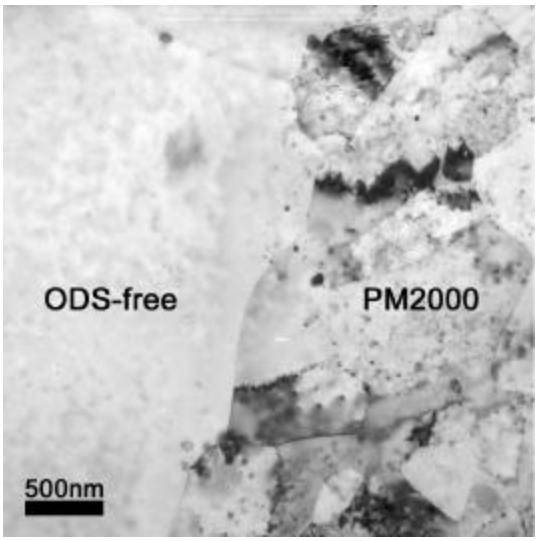

Figure 3
TEM micrograph of the interface between PM2000 and ODS-free material

Samples of the variant were annealed at 1380°C for 5 minutes and 60 minutes respectively.
After 5 minutes annealing, the microstructure had not changed noticeably but the uneven polishing effects were no longer apparent, presumably due to chemical homogenisation by inter-diffusion during annealing.
After 60 minutes, however, the whole sample appeared to have recrystallised. The PM2000 was extremely coarse-grained and, in transverse sections, the positions of the ODS-free regions appear to be marked by equiaxed but irregularly shaped grains of ~100µm diameter (see Fig 4a, and longitudinal section, Fig. 4b). The EBSD map of a transverse section in Fig. 5 shows that the scattered finer grains share no obvious orientation relationship with the surrounding coarse-grained PM2000. Indeed, the pole figures in Fig. 6 suggest that the ODS-free material effectively has no texture component, whereas the PM2000 has a clear <111> fibre texture aligned with the extrusion direction. This adds to the suggestion that the finer-grains have originated from the ODS-free material. Moreover, many of the finer grains contain a small area of different orientation. It is thought that these are sections through elongated recrystallising grains growing axially within adjacent PM2000, yet originating in the ODS-free material.
In corresponding longitudinal sections, it could be seen that the large, irregular grains did indeed coincide with the ODS-free regions as can be seen in Fig 4b.

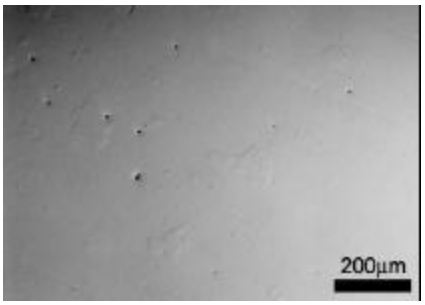

Figure 4a

Figure 4b

a) Transverse and b) longitudinal sections of PM2000 variant after annealing at 1380ºC for 1 hour.

Importantly, these experiments reveal that recrystallised grains that originate in the ODS-free regions are capable of growth into surrounding regions of PM2000 alloy; however, despite early nucleation, the extent of this out-growth is limited. Away from these regions the recrystallisation of the PM2000 is more or less unaffected by presence of the ODS-free regions. It is as if the two types of region, ODS-free and PM2000 recrystallise virtually independently, to form separate grain structures and textures. Even though the average grain size must be reduced slightly by the presence of the smaller grains associated with the ODS-free material, the overall grain structure in the PM2000 remained essentially unrefined. There appeared to be limited interaction between the recrystallising ODS-free regions and the PM2000, which may, in part, be due to the disparity between the recrystallisation temperatures of these two regions. It is suspected that if the recrystallisation temperatures of the two regions were closer, then the level of interaction during recrystallisation could be increased, leading to more control of grain structure evolution.

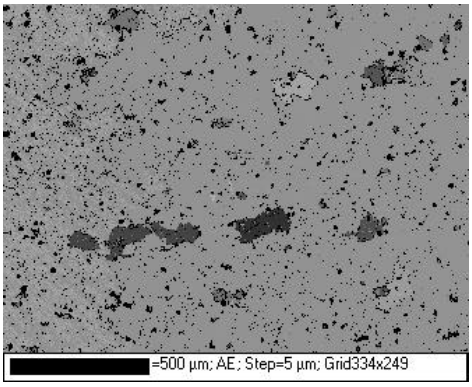

Figure 5
Euler contrast EBSD map showing fine grains with random orientations scattered throughout recrystallised PM2000.

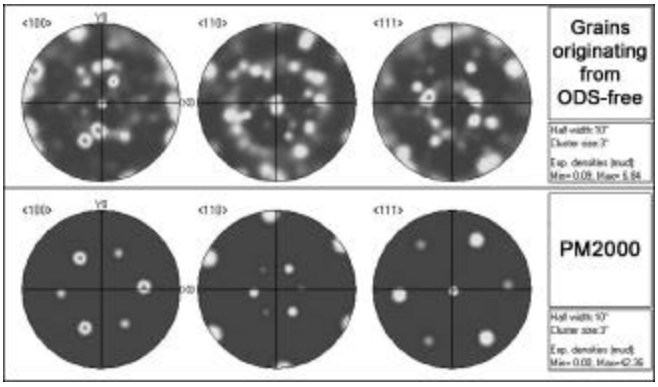

Figure 6
Pole figures taken from fine grains originating from ODS-free material and from the surrounding PM2000.

STRAINING AND RECRYSTALLISATION OF PM2000/ODS-FREE VARIANT

Recrystallisation temperature is strongly affected by the cumulative level of plastic strain in an alloy. On this basis, it was reasoned that light re-working of the recrystallised ODS-free regions in as-extruded alloy to a level just above that of the critical strain for these regions should add slightly to the plasticity in the as-extruded PM2000 regions, but would bring the recrystallisation temperatures of both regions into closer proximity. To determine the critical strain for recrystallisation in ODS-free regions in the PM2000, a FeCrAl alloy, Kanthal, was used as a model for bend and recrystallisation tests that would provide a range of strains across a single sample for subsequent annealing trials.

Initially, the Kanthal strip was cold rolled and recrystallised to provide a deformation free, uniform starting grain. This strip was then bent to an internal diameter (ID) of 10mm and annealed at 1000ºC for 1 hour. This resulted in recrystallisation in the more highly strained regions of the strip, as seen in Fig. 7.

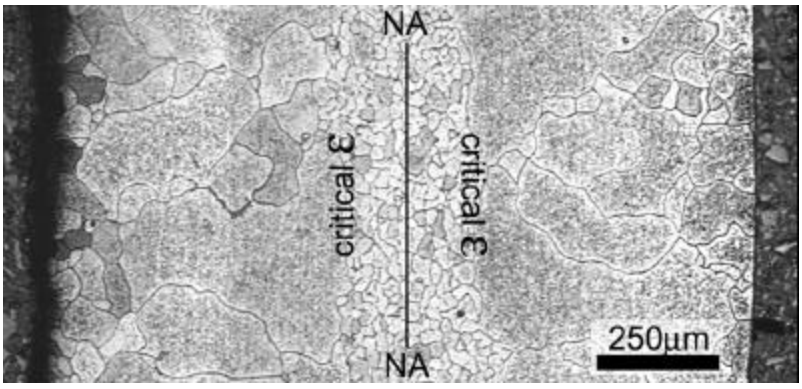

Figure 7
Kanthal that has been bent and recrystallised.
The neutral axis (NA) and the position of critical strain are shown.

This recrystallised material was concentrated towards the inner and outer band radius of the sample, away from the neutral axis, as might be expected. By measuring the distance of the first, coarsest recrystallised grain from the neutral axis, the strain at this point and, hence, the critical strain could be calculated. It was estimated to be 0.04 using the simplified formula $e=z/(r+0.5t)$, where z is the distance from the neutral axis, r is the internal radius and t is the sample thickness.
Using this information, it was thought possible to deform ODS-free regions to their critical strain in order to drive up the recrystallisation temperature. For practical purposes, it was decided that the simplest first approach would be to replicate the bending technique used with the Kanthal samples to introduce an appropriate range of strains in the ODS-free/PM2000 alloy samples, taking due account of the data gathered from the Kanthal analysis.

As a first step, the as-extruded ODS-free/PM2000 alloy was cold rolled and annealed to provide a predictable recrystallised microstructure in the ODS-free regions; but at the same time, this cold rolling and annealing was carefully chosen so as not to trigger recrystallisation in the surrounding PM2000 regions, instead adding to the plasticity already introduced by consolidation and extrusion. Hence, the variant was annealed at 1100ºC/1 hour after cold-rolling so that the ODS-free material recrystallised but the ODS PM2000 did not, thus rendering the ODS-free material strain-free but the PM2000 additionally deformed and recovered. Subsequently, samples were bent to an ID of 10mm and annealed at 1300ºC so that the entire variant would recrystallise concurrently. Samples were annealed for different lengths of time; some short so that the initial, stages of recrystallisation and interaction between the ODS-free regions and the surrounding PM2000 could be observed. Such samples were then sectioned longitudinally and prepared for EBSD and SEM examination.

In a sample cold rolled by 26%, annealed at 1100ºC/1 hour, bent to an ID of 10mm and then annealed at 1300ºC for 5 minutes (CW26%, 1100ºC/1hour, ID10mm, 1300ºC/5min) recrystallisation had initiated and the microstructure comprised a mixture of recrystallised and unrecrystallised grains in the PM2000 and the ODS-free regions. It was observed that grains from within the ODS-free regions appeared to have 'burst' out from their as-extruded 'band' and had begun to spread into the PM2000. Even though such interaction was limited in extent, it nevertheless showed that interaction was possible and that grain refining by the addition of ODS-free material ought to be feasible. Figs 8a and 8b show an area where grains have 'burst' from the ODS-free material into the PM2000.

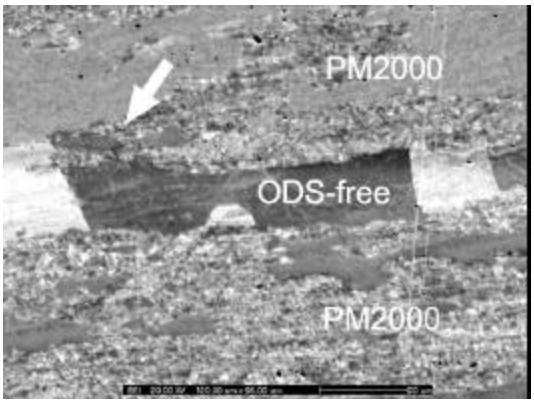

Figure 8a

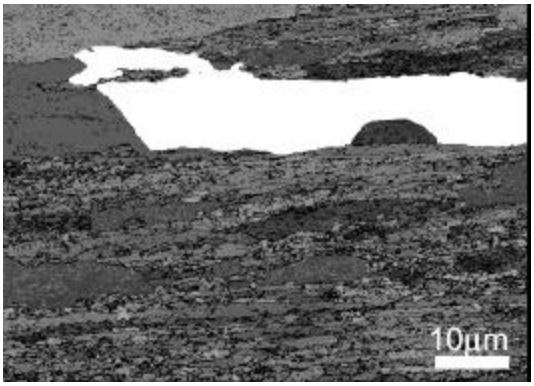

Figure 8b

FESEM images showing growth (arrowed) of grains from the ODS-free region into unrecrystallised PM2000. (a) Orientation contrast and (b) Euler contrast.

Fig. 8a is a FESEM orientation contrast image showing an ODS-free region surrounded by coarse and fine PM2000. The microstructure and the extent of individual grains is better illustrated in Fig. 8b which is an EBSD image where the grains are marked in Euler contrast according to their orientation except for the large, white grain which has been highlighted in white to mark it clearly. The lines of the as-extruded ODS-free region are clearly visible and it can be seen that the white grain has grown into the PM2000 at its top-left corner, spreading into unrecrystallised PM2000. An adjacent ODS-free grain to the left of the white grain also shows a similar effect at its top edge.

A sample was annealed at 1200ºC for 15 minutes (CW26%, 1100ºC/1hour, ID10mm, 1200ºC/15min) in order to slow the recrystallisation processes. Recrystallisation was found to be similar to that seen in the 1300ºC/5min sample, but unrecrystallised PM2000 was a little more prevalent. Growth of grains from the ODS-free regions was again observed, as seen in Fig. 9. Here growth (arrowed) had originated from the ODS-free grain (*) spreading into adjacent unrecrystallised PM2000. The orientation contrast image was slightly misleading, showing a change in contrast between the arrowed grains and across the ODS-free grain, while point EBSD analyses demonstrated that the grains marked all shared the same orientation and were, therefore, one grain.

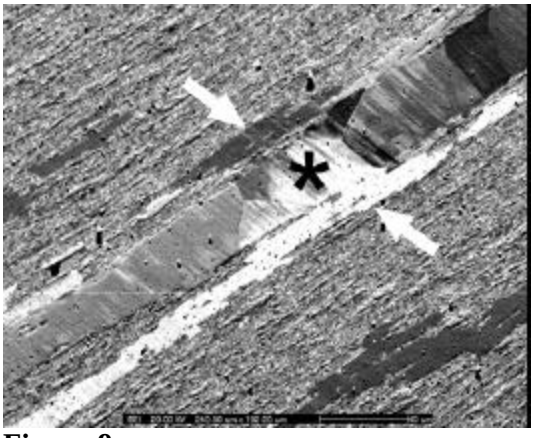

Figure 9
Orientation contrast image of a sample annealed at 1200ºC/5min showing grain growth from ODS-free into PM2000.

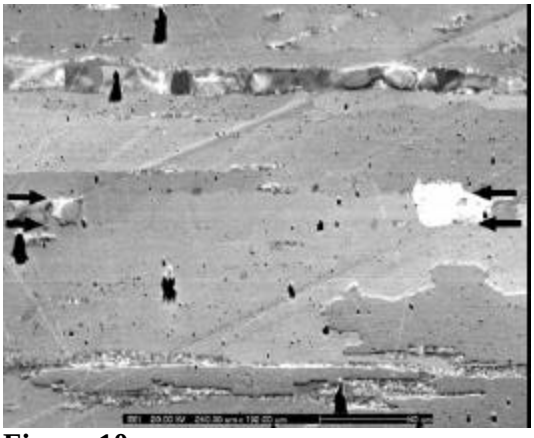

Figure 10
Orientation contrast image of a sample annealed at 1300ºC/15min showing more interaction between ODS-free and PM2000.

After annealing at 1300ºC for 15 minutes (CW26%, 1100ºC/1hour, ID10mm, 1300ºC/15min), recrystallisation was almost complete. Very little fine-grained, as-extruded PM2000 microstructure remained, though some is seen in Fig. 10. The figure also shows that elongated ODS-free regions still persist and appear not to interact with the PM2000 on the whole. There is some interaction however, and the ODS-free region arrowed in Fig. 10 contains a 'gap' ~160µm in length which is filled by one of the large, recrystallised grains which extends far into the PM2000 mainly below the ODS-free region.
This is more clearly illustrated in Fig. 11, an EBSD map which shows the same region in Euler contrast at slightly lower magnification. The 'interrupted' ODS-free region is clearly visible as is an unbroken ODS-free region which appears not to have interacted with the PM2000 at all. Some of the remaining fine-grained as-extruded PM2000 microstructure can also be seen, lower down on the map.

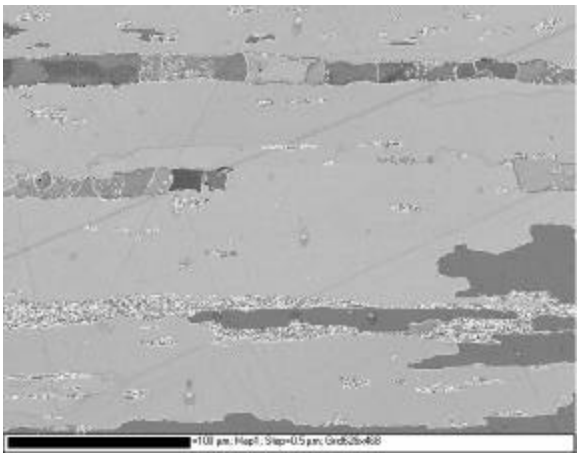

Figure 11
EBSD Euler contrast map showing a discontinuity in an elongated ODS-free region where ODS-free grains have interacted with PM2000 grains.

Those grains within elongated ODS-free regions that did not encroach into the PM2000 during annealing appeared to have undergone the opposite effect and the well defined stringer edges, typified in Fig. 1b, became much more convoluted and irregular. This effect can be seen in Fig. 12, a higher magnification EBSD map of the discontinuous ODS-free region shown in Fig. 11. It seems that grains from the recrystallised PM2000 are in the process of growing *into* the ODS-free region. As this sample represents only the early stages of recrystallisation, it is possible that such ODS-free regions could eventually disappear as PM2000 grains grow. This offers the intriguing possibility that deformed grains in ODS-free stringers that do not undergo recrystallisation and grow out into the PM2000, may subsequently be consumed by large grains originating in the PM2000 that grow-through the stringer; and this is an alternative explanation for the gap seen in the stringer in Fig. 11.

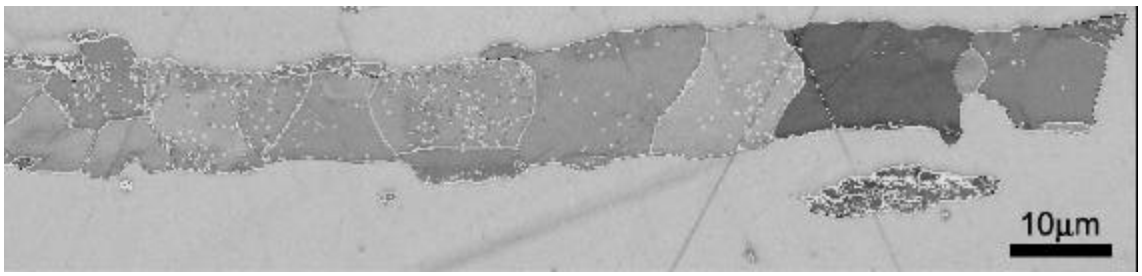

Figure 12
EBSD map showing in growth of PM2000 grains into an ODS-free region all along its length, creating an irregular interface.

It should be noted that in all the samples where ODS/ODS-free interaction was observed, the distribution of the interacting regions bore no obvious correlation with critical strain patterns seen earlier in the Kanthal. For example, the ODS-free region in Fig. 11 lay along a position of an estimated strain of 0.11, far higher than the estimated critical strain of 0.04. This may be due to the small volume of ODS-free material available for nucleation reducing the probability of nucleation in the ODS-free regions at the nucleation densities seen at the critical strain. It is therefore clear that the effects on recrystallisation introduced by the strain induced by the bending are more complex than originally envisaged and require additional interpretation. However, the bending strain does have the effect that the PM2000 recrystallises to a finer grain size at the outer edges of the sample than it does at the sample centre, where strain is low.

RECRYSTALLISATION AND PHASE TRANSFORMATIONS IN MILD STEEL EXTRUSION CANS

During recrystallisation experiments, it was noted that the microstructure of the mild steel extrusion can changed with time at temperature. This is clearly illustrated in Fig. 13. Immediately after extrusion the steel has a typical ferrite-pearlite structure. During annealing, aluminium and chromium progressively diffused into the mild steel can from the PM2000. This was accompanied by counter-diffusion of C into the PM2000 from the mild steel. In the can adjacent to the PM2000, these progressive compositional changes suppressed the γ/α transformation, allowing stable, coarse ferritic grains to grow. Further into the can, the inter-diffusion modified alloy hardenability sufficiently to result in transformation after austenitisation to local bainitic/martensitic components in the microstructure (circled). With additional annealing, inter-diffusion extended the stable ODS-free ferrite region further into the steel can.

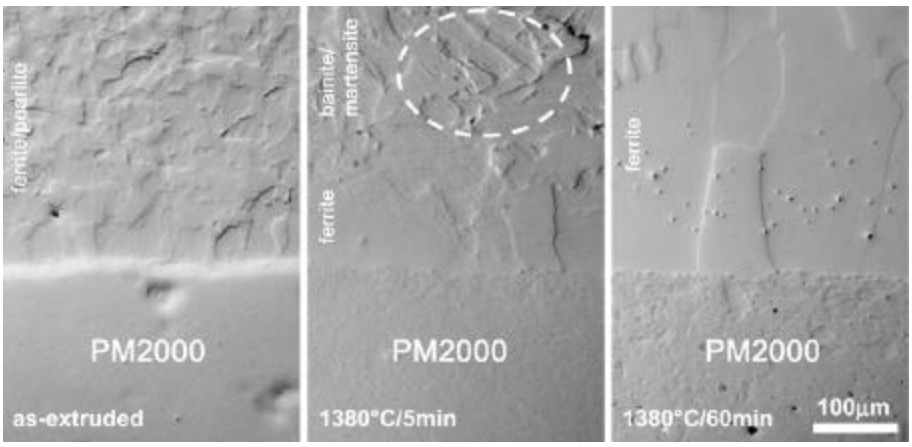

Figure 13
Optical micrographs showing the changes in microstructure of the extrusion can with time at temperature.

The simple, calculated diffusion profiles for Al and Cr in Figs 14a-b show that Al diffuses more quickly and the extent of its diffusion matches the observed changes in steel microstructure. This suggests that the microstructural changes are linked primarily to the Al concentration rather than to that of the Cr. This is not unreasonable, as Al is a ferrite stabiliser, with a Cr-equivalence around five times that of Cr itself. Simultaneously, C diffuses rapidly out of the mild steel can into PM2000, decarburising the steel and substantially reducing the local Ni-equivalent value as the Cr-equivalence rises. However, over the distances studied here the carbon concentration may be assumed to be almost constant and not related to microstructural changes.

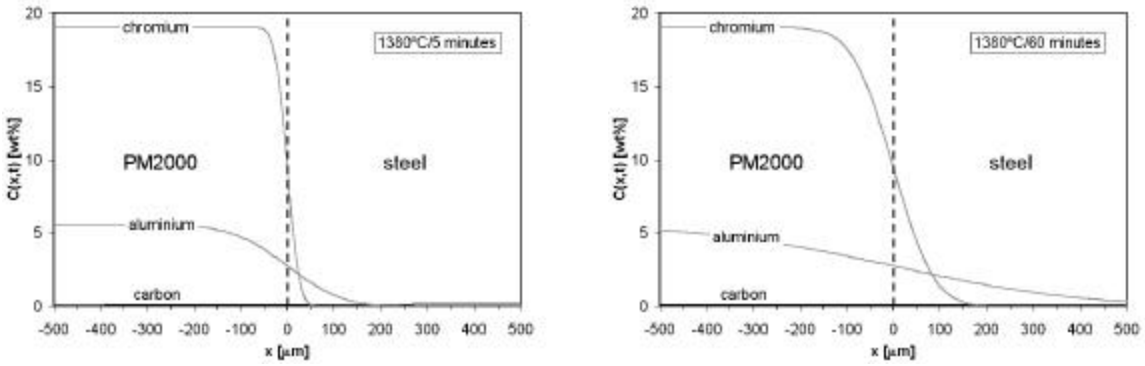

Figure 14
Diffusion profiles for chromium, aluminium and carbon across the PM2000/steel can interface after a) 5 minutes and b) 60 minutes at 1380ºC.

The progressive nature of these changes is reflected in the development of an almost columnar grain structure in the 'mild steel' can adjacent to the ODS alloy during annealing at 1300ºC for 60 minutes. Essentially, this represents the progressive migration into the mild steel can during annealing of the position of the stable α/γ interface. The effect of these changes in terms of the recrystallisation behaviour under consideration is that, immediately following consolidation, no extrusion deformation is likely to be retained in the can, since it will have been removed by the γ/α transformation that took place on cooling following annealing.

CONCLUSIONS

Recrystallisation behaviour has been studied in a special variant of PM2000 ODS alloy containing deliberately introduced ODS-free regions. A number of conclusions have been made concerning the changes that can be induced in deformation and annealing behaviour. Specifically:

(i) Migrating recrystallising interfaces can be induced to form in ODS-free regions and grow out into surrounding primary recrystallised PM2000 alloy; however, the rate of growth of these nuclei is slow and these regions do not dominate formation of final grain size or texture.
(ii) Final texture in extruded and recrystallised PM2000 containing ODS-free regions has a strong <111> fibre component and a weak superimposed random texture; the latter arises from grains originating in ODS-free regions.
(iii) Thermo-mechanical manipulation, including critical strain annealing, can be used to induce a near overlap in the recrystallisation temperatures of PM2000 alloy and the introduced ODS-free regions in the same sample; stimulating interaction that would appear to include migration of recrystallising interfaces both out of and into ODS-free regions at different points.
(iv) Inter-diffusion of Cr, Al and C at the mild steel can wall during sustained annealing influences subsequent transformation behaviour and the potential for any interaction that could affect recrystallisation in the ODS alloy.

ACKNOWLEDGEMENTS

This research was sponsored by the Advanced Research Materials (ARM) Programme, U.S. Department of Energy, Office of Fossil Energy under contract DE-AC05-96OR22464 managed by U.T.–Battelle, LLC.
The technical help and advice of Prof. D.J. Prior and Mr. N. Seaton of the Earth Sciences Department, University of Liverpool, during the collection and analysis of EBSD data is gratefully acknowledged.

REFERENCES

1. K H Matucha and M Ruhle, *Metal Powder Reports*, 1993, November, 24
2. I C Elliott and G A J Hack, *'Structural Applications of Mechanical Alloying'* in ASM International Conference, Myrtle Beach, March 1990, Eds. Froes and deBarbadillo, 15
3. M J Bennett, H Rosemary and J B Price, *Heat Resistant Materials*, 1991,ASM International, 95
4. G Korb and D Sporer, *Proc. Conf. 'High Temperature Materials for Power Engineering'*, 1990, Liege, Eds. Bachelet et al., Kluwer Academic Pub., 1417
5. R Timmins and E Arzt, *'Structural Applications of Mechanical Alloying'* in ASM International conference, Myrtle Beach, March 1990, Eds. Froes and deBarbadillo, 67
6. B Kazimierzak, J M Prignon, F Starr, L Coheur, D Coutsouradis and M Lamberigts *ibid*, 137
7. H K D H Bhadeshia, *Materials Science and Engineering*, 1997, **A223**, 64
8. B Kazimierzak private communication
9. F Starr, A R White and B Kazimierzak, *Proc. Conf. 'Materials for Advanced Power Engineering'*, 1994, Liege, Eds Coutsouradis et al., Kluwer Academic Pub., 1393
10. A.R. Jones, J. Ritherdon and D.J. Prior, *Proc. 17th Annual Conf. on Fossil Energy Materials*, Baltimore, Maryland, April 22-24, 2003, Eds. Judkins et al., (ORNL, 2003)
11. Y.L. Chen and A.R. Jones, *Met and Mat Trans. A*, 2002, **32A**(12), 3777

Coal Ash Corrosion Resistant Materials Testing Program
Evaluation of the Second Section Removed in August 2003

Dennis K. McDonald
The Babcock & Wilcox Company, 20 S. Van Buren Ave., P.O. Box 351, Barberton, Ohio 44203-0351
Email: dkmcdonald@babcock.com; Telephone (330) 860-6175
Edward S. Robitz
Babcock & Wilcox Research Center, 1562 Beeson St., Alliance, Ohio 44601
Email: esrobitz@babcock.com; Telephone (330) 860-6636

ABSTRACT

The "Coal Ash Corrosion Resistant Materials Testing Program" is being conducted by The Babcock & Wilcox Company (B&W), the U.S. Department of Energy (DOE) and the Ohio Coal Development Office (OCDO) at Reliant Energy's Niles plant in Niles, Ohio to provide full-scale, in-situ testing of recently developed boiler superheater materials. Fireside corrosion is a key issue for improving efficiency of new coal fired power plants and improving service life in existing plants.

In November 1998, B&W began development of a system to permit testing of advanced tube materials at metal temperatures typical of advanced supercritical steam temperatures (1100°F and higher) in a boiler exhibiting coal ash corrosive conditions. Several materials producers including Oak Ridge National Laboratory (ORNL) contributed advanced materials to the project.

In the spring of 1999 a system consisting of three identical sections, each containing multiple segments of twelve different materials, was installed. The sections are cooled by reheat steam, and are located just above the furnace entrance in Niles' Unit #1, a 110 MWe unit firing high sulfur Ohio coal. In November 2001 the first section was removed for thorough metallurgical evaluation after 29 months of operation. The second section was removed in August of 2003 and its evaluation is just being completed. The final section remains in service and is expected to be removed in the spring of 2005. This paper briefly describes the program and its importance; the design, fabrication, installation and operation of the test system, and materials utilized; experience to date; and briefly reviews the results of the evaluation of the first section; and then presents the results of the evaluation of the second section.

INTRODUCTION

The benefits of cycle efficiency improvement in terms of both fuel cost savings and emissions reductions are well demonstrated and, as more recent programs are demonstrating, more than offset the added equipment capital costs. It has also been widely recognized, in part as a result of this program, that the most effective way to improve plant efficiency is by raising steam temperature. Work by several organizations, including the DOE, have demonstrated that raising steam pressure is not nearly as beneficial to efficiency as raising steam temperature and its impact on cost is much greater since all pressure parts must be thicker.

The greatest obstacle to raising steam temperature has been identified as the availability of materials suitable for service in superheaters and reheaters. In the final stages of superheating, the materials must not only be capable of providing sufficient strength at surface metal temperatures that can exceed the delivered steam temperature by 100°F or more, but also provide corrosion resistance against the sulfur compounds formed by many U.S. coals. This corrosion issue has not been addressed by European or Asian development programs since most of their coals are very low in sulfur.

To begin to address the corrosion issue for higher steam temperature applications, Babcock & Wilcox (B&W) began to conduct the "Coal Ash Corrosion Resistant Materials Testing Program" in 1999 at Reliant Energy's Niles plant in Niles, Ohio. The total estimated cost of $1,864,603 is co-funded by the DOE who is contributing 37.5%. OCDO is providing 33.3%. B&W is providing 17% with the remaining 12% being in-

kind contributions by Reliant Energy and suppliers of tubing for the tests. As a result of this program B&W is now also participating in a much larger follow-on program called "Boiler Materials for Ultra-supercritical Power Plants" that has been initiated by a government-industry based consortium.

This paper provides a brief overview of the program, reports progress to date, reports findings from the removal of the second of three identical tube sections, makes some comparisons with the first section removed in November 2001, and draws some preliminary conclusions.

The Program

The objectives of the program are to 1) evaluate the corrosion performance of newer superheater/reheater materials for coal-fired boilers at surface temperatures equivalent to 1100ºF (593ºC) steam, 2) select materials resistant to fireside corrosion, and 3) generate long-term corrosion field data.

The corrosion rate for most austenitic materials used for high temperature tubing increases exponentially with temperature to a peak around 1300ºF, then decreases rapidly beyond the peak. To accelerate corrosion the system was designed to achieve high surface metal temperatures.

Design began in November 1998 and installation of the sections began in April. The sections are cooled by 600ºF, 315 psi reheat steam but are located within the superheater bank of the B&W 110 MWe cyclone-fired Niles boiler, a 1950s vintage subcritical unit burning a 3-3.5% sulfur Ohio coal. Figure 1 shows the location of the test sections and Figure 2 shows the system arrangement.

Three identical four-row sections contain specimens of the twelve alloys tested; most are included three times within the top two rows to expose them to three temperature regimes. The only difference between sections is that the first section was scheduled for removal and evaluation after one year of operation, the second after three years and the third after five years.

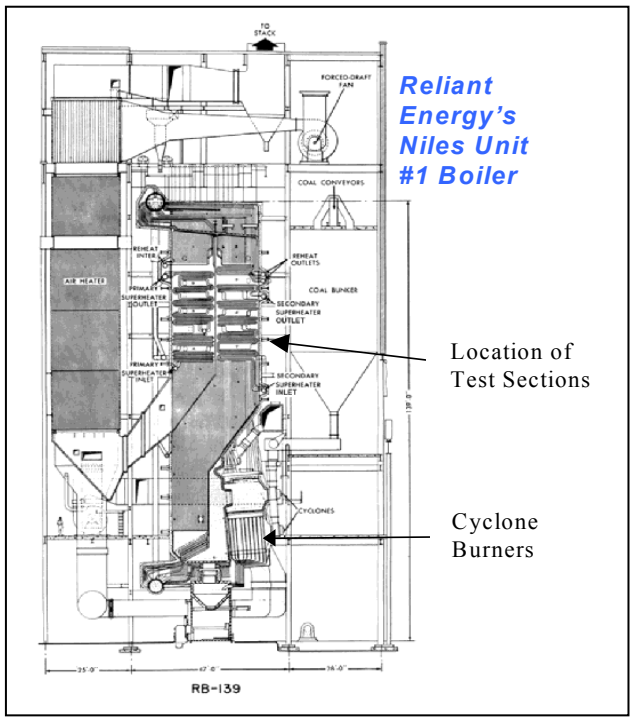

Figure 1: Niles Boiler

Surface metal temperatures are continuously calculated by the data acquisition system and correlated to the internal steam temperature, measured by thermocouples at the inlet, intermediate bend and outlet, and controlled by varying the steam flow by inlet valves.

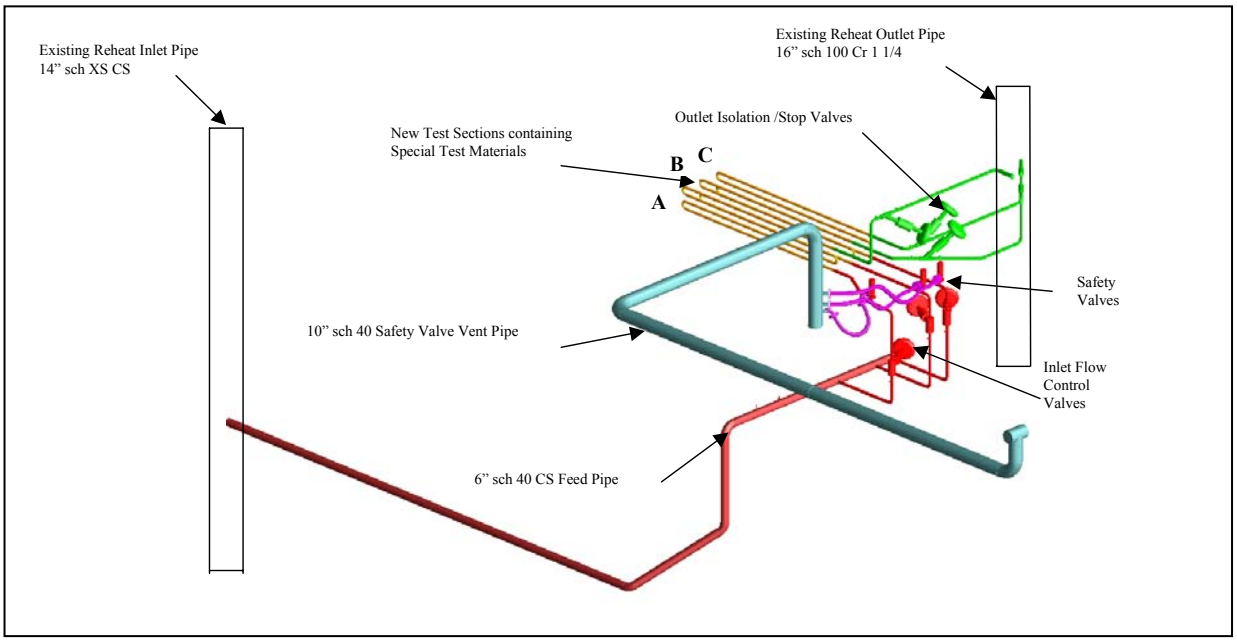

Figure 2: System Arrangement

Each of the three (3) identical test sections contains ten (10) primary and two (2) secondary advanced material samples. The primary samples are placed in three different locations within the section (see Figure 3 and Table 1). The three sections extend through the furnace front wall for the full depth of the furnace up-pass. The sections are supported from the baffle wall at their rear and the furnace front wall at their front; the wall penetration is sealed with an insulated casing box.

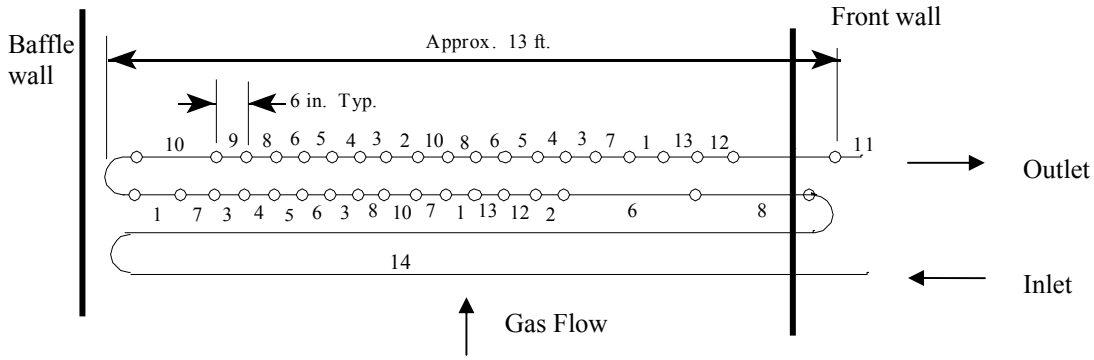

Figure 3: Location of Specimens within the Section

The sections were fabricated at the McDermott Technology, Inc., research facility in Alliance, Ohio. All but one of the 6 in. long specimens are 2.5 in. diameter by 0.400 wall. They were joined using alloy 625 filler metal by rotating the tube in a tungsten-arc orbital welder; every one of the 116 welds was x-ray clear (see Figure 4).

Installation was completed in May 1999, followed by shakedown and controls tuning (see Figure 5). During this period the steam temperature was controlled first to 1000°F and then to 1050°F before being

raised to the current temperature of 1075°F, which produced surface metal temperatures in the top row that would accelerate corrosion.

Table 1: Advanced Materials

#	MATERIAL	SUPPLIER	ASME RECOGNIZED	SIMILAR MATERIAL
1	Incoclad – Core is Incoloy 800H	INCO	Yes - Code Case 1325	SB407-UNS N08800
2	Thermie	ORNL	No	Inconel 617
3	HR3C – SA213TP310HCbN	Sumitomo	Yes	
4	Ta Modified 310	ORNL	No	SA213TP310H or SA213TP310HCbN
5	Modified 800H	ORNL	No	Incoloy 800H
6	Save 25	Sumitomo	No	SA213TP310H or SA213TP310HCbN
7	HR120	Haynes	No	SA213TP310H
8	NF709	Nippon Steel	No	SA213TP310H or SA213TP310HCbN
9	Fe3Al-2Cr/304H	ORNL	Yes	Core is SA213TP304H
10	TP347HFG – SA213TP347HFG	Sumitomo	Yes	
11	Transition Piece	SA312TP304H	Yes	
12	690 clad 800HT weld metal INCO 52	INCO	Yes	Incoloy 800H
13	671 clad 800HT weld metal INCO 72	INCO	Yes	Incoloy 800H
14	SA213TP310H	NA	Yes	

The system was plagued from startup with valve controller overheat failures as a result of unexpectedly high ambient temperatures that caused the inlet valve to open, cooling the section to around 800°F at the outlet. This condition has seldom lasted more than a day or two, thanks to the rapid response of the operators at the Niles plant. To eliminate this problem, a cooling fan and ductwork were installed to blow cooling air across each of the valves. This resulted in significant improvement but occasional problems continued. The electronic controllers were eventually replaced with mechanical devices.

Figure 4: Tungsten-arc Orbital Welder

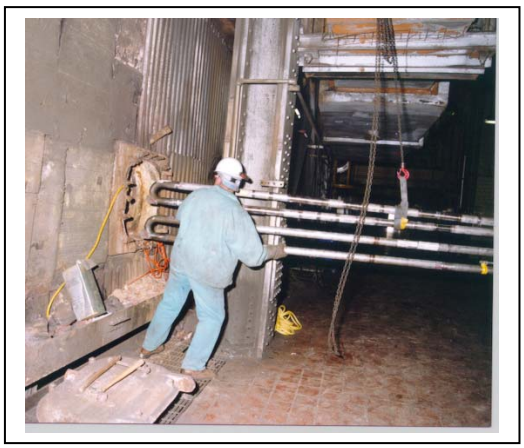

Figure 5: Installation into Niles Boiler

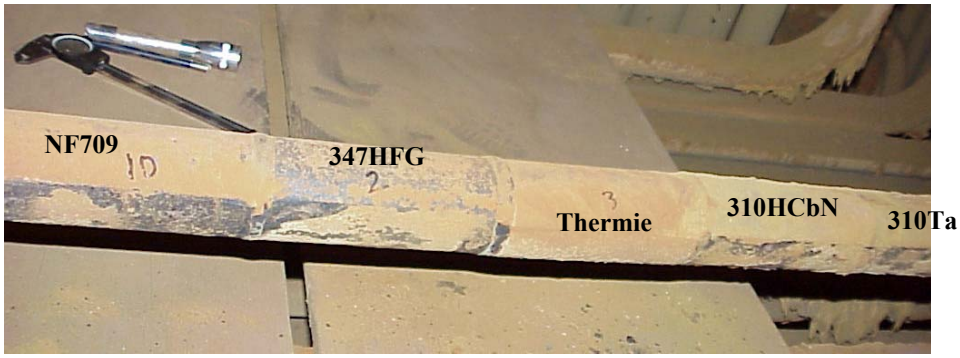

Figure 6: March 12, 2001 In-situ Inspection

Between startup and removal, inspections have been made on about 6-month intervals to monitor the extent of corrosion to avoid a failure. Figure 6 shows the in-situ condition in March 2001.

Due to outage scheduling, Section A was removed in November 2001 after 22 months of operation, equivalent to 15.5 months at temperatures conducive to corrosion rather than the intended 12. Varying corrosion was exhibited among the specimens with extreme corrosion experienced in the Save 25 piece. The Save 25 specimen actually developed a pinhole leak just prior to removal and in order to ensure operability of the remaining two sections a six-segment length containing the Save 25 specimens was removed from both Sections B and C, and replaced by Incoclad tubing "dutchmen."

Following removal of Section A and repair of Sections B and C, Sections B and C were returned to service. Sections B and C next were examined again in situ, in June 2002, after about seven additional months of service. This inspection also raised concerns, and two additional tube lengths were removed from both sections and replaced by "dutchmen." The sections then continued in service until May 2003 which marked the end of the next planned section removal and assessment period. At that time, for practical reasons, it was decided to remove and evaluate Section C rather than Section B. After replacement of some corroded segments to ensure Section B could operate for another 12 to 18 months, Section B was returned to service in December 2003 and will be removed and evaluated at the end of this program.

The results of the evaluation of the specimens from Section A were reported in a paper presented in 2003 (see references) and will not be repeated in detail. However, after presenting the results from Section C, a brief comparison is presented.

Section C Results

Total Exposure Time

After operating for about 40 months, the total exposure period for Section C summed to 28.5 months at conditions producing an average surface metal temperature that was at or above the minimum required for coal ash corrosion. Figure 7 is a schematic of Section C depicting the locations of the segments removed early. These segments were set aside and included in the overall evaluation of Section C performance. The segments removed in June 2002 experienced 21.6 months of exposure while those removed in November 2001 experienced 18.6 months at temperature, differing from the exposure time for Section A due to operational differences.

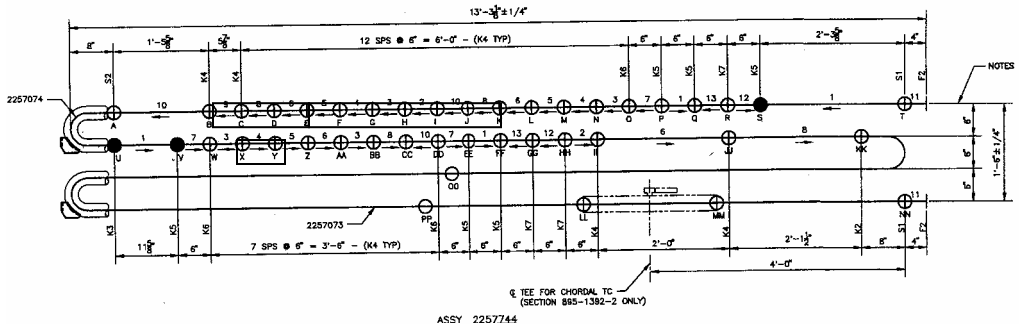

Figure 7: Schematic of Test Section Showing Position of Welds and Location of Dutchmen (i.e. Samples Removed Early)

Note: 1) Tube segments removed in November 2001 are highlighted in red.
2) Tube segments removed in June 2002 are highlighted in yellow.

Surface Metal Temperature

The daily average surface metal temperature for Section C was monitored and controlled in the same manner as was done for Section A. Calculations based on the Section C data showed that, in general, the tube segments in Section C ran approximately 10°F hotter than those at the same positions in Section A.

Evaluation

The evaluation of Section C proceeded much as it had for Section A with only a few exceptions. The most significant of these stemmed from the fact that examination of the INCO 72 weld overlay revealed that it was experiencing degradation due to a cracking mechanism that appeared to be unrelated to coal ash corrosion wastage. Additional work was performed to further characterize and understand this phenomenon.

Summary of Results

Analysis of deposits from the surface of Section C revealed the presence of constituents of the alkali-iron-trisulfates, known to promote coal ash corrosion. This and the loss of wall thickness confirm that the test environment was aggressive and challenged the ability of the candidate materials to resist wastage over the critical temperature range of 1000°F to 1300°F. Dimension rings provided the primary means of measuring the resistance of the candidate materials under these conditions.

Figure 8 shows the appearance of three Save 25 tube segment dimension rings. These three segments demonstrate that, for Save 25, the wastage rate was a strong function of temperature. The tube segment with the highest average surface metal temperature (1180°F) was completely perforated and had to be removed after only18.6 months at temperature. The tube segment at an intermediate temperature (1096°F) was removed after 21.6 months of exposure due to concerns about its high wastage rate. The tube segment at the lowest exposure temperature (1058°F) survived until the end of the Section C exposure period.

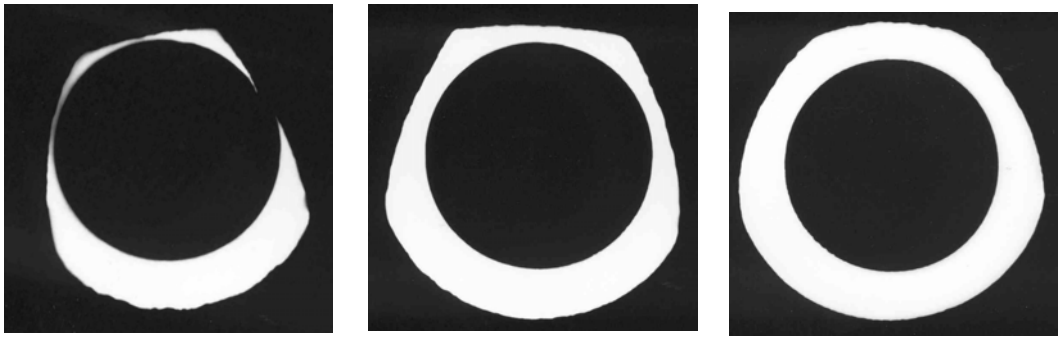

ASMT* Wastage Rate	1180 F >259 mils/yr Nov. 2001	1096 F 148 mils/yr Jun. 2002	1058 F 56 mils/yr May 2003

Figure 8: Save 25 Dimension Rings from Section C
*** ASMT = Average Surface Metal Temperature**

For these, and all of the other Section C segments, wall thickness measurements were taken at eight evenly spaced locations around the circumference of the dimension rings. These wall thickness data were used to calculate wastage rates for each of the tube segments. Figure 9 provides a bar chart showing the maximum wastage rate for the tube segments as a function of position within Section C.

Figure 10 plots the maximum wastage rate data as a function of temperature and suggests the following generalizations. The wastage rate increased with temperature for materials such as Save 25 and Modified 800H that exhibited a high overall wastage rate. Some materials such as 347HFG and HR120 exhibited an apparent decrease in wastage rate at intermediate temperatures. This suggests the possibility of more than one degradation mechanism for these materials. Other materials such as 310HCbN and 310Ta exhibited an apparent increase in wastage rate at an intermediate temperature. Finally, the more resistant high-chromium, high-nickel alloys like Incoclad 671, INCO 72 weld overlay, and INCO 52 weld overlay appeared to exhibit a decrease in rate as temperature increased.

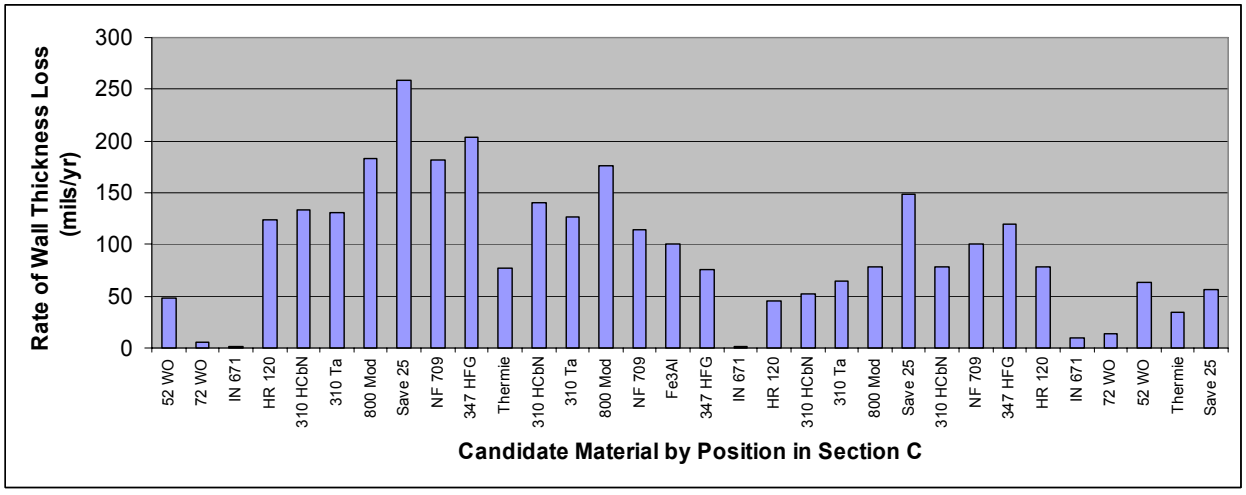

Figure 9: Maximum Wastage Rate as a Function of Position within Section C

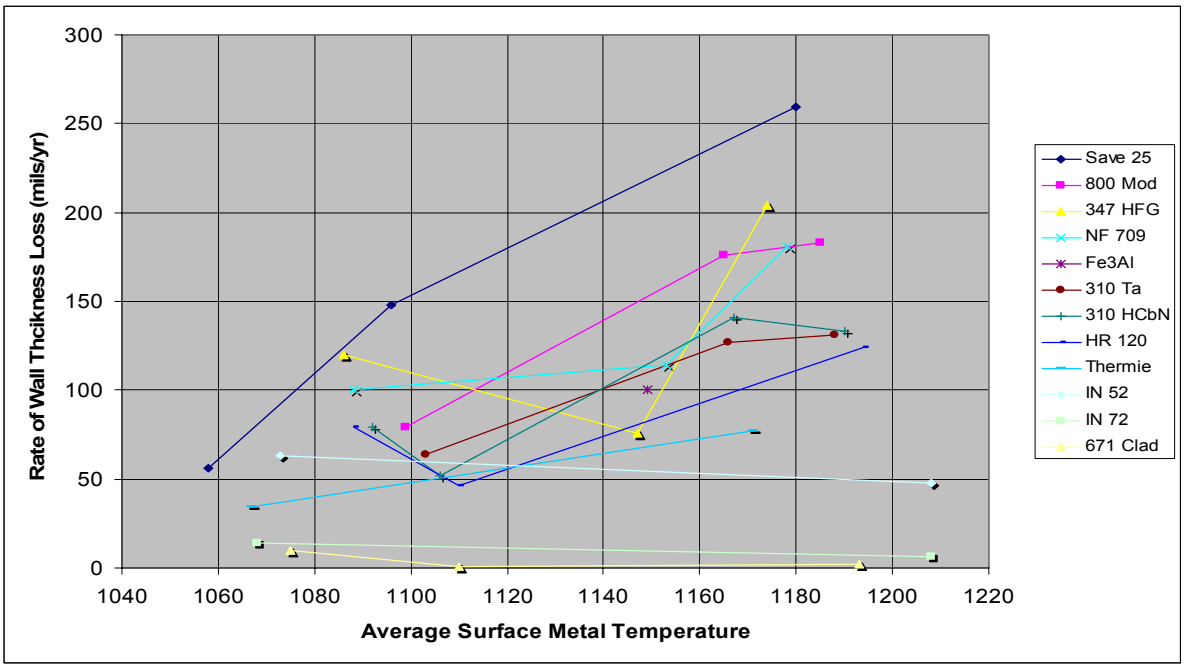

Figure 10: Maximum Wastage Rate as a Function of Temperature for Section C

There are a few issues that should be taken into account in assessing the wastage data in Figures 9 and 10. First, some of the candidate materials relied on a surface coating that had been breached at some point during the Section C exposure period. The coating therefore was no longer present to provide corrosion resistance, and at the point that the coating was breached, the remaining tube life depended on the corrosion resistance of the underlying substrate.

Analysis of Section A showed that the coating on the Fe_3Al-coated specimen was breached rapidly resulting in wastage of the underlying 304H substrate. This was also true for Section C, and in fact, no evidence could be found of the original Fe_3Al coating on these segments.

Although the INCO 52 weld overlay segments appear to have performed well compared with many of the other materials, it should be noted that within the timeframe of the Section C exposure the original 80 mil thick protective cladding was completely breached leaving only the 800H substrate to provide corrosion resistance. Note from Figure 9 or 10 that 800H has demonstrated one of the higher wastage rates.

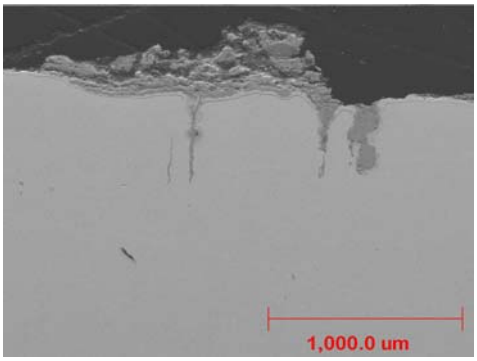

Figure 11: Weld Cracks Intersecting External Corrosion for INCO 72 Weld Overlay Test Segment

Finally, while the INCO 72 weld overlay segments consistently demonstrated excellent corrosion resistance, they appear to be suffering from a cracking problem not apparently related to the hot-side corrosion mechanism. In at least one case, corrosion had removed enough INCO 72 weld overlay to reveal an underlying crack. If this additional loss of wall thickness had been taken into account, the calculated corrosion rate would have increased by more than 50%. Figure 11 shows an SEM image of an underlying crack intersecting the tube surface. This spurred further investigations and Figure 12 shows evidence of cracking at other locations in this same segment. The cracking of concern appears to be at roughly the mid-point of the INCO 72 weld overlay.

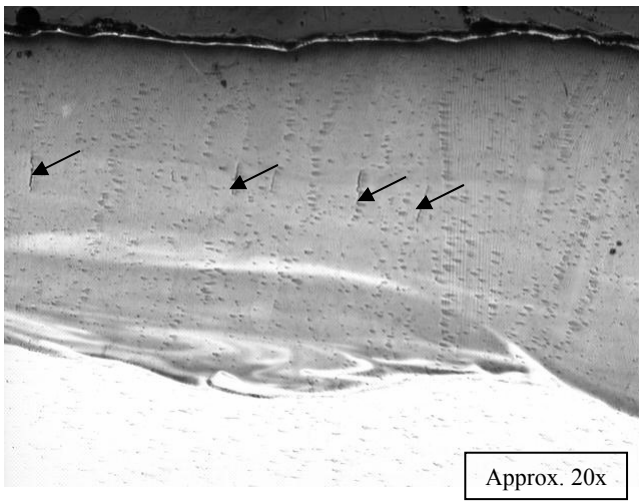

Figure 12: Internal Cracking in INCO 72 Weld Overlay Test Segment from Section C

More detailed evaluations of the other INCO 72 weld overlay segments in Section C, Section A, and in archive material revealed that these grain boundary cracks existed for all of the samples evaluated. Only a few cracks were found in the archived material which had not seen exposure in the boiler. Section A samples had somewhat more cracks and they were somewhat longer than those in the archived material. Section C had many more cracks, most of which were longer than those in Section A. This suggests that the weld cracking comes about due to an inherent weakness in the grain boundaries at the mid-cladding level, and that exposure to time at temperature causes these cracks to initiate and grow. Eventually these intersect with corrosion proceeding inward from the external surface leading to the evidence shown in Figure 11.

The implications of the INCO 72 weld overlay cracking problem are not clear. The fact that Incoclad 671, which has a very similar composition to that of the INCO 72 weld overlay, appears to be performing well without cracking suggests that this may be more of a process related problem than a material chemistry issue. Additional work would be required to resolve this.

Tube-to-Tube Weld Cross Sections

Since the sections were manufactured by welding short tube segments of candidate materials together, the question as to whether, for some of the candidate materials, these tube-to-tube welds corroded more quickly than material at mid-length of the tube segment was raised during the evaluation of Section A. There was concern that the welding heat input might have degraded the properties of the adjacent tube or cladding material. To address this issue, tube-to-tube weld cross sections were prepared. For ten of the twelve candidate materials, the Inconel 625 weld metal was more resistant to corrosion than the tube metal and the weld heat affected zone corroded less rapidly than candidate material. See Figure 13.

When the more corrosion resistant materials were considered, it was found that at some temperatures the Inconel 625 weld metal fared well compared to candidate material as indicated in Figure 14a. At other temperatures the Inconel 625 weld metal began corroding, eventually to the extent that the adjacent tube metal was affected (Figure 14b).

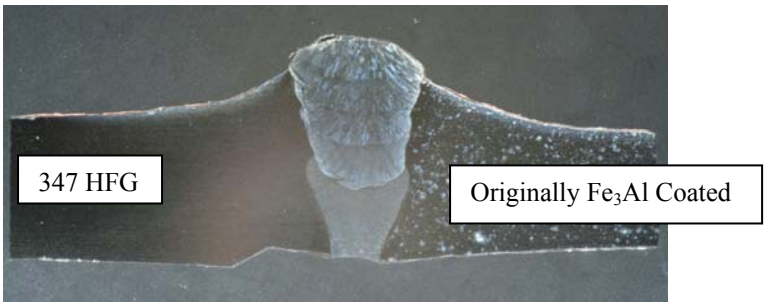

Figure 13: Typical Tube-to-Tube Weld Profile after Exposure

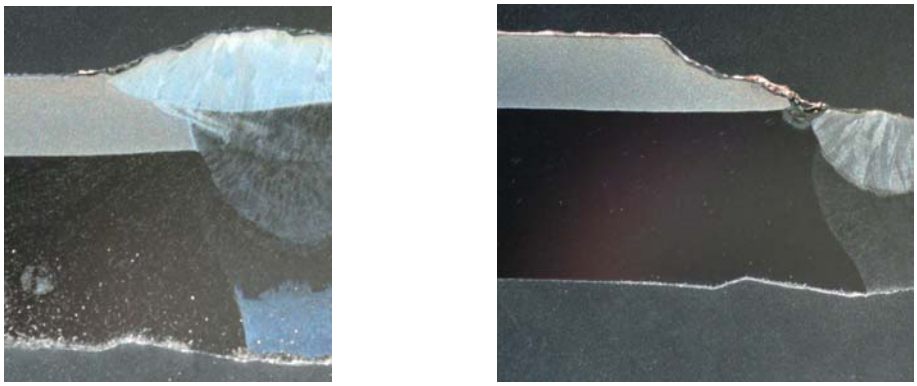

a) Weld "V" (at 1121 F) **b) Weld "P" (at 1203 F)**

Figure 14: Incoclad 671 Weld Cross Sections in Section C

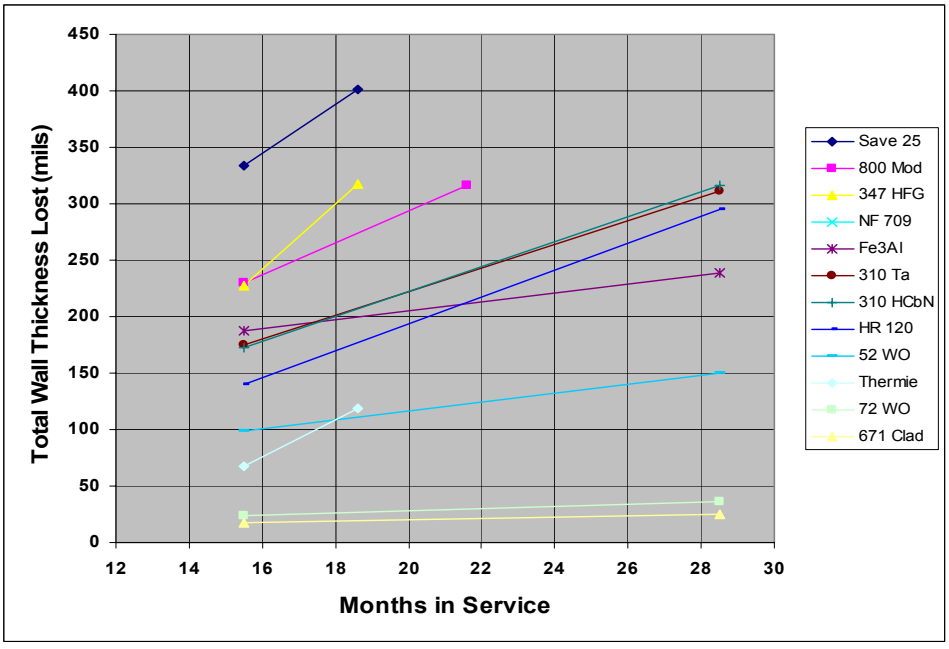

Figure 15: Wastage as a Function of Time for the Candidate Materials

Wastage as a Function of Time

The reason for evaluating multiple test sections was to characterize wastage as a function of time for each of the candidate materials. Figure 15 plots worst case wastage for the materials from Section A and Section C. The straight line fit to the data is not intended to suggest that the corrosion rate was linear for these materials. In comparing the rates for Section A and Section C, it can be said that the Section C corrosion rates typically were lower for the tube segments that showed better corrosion resistance, and higher for those that showed poorer resistance as indicated by the raw data for all the specimens in both sections, in Table 2.

Material	Tube Sample	Section A Rate Metal Lost* (mils/yr)	Section A Exposure Temperature (F)	Section C Rate Metal Lost* (mils/yr)	Section C Exposure Temperature (F)
INCO 52 Weld Overlay	AH	44	1198	48	1208
INCO 72 Weld Overlay	AG	10	1198	6	1208
Incoclad 671	AF	4	1193	2	1203
HR 120	AE	102	1184	124	1194
310 HCbN	AD	108	1180	133	1190
310 Ta	AC	123	1178	131	1188
Modified 800H	AB	169	1174	183	1185
Save 25	AA	259	1170	>259	1180
NF 709	Z	170	1167	181	1178
347 HFG	Y	174	1164	204	1174
Thermie	X	53	1160	77	1171
310 HCbN	W	133	1157	141	1167
310 Ta	V	136	1154	127	1166
Modified 800H	U	178	1150	176	1162
Save 25	T	224	1146	N/A**	1158
NF 709	S	136	1142	114	1153
Fe3Al	R	145	1139	100	1149
347 HFG	Q	83	1137	76	1147
Incoclad 671	P	2	1110	1	1121
HR 120	O	61	1100	46	1110
310 HCbN	N	98	1095	52	1106
310 Ta	M	120	1092	64	1103
Modified 800H	L	154	1088	79	1099
Save 25	K	208	1084	148	1096
310 HCbN	J	129	1081	79	1092
NF 709	I	145	1077	100	1088
347 HFG	H	176	1075	120	1086
HR 120	G	109	1077	79	1088
Incoclad 671	F	13	1075	10	1086
INCO 72 Weld Overlay	E	21	1068	14***	1079
INCO 52 Weld Overlay	D	77	1062	63	1073
Thermie	C	31	1056	34	1067
Save 25	B	67	1047	56	1058

Table 2: Maximum Wastage Rate as a Function of Time and Position

Note: Those test segments highlighted in blue experienced an increase in wastage rate with time.

* Metal loss rate is based on time at temperature, not total time within the boiler.
** N/A = Sample overlain with weld metal, thus no data available.
*** The calculated rate is based solely on wall thickness measurements and does not take into account that corrosion had removed sufficient material to connect an underlying weld crack with the surface.

Conclusions

The evaluation of Section C and consideration of Section A results, suggests the following:

- Materials which fared poorly in Section A also fared poorly in Section C. Data suggest that the wastage rate is initially high and increases with time at temperature, e.g. Save 25 and Modified 800H.
- Materials which fared well in Section A continued to fare well in Section C. For the better materials, limited data suggest that the wastage rate begins low then decreases with time, e.g Incoclad 671 and IN 72 Weld Overlay.
- Some materials, which demonstrated a moderate wastage rate, experienced a reduced wastage rate at an intermediate exposure temperature. The same performance was noted for these materials in both Section A and Section C, e.g. 310 Ta and 310 HCbN.
- Cracking was found in the IN 72 Weld Overlay. This degradation mechanism is believed to be independent of the corrosion mechanism. Cracking was observed in the as-received material and appears to increase in numbers and length with additional time at temperature. This cracking has not been taken into account in the wastage rate calculations of this report. The fact that Incoclad 671 has a very similar composition and does not exhibit cracking suggests the possibility that modifications to the cladding process may eliminate the cracking problem, and thus would firmly establish IN 72 Weld Overlay as a viable cost-effective option.
- By the end of Section C exposure, the full cladding thickness of the IN 52 Weld Overlay specimens had wasted away causing the 800H substrate to be exposed to corrosive conditions. The wastage rate thus would be expected to have increased significantly.
- Weld cross-sections suggest that the Inconel 625 filler metal would serve well for most of the candidate materials; however, when joining the more resistant tube materials, care must be taken to ensure that the weld filler metal has an equivalent wastage resistance.

REFERENCES:

"Coal Ash Corrosion Resistant Materials Testing Program - Evaluation of the First Section Removed in November 2001" by Dennis K. McDonald, The Babcock & Wilcox Company, presented at the 28th International Technical Conference on Coal Utilization & Fuel Systems", March 10-13 2003

"Topical Report: Removal of Section A" by Edward S. Robitz Jr., The Babcock & Wilcox Company, submitted to DOE (DE-FC26-99FT40525) and OCDO (CDO/D-97-02) October 31, 2001.

"Update on Coal Ash Corrosion Resistant Materials Testing Program" by Dennis K. McDonald, The Babcock & Wilcox Company, presented at the 16th Annual Conference on Fossil Energy Materials, Baltimore, Maryland, April 2002.

"Status of Coal Ash Corrosion Resistant Materials Test Program" by Dennis K. McDonald and David K. Meisenhelter, The Babcock & Wilcox Company, and Vinod K. Sikka, Oak Ridge National Laboratory, presented at the 1999 Pittsburgh Coal Conference.

This report was prepared by Babcock & Wilcox, Inc. pursuant to a Grant partially funded by the U.S. Department of Energy (DOE) under Instrument Number DE-FC26-99FT40525 and the Ohio Coal Development Office/Ohio Department of Development (OCDO/ODOD) under Grant Agreement Number CDO/D-98-2.

Fireside and Steamside Corrosion of Advanced Steam-Cycle Materials*

K. Natesan and D. L Rink
Argonne National Laboratory, 9700 South Cass Avenue, Argonne, IL 60439
E-mail: natesan@anl.gov; Telephone: (630) 252-5103; Fax: (630) 252-8681

Abstract

A program on corrosion is being conducted at Argonne National Laboratory to evaluate the performance of several structural alloys in the presence of mixtures of synthetic coal ash, alkali sulfates, and alkali chlorides and in a steam environment. Experiments in the present program, which addresses the effects of deposit chemistry, temperature, and alloy chemistry on the corrosion response of alloys, were conducted at temperatures in the range of 575-800°C for time periods up to ≈1850 h. Fe-base alloys selected for the study included HR3C, 310TaN, HR120, SAVE 25, NF709, modified 800, 347HFG, and HCM12A. In addition, 800H clad with Alloy 671 was included in several of the exposures. Ni-base alloys selected for the study included 600, 601, 617, 690, 625, 602CA, 214, 230, 45TM, HR 160, and 693. Data were obtained on weight change, scale thickness, internal penetration, microstructural characteristics of corrosion products, mechanical integrity of the scales, and cracking of scales. Results showed that the relationship of corrosion rates to temperature followed a bell-shaped curve for Fe-base alloys, with peak rates at ≈725°C, but the rate itself was dependent on the alloy chemistry. Results are summarized on the fireside corrosion of both the Fe- and Ni-base alloys. Experiments were also conducted to evaluate the corrosion performance of several Fe-base alloys in a steam environment. Specimens, exposed for 1850 h, were analyzed to determine the scale thickness and internal oxidation in the substrate alloys. Results, presented on both the fireside and steamside corrosion, can be used to compare the performance of the various Fe-base alloys. Attaining adequate creep strength, fireside corrosion resistance, and steamside corrosion resistance is still a challenge in materials development for advanced steam-cycle applications.

Background

Conceptual designs of advanced combustion systems that utilize coal as feedstock must include improved thermal efficiency and significant reduction in release of sulfur oxides, nitrogen oxides, and carbon dioxide. Such systems require materials and components that are capable of operating at much higher temperatures than those found in current coal-fired power plants. Component reliability and long-term, trouble-free performance of structural materials for these systems necessitate development/evaluation of materials in simulated coal-combustion environments. Apart from the environmental aspects of the effluent from coal

*Work supported by the U.S. Department of Energy, Office of Fossil Energy, Advanced Research Materials Program, Work Breakdown Structure Element ANL-4, under Contract W-31-109-Eng-38.

combustion, one concern from the systems standpoint is the aggressiveness of the combustion environment toward boiler structural components, such as steam superheaters and reheaters.

Recently, the U.S. Department of Energy has started to reevaluate coal-fired steam generation plants and, in particular, the designs based on supercritical and ultra-supercritical steam conditions. The ultimate goal of the staged development of power systems is to change steam pressure and temperature from the current values of 16.5-24 MPa (2400-3500 psig) and 540°C (1000°F), respectively, to 34.5 MPa (5000 psig) and 650°C (1200°F). Development of a revolutionary boiler design for U.S. markets, based on superheater/reheater temperatures >760°C, has been proposed. The higher steam temperature is expected to lead to another 2-3% increase in efficiency over a 700°C design, thus improving fuel usage and CO_2 emissions [1].

Fireside metal wastage in conventional coal-fired boilers can occur by gas-phase oxidation or deposit-induced liquid-phase corrosion. Using materials that are resistant to oxidation at the service temperatures of interest can minimize the former. On the other hand, deposit-induced corrosion of materials is an accelerated type of attack, influenced by the vaporization and condensation of small amounts of impurities such as sodium, potassium, sulfur, chlorine, and vanadium (or their compounds) that are present in the coal feedstock. At the temperatures of interest in advanced combustion systems, mixtures of alkali sulfates, along with alkali chlorides, will dominate the fireside deposit, and viable structural alloys must be resistant to attack by such deposits.

In advanced combustion systems, because the metals in the superheater regions will be subjected to much higher steam temperature, the alkali sulfate and coal ash will be the predominant deposit. Several factors (including sulfur, alkali, and chlorine in coal feedstock; excess air level during the combustion process; and metal temperature) determine the extent of corrosion of superheater materials in coal-fired boilers. The objective of the present work is to evaluate the corrosion performance of state-of-the-art candidate materials in coal ash, alkali sulfate, and alkali chloride environments at temperatures in the range of 575-800°C. The experimental program is aimed at developing a scientific understanding of corrosion mechanisms as a function of alloy composition and deposit chemistry, and at quantitatively determining the scaling and internal penetration of the alloys.

Experimental Procedure

Materials

Numerous alloys, both ASME coded and uncoded, were selected for corrosion evaluation. The compositions of the Fe-base alloys selected for the study are listed in Table 1. Among those selected, HCM12A is a super-ferritic alloy in which creep strength is obtained by both solution strengthening (W and Mo) and precipitation strengthening (V, Nb, and N). The alloy contains Cu (instead of Ni) to stabilize the long-term creep strength and to minimize δ-ferrite. The included austenitic alloys were broadly based on 18-20Cr and 20-25Cr steels. Super 304H, 347HFG, and NF709 fall into 18-20Cr steels, with improved creep strength achieved by addition of Nb and/or Ti. HR3C, 310TaN, and SAVE 25 fall into 20-25Cr steels, with improved creep strength achieved by addition of Nb, Ti, Ta, and N. Modified 800 has the Alloy 800 base, with additions of the strengthening elements Nb, V, N, and B. HR120 is a

Fe-Ni-Cr alloy with additions of Co, W, N, and Nb. In addition, specimens of 800H clad with Alloy 671 were also included in the study.

Table 2 lists the Ni-base alloys selected for the corrosion study. The alloys included 600, 601, 690, 617, 625, 602CA, 214, 230, 45TM, HR 160, and 693. Among them, Alloy 600 and 214 contained 15.4 and 15.9 wt.% Cr, respectively, whereas all the others contained Cr in a range of 21.5-28.8 wt.%. In addition, Alloys 617 and 625 had high concentration of Mo; Alloys 601, 602CA, and 214 contained Al concentration in a range of 1.4-3.7 wt.%; and Alloys 45TM and HR 160 contained Si in a range of 2.7-2.8 wt.%.

Table 1. Nominal composition (in wt.%) of Fe-base alloys selected for corrosion study

Material	C	Cr	Ni	Mn	Si	Mo	Fe	Other
HCM12A	0.10	12	0.3	0.5	0.3	0.4	Bal	W 2.0, V 0.2, Nb 0.05, Cu 0.9, N 0.05
Super 304H	0.10	18	9	1.0	0.3	-	Bal	Nb 0.45, Cu 3.0, N 0.09
347HFG	0.08	18	11	2.0	1.0	-	Bal	Nb + Ta = 10 x C minimum
HR3C	0.06	25	20	1.2	0.4	-	Bal	Nb 0.45, N 0.2
310TaN	0.05	25	20	1.0	0.2	-	Bal	Ta 1.5, N 0.2
NF709	0.07	20	25	1.0	0.6	1.5	Bal	Ti 0.6, Nb 0.2, N 0.18, B 0.004
SAVE 25	0.10	23	18	1.0	0.4	-	Bal	Nb 0.45, W 1.5, Cu 3.0, N 0.2
Modified 800H	0.10	20	30	1.5	0.2	1.5	Bal	Ti 0.25, Nb 0.25, V 0.05, N 0.03, B 0.004
HR120	0.05	25	37	0.7	0.6	2.5	Bal	Co 3, W 2.5, N 0.2, Cu, Al 0.1, Nb 0.7
MA956	-	20	-	-	-	-	Bal	Al 4.5, Ti 0.5, Y_2O_3 0.6
671-clad 800H								
671	0.05	48	Bal	0.02	0.2	-	0.2	Ti 0.4
800H	0.05	21	32	0.5	0.2	-	Bal	Ti 0.4, Al 0.4

Table 2. Nominal composition (in wt.%) of Ni-base alloys selected for corrosion study

Material	C	Cr	Ni	Mn	Si	Mo	Fe	Other
600	0.04	15.4	Bal	0.2	0.1	-	9.7	-
601	0.03	21.9	Bal	0.2	0.2	0.1	14.5	Al 1.4, Ti 0.3, Nb 0.1
690	0.01	27.2	61.4	0.2	0.1	0.1	10.2	Ti 0.3, Al 0.2
617	0.08	21.6	53.6	0.1	0.1	9.5	0.9	Co 12.5, Al 1.2, Ti 0.3
IN 625	0.05	21.5	Bal	0.3	0.3	9.0	2.5	Nb 3.7, Al 0.2, Ti 0.2
602CA	0.19	25.1	62.6	0.1	0.1	-	9.3	Al 2.3, Ti 0.13, Zr 0.19, Y 0.09
214	0.04	15.9	Bal	0.2	0.1	0.5	2.5	Al 3.7, Zr 0.01, Y 0.006
230	0.11	21.7	60.4	0.5	0.4	1.4	1.2	W 14, Al 0.3, La 0.015
45TM	0.08	27.4	46.4	0.4	2.7	-	26.7	Rare earths 0.07
HR 160	0.05	28.0	Bal	0.5	2.8	0.1	4.0	Co 30, Al 0.2
693	0.02	28.8	Bal	0.2	0.04	0.13	5.8	Al 3.3, Nb 0.67, Ti 0.4, Zr 0.03

Fireside Corrosion Tests

Details on the experimental setup and on the procedure for the fireside tests were presented earlier [2, 3]. The synthetic coal-ash deposit consisted of a mixture of reagent-grade SiO_2, Al_2O_3, and Fe_2O_3 in the ratio of 1:1:1 by weight. The alkali sulfate mixture consisted of Na_2SO_4 and K_2SO_4 in the ratio of 1:1 by weight. Three types of deposits were used in the corrosion experiments. In the first, ash and sulfate were mixed in the ratio of 90:10 by

weight; in the second, ash, sulfate, and NaCl were mixed in the ratio of 85:10:5 by weight; in the third, ash, sulfate, and NaCl were mixed in the ratio of 89:10:1 by weight. The specimens were exposed at temperatures of 575, 650, 725, and 800°C for time periods in the range of 336-1852 h.

Upon completion of the corrosion kinetics experiments, the specimens were examined by optical metallography and by a scanning electron microscope (SEM) equipped with energy–dispersive X–ray analyzer. In some cases, the deposit materials and the scales (developed on alloy specimens) were analyzed by X-ray diffraction. Optical examination of cross sections of exposed specimens and analyses with the SEM were used to identify the morphological features of corrosion-product phases in the scale layers and to establish the thickness of scales and depth of intergranular penetration, if any, in the alloys and cladding.

Corrosion Tests in Steam

A tubular resistance-heated furnace (see Fig. 1) was used to expose coupon specimens of several Fe-base alloys fto steam oxidation. The system consists of a furnace with a constant temperature zone of ≈20 cm and a reaction chamber made of high-purity alumina. The steam for the experiment was generated by pumping distilled water and converting it to steam in the preheat portion of the furnace, ahead of the specimen exposure location. The exhaust steam from the chamber was condensed in a steam condenser. The flow rate was 6 cc/h of water.

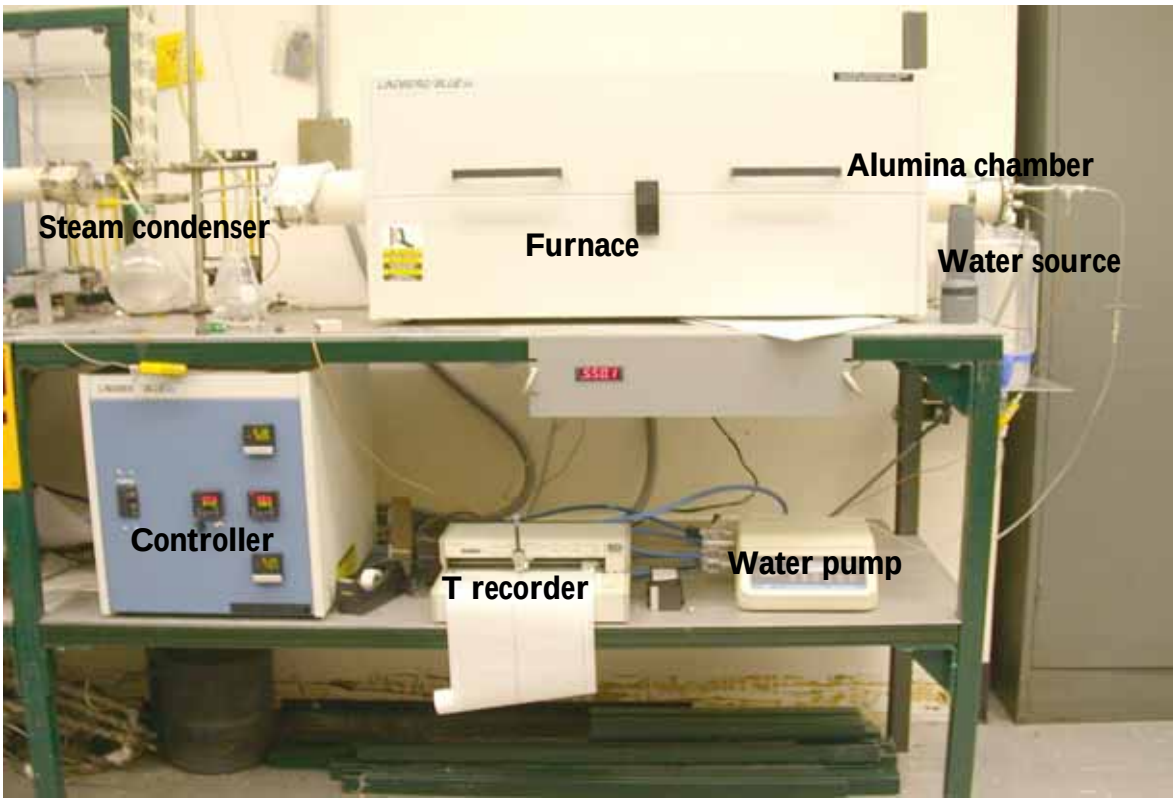

Figure 1. Test facility used for steam oxidation of candidate alloy specimens.

A mass balance on the water flow showed that almost all the input water was collected as the effluent, indicating that the steam consumption was negligible during the oxidation of specimens. Argon gas was used to disperse the steam in the reaction chamber.

Results and Discussion

Fireside Corrosion

Results from fireside corrosion studies on the Fe- and Ni-base alloys have been reported extensively in the conference proceedings that were published in past years [2, 3]. The results from the past work and any additional data developed are summarized in this paper. In general, at each exposure temperature, specimens of various alloys were exposed to a mixture of coal ash and alkali sulfate for 168 or 336 h, after which the specimens were retrieved, cleaned of deposit, and weighed. Subsequently, the exposures were continued with a fresh deposit mixture for another 168 or 336 h. The procedure was repeated several times at various temperatures to accumulate weight change data, which were plotted as a function of exposure time to develop a corrosion rate at each temperature for each alloy. Weight change followed linear kinetics for all the Fe-base alloys. At temperatures of 575, 650, and 725°C, most of the alloys lost weight, and the losses were strongly dependent on the alloy composition. At 800°C, several of the Fe-base alloys gained weight, and a few of them lost weight, but not to the same extent as observed at 725°C.

The results indicated that the weight loss rates increased with temperature up to 725°C and decreased to low values at 800°C. In fact, several of the alloys showed either negligible weight loss and/or gained weight after exposure at 800°C. The corrosion rates followed a bell-shaped curve with peaks near 725°C for all of the Fe-base alloys studied [2]. Weight loss rates for several alloys at 650 and 800°C, obtained when exposed in a deposit mixture that contained 5 wt.% NaCl, were also reported earlier [2]. Total corrosion (scale thickness plus penetration) data were reported earlier for several Fe-base alloys after exposure at 650, 725, and 800°C in an environment that contained coal ash and alkali sulfate. Results showed that at 650°C alloys such as 347HFG, SAVE25, and 800H exhibited total corrosion rate <0.2 mm/y, and all of the other alloys showed rates $\leq$0.44 mm/y. At 725°C, the corrosion rate for all of the alloys increased, and several of them exhibited a dramatic increase. For example, the rates for SAVE25 and modified 800H were 2.1 and 1.65 mm/y, respectively. At 800°C, the corrosion rates for several alloys slightly decreased from the values obtained at 725°C. Results indicated that NF709 was a superior-performing alloy, with rates of 0.26, 0.25, and 0.55 mm/y at 650, 725, and 800°C, respectively. The corresponding values for 310TaN were 0.43, 0.50, and 0.55 mm/y, respectively. The effect of 5 wt.% NaCl in the deposit mixture on the corrosion performance showed that NaCl accelerated corrosion in all of the Fe-base alloys used in this study. NF709, the best-performing alloy in the absence of NaCl, had corrosion rates of 2 and 15 mm/y at 650 and 800°C in the presence of NaCl. The best-performing alloy in environments with and without NaCl was HR3C. The corrosion rates of this alloy were 0.37 and 0.7 mm/y at 650°C in environments without and with 5 wt.% NaCl, respectively.

The accelerated corrosion in the heat-resistant alloys in the presence of NaCl has two causes: The NaCl in the deposit mixture establishes a Cl activity, which can attack the carbides that are present in the alloy as strengtheners. Furthermore, the Cl activity in the deposit near the

alloy can be high enough to form volatile chlorides of Fe, Cr, and Al (if present in the alloy). The volatile chlorides lead to a porous microstructure with virtually no scale development to protect the alloy.

To examine the influence of NaCl concentration in the deposit on the corrosion performance of Fe-base alloys, additional tests were conducted at 650, 725, and 800°C with a deposit that contained 1 wt.% NaCl. One major difference between the experiments conducted in the presence of Ash 1 (with no NaCl) and Ash 3 (with 1 wt.% NaCl) is the stickiness and adherence of the deposit with the substrate alloy. The deposit was significantly more adherent in the presence of NaCl than its absence. This was evident in the measured weight change data as a function of exposure time. The weight change data may not be representative of the corrosion process in the specimens exposed to ash that was sticky, primarily because of the stickiness of the deposit and the inability to clean the deposit off the specimens without damaging the corrosion product layers. Therefore, all of the tested alloys were mounted and polished to examine the rates of scaling and internal penetration in the alloys using optical and scanning electron microscopy. Figure 2 shows the total corrosion (scale thickness plus penetration) for Fe-base alloys after exposure at 650°C in the presence of deposits that contained 0 (Ash 1), 1 (Ash 3), and 5 (Ash 2) wt.% NaCl.

Exposures of Ni-base alloys followed a procedure similar to that used for the Fe-base alloys. The Ni-base alloys were tested in two deposit mixtures identified as Ash 1 (a mixture of ash constituents and 10 wt.% alkali sulfate) and Ash 3 (Ash 1 plus 1 wt.% NaCl). Results indicated that the weight loss rates are significantly lower than those observed for the Fe-base alloys under similar exposure conditions [3]. However, the results are misleading for two reasons. The deposits (due to their stickiness) are much more adherent to the scale and substrate in the case of Ni-base alloys than the Fe-base alloys, and effective removal of the deposit is difficult. Furthermore, the corrosive attack in the case of Ni-base alloys is more localized in the form of pits, which can be rather large and deep and may not be reflected in the overall weight change of the specimen.

The specimens were also analyzed to evaluate the total corrosion (scale thickness plus penetration) for Ni-base alloys after exposure at 650°C in the presence of deposits that contained 0 (Ash 1) and 1 (Ash 3) wt.% NaCl. Results (Fig. 3) showed that several of the alloys exhibit total corrosion rates <0.3 mm/y, based on parabolic kinetics. The measured corrosion rates include penetration depth values that were observed in the pits and represent maximum rates for these alloys. A comparison of the data for Ni- and Fe-base alloys indicates that the rates for the Ni-base alloys are generally much lower at 650°C, even in the presence of 1 wt.% NaCl. Nickel-base alloys are expected to resist chloride attack because the vapor pressure of $NiCl_2$ is much lower than that of Fe, Cr, and Al chlorides for the same Cl activity and gas temperature [4, 5]. Additional work is planned at higher temperatures to evaluate corrosion performance of Ni-base alloys in the presence of deposits with and without NaCl.

Additional corrosion experiments on Ni-base alloys at 725 and 800°C are in progress. The information developed from these tests will be used to develop corrosion rate (and metal wastage rate) correlations for the alloys as a function of temperature, alloy chemistry, and exposure environment.

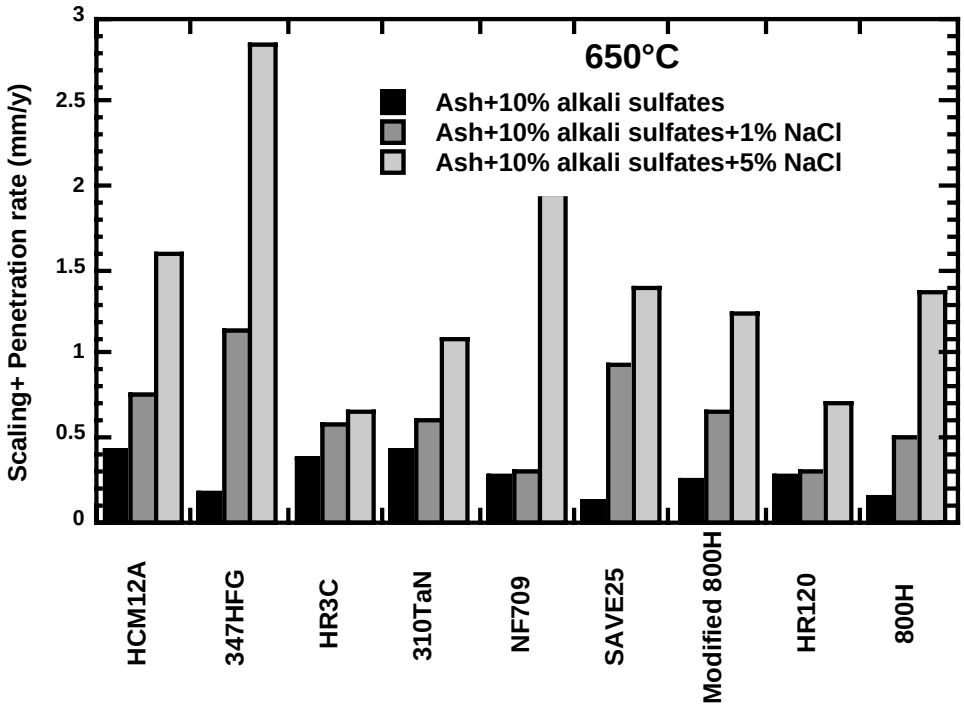

Figure 2. Scaling rate plus penetration rate for several Fe-base alloys after exposure at 650°C in presence of deposits containing 0, 1, and 5 wt.% NaCl.

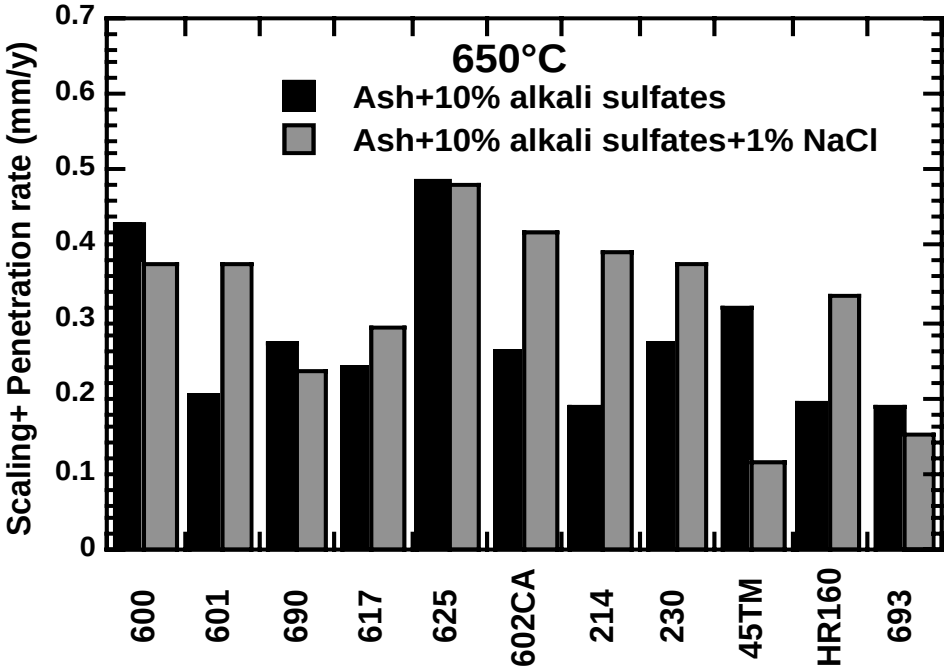

Figure 3. Scaling rate plus penetration rate for Ni-base alloys after exposure at 650°C in the presence of deposits containing ash constituents and alkali sulfates, with and without 1 wt.% NaCl.

Oxidation in Steam

Several of the Fe-base alloys have been exposed to a steam environment at 725°C for times up to 1850 h. Weight change data initially showed a sharp increase, indicating formation of an oxide film. However, the rates showed minimal change after the initial ≈200 h. The overall corrosion rates were negligible for all the specimens even after 1850 h (see Fig. 4). A detailed microscopic examination of the cross sections of exposed specimens showed significant internal oxidation in all of the tested alloys (see Figs. 5 and 6). SAVE 25 and HR3C exhibited the least amount of oxidation, whereas the modified 800 showed the most penetration of the substrate. Figure 7 shows the scale plus penetration loss for various alloys, calculated from the microstructural data using parabolic kinetics.

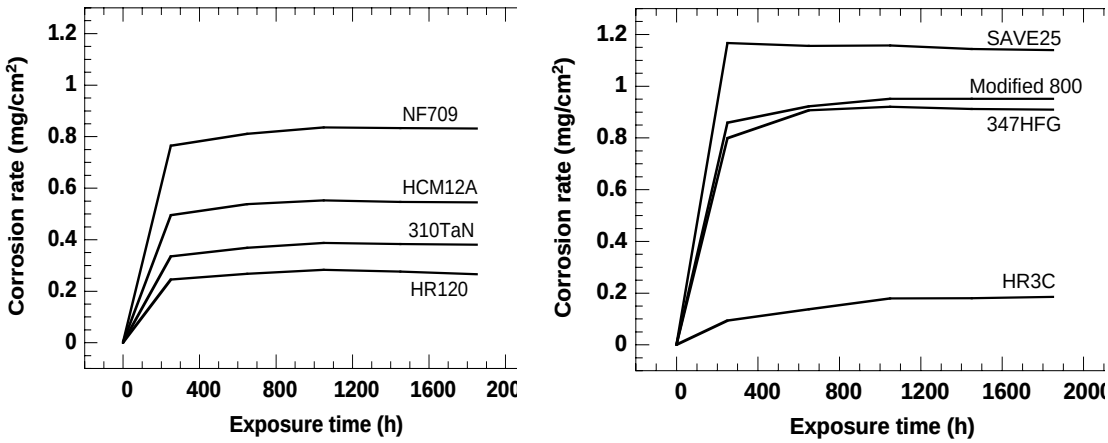

Figure 4. Corrosion rate of several Fe-base alloys tested in steam at 725°C.

Summary

Fireside and steam-side corrosion are major issues when selecting materials for advanced steam-cycle systems. We have conducted studies at Argonne National Laboratory to evaluate the corrosion performance of candidate Fe- and Ni-base alloys in coal-ash and in steam environments. The laboratory tests simulated the combustion atmosphere of advanced steam-cycle systems and three deposit chemistries, which included ash constituents, alkali sulfates, and NaCl.

Corrosion rate data showed a bell-shaped curve for the Fe-base alloys, with peak rates at ≈725°C, and the rate itself was dependent on the alloy chemistry. Several alloys showed acceptable rates in the sulfate-containing coal-ash environment; but NaCl in the deposit led to catastrophic corrosion at 650 and 800°C. To attain acceptable corrosion, it is essential to establish maximum levels for alkali sulfates and alkali chlorides in combustion environments (and their relationship to coal feedstock). The data obtained on Ni-base alloys at 650°C showed the corrosion rates for these alloys to be significantly less than those of Fe-base alloys for the same exposure conditions. However, the type of attack in the Ni-base alloys was much more localized in the form of pits. Detailed microstructural examination and X-ray diffraction analysis of the corrosion product layers indicated that Ni-base alloys corroded via a "low-temperature hot corrosion" mechanism that involves formation of liquid alkali sulfate and base metal sulfate eutectic. This reaction leads to sulfidation attack of the structural alloy.

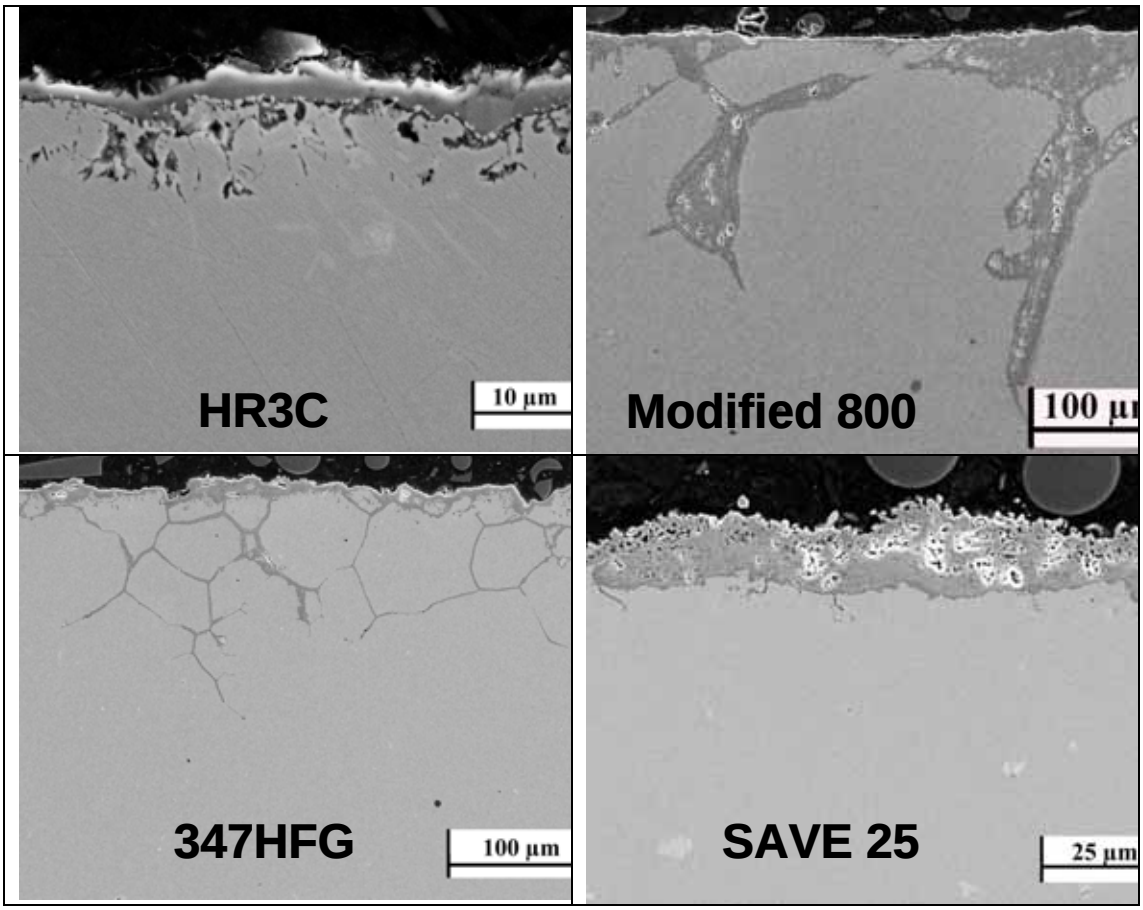

Figure 5. SEM photomicrographs of cross sections of HR3C, modified 800, 347HFG, and SAVE 25 after 1850-h exposure to steam at 725°C.

There is a need to establish the maximum levels for alkali sulfates and alkali chlorides in the combustion environment (and their relation to coal feedstock) for acceptable corrosion.

Results on steamside corrosion showed little weight change but significant internal oxidation of the alloys. At 725°C, rates varied between 0.03-0.68 mm/y, based on parabolic kinetics. Additional tests are in progress to evaluate the corrosion performance of Ni-base alloys at higher temperatures. Attaining adequate creep strength, fireside corrosion resistance, and steamside corrosion resistance is still a challenge in materials development for advanced steam-cycle applications.

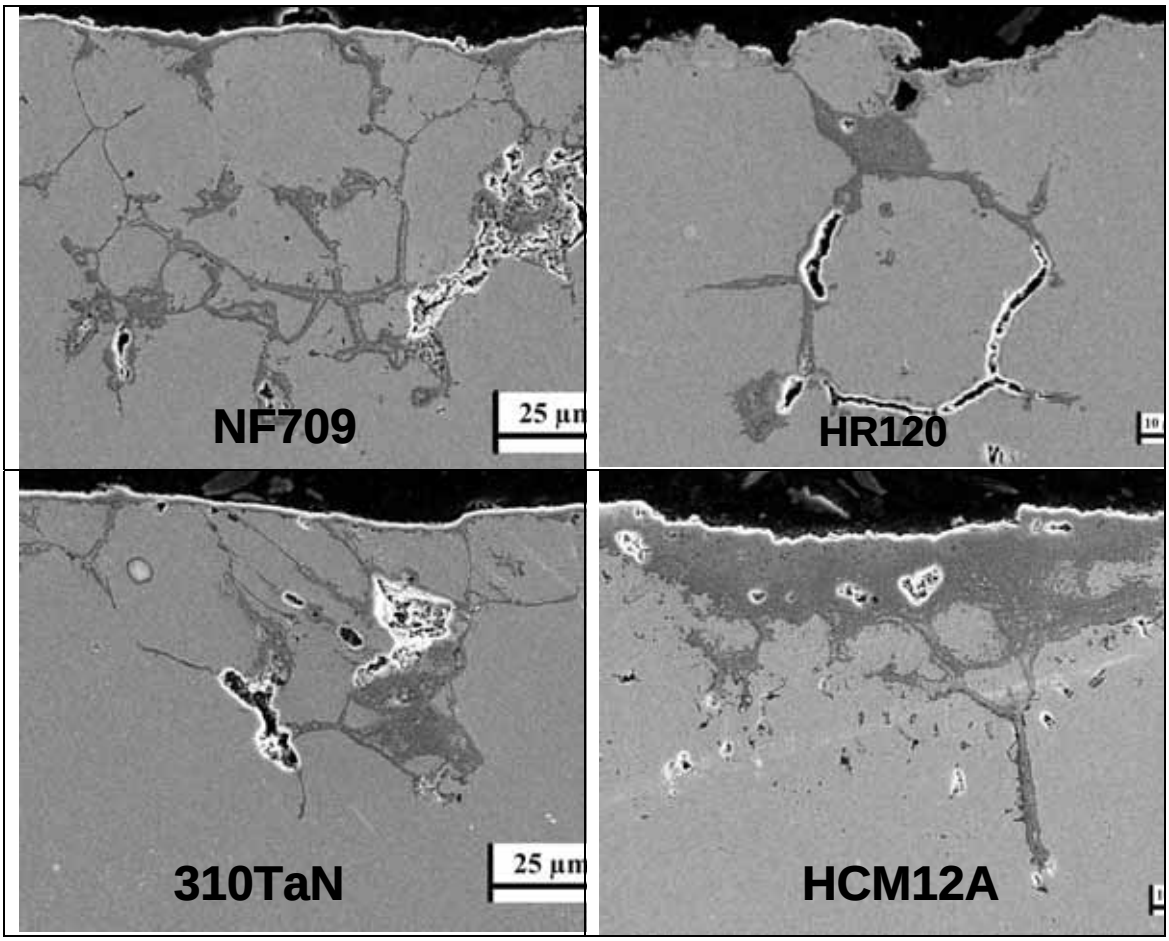

Figure 6. SEM photomicrographs of cross sections of NF709, HR120, 310TaN, and HCM12A after 1850-h exposure to steam at 725°C.

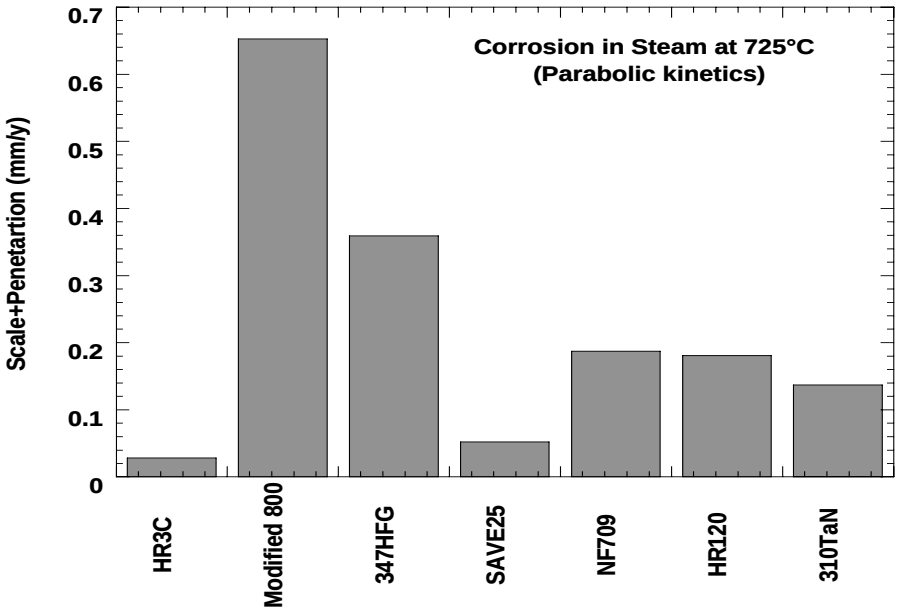

Figure 7. Scale plus penetration rate for Fe-base alloys in steam exposure at 725°C.

References

[1]. R. Viswanathan and W. Bakker, J. Mater. Eng. Perf. 10 (1), 2001, 81.

[2]. K. Natesan, A. Purohit, and D. L. Rink, Fireside Corrosion of Alloys for Combustion Power Plants, Proc. 16th Annual Conference on Fossil Energy Materials, Baltimore, MD, April 22-24, 2002.

[3]. K. Natesan, A. Purohit, and D. L. Rink, Coal-ash Corrosion of Alloys for Combustion Power Plants, Proc. 17th Annual Conference on Fossil Energy Materials, Baltimore, MD, April 22-24, 2003.

[4]. K. Natesan and C. Reignier, Corrosion Performance of Structural Alloys in Oxygen/Sulfur/Chlorine-Containing Environments, Proc. 12th Ann. Conf. on Fossil Energy Materials, Knoxville, Paper 1.8, 1998.

[5]. K. Natesan and C. Kraus, Corrosion Performance of Structural Alloys and Coatings in the Presence of Deposits, Proc. 15th Ann. Conf. on Fossil Energy Materials, Knoxville, April 30 - May 2, 2001.

Acknowledgments

This work was supported by the U.S. Department of Energy, Office of Fossil Energy, Advanced Research Materials Program, Work Breakdown Structure Element ANL–4, under Contract W–31–109–Eng–38.

PHASE STABILITY OF Nb-MODIFIED Mo-Si-B ALLOYS AND THEIR IMPROVED OXIDATION RESISTANCE USING A NOVEL CHLORINATION PROCESS

Matthew J. Kramer
Ames Laboratory, 37 Wilhelm Hall, Iowa State University, Ames, IA 50011
Email: mjkramer@ameslab.gov; Telephone: (515) 294-0276; Fax: (515) 294-4291

Vikas Behrani, Yonghua Liu, Andrew J. Thom, and Mufit Akinc
Ames Laboratory, 330 Spedding Hall, Iowa State University, Ames, IA 50011
Email: ajthom@ameslab.gov; Telephone: (515) 294-4064; Fax: (515) 294-4709

ABSTRACT

A fundamental limitation of bcc-Mo+T2(Mo_5SiB_2)-based alloys is their poor oxidation resistance at temperatures envisioned for Vision 21 goals. On the other hand, the oxidation resistance of T1 ($Mo_5Si_3B_x$) alloys is exceptional. The present work explored Nb alloying additions to bcc-Mo + T2 (Mo_5SiB_2)-based alloys to develop potentially oxidation resistant alloys. Investigation of the phase stability of Nb-Mo-Si-B alloys has shown that metal-rich phase field of ss-(Nb,Mo) can be extended to coexist with a quaternary T1-like silicide phase $(Nb,Mo)_5Si_3B_x$. In fact, the complete solid-solubility between Nb and Mo leads to substitution of Nb for Mo in all silicide phases: T1 as $(Nb,Mo)_5Si_3B_x$, T2 as $(Nb,Mo)_5(Si,B)_3$, $D8_8$ as $(Nb,Mo)_5Si_3B_x$, and M_3Si as $(Nb,Mo)_3Si$. Oxidation resistance testing shows that the quaternary T1 phase can not adequately protect the bcc-(Nb,Mo) phase. A complex, multilayered scale of several hundred microns thickness forms on oxidation in air at 1000°C. The formation of Nb_2O_5, which persists in the scale in contrast to volatile MoO_3, contributes to macro-porosity in the scale. The fine Nb_2O_5 crystals appear to increase the viscosity of the borosilicate glass, and this inhibits the ability of the scale to adequately re-flow and heal pores formed by MoO_3 evaporation. To overcome this limitation, a novel chlorination process was developed in order to enrich the surface scale in borosilicate glass. This process involves pre-oxidizing the quaternary alloy to form a relatively thin scale, then exposing it to a carbon monoxide + chlorine gas mixture at 1000°C. This process preferentially removes Nb_2O_5 from the scale via the formation of volatile $NbCl_5$. The scale is then healed by a post-anneal at 1100°C, with the overall scale porosity reducing from about 30% after pre-oxidation to about 9% after the post-chlorination heat treatment. The chlorination process significantly improves the alloys oxidation resistance, demonstrated by a reduction of the parabolic rate constant by two-thirds for air oxidation at 1000°C.

INTRODUCTION

Molybdenum and niobium borosilicides are being investigated by researchers in both government and industry in the United States for use in high temperature applications. In the Mo-Si-B system, compositions based on the T1 phase, $Mo_5Si_3B_x$, have excellent oxidation resistance and creep strength [1, 2]. However, these alloys also have low fracture toughness, and the thermal expansion anisotropy of the T1 phase make these alloys susceptible to thermal stress induced microcracking [3]. These deficiencies in mechanical behavior can be improved by moving towards the Mo-rich portion of the system. Alloys which incorporate the bcc-Mo phase have dramatically improved fracture toughness, but they present a challenge in achieving

oxidation resistance on par with $Mo_5Si_3B_x$–based alloys. The oxidation resistant phase of these alloys is the T2 phase (Mo_5SiB_2), and its high boron content renders a borosilicate glass with a viscosity much lower than that formed on the T1 phase. This enables excessive volatility of MoO_3 through the scale, contributing to unacceptable metal recession rates above about 1300°C [4]. Other recent works have explored microstructurally designing a bcc-Mo containing composite to balance both oxidation resistance and adequate mechanical behavior [5].

The Nb-Si-B system is of interest since in this system it is possible to develop a two-phase assemblage of Nb + T2 ($Nb_5(Si,B)_3$). Recent work has explored whether the ternary phase T2, which contains a variable amount of silicon and boron, may act analogously on oxidation to the T1-based alloys in the Mo-Si-B system. However, the oxidation resistance of the T2 phase was poor compared to the $Mo_5Si_3B_x$–based alloys [6]. Extensive scale growth, along with scale cracking and rapid oxidation kinetics, were observed and this was attributed to the excessive growth of the condensed phase Nb_2O_5.

This leads to the consideration of the Nb-Mo-Si-B system, since the Nb and Mo are expected to freely substitute for each other due to their similar size. Appropriate substitution of Nb and Mo may enable the design of an alloy that combines the merits of the two ternary systems. In addition, Nb for Mo substitution improves the thermal expansion behavior of T_1 phase. The CTE (coefficient of thermal expansion) anisotropy of Mo_5Si_3 is significantly reduced by Nb additions [3,7,8,9]. Therefore, one objective of this study was to synthesize (Mo, Nb) silicides and investigate the effect of Nb/Mo substitution on their phase stability and microstructures. Throughout this study, the W_5Si_3-type tetragonal structure, as $(Nb,Mo)_5Si_3B_x$, is termed T1, the Cr_5B_3-type tetragonal structure, as $(Nb,Mo)_5(Si,B)_3$, is termed T2, and the Mn_5Si_3-type hexagonal structure, as $(Nb,Mo)_5Si_3B_x$, is termed $D8_8$.

The second objective of this research was to improve the oxidation behavior of Nb-Mo-Si-B alloys. Based on previous work [10], quaternary alloys are not adequately resistant to oxidation, due in part to the formation of a fast-growing scale containing Nb_2O_5. The present work investigated the removal of Nb_2O_5 from the oxide scale by reaction (1):

$$Nb_2O_5(s) + 5Cl_2(g) + 5CO(g) \rightarrow 2NbCl_5(g) + 5CO_2(g) \qquad (1)$$

The direct reaction of niobium pentoxide in the scale with chlorine and carbon monoxide [11,12] was studied in order to enrich the scale in borosilicate glass, thereby potentially improving the oxidation resistance of the alloy. Although all the halides of niobium are volatile by 1000°C, the niobium pentachloride ($NbCl_5$) reaction route was chosen for this study, as it is relatively easy to form.

EXPERIMENTAL PROCEDURE

Six compositions in the Nb-Mo-Si-B system were prepared for study. Their nominal compositions are given in Table 1. The arc-melted alloys were powder-metallurgically processed into dense pellets. More details on the synthesis and processing of these compositions can be found elsewhere [10].

Sample density was measured by the Archimedes method and image analysis. Phase identification and microstructural characterization were performed using X-ray diffraction (XRD, Scintag XDS 2000, Cupertino, CA), scanning electron microscopy (SEM, JEOL, JSM 6100, Peabody, MA) and energy dispersive spectroscopy (EDS, Oxford Instruments, Valley, CA). The compositions of individual phases were determined using electron probe microanalysis (EPMA, ARL, Sunland, California). Approximately 100 data points were collected for each sample by automated analysis. Rietveld refinement of the XRD patterns was performed using Rietica software (Lucas Height Research Laboratory, Menai, Australia) and GSAS (General Structure Analysis System, Los Alamos National Laboratory, Los Alamos, NM) software to determine the fraction of phases present and the lattice parameters. Peak profile coefficients, thermal parameters, specific atom sites, and lattice parameters were varied to obtain the best numerical fit for the X-ray data. Oxidation coupons were cut from the pellets and were polished using standard metallographic techniques. The oxidation coupons were suspended from a sapphire wire in a vertical tube thermo-gravimetric analyzer using an electrobalance sensitive to 0.01 mg (Cahn-2000, Cahn Instruments, Inc., Cerritos, CA).

Details of the experimental setup for chlorinating the pre-oxidized Nb-Mo-Si-B alloy can be found elsewhere [13]. Chlorine and carbon monoxide gas were flowed over the pre-oxidized alloy at 1000°C. Volatile $NbCl_5$ is carried down stream and converted into Nb_2O_5 and HCl in a water bubbler. Microstructure of the oxide scale was characterized after chlorination using XRD, X-ray photoelectron spectroscopy (XPS, Physical Electronics, PHI 5500, ESCA System, Multitechnique Surface Analytical System), SEM and EDS. Treated samples were then oxidized in the TGA apparatus to determine the effect of chlorination on the alloy oxidation behavior.

RESULTS AND DISCUSSION

PHASE ANALYSIS AND MICROSTRUCTURES

The phase assemblages determined by XRD analysis and Rietveld refinement are given in Table 1. EDS indicated that all phases present in all samples contain both Mo and Nb. Figure 1 shows the BSE images of the microstructures of as-sintered alloys A-F. Compositions A and B differ in Nb/Mo ratio, 2.94 to 1, but are three phase mixtures with a T1 matrix and T2 and $D8_8$ as the secondary phases, yielding a M:Si:B ratio of 63:30:7. The fact that these two compositions have nearly the same phase fractions suggests that each individual phase has a different Nb/Mo ratio. There is no hexagonal phase in the Mo-Si-B system, and therefore the $D8_8$ phase in Nb-Mo-Si-B system is expected to be Nb-rich. Severe microcracks were observed in both T1 and $D8_8$ phases because of their substantial thermal expansion anisotropy [3]. Compared to A and B, the composition C has the highest Mo content but the same M:Si:B ratio. The hexagonal $D8_8$ phase is absent and a small amount of Mo-rich $(Mo,Nb)_3Si$ was detected by XRD. Extensive microcracking was also observed in the T1 matrix.

Samples D, E, and F are more metal rich with the M:Si:B ratio as 70:23:7, with D through F having a Nb:Mo ratio of 3.12, 1.0, and 0.37, respectively. Despite the same Nb/Mo ratio, composition D has a completely different microstructure than composition A.

Table 1. Nominal compositions and phases present in Nb-Mo-Si-B samples

Sample	atomic percent, at%					Vol. Fractions (%)				
	Nb	Mo	Si	B	Nb/Mo	T1	T2	$D8_8$	M	M_3Si
A	47	16	30	7	2.94	58	29	13		
B	31.5	31.5	30	7	1.00	60	29	11		
C	16.7	46.3	30	7	0.36	68	27			5
D	53	17	23	7	3.12		61	15	24	
E	35	35	23	7	1.00	41	26	9	23	
F	18.9	51.1	23	7	0.37	18	27			55

T1- Tetragonal $(Nb,Mo)_5Si_3B_x$, W_5Si_3 type; T2- Tetragonal $(Nb,Mo)_5(Si,B)_3$, Cr_5B_3 type;
$D8_8$- Hexagonal $(Nb,Mo)_5Si_3B_x$, Mn_5Si_3 type; M- (Nb, Mo) solid solution; M_3Si- $(Mo,Nb)_3Si$

The total (Nb + Mo) content in D is greater than in A by 7 at%. Sample D is composed of a T2 matrix with 24 vol% (Nb + Mo) metal and 15 vol% $D8_8$ and no T1 phase. Upon further increasing the Mo content to the same level of Nb in composition E, four phases were identified: T1, T2, $D8_8$ and metal phase (Nb + Mo). Composition E appears to combine the proper mix of total metal content with Nb/Mo substitution since this was the only composition providing for the co-existence of a T1 phase and metal phase. No cracking was observed in the T1 in this composition. It is possible that the thermal expansion anisotropy of T1 was relieved by the ductile metal phase. Nb for Mo in Mo_5Si_3, which reduces the anisotropic thermal expansion, may also play a role in minimizing cracking in composition E. As the Mo content was further increased to composition F, both the metal phase and the $D8_8$ phase disappeared, and Mo-rich $(Mo,Nb)_3Si$ became the matrix phase. These results show that by proper substitution of Nb for Mo, the formation of $(Mo,Nb)_3Si$ can be suppressed to yield a microstructure containing both a T1-like phase and a metal phase. The critical value of total metal content and Nb/Mo ratio for avoiding the formation of $(Mo,Nb)_3Si$ needs to be studied in greater detail.

Figure 2 shows the combined results of lattice parameter and chemical compositional determinations for the individual phases in all alloys. Due to difficulties in quantitative determination of boron content using EPMA, only the Nb, Mo and Si content were measured. Using the phase compositions obtained by EPMA and the lattice dimensions determined by XRD/Rietveld analysis, the unit cell volume for T1, T2 and $D8_8$ are plotted as a function of relative atomic Nb concentration, Nb/(Nb + Mo). The horizontal errors bars reflect composition uncertainties in EPMA measurements. The unit cell volumes of all phases, except for T2 in composition D, increase linearly with relative Nb concentration. This result is in accordance with Vegard's law that lattice cell dimension varies linearly with the concentration of solute added. Because of the homogeneity regions for silicide T1, $D8_8$, and especially for T2, the maximum and minimum lattice cell dimensions available in literature were marked as open symbols for each terminal phase.

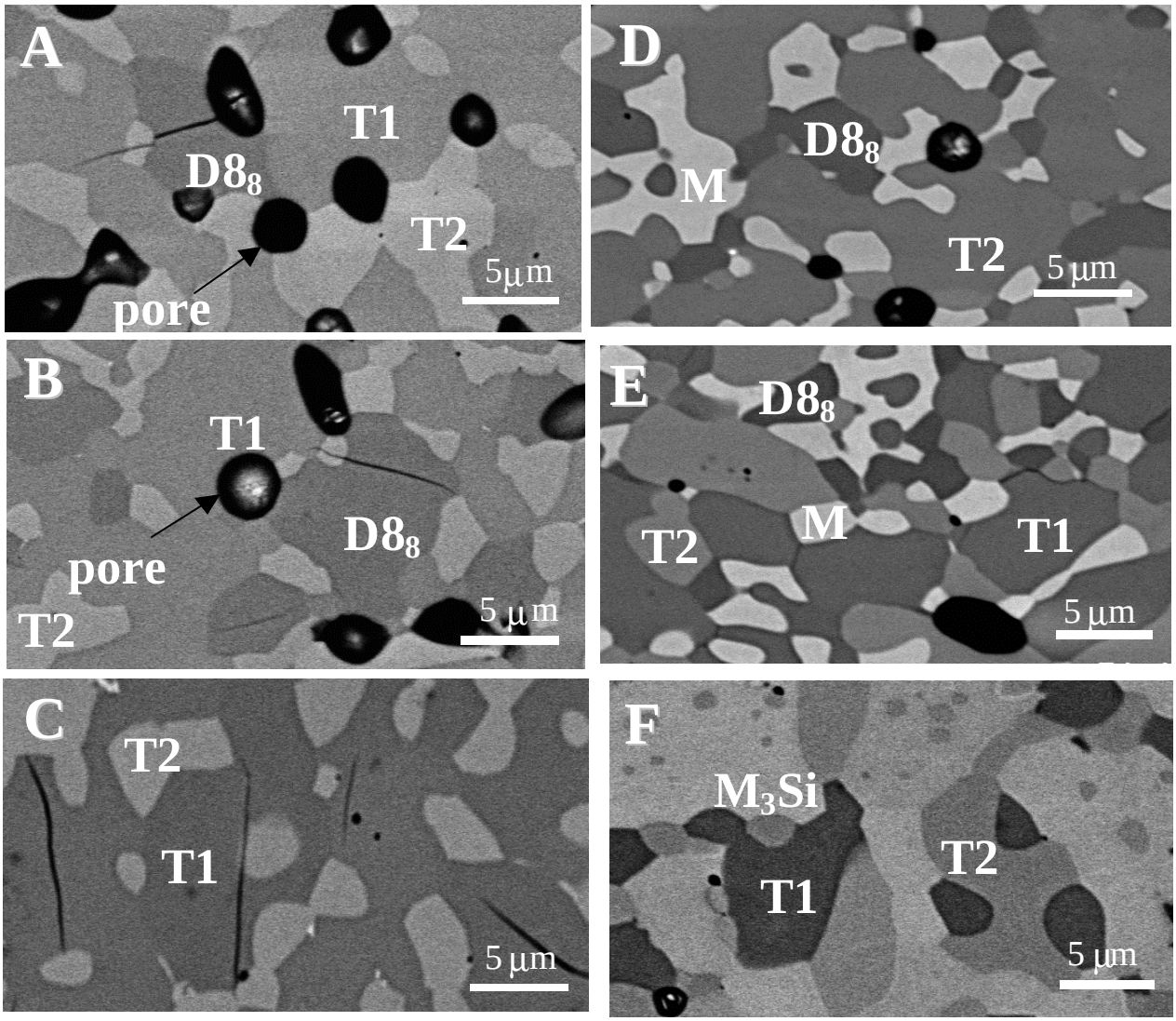

Figure 1. BSE images of compositions A-F described in Table 1.

Figure 2 includes the lower and upper limits of unit cell volumes for Nb-free T1 [3], Mo-free $D8_8$ [14] and Mo-free T2 [14], while the lattice dimension variations for Mo-free T1, Nb-free $D8_8$ and Nb-free T2 are ignored due to their very small homogeneity regions. The variation of the lattice dimensions for silicides due to the Nb/Mo substitution should be always within a band formed by the minimum and maximum unit cells of the terminal phases. The location of each phase in the band can reflect its approximate composition, such as boron content. For T1 phase, a narrow band was formed by the compositions $Mo_5Si_{2.94}$ (upper) [3], $Mo_5Si_{2.97}B_{0.16}$ (lower) [3] and Nb_5Si_3 [15], indicating the solubility of B in T1 is very low. For $D8_8$ phase, a wider band was formed by the compositions $Nb_5Si_{2.92}B_{0.42}$ [14], $Nb_5Si_{2.76}B_{0.86}$ [14] and Mo_5Si_3C [16]. The upper boundary implies a higher interstitial boron content than lower boundary. Because both binary Mo_5Si_3 and boron doped Mo_5Si_3 do not have a $D8_8$ structure, the lattice parameters of

carbon stabilized Mo_5Si_3, which has a $D8_8$ structure, were used for comparison instead. All $D8_8$ phases in this study were located in Nb-rich portion, suggesting $D8_8$ is a Nb-rich phase. This result was consistent with the previous EPMA measurements. For T2 phase, a very wide band was formed by compositions Nb_5Si_3 [6], $Nb_5Si_{1.27}B_{1.67}$ [14] and Mo_5SiB_2 [17]. Because of the substitution of B for Si in T2 structure, the lower boundary represents the higher B contents than upper boundary. T2 phases except in sample D are close to the lower boundary, indicating these T2 phases are high in boron content. This can be explained by the microstructures of samples. The samples A, B, C, E and F are all T1 or M_3Si matrix materials which are considerably lower in boron content. Therefore boron mainly concentrated in minor phase T2, resulting in the high boron content in T2. However, sample D showed different characteristics from other samples. The T2 phase in sample D is located closely to the upper boundary, suggesting this phase is low in boron content. Sample D is a T2 matrix material, therefore the average boron content can be lower compared to T2 as a minor phase in the other samples.

CHLORINATION TREATMENT AND POST-OXIDATION

Oxidation resistance of the Nb-Mo-Si-B quaternary alloys is inadequate and these results are discussed elsewhere [10]. For this study, a composition similar to B was selected for chlorination treatment. A new alloy was synthesized and powder-metallurgically processed for the chlorination study, and these details can be found elsewhere [13]. This alloy contained three quaternary phases (vol%): 40% T_1 (tetragonal $(Nb,Mo)_5Si_3B_x$; x<1), 40% T_2 ($(Nb,Mo)_5(Si,B)_3$) and 20% $D8_8$ (hexagonal $(Nb,Mo)_5Si_3,B_x$) and was 97±1% of theoretical density after sintering at 1900°C for 2 hours.

Reactivity of pure Nb_2O_5 in the Cl_2+CO environment was measured to ensure gas mixture and reaction times were appropriately set. Starting with 100 mg of pure powder, 98.5% of Nb_2O_5 was removed from the reaction chamber after chlorination at 1000°C for 30 min. Pure SiO_2 and borosilicate glass were also tested to ensure their resistance to the chlorination process. A minimal loss of 1-1.5% at 1000°C during chlorination is believed due to vaporization of moisture and impurities. EDS, XRD and XPS were used to investigate the composition of the oxide scale after chlorination. After 5 hours of pre-oxidation exposure, a 100-200 µm thick scale was formed and 15 min chlorination treatment was sufficient to remove most of the Nb_2O_5 from the scale. XPS analysis of oxide layer after chlorination shows that the outer scale is essentially borosilicate glass with a trace amount of Nb.

Oxidation resistance of the alloy was tested by TGA during pre-oxidation and after chlorination. The mass change of the alloy oxidized in air establishes the baseline behavior. The baseline rate was 1.1 $mg^2/cm^4/hr$, which compares favorably to previous results [10]. XRD detected Nb_2O_5 on the surface of unchlorinated alloy oxidized in air at 1000°C but no crystalline MoO_3, SiO_2 and B_2O_3 after 10 hours of oxidation at 1000°C. A new sample was then pre-oxidized in air at 1000°C, chlorinated, and then TGA tested at 1000°C in air. These results showed that after Nb_2O_5 removal, the oxidation resistance of the alloy improves significantly. After 10 hours of oxidation, the weight gain of the untreated alloy was 2.6 mg/cm^2. The chlorination treatment reduced this mass gain 1.3 mg/cm^2. The alloy parabolic oxidation rate after chlorination (0.28 $mg^2/cm^4/hr^2$) is one-third of the rate before the chlorination.

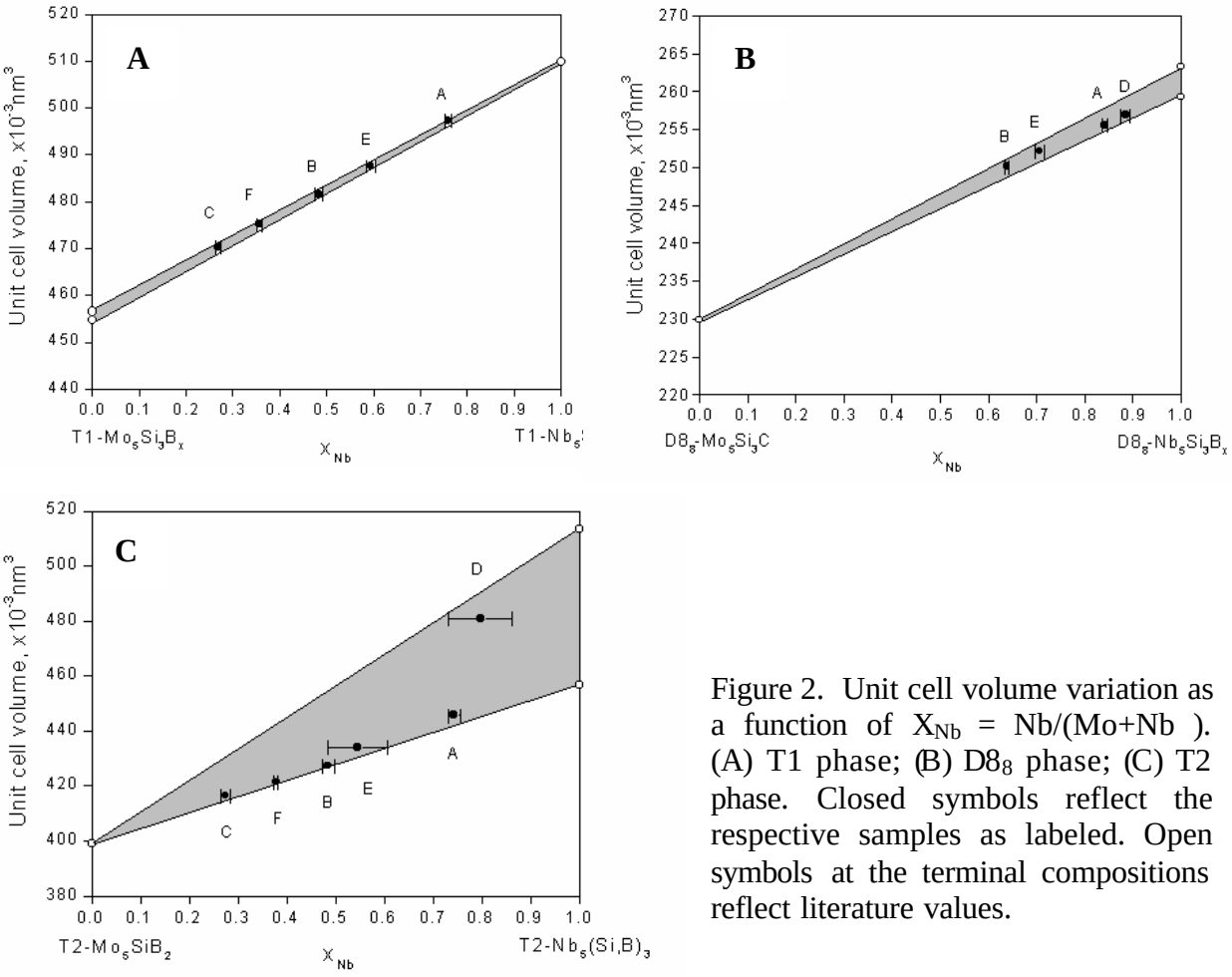

Figure 2. Unit cell volume variation as a function of X_{Nb} = Nb/(Mo+Nb). (A) T1 phase; (B) $D8_8$ phase; (C) T2 phase. Closed symbols reflect the respective samples as labeled. Open symbols at the terminal compositions reflect literature values.

This reduced rate is comparable to the oxidation rate of the unchlorinated alloy in argon (0.13 $mg^2/cm^4/hr^2$) with a residual oxygen pressure of $PO_2=10^{-4}$ atm. This demonstrates that the chlorination process effectively reduced the inward transport of oxygen to the alloy/scale interface and after initial incubation period, the scale becomes protective in nature.

CONCLUSION

Six compositions in the Nb-Mo-Si-B system with differing ratios of Nb/Mo were prepared by arc melting and sintering. The microstructures depended on the overall metal content and the Nb/Mo ratio. The co-existence of a quaternary T1-like silicide phase with a metal phase was obtained in the alloy 35Nb-35Mo-23Si-7B. A new chlorination treatment of the oxidized alloy was used to remove the non-volatile Nb_2O_5 from the oxidized scale and obtain a scale rich in borosilicate glass. Chlorination was able to remove Nb_2O_5 from most of the scale on the 5 hour pre-oxidized alloy. Oxidation rates were reduced by two-thirds after the chlorination treatment. Low oxidation rates after chlorination indicates the formation of a protective scale. This also suggests that oxidative instability of Nb-Mo-Si-B alloys can be attributed to presence of non-volatile Nb_2O_5.

ACKNOWLEDGEMENTS

The Ames Laboratory is operated by the US Department of Energy (DOE) by Iowa State University under Contract No. W-7405-ENG-82. This work was supported by the U.S. Department of Energy (DOE) National Energy Technology Laboratory under Field Work Proposal number AL-00-360-011.

REFERENCES

1. A.J. Thom, E. Summers, and M. Akinc: Intermetallics, 2002, **10**, 555-70.
2. M.K. Meyer, M.J. Kramer, and M. Akinc: Intermetallics, 1996, **4**, 273-81.
3. H.L. Zhao, M.J. Kramer, and M. Akinc: Intermetallics, 2004, **12**, 493-98.
4. T.A. Parthasarathy, M.G. Mendiratta, and D.M. Dimiduk: Acta Materialia, 2002, **50**, 1857-68.
5. J.H. Schneibel, J.J. Kruzic, and R.O. Ritchie: Proceedings of the 17th Annual Conference on Fossil Energy Materials, 2003, "http://www.netl.doe.gov/publications/proceedings/03/materials/".
6. Y. Liu, A.J. Thom, M.J. Kramer, and M. Akinc: Eleventh Int. Symp. on Processing and Fabrication of Advanced Materials, 2003, 258-71.
7. C.L. Fu and X. Wang: Philos. Mag. Lett., 2000, **80,** 683.
8. J.H. Schneibel, C.J. Rawn, T.R. Watkins, and E.A. Payzant: Phys Rev B, 2002, **65**.
9. F. Chu, D.J. Thoma, K McClellan, P. Peralta, Y. He, Intermetallics, 1999, **7,** 611.
10. Y. Liu, M.J. Kramer, A.J. Thom, and M. Akinc: accepted for publication, Metallurgical and Materials Transactions A.
11. L. Freitas and F. Ajersch: Chem. Eng. Comun., 1984, **30,** 19.
12. I. Gaballah, E. Allain, and M. Djona: Min. Met. Mat. Soc., 1992, 759.
13. V. Behrani, A.J. Thom, M.J. Kramer, and M. Akinc: accepted for publication, Metallurgical and Materials Transactions A.
14. H. Nowotny, F. Benesovsky, E. Rudy, and A. Wittmann: Monatch. Chem., 1960, **91**, 975.
15. M.E. Schlesinger, H. Okamoto, A.B. Gokhale, and R. Abbaschian: J. Phase Equilibria, 1993, **14**, 502.
16. H. Schachner, E. Cerwenka, and H. Nowotny: Monatch. Chem., 1954, **85**, 245.
17. H. Nowotny, E. Dimakopoulou, and H. Kudielka: Monatsh. Chem., 1957, **88**, 180.

EXPERIMENTAL AND NUMERICAL ANALYSIS OF THERMOMECHANICAL PROPERTIES OF SPINEL DISPERSED MOLYBDENUM ALLOYS

B.S.-J. Kang[1], B. Cooper[2], C. Feng[1], and N. Ma[2]
[1]Mechanical and Aerospace Engineering Department
[2]Physics Department
West Virginia University
Morgantown, WV 26506

ABSTRACT

Molybdenum alloys containing different volume fraction of $MgAl_2O_4$ or MgO spinel particles were studied. Tensile tests with different strain rate were carried out at room temperature and 650°C. Thermal cycle and TMA tests were conducted to study thermomechanical behavior of the alloys. Postmortem microstructure analysis revealed that large spinel particles may induce molybdenum oxides precipitation and initiate microcracks. Preliminary numerical atomistic simulation was carried out to study the factors effecting thermomechanical properties including impurity management, dispersion quality and thermomechanical mismatch between inclusion and molybdenum matrix. Although spinel particles can improve the room temperature ductility of molybdenum, further improvement of material processing conditions is needed.

INTRODUCTION

A number of silicide-based intermetallics is currently being developed for high temperature applications (>1000°C) in advanced fossil energy combustion systems. These alloys consist typically of Mo_3Si, Mo_5SiB_2, and a molybdenum solid solution phase. The Mo_5SiB_2 phase is required for oxidation resistance. The ductile molybdenum solid solution phase provides toughening. The goal is to maintain the desired high-temperature mechanical properties while also achieving the required high-temperature oxidation/hot corrosion resistance. Some key challenges of the alloy development are (i) improvement of room-temperature ductility and toughness, (ii) lowering the ductile-to-brittle transition temperature (DBTT), (iii) greater tensile strength and fracture toughness at elevated temperature, and (iv) high degree of stability at high temperatures.

However, since the ductility of molybdenum phase is marginal, ways have to be found to improve it. In the 1960's, Scruggs found that powder-metallurgical Cr is ductilized by addition of MgO particles that transform into $MgCr_2O_4$ spinel particles[1]. Recently Brady et al. verified this ductilization effect[2]. They determined that segregation of detrimental impurities such as nitrogen to the particle-matrix interface is one of the factors responsible for ductilization. Scruggs also suggested that Mo can be ductilized by adding $MgAl_2O_4$ or $NiAl_2O_4$ spinel particles[3].

To study the effect of spinel particles, several molybdenum alloys were fabricated by hot-pressing of mixtures of Mo powder with different volume factions of spinel ($MgAl_2O_4$) or MgO powders. Tensile tests were carried out at room temperature and 650°C at two strain rates for selected alloys. Thermal cycle and TMA tests were also conducted to study the

thermomechanical behavior of the alloys. The test results were correlated to the size, density, distribution of the spinel particles and processing time. For each test, a follow-up detailed fractography and microstructural analyses were carried out to study the influence of these competing effects.

In addition, related atomistic modeling simulations using combined ab-initio full-potential muffin-tin orbital and semi-empirical tight-binding (TB) methods were also carried out to study the effect of spinel impurity management and thermomechanical mismatch.

EXPERIMENTAL

Table 1 shows the molybdenum alloys examined. Three sets were disks with 62 mm diameter and 13 mm height as shown in Figure 1 whereas dog-bone tensile specimens were obtained using a wire-cut EDM machine. All tensile test specimens were polished down to 1μm surface finish. TMA tests were also conducted for coefficient of thermal expansion measurements.

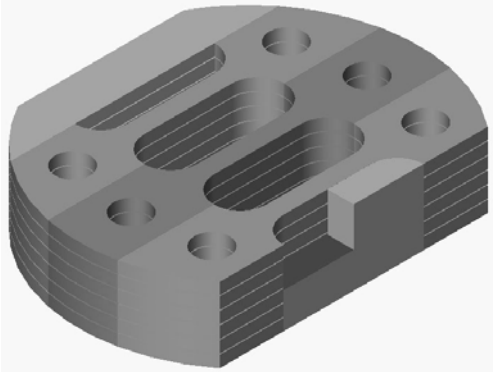

Figure 1 Specimen design

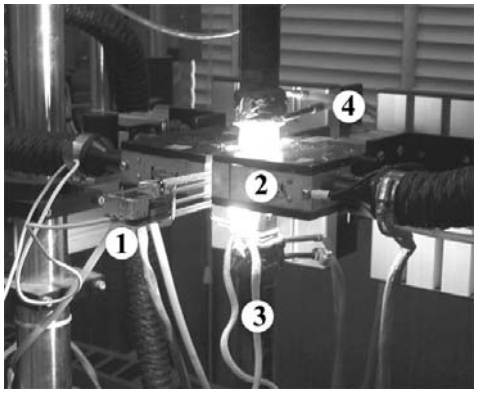

Figure 2 MTS 810 high temperature material testing system
1. High temperature extensometer, 2. Quartz lamp heater with specimen mounted,
3. Thermal couple, 4. Water cooling lines

Table 1 Material Matrix

NO.	MATERIALS	PROCESSING CONDITION
#678	Mo-3.4wt%$MgAl_2O_4$	Mo powder(2-8μm), 3.4 wt%$MgAl_2O_4$(1~5μm) Hot Pressed/4hr/1800ºC/3ksi/Vacuum
#695*	Mo	Mo powder (2- 8μm) Hot Pressed/1hr/18000ºC/3ksi/Vacuum
#696	Mo-3wt%$MgAl_2O_4$	Mo powder (2-8μm) 3wt% $MgAl_2O_4$(1~5μ m) Hot Pressed/1hr/1800ºC/3ksi/Vacuum
#697*	Mo-6wt%$MgAl_2O_4$	Mo powder (2-8μm) 6wt% $MgAl_2O_4$ (1~5μm) Hot Pressed/1hr/18000ºC/3ksi/Vacuum
#698*	Mo- 3wt%MgO	Mo powder (2-8μm) 3 wt% MgO Hot Pressed/1hr/1800ºC/3ksi/Vacuum
#729	Mo	Mo powder(3~7μm) Hot pressed 3ksi/1800C/1hr/vacuum
#732	Mo-15wt%$MgAl_2O_4$	Mo powder(3~7μm), $MgAl_2O_4$, 325mesh Hot pressed 3ksi/1800C/1hr/vacuum

*
tensile tests were carried on these alloys
**(Alloys provided by Dr. Joachim H. Schneibel, ORNL)

Tensile tests were carried out on a MTS 810 materials test system as shown in Figure 2. The system consists of a customized quartz heater system (which can be used for high temperature material testing up to 1,200°C), an Epsilon Model 3448 high temperature extensometer (gage length: 10 mm) and a PC data acquisition system. A customized computer program is used to control the heating, conduct the tensile test, and record the stress-strain curve.

NUMERICAL SIMULATIONS

It has been found [1-3] that ductility enhancement depends on the nature and composition of the spinel dispersion. At present the mechanism of spinel dispersion for improving the ductility of Mo phase is not well understood and some of the critical issues such as composition of the dispersion and the effect of oxide particle size are yet to be studied. In this paper, a proposed possible impurity management mechanism through interface electrostatic potential is illustrated in Figure 3. In the upper panel, for positive electrostatic potential oxide-Mo interface, the negatively charged oxygen impurities in Mo phase move towards the interface, therefore, oxygen impurities aggregate and precipitate/segregate near the spinel-Mo boundary, leaving the bulk and grain boundaries of Mo clean. But the exact value of surface potential depends greatly on the local environment, such as the surface structure, other ionic concentrations, as well as temperature. It is further complicated by the fact that the surface charge is compensated by an adjacent space-charge layer. The evaluation of the surface electrostatic potential can be achieved by using atomistic simulations.

To study the various defect properties in the bulk and grain/interface boundaries of Mo system, as well as to carry out Monte Carlo/molecular dynamics simulations for nano-sized spinel

particles, a new tight-binding (TB) scheme is developed. It combines the accuracy provided by ab-initio full-potential muffin-tin orbital (FP-LMTO) method [5-6] and the efficiency inherited from semi-empirical tight-binding method [7-8].

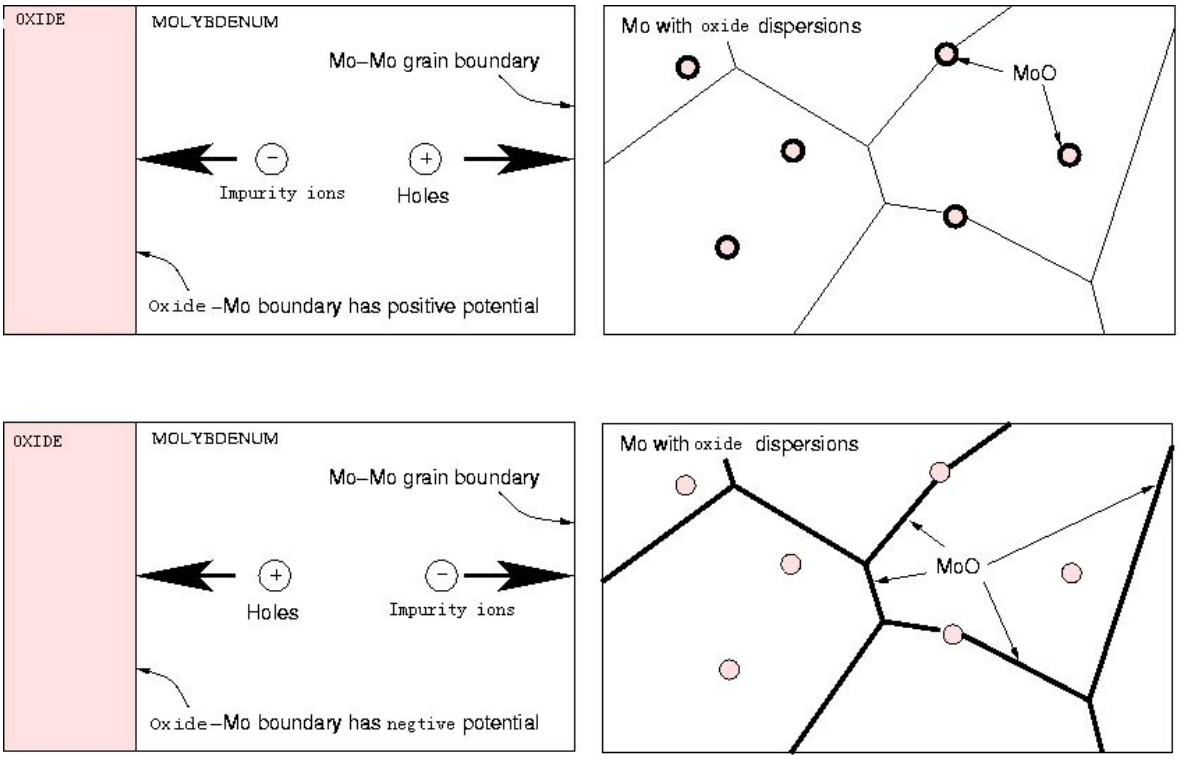

Figure 3. How surface electrostatic potential contributes to impurity management

With this new TB method, up to 1000 atoms could be simulated. With parallel computing power, this limit could be raised up even more. In this scheme, numerical fitting are completely eliminated by iteratively solve equations that related them to the diagonal ab-initio matrix elements and the cohesive energy curve. Thus the accuracy has been improved and has greatly transferability.

RESULTS AND DISCUSSIONS

Tensile Test Properties

Tensile tests were conducted at room temperature and 650°C at two displacement rates (0.254mm/min and 0.00254mm/min). Figures 4 and 5 show the stress-strain curves of alloys #695, #697, and #698 at room temperature and 650°C with two different loading rates. Table 2 shows the measured material properties, including hardness data. As shown, all the tested alloys showed improved ductility at the slow loading rate of 0.00254mm/min. Figure 5 shows jitters in the stress-strain curves of alloy #697 tested at the much slower loading rate both at room temperature and 650 °C. Figure 6 shows a typical post-mortem optical micrograph of a #697 specimen under the slower loading rate. As shown, widely spread microcracks are observed that can be traced to the sites of larger spinel particles. This phenomenon was not observed for #697 specimen tested under faster loading rate. The room temperature ductility increase of alloy #697 at the lower strain rate may be related to this microcracking effect.

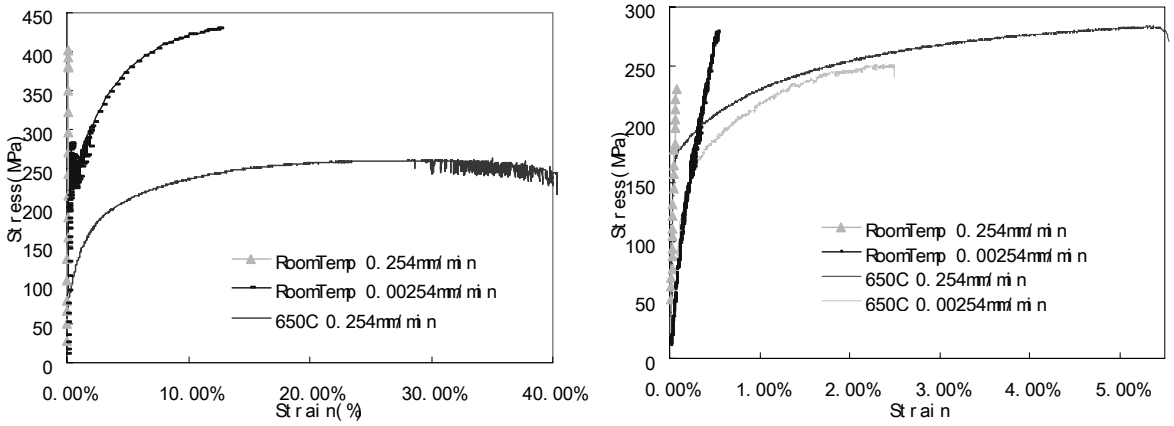

(a) #695 (b) #698

Figure 4 Engineering stress-strain curves of alloy #695 and #698 at room temperature and 650°C

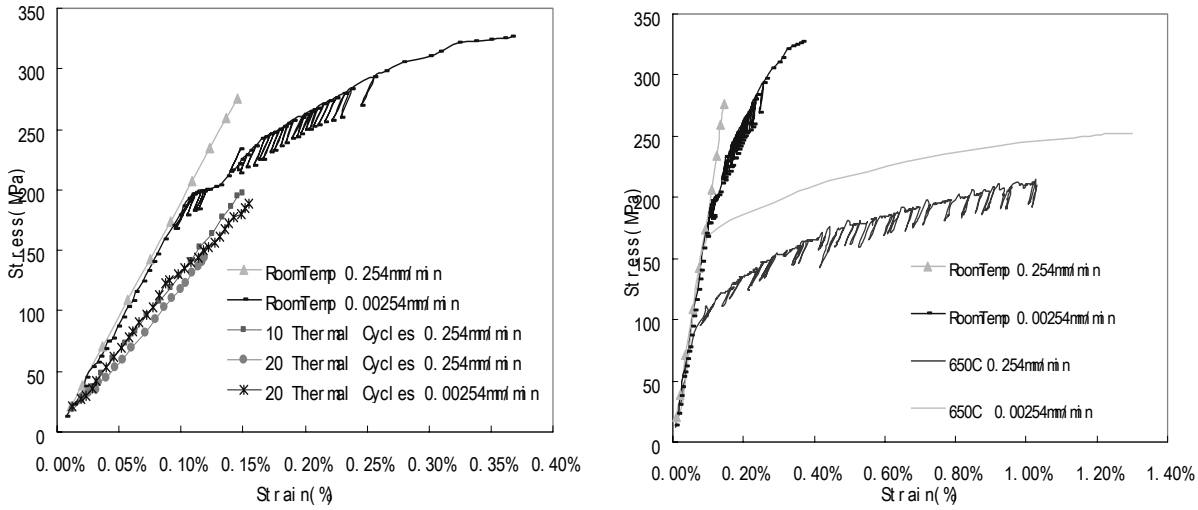

(a) Room Temperature (b) 650°C and Room Temperature

Figure 5 Engineering stress-strain curves of alloy #697 at room temperature and 650°C

Thermal Cycle Effect

Thermal cycling effects were studied for alloys #697, #678 and #732. Specimens were first heated to 650°C with a 250°C/min heating rate, held for 5 minutes at 650°C and then air- cooled to room temperature. Three tests, consisting of either 10 or 20 thermal cycles were conducted. A significant amount of thermally induced microcracks was observed in alloy #697 and these microcracks are all generated at the sites of larger spinel particles, as typically shown in Figure 7a. However, no thermally induced microcracks have been found in alloy #678 and #732, as shown in Figure 7b and 7c. Furthermore, as shown in Figure 5a, three #697 specimens were first subjected to thermal cycles prior to tensile tests. As shown in Figure 5(a) and Table 2, specimens with thermal cycles showed lower failure strength, irrespective of the loading rates.

Table 2 Mechanical properties

(TC = Thermal Cycle, RM= Room Temperature)

ID	0.254mm/min				0.00254mm/min				Hardness
	Young's Modulus (GPa)		Ultimate Strength (MPa)		Young's Modulus (GPa)		Ultimate Strength (MPa)		HV0.3
	RM	650°C	RM	650°C	RM	650°C	RM	650°C	RM
#695	243	260	402	263	115	-----	430	-----	185
#697	189	139	276	212	184	200	327	252	233
	120 (TC)	-----	150-197 (TC)	-----	120 (TC)	-----	150-197 (TC)	-----	
#698	317	317	230	283	115	112	278	251	221

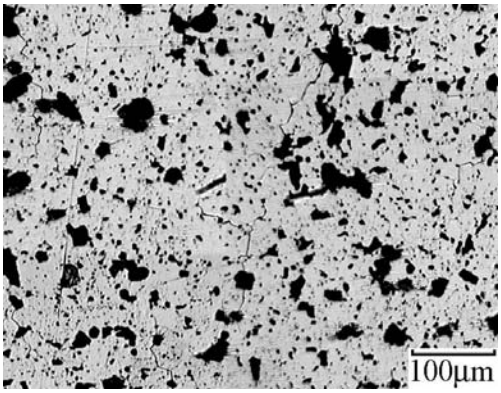

Figure 6 Microcracks caused by the slower loading rate (0.00254mm/min) #697 specimen tested under room temperature

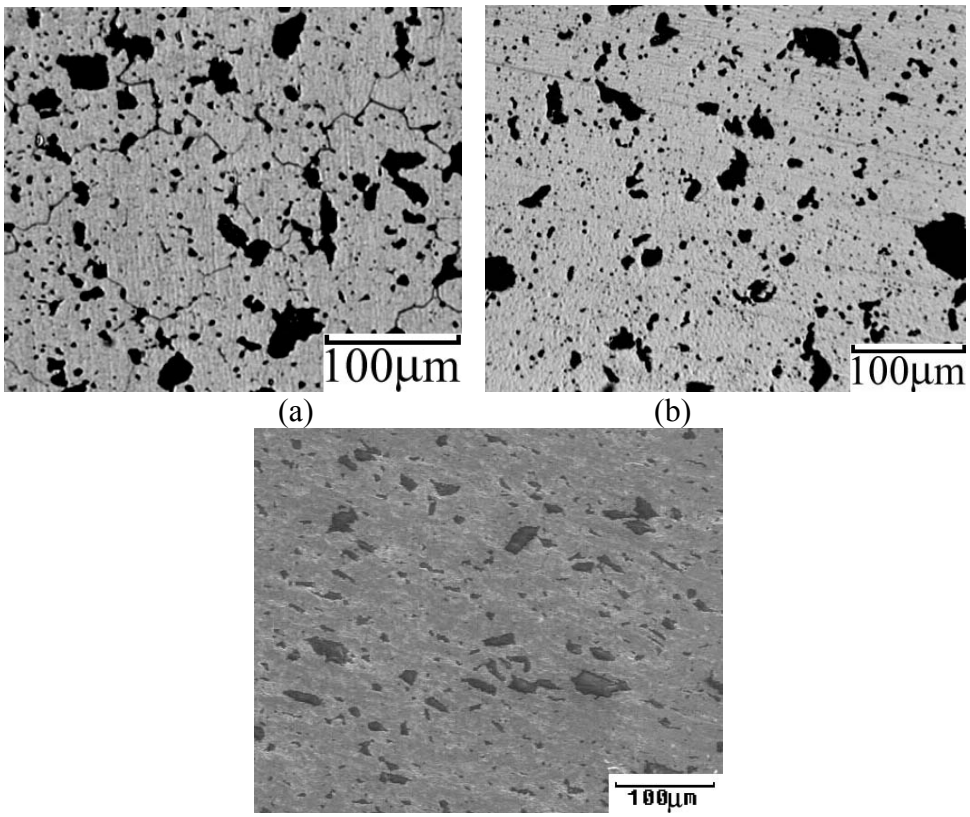

(a) (b)

(c)

Figure 7(a) Microcracks caused by thermal cycles, alloy #697, 20 cycles
Figure 7(b) No microcracks observed after 20 thermal cycles, alloy #678
Figure 7(c) No microcracks observed after 20 thermal cycles, alloy #732

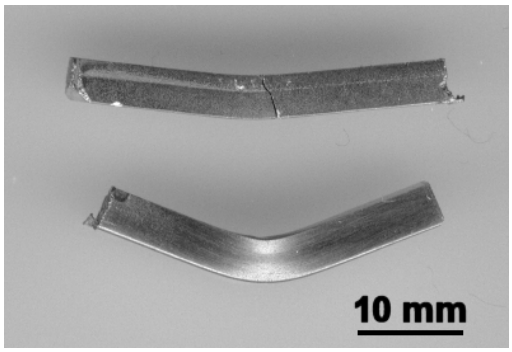

Figure 8 Comparison of the bending ductility of Mo (top) and Mo-3.4 wt% $MgAl_2O_4$ (bottom) [4]

The test results of alloy #697 (Figures 4 to 5 and Figure 7(a), and Table 2) showed a negative effect of the large spinel particles on the Mo alloys. However, as shown in Figure 8[4], a drastic room temperature ductility was found on alloy #678 which has similar volume fraction of spinel particles as that of alloy #696 but with longer processing time (hot pressed for 4 hours). Similar to the tension test results, room temperature bending tests of alloys #696 and #697 all showed brittle failure characteristics.

Figures 10 and 11 showed the spinel particle distribution and the corresponding cumulative size distribution curves. Alloy #732 has similar particle distribution characteristics as that of alloy #678. Comparing to alloy #697, it is clearly seen that alloy #678 has better spinel particle dispersion and smaller spinel particles, and this may be the reason for its better room temperature ductility performance.

The above test results indicate that further improvement of the processing conditions for spinel-dispersed Mo alloy is needed. In particular, the size of the spinel particles needs to be reduced and their spatial distribution needs to be more evenly dispersed.

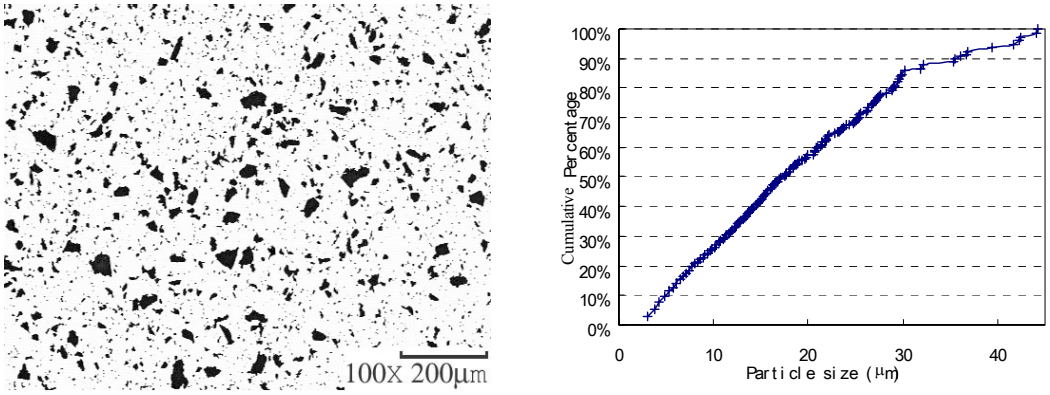

Figure 10 Typical spinel particle size and distribution, alloy #697

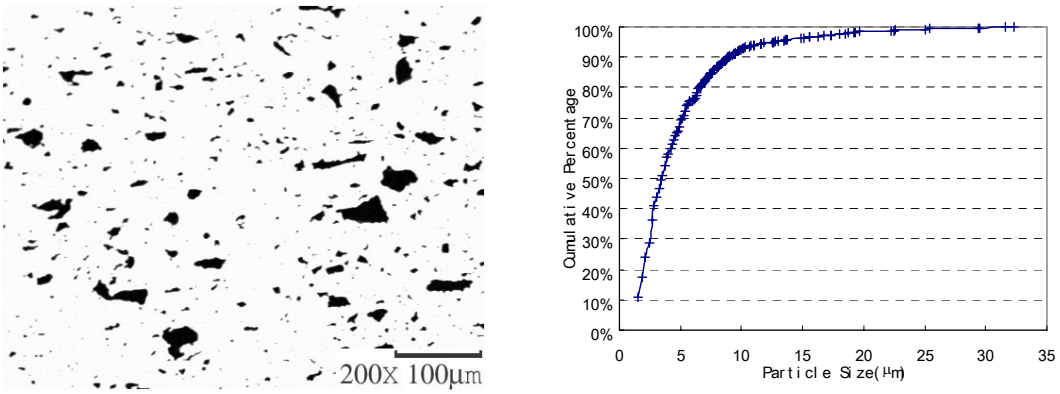

Figure 11 Typical spinel particle size and distribution, alloy #678

MOLYBDENUM OXIDE IN THERMAL CYCLE TEST AND TMA TEST

A series of thermal expansion tests were conducted using Thermo-Mechanical Analyzer (TMA). Figure 12 shows the typical TMA test results. It should be noted that the argon gas used for the TMA test contained trace amount of oxygen (about 40 ppm) such that formation of Mo oxides started to occur above 600^{o}C. Further studies revealed that the Mo oxides formation occurred in

two stages, i.e. MoO_2 was first formed and then changed to volatile MoO_3 at higher temperature, as shown in the figure. The formation of Mo oxides was also verified by X-ray diffraction (XRD) method as shown in Figure 13.

Figure 14 shows typical suspected Mo oxide sites of alloy #697 specimen under different test conditions using SEM backscattered electron detection and energy dispersive spectroscopy. Quantitative Analysis with Phi-Rho-Z method was also used to determine the proportions of Mo and oxygen constituents. However, no Mo oxide site was found on alloys #678 and #732 under similar test conditions. These preliminary results showed alloy with finer spinel ($MgAl_2O_4$) particle size and more evenly spinel particle distribution is desirable to achieve better room-temperature ductility.

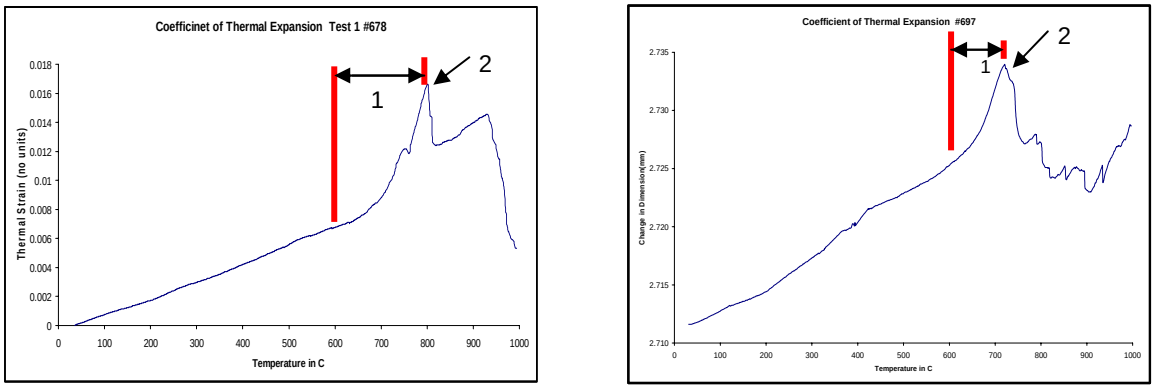

Alloy #678(Mo+Spinel) Alloy #697(Mo+Spinel)

1: Formation of MoO_2 above 600°C 2: Formation of volatile MoO_3 from MoO_2 by further oxidation

Figure 12 TMA tests results for alloy #678 and #697

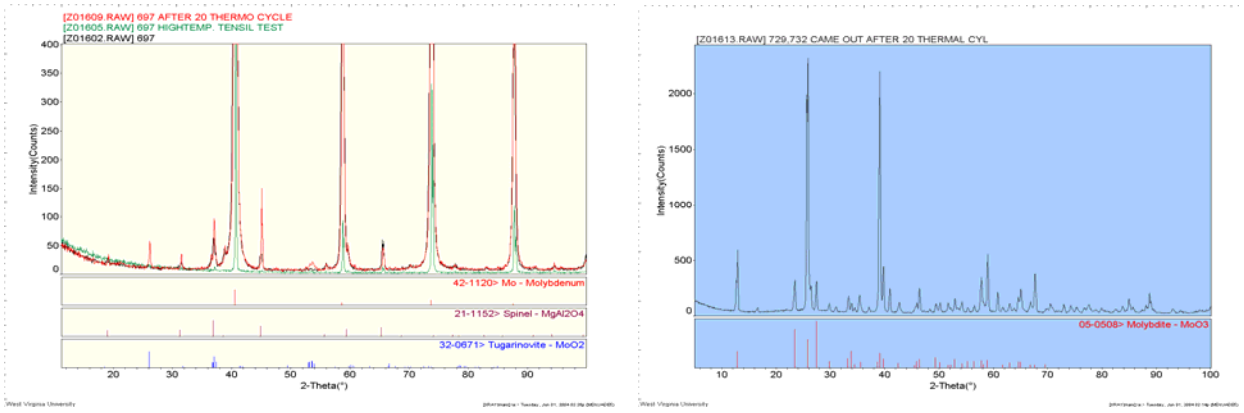

(a) MoO_2 (b) MoO_3

Figure 13. Molybdenum oxide distinguished using X-ray diffraction

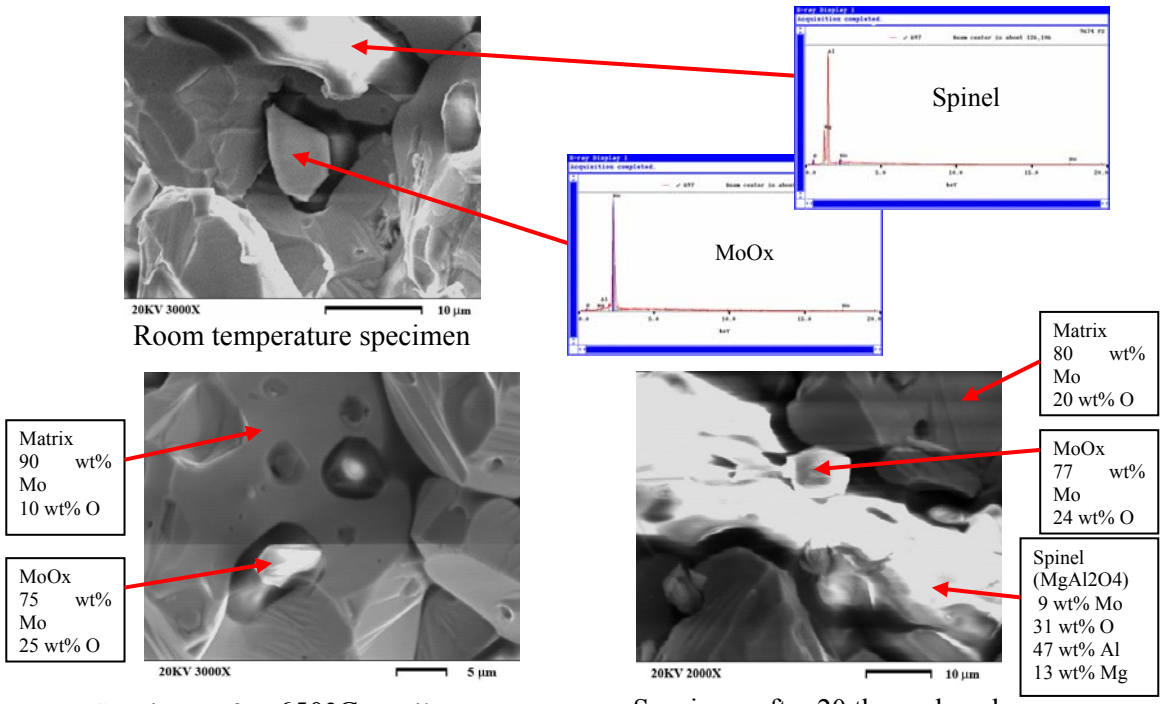

Figure 14 Alloy #697 under different testing conditions

Numerical Simulation Results

Our preliminary studies on $MgAl_2O_4$ spinel system have yielded fruitful results, but also encountered many new challenges as well. In determining the TB parameters, it was found that the parameters for oxygen-oxygen bond depend strongly on the geometric and environmental conditions as shown in Figure 15. Our initial parameterization for spinel accurately reproduces the cohesive energy curve and elastic modulus. However, it fails to render the correct formation energy for charged point defects. This is because our TB formula does not appropriately account for charge transfer effects, which are normally neglected in covalent crystals, but are important in ionic crystals. Further modification on our TB scheme to include self-consistent determination of charge transfer is currently underway.

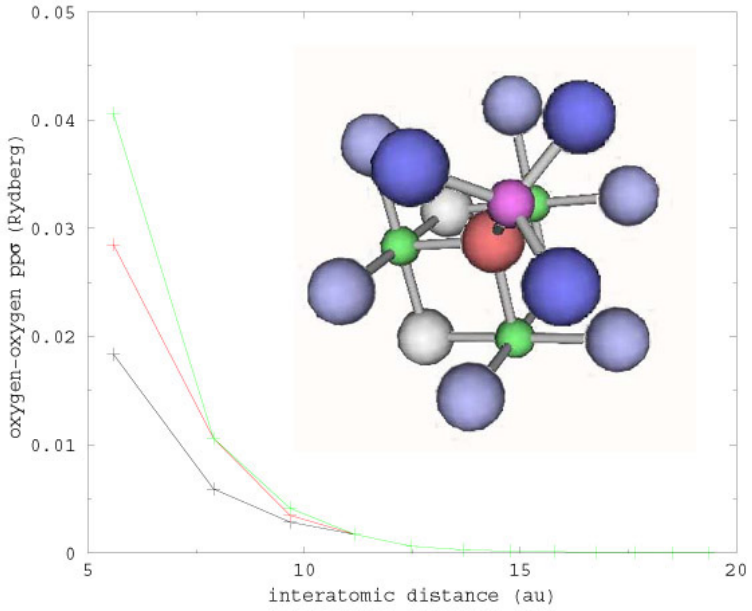

Figure 15. Environmental dependent oxygen-oxygen bond

SUMMARY

Preliminary thermomechanical tests of molybdenum alloys with $MgAl_2O_4$ or MgO spinel particles were conducted at room temperature and 650°C and correlated with the material microstructure. Although $MgAl_2O_4$ particles can improve the room temperature ductility significantly, test results revealed that further improvement of material processing conditions is needed to obtain spinel-dispersed Mo alloys with desirable room-temperature ductility.

The oxygen impurities tend to segregate/precipitate as molybdenum oxides presumably near the Mo grain boundaries and near the Mo-spinel interface area, especially for large spinel particles. The large spinel particles may initiate micro-cracks during thermal and/or mechanical properties mismatch and have an advert effect on the ductility enhancement. Finer particle, such as nano-particle is preferable.

ACKNOWLEDGMENTS

The work is sponsored by the Office of Fossil Energy, Advanced Research Materials (ARM) Program, U.S. Department of Energy, under contract DE-AC05-00OR22725 managed by UT-Battelle, LLC.

REFERENCES

1. D. M. Scruggs, L. H. Van Vlack, and W. M. Spurgeon, J. Amer. Ceram.Soc. 51 (1968) 473.
2. M. P. Brady, I. M. Anderson, M. L. Weaver, H. M. Meyer, L. R. Walker, M. K. Miller, D. J. Larson, I. G. Wright, V. K. Sikka, A. Rar, G. M. Pharr, J. R. Keiser, and C. A. Walls, Nitrogen impurity gettering in oxide dispersion ductilized chromium, Materials Science and Engineering A, Vol. 358, pp.243(2003)

3. D. M. Scruggs, Ductile tungsten composition containing a spinel dispersed uniformly throughout, United States Patent 3,320,037, Patented May 16, 1967.
4. J. H. Schneibel, J. J. Kruzic, R. O. Ritchie, Proceedings of the 17th Annual Conference on Fossil Energy Materials Baltimore, MD, April 22-24, 2003.
5. D.L. Price, B.R. Cooper, Phys.Rev. B, vol 39 pp 4945 (1989)
6. D.L. Price, B.R. Cooper and J.M. Wills, Phys. Rev. B, vol 46 pp11368 (1992)
7. J.C. Slater, G. F. Koster, Phys. Rev. vol 94 pp1498 (1954)
8. D.A. Papaconstantopoulos, Handbook of the Band Structure of Elemental Solids, Plenum, New York, (1986); R.E. Cohen, M.J. Mehl and D.A. Papaconstantopoulos, Phys. Rev. B (50) 14694.

MICROSTRUCTURES AND MECHANICAL PROPERTIES OF THE TiAlNb ALLOYS

Lan Huang
Department of Materials Science and Engineering, The University of Tennessee, Knoxville, TN 37996-2200
E-mail: lhuang2@utk.edu; Telephone: (865) 974-0645; Fax: (865) 974-4115

P. K. Liaw
Department of Materials Science and Engineering, The University of Tennessee, Knoxville, TN 37996-2200
E-mail: pliaw@utk.edu; Telephone: (865) 974-6356;
Fax: (865) 974-4115

and

C. T. Liu
Metals and Ceramics Division, Oak Ridge National Laboratory,
Oak Ridge, TN 37831-6115
E-mail: liuct@ornl.gov; Telephone: (865) 574-4459; Fax: (865) 574-7659

ABSTRACT

The TiAl alloys have been receiving considerable attentions because of their attractive properties, such as low densities, excellent high-temperature strengths, and good oxidation resistances. However, the TiAl alloys are quite brittle at room temperature and have relatively low fracture toughnesses. The relationship between the microstructures and mechanical properties of the intermetallic alloy has been investigated. With the addition of elements, such as niobium, tungsten, and boron, microstructures of the intermetallic alloys can be changed, and an enhancement in the mechanical properties of the alloy can be found. The addition of Nb is effective in improving the room-temperature ductilities, fracture toughnesses, elevated-temperature strength and oxidation resistances. The addition of W can result in an enhancement of mechanical properties, such as yield strengths, ultimate tensile strengths, and an refinement in microstructures. The boron addition in the lamellar TiAl alloys has a significant effect on room-temperature tensile ductilities.[1-2] The research plan and preliminary results of the Ti-Al-Nb-W-B alloys are discussed.

INTRODUCTION

The TiAl-based alloys have attracted a great deal of interests for use in high-temperature structural applications due to their good elevated-temperature mechanical properties, low densities, and good creep and oxidation resistances. The initial application of these alloys was limited due to their poor fracture resistances at ambient temperatures. Efforts to enhance the ductility and refine the grain size in

these materials have focused on the microstructural control and alloying addition of B, Si, W, Cr, V, Mn, and Mo. In this program, a review on the microstructures and mechanical behaviors of the TiAl-based alloys has been conducted. The research plan and preliminary results of the TiAl-based alloys are presented.

REVIEW

Relationship between the microstructures and mechanical properties of TiAl-based alloys.

Three important microstructures of the TiAl-based alloys are: (1) fully lamellar (FL) microstructures, $\alpha_2+\gamma$; (2) duplex microstructures (DP), $\alpha_2+\gamma$ and γ; and (3) near-gamma (NG) microstructures, γ. It is found that the γ phase is a very brittle phase, which leads the titanium-aluminide alloy to fracture. The TiAl-based alloys with a fully lamellar microstructure have the most balanced properties at both room and elevated temperatures.[9]

Fully lamellar structures are generally observed in cast conditions, and duplex structures are formed in thermomechanically-treated conditions. The FL microstructure consists of equiaxed polycrystalline grains with densely-packed lamellae. The lamellae are composed of α_2 plates interspersed between many γ plates. The DP microstructure, however, is made up of lamellar grains with single-phase γ grains distributed around them.[10]

The coarse FL structures with a grain size, (d), $d > 500$ μm, exhibit adequate fracture toughnesses but usually poor tensile ductilities at room temperature. On the other hand, the DP structures with fine grain sizes ($d < 50$μm) show adequate tensile ductilities but poor fracture toughnesses, and more importantly, poorer high-temperature strengths and creep resistances, as compared with the FL materials. The room-temperature tensile yield strength (σ_y), fracture strength (σ_f), and ductility (δ) of the TiAl-based alloys increase with decreasing the colony size of the fully-lamellar structure. Based on these correlations, a material with fine fully lamellar (FFL) microstructures would be expected to have balanced mechanical properties.[11-14]

Room-temperature (RT) tensile ductilities and toughnesses are two properties of considerable importance to the application of TiAl-based alloys. A great deal of research has been focused on optimizing the fully lamellar (FL) structure to have a fine grain size. This is because a FL structure with a fine grain size is known to have better balanced properties than the FL structure with a large grain size and the duplex (DP) one with a fine grain size.[15-20] Methods of refining fully lamellar structures includes:(1) solidification with grain refiner (e.g., borides)[21,22]; (2) rheocasting[23,24]; (3) supertransus processing (e.g. hot extrusion and forging of powders and ingots at a temperature, T, higher than the α transus temperature, Tα, or lower than Tα but above the eutectoid temperature, Te [$\alpha \rightarrow \alpha_2+\gamma$][25-27]; (4) thermomechanical treatment (e.g., forging plus heat treatment).[28-30] The third and fourth methods were widely used in previous studies, which involve mechanical treatments. The finest grain sizes reported

so far are those obtained the by hot extrusion of ingots and by hot forging plus heat treatments. Recently, an alternative method by which a coarse FL with a grain size of ~500 μm can be refined to ~10 μm merely by the rapid heat treatment.[10]

The fracture mechanisms in the duplex microstructures are the plasticity-induced grain-boundary decohesion and cleavage, while those in the lamellar microstructures are the interface delamination and cracking along the lamellae.[31] The lamellar microstructure is tougher than the equiaxed gamma or duplex microstructure because of the higher near-tip plasticity and an anisotropic composite-like fracture characteristic that yields a tortuous crack path, shear-ligament toughening, and an improved resistance-curve behavior. The tensile ductility of the lamellar microstructure increases with decreasing the colony size, while the fracture toughness shows a maximum at a large colony size.[32]

The initiation toughness, K_{IC}, of the lamellar TiAl-based alloys increases with increasing the grain size and the volume fraction of lamellar grains.[32] Both K_{IC} and the crack-growth toughness, K_S, increase with decreasing the lamellae spacing by affecting translamellar microcracking and the size of the shear ligaments. K_S increases with increasing the colony size, the volume fraction, and the width of crack-wake ligaments. At a large grain size, K_S depends on the grain size indirectly through the influence of the grain size on the ligament width. The tensile ductility in the TiAl-based alloys is limited by the instability of microcracks nucleated in the microstructure. The level of the tensile ductility depends on the K_{IC} value and the grain size. High fracture toughnesses can be attained in large-grained lamellar TiAl-based alloys with a fine lamellae spacing (< 2 μm). The balanced properties of a moderate K_{IC} and plastic elongation (16 MPa√m and 1.5%) can be attained in the fully-lamellar TiAl alloys with a size of approximately 300 μm and a lamellae spacing of less than 2 μm.[33]

Influence of Al, Nb, W, and B on microstructures and mechanical behavior of the TiAl-based alloys.

The Al content in TiAl-based alloys has great effects on the microstructure and high-temperature strength.[34] With decreasing the Al content, the volume fraction of the α_2 phase increases. The average lamellae spacing decreases linearly with increasing the volume fraction of the α_2 phase. The best ductility typically occurs in the range of the 46-50 atomic percent (at.%) within the ductile Al range, and increasing Al generally decreases the fracture toughness. The lamellar colony size in the cast TiAl-based alloys (with 44–50 at.% Al and 1 at.% B) increases monotonically with increasing the Al concentration because the increased tendency to form the alpha phase with the increase of the Al content reduces the boron concentration in the liquid, thus reducing the role of boron in the grain refinement.[35]

The Nb content in the high Nb-containing TiAl-based alloys significantly increases the high-temperature strength. The Nb addition only shows slight effects on the volume fraction of the α_2 phase and the average lamellae spacing. The main effect of high Nb contents on high-temperature strengths relies on the increase of the value of σ_0 in the Hall-Petch equation, as shown below:

$$\sigma_{0.2} = \sigma_0 + k_\lambda \lambda^{-1/2}$$

where $\sigma_{0.2}$ is the 0.2% offset yield strength, σ_0 and k_λ are material constants, and λ is the lamellae spacing. It means that the friction stress of moving dislocations arises mainly from the Peierls stress of the lattice, and the interactions between dislocations are much stronger than those for the TiAl-based alloys with less Nb contents.[34] The high Nb content also improves the high-temperature stability of microstructures of the TiAl-based alloys, resulting in the improvement of the high-temperature strength. The oxidation resistance of the TiAl-based alloys is improved with the Nb addition. The amount of Nb to be added is generally determined, depending on the oxidation resistance required. Nb slightly improves the creep resistance.

Tungsten was found to improve the creep properties significantly. The addition of W might act as a solid-solution strengthener so as to stabilize the $\alpha_2+\gamma$ lamellar structure.[36] The motion of dislocations and/or interfaces could be impeded by β_2 particles stabilized with tungsten. The addition of W also greatly improves the oxidation resistance.[37]

Alloying by boron in the TiAl-based alloys was proved to be an effective and economic method to achieve the grain refinement, reduce the lamellar colony size, and prevent the uncontrolled grain growth during heat treatments performed within the single-phase α-field.[38-40] The effect of the boron addition on room-temperature tensile ductilities in the lamellar TiAl-based alloys depends predominately on the size of titanium-boride precipitates.[40] Alloys with fine titanium-boride precipitates have good ductilities, which is due to the refinement in the grain size induced by the boron addition in both wrought and cast conditions. Boron does not affect the yeild strength while lowering the ductilities of the TiAl-based alloys containing > 0.10 at. % B. Large titanium-boride precipitates proved to be detrimental to ductilities. Cracking along large titanium-boride precipitates can suppress the beneficial effect reflected from the grain refinement. Any refinement in titanium-boride precipitates, i.e., breaking down long titanium-boride precipitates by thermomechanical processing or limiting the boride-precipitate growth by fast cooling during solidification, will increase the ductilities significantly. The addition of > 0.5 at.% of boron refines grain sizes, and improves strengths and workabilities.

OBJECTIVE

The objectives of the research are to (1) design and fabricate the Ti-Al-Nb-W-B intermetallic alloys, (2) observe the phase composition of the intermetallic alloys after high-temperature heat treatments, (3) study and characterize the mechanical properties of the alloys, and (4) predict the relationship between the microstructures and mechanical behaviors. The present investigation will lead to a mechanistic understanding and theoretical modeling of processing and microstructural effects on the mechanical performance of these alloys, and a metallurgical way to improve their mechanical properties.

RESEARCH PLANS

The research work will emphasize the processing and optimization of the microstructures of the Ti-Al-Nb-W-B intermetallic alloys for improving fatigue and fracture resistances. The materials used in this investigation have been prepared by drop-cast and powder-metallurgy techniques. Heat treatments will be conducted to refine the microstructures of the Ti-Al-Nb-W-B alloys. Fatigue and fracture properties will be developed as functions of processing methods and microstructures. To facilitate a mechanistic understanding of the fatigue-crack-initiation behavior, nondestructive-evaluation (NDE) techniques, such as replication methods, thermography, and scanning-electron microscopy (SEM), will be utilized to investigate crack-initiation mechanisms. Theoretical models will be attempted to predict fatigue-crack-initiation behavior. Moreover, the possibility for developing new extremely high-temperature intermetallic materials with good mechanical properties will be explored.

NDE techniques will be used to monitor the crack initiation and propagation process during the fracture-toughness and cyclic-fatigue experiments of the Ti-Al-Nb-W-B alloys. A series of fracture-toughness and fatigue specimens will be interrupted during testing at pre-determined points, followed by carefully cross-sectioning and studying by means of SEM. The fracture and fatigue-crack-propagation paths at various stages of testing will be statistically characterized, *e.g.,* the length along boundaries/interfaces, the cracking orientation with respect to loading directions, etc. It is expected that the fracture and fatigue-crack-propagation processes will be quantitatively investigated and modeled in the Ti-Al-Nb-W-B alloys.

The grain size, lamellae spacing, and colony size play a dominating role in controlling the fatigue and fracture characteristics of the Ti-Al-Nb-based alloys. Transmission-electron microscopy (TEM) will be utilized to characterize the fine structures of the grain boundaries and interfacial areas. It is planned to use a nanoindentation technique to probe mechanical properties in the grain-boundary areas.

On the basis of the above quantitative results, it will be attempted to conduct process modeling, which will relate processing parameters and alloy compositions to final microstructures. Furthermore, numerical simulations of the fracture processes in the Ti-Al-Nb-W-B systems will be performed to predict the fracture behavior and fatigue life under given loading, which will be used to optimize the microstructural design of the Ti-Al-Nb-W-B alloys with superior fatigue and fracture properties.

It is expected that the present investigation will lead to a mechanistic understanding and theoretical modeling of the processing, fatigue, and fracture behavior of Ti-Al-Nb-W-B systems, and a metallurgical way to improve their mechanical properties. The influence of processing parameters and microstructures on mechanical behavior of the Ti-Al-Nb-W-B systems will be emphasized.

EXPERIMENTAL PROCEDURES

Niobium, tungsten, and boron are added to the arc-melted and drop-casted TiAl-based alloy, fabricated at Oak Ridge National Laboratory. The atomic percents of Nb, W, and B are 8.5%, 1.5%, and 0.05%, respectively. The Ti-44at.%Al-8.5at.%Nb-1.5at.%W-0.05at.%B sample was cut into four pieces, and capsulated into a quartz tube with argon inside. According to the Differential Scanning Calorimetry (DSC) graph, we are able to predict the phase-changing temperatures, and, thus, determine the proper heat-treatment temperatures. The four heat-treatment temperatures and related times are as follow: at $1{,}100^0$C for 48 hrs; at $1{,}240^0$C for 10 hrs; at $1{,}310^0$C for 5 hrs; and at $1{,}400^0$C for 2 hrs.

The newly fabricated TiAl-based alloys at Oak Ridge National Laboratory are: Ti-45Al-7Nb-0.15B; Ti-45Al-7Nb-0.15B-0.2W; Ti-45Al-7Nb-0.15B-0.4W; Ti-45Al-7Nb-0.15B-0.7W, in atomic percent. The atomic percents of the niobium, tungsten, and boron have been reduced. Since W and B are β phase stabilizers, the toughness of the newly fabricated materials should be improved. Heat treatments of the alloys have been scheduled. After capsulating all of the four pieces of alloys in one quartz tube, the samples are to be annealed at $1{,}100^0$C for 48 hrs, we will then section the $1{,}100^0$C-annealed alloys into five pieces for additional heat treatments at 900^0C, $1{,}240^0$C, $1{,}310^0$C, and $1{,}400^0$C, respectively. At 900^0C, alloy specimens will be annealed for 15 days, at $1{,}240^0$C for 10 hrs; $1{,}310^0$C for 5 hrs; and $1{,}400^0$C for 2 hrs.

When heat-treatments of the alloys are finished, the microstructures of the alloys will be defined with the use of the optical microscopy, SEM, TEM, and an electron microprobe. Hardness tests on the heat-treated alloys will be performed. Since the strength of the material is controlled by the lamellae spacing, and the ductility is controlled by the grain size. The pertinent temperature and ways to produce the desired fully lamellae structures will be obtained. Mechanical experiments, such as tension, fatigue, and creep tests, will be performed, at both room and elevated temperatures.

PRELIMINARY RESULTS

Microstructures of the Ti-44at.%Al-8.5at.%Nb-1.5at.%W-0.05at.%B sample, after the scheduled heat-treatments, are shown in Figs. 1-5, for the as-received, $1{,}100^0$C. $1{,}240^0$C, $1{,}310^0$C, and $1{,}400^0$C-annealed samples, respectively. This alloy contains mainly three phases, α_2, δ and β, and the detailed analysis of the microsturctures is in progress.

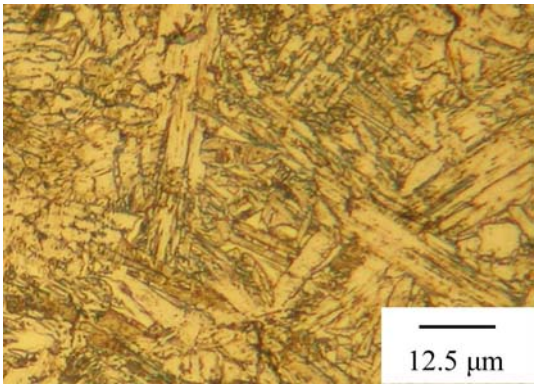

Fig. 1 Microstructure of the As-received Ti-44at.%Al-8.5at.%Nb-1.5at.%W-0.05at.%B Alloy
The estimated phases are $\alpha_2+\gamma$ and γ.

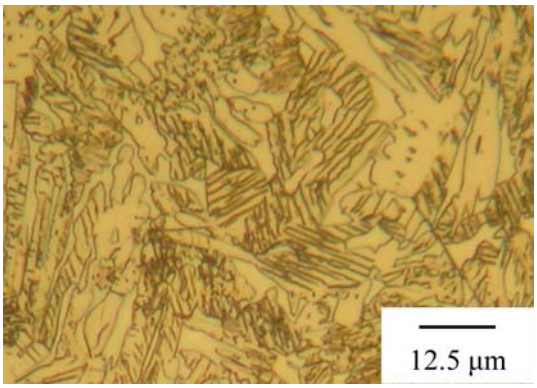

Fig. 2 Microstructure of the Heat-treated Alloy, 1,100^{0}C for 48 hrs
The estimated phases are $\alpha_2+\gamma$ and γ.

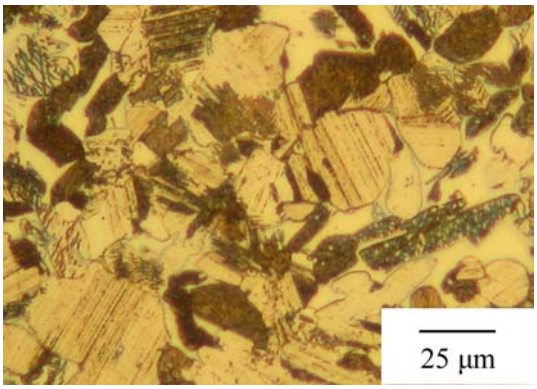

Fig. 3 Microstructure of the Heat-treated Alloy, 1,240^{0}C for 10 hrs
The estimated phases are $\alpha+\gamma$ and γ.

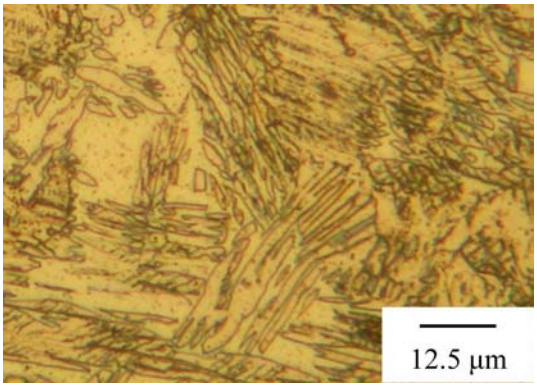

Fig. 4 Microstructure of the Heat-treated Alloy, 1,310^{0}C for 5 hrs
The estimated phases are α+β and β.

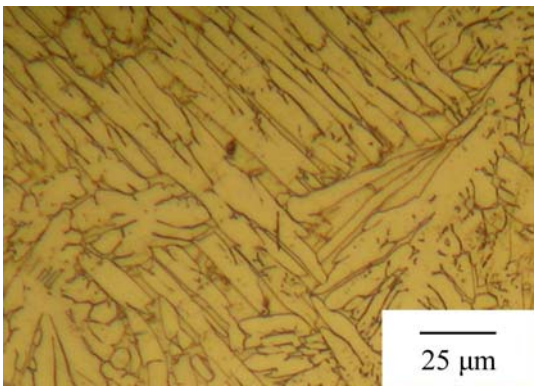

Fig. 5 Microstructure of the Heat-treated Alloy, 1,400^{0}C for 2 hrs
The estimated phase is β.

SUMMARY

The literature survey on the TiAl-based alloys has been completed. The heat treatments and microstructures of the Ti-44at.%Al-8.5at.%Nb-1.5at.%W-0.05at.%B alloy are being studied. Preliminary results on microstructure investigations have been reported. Research plans on the newly prepared TiAl-based alloys have been scheduled.

ACKNOWLEDGEMENTS

The present research is sponsored by the Fossil Energy Materials Program, with Dr. R. Judkins and Dr. J. Zollar as Program Managers, and the National Science Foundation Combined Research-Curriculum Development (CRCD) Program, with Ms. Mary Poats as the contract monitor, under the contract number of DGE-0203415. P. K. Liaw would like to thank Ms. Roberta Campbell for her kind help in revising this manuscript.

REFERENCES

[1] Z. C. Liu, J. P. Lin, S. J. Li and G. L. Chen, Intermetallics, 10, 653-659, 2002.
[2] D. Hu, Intermetallics, 10, and 851-858, 2002.
[3] D. J. Larson, C. T. Liu, and M. K. Miller, Intermetallics, 5, 497-500, 1997.
[4] Y-K. Kim, Acta. Metall., 40, 1121, 1992.
[5] D. M. Dimiduk, Gamma Titanium Aluminides, eds., Y-K. Kim, R. Wagner, and M. Yamaguchi, TMS, Warrendale, PA., p. 21, 1995.
[6] Y-K. Kim, Gamma Titnnium Aluminides, eds., Y-K. Kim, R. Wagner, and M. Yamaguchi, TMS, Warrendale, PA., p. 637, 1995.
[7] S. C. Huang, Structural Intermetallics, eds., R. Darolia, J. Lewandowski, C. T. Liu, P. Martin, D. Miracle, and M. Nathal, TMS, Warrendale, PA., p. 299, 1993.
[8] C. T. Liu, P. J. Maziasz, D. R. Clemens, J. H. Schneibel, V. K. Sikka, T. G. Nieh, J. L. Wright, and L. R. Walker, Gamma Titanium Aluminides, eds., Y-K. Kim, R. Wagner, and M. Yamaguchi, TMS, Warrendale, PA., p. 679, 1995.
[9] Shyh-Chin Huang, Structural Intermetallics, eds., R. Darolia, J. J. Lewandowski, C. T. Liu, P. L. Martin, D. B. Miracle, and M. V. Nathal, TMS, 299-307, 1993.
[10] J. N. Wang and K. Xie, Intermetallics, 545-548, 2000.
[11] S. C. Huang, Metall Trans., 23A, 375, 1992.
[12] S. C. Huang, eds., R. Darolia, J. J. Lewandowski, C. T. Liu, P. L. Martin, D. B. Miracle, and M. V. Nathal, Structural intermetallics, Warrendale, PA, TMS, p. 299, 1993.
[13] J. N. Wang, A. J. Schwartz, T. G. Nieh, C. T. Liu, V. K. Sikka, D. Clemens, K-W. Kim, R. Wagner, and M. Yamaguchi, eds., Gamma Titanium Aluminides, Warrendale, PA, TMS, p. 949, 1995.
[14] Y-W. Kim, JOM, 46, 30, 1994.
[15] J. N. Wang, J. Yang, Q. F. Xia, and Y. Wong, Mater. Sci. & Engng. A, 329, 118-123, 2002.
[16] S.C. Huang, Metall. Trans., 23A, 375, 1992.
[17] Y.-W. Kim, J. Organometall. Chem., 46, 30, 1994.
[18] J. N. Wang, A. J. Schwartz, T. G. Nieh, C.T. Liu, V. K. Sikka, and D. Clemens, eds., Y.-W. Kim, R. Wagner, and M. Yamaguchi, Gamma Titanium Aluminides, TMS, Warrendale, PA, p. 949, 1995.
[19] C. T. Liu, J. H. Schneibel, P. J. Maziasz, J. L. Wright, and D. S. Easton, Intermetallics, 4, 429, 1996.
[20] D. M. Dimiduk, P. M. Hazzledine, T. A. Parthasarathy, S. Seshageri, and M. G. Mendiratta, Metall. Mater. Trans., 29A, 37, 1998.
[21] D. W. Larsen, S. Kampe, and L. Christodoulou. Mater. Res. Soc. Symp. Proc. 194-285, 1990.
[22] S. C. Huang and E. L. Hall, Mater. Res. Soc. Symp. Proc., 213-827, 1991.
[23] K. Ichikawa and Y. Kinoshita. Mater. Trans. Jpn. Inst. Met., 37-1311, 1996.
[24] K. Ichikawa and Y. Kinoshita. Mater. Sci. Engng. A, 240-493, 1997.
[25] Y-W Kim and D. M. Dimiduk. US Patent No. 5226985, 13 July 1993.
[26] P. A. McQuay, D. M. Dimiduk, and Y-W Kim, US Patent No. 5417781, 23 May 1995.
[27] D. Rugg, M. Kearns, S. A. Blackham, N. A. Walker, and S. Kerry, Blenkinsop, PA, eds., W. J. Evans and H. M. Flower, Titanium '95: Science and Technology, London: The Institute of Materials, p. 201, 1996.

[28] S. L. Semiatin, V. Seetharaman, and I. Weiss, eds., I. E. Weiss, R. Srinivasan, P. J. Bania, D. Eylon, and S. L. Semiatin, Advances in the Science and Technology of Titanium Alloy Processing, Warrendale, PA, TMS, p. 3, 1996.
[29] L. Semiatin, V. Seetharaman, D. M. Dimiduk, and K. H. G. Ashbee, Metall. Mater. Trans A, 29, 7, 1998.
[30] D. M. Dimiduk, P. L. Martin, and Y-W Kim, Mater. Sci. Engng. A, 243, 66, 1998.
[31] K. S. Chan and Y. M. Kim, Metallurgical Transactions A, 23, 1663-1677, 1992.
[32] K. S. Chan and Y. M. Kim, Acta Metall. Mater., 43 (2), 439-451, 1995.
[33] K. S. Chan, Gamma Titanium Aluminides, Y. M. Kim, R. Wagner, and M. Yamaguchi, eds., TMS, 835-847, 1995.
[34] D. Hu, Intermetallics, 9, 1037-1043, 2001.
[35] S. J. Yang, S. W. Nam, and M. Hagiwara, Journal of Alloys and Compositions, 350, 280-287, 2003.
[36] R. Yu, L. L. He, Z. Y. Cheng, J. Zhu, and H. Q. Ye, Intermetallics, 10, 661-665, 2002.
[37] D. Hu, Intermetallics, 9, 1037, 2001.
[38] Y. W. Kim, Acta Metall. Mater., 40, 1121, 1992.
[39] J. Lapin and A. Klimova Kovove, Mater., 4, 41, 2003.
[40] P. J. Maziasz, R. V. Ramanujan, C. T. Liu, and J. L. Wright, Intermetallics, 5, 83-95, 1997.

SESSION III

COATINGS AND PROTECTION OF MATERIALS

CORRODION BEHAVIOR OF Fe-Al-Cr WELD OVERLAY COATINGS FOR THE PROTECTION OF BOILER TUBES IN LOW NOX ENVIRONMENTS

J.R. Regina, J.N. DuPont, and A.R. Marder
Lehigh University
Materials Science and Engineering
5 E. Packer Ave.
Bethlehem, PA 18015

ABSTRACT

Iron-aluminum based alloys have recently been evaluated as weld overlay coatings for the protection of waterwall boiler tubes in highly aggressive sulfur-bearing environments. The objective of this study was to investigate the corrosion resistance of iron-aluminum based alloys containing chromium and titanium additions for use as low cost weld overlay coatings on boiler tubes exposed to furnace environments operating under low NOx burning conditions. These alloys were exposed to several simulated high-temperature gaseous corrosion atmospheres and were also placed in contact with solid FeS_2 to simulate corrosive slag that can form on the boiler tube walls. Corrosion kinetics and scale morphology were used to evaluate the corrosion resistance of each alloy. Critical aluminum and chromium concentrations required for protective corrosion behavior were found in all testing environments. Once corrosion resistant alloys were identified from the corrosion-testing phase of the study, the weldability of the Fe-Al-Cr weld overlay claddings were evaluated. It was found that Fe-Al-Cr weld overlays were susceptible to hydrogen cracking at certain weld compositions. The crack-free composition range was identified and will be used to develop Fe-Al-Cr based coatings for boiler tubes in low NOx furnaces that are both weldable and corrosion resistant.

INTRODUCTION

Coal-burning power companies have successfully been able to reduce the amount of hazardous nitrous-oxide (NOx) compounds released into the atmosphere by utilizing a staged-combustion system. These systems rely on starving the combustion process of oxygen in the lower elevation of the furnace, allowing for NOx compounds to reduce to inert N_2. Consequently, sulfur found in the coal can form highly corrosive compounds such as H_2S during combustion, which has led to an increased frequency of boiler tube ruptures and unscheduled downtime. Iron-aluminum based weld overlay claddings have recently been considered as coatings for the boiler tubes located within these coal-burning furnaces, because they have been shown to provide excellent sulfidation resistance and are relatively inexpensive to deposit[1-3]. The current study compared the high-temperature corrosion resistance of several Fe-Al alloys containing Cr and Ti additions in three gaseous environments, selected to simulate low NOx burning conditions. Gas-slag corrosion experiments were conducted using FeS_2 powder to simulate slag located on the boiler tube surface.

Once corrosion resistant alloy compositions were identified, Fe-Al-Cr welds were produced using a gas-tungsten arc welding (GTAW) process and evaluated for cracking. It has previously been shown that binary Fe-Al weld overlay claddings are susceptible to hydrogen cracking at elevated aluminum concentrations, but the effect of Cr on the cracking behavior of these alloys has yet to be thoroughly studied[4]. Therefore, the hydrogen cracking susceptibility of Fe-Al-Cr welds was identified as a function of aluminum and chromium concentrations. The objective of this study was to identify weld overlay compositions that can be deposited crack-free and provide adequate corrosion resistance in low NOx environments.

EXPERIMENTAL PROCEDURE

Alloys were made by arc-melting high purity components under an argon atmosphere and drop cast into a water-cooled copper mold. Cast alloys were used because it was previously shown that the high temperature corrosion behavior of weld overlays could be explained by using cast alloys of equivalent composition[5]. It has also been reported that the corrosion behavior between Fe-Al weld overlays and cast alloys are similar due to no microsegregation within the welds and both having coarse grained microstructures[4]. Alloys contained 7.5wt% or 10wt%Al, chromium levels ranged from 0-5wt% (all alloy values reported in wt%), and two quaternary alloys contained both chromium and titanium additions (Table I). Corrosion experiments were carried out using a Netzsch STA 409 high-temperature thermogravimetric (TG) balance, which measured the corrosion kinetics. Corrosion coupons were prepared identically, heated at a rate of 50°C/min, and held at 500°C for 100 hours. Water vapor present in the mixed oxidizing/sulfidizing and the oxidizing environments was injected into the furnace at a controlled rate via a capillary tube and a syringe pump. The three gas compositions used for this study can be seen in Table II.

Gas-slag corrosion experiments were conducted using Lindberg/Blue Horizontal Tube Furnaces. The corrosion test setup consisted of a quartz ring super-glued onto the top of the ground alloy surface. A predetermined amount (1680mg) of FeS_2 powder, supplied by American Minerals, was poured into the quartz ring without being packed and this setup was placed into the furnace. Either the mixed oxidizing/sulfidizing gas or the oxidizing gas was then introduced into the furnace, the samples were heated at a rate of 50°C/min to 500°C, and they were exposed for 100 hours. Samples were carefully mounted in cold setting epoxy and their polished cross sections were observed using Light Optical Microscopy (LOM). LOM images were taken with an integrated camera on a LECO digital imaging system. The thickness of the internal corrosion products observed in non-protective alloys were measured using a Quantitative Image Analysis (QIA) program interfaced with a Light Optical Microscope.

Single-pass Fe-Al-Cr welds were made using a mechanical Gas-Tungsten Arc Welding (GTAW) system equipped with a computer controlled power source and table. Substrates used during welding were commercially available low-carbon steel (Grade A285C). Two filler metal wires (Fe-Cr wire and Al wire) were simultaneously fed into the weld pool in order to have the ability of varying the aluminum and chromium concentrations separately. The energy input was kept constant by carefully controlling the weld power and travel speed. A non-destructive dye penetration test was performed the weld overlays after they were produced to determine if welds were susceptible to cracking. Quantitative chemical analysis was performed on each weld sample using a JEOL 733 Microprobe at 20keV. A phi(ρz) correction scheme was used to correct for absorption and fluorescence of x-rays that occurs during Electron Probe Microanalysis (EPMA).

Table I – Alloy compositions used for corrosion testing. All values are in weight percent.

Alloy Designation	Fe	Al	Cr	Ti
Fe-7.5Al	Bal.	7.38	--------	--------
Fe-7.5Al-1Cr	Bal.	7.45	0.96	--------
Fr-7.5Al-2Cr	Bal.	7.59	2.09	--------
Fe-7.5Al-5Cr	Bal.	7.77	5.03	--------
Fe-7.5Al-2Cr-1.5Ti	Bal.	7.81	2.19	1.65
Fe-10Al	Bal.	10.04	--------	--------
Fe-10Al-1Cr	Bal.	10.04	0.99	--------
Fe-10Al-2Cr	Bal.	10.19	2.16	--------
Fe-10Al-5Cr	Bal.	10.74	5.18	--------
Fe-10Al-2Cr-1.5Ti	Bal.	10.34	2.18	1.67

Table II – Gas compositions used for corrosion testing (vol. %).

Gas Component	Sulfidizing Gas	Mixed Oxidizing/Sulfidizing Gas	Oxidizing Gas
O_2	--------	--------	2
CO	15	10	--------
CO_2	--------	5	15
H_2	3	--------	--------
H_2O	--------	2	6
H_2S	0.12	0.12	--------
SO_2	--------	--------	0.12
N_2	Bal.	Bal.	Bal.
Log Po_2	-28	-19	-2
Log Ps_2	-6	-8	-46

RESULTS AND DISCUSSION

GASEOUS CORROSION EVALUATION

The ten Fe-Al based alloys containing Cr and Ti (Table I) were used for the gaseous corrosion phase of the study. Each alloy was exposed to the three gases (Table II) at 500°C for 100 hours. The kinetic results for select alloys exposed to the sulfidizing environment can be seen in Figure 1. Alloys containing 10%Al demonstrated excellent corrosion resistance during 100 hours of exposure regardless of the chromium or titanium additions. These alloys gained no significant amount of weight during corrosion testing. On the other hand, ternary FeAlCr alloys containing 7.5%Al were only protective when the chromium concentration was increased to 5%Cr. It was also observed that titanium additions were beneficial to the corrosion behavior of Fe-7.5Al-2Cr during exposure to the sulfidizing gas (Figure 2).

The corrosion results for alloys exposed to the mixed oxidizing/sulfidizing environment can be seen in Figure 3. It was observed that chromium additions had no positive effect on the corrosion behavior of alloys containing 7.5%Al and titanium addition had only a slight effect on the corrosion resistance of Fe-7.5Al-2Cr. Alloys containing 10%Al were protective when chromium was present and it was observed that titanium had no significant effect on the corrosion behavior of the ternary alloy, as they were both protective during 100 hours of exposure. The alloys exposed to the oxidizing environment can be seen in Figure 4, which shows that chromium additions helped increase the oxidation resistance of alloys containing 7.5%Al. Similarly to the mixed oxidizing/sulfidizing gas, titanium additions did not have any significant effect on the oxidation behavior of the alloys. Overall, the alloys that consistently demonstrated the best corrosion protection in all three gaseous corrosion environments contained 10%Al and required chromium additions.

GAS-SLAG CORROSION EVALUATION

The same ten alloys were then tested in simulated gas-slag corrosion environments where they were exposed to either the mixed oxidizing/sulfidizing or the oxidizing environments while in direct contact with FeS_2 powder for 100 hours at 500°C. Alloys containing 10%Al were completely protective when exposed to mixed oxidizing/sulfidizing environment, regardless of the chromium or titanium additions. On the other hand, all alloys containing 7.5%Al formed significant corrosion product despite chromium or titanium additions. Typical corrosion product morphology consisted of a porous external corrosion scale above a substrate corrosion scale, which seemed to form uniformly and was multi-layered in nature (Figure 5).

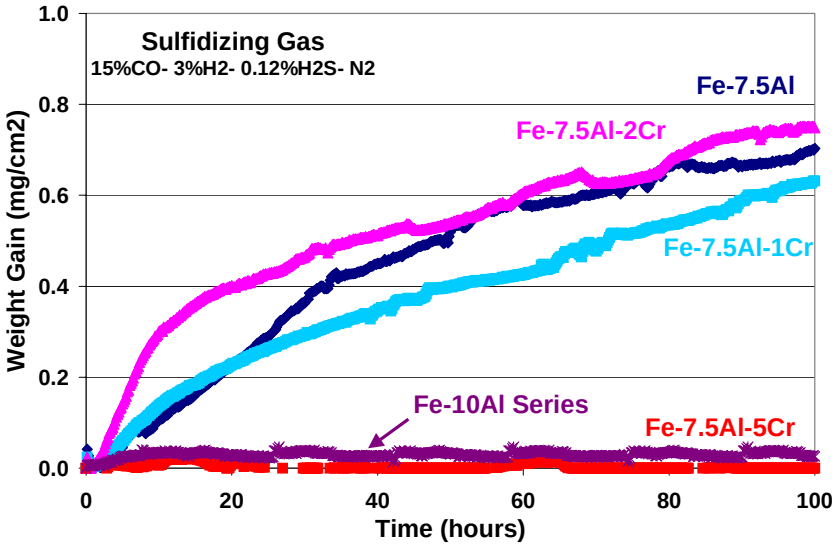

Figure 1 – Kinetic results for the alloys exposed to the sulfidizing gas at 500°C showing that the alloys containing 10%Al and Fe-7.5Al-5Cr demonstrated excellent corrosion resistance.

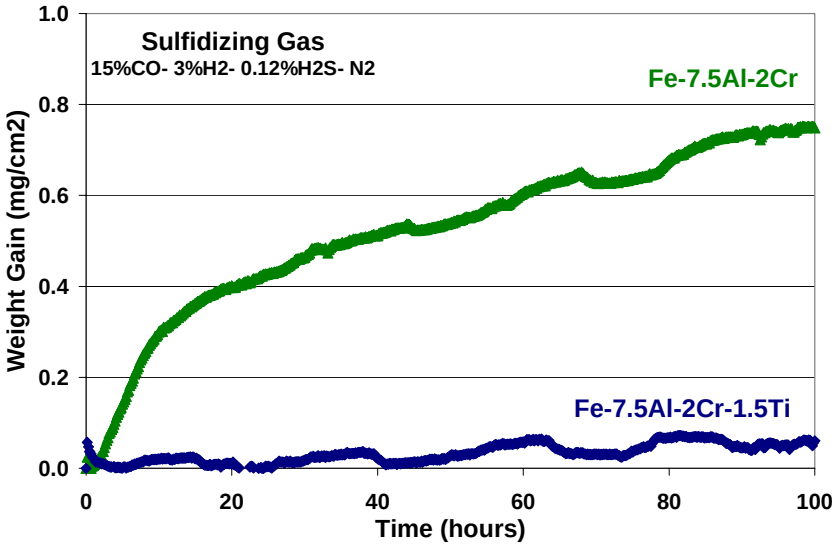

Figure 2 – Kinetic results showing that additions of titanium to Fe-7.5Al-2Cr were beneficial to the corrosion behavior in the sulfidizing environment.

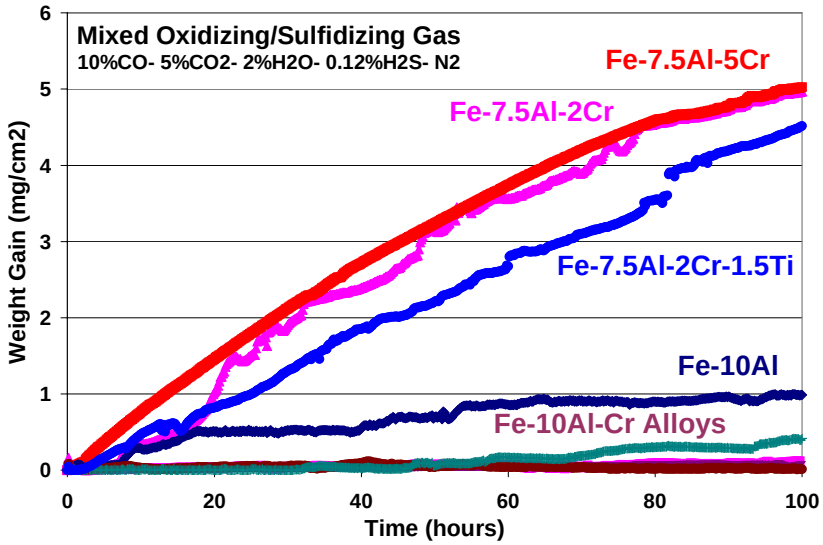

Figure 3 – Kinetic results for alloys exposed to the mixed oxidizing/sulfidizing gas at 500°C where Fe-10Al-Cr alloys includes the ternary and quaternary alloys. Note scale change.

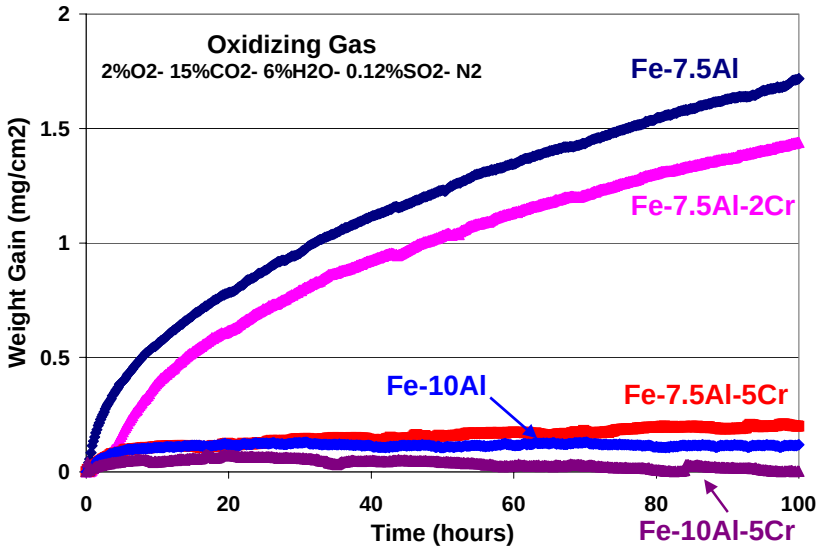

Figure 4 – Kinetic results for select alloys exposed to the oxidizing gas at 500°C showing that the alloys containing 10%Al and Fe-7.5Al-5Cr were protective. Note scale change.

From LOM observations it appeared that the amount of substrate and external corrosion product that formed on the 7.5%Al alloys decreased as the amount of chromium increased (Figure 5b). Unfortunately the external corrosion scale thickness could not be measured accurately because of the interaction with the FeS_2 powder. Because the substrate corrosion scales were uniform, the thickness was easily measured and can be seen in Table III. From these measurements it was determined for alloys containing 7.5%Al, a chromium concentration of 5% provided the best corrosion protection in the mixed oxidizing/sulfidizing environment. Increasing the aluminum concentration to 10% provided even further corrosion protection and alloys remained completely passive during exposure to this simulated gas-slag environment (Figure 5c).

Table III – Substrate corrosion scale thickness for samples exposed to FeS_2 powder and the mixed oxidizing/sulfidizing environment.

Alloy	Thickness (μm)	Standard Deviation
Fe-7.5Al	30.5	2.1
Fe-7.5Al-1Cr	19.7	4.3
Fe-7.5Al-2Cr	26.3	2.8
Fe-7.5Al-2Cr-1.5Ti	28.6	2.2
Fe-7.5Al-5Cr	11.3	1.8

Corrosion behavior of the alloys exposed to FeS_2 and the oxidizing environment was identical to that observed in the mixed gas. Alloys containing 7.5%Al were not protective during 100 hours of exposure to the oxidizing environment and formed both substrate and external corrosion scales (Figure 6). The external corrosion scales that formed on these alloys appeared to be comprised of a dense outer layer above a porous layer, while the substrate corrosion scale was multi-layered and uniformly attacked the alloy. Cracks running perpendicular to the metal-scale interface were observed in several of the exposed alloys. Additions of chromium appeared to improve the corrosion resistance of the Fe-7.5Al alloy, as the extent of corrosion was significantly reduced when 5%Cr was added (Figure 6b). Internal corrosion scale thickness measurements confirmed that 5%Cr significantly reduced the amount of internal corrosion. It was also observed that Fe-7.5Al-5Cr was the only non-protective alloy that did not form perpendicular cracks in the substrate corrosion scale. Alloys containing 10%Al were completely protective during 100 hours of exposure to FeS_2 and the oxidizing environment (Figure 6c). Overall, it was concluded that chromium additions up to 5% could improve the corrosion resistance of alloys containing less than 10%Al, but alloys required 10%Al to provide excellent corrosion protection in the gas-slag environments.

Table IV – Substrate corrosion scale thickness for samples exposed to FeS_2 powder and the oxidizing environment.

Alloy	Thickness (μm)	Standard Deviation
Fe-7.5Al	103.1	12.5
Fe-7.5Al-1Cr	69.2	2.0
Fe-7.5Al-2Cr	91.3	1.6
Fe-7.5Al-2Cr-1.5Ti	88.4	19.3
Fe-7.5Al-5Cr	43.3	2.0

CRACKING BEHAVIOR OF FEALCR WELD OVERLAYS

Single pass GTAW welds were deposited onto plain-carbon steel substrates using commercially available Fe-Cr and Al filler metal wires. The welding parameters were adjusted to produce a wide range of welding compositions and the coatings were tested for cracking. The cracking behavior of the welds as a function of aluminum and chromium concentration can be seen in Figure 7. From this figure it can be

seen that binary Fe-Al welds were deposited crack-free up to approximately 15%Al. When the aluminum concentration was decreased to approximately 10%, chromium additions up to approximately 5%Cr could be incorporated into the weld and remain crack-free. As the aluminum concentrations of the welds were decreased further to approximately 7.5%Al, even more chromium (approximately 11%Cr) could be added to the weld without the formation of cracks.

Cracking within these welds can be extremely detrimental to the corrosion behavior of the weld overlay coating because the cracks can run from the surface of the weld into the underlying base metal. These cracks provide pathways for corrosive gas to come in direct contact with the non-protective underlying metal, rendering the coating completely useless. This can be seen in Figure 8, which shows the cross-section of a typical crack that formed in the weld overlay and extended into the substrate. The weldability results showed that all ternary alloys used in this study were weldable compositions. Therefore, the corrosion behavior of select weldable FeAlCr alloys should be evaluated further and compared to currently used Ni-base superalloys for longer exposure times to determine if these alloys remain good candidates for boiler tube coatings in low NOx environments.

CONCLUSIONS

In the gaseous corrosion-testing portion of the study, several Fe-Al based alloys containing Cr and Ti additions were exposed to three different gaseous corrosion environments. It was found that:

- In order to demonstrate protective corrosion behavior in all three environments, alloys required 10%Al and the best corrosion protection was observed on the alloy containing both 10%Al and 5%Cr.
- Titanium additions seemed to improve the corrosion behavior of the Fe-7.5Al-2Cr alloy when exposed to the sulfidizing environment, but did not seem to make significant improvements of alloys exposed to the other environments.

Gas-slag corrosion tests performed on the same group of Fe-Al alloys while in contact with FeS_2 powder and exposed to the two corrosive environments showed that:

- Improvements to the corrosion behavior of alloys containing 7.5%Al were most significant when 5%Cr was added. Increasing the aluminum concentration to 10% provided protection in these environments, regardless of Cr and Ti content.

FeAlCr welds produced using a GTAW system were evaluated for cracking and it was found that:

- Ternary alloy compositions used in this study were weldable compositions and would potentially make good coating candidates for boiler tubes found in low NOx furnace environments.

REFERENCES

1. P.F.Tortorelli and K.Natesan *Mater.Sci.Eng., A* **A258** (1998) 115-125..
2. S.W.Banovic, J.N.DuPont, and A.R.Marder *Scr.Mater.* **38** (1998) 1763-1767.
3. J.H.DeVan and P.F.Tortorelli *Corros.Sci.* **35** (1993) 1065-1071.
4. S.W.Banovic, J.N.DuPont, P.F.Tortorelli, and A.R.Marder *Weld.Res.(Miami)* **78** (1999) 23S-30S.
5. P.F.Tortorelli, G.M.Goodwin, M.Howell, and J.H.DeVan In: Proc. Int. Conf. *Heat-Resistant Materials II*, 1995, (Ed. K.Natesan, G.Krishnamurti, G.Y.Lai) p 585-590.

ACKNOWLEDGMENTS

This research was sponsored by the Fossil Energy Advanced Research and Technology Development (AR&TD) Materials Program, U.S. Department of Energy, under contract DE-AC05-96OR22464 with U.T. Battelle. The authors would like to thank V.K. Sikka, P.F. Tortorelli, and B.A. Pint from ORNL for the cast alloys used in corrosion testing and American Minerals for supplying the FeS_2 powder.

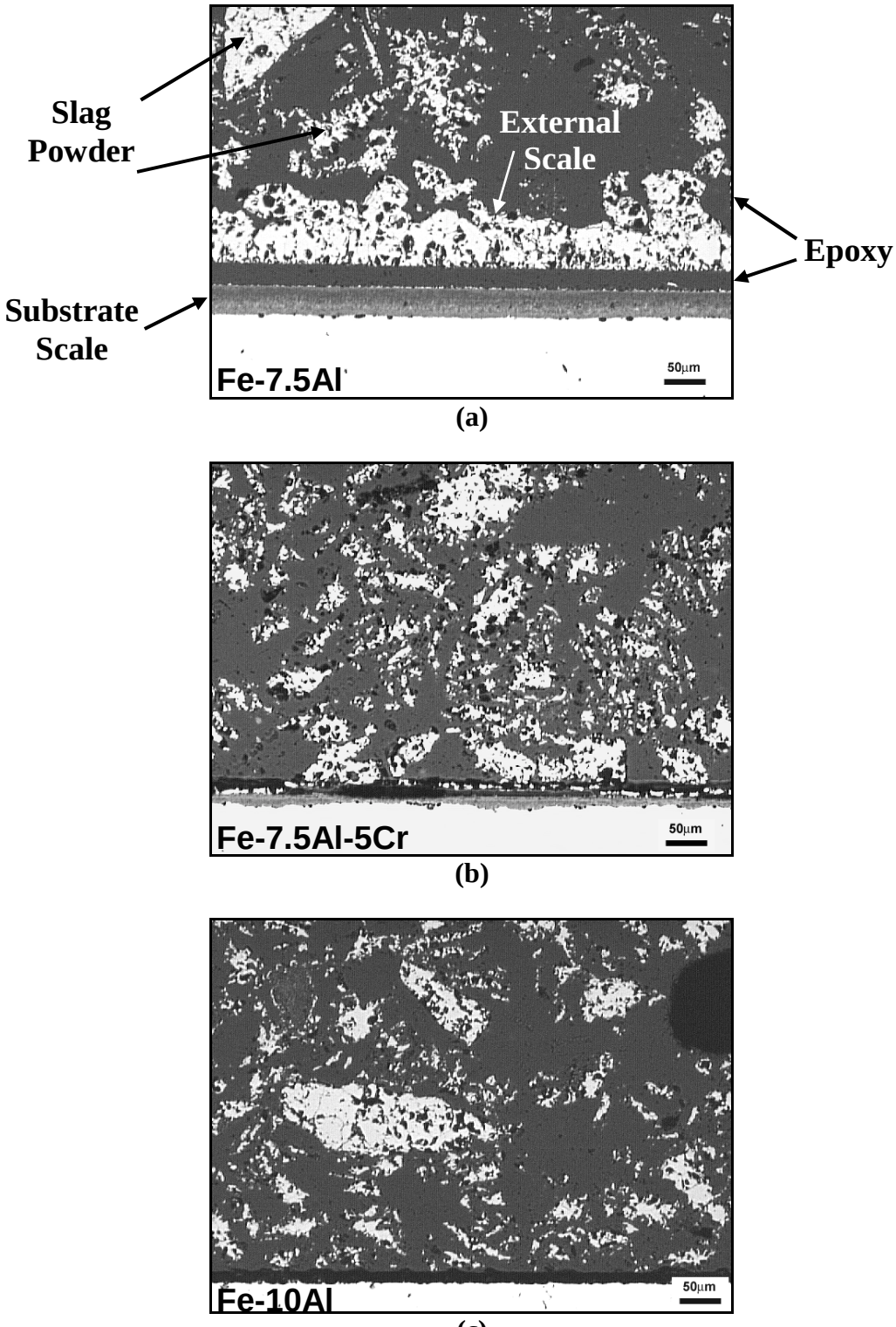

Figure 5 – Typical corrosion scale microstructures for alloys exposed to FeS_2 and the mixed oxidizing/sulfidizing environment, showing non-protective alloys containing 7.5%Al (a), improvements in corrosion behavior observed when chromium was added (b) and when the aluminum concentration was increased to 10%Al (c).

(a)

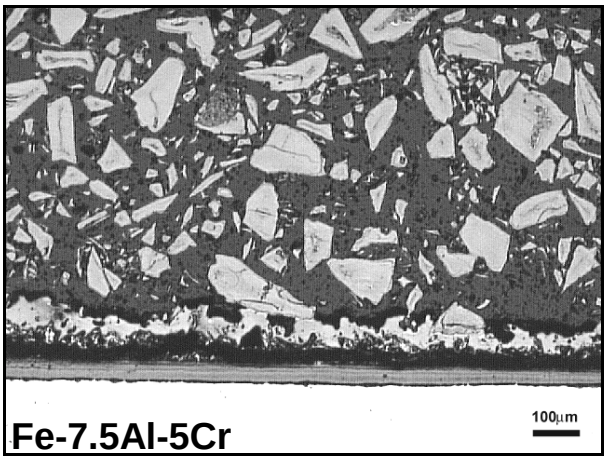

(b)

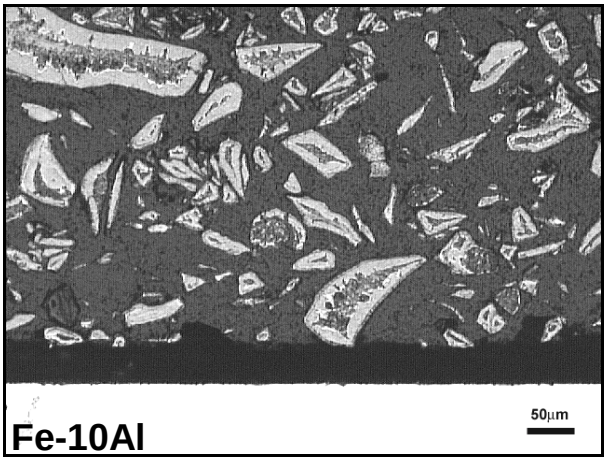

(c)

Figure 6 – Typical corrosion scale microstructure observed alloys exposed to FeS_2 and the oxidizing environment, showing non-protective samples containing 7.5%Al (a), improvements in corrosion behavior observed when chromium was added (b) and when the aluminum concentration was increased to 10%Al (c).

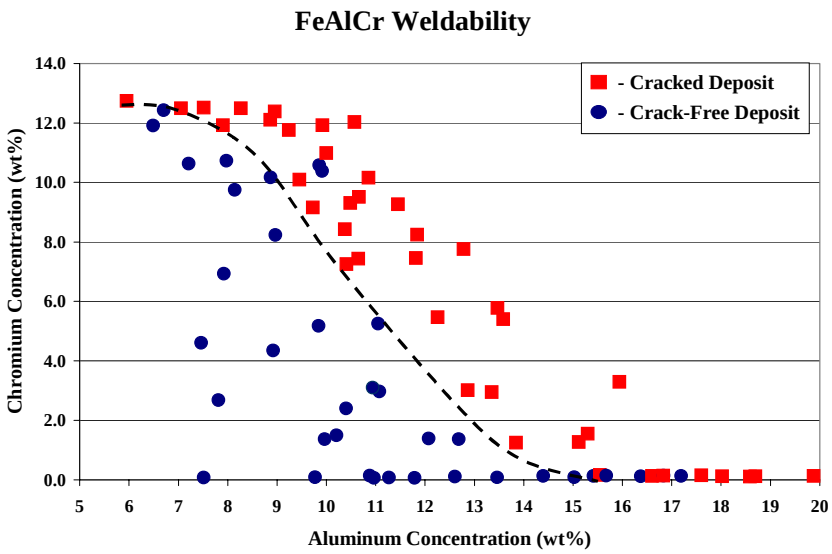

Figure 7 – Cracking behavior of FeAlCr weld overlay coatings as a function of aluminum and chromium concentrations.

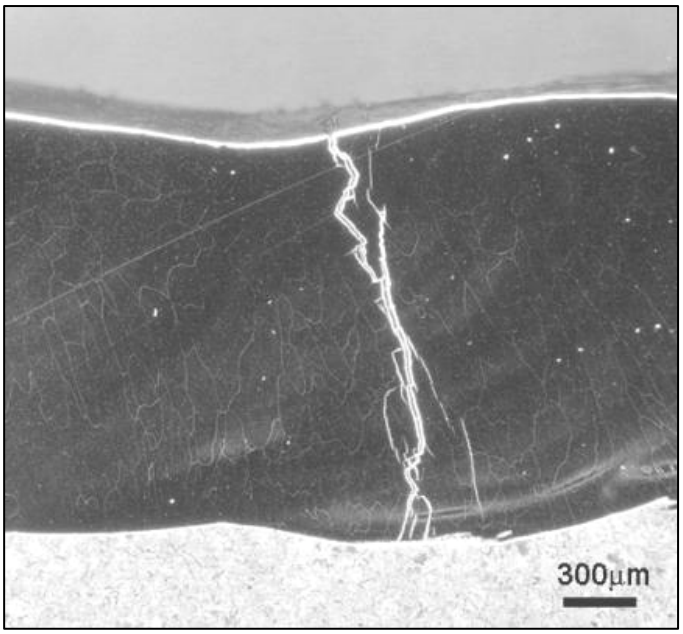

Figure 8 – Typical crack found in FeAlCr weld overlay claddings that were susceptible to hydrogen cracking. Note that the crack extends through the entire weld coating.

COATING MICROSTRUCTURE-PROPERTY-PERFORMANCE ISSUES

Terry C. Totemeier
Idaho National Engineering and Environmental Laboratory
P.O. Box 1625, MS 2218, Idaho Falls, ID 83415
Email: totetc@inel.gov; Telephone: 208-526-3074; Fax: 208-526-4822

Richard N. Wright
Idaho National Engineering and Environmental Laboratory
P.O. Box 1625, MS 2218, Idaho Falls, ID 83415
Email: rnw2@inel.gov; Telephone: 208-526-6127; Fax: 208-526-4822

ABSTRACT

Results of studies on the relationships between spray parameters, residual stress, microstructure, and performance of thermally-sprayed coatings for high-temperature oxidation and corrosion resistance are presented. Efforts have been focused on two areas: measurement and modeling of residual stresses in metallic and intermetallic coatings prepared by the high-velocity oxy-fuel (HVOF) spray process and measurement of the performance characteristics of these coatings.

The variation of residual stresses with spray parameters (primarily spray particle velocity), coating thickness, and substrate type was determined by x-ray diffraction analysis of sprayed coatings. The x-ray results were compared to the predictions of various models of increasing complexity which relate curvature of coating-substrate couples to residual stress. These included a simple two-beam model, an elastic, analytical model of progressive coating deposition, and a finite-element-based, elastic-perfectly plastic model of progressive coating deposition. While the two-beam model did not accurately characterize with variation of residual stress with coating thickness and therefore showed poor agreement with the x-ray data, both progressive models predicted residual coating stresses which were in good agreement with x-ray results.

Initial coating performance characteristics measured included coating adhesion using the ASTM C633 test standard and resistance to cracking under thermal cycling conditions. FeAl coatings prepared using the HVOF spray process and Mo-Si-B coatings prepared by plasma spraying in air were studied. Coating adhesion was observed to depend both on spray particle velocity and substrate material. Initial results indicate that resistance to cracking in thermal cycling is primarily related to coefficient of thermal expansion (CTE) mismatch between the coating and the substrate.

INTRODUCTION

Recent research at the Idaho National Engineering and Environmental Laboratory (INEEL) in the fossil energy advanced materials program has focused on characterization of thermal spray coatings for high-temperature environmental resistance. These coatings have mainly been formed via high-velocity oxy-fuel (HVOF) thermal spray, although some coatings have been formed by air plasma spray (APS). Coating materials studied to date include the Fe_3Al and FeAl iron aluminides, 316 stainless steel, and Mo-Si-B intermetallics. The characterization has specifically focused on determining the effects of coating process variables (primarily spray particle velocity) on coating characteristics such as microstructural features (porosity, oxide, unmelted particles), mechanical and physical properties (microhardness, elastic modulus, coefficient of thermal expansion), and residual stress. The findings of these studies have been presented in several publications;[1-4] the general trend observed is one of improved coating microstructures and higher compressive residual stresses with increasing spray particle velocity, a dependence which is attributed to an increased peening effect.

The aim of current research is to determine the links between these coating characteristics and the coating performance in service conditions typical of power-plant use. Coating performance is broken down into two aspects, both critically important–environmental resistance and durability. Clearly, a coating intended for environmental resistance must possess intrinsic stability in the service environment of interest, but it is also required to demonstrate that thermal spray coatings of a particular material (e.g., FeAl) show oxidation resistance comparable to that of the bulk, wrought form. Durability is an additional requirement–an impervious coating is only useful when sound (i.e., crack-free) and attached to the substrate.

Residual stresses have been shown to play an important role in the cracking, adhesion, and spallation behavior of coatings.[5-9] Residual stresses in thermally-sprayed coatings can be considered as the sum of three components: a tensile quench stress arising from the solidification and rapid cooling of individual spray particles upon impact with the much cooler substrate; a compressive peening stress imparted by impact of high-velocity spray particles, and a thermal mismatch stress incurred during cooling of the coating-substrate couple from the deposition temperature.

Several different techniques have been used for measurement of residual stress, all with intrinsic advantages and disadvantages; comprehensive reviews are given in Refs. [10] and [11]. These techniques can be divided into three categories: measurement of crystallographic lattice parameters using X-ray or neutron diffraction;[12-16] methods which relate the curvature of as-sprayed coating-substrate couples to stress in the coating and substrate;[1, 2, 17-20] and techniques which monitor changes in substrate strain upon layer-by-layer removal of the coating.[21] Lattice parameter methods directly measure coating strain (which can be related to stress), but require knowledge of coating physical constants and expensive instrumentation. Curvature-based methods are simple, but rely on analytical or numerical models (with necessary assumptions) to calculate coating and substrate stresses. Material removal methods permit determination of the residual stress variation through the thickness of the coating and substrate, but involve relatively time-consuming sample preparation and again rely on models to relate measured substrate strains to coating stresses.

The effects of HVOF spray parameters on residual stresses in Fe_3Al and FeAl intermetallic coatings have been reported[1, 2, 22] There were difficulties, however, in relating curvature measurements of coating-substrate couples to actual coating stresses on thick, non-bending substrates. The aim of the work presented in this paper is to further assess and compare two techniques for residual stress measurement in HVOF coatings with the aim of determining a simple and (relatively) accurate procedure for characterizing residual stresses in thermal spray coatings. This was performed by making XRD-based residual stress measurements on the same specimens on which curvature measurements were obtained. The measured curvatures were used to calculate residual stresses using three different models: a simple, elastic, two-beam bending model; the elastic progressive deposition model developed by Tsui and Clyne;[23] and an elastic-plastic extension of the progressive model.

In addition to the residual stress results, this paper also presents initial results of the coating performance testing, specifically coating adhesion and thermal cycling resistance results.

EXPERIMENTAL TECHNIQUES

RESIDUAL STRESS MEASUREMENT AND CALCULATION

Residual stresses were measured on Fe_3Al and 316 SS HVOF coatings applied to thick (6.4 mm) and thin (1.4 mm) low-carbon and stainless steel substrates. Coatings were applied at spray particle velocities varying from 520 to 640 m/s; coating thicknesses varied from 250 to 1500 μm. Coating residual stresses were measured using standard d versus $\sin^2\psi$ XRD techniques, as described in Ref. [24]. Measurements were made on a Bruker AXS diffractometer (Madison, WI) with Cr K_α radiation. For 316 SS coatings, the (220) peak at $2\theta = 129°$ was measured; for Fe_3Al coatings the (211) peak at $2\theta = 150°$ was measured. The Bruker-supplied STRESS application was used to calculate residual stresses from peak positions. Young's moduli for 316 SS and Fe_3Al were taken as 200[25] and 140 GPa,[2] respectively. Crystallographic anisotropy factors (ARX) for 316 SS and Fe_3Al were taken as 1.72 and 1.49, respectively.[26]

Stresses were generally measured on coating surfaces from which 75 to 100 μm had been removed by grinding with 600 grit paper and polishing to a 1 μm finish. Surface removal was performed in order to provide a flat X-ray measurement surface and avoid the effects of surface roughness on the measured stresses. The potential effect of the grinding and polishing procedure on residual stress was assessed by measuring stresses on annealed 316 SS specimens before and after surface removal—in both cases no residual stresses were observed.

The curvatures of coating-thin substrate couples were measured using an optical comparator. These curvatures were used to directly calculate coating and substrate residual stresses using the two-beam model as described in Refs.[10] and [1] . The Stoney approximation to the simple two-beam model was also calculated for comparison. This assumes the coating is very thin relative to the substrate. See Ref [10] for details. Residual stresses were calculated with the progressive deposition model of Tsui and Clyne[23] by iteratively adjusting the "deposition stress" input to the model until the model-calculated curvature matched the measured curvature of the coating-substrate couple being analyzed. At this point the model output also gave the near-surface coating residual stress. A finite element (FEM) numerical analysis was used to extend the elastic progressive model to include the effects of substrate plasticity. The analysis was performed using the ABACUS software package; full details will be presented in a forthcoming publication.

COATING PERFORMANCE TESTING

Coating adhesion testing was performed to the ASTM C633 test standard. FeAl and Mo-Si-B (Mo - 13.4 wt% Si – 2.6 wt% B, obtained from Ames Laboratory) coatings were sprayed onto cylindrical low-carbon and stainless steel substrates. The substrates were sized to fit the test standard, approximately 25 mm in height and diameter; threaded on the back side for pull rod attachment. FeAl coatings were prepared using HVOF spraying at varied spray particle velocity; Mo-Si-B coatings were prepared by APS spraying at a single particle velocity. The coating thickness in all cases was approximately 500 μm.

The thermal cycling resistance of several coating-substrate combinations was assessed by subjecting coated substrates to a multiple thermal cycles consisting of heating to 800°C, holding at temperature for one hour, and slow furnace cooling. The coating materials tested were 316 SS, Fe_3Al, FeAl, and Mo-Si-B. Varied spray particle velocities were considered, and both low-carbon and stainless steel substrates were used. As with the adhesion test coupons, the coatings were approximately 500 μm thick and the substrates were cylindrical and approximately 25 mm in height and diameter. Coatings were applied to a flat surface. Post-test metallographic examination of cross-sections was performed to reveal coating cracking. Specimens were examined that had received 1, 15, and 30 cycles.

RESULTS AND DISCUSSION

RESIDUAL STRESS

Figure 1 shows a comparison of the through-thickness residual stress predictions for the three different curvature models. This example is for an Fe_3Al coating sprayed at a relatively high particle velocity of 620 m/s. Two cases are shown: a thin coating (left) and a thick coating (right). All models agree fairly well for the thin coating; the coating residual stress is approximately 300 MPa compressive and the substrate stresses vary from compressive at the outer surface to tensile at the coating-substrate interface. In constrast, the models predict significantly different variations of coating residual stress for the thick coating. The two-beam model predicts a strong variation of stress through the coating, from highly compressive at the coating-substrate interface to highly tensile at the coating surface. Both progressive models predict coating stresses that are slightly tensile at the interface and compressive at the surface. The Stoney approximation stress is constant through the coating thickness (this is implicit in the approximation), at a magnitude of approximately 200 MPa compressive.

The difference between the elastic and elastic-plastic progressive models is evident in the substrate stress. While stress levels in the elastic model reach magnitudes as high as nearly 1000 MPa, these stresses are limited to 300 MPa in the elastic-plastic model. Surprisingly, the difference in coating residual stress predicted by the two progressive models is minimal, despite the large difference in substrate stresses.

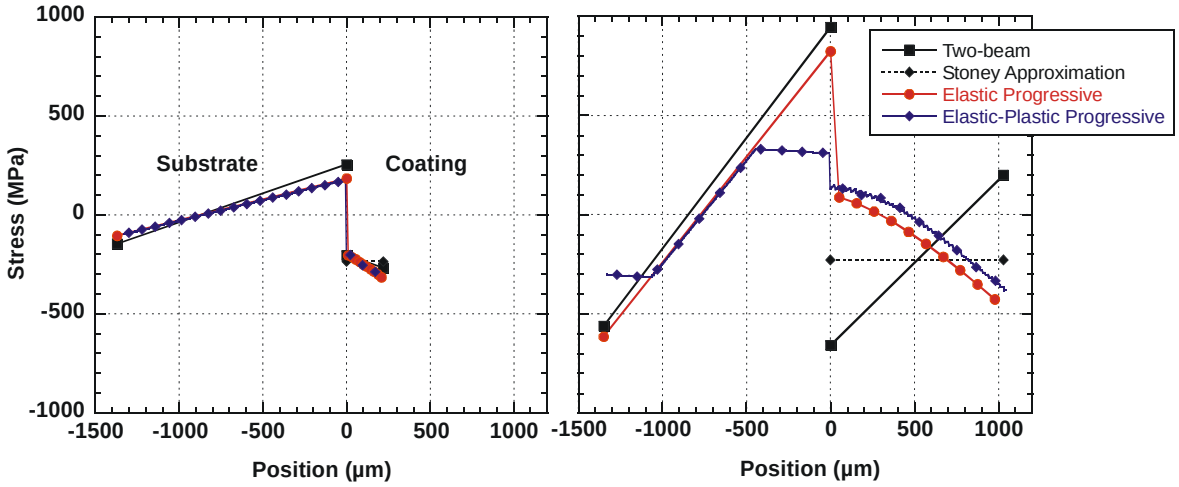

Figure 1: Comparison of curvature-residual stress models for a Fe_3Al coating sprayed at 620 m/s.

Figure 2 compares the coating near-surface stresses (stresses evaluated after 100 μm removed to provide the best comparison with XRD-measured stresses) predicted by the Stoney approximation, the two progressive models, and measured by XRD analysis. These stresses are plotted for two spray particle velocities as a function of coating thickness. Each data point represents stresses predicted or measured on a unique coating-substrate couple. Note that the two-beam model predictions are not shown; this model predicts near-surface stresses which vary with coating thickness from compressive for thin coatings to very tensile for thick coatings, clearly at odds with the measured stresses. The two-beam model does not sufficiently capture the physical reality of coating residual stress development. The Stoney approximation is listed, however, as a simplification over the progressive model which has the potential to sufficiently capture the nature of coating stresses.

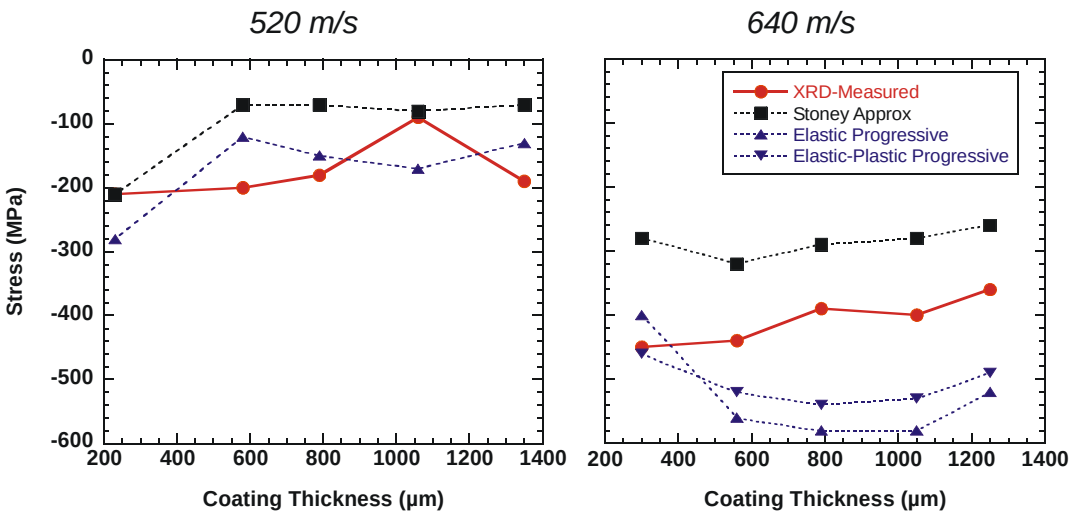

Figure 2: Comparison of model-predicted residual stresses with XRD-measured stresses for 316 SS coatings sprayed at 520 m/s and 640 m/s.

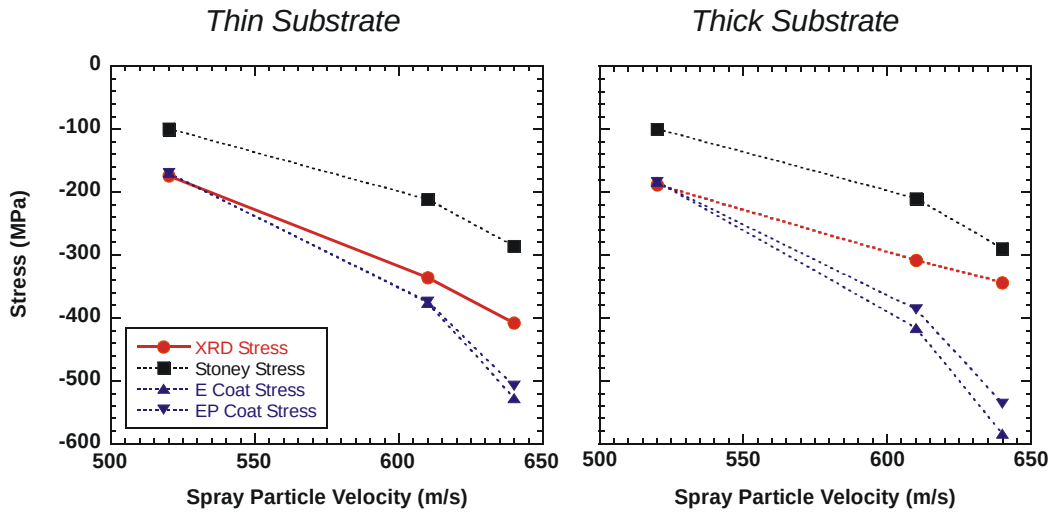

Figure 3: Comparison of mean model-predicted coating residual stresses with XRD-measured stresses as a function of spray particle velocity for 316 SS coatings sprayed onto thin and thick 316 SS substrates.

Reasonably good agreement exists between the various models and the XRD measurement for the coatings sprayed at low particle velocity (Figure 2, left). The stresses in this case are relatively low in magnitude and do not vary significantly with coating thickness. A greater divergence between model predictions and the XRD measurements is observed for coatings sprayed at the high particle velocity (Figure 2, right), which have higher compressive stresses. The XRD-measured stresses are more compressive than the Stoney approximation stress but less compressive than the predictions of both progressive models. In all cases the measured or predicted coating residual stresses again do not significantly vary with coating thickness. The similarity of predictions of the elastic and elastic-plastic progressive models noted in Figure 1 above is also observed in Figure 2. Note that the elastic-plastic prediction for the lower velocity coatings is identical to the elastic prediction (no plasticity), so it is not shown in this case.

Given that the coating near-surface stresses do not vary significantly with thickness, the model-predicted and XRD-measured residual stresses may be summarized as in Figure 3, which shows the predicted and measured coating near-surface stresses as a function of spray particle velocity for 316 SS coatings applied to thin and thick substrates. In the case of the thick substrates, the Stoney approximation stress was assumed to be the same as determined from

the coating-thin substrate curvature couples; for the progressive models the deposition stress derived from the curvature of coating-thin substrate couples was used to predict coating near-surface stresses on thick substrates.

In both the thin and thick substrate cases good agreement is observed between the progressive models and the XRD measurement at low particle velocity. The progressive model predictions increasingly deviate from the XRD measurement with increasing particle velocity; model predictions are much more compressive than XRD measurements at the highest velocity. The Stoney approximation stresses, however, are consistently less compressive than the measured stresses. It is unclear at the moment what contributes to the difference between the measured and predicted stresses, but there are reasons to suspect both the XRD measurement procedure for thicker coatings and the ability of the progressive model to accurately model highly curved coating-substrate couples.

Based on the above observations, we believe that the "best" residual stress assessment technique for thermal spray coatings is to use the elastic progressive model to determine deposition stresses on curvature couples in which the coating is thin relative to the substrate (i.e. less than 500 μm on a 1500 μm substrate). This deposition stress may then be used with the elastic progressive model to predict coating stresses in other configurations, for example different substrates, different coating or substrate thicknesses, etc. There appears to be little benefit in using the considerably more complex elastic-plastic progressive model. The term "best" in this case means a technique which reasonably accurately represents the actual stresses and is simple to implement.

COATING PERFORMANCE

Coating Adhesion

Figure 4 shows coating adhesion results obtained to date. In the case of FeAl, the adhesive strength on stainless steel substrates slightly increases with increasing spray particle velocity, while the opposite trend is apparent for FeAl coatings applied to low-carbon steel substrates. In all cases the coatings fail by debonding at the coating-substrate interface. The increasing adhesive strength of FeAl coatings on stainless steel with increasing velocity is believed to result from increased mechanical bonding to the substrate by the higher-velocity particles, while the decreasing strength on low-carbon steel is believed to result from increasing substrate oxidation caused by the HVOF torch. The size of the HVOF flame markedly increases at the higher torch chamber pressures required to accelerate spray particles to higher velocities. Substrate oxidation decreases the coating adhesion, a fact supported by the adhesion measured for an FeAl coating on low-carbon steel after 90 day exposure to ambient environmental conditions. The adhesive strength decreased from over 60 MPa to 10 MPa, likely due to oxidation at the exposed coating-substrate interface.

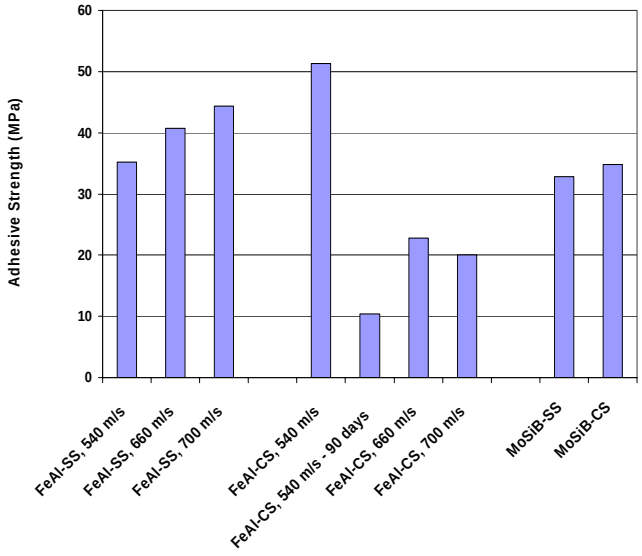

Figure 4: Coating adhesion strength results.

The adhesive strength of APS-sprayed Mo-Si-B coatings was approximately the same on both stainless and low-carbon steel substrates. Substrate oxidation is believed to play less of a role in this case because the size of the plasma plume is considerably reduced relative to the HVOF torch.

Thermal Cycling Resistance

Table 1 lists the results of the thermal cycling trials. FeAl coatings sprayed at the two higher velocities consistently cracked and de-bonded from the stainless steel substrate, while the coating sprayed at the lower velocity was unaffected by the cycling. This lower-velocity coating had porosity (~5%) which resulted in a lower elastic modulus (120 GPa compared to 150 GPa for higher-velocity coatings without porosity) [22]. Stainless steel and Fe_3Al coatings sprayed on stainless steel substrates at all particle velocities showed no cracking after thermal cycling, but the Mo-Si-B coating sprayed using APS cracked and debonded from the stainless steel substrate. All coatings sprayed onto low-carbon steel substrates debonded due to heavy substrate oxidation resulting from the repeated heating to 800°C in air.

Table 1: Results of coating thermal cycle tests.

Coating	Velocity (m/s)	Cycles		
		1	15	30
FeAl	540	-	-	✓
	660	-	-	X
	700		X	X
316 SS	520	✓	-	✓
	640	✓	-	✓
Fe_3Al	520	✓	-	✓
	620	✓	-	✓
Mo-Si-B	350 (APS)	-	-	X

- = not tested; X = cracking or debonding; ✓ = no cracking or debonding

The source of the different behavior of the FeAl, Fe_3Al, and stainless steel coatings is believed to be the coefficient of thermal expansion. There is no coating-substrate thermal expansion mismatch for the stainless steel coatings (confirmed by coating CTE measurements), and the Fe_3Al coating has a mean CTE from room temperature to 800°C of approximately 18-19 ppm/°C, very similar to the 316 SS CTE of 19 ppm/°C. In contrast, the CTE of the FeAl coating over the same temperature range is 23-24 ppm/°C. The CTE mismatch for the Mo-Si-B coating on SS is even greater—the CTE of the coating in this case is approximately 8.5 ppm/°C. Lack of debonding or cracking in the case of the low-velocity FeAl coating is attributed to the greater coating compliance (lower modulus) resulting from porosity. The compliance reduces stress build-up in cycling.

CONCLUSIONS

The investigation of residual stress measurement techniques for HVOF thermal spray coatings has shown that models more complex than the simple, elastic two-beam bending model are needed to accurately predict the through-thickness residual stress variation in coatings. The progressive deposition model was shown to be effective in this regard for thinner coatings at lower residual stresses. The difference in predicted coating residual stress between the elastic and elastic-plastic versions of the progressive model was insignificant.

The results of initial coating performance tests were presented; increasing spray particle velocity was observed to increase the adhesion of FeAl coatings sprayed onto stainless steel substrates but decrease adhesion of coatings sprayed onto low-carbon steel substrates. Initial thermal cycling results indicate that CTE mismatch is a strong factor influencing coating cracking and adhesion in thermal cycle conditions.

ACKNOWLEDGEMENTS

The authors would like to acknowledge the assistance of W.D. Swank and D.C. Haggard with thermal spraying, J.A. Simpson with coating performance testing, J.K. Wright with FEM analysis, and T.C. Morris with metallography. This work was supported by the Department of Energy, Office of Fossil Energy, under DOE Idaho Operations Office Contract No. DE-AC07-99ID13727.

REFERENCES

1. T.C. Totemeier, R.N. Wright, and W.D. Swank: *Journal of Thermal Spray Technology*, 2002, vol. 11, pp. 400-08.
2. T.C. Totemeier, R.N. Wright, and W.D. Swank: *Metallurgical and Materials Transactions A*, 2003, vol. 34A, pp. 2223-31.
3. T.C. Totemeier, R.N. Wright, and W.D. Swank: in *17th Annual Conference on Fossil Energy Materials*, National Energy Technology Laboratory, Pittsburgh, PA, 2003, pp. available at www.netl.doe.gov.
4. T.C. Totemeier, R.N. Wright, and W.D. Swank: *Metallurgical and Materials Transactions A*, 2004, vol. 35A, pp. 1807-14.
5. L. Pejryd, J. Wigren, D.J. Greving, J.R. Shadley, and E.F. Rybicki: *Journal of Thermal Spray Technology*, 1995, vol. 4, pp. 268-74.
6. R.T.R. McGrann, D.J. Greving, J.R. Shadley, E.F. Rybicki, T.L. Kruecke, and B.E. Bodger: *Surface and Coatings Technology*, 1998, vol. 108-109, pp. 59-64.
7. S.J. Howard, Y.C. Tsui, and T.W. Clyne: in *1994 Thermal Spray Industrial Applications*, C.C. Berndt and S. Sampath, Editors, ASM International, Materials Park, OH, 1994, pp. 703-08.
8. S. Kuroda, T. Fukushima, and S. Kitahara: in *Thermal Spray: International Advances in Coatings Technology*, C.C. Berndt, Editor, ASM International, Materials Park, OH, 1992, pp. 903-09.
9. D.J. Greving, J.R. Shadley, and E.F. Rybicki: *Journal of Thermal Spray Technology*, 1994, vol. 3, pp. 371-78.
10. T.W. Clyne and S.C. Gill: *Journal of Thermal Spray Technology*, 1996, vol. 5, pp. 401-18.
11. S. Kuroda: in *Thermal Spray: Meeting the Challenges of the 21st Century*, C. Coddet, Editor, ASM International, Materials Park, OH, 1998, pp. 539-50.
12. O. Kesler, J. Matejicek, S. Sampath, S. Suresh, T. Gnaeupel-Herold, P.C. Brand, and H.J. Prask: *Materials Science and Engineering A*, 1998, vol. A257, pp. 215-24.
13. I. Iordanova and K.S. Forcey: *Surface and Coatings Technology*, 1997, vol. 91, pp. 174-82.
14. J. Matejicek, S. Sampath, P.C. Brand, and H.J. Prask: in *Thermal Spray: A United Forum for Scientific and Technological Advances*, C.C. Berndt, Editor, ASM International, Materials Park, OH, 1997, pp. 861-66.
15. J. Matejicek, S. Sampath, and J. Dubsky: *Journal of Thermal Spray Technology*, 1998, vol. 7, pp. 489-96.
16. S. Kuroda, Y. Tashiro, H. Yumoto, S. Taira, H. Fukanuma, and S. Tobe: *Journal of Thermal Spray Technology*, 2001, vol. 10, pp. 367-74.
17. R. Knight and R.W. Smith: in *Thermal Spray Coatings: Research, Design, and Applications*, C.C. Berndt and T.F. Bernecki, Editors, ASM International, Materials Park, OH, 1993, pp. 607-12.
18. S.C. Gill and T.W. Clyne: *Thin Solid Films*, 1994, vol. 250, pp. 172-80.
19. W.D. Swank, R.A. Gavalya, J.K. Wright, and R.N. Wright: in *Thermal Spray: Surface Engineering Via Applied Research*, C.C. Berndt, Editor, ASM International, Materials Park, OH, 2000, pp. 363-69.
20. O. Kesler, M. Finot, S. Suresh, and S. Sampath: *Acta Materialia*, 1997, vol. 45, pp. 3123-34.
21. D.J. Greving, E.F. Rybicki, and J.R. Shadley: *Journal of Thermal Spray Technology*, 1994, vol. 3, pp. 379-88.
22. T.C. Totemeier, R.N. Wright, and W.D. Swank: *Intermetallics*, 2004, in press.
23. Y.C. Tsui and T.W. Clyne: *Thin Solid Films*, 1997, vol. 306, pp. 23-33.
24. I.C. Noyan and J.B. Cohen: *Residual Stress - Measurement by Diffraction and Interpretation*, Springer-Verlag, New York, 1987.
25. S.H. Crandall, N.C. Dahl, and T.J. Lardner: *An Introduction to the Mechanics of Solids*, 2nd ed., McGraw-Hill, New York, 1978.
26. *Stress User's Manual*, Bruker AXS GmbH, Karlsruhe, Germany, 1999.

HIGH TEMPERATURE OXIDATION PERFORMANCE OF ALUMINIDE COATINGS

Bruce A. Pint
Oak Ridge National Laboratory, P.O. Box 2008, Oak Ridge, TN 37831-6156
E-mail: pintba@ornl.gov; Telephone: (865) 576-2897; Fax: (865) 241-0215

Ying Zhang
Dept. of Mech. Eng., Tennessee Tech. Univ., P.O.Box 5014, Cookeville, TN 38505-0001
E-mail: yzhang@tntech.edu; Telephone: (931) 372-3265; Fax: (931) 372-6340

J. Allen Haynes
Oak Ridge National Laboratory, P.O. Box 2008, Oak Ridge, TN 37831-6063
E-mail: haynesa@ornl.gov; Telephone: (865) 576-2894; Fax: (865) 574-6918

Ian G. Wright
Oak Ridge National Laboratory, P.O. Box 2008, Oak Ridge, TN 37831-6156
E-mail: wrightig@ornl.gov; Telephone: (865) 574-4451; Fax: (865) 241-0215

ABSTRACT

The performance of iron aluminide coatings is being studied in the laboratory using high purity, well-controlled coatings made by chemical vapor deposition (CVD). Coatings are being tested on representative ferritic (Fe-9Cr-1Mo) and austenitic (type 304L stainless steel) substrates. Previous work showed that with a high thermal cycling test frequency (1h cycle at 700°C), coating degradation occurred in less than 2000 cycles in air + 10% water vapor due to the thermal expansion mismatch between coating and substrate. By increasing the test cycle frequency to 100h, the coatings have remained protective for over 6,000h at 700°C. The effect of coating thickness on this relationship, as well as the role of substrate impurities on coating performance, is being investigated. Further work is being conducted with model alloys to determine the minimum Al content needed to maintain a protective alumina scale under these conditions.

INTRODUCTION

Coatings are required in many high temperature applications to protect high strength or low cost structural alloys that do not have sufficient inherent oxidation resistance. Aluminide (Fe_3Al or FeAl) coatings are of interest for many environments, because of the formation of a highly stable, external alumina scale.[1-6] For Fe-base alloys, aluminide coatings can be protective in sulfidizing environments.[2,5,6] Environments containing water vapor (steam, exhaust gas) also are of particular interest because of the accelerated attack observed on Fe-base alloys[7-12] associated with volatile chromium hydroxide formation. Alumina is more stable in such environments[13] and alumina-forming coatings provide excellent protection.[5,14,15] Recent long-term results on representative CVD aluminide coated ferritic (Fe-9Cr-1Mo) and austenitic (type 304L stainless steel) substrates in humid air showed coating failure and substrate attack after 2,000h at 700°C when the specimens were cycled every hour.[14,15] Very little Al was lost to the substrates, due to interdiffusion after this exposure. The coating failure was attributed to thermal fatigue cracking due to the difference in coefficient of thermal expansion (CTE) between the substrate and coating.[5] The current work is continuing to examine this type of failure, by examining the performance of (1) thinner coatings under the same conditions, where less strain would be expected in the coating layer, (2) similar coatings in 100h cycles (i.e. fewer thermal cycles), and (3) similar coatings on impurity controlled substrates. In addition to the oxidation experiments, 10,000h diffusion experiments are being conducted to assist in the development of a coating lifetime model.[16] An additional issue for the model is the critical Al content of

the coating needed for protection in humid environments. This issue is being addressed by testing model alloys and by accelerated testing of coatings at 800°C.

EXPERIMENTAL PROCEDURE

The substrates used in this study were commercial Fe-9Cr-1Mo, commercial type 304L stainless steel (Fe-18Cr-9Ni nominally) and laboratory castings of 304L with controlled impurity contents. The laboratory-scale CVD reactor and coating process for low-activity (thin coatings) and high-activity (thick coatings) have been described elsewhere.[5,15,17] Coatings made by CVD have been used in this work in order to have a well-controlled, high purity coating for long-term testing. It is anticipated that similar aluminide coatings could be made by a higher-volume, commercial process, such as pack cementation. Characterization of the as-deposited coatings has been described elsewhere.[16-19]

The oxidation testing focuses on 700°C, where the substrate alloys are adversely affected by environmental effects, but some strength is retained. Some tests were conducted at 800°C in order to accelerate interdiffusion with the substrate. Cyclic oxidation testing in air with 10±0.5vol.%H_2O was conducted two ways: (1) in a vertical, automated test rig with the specimens suspended from alumina rods using Pt-Rh wire and a cycle consisting of 1h at temperature and 10min cooling at room temperature, or (2) in a horizontal tube furnace with the specimens in an alumina boat, the cycle consisting of 100h at temperature with the specimens cooled and weighed after each cycle. In each case, both ends of the high-purity alumina reaction tube were closed and the addition of water vapor was controlled in the carrier gas by a water injection system described elsewhere.[11] Humid air produces similar reaction products as steam environments.[9,12]

Before and after exposures, specimens were weighed on a Toledo-Mettler model AG245 balance. Selected specimens were examined by light microscopy, field emission gun, scanning electron microscopy (SEM) equipped with energy dispersive x-ray analysis (EDXA) and electron probe microanalysis (EPMA) using wavelength dispersive x-ray analysis. For cross-sections, the surface reaction product was protected by Cu-plating the specimen prior to mounting in epoxy.

RESULTS AND DISCUSSION

EFFECT OF COATING THICKNESS ON PERFORMANCE IN 1h CYCLES AT 700°C

Previous experimental results suggested a role of the coating-substrate thermal expansion mismatch. Additional experiments are being conducted to explore the role of CTE mismatch on coating performance. If the CTE difference leads to coating failure, then coating thickness could play a role. The stress on cooling is proportional to the CTE difference and is independent of coating thickness. However, the strain generated on cooling should increase with coating thickness. Previous work on thin CVD aluminide coatings, with a ≈5μm Al-rich outer layer, did not show significant degradation after 1,000, 1h cycles at 700°C in air + 10vol.%H_2O.[19] Without a coating, 304L and Fe-9Cr-1Mo were severely attacked after short exposures in this environment, Figure 1. After 1,000 cycles, the coated specimens were sectioned for metallographic analysis.[18] However, thicker coatings (≈40μm Al-rich outer layer) made by a high activity CVD process did not show complete penetration until after 2,000 1h cycles. In order to clarify the role of coating thickness, a new set of thin CVD coatings was made and testing is in progress, Figure 1. In general, there is good agreement for the mass gain of these new thin coated samples with the previous results for thin coatings. For the coating on 304L, the mass gain for the thin and thick coatings were similar after 1,600h. However, for the coating on Fe-9Cr-1Mo, the mass gain was lower for the thin coatings. This suggests that coating thickness may be more of a factor on coatings on ferritic substrates than on 304L. The new specimens with thin coatings will be characterized after completing 2,000 1h

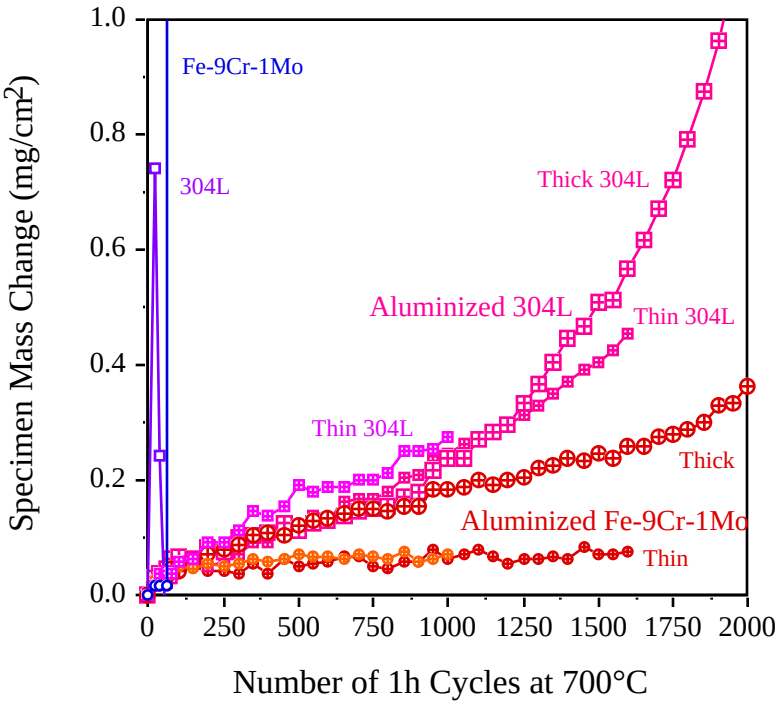

Figure 1. Specimen mass changes during 1h cycles at 700°C in air+10%H_2O. Results are shown for specimens coated with both the high (larger symbol) and low (smaller symbol) Al activity processes to yield thick and thin aluminide coatings, respectively.

cycles to compare their performance to the thick coatings.

EFFECT OF CYCLE FREQUENCY ON COATING PERFORMANCE AT 700°C

A second method for testing the role of CTE is to change the cycle frequency of the test. In the case of the CTE difference between an alumina-forming alloy and the alumina scale, decreasing the cycle frequency generally results in less scale spallation.[20] Previously, results from exposures using 100h cycles at 700°C in air + 10vol.%H_2O have been reported to ≈2,000h.[14] Figure 2 shows the continuation of this test past 6,000h with relatively low mass gains for both coated substrates and no indication of coating failure as was observed in 1h cycles. Also shown in Figure 2 are the results for uncoated 304L and Fe-9Cr-1Mo substrates in 100h cycles. After less than 1000h, both substrates experienced accelerated attack, similar to that observed in 1h cycles. Figures 3a and 3b show the type of macroscopic degradation observed on the edges of coated specimens after 2,000, 1h cycles.[14,15] In contrast, only minor cracking was observed on coated 304L after 60, 100h cycles (arrows in Figure 3c). Figure 3d shows virtually no cracking in the coating at the edge of the Fe-9Cr-1Mo substrate after 6,000h. While there was much less macroscopic damage observed in the coatings exposed in 100h cycles, some damage is developing with time. Figures 4a and 4b show the coating surfaces after 40, 100h cycles at 700°C. After 60, 100h cycles, there was some increase in the number of cracks observed on the specimen surfaces, Figure 4c and 4d, with more cracks observed on the 304L substrate. Without stopping the test and sectioning the specimens, it is not possible to determine the depth of these cracks. However, based on the low mass gains (Figure 2) these cracks are unlikely to have breached the coating. Thus, by reducing the cycle frequency, coating performance was improved, supporting a detrimental role of substrate-coating CTE mismatch.

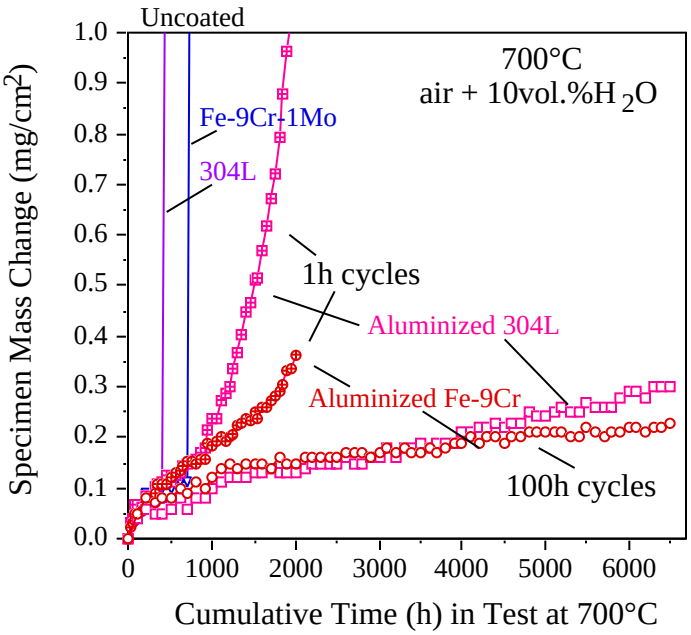

Figure 2. Specimen mass changes during 1h cycles at 700°C in air+10%H_2O. Results are shown for specimens coated with both the high (larger symbol) and low (smaller symbol) Al activity processes.

EFFECT OF SUBSTRATE IMPURITIES ON COATING PERFORMANCE

Characterization of the coatings on commercial substrates showed AlN particles in both the as-deposited and exposed coatings.[16] The source of the nitrogen was determined to be the substrate and initially, laboratory castings of 304L and Fe-9Cr-1Mo compositions were made with lower nitrogen contents: 300ppmw in 304L compared to 800ppm in commercial material and 200ppm in Fe-9Cr-1Mo compared to 475-575ppm in commercial heats. However, coatings on these laboratory cast substrates did not have significantly fewer precipitates nor did they perform significantly better than coatings on commercial alloy

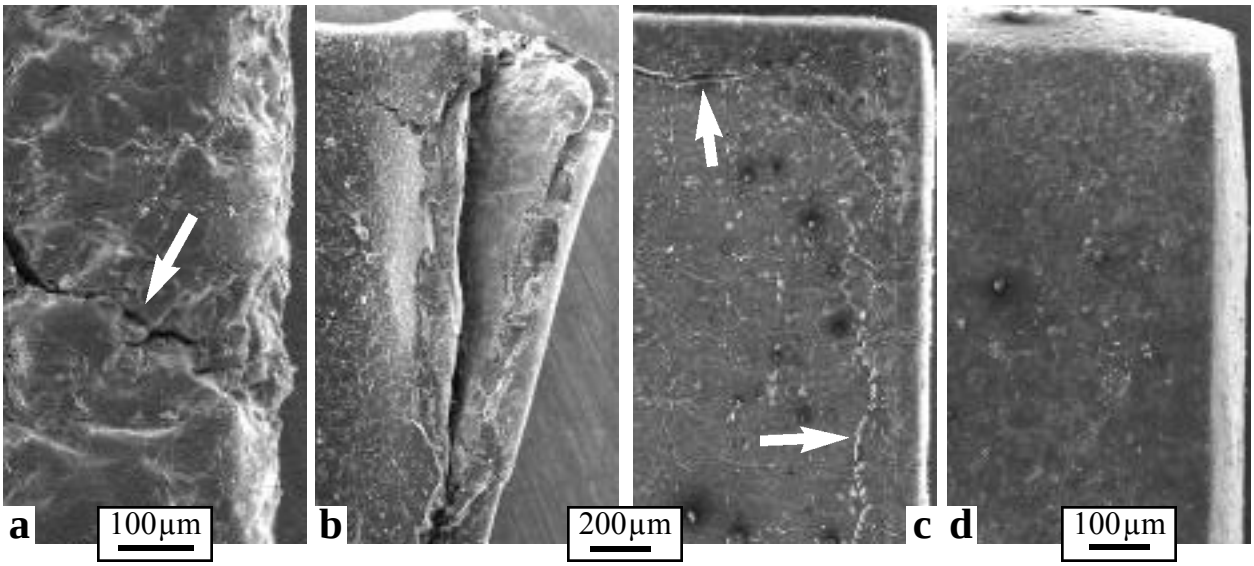

Figure 3. SEM secondary electron plan-view images of coated specimens exposed at 700°C in humid air; (a) Fe-9Cr-1Mo after 2000, 1h cycles, (b) 304L after 2000, 1h cycles, (c) 304L after 60, 100h cycles and (d) Fe-9Cr-1Mo after 60, 100h cycles. Arrows point to cracks in the coating.

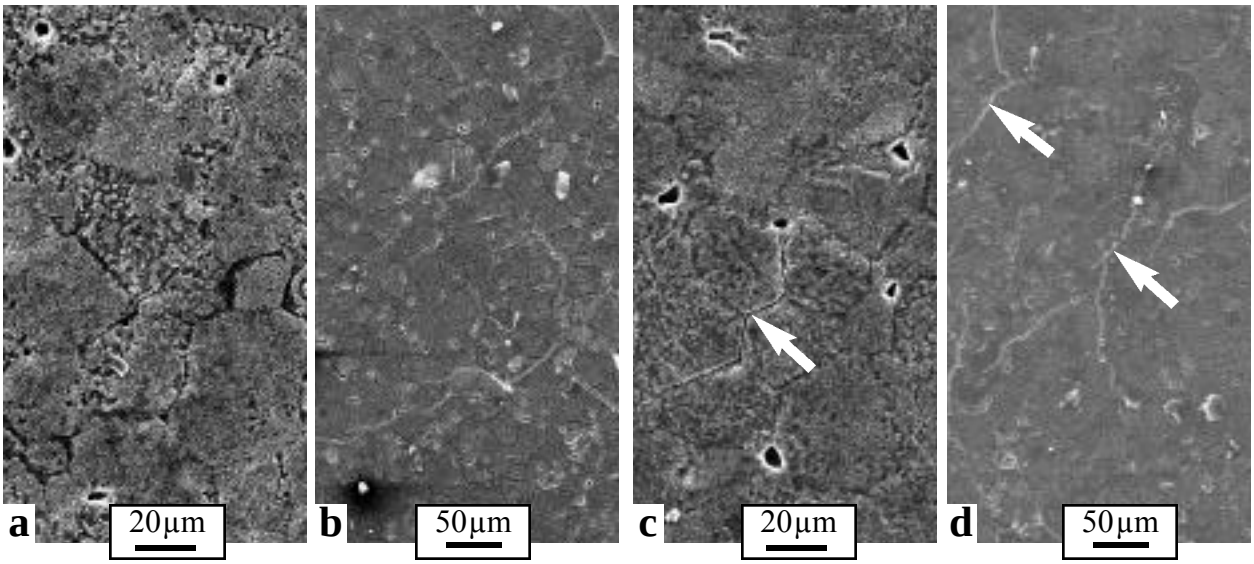

Figure 4. SEM secondary electron plan-view images of coated specimens exposed in 100h cycles at 700°C in humid air; (a) Fe-9Cr-1Mo after 40 cycles, (b) 304L after 40 cycles, (c) Fe-9Cr-1Mo after 60 cycles and (d) 304L after 60 cycles. Arrows point to cracks in the coating.

substrates. A subsequent group of alloys was made with very low N contents. High activity CVD coatings on laboratory-cast, low N 304L, exhibited no nitride precipitates in the coating and fewer voids.[16] Testing has begun to determine if the precipitate-free coatings on this substrate have superior performance to those on commercial 304Lsubstrates. Figure 5 shows the current results of that test in humid air using 1h cycles at 700°C. After 600 cycles, the coating on laboratory 304L shows a similar mass gain to the coatings on commercial 304Lsubstrates. This test will be continued to determine if low substrate nitrogen levels affect coating performance.

DETERMINATION OF THE CRITICAL Al CONTENT FOR COATING FAILURE

A further issue that needs to be resolved for the development of a coating lifetime model is the critical Al content at failure, i.e., the amount of Al remaining at the coating surface when the coating is no longer protective. Initially, this issue was studied using model binary Fe-Al alloys.[5,19,21] However, it was suspected that Cr in the coating also would have a significant effect on the critical Al content and thus model Fe-Al-Cr alloys were fabricated. Figure 6 shows a summary of these results. Binary Fe-Al alloys require ≈20at.%Al in order to prevent FeOx formation during 100, 1h cycles at 700°C in humid air.[19,21] However, when Cr was added, protective behavior was observed for Fe-13Al-10Cr and Fe-20Cr-10Al (FeCrAl). The protective alloys were tested to 1,000 1h cycles and continued to form a thin, protective alumina scale. Initial work showed that Hf added to these model alloys played a significant role. The mass gain for Fe-15Al was much higher for the Hf-free alloy. However, there was less difference for Fe-17Al with and without Hf and protective behavior was observed for FeCrAl with and without Hf. To continue this work, additional Fe-Al-Cr model alloys could be fabricated with lower Al contents to determine a critical Al level when ≈10%Cr was present. However, prior work on low alloyed Fe-Al-Cr alloys showed a significant role of alloy grain size in this temperature range, with fine grained alloys forming protective scales where coarse-grained alloys did not.[22] Given the large difference in grain size between coatings (≈50μm) and cast alloys (≈1-2mm), the results from cast alloys may not be representative of coating performance.

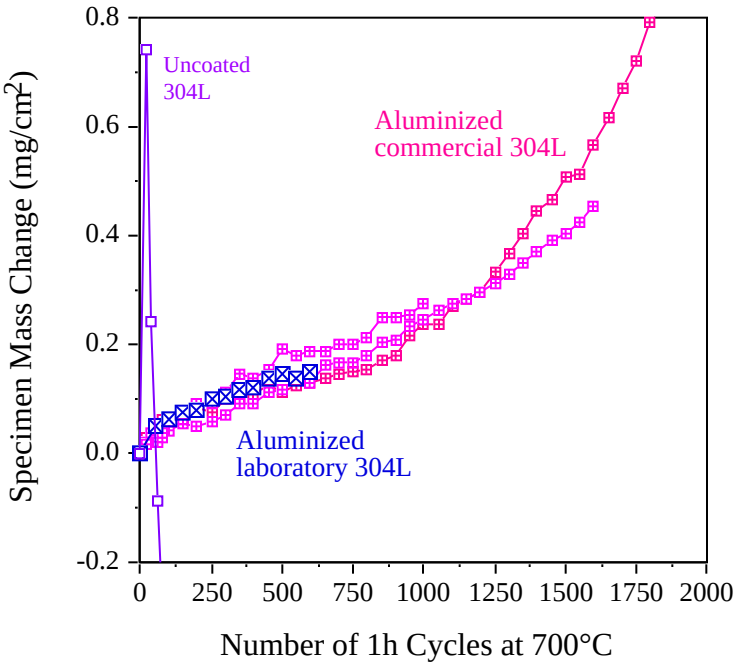

Figure 5. Specimen mass changes during 1h cycles at 700°C in air+10%H_2O for coatings on commercial 304L and laboratory-cast, low N 304L.

A second set of experiments is being conducted to provide more information about the critical Al content for these coatings. By accelerating the test temperature to 800°C, the loss of Al to the substrate by interdiffusion should be significantly increased, thereby reducing the time to failure. A CVD-coated (high activity) specimen of commercial Fe-9Cr-1Mo has been tested for over 2,000h in humid air at 800°C in 100h cycles, Figure 7a. As at 700°C, an uncoated Fe-9Cr-1Mo specimen begins accelerated attack in less than 500h in these conditions while the coated specimen continues to show a low mass gain. A prior diffusion anneal showed that the surface Al content of the aluminide coating decreased to ≈12%Al after a

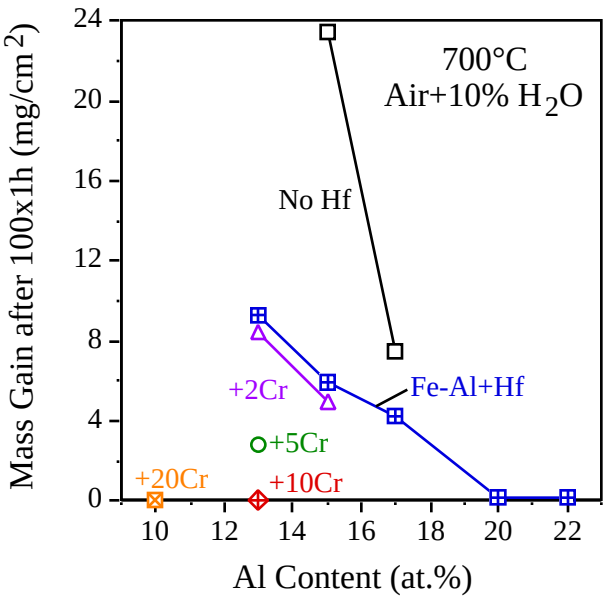

Figure 6. Summary of mass gains for cast Fe-Al-Cr alloys after exposure for 100, 1h cycles at 700°C in air + 10 vol.%H_2O.

2,000h isothermal exposure at 800°C. Exposure of the coated specimen will continue until the coating is breached. At that point, the remaining Al content will be measured. Results from these tests may provide a more accurate value of the critical Al content. A coated 304L specimen also will be tested in these conditions.

SUMMARY

Long-term testing of CVD aluminide coatings on one ferritic (Fe-9Cr-1Mo) and one austenitic (304L) Fe-base substrate is being conducted in air+10%H_2O, where these substrates are readily attacked when not coated. The role of the coating-substrate thermal expansion mismatch is being studied by changing the coating thickness and the test cycle frequency. Increasing the cycle time from 1h to 100h, significantly increased the coating lifetime and reduced cracking in the coating at 700°C. The role of substrate chemistry also is being evaluated. Reducing the N content in 304L produced a coating with fewer voids and AlN precipitates. The performance of the reduced defect coating is being evaluated. To complete a coating lifetime model, testing is under way to determine the critical Al content in these coatings. Initial work focused on results from model alloys. However, accelerated testing of the coatings at 800°C in 100h cycles may provide more accurate values, because of differences in the grain size between coatings and castings.
An unresolved issue is the more severe thermal cycling damage on 304L substrates compared to Fe-9Cr-1Mo. Several hypotheses have been suggested but none have been confirmed. One explanation is that 304L retains more strength at the 700°C test temperature than the ferritic alloy: a weaker substrate may allow more stress relaxation in the coating at temperature. A second explanation is that the diffusion of Al into the 304L substrate should cause the inner coating layer to become ferritic. This would result in three zones with different CTE's in the coating-substrate system resulting in the generation of more strain during each cycle. In the case of the coating on Fe-9Cr-1Mo, both the substrate and the inner coating layer would remain ferritic. Only the thinner, outer aluminide layer would have a CTE mismatch in this system.

ACKNOWLEDGMENTS

The authors would like to thank K. Cooley, L. D. Chitwood, G. Garner, K. S. Reeves and H. Longmire at ORNL for assistance with the experimental work and M. P. Brady and P. F. Tortorelli at ORNL for

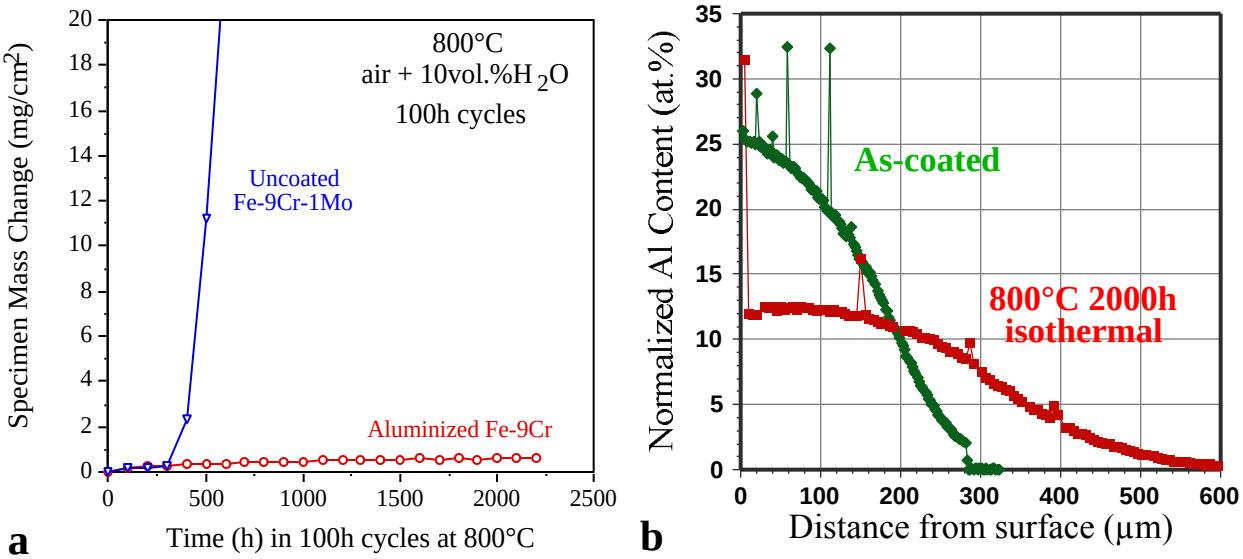

Figure 7. (a) Specimen mass changes during 100h cycles at 800°C in air+10%H_2O for coated and uncoated commercial Fe-9Cr-1Mo. (b) EPMAAl profiles before and after a 2000h, 800°C isothermal anneal.

manuscript comments. This research was sponsored by the U.S. Department of Energy, Fossil Energy Advanced Materials Research Program under contract DE-AC05-00OR22725 with UT-Battelle, LLC.

REFERENCES

1. P. F. Tortorelli and K. Natesan, *Mater. Sci. Eng.*, A258 (1998) 115.
2. P. F. Tortorelli, I. G. Wright, G. M. Goodwin, and M. Howell, in: *Elevated Temperature Coatings: Science and Technology II*, Eds. N. B. Dahotre and J. M. Hampikian; TMS, Warrendale, PA, 1996, p.175.
3. F. D. Geib and R. A. Rapp, *Oxid. Met.*, 40 (1993) 213.
4. M. Zheng and R. A. Rapp, *Oxid. Met.*, 49 (1998) 19.
5. B. A. Pint, Y. Zhang, P. F. Tortorelli, J. A. Haynes and I. G. Wright, *Mater. High Temp.*, 18 (2001) 185.
6. P. F. Tortorelli, G. M. Goodwin, M. Howell and J. H. DeVan in: *Heat Resistant Materials II*, Eds. K. Natesan, P. Ganesan and G. Lai; ASM International, Materials Park, OH, 1995, p.585.
7. G. C. Wood, I. G. Wright, T. Hodgkiess, D. P. Whittle, *Werk. Korr.*, 21 (1970) 900.
8. J. Shen, L. Zhou and T. Li, *Oxid. Met.*, 48 (1997) 347.
9. H. Nickel, Y. Wouters, M. Thiele and W. J. Quadakkers, *Fresenius J. Anal Chem.*, 361 (1998) 540.
10. H. Asteman, J.-E. Svensson, L.-G. Johansson and M. Norell, *Oxid. Met.*, 52 (1999) 95.
11. B. A. Pint and J. M. Rakowski, NACE Paper 00-259, Houston, TX, presented at NACE Corrosion 2000, Orlando, FL, March 2000.
12. S. Henry, A. Galerie and L. Antoni, *Mater. Sci. Forum*, 369-372 (2001) 353.
13. E. J. Opila and N S Jacobson in: *Fundamental Aspects of High Temperature Corrosion*, Eds. D A Shores, R A Rapp, and P Y Hou; Proc. Vol.96-26, Electrochemical Society, Pennington, NJ, 1996, p.344.
14. B. A. Pint, Y. Zhang, J. A. Haynes and I. G. Wright in: *Proc. Seventeenth Annual Conf. Fossil Energy Materials*, R. R. Judkins (comp.), U. S. Department of Energy, 2003.
15. Y. Zhang, B. A. Pint, G. W. Garner, K. M. Cooley and J. A. Haynes, *Surf. Coat. Tech.*, in press (2004).
16. Y. Zhang, B. A. Pint, J. A. Haynes, K. M. Cooley and I. G. Wright, in: *Proc. Eighteenth Annual Conf. Fossil Energy Materials*, R. R. Judkins (comp.), U. S. Department of Energy, 2004.
17. Y. Zhang and B. A. Pint in: *Proc. Sixteenth Annual Conf. Fossil Energy Materials*, R. R. Judkins (comp.), U. S. Department of Energy, 2002.
18. Y. Zhang, B. A. Pint, J. A. Haynes, K. M. Cooley and I. G. Wright, in: *Proc. Seventeenth Annual Conf. Fossil Energy Materials*, R. R. Judkins (comp.), U. S. Department of Energy, 2003.
19. B. A. Pint, Y. Zhang, P. F. Tortorelli, J. A. Haynes and I. G. Wright in: *Proc. Sixteenth Annual Conf. Fossil Energy Materials*, R. R. Judkins (comp.), U. S. Department of Energy, 2002.
20. B. A. Pint, P. F. Tortorelli and I. G. Wright, *Oxid. Met.*, 58 (2002) 73.
21. B. A. Pint and I. G. Wright, *Mater. Sci. Forum*, in press (2004).
22. M. J. Maloney and G. J. Yurek, in: *Composites/Corrosion-Coatings of Advanced Materials*, Eds. S. Kimura, A. Kobayashi, S. Umekawa, K. Nii, Y. Saito and M. Yoshimura, Proc. Vol. IMAM-4, Materials Research Society, Pittsburgh, PA, 1989, p.383.

ALUMINIDE COATINGS FOR POWER GENERATION APPLICATIONS

Y. Zhang
Department of Mechanical Engineering, Box 5014
Tennessee Technological University, Cookeville, TN 38505-0001
E-mail: yzhang@tntech.edu; Tel.: (931) 372-3265; Fax: (931) 372-6345

B. A. Pint, J. A. Haynes, K. M. Cooley, and I. G. Wright
Metals and Ceramics Division
Oak Ridge National Laboratory, Oak Ridge, TN 37831-6156
E-mail: pintb@ornl.gov; Tel.: (865) 576-2897; Fax: (865) 241-0215

ABSTRACT

One of the critical issues for the application of iron aluminide coatings is the possible compatibility problem between Fe-Al coatings and substrates which can have substantially different coefficients of thermal expansion (CTE). Formation of the precipitates or thin layers of nitride between aluminide coatings and substrates could worsen the problem. Preliminary results had indicated that the small amount of interstitial elements, particularly N, in the substrate alloys showed a profound effect on coating formation and quality. The present study focused on the effect of N in the substrate alloys on the coating formation by comparing the aluminide coatings fabricated by chemical vapor deposition (CVD) on commercial and laboratory ferritic and austenitic alloys with different N contents. The N diffused from the substrates during CVD aluminization not only caused the formation of nitride in the coating, but also affected coating adhesion. Spallation sometimes occurred in the as-deposited coating on 304L when an AlN layer was present underneath the coating. The coating growth during the early stages of aluminization also was affected.

INTRODUCTION

Increasing the temperature capabilities of ferritic and austenitic alloys for advanced power generation applications has been of ongoing interest for many years due to potential gains in energy efficiency and concomitant decreases in emissions. These classes of alloys generally owe their oxidation resistance to the formation of Cr-containing oxides which, especially for the ferritic steels, become less protective at higher temperatures and in steam or exhaust environments so that protective coatings will have to be considered.[1, 2] Iron aluminides are well known to have excellent oxidation and sulfidation resistance due to the formation of an external, protective alumina scale.[3, 4, 5, 6] Thus, an aluminide coating could be a good candidate for improving the oxidation/corrosion resistance of ferritic and austenitic steels provided that it can be applied with the desired composition and microstructure and be mechanically sound (that is, minimal cracking and adherent to the substrate).

Two lifetime issues of particular concern for application of iron aluminide coatings are (1) the loss of Al from the coating into the substrate alloys which do not contain any Al, and (2) possible compatibility problems between Fe-Al coatings and substrates which can have substantially different coefficients of thermal expansion (CTE).[7] Preliminary results indicated that the interstitial elements from the steel substrates appeared to affect aluminide coating quality.[8] In particular, nitrogen in the alloys caused the formation of AlN precipitates and/or thin layers in the coating, which resulted in poor adhesion of as-deposited coatings. The present study focused on the effect of N contents in the substrate alloys on coating formation and quality. In addition to commercial ferritic and austenitic alloys, laboratory cast alloys which were N-free were coated for comparison. All coatings were synthesized in a laboratory-

scale CVD reactor in order to more rigorously control the coating process in terms of composition, purity and microstructure.

EXPERIMENTAL PROCEDURE

The commercial ferritic and austenitic alloys used in this work were Fe-9Cr-1Mo (Fe-9.26Cr-0.96Mo-0.47Mn-0.23V-0.19Si-0.16Ni, all compositions in wt.%) and type 304L (Fe-18.29Cr-8.75Ni-1.84Mn-0.24Mo-0.18Co-0.29Cu-0.47Si) austenitic stainless steel; Table 1 shows their N and C contents. The laboratory cast alloys had nearly identical compositions except that they were N-free. These alloys were prepared at Oak Ridge National Laboratory (ORNL) by arc melting using high-purity raw materials and a drop casting process. Each ingot was inverted and remelted five times to ensure macroscopic compositional homogeneity before casting into a 13 mm diameter cylinder. The alloys were then given the same thermo-mechanical treatment of the commercial alloys, i.e., hot rolling to 2.5mm plate at 1050°C and air cooling to room temperature. The iron aluminide coatings were synthesized at 1050°C for 6h in a clean laboratory CVD reactor at ORNL, and details of the coating fabrication process have been reported elsewhere.[9, 10] Prior to coating, the substrate surface was polished to a 0.3 μm alumina finish and ultrasonically cleaned in acetone and methanol. Selected coated specimens were examined by X-ray diffraction (XRD), field emission gun scanning electron microscopy (FEM-SEM) equipped with energy dispersive spectroscopy (EDS), and electron probe microanalysis (EPMA). The coatings on specimens for cross-sectional examination were protected by Cu-plating the specimen prior to mounting in epoxy. The hardness profiles across the coating layer were determined by Vickers microhardness measurements with a load of 50gf.

RESULTS AND DISCUSSION

Elements such as C and N are added to austenitic and ferritic steels primarily for strengthening.[11] Nitrogen is often used austenitic steels, and additions up to 0.2% are employed.[12] In ferritic steels with a low N solubility limit, addition of N to ~0.08% is very popular to improve the high temperature strength of 9-12% Cr steels.[12, 13] However, N additions above 0.06% can cause problems, such as bubbling, in ferritic steels. Also, it is believed that there should be an optimal content relative to other nitride-forming elements such as boron.[14] As indicated in Table 1, the N contents in the commercial steels were relatively high, ~500 ppm in Fe-9Cr-1Mo and ~800 ppm in 304L, respectively. Figures 1(a) and (b) are the back-scatter (BS) electron micrographs of surface morphologies of as-deposited aluminide coatings on commercial Fe-9Cr-1Mo alloy, showing a normal coated area and an abnormal uncoated region, respectively. As indicated by the X-ray maps in Fig. 1(c), the uncoated area on the specimen is rich in Al and N. In cross-section, AlN precipitates were found underneath this region, Fig. 2. The morphology of the AlN precipitates were very similar to that formed on MA956, an oxide dispersion strengthened (ODS) alloy, after exposure to a nitrogen-containing environment.[15]

Table 1. The N and C contents (in ppm) in the commercial Fe-9Cr-1Mo and 304L alloys.

Alloy	N	C
Fe-9Cr-1Mo	480	516
304L	790	204

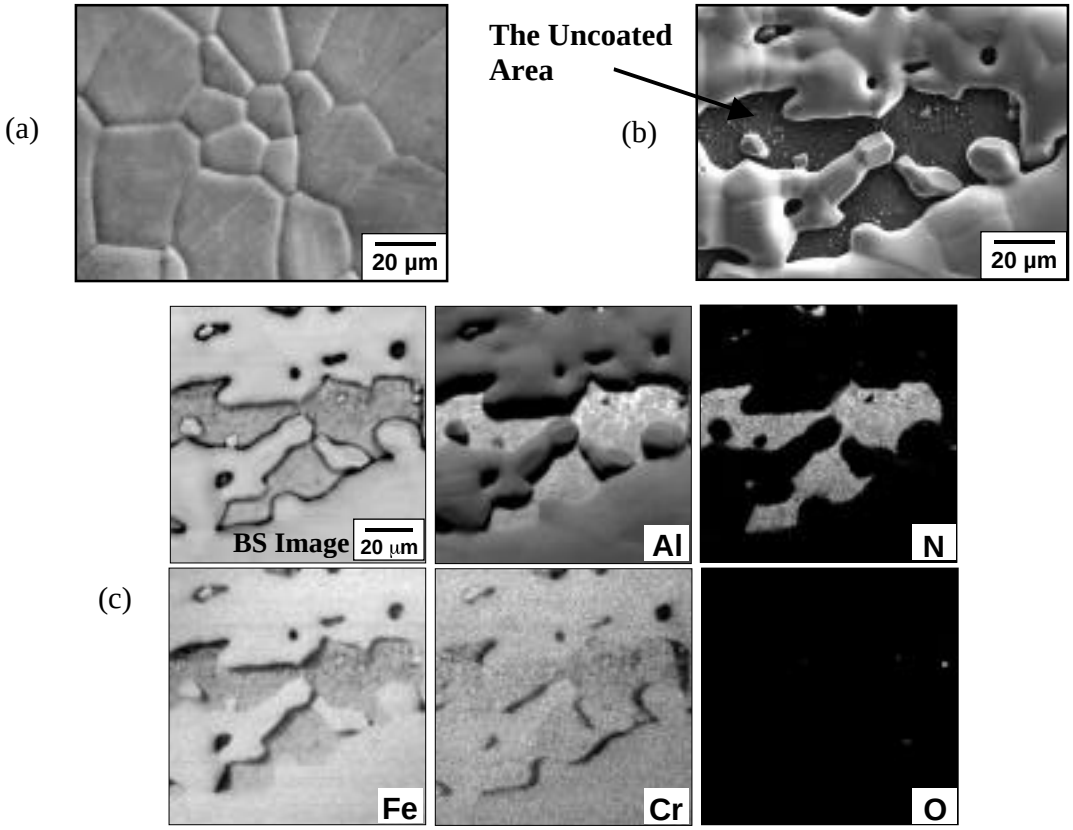

Figure 1. (a) and (b) EPMA back-scattered electron images of an as-deposited CVD coating specimen on commercial Fe-9Cr-1Mo showing the coated and uncoated areas, respectively; (c) the X-ray maps of the uncoated area shown in (b).

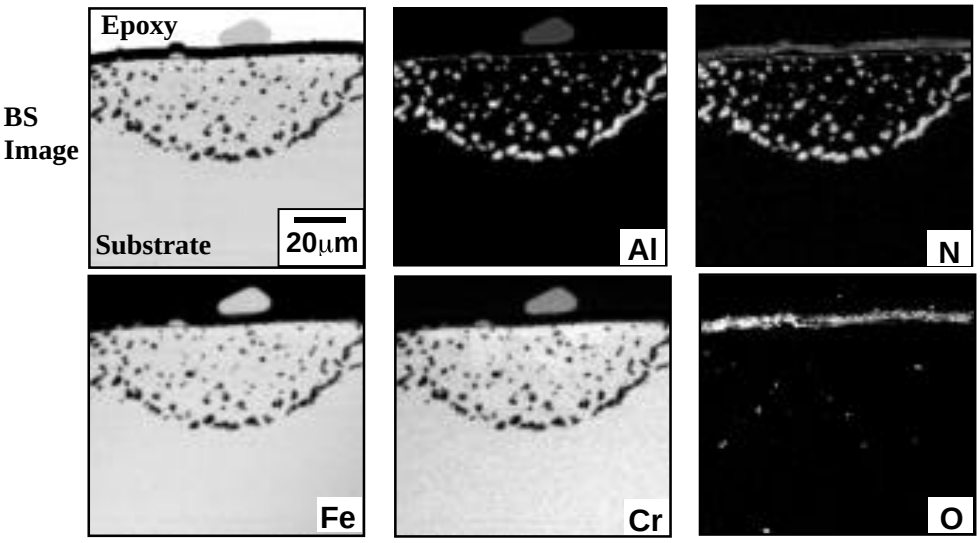

Figure 2. EPMA back-scattered electron image and X-ray maps of the cross-section of the coating on commercial Fe-9Cr-1Mo, showing the AlN precipitates underneath the uncoated area in Fig. 1(b).

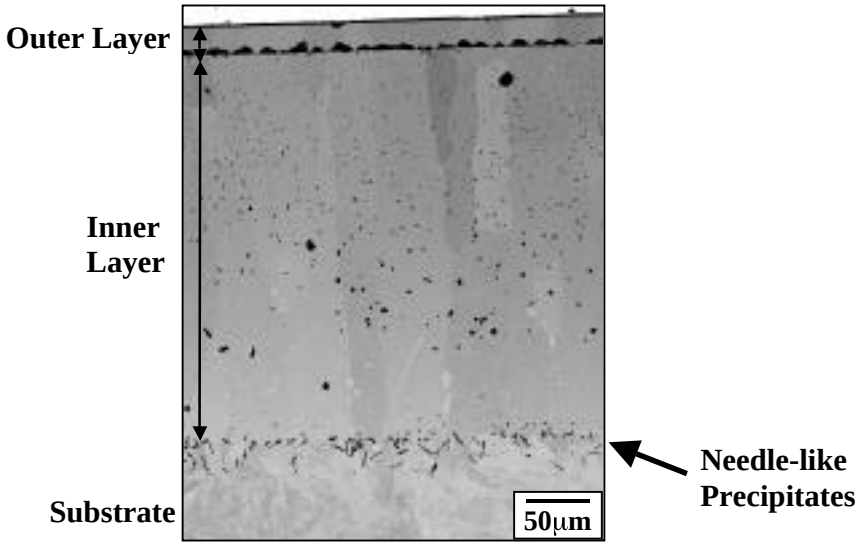

Figure 3. EPMA back-scattered electron image of the CVD aluminide coating on commercial Fe-9Cr-1Mo after 5000h oxidation in laboratory air at 700°C.

The as-deposited CVD aluminide coatings typically consisted of an Al-rich outer layer (20-25 μm) with Fe_3Al or $(Fe,Ni)_3Al$ structure and a thick (150-250 μm), lower Al inner layer with a bcc crystal structure.[16] For the coatings on commercial Fe-9Cr-1Mo alloys, in addition to the fine precipitates in the inner layer, needle-like precipitates were consistently found near the interface of aluminide coating and substrate, Fig. 3. The precipitates tended to grow and aggregate during thermal exposures at elevated temperatures. Agüero et al. recently observed precipitates of an unidentified phase rich in Al with similar morphologies in their slurry iron aluminide coatings,[17] which was probably the AlN phase. Although these particles were observed, no detrimental effect has been attributed to them.

The N content in commercial 304L appeared to have a more significant effect on coating adhesion. As shown in Fig. 4(a), the aluminide coating sometimes spalled after the high-Al activity CVD aluminization, leaving a darker-contrast layer underneath. A high-Al activity in the reactor produced thicker aluminide coatings with a higher Al content in the coating, which resulted in a more brittle coating.[10] This dark layer was identified as AlN by XRD, Fig. 5. The surface chemical compositions of the dark layer and the coating layer were measured by EPMA, as given in Table 2. As compared with the coating surface, the dark layer underneath the coating contained significant amounts of N and O.

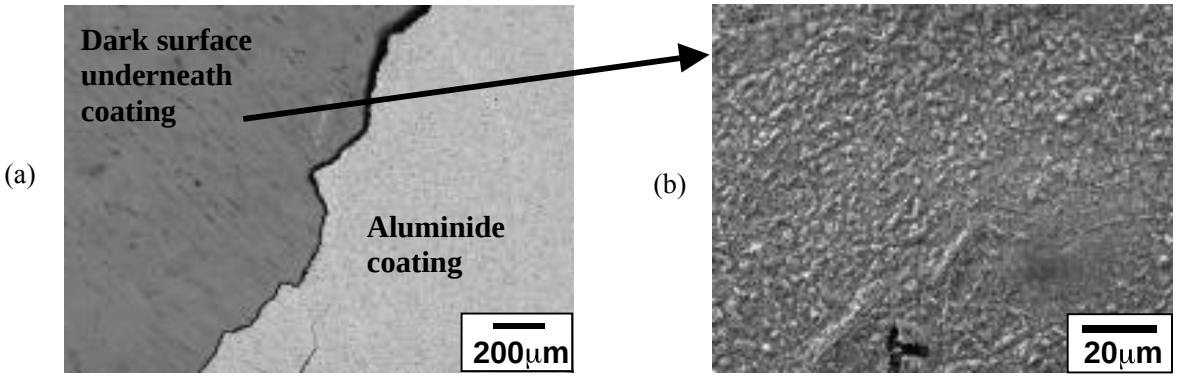

Figure 4. SEM secondary electron images of (a) the dark surface on coated 304L after the coating spalled, and (b) the morphology of the dark surface.

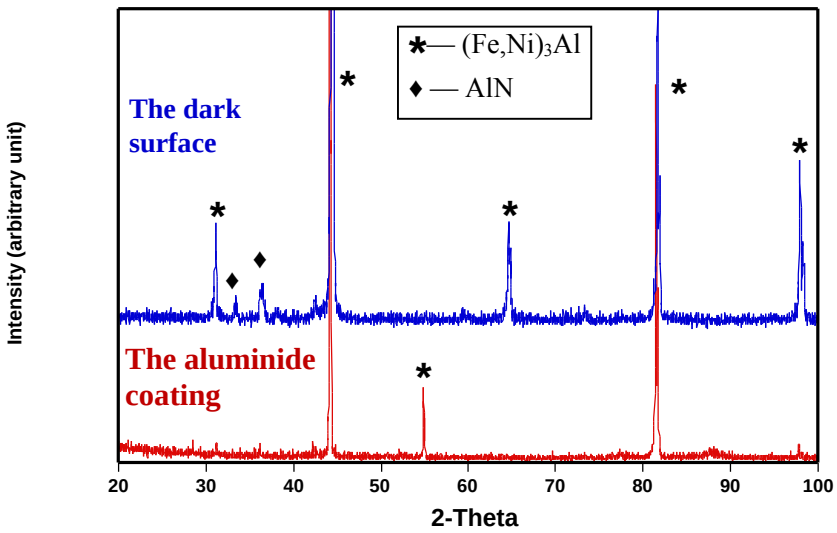

Figure 5. XRD patterns of the as-deposited aluminide coatings on 304L and the dark surface underneath after the coating spalled.

Table 2. The composition of the dark surface and the surface of aluminide coating in Figure 4(a).

wt.%	Fe	Al	Ni	Cr	N	O	C
Dark Surface	41.1	34.5	15.0	7.6	13.2	4.0	0.3
Coating Surface	58.2	22.5	9.3	9.3	0	0	0.6

The effect of N was examined in the early stages of CVD aluminization. After only a short aluminization (less than 30min), nitrogen appeared to affect the formation of aluminide islands on the 304L substrate, Fig. 6. A N-rich phase was observed to hinder coating formation at the substrate grain boundaries.

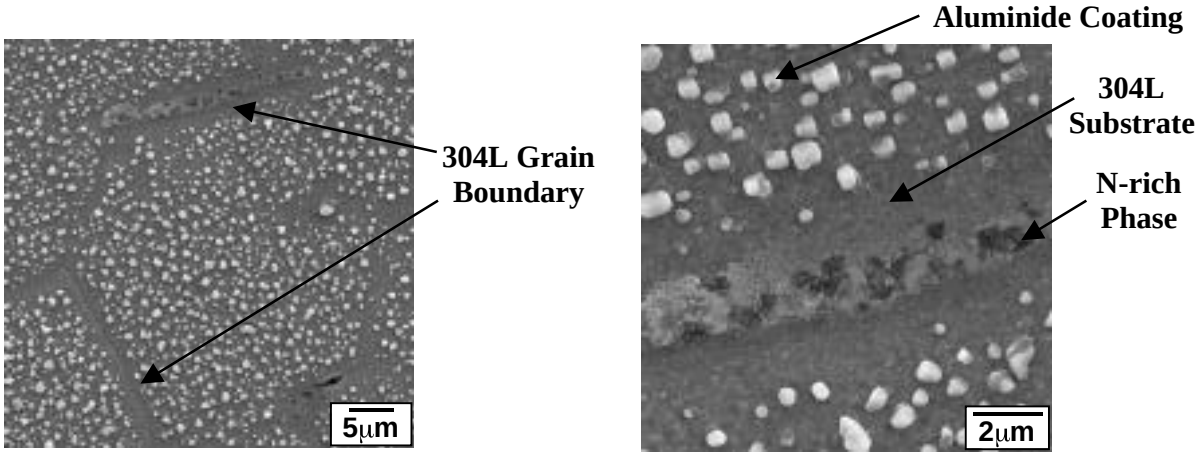

(a) (b)

Figure 6. (a) SEM secondary electron image of the 304L surface during the early stage of CVD aluminization, and (b) a higher-magnification image showing the N-rich phase at the grain boundaries.

Previous work has reported that the thickness of an Fe-Al diffusion coating is reduced in the presence of oxygen and nitrogen due to the formation of an oxy-nitride phase which acted as a diffusion barrier.[18, 19] As indicated by Bangaru and Krutenat,[20] when Al diffuses into the austenitic stainless steel substrates, a localized transformation from austenite to ferrite occurs, and the higher Al diffusivity in ferrite enhances further Al diffusion. According to a study on pack aluminide coatings,[21] the solubility of C in ferrite is substantially lower than that in austenite and thus at the transformation front, the C has been found to precipitate out in the form of stable carbides. Nitrogen could possibly behave in a similar way during the CVD aluminizing process.

To further study the role of N, N-free alloys were coated. Figure 7 compares the cross-sections of the as-deposited commercial 304L and the N-free laboratory alloy during the same CVD aluminizing run. Nitrogen in the commercial 304L led to the formation of AlN precipitates, whereas in the N-free alloy a clean inner layer was observed. Also, Kirkendall voids were formed near the interface of the outer layer and inner layer on the commercial 304L, which could reduce coating adhesion. AlN precipitates were observed by Geib and Rapp during aluminizing a boiler steel Fe-2.25Cr-1.0Mo-0.15C alloy via pack cementation.[22] The source of N for the formation of these precipitates was suggested to be the NH_4Cl activator in the pack. Based on the results from the present study, the substrate alloys could be another source of N contributing to the formation of the nitride precipitates. Since the two specimens shown in Fig. 7 were coated in the same CVD reactor at the same time, apparently the N that caused the formation of AlN precipitates (Fig. 7a) was not from the coating process but from the substrate itself.

In order to investigate the role of these precipitates, hardness profiles were made across both coatings in Fig. 7; the profiles are shown in Fig. 8. The presence of AlN precipitates in the coating did not significantly affect the coating hardness. The hardness of bare 304L alloys was ~225 HV; the decrease of the hardness in the substrate to ~160 HV after the CVD aluminization (Fig. 8) was possibly due to the grain growth at the coating deposition temperature (1050°C). Oxidation testing will be conducted to assess the performance of these coatings.

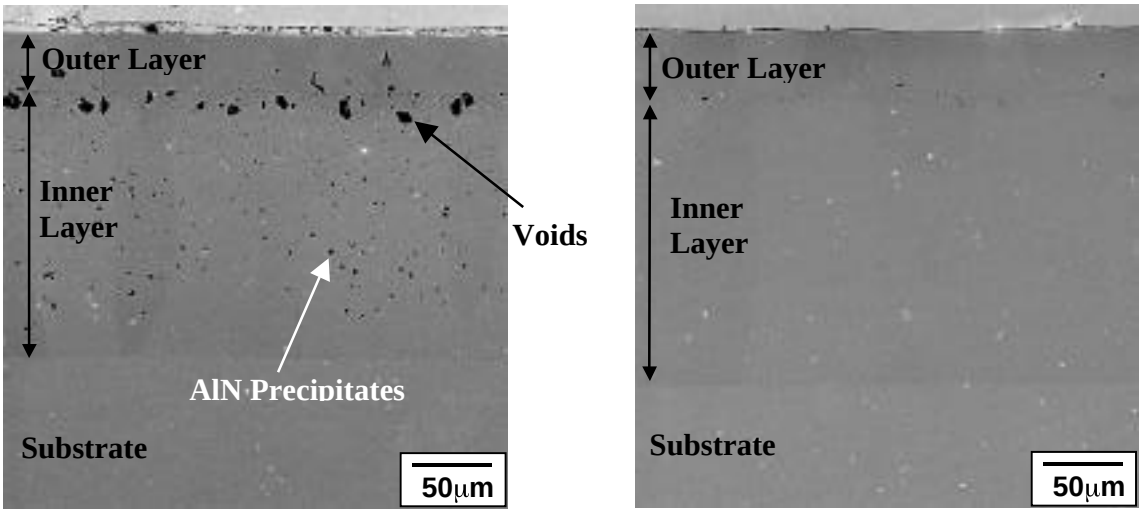

(a) (b)

Figure 7. SEM secondary electron images of the coatings on (a) commercial 304L alloy and (b) the cast N-free 304L alloy.

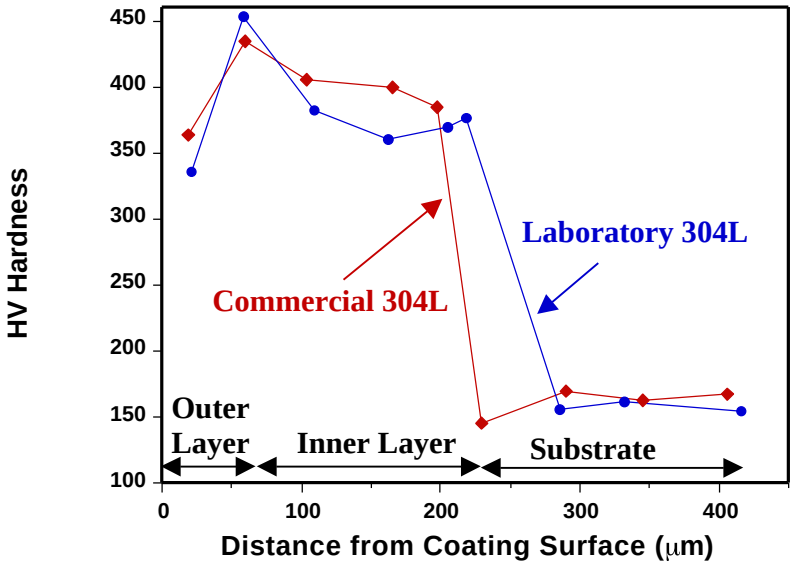

Figure 8. Microhardness profiles of the iron aluminide coatings on commercial and laboratory 304L alloys.

SUMMARY

The effect of N contents in the steel substrates was investigated by comparing the formation of iron aluminide coatings on commercial Fe-9Cr-1Mo and 304L steels with relatively high N contents (500-700 ppm) and N-free laboratory alloys. AlN precipitates were consistently observed in the coating on both commercial Fe-9Cr-1Mo and 304L alloys. Occasionally, a continuous AlN layer was formed underneath the coating on 304L which led to coating spallation. The observation of the early stage of the CVD aluminization indicated that these AlN precipitates could act as a diffusion barrier and hinder the formation of aluminide coatings. For the laboratory N-free alloys, a clean coating layer was formed during the same CVD aluminizing process with no precipitates and significantly reduced Kirkendall voids.

ACKNOWLEDGMENTS

The authors acknowledge L. D. Chitwood, G. W. Garner, L. R. Walker, K. S. Reeves, and K. S. Yarborough at ORNL and B. Bates and W. E. Hawkins at Tennessee Technological University (TTU) for assisting with the experimental work, and P. F. Tortorelli at ORNL for reviewing the manuscript. This research was sponsored by the U.S. Department of Energy, Fossil Energy Advanced Materials Research Program, under contract DE-AC05-00OR22725 with UT-Battelle LLC and subcontract 4000007035 with TTU.

REFERENCES

[1] G. C. Wood, I. G. Wright, T. Hodgkiess, and D. P. Whittle, *Werk. Korr.*, 21 (1970) 900.

[2] B. A. Pint and J. M. Rakowski, *NACE Paper 00-259*, Houston, TX, presented at NACE Corrosion 2000, Orlando, FL, March 2000.

[3] P. F. Tortorelli and J. H. DeVan, *Mat. Sci. Eng.*, A153 (1992) 573.

[4] J. H. DeVan and P. F. Tortorelli, *Corr. Sci.*, 35 (1993) 1065.

[5] P. F. Tortorelli and K. Natesan, *Mater. Sci. Eng.*, A 258 (1998) 115.

[6] B. A. Pint, P. F. Tortorelli, and I. G. Wright, *Mater. High Temp.*, 16 (1999) 1.

[7] B. A. Pint, Y. Zhang, P. F. Tortorelli, J. A. Haynes, and I. G. Wright, *Mater. High Temp.*, 18(3) (2001) 185.

[8] B. A. Pint, Y. Zhang, P. F. Tortorelli, J. A. Haynes and I. G. Wright, in *Proc. Sixteenth Annual Conf. Fossil Energy Materials*, R. R. Judkins (comp.), U.S. Department of Energy, April 22-24, Baltimore, Maryland, 2002.

[9] W.Y. Lee, Y. Zhang, I.G. Wright, B.A. Pint, and P.K. Liaw, *Metall. Trans.*, 29A (1998) 833.

[10] Y. Zhang and B.A. Pint, in *Proc. Sixteenth Annual Conf. Fossil Energy Materials*, R. R. Judkins (comp.), U.S. Department of Energy, April 22-24, Baltimore, Maryland, 2002.

[11] D. Peckner and I. M. Bernstein, in *Handbook of Stainless Steels*, McGraw-Hill Book Company, 1977, pp. 14.

[12] F. Masuyama, K. Hiromatsu, and Y. Hasegawa, *ISIJ International*, 36 (1996) 825.

[13] K-I Hara, H. Aoki, F. Masuyama, and T. Endo, *ISIJ International*, 37 (1997) 181.

[14] F. Masuyama, *ISIJ International*, 41 (2001) 612.

[15] M. Turker, H. Cama, and T. A. Hughes, Corrosion Sci., 37 (1995) 413.

[16] Y. Zhang, B. A. Pint, G. W. Garner, K. M. Cooley, J. A. Haynes, "Effect of Cycle Length on the Oxidation Performance of Iron Aluminide Coatings", submitted to *Surf. Coat. Technol.*, 2004.

[17] A. Agüero and R. Muelas, in *Materials for Advanced Power Engineering 2002*, Eds. J. L. Beckers, M. Carton, F. Schubert, and P. J. Ennis, 2002, pp. 1143.

[18] M. Bedford and J. Boustead, *J. Mater. Sci.*, 13 (1978) 253.

[19] M. V. Akdeniz and A. O. Mekhrabov, *Acta mater.*, 46 (1998) 1185.

[20] N. V. Bangaru and R. C. Krutenat, *J. Vac. Sci. Technol.*, 2B (1984) 806.

[21] M. Zheng and R. A. Rapp, *Oxid. Met.*, 49 (1998) 19.

[22] F. D. Geib and R. A. Rapp, *Oxid. Met.*, 40 (1993) 213.

CORROSION RESISTANT CERAMIC COATINGS: FORMATION OF MULLITE COATINGS ON SiC SUBSTRATES FROM COLLOIDAL SUSPENSION

Beth L. Armstrong
Oak Ridge National Laboratory
Bethel Valley Road, P.O. Box 2008, Oak Ridge, TN 37831-6063
Email: armstrongbl@ornl.gov; Telephone: (865) 241-5862; Fax: (865) 574-6918

Glen H. Kirby
Oak Ridge National Laboratory
Bethel Valley Road, P.O. Box 2008, Oak Ridge, TN 37831-6063
Email: kirbygh@ornl.gov; Telephone: (865) 576-6545; Fax: (865) 574-6918

Kevin M. Cooley
Oak Ridge National Laboratory
Bethel Valley Road, P.O. Box 2008, Oak Ridge, TN 37831-6063
Email: cooleykm@ornl.gov; Telephone: (865) 574-4559; Fax: (865) 574-6918

ABSTRACT

Silicon-based ceramics such as silicon carbide are attractive for use in hot-gas filters, heat exchangers, and other devices for advanced energy producing systems due to their higher temperature capability relative to metals, high thermal conductivity, retention of mechanical properties at operating temperatures, and excellent thermal shock resistance. A major drawback of SiC ceramics is the susceptibility to corrosion by alkali metals and steam at high temperatures, which limits the applicability for extended service in many fossil energy conversion and combustion system environments. Thus, in order to utilize the attractive properties of SiC, additional measures must be employed to protect the materials from corrosive environments. To address this issue, the development of novel coatings for SiC ceramics utilizing low-cost aqueous processing methods such as dip coating is being pursued. Colloidal processing of ceramic particles in aqueous suspension offers an economical route for forming uniform, thick ceramic coatings on complex-shaped components via a simple dip-coating process. In the current study, concentrated mullite suspensions were developed using varying amounts of a cationic polyelectrolyte, polyethylenimine (PEI), as a rheological modifier. SiC substrates were dipped into these suspensions and the resultant coatings were dried, sintered, and evaluated. Suspension precursors containing 0.175 mg PEI/m^2 mullite were optimal for dip coating SiC substrates. Dense coatings were obtained after sintering at 1350^{o}C.

INTRODUCTION

Advanced fossil energy processes have hostile environments with temperatures as high as 1400°C and atmospheres that contain water vapor, sulfur, nitrogen, trace heavy metals, and alkali salts. Silicon-based ceramics such as SiC or SiC/SiC composites are attractive for use in these environments for applications such as hot-gas filters, heat exchangers, and other devices for advanced energy producing systems. They are candidates due to their higher temperature capability relative to metals, high thermal conductivity, retention of mechanical properties at operating temperatures, and excellent thermal shock resistance. A slow growing silica scale is the typical protection mechanism for the SiC material. This scale limits oxygen diffusion and thus prevents further attack of the substrate. A major drawback of SiC ceramics, however, is the susceptibility of the silica scale to volatilization and corrosion by water vapor and alkali salts such as Na_2SO_4 at high temperatures. This factor limits the applicability of SiC ceramics for extended service in many fossil energy conversion and combustion system environments.[1-3] Thus, the use of protective coatings or the development of material with improved stability in these harsh environments is necessary.

Colloidal processing of ceramic suspensions offers a low cost alternative approach for producing uniform, thick ceramic coatings on complex-shaped components via a simple dip coating process. This approach has been demonstrated in many multi-disciplinary areas such as coatings (paints, glazes), fabrication of monolithic components (casting, deposition), and emulsions (gels, food additives, cosmetics). Control of the suspension rheological behavior is paramount to produce quality coatings and can be accomplished by tailoring interparticle (or surface) forces. In aqueous-based suspensions, long-range attractive van der Waals forces are ubiquitous and must be balanced by repulsive forces to tailor the desired degree of suspension stability. For example, ionizable polymeric dispersants, or polyelectrolytes, are commonly used to modify the surface of particles to impart repulsive electrosteric interparticle forces.[4,5]

In this study, concentrated, aqueous suspensions comprised of mullite particles are developed for use in a dip-coating process. Mullite is chosen to demonstrate the feasibility of this process as its behavior is well-characterized in fossil environments. The approach consists of zeta potential measurements as a function of pH to understand the electrochemistry of mullite surfaces in aqueous suspension, rheological characterization of concentrated suspensions to understand the influence of a polyelectrolyte (polyethylenimine) on the bulk suspension properties, and characterization of green and sintered mullite dip coatings on SiC substrates.

EXPERIMENTAL PROCEDURE

Mullite, i.e., $3Al_2O_3{\cdot}2SiO_2$, (MULCR®, Baikowski International Corporation, Charlotte, NC) was used as the ceramic powder in this study. The mullite powder was attritor milled to an average particle size of 1 μm and surface area of 26.0 m^2/g, determined using dynamic light scattering (LA-700, Horiba Instruments Incorporated, Irvine, CA) and BET (Autosorb-1, Quantachrome Instruments, Boynton Beach, FL), respectively. Polyethylenimine (PEI), a

cationic polyelectrolyte with a weight average molecular weight of 10,000 g/mole and one protonizable amine group (NH) per monomer unit was used as a rheological modifier. The fraction of protonated amine groups, α, was determined by potentiometric titration and is shown as a function of pH in Fig. 1 (Note, $\alpha = [NH_2^+]/([NH] + [NH_2^+])$).

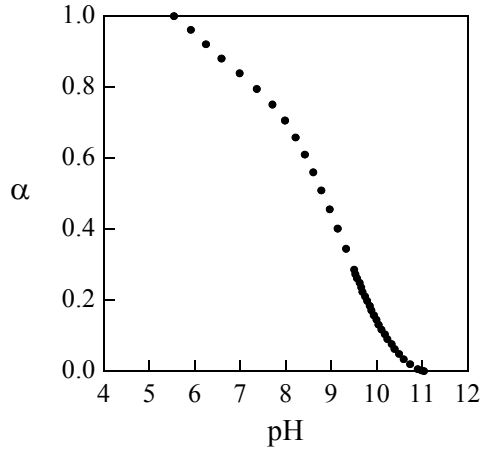

Fig. 1. Fraction of protonated amine groups, α, as a function of pH in dilute PEI solution (10^{-3} *M*). $\alpha = [NH_2^+]/([NH] + [NH_2^+])$.

Zeta potential measurements were carried out on the mullite particles in dilute aqueous suspension using capillary electrophoresis (Zetasizer 3000HS, Malvern Instruments Ltd., Worcestershire, UK). Dilute suspensions (10^{-3} vol% solids) were prepared by adding the appropriate amount of powder to aqueous, KNO_3 solutions (0.01 *M*) of varying pH ranging from 2 – 11. The solutions were adjusted to the appropriate pH using stock solutions of nitric acid or ammonium hydroxide. The suspensions were ultrasonically treated for 120 s to break up soft agglomerates prior to measurement.

Rheological measurements were carried out on concentrated mullite suspensions using a controlled-stress rheometer (Rheometric Scientific SR5, TA Instruments, New Castle, DE) fitted with concentric cylinder geometry. Concentrated mullite suspensions (45 vol% solids) were formulated by mixing an appropriate amount of mullite powder into aqueous solutions (pH 7) of varying PEI concentration. The suspensions were ultrasonically treated for 300 s to break up soft agglomerates, and then stirred for 24 hours to achieve equilibrium. Prior to measurement, the suspensions were presheared at a stress of 200 Pa for 300 s and then allowed to equilibrate for 900 s. Furthermore, a specially designed solvent trap was used to minimize the evaporation of water. In this way, variations in sample handling were minimized to ensure reproducibility of the data. Stress viscometry measurements were carried out by ramping an applied shear stress (logarithmically) from 0.025 to 200 Pa. A delay time (i.e., the time between two consecutive data acquisition events) of 60 s was used in this study. After repeating the preshear procedure mentioned above, storage modulus (G') measurements were carried out by ramping an oscillatory shear stress (logarithmically) from 0.025 to 200 Pa at a constant frequency of 1 Hz. All rheological measurements were performed at a constant temperature of 25°C.

Silicon carbide substrates (Hexaloy, Carborundum Co., Niagara Falls, NY) that were 20 mm x 6.5 mm x 6.5 mm in size were dipped into the concentrated mullite suspensions (45 vol%) of varying PEI concentration. The substrates were inserted into suspensions at a rate of 1.4 mm/s,

submerged for 60 s, and withdrawn at a rate of 1.4 mm/s. The coated substrates were dried under ambient conditions, heat treated at 600°C to burn out any organics, and sintered at varying temperature and atmosphere (e.g., air, argon, and nitrogen).

RESULTS AND DISCUSSION

ZETA POTENTIAL

Zeta potential measurements were carried out on dilute mullite suspensions (10^{-3} vol% solids) of varying pH and the results are shown in Fig. 2. Interestingly, the isoelectric point (IEP) was observed at pH 3.8, which is near the IEP reported for pure SiO_2 (pH 2-3) (ref. 6). Favorable conditions for adsorption of PEI exist between pH 3.8 and 8.8 where the mullite particles are negatively charged and PEI is highly positively charged (i.e., $1 > \alpha > 0.5$).

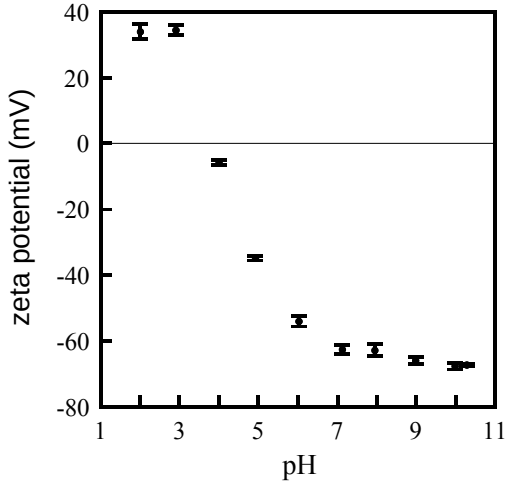

Fig. 2. Zeta potential as a function of pH for dilute mullite suspensions (10^{-3} vol% solids). Note, the data points and error bars represent the average and standard deviation, respectively, of ten measurements.

RHEOLOGICAL BEHAVIOR

Rheological measurements were carried out on concentrated mullite suspensions and the results are shown in Figs. 3-5. The apparent viscosity is plotted as a function of applied shear stress in Fig. 3 for suspensions of varying PEI concentration. The degree of shear-thinning decreased with increasing PEI concentration until nearly Newtonian flow behavior was observed at 0.2 mg PEI/m^2 mullite. These suspensions exhibited stable flow behavior over a 15-day time span, as shown by the results in Fig. 4. The elastic modulus is plotted as a function of applied shear stress in Fig. 5 for suspensions of varying PEI concentration. Solid-like behavior, indicative of colloidal gels, was observed for suspensions with less than 0.2 mg PEI/m^2 mullite. The linear elastic modulus and yield stress decreased with increasing PEI concentration until the transition from gel- to fluid-like behavior occurred at 0.2 mg PEI/m^2 mullite.

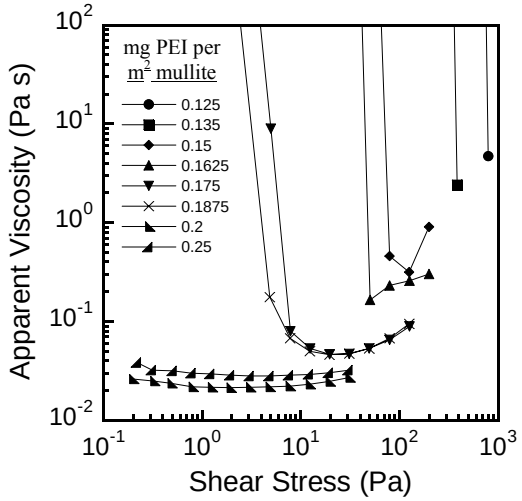

Fig. 3. Apparent viscosity as a function of shear stress for concentrated mullite suspensions (45 vol% solids) of varying PEI concentration. Note, the solid lines merely guide the eye.

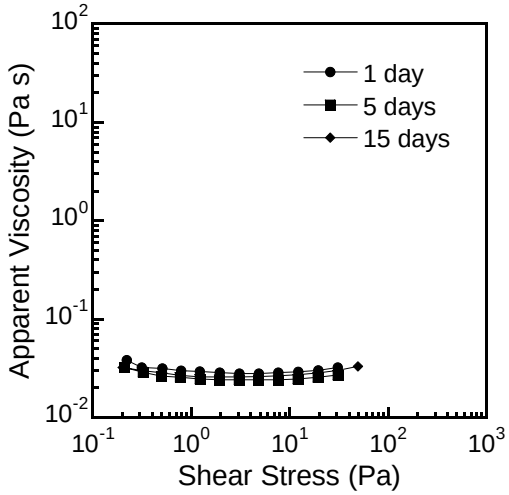

Fig. 4. Apparent viscosity as a function of shear stress for concentrated mullite suspensions (45 vol% solids, 0.25 mg PEI/m^2 mullite) aged for varying times.

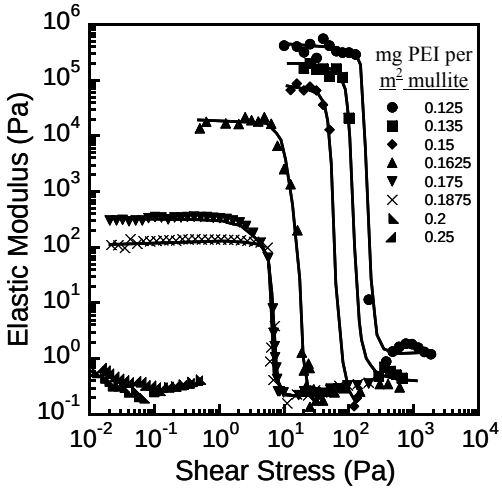

Fig. 5. Elastic modulus as a function of shear stress for concentrated mullite suspensions (45 vol% solids) of varying PEI concentration. Note, the solid lines merely guide the eye.

COATING FORMATION

Silicon carbide substrates were dipped into mullite suspensions of varying rheological behavior and the resulting coatings are displayed in Fig. 6. Excellent coatings were obtained from mullite suspensions with 0.1625 - 0.175 mg PEI/m^2 mullite surface. Mullite suspensions with less than 0.1625 mg PEI/m^2 mullite resulted in thick, uneven coatings that decreased in quality with decreasing PEI concentration. These features stem from a particle-gel network that is too strong,

i.e., when the linear elastic modulus is greater than ~ 10 kPa. Mullite suspensions with 0.1875 mg PEI/m^2 mullite or greater resulted in coatings with three types of defects: thickness gradients, pores, and drying "dimples". These defects stem from a particle-gel network that is too weak, i.e., when the linear elastic modulus is less than ~ 100 Pa. For example, thickness gradients result from dripping and beading of the suspensions at the bottom of the substrate. Pores arise from entrained air bubbles in the suspension, possibly stabilized by PEI, that quickly migrate through a liquid-like medium to the suspension/substrate interface during dipping. After drying, the air bubbles become locked into position at the interface. Dimple-shaped defects form during drying in a process described by Martinez and Lewis.[7] Drying begins with fast evaporation of solvent at the corners and edges of a ceramic coating, but over time, the drying front converges inward until the center of the coating is completely dry. Concurrently, solvent wicks from the region of high solvent concentration (the center) to the region of low concentration (the drying front). If the gel structure is too weak, particles migrate with the fluid flow and ultimately, a dimple-shaped defect forms in the center of the coating.

Fig. 6. Resultant coatings from dipping SiC substrates into concentrated mullite suspensions (45 vol%) of varying PEI concentration ranging between 0.15-0.20 mg PEI/m^2 mullite.

SINTERING BEHAVIOR

The sintering conditions, i.e., atmosphere and temperature, strongly influenced the ultimate coating quality. Dramatic differences were observed in the adherence of coatings depending on the sintering atmosphere. Adherent coatings were obtained in air, likely because a thin, silica-rich reaction layer formed to provide bonding. On the other hand, the coatings sintered in argon and nitrogen atmospheres easily detached from the SiC substrates because a bond layer does not form. Furthermore, mullite and nitrogen likely reacted to form AlN, which could result in coating expansion and spallation.

Dense, adherent, macro crack-free coatings were obtained after sintering at 1350^{o}C in air, as shown in Fig. 7. This temperature was significantly lower than the requirement for densification of bulk mullite (1600^{o}C) (ref. 8) and was only slightly higher than the target operating temperature in fossil environments (~1200^{o}C). The coating thickness varied from a few micrometers at the corners to ~ 150 μm at the midpoint of each edge. Future steps to optimize the suspension solids loading and the sintering conditions will be employed to minimize this thickness gradient.

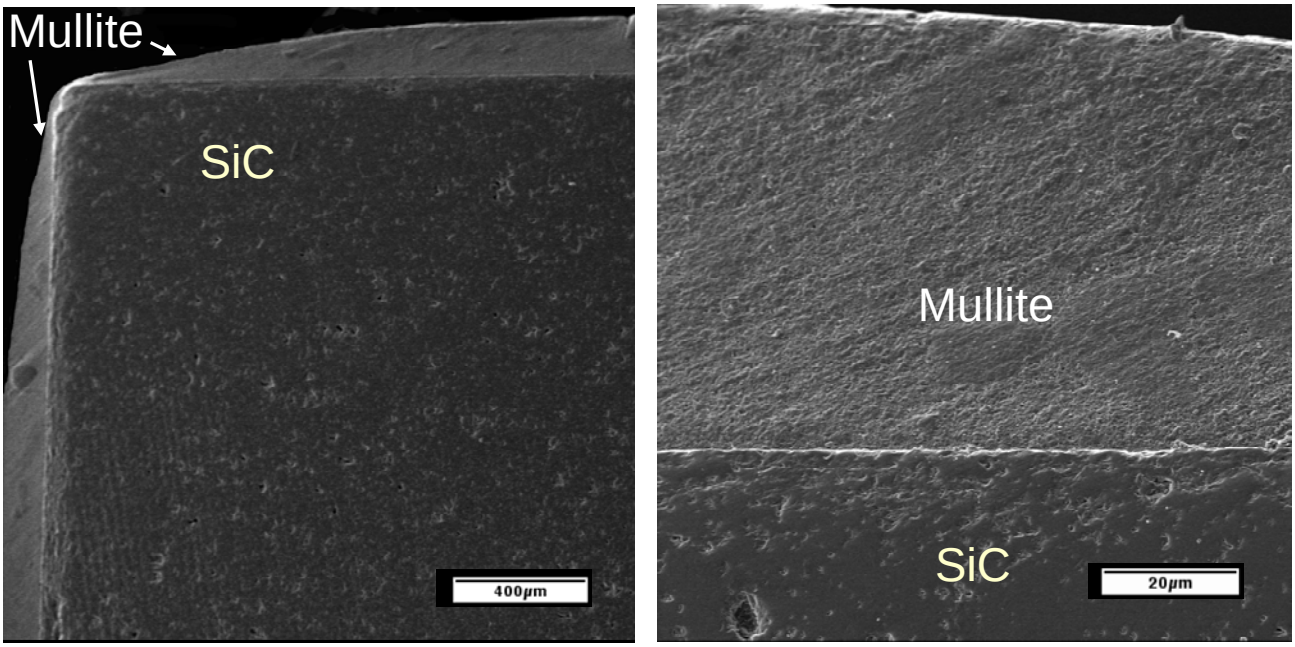

Fig. 7. SEM micrographs of mullite coated SiC, dipped from concentrated suspension precursors (45 vol% solids) with 0.175 mg PEI/m^2 mullte and sintered at 1350^{o}C.

CONCLUSIONS

Dip coating is a feasible, low-cost method to coat SiC ceramics for use in fossil energy applications using concentrated, aqueous suspensions prepared via a colloidal processing approach. The surface of mullite particles in aqueous suspension was characterized using zeta potential measurements and PEI was identified as an effective additive to modify the particle surfaces to facilitate fabrication of concentrated colloidal suspensions. Rheological measurements indicated that fluids and gels of varying linear elastic modulus and yield stress can be tailored by varying the PEI concentration. The optimal PEI concentration for dip coating ranged from 0.1625 - 0.175 mg PEI/m^2 mullite surface area. Dense, adherent, and macro crack-free mullite coatings were obtained on the SiC substrates after sintering at 1350^{o}C in air.

ACKNOWLEDGMENTS

The authors would like to thank Shirley Waters for her assistance with SEM measurements. This research was sponsored by the U.S. Department of Energy, Office of Fossil Energy Advanced Research Materials Program under Work Breakdown Structure Element ORNL-1(B). The Oak Ridge National Laboratory is operated by UT–Battelle LLC for the U.S. Department of Energy under contract DE-AC05-00OR22725.

REFERENCES

1. Fox, D., Cuy, M., and Strangman, T., "Sea Salt Hot Corrosion and Strength of an Yttria-Containing Silicon Nitride," *J. Am. Ceram. Soc.*, **80** (11) 2798-804 (1997).
2. Opila, E., "Variation of the Oxidation Rate of Silicon Carbide with Water-Vapor Pressure," *J. Am. Ceram. Soc.*, **82** (3) 625-36 (1999).
3. More, K., Tortorelli, P., Ferber, M., and Keiser, J., "Observations of Accelerated Silicon Carbide Recession by Oxidation at High Water-Vapor Pressures," *J. Am. Ceram. Soc.*, **83** (1) 211-13 (2000).
4. Cesarano, J., "Stability of Aqueous α-Al_2O_3 Suspensions with Poly(methacrylic acid) Polyelectrolyte," *J. Am. Ceram. Soc.*, **71** (4) 250-55 (1988).
5. Cesarano, J., "Processing of Highly Concentrated Aqueous α-Alumina Suspensions Stabilized with Polyelectrolytes," *J. Am. Ceram. Soc.*, **71** (12) 1062-67 (1988)
6. Reed, J.S., *Principles of Ceramic Processing*. 2nd ed. 1995, New York, NY: John Wiley & Sons.
7. Martinez, C. J. and Lewis, J. A. “Rheological, Structural, and Stress Evolution of Aqueous Al_2O_3:Latex Tape-Cast Layers,” *J. Am. Ceram. Soc.*, **85** [10] 2409-16 (2002).
8. Armstrong, B. L. Unpublished Data.

METAL-ORGANIC CHEMICALLY VAPOR DEPOSITED YTTRIA-STABILIZED ZIRCONIA (YSZ) FOR THERMAL BARRIER COATINGS

V. G. Varanasi and T. M. Besmann
Oak Ridge National Laboratory
P.O. Box 2008
Oak Ridge, TN 37831-6063

W. Xu and T. L. Starr
University of Louisville
Louisville, KY 40292

ABSTRACT

Metal-organic chemical vapor deposition (MOCVD) process development utilized a cold wall reactor with liquid delivery of a metal-organic precursor solution to deposit yttria-stabilized zirconia. At high temperature (> 950°C) the deposition process is transport limited and the rate is ultimately controlled by the solubility of the selected precursor in the selected solvent. Proposed, thick thermal barrier coatings with a columnar structure have been successfully deposited on developmental FeCrAlY material and resistance to spallation during thermal cycling in initial testing has been demonstrated on pre-oxidized surfaces.

INTRODUCTION

Yttria-stabilized zirconia (YSZ) is used as a thermal barrier coating (TBC) to protect super-alloy blades such as Mar-M247 or Rene-N5 during engine operation. The current method for YSZ fabrication for TBC applications is by air-plasma spraying (APS) or electron beam-physical vapor deposition (EB-PVD).[1-5] APS gives reasonable deposition rates, but has a limited life and aging effects due to its porous and lamellar structure. The EB-PVD coatings are more stable and can accommodate thermomechanical stresses due to their characteristic strain-tolerant, columnar microstructure. EB-PVD, however, is primarily line-of-sight, which often leaves "hidden areas" uncoated, has low throughput, and has high capital cost. The process of metal-organic chemical vapor deposition (MOCVD) is investigated here as an economical alternative to EB-PVD and APS, with the potential for better overall coverage as well as the ability to produce thick (100-250 μm), strain-tolerant, columnar coatings.

MOCVD of YSZ involves the use of zirconium and yttrium organometallic precursors reacting with an oxygen source. Previous researchers have used β-diketonate or chloride precursors and oxygen.[6-8] These precursors have low transport rates due to their low carrier solvent solubility.[9] Solvated zirconium and yttrium butoxide precursors were investigated here due to their higher vapor pressures and high solvent solubility. This work uses previously performed predictive

equilibrium modeling and experiments involving butoxide precursors for tetragonal YSZ fabrication.[10]

EXPERIMENTAL

From the equilibrium analysis a minimum of 18 moles per minute of molecular oxygen is required for every mole per minute of Y-butoxide + Zr-butoxide (O/(Y+Zr)=35) to ensure formation of tetragonal YSZ at 950°C. To assure full oxidation, the oxygen flow rate was selected to be twice the minimum, O/(Y+Zr)=72.

YSZ was deposited in the MOCVD reactor shown in Fig. 1. Substrates included alpha-alumina (99.6 % purity: Coors) and a FeCrAlY. The precursors were Y- and Zr-tert butoxides dissolved in toluene and n-butanol, respectively. The precursors were pre-solvated and their solubility was 0.5 M Y in toluene and 2.23 M Zr in n-butanol. From the as-delivered batches, the reactants were mixed together based on their solubility and the desired coating composition. The solution was delivered continuously by a syringe pump through a poppet-seal relief valve into the deposition chamber. To ensure efficient vaporization, the solution was then misted using an ultrasonic atomizing nozzle. The misted solution was carried by 300°C O_2 at 1200 sccm to the substrate through a stainless-steel stagnation flow nozzle. The substrate was inductively heated using a Mar-M247 susceptor. The CVD chamber wall and susceptor holder were made of fused silica glass. A thermocouple was placed within the susceptor to control the susceptor temperature, while the substrate temperature was read using an optical pyrometer. Samples were analyzed using X-ray diffraction (XRD) to identify the phases. Scanning electron microscopy (SEM) revealed coating thickness and microstructure. In addition, electron probe microanalysis (EPMA) was used to determine the relative homogeneity of yttrium and zirconium throughout the as-deposited coating.

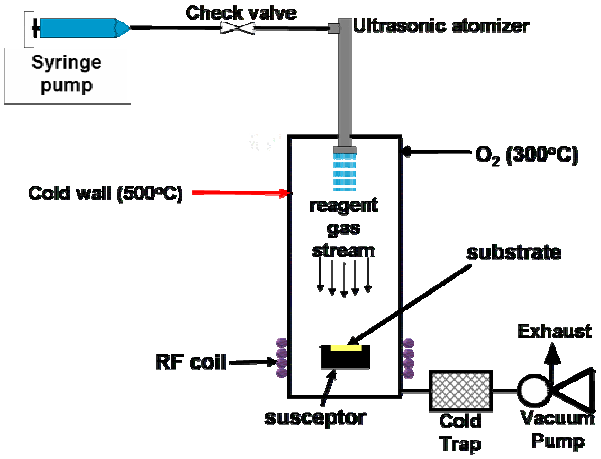

Fig. 1. Schematic of MOCVD system.

RESULTS

Deposition rate as measured from images of the cross-sections vs. substrate temperature is shown in Fig. 2. These agreed well with simple weight gain measurements, where the thickness was calculated from the density of YSZ and the exposed substrate surface area (only the top surface is coated). Coatings up to ~75 μm thick, limited only by the charge to the syringe, were deposited at the higher temperatures. An activation energy assuming an Arrhenius dependence and first order kinetics between 840 and 975°C was calculated to be 53.8 ± 0.2 kJ/mol.

A secondary electron image of a cross-section of the coating on an alumina substrate is presented in Fig. 3, and displays a typical CVD columnar structure. The microprobe images for yttrium and zirconium signals are also shown, and the non-uniformity, i.e., banding, corresponded to the difference in gray-scale seen in the secondary electron image. In order to further characterize composition, quantitative microprobe measurements were made as a function of position on the cross-section and are shown in Fig. 4. The variation in yttrium and zirconium content is apparent, and the average yttrium proportion was less than half that of the inlet solution. Results of XRD of the coatings indicated a major tetragonal YSZ phase and a minor monoclinic phase.

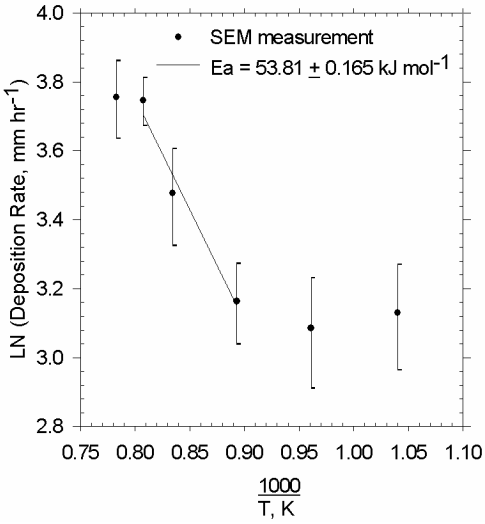

Fig. 2. Arrhenius plot of deposition rates vs. temperature.

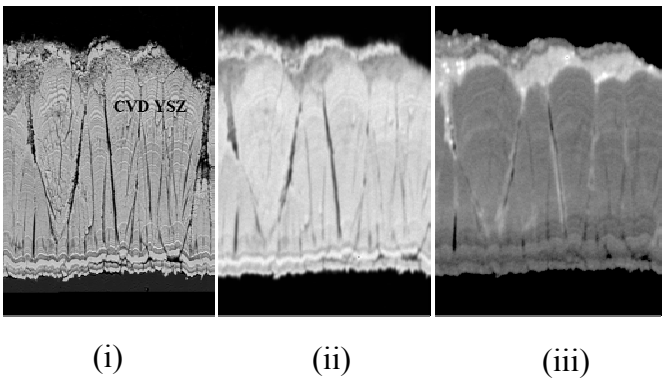

Fig. 3. (i) Secondary electron image, (ii) Zr concentration, and (iii) Y concentration of polished coating cross-section. Coating is ~50 μm thick.

Results of initial thermal cycling tests of YSZ-coated FeCrAlY samples are presented in Fig. 4. The uncoated sample experienced slow oxide scale growth, which resulted in small weight gains. A YSZ-coated FeCrAlY sample, on which no polishing or pre-oxidation was performed before coating, suffered substantial weight loss over the thermal cycling period due to severe spallation of the coating. A second substrate with a polished surface that was pre-oxidized in 1 kPa oxygen at 1000°C for 1 h prior to coating to form the desired alumina surface oxide performed significantly better, with minimal weight loss to almost 300 cycles so far (Fig. 5).

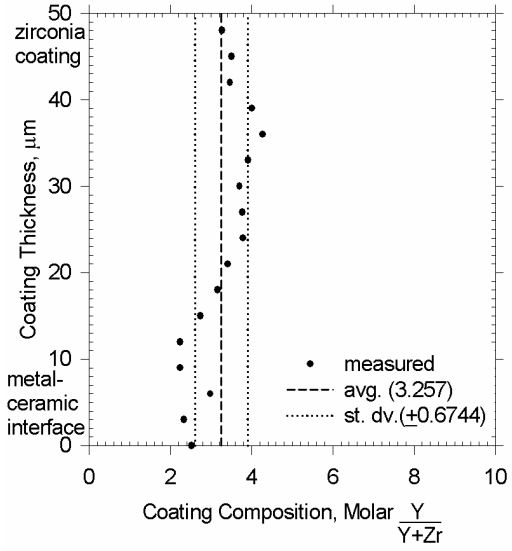

Fig. 4. Yttrium molar ratio as a function of position in a cross-section of a coating.

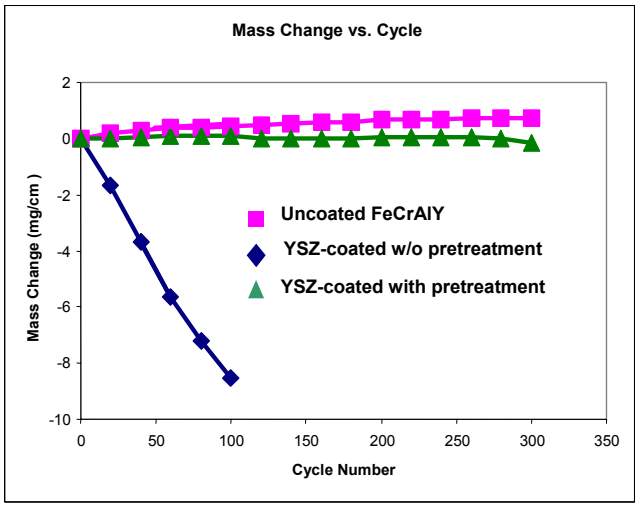

Fig. 5. Mass change as a function of thermal cycles

DISCUSSION

Deposition of YSZ with little to no carbon co-deposition is demonstrated under the current conditions. Samples are white in appearance and calcining at 1000°C for several hours yielded minimal to no weight change. The deposition rate dependence on temperature (Fig. 3) appears to indicate a chemical kinetic rate-limiting regime, at least between 840 and 975°C, where the activation energy is relatively large. At higher temperatures, as is typically the case for CVD processing, the chemical kinetic rate becomes more rapid than mass transport to the substrate surface, and thus the apparent activation energy is significantly smaller. The weak temperature dependence behavior observed at low temperatures may be due to complex formation, or failure to form species that would allow efficient oxide deposition.

The non-uniformity in Y:Zr ratio is due to inconsistent precursor delivery or cyclic mass transport issues. The low yttria content of the coatings may have been the result of the recognized greater difficulty in oxidizing yttrium, as compared to zirconium precursors,[11,12] causing formation of tetragonal coatings with minor monoclinic phase content, as one would expect from the phase equilibria.[13] Despite the two-phase nature, a YSZ-coated FeCrAlY sample with a pre-oxidized surface exhibited excellent initial thermal cycling behavior.

SUMMARY

The MOCVD of relatively thick columnar YSZ thermal barrier coatings has been successfully demonstrated. The coatings were not fully tetragonal phase, yet they appeared to be stable over the temperature range of interest. Initial thermal cycling tests of a YSZ coating on a FeCrAlY developmental material that had been pre-oxidized to form an alumina film showed excellent adhesion. Further development will require determination of coating thermal diffusivity, further understanding of behavior in turbine environments, and scale-up to coating components of realistic size and shape.

ACKNOWLEDGMENTS

The authors wish to thank L. Chitwood for the exposures, and B. Pint for sample substrates. Valuable comments were provided by R. Judkins, I. Wright, and M. Brady. Research was sponsored by the Office of Fossil Energy, National Energy Technology Laboratory, U.S. Department of Energy, under contract number DE-AC05-00OR22725 with UT-Battelle, LLC.

REFERENCES

1. J. R. Nicholls, “Advances in Coating Design for High-Performance Gas Turbines,” *MRS Bull.*, **28** 659-670 (2003).
2. D. R. Clarke and C. G. Levi, “Materials Design for the Next Generation Thermal Barrier Coatings,” *Annu. Rev. Mater. Res.*, **33** 383-417 (2003).
3. A. G. Evans, D. R.Mumm, J. W. Hutchinson, G. H. Meier and F. S. Pettit, “Mechanisms Controlling the Durability of Thermal Barrier Coatings”, *Progr. Mat. Sci.*, **46** 505-553 (2001).
4. N. P. Padture, M. Gell and E. H. Jordan, “Thermal Barrier Coatings for Gas-Turbine Engine Applications”, *Science*, **296** 280-284 (2002).
5. P. K. Wright and A. G. Evans, “Mechanisms Governing the Performance of Thermal Barrier Coatings” *Curr. Opin. Sol. State Phys.*, **4** 255-65 (1999).
6. G. W. Wahl, W. Nemetz, M. Giannozzi, S. Rushworth, D. Baxter, N. Archer, F. Cernuschi, and N. Boyle "Chemical Vapor Depostion of TBC: An Alternative Process for Gas Turbine Components," *Transactions of the ASME,* **123** 520-4 (2001).
7. G. Wahl, Ch. Metz, and S. Samoilenkov "Thermal Barrier Coatings," in Proceedings: Thirteenth European Conference on Chemical Vapor Deposition, EDP Sciences, Les Ulis, France, 2001, pp. Pr3-835-46.
8. H.Yamane and T. Hirai. "Yttria Stabilized Zirconia Transparent Films Prepared by Chemical Vapor Deposition." *Journal of Crystal Growth,* **94** 880-4 (1989).
9. V. G. Varanasi, , T. M. Besmann, (2003). “Parametric Study of the Chemical Vapor Deposition of Yttria-Stabilized Zirconia From Organometallic Precursors,” in Proceedings of

the Electrochemical Society: Chemical Vapor Deposition XVI and EuroCVD 14, Vol. 2, The Electrochemical Society, Pennington, NJ, 2003, pp. 783-9.
10. V. G. Varanasi, T. M. Besmann, T. L. Starr, W. Xu, and T. J. Anderson, "Yttria-Stabilized Zirconia Thermal Barrier Coatings by Metal-Organic Chemical Vapor Deposition," Proc. High Temperature Ceramic Matrix Composites V, in press.
11. C. Dubourdieu, S.B. Kang, Y.Q. Li, G. Kulesha, B. Gallois, "Solid Single-Spurce Metal Organic Chemical Vapor Deposition of Yttria-Stabilized Zirconia," *Thin Solid Films*, **339** 165-73 (1999).
12. H. Holschuh and H. Sur, "Textured (100) Yttria-Stabilized Zirconia Thin Films Deposited by Plasma-Enhanced Chemical Vapor Deposition," *Appl. Phys. Lett.*, **59** 470-2 (1991).
13. Y. Du and Z. P. Jin, "Thermodynamic Calculation of the ZrO_2-$YO_{1.5}$-CaO Phase Diagram." *CALPHAD,* **16** (4) 355-62 (1992).

MODELING OF CHEMICAL VAPOR DEPOSITED ZIRCONIA FOR THERMAL BARRIER AND ENVIRONMENTAL BARRIER COATINGS

Thomas L. Starr
Chemical Engineering Department, University of Louisville, Louisville, KY 40292
E-mail: tom.starr@louisville.edu; Telephone: (502) 852-1073; Fax (502)852-6355

Weijie Xu
Chemical Engineering Department, University of Louisville, Louisville, KY 40292
E-mail: wjx243@yahoo.com; Telephone: (502) 852-2648; Fax (502)852-6355

ABSTRACT

YSZ (Yttria-stabilized zirconia) coatings can provide effective thermal and environmental protection for advanced energy systems. A CVD (chemical vapor deposition) method for applying these coatings offers advantages over the current EB-PVD (electron beam physical vapor deposition) and APS (air plasma spray) application methods. Computer modeling of the process provides understanding of mass transport and reaction kinetics and guides process development at Oak Ridge National Laboratory. Critical requirements for a successful CVD process are high coating deposition rate and uniform coating thickness.

A computer model has been developed to simulate the direct liquid injection CVD process for YSZ. This model has been validated by experimental work at ORNL using a coupon-scale (2 cm), one-sided substrate and mixed zirconium and yttrium butoxide precursors. As compared to the diketonates used previously, butoxide precursors are more soluble in liquid solvents and provide higher gas phase concentrations. This yields higher deposition rate and allows greater inlet-to-substrate distances.

Current efforts focus on design of a subscale development reactor to demonstrate uniform, high rate deposition on both sides of a 10-12 cm substrate. This configuration and dimension is comparable to the cross-flow dimension in a full-scale gas turbine blade. The computer model is used to evaluate design options for holding and heating the substrate and for introducing the precursor vapor. Methods developed with the subscale reactor should be transferable to future design of a full scale turbine blade coating system.

Model results for a number of reactor configurations are presented. These illustrate design tradeoffs that must be evaluated. Control of precursor vapor flow pattern is a critical issue that fundamentally controls the uniformity of coating thickness.

Overall, these modeling results support the feasibility of a direct liquid injection CVD process for deposition of thermal and environmental barrier coatings on advanced energy system components.

INTRODUCTION

Thermal and environmental barrier coatings are important components of current and future energy systems. Such coatings – applied to hot, metallic surfaces in combustors, heat exchanger and turbines – increase the allowable operating temperature and increase the efficiency of the energy system. Because of its low thermal conductivity and high thermal expansion yttria-stabilized zirconia (YSZ) is the material of choice for protection of structural components in many high temperature applications. Current coating application methods have their drawbacks, however. Air plasma spray (APS) is a relatively low-cost process and is suitable for large and relatively complex shapes. It is difficult to produce uniform, relatively thin coatings with this process, however, and the coatings do not exhibit the columnar microstructure that is needed for reliable, long-term performance. The electron-beam physical vapor deposition (EB-PVD) process does produce the desirable microstructure, however, the capital cost of these systems is very high and the line-of-sight nature of the process limits coating uniformity and the ability to coat large and complex shapes.

The chemical vapor deposition (CVD) process also produces the desirable columnar microstructure and – under proper conditions – can produce uniform coatings over complex shapes. The overall goal of this project – a joint effort of the University of Louisville and Oak Ridge National Laboratory (ORNL) – is to develop the YSZ CVD

process for application of thermal barrier coatings for fossil energy systems. Last year's report described our refinement of a computer model to simulate experimental results at ORNL over the full range of process temperatures and pressures and our use of that model to discover factors that limit coating deposition rate in the direct-liquid-injection CVD process.

DISCUSSION OF CURRENT ACTIVITIES

Based on process modeling results we identified a new precursor solution with potential for significantly increasing the YSZ deposition rate. Experimental results at ORNL confirmed this prediction. Adjusting reaction kinetics parameters to match these experiments we initiated design of a reactor for uniform coating of a sub-scale turbine blade substrate.

INCREASE COATING DEPOSITION RATE

Computer modeling research at the University of Louisville is being performed in order to provide understanding of transport and kinetics factors that control the deposition process and to develop a tool for reactor design and optimization. This research uses a commercial fluid dynamics code (CFD-ACE from CFD Research Corporation, Huntsville, AL) with an axisymmetric 3-D model for heat, momentum and mass transport throughout the reactor. Details of the reactor geometry and reactor simulation model were given in the previous report[1]. Many variables in the model are determined by experimental parameters of the reactor. Vapor composition and gas flow rate, substrate and nozzle temperatures, pressure and geometry are experimentally set and determine the boundary conditions for the model. Physical parameters of the materials and fluids in the model, such as viscosity, thermal conductivity and species diffusion coefficients, are known from measurement or from well-established estimation methods. The principal uncertainty in the model is specification of the chemical reactions that lead to deposition of solid YSZ on the substrate.

Model results (Figure 1) show that, in the region between the inlet and substrate, temperature, fluid flow and concentration profiles closely approximate those expected for ideal stagnation point flow, i.e. temperature and axial velocity are independent of radial position and depend only on height above the substrate surface. Precursor

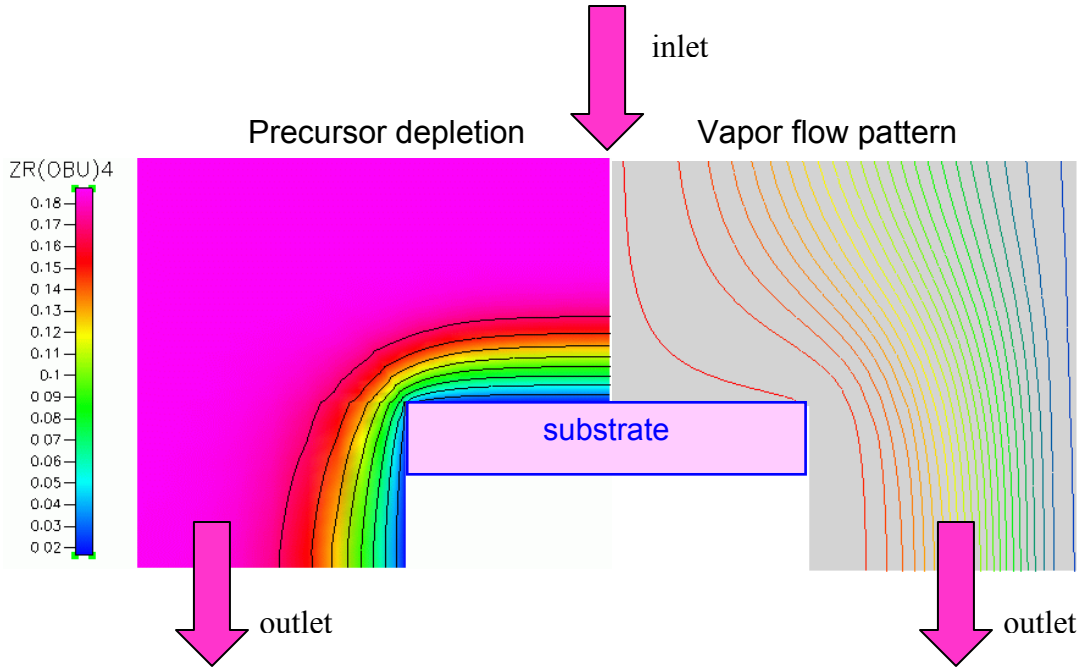

Figure 1. Local deposition rate is controlled by precursor depletion and vapor flow pattern.

concentrations above the substrate are nearly independent of radial position and show 90% depletion at the surface for temperatures above approximately 930°C. Under these conditions the YSZ deposition rate is controlled primarily by the rate of diffusion across a mass-transport pseudo-boundary, $DC_o/\Delta L$, where D is the precursor species gas phase diffusion coefficient, C_o is the gas phase precursor concentration at the inlet and ΔL is the width of the boundary layer.

In experimental work at ORNL using $Zr(tmhd)_4$ and $Y(tmhd)_3$ as precursors, the maximum deposition rate was less than 10 μm/hr – too low for a practical system which must apply coatings up to 300 μm in thickness. Since substantially increasing the precursor diffusion coefficient, D, or decreasing the boundary layer thickness, ΔL, is not possible the only feasible method for substantially increasing deposition rate is to increase the inlet precursor concentration. For liquid injection CVD the gas phase precursor concentration is closely related to its concentration in the liquid solution.

Many metal-organic materials have been used as precursors for the CVD of YSZ. Basically, there are two kinds of precursors: β-diketonates and alkoxides. Table 1 lists physical and chemical properties of the two β-diketonate precursors used in the initial experimental work at ORNL: $Zr(tmhd)_4$ and $Y(tmhd)_3$. The air and moisture stability of these compounds make them attractive for use in CVD. Another result of this stability is their high melting temperatures which limit their vapor pressures, solubilities in liquid solvents and, ultimately, the achievable coating deposition rate.

In general, metal alkoxides have lower stability and melting points than β-diketonates, and thus, higher volatility and liquid solubility. For example, zirconium n-butoxide has very high solubility in butanol solvent at room temperature and a commercially-available solution (Table 1) has 100X higher concentration of precursor than the $Zr(tmhd)_4$ solution used previously (2.2 M versus 0.022 M). Yttrium butoxide also is available as a liquid solution at moderately high concentration (0.5 M). Handling of these precursors in liquid solution form is expected to reduce exposure to moisture and air and to provide better stability in use. In addition these alkoxide precursors are less expensive than the β-diketonates.

Table1. Selected metal organic precursors for YSZ

Description	Chemical Formula	BP/MP (°C)	Other	Price
β-diketonates				
Tetrakis (2,2,6,6-tetramethyl-3,5-heptanedionato) zirconium	$Zr(C_{11}H_{19}O_2)_4$	MP 318-320	stable	$62/5g
Tris (2,2,6,6-tetramethyl-3,5-heptanedionato) yttrium	$Y(C_{11}H_{19}O_2)_3$	MP 170-173	stable	$115/5g
Metal alkoxides				
Zirconium n-butoxide	$Zr(OC_4H_9)_4$	BP 243 (0.1 mm)	moisture sensitive	$14/50g (76-80% in n-butanol)
Yttrium butoxide	$Y(OC_4H_9)_3$	BP 109 (760 mm)	moisture sensitive	$48/25ml (0.5 M in toluene)

Our previous modeling of ORNL experiments showed that deposition rate was limited by the gas phase concentration which, in turn, was limited by the low liquid solubility of the β-diketonates precursors. These model results suggested a switch to alkoxide precursors. This proposed change was validated by ORNL experiments which showed much higher deposition rate even with increasing the substrate-nozzle distance from 1 to 20 cm. Varanasi et al.[2] used yttrium and zirconium butoxide dissolved in toluene and n-butanol, respectively as precursors to give a high deposition rate (~45 μm/hr) as shown in Figure 2.

In general the CVD model can include all gas phase and surface reactions involved in the process. In the ORNL system the reactions are carried out at low pressure (7 torr) and the solvent concentration in the gas phase is low due to the large amount of the oxygen carrier gas. Therefore, gas phase reactions and the solvent pyrolysis reactions at the substrate surface are not included in our model.

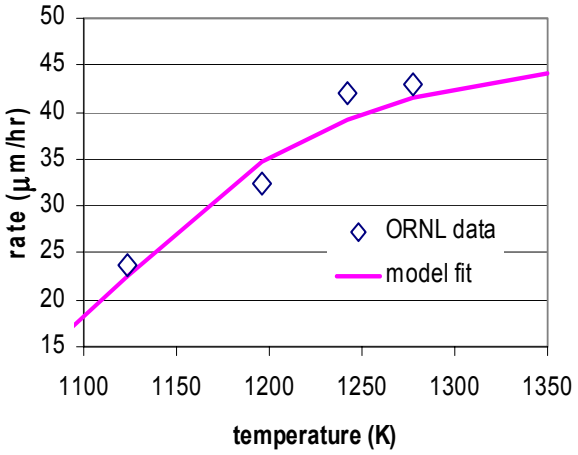

Figure 2. Experiment (solid symbol) and model (open symbol) deposition rate at low pressure (7 torr).

At the solid surface zirconia and yttria precursor reaction rates are given by Arrhenius-type equations, first-order with respect to the concentration of the precursor species at the surface.

$$Zr(OBut)_4 \rightarrow ZrO_2(s) + \text{volatile species} \quad (1a)$$
$$2\ Y(OBut)_3 \rightarrow Y_2O_3(s) + \text{volatile species} \quad (1b)$$

Rate constants and activation energies for these reactions are selected to best fit the experimental results.

Model boundary conditions are set to match ORNL experimental conditions for YSZ with nozzle temperature of 200 ^oC, substrate temperatures of 770 to 1000 ^oC, oxygen flow of 1200 sccm and precursor solution flow of 0.87 ml/min. The precursor solution is a mixture of 63 ml zirconium n-butoxide 80%wt in butanol and 25 ml yttrium butoxide 0.5M in toluene, yielding a metal composition Y/(Y+Zr) =0.165.

Experiment and model results are shown in Figure 2. The deposition rate increases significantly from 770 to 970 ^oC but is nearly unchanged above this temperature. Model results show precursor species at the surface are more than 80% depleted at 1000 ^oC leading to transport control of the deposition rate.

DESIGN OF A SUB-SCALE REACTOR

With the successful completion of lab-scale YSZ-CVD experiments and model development, we have started the design of a CVD reactor for coating of a larger specimen. Figure 3 shows our proposed specimen which is a 12 cm x 3 cm x 2 mm rectangle. This geometry is closer to the actual turbine blade geometry than the 2 cm diameter substrate used previously. The CVD model will be used to evaluate reactors with different inlet and outlet configurations with the goal of achieving high deposition rate (20-100 μm/hr) and high uniformity (variation less than 10%).

Local deposition rate is controlled by precursor depletion and vapor flow pattern. Balancing these can achieve uniform coating thickness. From Figure 4 we can see that temperature is an important factor affecting both the deposition rate and the uniformity. At the low substrate temperature (1000 K), the deposition rate is relatively low but the uniformity is good. Increasing the temperature to 1300 K substantially increases the average deposition rate but the uniformity is poorer. The mass transport boundary layer becomes thinner as the flow passes over the substrate edge and turns toward the outlet, producing an increase in coating rate along the outer part of the specimen. Successful coating of larger substrates will require careful control of the vapor flow pattern.

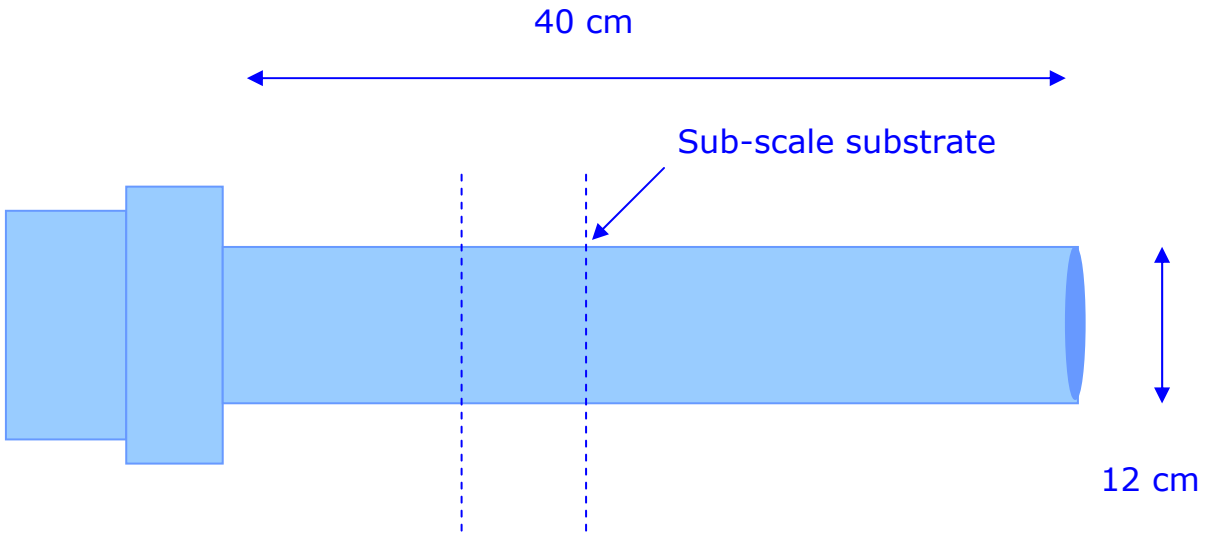

Figure 3. Sub-scale substrate will demonstrate two-sided deposition over a length comparable to the width of a full-scale gas turbine blade.

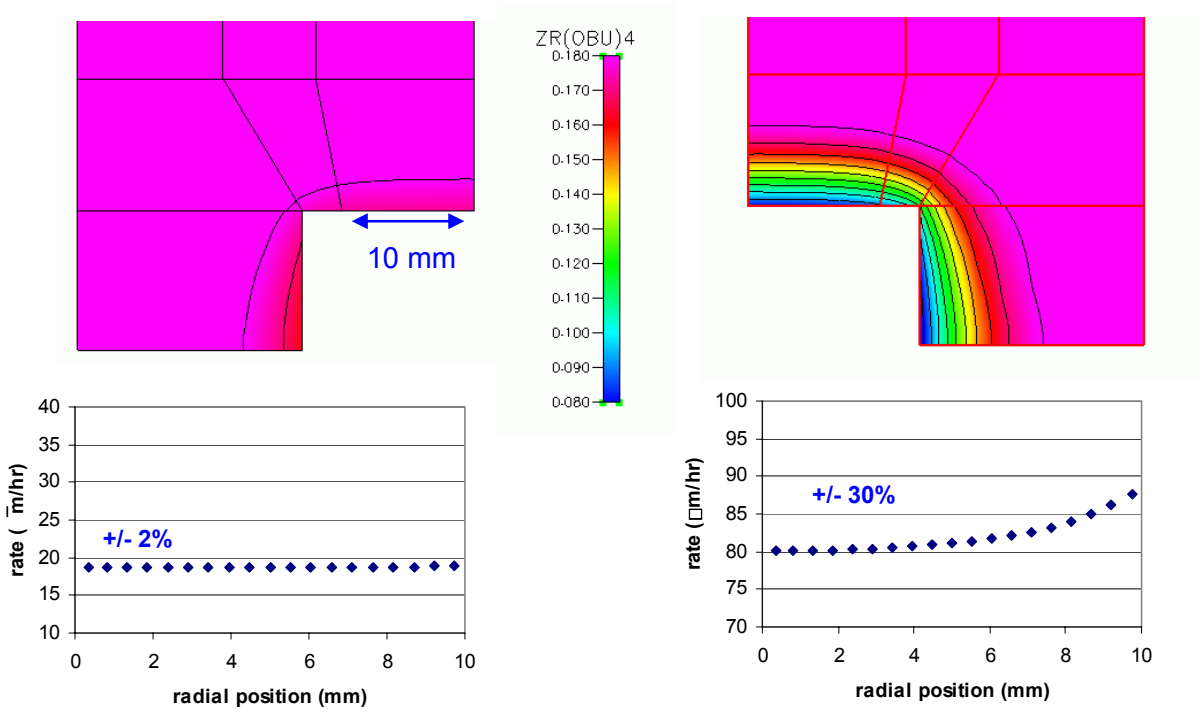

Figure 4. At 1000 K deposition rate is uniform across the substrate but relatively low (left). At 1300 K the deposition rate is higher but uniformity is poor (right).

With the 12 cm x 3 cm substrate dimensions a rectangular reactor design (Figure 5) provides a small volume for better precursor usage and allows control of the flow pattern by changing the inlet and outlet positions. The finite element model for analysis of vapor flow and deposition rate takes advantage of the symmetry of the system. Basic flow geometry variations include two side inlets with top or bottom outlet.

Figures 6 through 9 show model results for various configurations and process conditions. With one outlet (top or bottom) the deposition is non-uniform with the highest deposition rate near the outlet. The poor uniformity for this geometry is the result of a recirculation zone near the part of the substrate away from the outlet, producing significant precursor depletion. Increasing the velocity increases the deposition rate and improves the uniformity somewhat. Higher temperature increases the deposition rate but decreases the uniformity. A two outlet (top and bottom) configuration shows improved deposition uniformity as a result of more uniform velocity and precursor depletion along the substrate surface. Variation over the 12 cm substrate is 14% and 7% for 1300 K and 1000 K respectively.

Additional improvement in deposition uniformity can be obtained by alternating the outlet position during the coating run. Figure 10 shows the results of switching the outlet from top to bottom midway through the run and of a three-part switching that include one-third of the run with both outlets open. This dynamic alternation of outlet position provides the opportunity to "average out" variations that are inherent in the various steady-state configurations.

CONCLUSIONS

High deposition rate was achieved with change to alkoxide precursors. Uniform coating over 12 cm can be achieved through control of gas flow pattern. Future work includes designing detail of sub-scale research reactor, investigating surface kinetics and nucleation processes that control coating microstructure and composition, investigating process monitoring and control methods and developing 3-D model for design of full turbine blade deposition system.

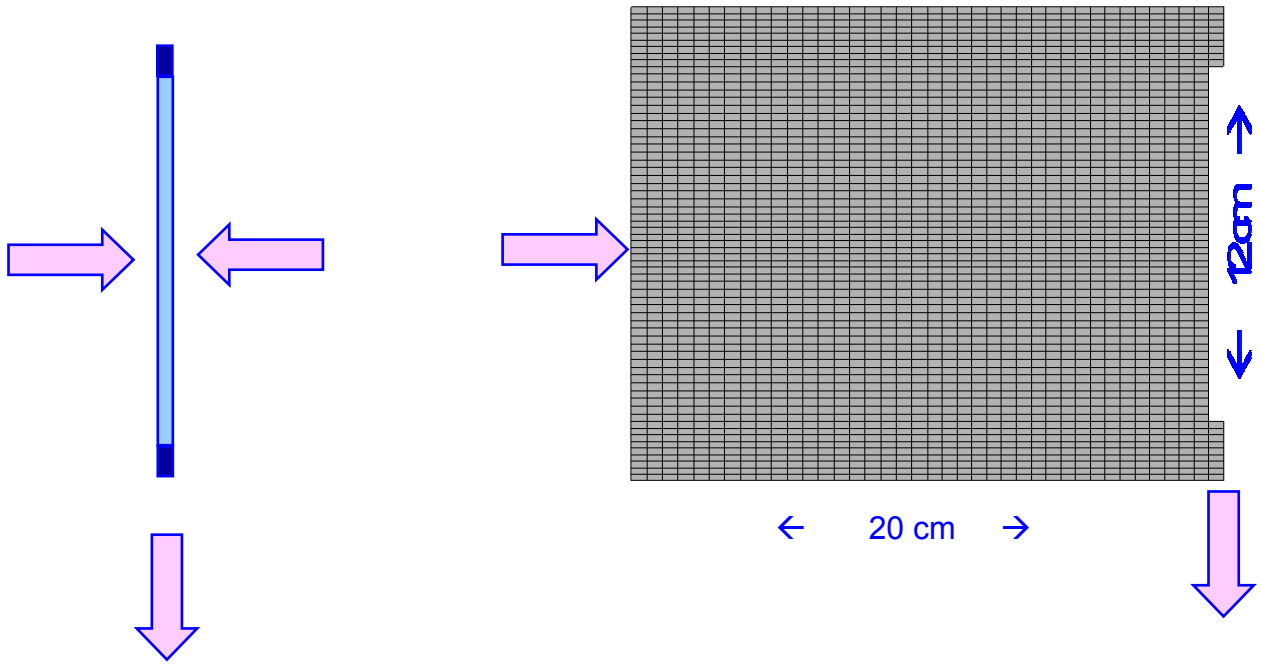

Figure 5. One design for a coating system uses impinging flow onto both faces of the sub-scale specimen (left). Modeling of a rectangular reactor with this configuration uses a finite element grid of one symmetric half (right).

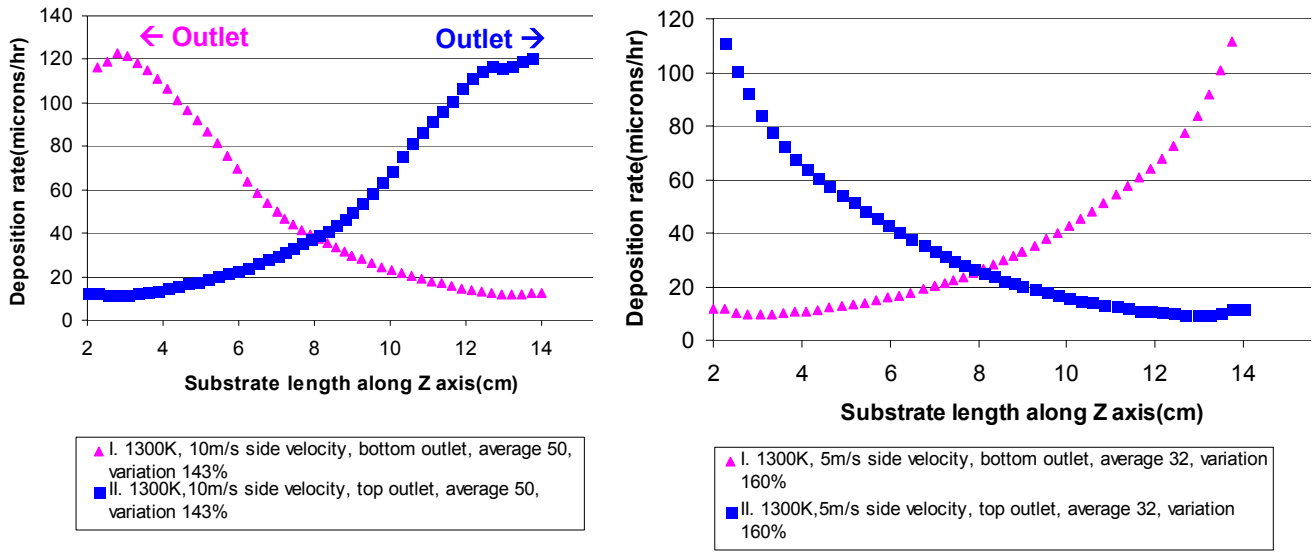

Figure 6. Coating rate and uniformity vary with inlet flow rate and location of outlet. Average deposition rate over the substrate is calculated from 3 cm to 13 cm. The variation is calculated as (maximum – average)/average x 100

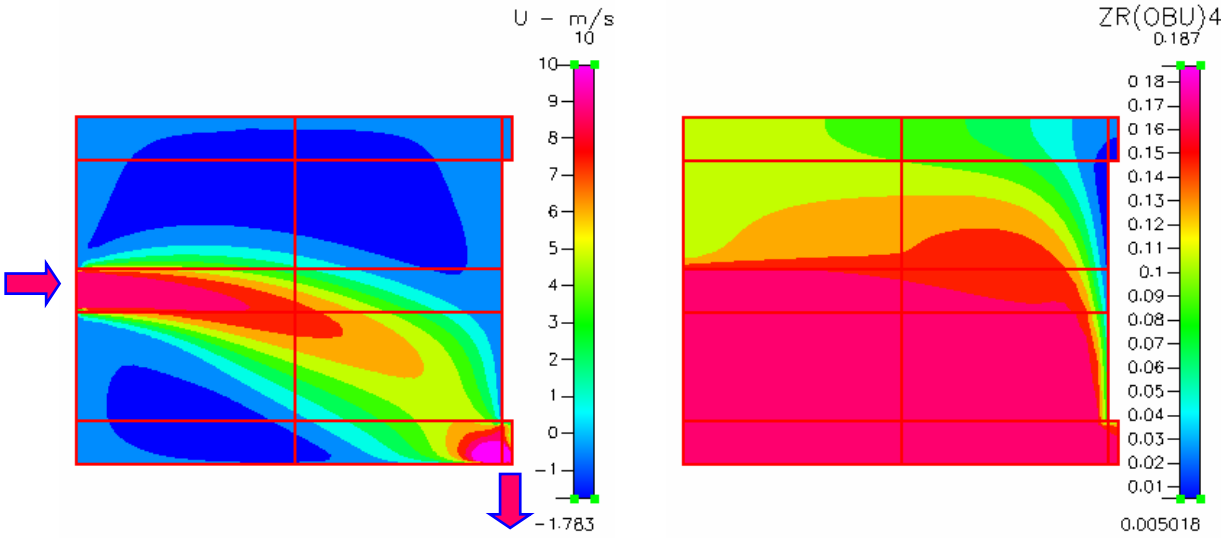

Figure 7. Model results for 1300 K and 10 m/s inlet velocity with the bottom outlet configuration show non-uniform deposition. Velocity vector plot (left) show recirculation zones in upper and lower left corners. Depletion of precursor (right) produces low deposition rate on the upper part of the substrate.

REFERENCES

1. T.L. Starr, W. Xu, T.M. Besmann and V. Varanasi, "Modeling of Chemical Vapor Deposited Zirconia for Thermal Barrier and Environmental Barrier Coatings" 17th Annual Conference on Fossil Energy Materials, Baltimore, MD April 22-24, 2003.
2. T.M. Besmann, V. G. Varanasi, J.J. Henry, W. Xu and T.L. Starr, 'YSZ Thermal Barrier Coatings by MOCVD" 18th Annual Conference on Fossil Energy Materials, June 2-4, 2004, Knoxville, TN.

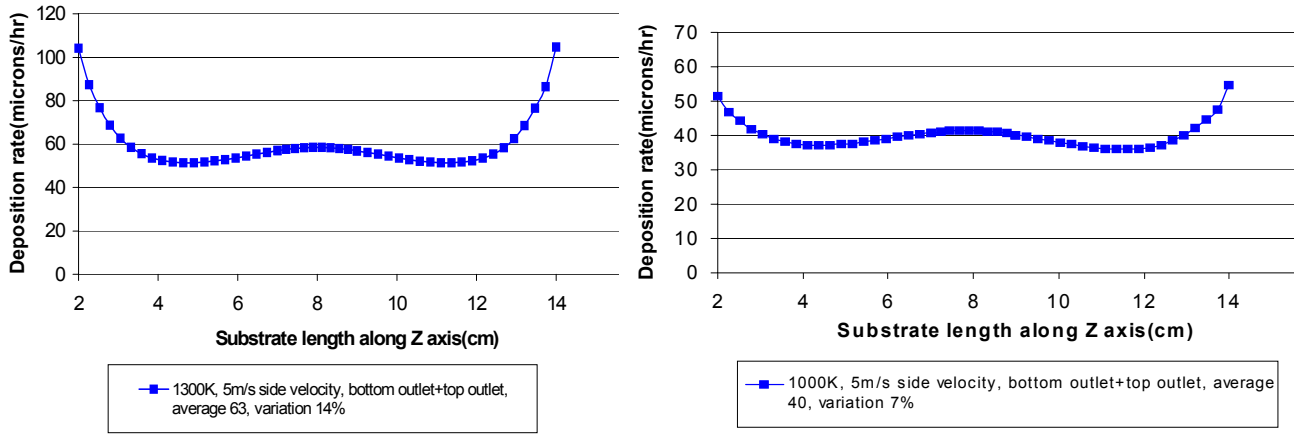

Figure 8. Coating uniformity improves with two outlets - top and bottom. The variation over the 12 cm substrate is 14% and 7% for 1300 K and 1000 K respectively.

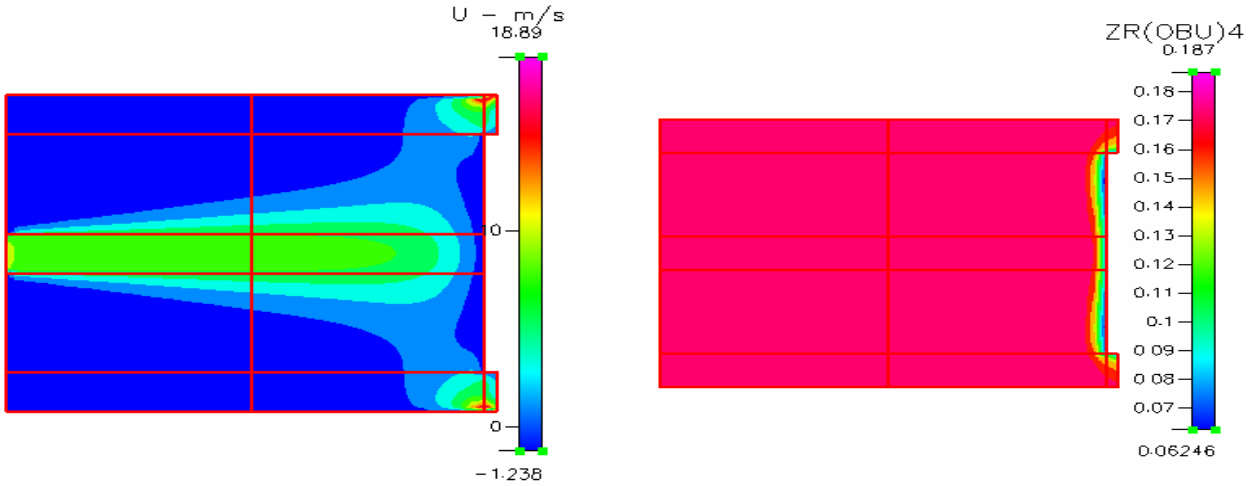

Figure 9. Improved coating uniformity with two outlets is the result of more uniform vapor flow velocity and precursor depletion along the substrate.

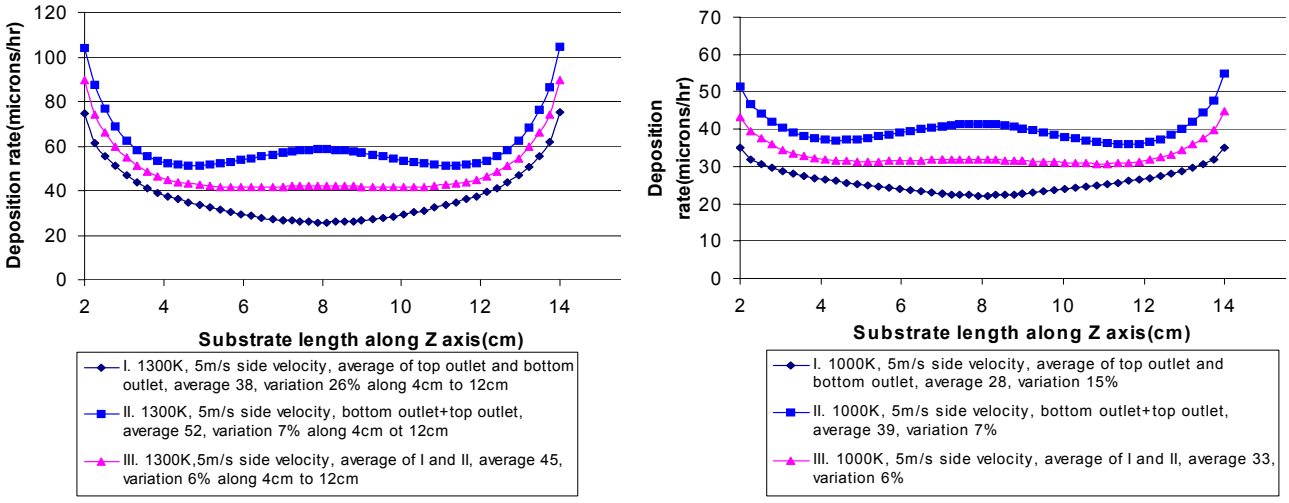

Figure 10. Alternating the outlet position during a coating run provides further improvement in coating uniformity by "averaging out" the variations in each steady state configuration.

CONCEPTS FOR SMART PROTECTIVE HIGH-TEMPERATURE COATINGS

P.F. Tortorelli
Oak Ridge National Laboratory, Oak Ridge, TN 37831-6156
tortorellipf@ornl.gov ; Tel: (865) 574-5119; FAX (865) 241-0215

M.P. Brady
Oak Ridge National Laboratory, Oak Ridge, TN 37831-6115
bradymp@ornl.gov; Tel: (865) 574-5153; FAX (865) 241-0215

I.G. Wright
Oak Ridge National Laboratory, Oak Ridge, TN 37831-6156
wrightig@ornl.gov; Tel: (865) 574-4451; FAX (865) 241-0215

ABSTRACT

Multiphase Mo-Si-B alloys comprise the first material system for evaluating smart coating concepts for high-temperature corrosion resistance in fossil environments. Results from high-temperature exposures in an oxidizing-sulfidizing environment are presented. The α-Mo-Mo_5SiB_2-Mo_3Si system displayed promising sulfidation resistance at 800°C.

INTRODUCTION

The need for high-temperature environmental resistance is a critical material barrier to the operation of fossil systems with the improved energy efficiency and emissions goals of the U.S. Department of Energy's Office of Fossil Energy. All fossil fuel-derived processes contain reactive species and high-temperature degradation arising from reactions of solids with gases and condensible products often limits performance or materials lifetimes such that efficiency, emission, and/or economic targets or requirements are not realized. Therefore, historically, the development of materials for fossil-fuel combustion and conversion systems has been closely linked to corrosion studies of alloys and ceramics in appropriate environments. This project is somewhat different; it focuses on the feasibility of new routes to controlling the critical chemical and mechanical phenomena that collectively form the basis for environmental protection in relevant fossil environments by exploring compositional and microstructural manipulations and cooperative phenomena that have not necessarily been examined in any detail to date. This can hopefully lead to concepts for "smart" coatings or materials that have the ability to sense and respond appropriately to a particular set or series of environmental conditions in order to provide high-temperature corrosion protection.

The strategies being explored involve cooperative or in-place oxidation or sulfidation reactions of multiphase alloys.[1,2] The first material systems to be evaluated involve silicides as there is some evidence that such materials have enhanced resistance in oxidizing-sulfidizing and sulfidizing environments and in air/oxygen at very high temperatures.[3] In this regard, molybdenum silicides may prove to be of particular interest. Molybdenum is known to sulfidize fairly slowly[4] and there has been recent progress in developing Mo-Si-B systems with improved oxidation resistance at high and intermediate temperatures.[5-11] Consequently, the high-temperature oxidation and sulfidation behaviors of multiphase

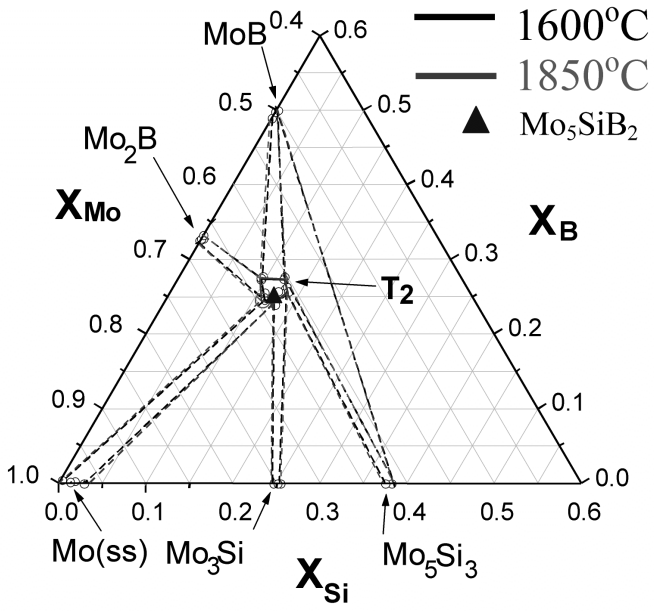

Fig.1. Partial Mo-Si-B phase diagram. Axes are in at.%.

Mo-Si-B alloys with different compositions and phase morphologies have been, and are being, studied.[12,13]

RESULTS AND DISCUSSION

Results from cyclic oxidation exposures of three-phase Mo-Si-B alloys have been reported previously.[8,12,13] There was a clear differentiation in oxidation behavior among the different compositions and phase assemblages at 1200°C. The multiphase alloys, α-Mo-Mo_5SiB_2-Mo_3Si, Mo_5Si_3(-B)-Mo_5SiB_2-Mo_3Si, and Mo_5Si_3(-B)-MoB-$MoSi_2$ (see Fig. 1), showed substantially better cyclic oxidation resistance than the single-phase Mo_5Si_3(-B) compositions. The results for the specimens with α-Mo suggested a multistage mechanism in which the Mo is rapidly removed by formation of volatile MoO_3 and the resulting near-surface enrichment in silicon and boron facilitates the formation of a protective borosilicate or silica layer that grows laterally to seal the remaining Mo-rich areas of the alloy from the environment.[13] Following Gesmundo and Gleeson,[1] this process would be categorized as a cooperative oxidation phenomenon.

The sulfidation resistance of α-Mo-Mo_5SiB_2-Mo_3Si alloys was evaluated by isothermally exposing specimens to an H_2-H_2S-H_2O-Ar gas mixture at 800°C for 100-150 h. At this temperature, the gas composition yielded a p_{S_2} of ~10^{-6} atm and a p_{O_2} of ~10^{-22} atm. This environment represents severe coal gasification conditions, but has been used previously to evaluate the corrosion of the most sulfidation-resistant alloys.[14,15] Furthermore, calculations based on equilibrium thermodynamics predict that Mo-Si alloys should form SiO_2 and MoS_2 under these conditions (Fig.2). Gravimetric results are shown in Fig. 3, which also includes typical data for a very sulfidation-resistant alloy, Fe_3Al,[14,16] another alumina-former (FeCrAl), and a model austenitic stainless steel (based on the nominal Cr and Ni concentrations of type 310). The different α-Mo-Mo_5SiB_2-Mo_3Si specimens (same Mo concentration, 34 vol%, but differing coarseness of the microstructure) showed similar gravimetric behavior representative of very good sulfidation resistance.

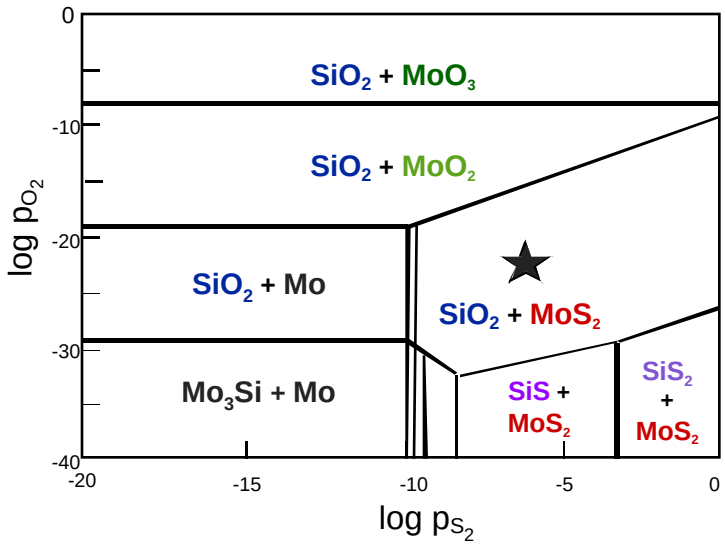

Fig. 2. Calculated product stability diagram for Mo-Si as a function of the partial pressures of oxygen and sulfur. The star represents partial pressures of H_2-H_2S-H_2O-Ar gas mixture used for oxidation-sulfidation exposures at 800°C.

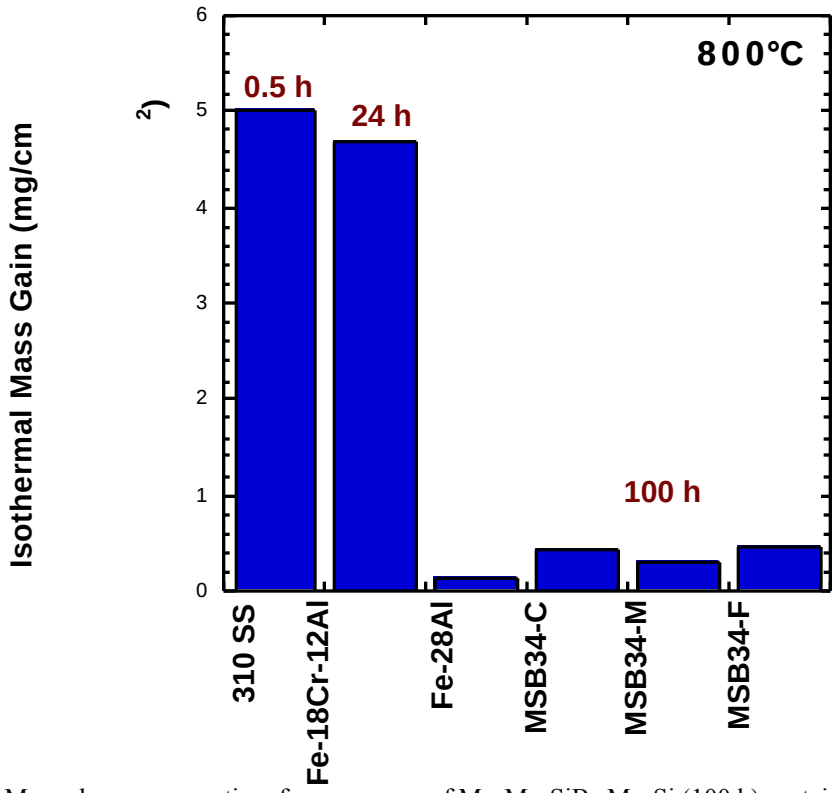

Fig. 3. Mass change versus time for exposures of Mo-Mo_5SiB_2-Mo_3Si (100 h), a stainless steel model alloy (Fe-27%Cr-19%Ni, 0.5 h), and a FeCrAl alloy (24 h) to H_2-H_2S-H_2O-Ar at 800°C. C,M, and F refer to coarse, medium, and fine phase dispersions. Concentrations are in at.%.

Because only thin corrosion products were observed on the α-Mo-Mo_5SiB_2-Mo_3Si (Fig. 4) after the exposures under oxidizing-sulfidizing conditions, x-ray diffraction (XRD) could not definitively determine their compositions. However, there was some XRD evidence that sulfides had formed. Typically, the Mo_3Si+T2 phase mixture was observed to be in relief above the α-Mo phase. This could be due to the formation of volatile MoO_3, but, as shown in Fig. 2, this is not expected under the present exposure conditions. Alternatively, there could be preferential spallation of the product that forms on the α-Mo phase (most likely MoS_2, see Fig. 2). A remnant of a scale formed on the α-Mo phase was observed – see Fig. 5, which also shows one part of this layer in the process of spalling. As these products are thin and can easily reform on the α-Mo phase, such spallation may not be an important issue, but will need to be investigated in more detail.

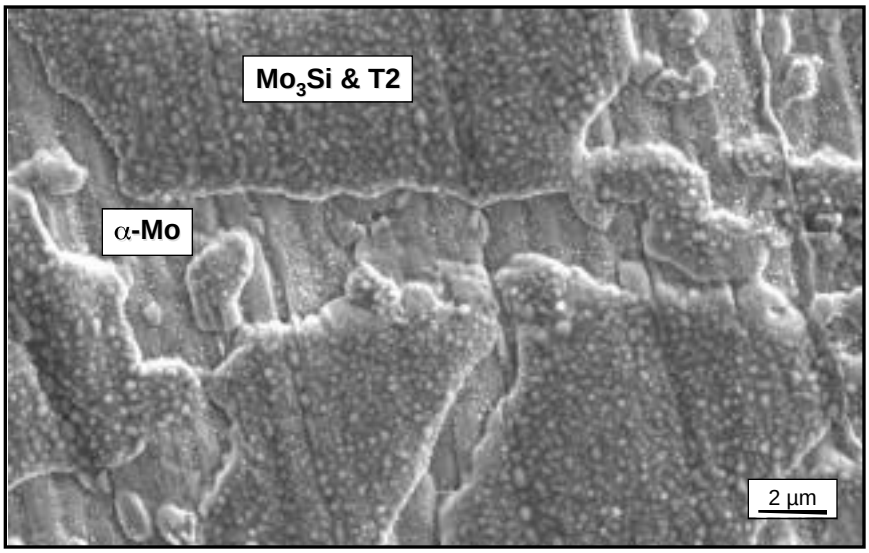

Fig. 4. Scanning electron micrograph of the surface of a specimen of α-Mo-Mo_5SiB_2-Mo_3Si after exposure to H_2-H_2S-H_2O-Ar at 800°C for 150h.

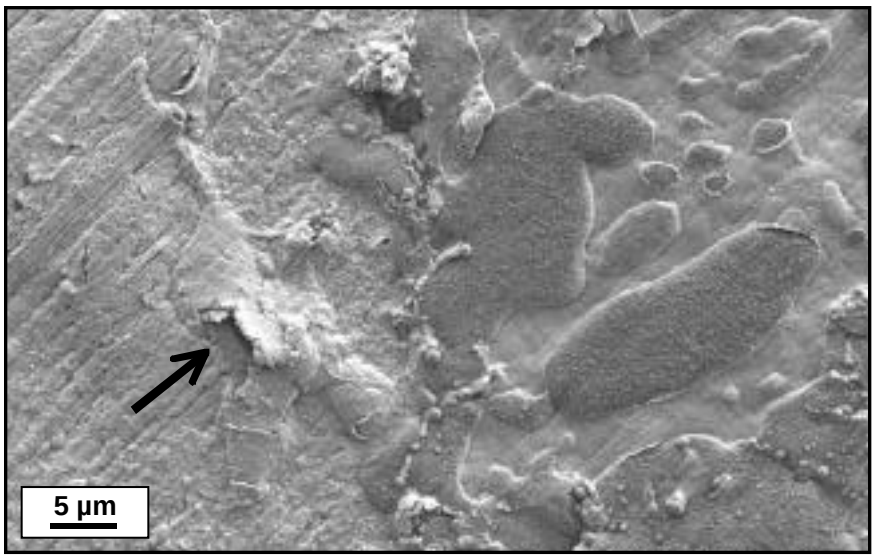

Fig. 5. Scanning electron micrograph of the surface of a specimen of α-Mo-Mo_5SiB_2-Mo_3Si after exposure to H_2-H_2S-H_2O-Ar at 800°C for 100h. Arrow indicates site of spalling of scale formed on α-Mo phase

As shown in Figs. 4 and 5, the various phases in the α-Mo-Mo_5SiB_2-Mo_3Si alloy appeared to react with the environment independently of each other. These observations suggest that, under the current exposure conditions, this alloy exhibits the "in-place" (or "independent") mode of multiphase oxidation.[1] This is in contrast to the cooperative process observed for purely oxidizing conditions at higher temperatures (see above). For in-place reactions, it is expected that the coarseness of the phase distribution should not have a major effect on corrosion behavior and this is what is observed in the gravimetric results under oxidizing-sulfidizing conditions: there is no significant difference in mass change among those specimens with fine, medium, and coarse phase dispersions (Fig. 3).

Future work will include detailed cross sectional analyses of the sulfidized specimens as well as exposures of other variants of the base α-Mo-Mo_5SiB_2-Mo_3Si phase field. Also, oxidation exposures at 800°C will be conducted so as to directly compare behavior at 800°C under oxidizing and oxidizing-sulfidizing conditions. The knowledge gained about the different modes of reaction in different environments will be used to help explore further phase-size and composition manipulations in the Mo-Si-B system in order to evaluate the possibilities of developing such alloys as smart protective coatings. A similar approach will be used with the Ti-Al-Cr system.

SUMMARY

Smart protective coatings may provide one of the breakthrough areas to overcome materials barriers imposed by the requirements of advanced fossil energy systems. To this end, multiphase molybdenum silicides with boron are being examined as the first material system for evaluating smart coating concepts for high-temperature corrosion resistance in fossil environments. The present work confirmed that Mo-rich, B-containing silicides can have good high-temperature sulfidation resistance.

ACKNOWLEDGEMENTS

Research sponsored by the Office of Fossil Energy Advanced Research Materials Program, U. S. Department of Energy, under contract DE-AC05-00OR22725 with UT-Battelle, LLC.

REFERENCES

1. F. Gesmundo and B. Gleeson, *Oxid. Met.* 44 (1995) 211-37.

2. M. P. Brady, B. Gleeson and I. G. Wright, *JOM* 52 (2000) 16-21.

3. M. P. Brady, B. A. Pint, P. F. Tortorelli, I. G. Wright and R. J. Hanrahan Jr., pp. Chapter 6 in Corrosion and Environmental Degradation of Materials, M. Schütze (eds.), Wiley-VCH, Weinheim, Germany, 1999.

4. S. Mrowec, *Oxid. Met.* 44 (1995) 177-209.

5. M. K. Meyer and M. Akinc, *J. Am. Ceram. Soc.* 79 (1996) 938-944.

6. D. M. Berczik, "Oxidation Resistant Molybdenum Alloys," U.S. Patent, 5,693,156, 1997

7. M. K. Meyer, A. J. Thom and M. Akinc, *Intermetallics* 7 (1999) 153-62.

8. K. Natesan and S. C. Deevi, *Intermetallics* 8 (2000) 1147-58.

9. M. G. Mendiratta, T. A. Parthasarathy and D. M. Dimiduk, *Intermetallics* 10 (2002) 225-32.

10. J. H. Schneibel, P. F. Tortorelli, M. J. Kramer, A. J. Thom, R. O. Ritchie and J. J. Kruzic, paper BB.2 in Proc. Symp. On Defect Properties and Related Phenomena in Intermetallic Alloys, E. P. George, H. Inui, M. J. Mills and G. Eggeler (eds.), The Materials Research Society, Pittsburgh, 2002.

11. V. Supatarawanich, D. R. Johnson and C. T. Liu, *Mater. Sci. Eng. A* 344 (2003) 328-39.

12. P. F. Tortorelli, B. A. Pint, K. L. More, A. J. Thom and M. Akinc, Proc. ORNL Fossil Energy Program Annual Report for April 2000 to March 2001, R. R. Judkins and P. T. Carlson (eds.), ORNL/TM-2001/89, 2001.

13. P.F. Tortorelli, J.H. Schneibel, K.L. More, and B.A. Pint, *Proc. Sixth Int'l. Symp. High Temp. Corrosion and Protection of Mat'ls.*, 2004, accepted for publication in *Mater. Sci. Forum.*

14. J.H. DeVan and P.F. Tortorelli, *Mater. at High Temp.* 11 (1993) 30-35.

15. K. Natesan and P.F. Tortorelli, pp. 265-80 in Nickel and Iron Aluminides: Processing, Properties, and Applications, S. C. Deevi, V. K. Sikka, P. J. Maziasz and R. W. Cahn (eds.), ASM International, Materials Park, OH, 1997.

16. J. H. DeVan, pp. 107-15 in Oxidation of Intermetallics, T. Grobstein and J. Doychak (eds.), TMS, Warrendale, PA, 1989.

CORRODION PROBES FOR FIRESIDE MONITORING IN COAL-FIRED BOILERS

Bernard S. Covino, Jr., Gordon R. Holcomb, Stephen D. Cramer, Sophie J. Bullard, Margaret Ziomek-Moroz
Albany Research Center, U. S. Dept of Energy, 1450 Queen Ave, S. W., Albany, OR 97321
E-mail: covino@alrc.doe.gov; Telephone: (541) 967-5828; Fax: (541) 967-5914
E-mail: holcomb@alrc.doe.gov; Telephone: (541) 967-5874; Fax: (541) 967-5914
E-mail: cramer@alrc.doe.gov; Telephone: (541) 967-5924; Fax: (541) 967-5914
E-mail: bullard@alrc.doe.gov; Telephone: (541) 967-5989; Fax: (541) 967-5914
E-mail: moroz@alrc.doe.gov; Telephone: (541) 967-5943; Fax: (541) 967-5914

David A. Eden and Michael S. Cayard
InterCorr International Inc., 14503 Bammel North Houston, Suite 300, Houston, TX 77014
E-mail: daeden@intercorr.com, Telephone: (281) 444-2282; Fax: (281) 444-0246
E-mail: mcayard@intercorr.com ; Telephone: (281) 444-2282; Fax: (281) 444-0246

ABSTRACT

Electrochemical corrosion rate (ECR) probes were constructed and exposed along with mass loss coupons in a $N_2/O_2/CO_2/H_2O$ environment to determine ECR probe operating characteristics. Temperatures ranged from 450º to 600ºC and both ECR probes and mass loss coupons were coated with ash. Results are presented in terms of the probe response to temperature, the measured zero baseline, and the quantitative nature of the probes. The effect of Stern-Geary constant and the choice of electrochemical technique used to measure the corrosion rate are also discussed. ECR probe corrosion rates were a function of time, temperature, and process environment and were found to be quantitative for some test conditions. Measured Stern-Geary constants averaged 0.0141 V/decade and the linear polarization technique was found to be more quantitative than the electrochemical noise technique.

INTRODUCTION

Increasing the efficiency of the Rankine cycle in coal combustors can be accomplished by increasing heat exchanger steam temperatures and pressures, as is done in supercritical and ultra supercritical units. The benefits of increasing energy conversion efficiencies are reduced consumption of fossil fuels (coal, oil, and gas) and reduced emission of greenhouse gases (CO_2). In order to achieve both of these benefits, it is necessary to overcome technological challenges related to materials of construction. New materials or material/coating combinations with adequate strength, creep, fatigue, and corrosion resistance will need to be developed. Additional issues are present when alternate fuels are used. While heat exchanger tubes in a coal-fired plants using clean high quality fuel may last 20 to 30 years, tubes in coal-fired plants using lower quality fuel and in some coal gasification plants last only 3 to 5 years.

Problems occur when equipment designed for either oxidizing or reducing conditions is exposed to alternating oxidizing and reducing conditions. The use of low NO_x burners is becoming more commonplace and can produce reducing environments that accelerate corrosion. Complicating the development of corrosion-resistant materials for fireside applications is the influence of ash deposits and thermal gradients on the corrosion mechanism. Ash deposits and thermal gradients have a synergism that greatly increases the corrosive attack on heat exchanging equipment such as waterwalls, reheaters, and

superheaters. One method of addressing corrosion of these heat exchange surfaces is the use of corrosion sensors to monitor when process changes cause corrosive conditions. In such a case, corrosion rate could become a process control variable that directs the operation of a coal combustion or coal gasification system. Alternatively, corrosion sensors could be used to provide an indication of total metal damage and thus a tool to schedule planned maintenance outages.

A number of research efforts have been aimed at developing high temperature corrosion probes for various industries. The majority of the research has been based on the use of electrochemical noise (EN)[1-6] techniques. Others have considered the use of electrochemical impedance spectroscopy (EIS)[3-5] and linear polarization resistance (LPR)[6], zero resistance ammetry (ZRA)[4], and electrical resistance (ER)[4]. However, only a limited effort has been made to quantify[2] the operation of corrosion rate probes. For these probes to be accepted routinely in the power generation industries, it will be necessary to determine if they accurately measure corrosion and the changes in corrosion rate that occur in environments of interest, if the sensor materials have an optimum composition for the intended exposure, and if the sensitivity or accuracy of the sensor changes with exposure time in fireside environments. Once this is established, electrochemical corrosion rate sensors can be used extensively and will allow corrosion rate to become a process variable for power plant operators.

Most electrochemical corrosion rate measurement techniques measure a resistance that is representative of the rate of the corrosion reaction. This is true of the LPR, EN, and EIS techniques. These resistances are related to corrosion rate by the Stern-Geary linear approximation to the Butler-Volmer equation,

$$R_p = R_n = \frac{\Delta E}{\Delta i_{applied}} = \frac{\beta_a \beta_c}{2.303(i_{corr})(\beta_a + \beta_c)} = \frac{B}{(i_{corr})} \qquad (1)$$

where R_p is a resistance obtained from the LPR and EIS techniques, R_n is a resistance obtained from the EN technique, B is the Stern-Geary constant, β_a and β_c are the anodic and cathodic Tafel constants, respectively, and i_{corr} is the corrosion current density from which a corrosion rate may be calculated. The Stern-Geary constant (determined by the Tafel constants) is the only variable that is normally not measured, but commonly assumed to be a value of 0.020 to 0.030 V/decade. Because B is related to Tafel constants, it can be measured using either standard electrochemical polarization techniques or the harmonic distortion analysis (HDA) technique that is used in this report.

The purpose of the research presented here is to address some of the issues that impact the understanding and the use of ECR probes. This report is part of an effort to characterize the long-term stability and performance of probes, and to optimize the choice of sensor materials.

EXPERIMENTAL DETAILS

Electrochemical corrosion rate (ECR) probes were designed and constructed for laboratory experiments using 4130 carbon steel (CS), 304L stainless steel (SS), and 316L SS sensors or electrodes. The probes were covered with ash and exposed, along with mass loss coupons made from the same material, to a mixed gas environment and temperatures that ranged from 450 to 600ºC. The purpose was to determine the operating characteristics of probes and to compare integrated or average corrosion rates obtained from ECR probes to those obtained from mass loss coupons.

Three-sensor electrochemical corrosion rate probes were fabricated using the components shown in Figure 1. The cylindrical piece of ceramic served as the form to contain the sensors. The stainless steel tubing served to isolate the wires from the test environment and provided a path for the wires to exit the high temperature environment. Sensors were embedded within the ceramic form using a water-based high-alumina cement. Final preparation included hand polishing the sensors to a 600 grit finish. The finished probe is shown in Figure 1.

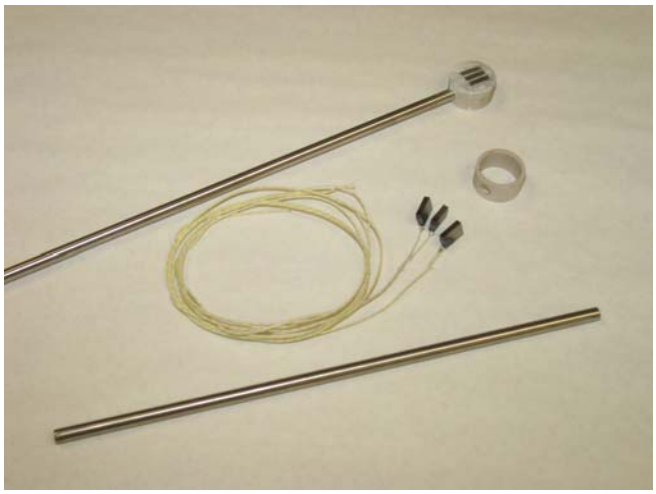

Figure 1 – A completed high temperature corrosion rate probe and the components of construction.

Experiments were conducted using an ash coating and a mixed gas environment identical to those reported previously[7]. The ash was obtained from a municipal incinerator and analyses showed high concentrations of corrosion-causing elements such as S, Cl, Pb, and K. The gas mixture consisted of 68 vol% N_2, 15 vol% H_2O, 9 vol% O_2, and 8 vol% CO_2. Temperatures ranged from 450 to 600ºC. Typical test periods were 100 to 120 hours.

Figure 2 – Electrochemical corrosion rate probe and mass loss coupons prior to testing but after the application of a layer of ash. One coupon (far right) intentionally ash free.

Tests designed to determine the quantitative nature of ECR probes involved exposing four mass loss coupons and the probe to the corrosive environment. Three of the four mass loss coupons were coated with ash on one side while one was left ash free. A slurry of the ash was applied to each of the ash-covered coupons and to the probe. Water was originally used to make the ash slurry; however, methanol was used for later tests. Two of the ash-covered coupons were used to determine the mass loss corrosion rate for comparison to the ECR probe corrosion rate. The third ash-covered coupon was cross-sectioned for analyses to provide mechanistic information. Figure 2 shows the ash-covered probe and ash-covered and ash-free mass loss coupons.

Following exposure to the corrosive environment, ash was scraped from the surface of the mass loss coupons in preparation for chemical cleaning. 4130 CS mass loss coupons were cleaned at 60ºC in a 12 vol% H_2SO_4 plus 0.25 vol% Rodine 95 (inhibitor) solution; the 304L and 316L SS mass loss coupons were cleaned at 25ºC in a 10 vol% HNO_3 solution containing 2 vol% HF.

The corrosion measurement equipment used for this research was the SmartCET system. This system

applies three techniques, EN, LPR, and HDA, to the measurement of corrosion. The application of the three techniques and the appropriate data analysis produces a set of corrosion measurements approximately every 7 minutes. Data, which include EN, LPR, and HDA corrosion rates, an EN pitting factor, and Tafel and Stern-Geary constants from the HDA technique, are collected, displayed, and stored using FieldCET software. A number of other variables, such as solution resistance, skew, and kurtosis, are collected and available for use. The ECR probe corrosion rates were determined by integrating the corrosion rates measured every 7 minutes to calculate the mass loss which was then divided by exposure time and converted to units of a penetration rate of mm/y.

RESULTS AND DISCUSSION

The major emphasis of the research presented here is to evaluate the quantitative nature of ECR probes. In doing so, it became apparent that there were a number of variables that could affect that evaluation. Some of the variables that were considered, electrolyte, zero baseline, electrochemical technique, and Stern-Geary factor, are discussed below.

ECR PROBE RESPONSE AND ELECTROLYTE

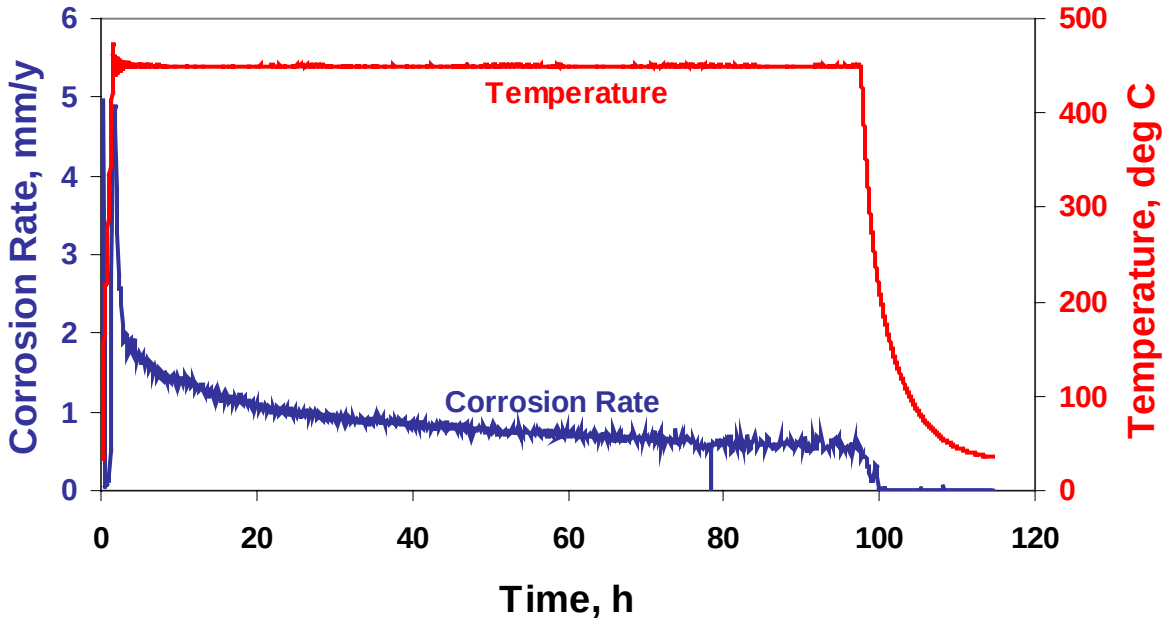

Figure 3 – Typical response of corrosion rate to time and temperature

Because an ECR probe is electrochemical in nature, all parts of an electrochemical cell must be present in order for the technique to work. For the probes used here, that includes the working, counter, and reference electrodes shown in Figure 1, and also an electrolyte that electrically connects the three electrodes. Other investigators[8] have applied salt films to act as the initial electrolyte. In the research presented here, it is the ash layer and then possibly the ash plus corrosion film layers that act as the electrolyte as the corrosion reaction progresses. Figure 3 shows the response of an ECR probe with mild steel sensors to time and temperature. This was the type of behavior that was observed for most of the

experiments conducted here. This type of response suggests that an electrolyte was present because electrochemical techniques were able to measure corrosion rates and changes in corrosion rates. Except for the initial start up time, ECR probe corrosion rates decreased with time to the end of the 100-hour exposure period, Figure 3. This decrease in corrosion rate is the type of response that is typical of materials that form semi-protective corrosion films where the corrosion reaction may be dependant on diffusion of reactants or corrosion products.

ZERO BASELINE

An important property of ECR probes is to have a relatively low baseline corrosion rate when there is no corrosion occurring or when there is no electrolyte present. In order to measure the

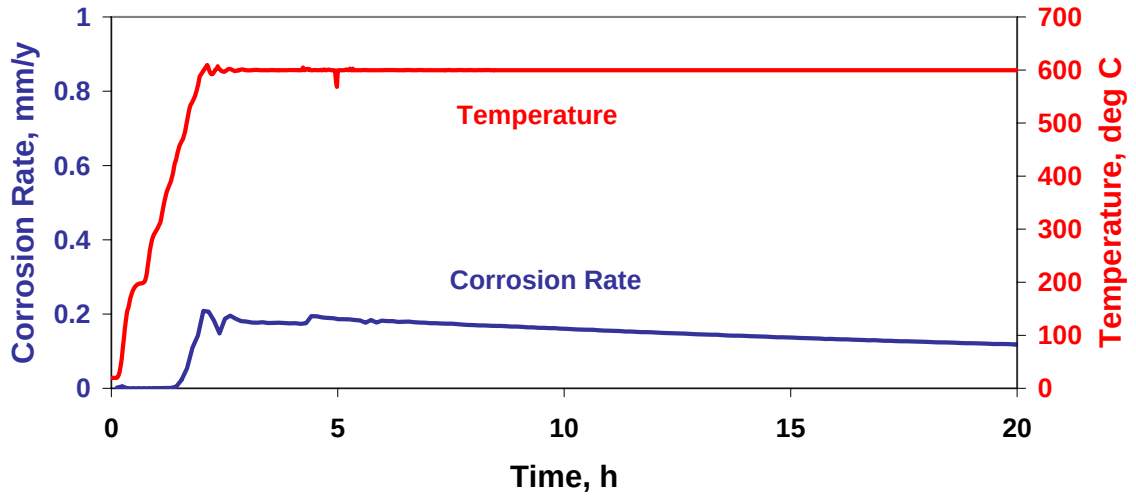

Figure 4 – Zero baseline measured on a 316L SS ECR probe with no ash

zero baseline response, a test was run in which a 316L SS ECR probe was inserted in a nitrogen-filled furnace without any ash or salt film to act as electrolyte. Ideally, the corrosion rates should be zero because there is no electrolyte and no gaseous species to cause corrosion. This was not, however, the case. Figure 4 shows the results of a zero baseline test in which the corrosion rates were not zero. Corrosion rates were zero during part of the heat-up phase of the experiment but started increasing as the temperature exceeded 430ºC and then increased to an average value of 0.16 mm/y as the test environment was changed, at the time that the temperature reached 600ºC, from nitrogen to the $N_2/CO_2/O_2/H_2O$ mixture.

There are two possible reasons for these non-zero corrosion rates. The first would be the formation of some type of film, such as a corrosion product, that covered and electrically connected the three sensor electrodes. For the results presented here, this does not seem likely because there was no visible corrosion product on the ECR probe surface after removing it from the test. A second and more likely possibility is that, at the test temperature, the potting compound surrounding the sensor electrodes was sufficiently electrically conductive to act as the electrolyte for the electrochemical measurement of corrosion rate. Additional zero baseline tests are planned using more resistive potting compounds.

QUANTITATIVE NATURE OF ECR PROBES

Experiments were conducted to compare ECR probe corrosion rates with actual mass loss corrosion rates for coupons and probes exposed in exactly the same environment. Mass loss coupons were cleaned of all ash and scale and corrosion rates were calculated. Data similar to that in Figure 3, for all of the alloys tested, was integrated to determine a cumulative mass loss. This was then used to calculate a corrosion rate for the ECR probe. The corrosion rates in Figure 4 show a good comparison between the ECR and the mass loss corrosion rates for all of the alloys except for the mild steel. Some possible explanations are differences between the ECR probe and the mass loss coupons, corrosion attack that is

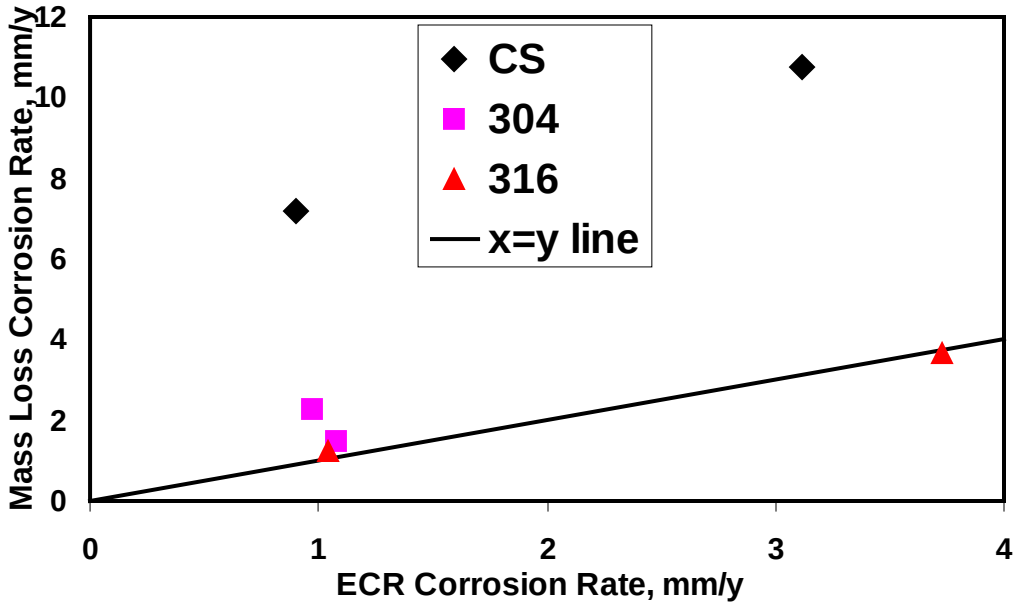

Figure 5 – Comparison of ECR probe to mass loss corrosion rates

non-electrochemical in nature (eg, internal corrosion that can remove whole grains from the matrix without reacting the material) among others. Studies[8] conducted using different conditions (probe construction, coating, and gaseous environment) but with the same SmartCET equipment had good agreement between ECR probe and mass loss corrosion rates. Research is being conducted to determine the reasons for such differences. One change being considered is the use of a profilometer to measure the actual material lost from the ECR probe electrodes rather than relying on mass loss coupons.

EFFECT OF ELECTROCHEMICAL TECHNIQUE

There are a number of electrochemical techniques that can be used to measure the corrosion rates of ECR probes. All of the currently significant techniques were mentioned earlier in this report. Of those, data from the LPR technique was compared to data from the EN technique because the current research equipment generates both types of data. This comparison is shown in Figure 6 for all of the materials and test conditions used in this research. EN corrosion rates were consistently lower than LPR corrosion rates by an average factor of 6-7. Thus if EN corrosion rates were plotted instead of LPR corrosion rates in

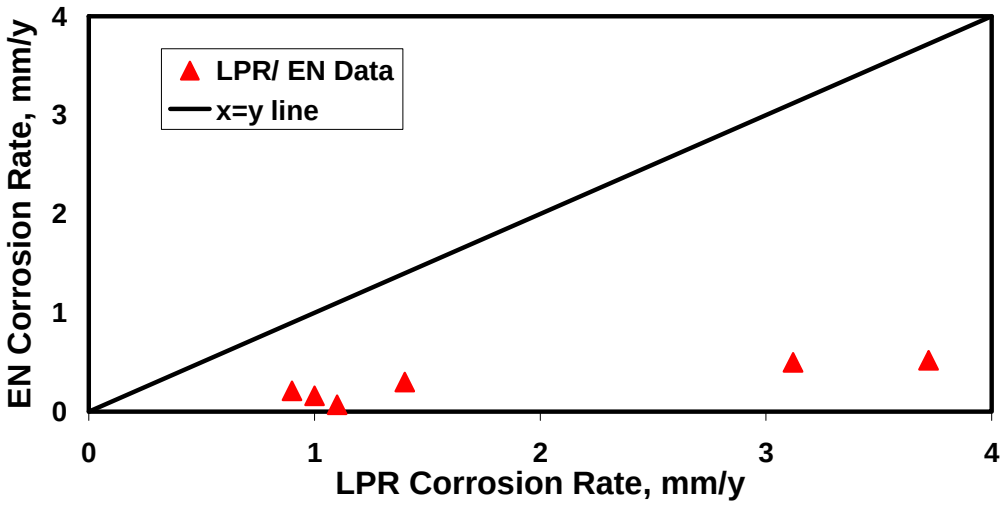

Figure 6 – Comparison of electrochemical noise to linear polarization corrosion rates.

Figure 5, the comparison to mass loss corrosion rates would have been worse. For the equipment used here, it is concluded that LPR corrosion rates better represent the actual corrosion reaction. Other researchers[2] have used EN probe data and profilometry to measure the corrosion penetration rate of their probe surfaces in an effort to quantify their electrochemical corrosion rates. Still others[4] have used EIS data for the probe measurement and the SEM to measure the metal lost from the actual probe. Both of these research groups generated mass loss and electrochemical probe corrosion rates that differed by only about 50%.

EFFECT OF CHOICE OF STERN GEARY CONSTANT

The choice of the Stern-Geary (B) constant may be the most powerful factor affecting reported electrochemical corrosion rates. As can be seen in equation 1, corrosion rate is directly proportional to B. Within reason, a B value could be chosen to make the ECR probe corrosion rates coincide with mass loss corrosion rates. This was not done in this report; rather the B values measured using the HDA technique were used to calculate the corrosion rates. Other studies[1,2] of ECR probes did not report the method used to calculate corrosion rates or the value of B used

The Stern-Geary constants measured for all of the experiments ranged from 0.0117 to 0.0182 V/decade with an average value of 0.0141V/decade. This average is significantly lower than the normally assumed values of 0.020 to 0.030 V/decade. The actual values, and not the average value, were used to calculate the LPR and EN corrosion rates that are shown in Figures 5 and 6. One use for this measured value of B is to allow a more accurate calculation of corrosion rate when using equation (1). The Stern-Geary constant and the Tafel constants that are used to calculate B can also be coupled with other information, such as scale analyses and electrochemical data from other techniques, to help explain corrosion mechanisms.

SUMMARY

Results presented here show that validation of ECR probes for use in high temperature fossil energy applications requires an understanding of: probe construction and how that affects the zero baseline response, the correlation between mass loss and ECR probe corrosion rates, the measurement and use of the most representative value of the Stern-Geary constant, and the choice of the most appropriate electrochemical technique to use with the ECR probes.

CONCLUSIONS

- LPR-based ECR probes are able to measure corrosion rates that are sensitive to temperature and process changes.
- The HDA technique is able to measure a unique value of the Stern-Geary constant that averaged 0.0141 V/decade in the high temperature corrosion environments considered here.
- Both 304L and 316L SS produced ECR probe corrosion rates that were similar to their mass loss corrosion rates.
- There were relatively large differences between the mass loss and ECR probe corrosion rates for the 4130 CS coupons and probes.
- A relatively low but steady baseline corrosion rate was measured when no electrolyte was present. Conductivity in the potting compound is suspected.
- For the hardware/software combination used here, LPR corrosion rates appeared to measure more accurate (compared to mass loss corrosion rates) corrosion rates than the EN technique.

REFERENCES

1. T.M. Linjeville, K.A. Davis, G.C. Green, W.M. Cox, R.N. Carr, N.S. Harding, and D. Overacker, "On-Line Technique for Corrosion Characterization in Utility Boilers, Proceedings of Power Production in the 21st Century: Impacts of Fuel Quality and Operations," United Engineering Foundation, Snowbird, UT, October 28-November 2, 2001.
2. T.M. Linjeville, J. Valentine, K.A. Davis, N.S. Harding, and W.M. Cox, "Prediction and Real-time Monitoring techniques for Corrosion Characterization in Furnaces," Materials at High Temperatures, Vol. 20, No. 2, pp. 175-184, 2003.
3. D.M. Farrell, W.Y. Mok, and L.W. Pinder, "On-line Monitoring of Furnace-Wall Corrosion in a 125 MW Power Generation Boiler," Materials Science and Engineering, Vol. A121, pp. 651-659, 1989.
4. D. M. Farrell, "On-line Monitoring of Fireside Corrosion in Power Plant," 12th International Corrosion Congress, Vol. 12, pp. 4131-4140, 1993.
5. G. Gao, F.H. Stott, J.L. Dawson, and D.M. Farrell, "Electrochemical Monitoring of High-Temperature Molten Salt Corrosion," Oxidation of Metals, Vol. 33, Nos. 1/2, pp. 79-94, 1990.
6. G.J. Bignold and G.P. Quirk, "Electrochemical Noise Measurements in a 500 MW Steam Turbine to Maximize Lifetime Under Changing Operational Demands," Paper no, 02333, CORROSION/2002, NACE International, Houston, TX, 20 pp, 2002.
7. B. S. Covino, Jr., J. H. Russell, S. D. Cramer, G. R. Holcomb, S. J. Bullard, M. Ziomek-Moroz, S. A. Matthes, and M. L. White, "The Role of Ash Deposits in the High Temperature Corrosion of Boiler Tubes," Paper no.03718, CORROSION/2003, NACE International, Houston TX, 12 pp., 2003.
8. D. A. Eden and B. Breene, "On-Line Electrochemical Corrosion Monitoring in Fireside Applications," Paper No. 03361, CORROSION/2003, NACE International, Houston, TX, 10 pp., 2003.

SESSION IV

BREAKTHROUGHS
IN
MATERIALS PERFORMANCE
AND
RELIABILITY

Mo-Si-B Alloy Development

J. H. Schneibel
Oak Ridge National Laboratory, Metals and Ceramics Division, P. O. Box 2008, Oak Ridge, TN 37831-6115
E-mail: schneibeljh@ornl.gov; Telephone: (865) 576-4644; Fax: (865) 574-7659
Jamie J. Kruzic
Lawrence Berkeley National Laboratory, 1 Cyclotron Road, Berkeley, CA 94720, U.S.A.
Email: jjkruzic@lbl.gov; Telephone: (510) 486-5544; Fax: (510) 486-4995
Robert O. Ritchie
Lawrence Berkeley National Laboratory, 1 Cyclotron Road, Berkeley, CA 94720, U.S.A.
Email: roritchie@lbl.gov; Telephone: (510) 486-5798; Fax: (510) 486-4881

ABSTRACT

Mo-Si-B silicides consisting of the phases α-Mo (Mo solid solution), Mo_3Si, and Mo_5SiB_2 exhibit melting points on the order of 2000°C and have potential as ultra-high temperature structural materials. Mo-Si-B silicides can be processed such that the α-Mo is present either in the form of isolated particles in a silicide matrix, or else as a continuous matrix "cementing" individual silicide particles together. These Mo-Si-B silicide alloys are fundamentally different from ceramics because of the presence of a ductile Mo-phase that improves the fracture toughness. They exhibit a trade-off between oxidation resistance and fracture toughness: increasing the volume fraction of the Mo phase improves the fracture toughness, while it degrades the oxidation resistance. One potential solution to this dilemma would be the application of oxidation-resistant coatings. For coatings to be successful, the coefficients of thermal expansion (CTE) for the substrate and coating should not be too different. Attempts to increase the CTE of Mo-Si-B alloys by alloying with Al or Mn, in order to make it more similar to that of Al_2O_3, were unsuccessful. On the other hand, there are potential coatings with CTEs lower than those of Al_2O_3, such as $CaAl_4O_7$. However, $CaAl_4O_7$ was found to be thermodynamically unstable in contact with Mo-Si-B. A second potential solution would be to improve the ductility of the α-Mo phase in order to reduce the volume fraction needed to achieve the required fracture toughness, and thus improve the oxidation resistance. The room temperature fracture toughness of Mo-Si-B alloys can be improved by microalloying with Zr suggesting that the toughening efficiency of the Mo phase can be improved. Early work carried out by D. M. Scruggs in the 1960s suggests that the room temperature ductility of Mo is improved by additions of spinel ($MgAl_2O_4$, $NiAl_2O_4$) particles. However, experiments with $MgAl_2O_4$ spinel particles in Mo have so far not shown conclusive results. Further work is in progress to resolve this issue.

INTRODUCTION

In order to increase the thermodynamic efficiency of fossil energy systems, strong, tough and oxidation resistant materials capable of service temperatures well beyond 1000°C are needed. While refractory elements such as Nb, Mo, Ta, and W have high melting points, they lack oxidation resistance. Refractory element silicides, on the other hand, can be oxidation resistant. For example, $MoSi_2$ is widely used in heating elements for resistance furnaces. Its good oxidation resistance is due to the formation of a protective silica glass scale. However, $MoSi_2$ is very brittle with a room temperature fracture toughness on the order of 3 MPa $m^{1/2}$.[1] Also, it is very weak at high temperatures[1]. Berczik[2,3] has pioneered alloys consisting of Mo_3Si, Mo_5SiB_2 ("T2"), and a toughening Mo solid solution (α-Mo). The boron in these alloys improves their oxidation resistance. This is because boron reduces the viscosity of the glassy silica scale that forms on these alloys during exposure to air.[4,5] The low viscosity helps to maintain a continuous protective oxide scale. Since these alloys contain a ductile phase, α-Mo, they can exhibit respectable fracture toughness values. For an α-Mo volume fraction of 49%, room temperature initiation and peak toughness values of, respectively, 12 and 21 MPa $m^{1/2}$ have been reported.[6] While the fracture toughness increases as the α-Mo volume fraction increases, the oxidation resistance decreases. The optimization of Mo-Mo_3Si-T2 alloys requires therefore a trade-off between fracture toughness on the one hand, and oxidation resistance on the other. This paper compiles data illustrating the opposite trends in the fracture toughness and oxidation resistance as the α-Mo volume fraction increases. In order to have a sufficiently high volume fraction of toughening α-Mo, oxidation-resistant coatings are being considered. Preliminary experiments

assessing the thermal expansion mismatch and the thermodynamic compatibility of potential coatings for Mo-Si-B silicides are presented. Another approach aims at improving the toughening efficiency of the α-Mo phase (thus reducing the volume fraction required to achieve adequate toughness) by making it more ductile. Microalloying with Zr is shown to be successful in this regard. Scruggs showed that the room temperature ductility of Mo increases, when $MgAl_2O_4$ or $NiAl_2O_4$ spinel particles are added.[7] However, our experimental results on the Scruggs effect are so far inconclusive.

EXPERIMENTAL PROCEDURES

The alloys in this work were prepared by arc-melting elemental starting materials in a partial pressure of argon (70 kPa) on a water-cooled copper hearth. The purity of the starting materials Mo, Si, Zr and B was 99.95, 99.99, 99.5, and 99.5 weight % (wt%), respectively. Unless stated otherwise, alloy compositions will be in atomic % (at. %). The alloys were re-melted several times in order to improve their homogeneity. Some alloys were drop-cast into cylindrical water-cooled copper molds with diameters of 12.5 or 25 mm. Alloys containing Al or Mn experienced significant weight losses during arc-melting due to evaporation. Their composition after casting was re-calculated assuming that the weight loss was exclusively due to losses in Al or Mn, respectively.

Metallography specimens were prepared by grinding, mechanical polishing, and etching in Murakami's reagent. Microstructural examination was carried out by optical microscopy as well as scanning electron microscopy (SEM). The phases were identified by a combination of energy dispersive spectroscopy (EDS) in an SEM, by wavelength-dispersive spectroscopy (microprobe), and powder x-ray diffraction.

Thermal expansion measurements were carried out with 25 mm long specimens in argon in a Theta Industries Inc. dilatometer.

Mo powders (2-8 μm) with and without $MgAl_2O_4$ spinel particles (-325 mesh, <45 μm) were hot-pressed in graphite dies *in vacuo* (rotary pump) for times ranging from 1 to 4 hours at 1800°C and a pressure of 21 MPa. Tensile test specimens were cut by electro-discharge machining and finished with 600 grit SiC paper prior to testing.

For the purpose of screening tests, the fracture toughness K_q was determined from flexure tests with chevron-notched flexure bars[8] with a cross-section of 3×4 mm and a span of 20 mm (see also Fig. 1):

$$K_q=[EG/(1-\nu^2)]^{1/2}, \qquad (1)$$

where E is Young's modulus, $G=W/A$ is the work W expended during fracture divided by the area A swept out by the crack, and ν = Poisson's ratio. The fracture toughness values determined with this technique tend to be higher than those determined with more rigorous techniques. On the other hand, this technique requires less sample material, is simpler to implement than more rigorous techniques, and is considered suitable for comparative purposes.

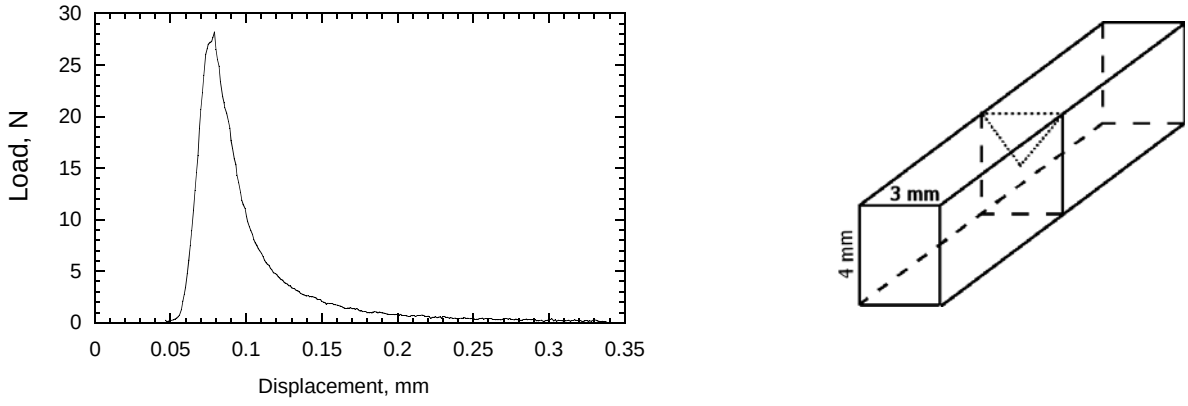

Figure 1. Determination of K_q from flexure tests with chevron-notched flexure bars

For some specimens, precise fracture toughness values were obtained under plane-strain conditions by monotonically loading fatigue-precracked, disk-shaped compact-tension DC(T) specimens to failure.[6,9] During these tests, crack lengths were periodically monitored using the elastic unloading compliance. Following pre-cracking, specimens were cycled for ~24 hr at the ΔK_{TH} threshold (where there is no discernable crack growth) in an attempt to remove any possible crack bridging in the wake of the pre-crack. The resistance curve (*R*-curve) behavior was then evaluated by measuring the crack-growth resistance, K_R, as a function of crack extension, Δa.

RESULTS AND DISCUSSION

FRACTURE TOUGHNESS AND OXIDATION RESISTANCE VS. α-MO VOLUME FRACTION

Figures 2 and 3 summarize oxidation and fracture toughness data for Mo-Si-B alloys.[10-12] The oxidation data include the large initial mass loss due to evaporation of MoO_3. A more thorough comparison would have to compare the oxidation rates following the initial mass loss. The fracture toughness of pure Mo was approximated by the value for a Mo-1Zr alloy.[13] Rigorously measured data for Mo-Si-B containing 49 vol.% of continuous α-Mo phase are shown as well.[6] The two figures show that oxidation resistance and fracture toughness depend in opposite ways on the α-Mo volume fraction. As the α-Mo volume fraction increases the fracture toughness increases, whereas the oxidation resistance decreases. Oxidation resistant coatings could be one potential solution to this dilemma. Another potential solution is to improve the toughening effectiveness of the Mo phase, i.e., make it more ductile. Then less α-Mo would be required in order to reach the desired fracture toughness. This, in turn, would result in an improvement of the oxidation resistance. The ductilization approach is realistic since the room temperature fracture surface of a high-toughness silicide alloy (that shown by the diamonds in Fig. 3 [ref. 6]) indicates a significant fraction of intergranular fracture in the α-Mo phase (Fig. 4). If intergranular fracture can be inhibited, an even higher fracture toughness is likely. In this work, two ductilization approaches will be assessed. One of them involves microalloying with Zr, and the other the addition of spinel particles to the Mo phase.

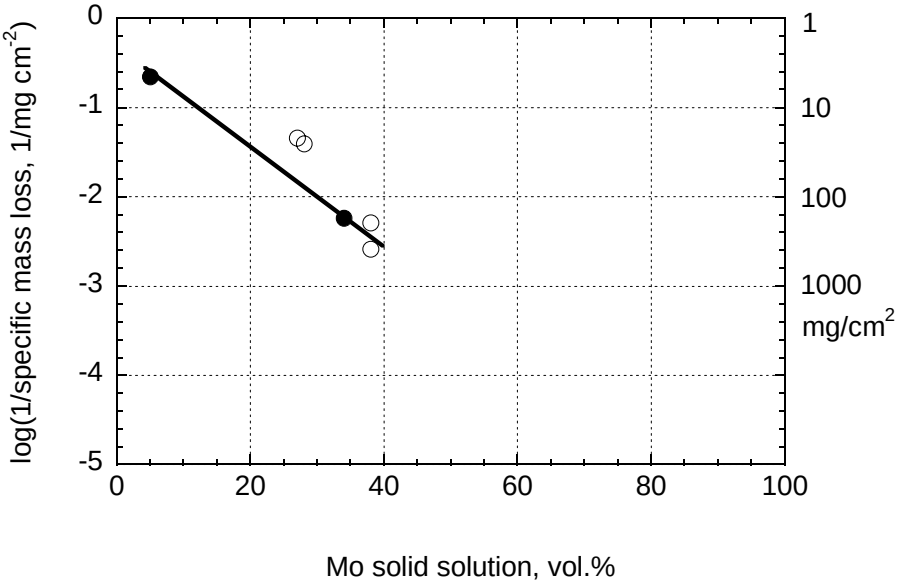

Fig. 2. Specific mass loss for Mo-Si-B alloys after oxidation for durations from 20 and 24 hours at 1200°C, as a function of the α-Mo volume fraction. The full circles correspond to specimens containing individual α-Mo particles, and the white circles to specimens containing continuous α-Mo.

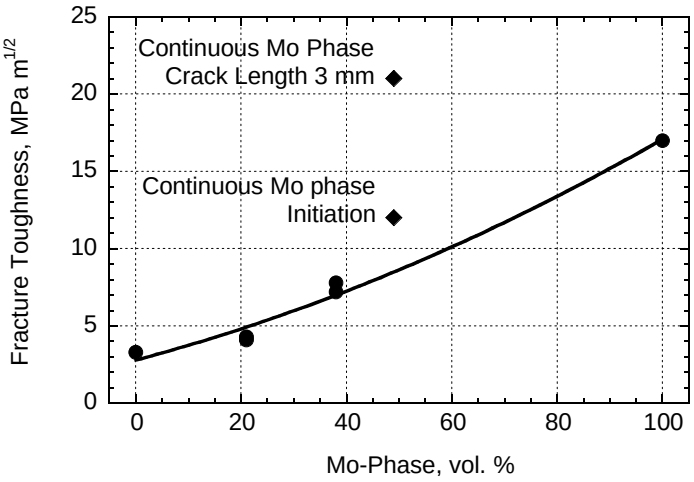

Fig. 3. Room temperature fracture toughness of Mo-Si-B alloys as a function of the α-Mo volume fraction. The values for the Mo-1 wt% Zr alloy ("100% Mo-Phase") and the silicide with 49 vol.% of a continuous α-Mo phase (diamonds) were obtained with rigorous testing techniques. The values for 49 vol.% α-Mo illustrate the extent by which the fracture toughness can be increased if the α-Mo is coarse and continuously distributed.

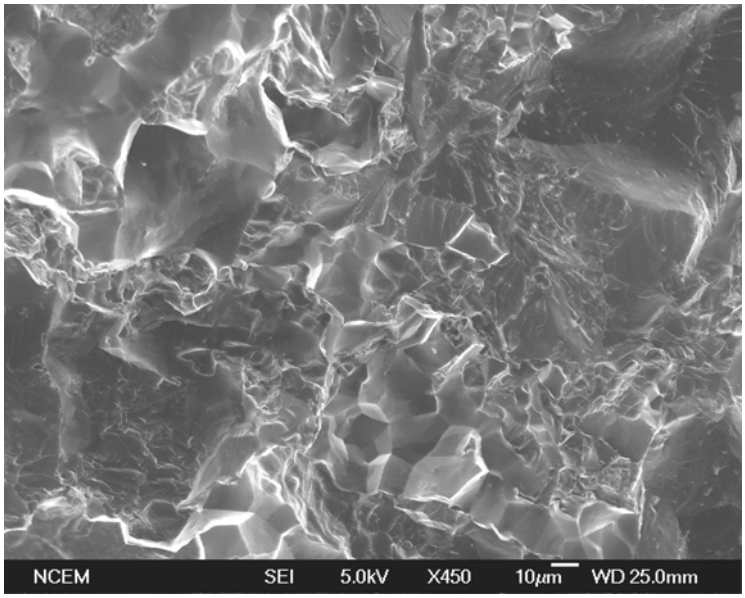

Fig. 4. SEM micrograph of fracture surface of Mo-Si-B specimen containing 49 vol.% of continuous α-Mo phase. Most of the flat cleavage facets correspond to fracture of the intermetallic phases. The α-Mo phase exhibits a significant fraction of intergranular fracture.

COATINGS

Fig. 5 compares the thermal expansion of Al_2O_3 to that of Mo, Mo_3Si, and Mo_5SiB_2.[14,15] Since Al_2O_3 has a higher expansion coefficient than the silicide phases, it is not suitable as a coating. This is because upon cooling, tensile stresses would be set up in the Al_2O_3 and cracking would presumably occur. If the thermal expansion coefficient of the silicide could be increased, a better match with that of Al_2O_3 would result. Figure 6 shows the thermal expansion of Mo-12Si-8.5B (at. %). Alloying with Al increased the thermal expansion slightly, whereas alloying with Mn reduced it. These results suggests that it would be difficult to increase the CTE of Mo-Si-B alloys to match that of Al_2O_3. Coatings other than Al_2O_3, with lower thermal expansion, may be a more realistic option. Figure 7 compares the thermal expansion of calcium aluminate, $CaAl_4O_7$, hafnium silicate $HfSiO_4$, and mullite, $3Al_2O_3{\cdot}2SiO_2$ (ref. 16) with that of Mo-12Si-8.5B. Since these coating materials have a lower CTE than Mo-12Si-8.5B, they are less likely to spall during cyclic oxidation. However, x-ray diffraction of a $CaAl_4O_7$ coating applied to Mo-12Si-8.5B showed the phases Mo, Al_2O_3, and $CaAl_2Si_2O_8$ (calcium aluminosilicate, also called anorthite) indicating that this coating is not thermodynamically stable in contact with molybdenum silicides. The thermodynamic stability of mullite is presently under investigation.

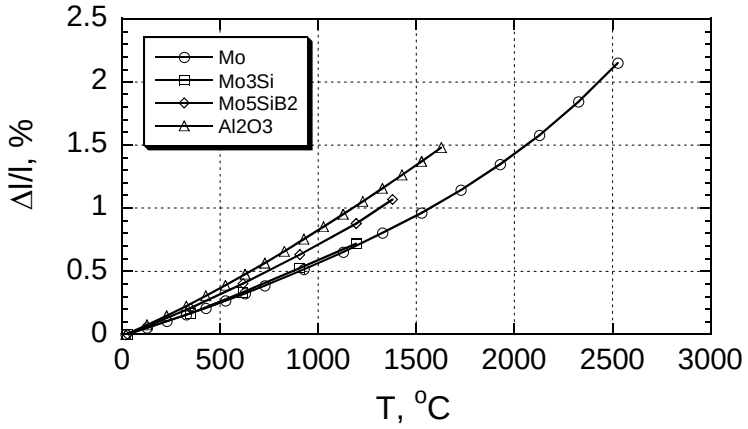

Fig. 5. Plot of thermal expansions, Δl/l, where Δl is the change in the initial specimen length l, as a function of temperature. The thermal expansion of alumina is higher than that of the phases in Mo-Si-B alloys.

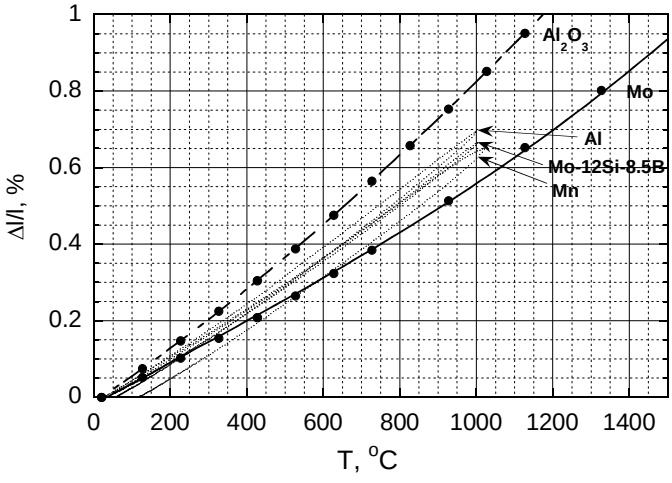

Fig. 6. Effect of alloying with Al or Mn on the thermal expansion of Mo-12Si-8.5B (at. %).

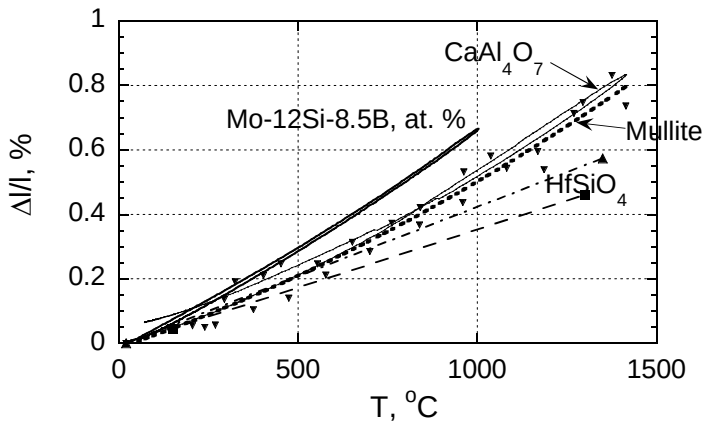

Fig. 7. Thermal expansion of potential coatings for Mo-12Si-8.5B (at. %).

MICROALLOYING WITH Zr

Alloys with different concentrations of Zr, substituting for Mo, were prepared by arc-melting followed by drop-casting and anneling in vacuum for 24 hours at 1600°C. The Zr additions did not change the microstructure significantly. The microstructures consisted essentially of Mo particles (bright) in a matrix of Mo_3Si/Mo_5SiB_2, see Fig. 8. As the Zr concentration increased, the propensity for macrocracks in the cast and annealed ingots increased. The specimens with the higher Zr concentrations were therefore quite fragile. Figure 9 shows the trend in the room temperature fracture toughness when increasing amounts of Mo are substituted with Zr. More detailed data on the fracture toughness tests are listed in Table I. For some compositions several data points were collected in order to obtain an estimate for the scatter. It should be noted that the chevron-notch specimen technique employed here does not provide a rigorous value for the fracture toughness. However, it does reflect the trend in the fracture toughness values. Additions of Zr increased the room temperature fracture toughness noticeably. The maximum fracture toughness was found for Zr concentrations on the order of 2 at. %. The mechanism responsible for the toughening has not yet been identified, and the partitioning of the Zr in the three constituent phases of the alloy has not been measured. However, it is considered unlikely that the Zr additions would improve the fracture toughness of the brittle phases Mo_3Si and Mo_5SiB_2 with their complex crystal structures - it is more likely that the Zr improved the ductility/toughness of the α-Mo phase, as for example observed in TZM alloys.

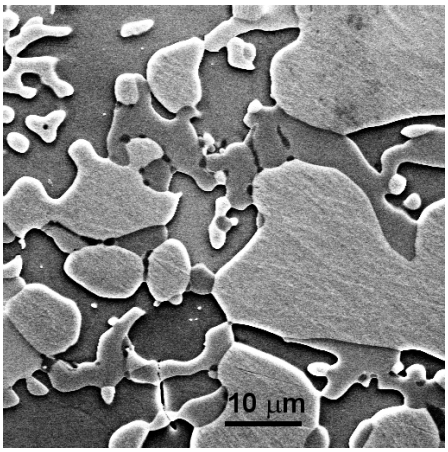

Fig. 8. SEM micrograph of etched Mo-1.5Zr-12Si-8.5B (at. %). The α-Mo appears as the bright particles.

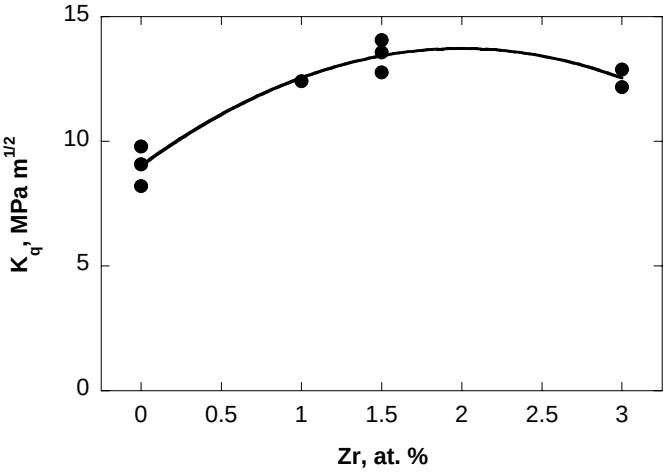

Fig. 9. Room temperature fracture toughness K_q of Mo-xZr-12Si-8.5B as a function of Zr concentration.

Table I. Fracture toughness K_q of Mo-Si-B alloys micro-alloyed with Ti or Zr. K_q was evaluated from Eqn. (1) assuming E=327 GPa and ν=0.29.

	Area of triangle broken during test, mm^2	Absorbed energy, mJ	G, J/m^2	K_q, MPa $m^{1/2}$	K_q, MPa $m^{1/2}$, average±standard deviation
Mo-12Si-8.5B	2.94	0.68	231	9.1	
″	2.88	0.775	267	9.8	9.0±0.8
"	3.19	0.603	189	8.2	
Mo-12Si-8.5B-1Zr	2.82	1.09	432	12.4	
Mo-12Si-8.5B-1.5Zr	3.05	1.575	516	13.6	13.5±0.7
″	2.89	1.32	457	12.8	
″	3.48	1.93	555	14.1	
Mo-12Si-8.5B-3Zr	2.54	1.284	466	12.9	12.6±0.5
″	2.76	1.149	416	12.2	

DUCTILIZATION WITH SPINEL PARTICLES

In the 1960's, Scruggs found that powder-metallurgical Cr is ductilized by addition of MgO particles that transform into $MgCr_2O_4$ spinel particles.[17] Under the Fossil Energy Materials Program, M. P. Brady verified this ductilizing effect.[18] He determined that segregation of detrimental impurities such as nitrogen to the particle-matrix interface is one of the factors responsible for ductilization. Scruggs suggested that not only Cr, but also Mo can be ductilized by adding spinel particles.[7] In a preliminary experiment, nominally pure Mo and Mo-9 vol.% $MgAl_2O_4$ coupons were prepared by hot-pressing at 1800°C. Figure 10 compares bend bars after room temperature testing and suggests that the spinel ductilization mechanism does occur.

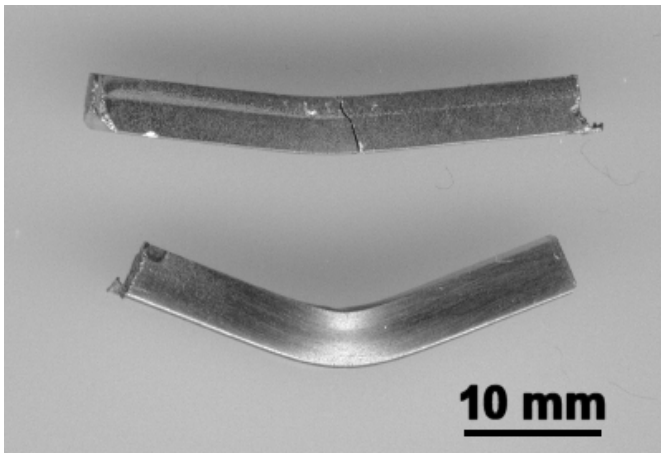

Figure 10. Qualitative comparison of the room temperature bend ductility of Mo (top) and Mo-9vol.% $MgAl_2O_4$ (bottom).

Although this initial experiment seemed convincing, further work carried out to substantiate this effect has so far not been conclusive. A set of specimens of nominally pure Mo and Mo containing 5, 10, and 15 vol.% of $MgAl_2O_4$ was hot-pressed (4h/1800°C/21 MPa). However, all these specimens were quite brittle. A combination of optical microscopy, SEM-EDS and x-ray diffraction showed that these materials contained significant amounts of MoO_2 inclusions. Near the edges of the coupons, i.e., close to the graphite hot-pressing dies, the MoO_2 was reduced to Mo and molybdenum carbide formed instead. It is concluded that the starting Mo powder was contaminated with oxygen. Another set of specimens was prepared with Mo powder obtained from a different source. Figure 11 shows the room temperature ductility of those specimens as a function of spinel volume fraction and strain rate. Significant scatter is observed, in particular for the "pure" Mo. Its ductility, at a strain rate of 10^{-4} s^{-1}, ranges from 11 to 52%. Figure 12 shows SEM micrographs of fracture surfaces of Mo. It is obvious that less ductile specimens fractured primarily along the grain boundaries, whereas more ductile specimens fractured transgranularly. Figure 13a shows the fracture surface of Mo-5 vol.% $MgAl_2O_4$ to be a 50/50 mixture of intergranular and transgranular fracture; Fig. 13b is a lower magnification micrograph illustrating the presence of large (50 μm) spinel particles.

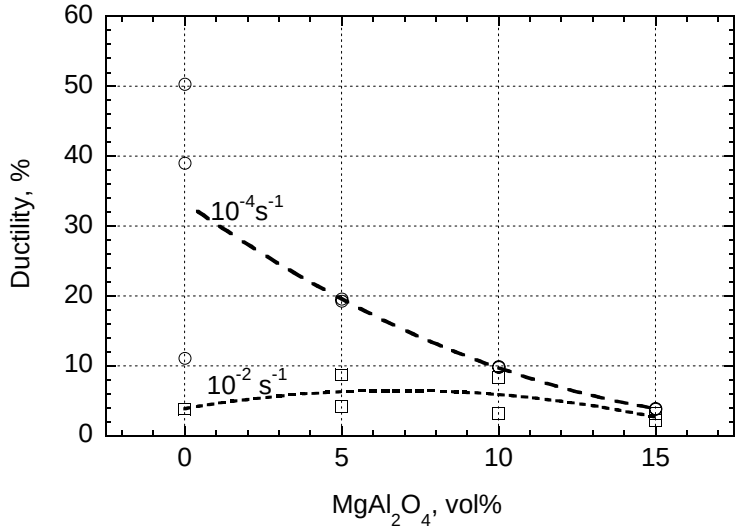

Fig. 11. Room temperature ductility as a function of $MgAl_2O_4$ volume fraction and strain rate

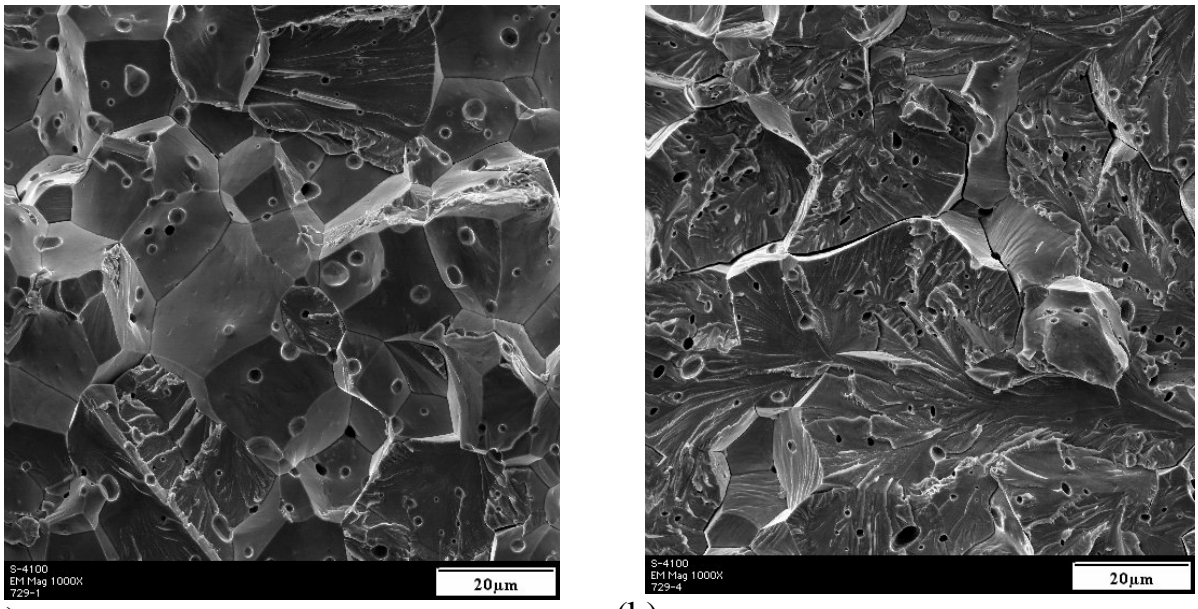

(a) (b)

Fig. 12. SEM micrographs of fracture surfaces of two Mo specimens from the same hot-pressed disc tested at room temperature and 10^{-4} s^{-1}. One specimen (a) exhibited a ductility of 11%, whereas another (b) exhibited a ductility of 52%.

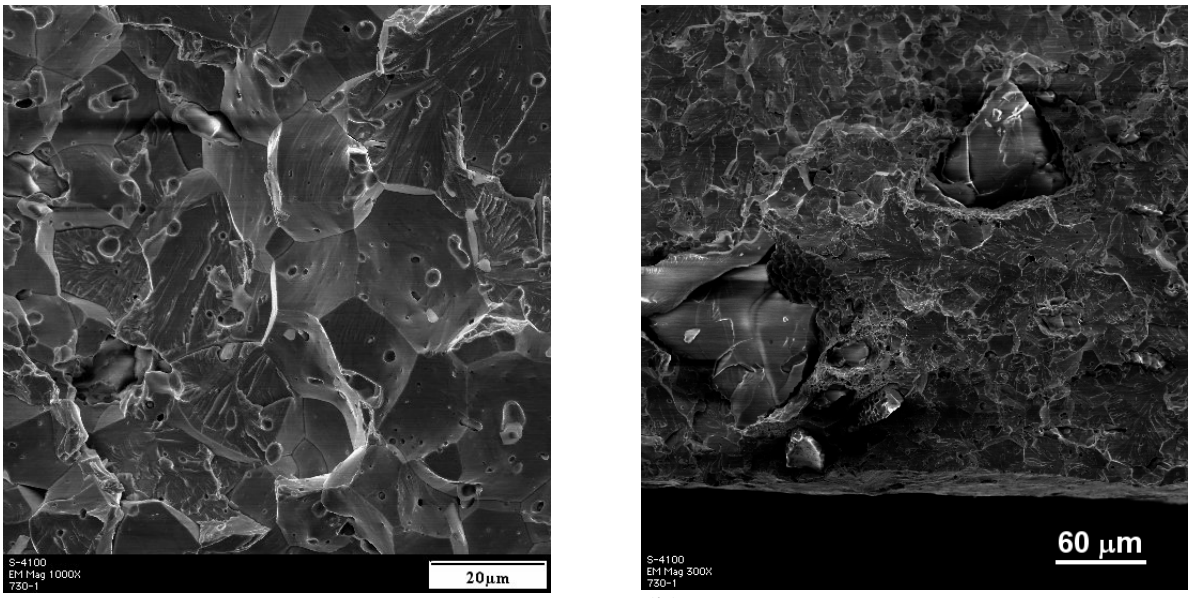

(a) (b)

Fig. 13. SEM micrographs of room temperature fracture surfaces of Mo-5 vol.% $MgAl_2O_4$ at different magnifications. The initial strain rate was 10^{-4} s^{-1}.

All the specimens were machined parallel to the hot-pressed discs. Because of interaction with the graphite die it is conceivable that the carbon concentration near the top and bottom of the discs is higher than that in the middle. According to Wadsworth, Nieh and Stephens[19] the C/O ratio is an important factor controlling the ductility of nominally pure Mo. Substantial room temperature ductility is only observed for atomic C/O ratios in excess of two. For values below two, intergranular fracture becomes important and the ductility decreases. Since we did not track the location of the specimens machined from the hot-pressed discs, their C concentration, and therefore their ductility, are likely to vary in a random manner.

Even though the results are inconclusive at this time, it is nonetheless surprising that the spinel-containing specimens are relatively ductile. The large $MgAl_2O_4$ particles in Mo-5 vol.% $MgAl_2O_4$ (Fig. 13b) would be expected to degrade the ductility substantially. However, this particular specimen did have a room temperature ductility of 20%. This suggests that a spinel ductilizing effect may exist, but more careful work is required to verify it. In future work, the C/O issue will be addressed. Also, it is imperative to quantify the fraction of transgranular and intergranular fracture. In particular, it is not clear whether the primary role of the spinel particles is to minimize the incidence of intergranular fracture, or whether spinel particles would ductilize a single crystal as well. Comparisons with "pure" Mo may be of doubtful value. Addition of even a small amount of $MgAl_2O_4$ might change the residual impurity content and make therefore a comparison with "pure" Mo objectionable. A better strategy may be to determine whether there is a regime in which the ductility increases as the spinel volume fraction increases.

SUMMARY AND CONCLUSIONS

Mo-Si-B intermetallics can be processed such that the α-Mo occurs either in the form of discrete particles or as a continuous matrix. With 49 vol.% of continuous α-Mo, very high fracture toughness values up to 21 MPa $m^{1/2}$ can be obtained. However, this high fracture toughness occurs at the expense of the oxidation resistance. Oxidation-resistant coatings may be one possible way of dealing with this dilemma. Attempts to increase the thermal expansion of Mo-Si-B silicides in order to match its value to that of Al_2O_3 have so far not been met with success. Other oxidation-resistant coatings with lower thermal expansion such as $CaSi_4O_7$, $HfSiO_4$, and mullite are being considered. However, $CaAl_4O_7$ is not stable in contact with Mo-Si-B alloys. As an alternative to coatings, it is considered very important to improve the mechanical properties of the α-Mo phase. This will increase toughening effectiveness. In order to achieve a certain value of the fracture toughness, less α-Mo will then be required, with a concomitant improvement in the oxidation resistance. It is shown that the mechanical properties of α-Mo can be improved by micro-alloying with Zr. Experiments to ductilize Mo by adding $MgAl_2O_4$ spinel particles have so far been inconclusive, and further experiments will be required to resolve this issue.

ACKNOWLEDGEMENTS

This work was sponsored by the Office of Fossil Energy, Advanced Research Materials (ARM) Program, U.S. Department of Energy, under contract DE-AC05-00OR22725 with Oak Ridge National Laboratory managed by UT-Battelle, LLC and under contract No. DE-AC03-76SF00098 with the Lawrence Berkeley National Laboratory. Thanks go to M. P. Brady for pointing out Scruggs' work on ductilization of Mo by spinel, and for many valuable discussions. Thanks go also to B. L. Armstrong and R. D. Carneim for providing calcium aluminate-coated specimens and thermal expansion data for calcium aluminate.

REFERENCES

1. A. K. Vasudévan and J. Petrovic, "A comparative overview of molybdenum silicide composites," Mater. Sci. and Eng. A155 (1992) 1-17.
2. D. M. Berczik, United States Patent 5,595,616 (1997), "Method for enhancing the oxidation resistance of a molybdenum alloy, and a method of making a molybdenum alloy."
3. D. M. Berczik, United States Patent 5,693,156 (1997), "Oxidation resistant molybdenum alloys."
4. T. A. Parthasarathy, M. G. Mendiratta, and D. M. Dimiduk, "Oxidation mechanisms in Mo-reinforced Mo_5SiB_2 (T2) Mo_3Si alloys," Acta Mater. 50 (2002) 1857-1868.

5. V. Supatarawanich, D. R. Johnson, and C. T. Liu, "Effects of microstructure on the oxidation behavior of multiphase Mo-Si-B alloys," Mater. Sci. Eng. A344 (2003) 328-339.
6. J. J. Kruzic, J. H. Schneibel, and R. O. Ritchie, "Fracture and Fatigue Resistance of Mo-Si-B Alloys for Ultrahigh-Temperature Structural Applications", Scripta Mater. 50 (2004) 459-464.
7. D. M. Scruggs, "Ductile molybdenum composition containing a spinel dispersion," United States Patent 3,320,036, Patented May 16, 1967.
8. J. H. Schneibel and E. d. Specht, "Slow crack growth in ternary B2 iron aluminides at room temperature," Scr. Metal. Mater. 31 (1994) 1737-1742.
9. H. Choe, J. H. Schneibel, and R. O. Ritchie, "On the fracture and fatigue properties of Mo-Mo_3Si-Mo_5SiB_2 refractory intermetallic alloys at ambient to elevated temperatures (25-1300^oC)," Metall. Mater. Trans. 34A (2003) 25-239.
10. J. H. Schneibel, P. F. Tortorelli, M. J. Kramer, A. J. Thom, J. J. Kruzic, and R. O. Ritchie, "Optimization of Mo-Si-B Intermetallics," in Defect Properties and Related Phenomena in Intermetallic Alloys, E. P. George, M. J. Mills, H. Inui, G. Eggeler, eds., MRS Symposium Proceedings, vol. 753, Materials Research Society, Warrendale, PA, 2003, BB2.2.1-6.
11. J. H. Schneibel, C. T. Liu, D. S. Easton, and C. A. Carmichael, "Microstructure and mechanical properties of Mo-Mo_3Si-Mo_5SiB_2 silicides," Mater. Sci. Eng. A, A261 (1999) 78-83.
12. J. H. Schneibel, D. S. Easton, H. Choe, and R. O. Ritchie, "Fracture Toughness, Creep Strength and Oxidation Resistance of Mo-Mo3Si-Mo5SiB2 Molybdenum Silicides," in "Structural Intermetallics, Third International Symposium," K. J. Hemker and D. M. Dimiduk, eds., TMS, Warrendale, PA, 2001, pp. 801-809.
13. A. Yu. Koval, A. D. Vasilev, and S. A. Firstov, "Fracture Toughness of Molybdenum Sheet under Brittle-Ductile Transition," Int. J. of Refractory Metals & Hard Materials, 15 (1997) 223-226.
14. Y. S. Touloukian, R. K. Kirby, R. E. Taylor, and P. D. Desai, "Thermophysical Properties of Matter Vol. 12 (Thermal Expansion)," Purdue University, Lafayaette, IN, 1975.
15. C. J. Rawn, J. H. Schneibel, C. M. Hoffmann, and C. R. Hubbard, „The crystal structure and thermal expansion of Mo_5SiB_2, Intermetallics 9 (2001) 209-216.
16. CINDAS LLC TPMD Database, www.cindasdata.com
17. D. M. Scruggs, L. H. Van Vlack, and W. M. Spurgeon, J. Amer. Ceram.Soc. 51 (1968) 473.
18. M. P. Brady, I. M. Anderson, M. L. Weaver, H. M. Meyer, L. R. Walker, M. K. Miller, D. J. Larson, I. G. Wright, V. K. Sikka, a. Rar, G. M. Pharr, J. R. Keiser, and C. A. Walls, "Nitrogen impurity gettering in oxide dispersion ductilized chromium," Materials Science and Engineering A 50 (2004) 459-464.
19. J. Wadsworth, T. G. Nieh, and J. J. Stephens, "Dilute Mo-Re alloys - a critical evaluation of their comparative mechanical properties," Scr. Metall. 20 (1986) 637-642.

MULTI-PHASE HIGH TEMPERATURE ALLOYS AND PROGRESS IN CONTROLLED OXIDATION FOR FUNCTIONAL AND PROTECTIVE SURFACES

Michael P. Brady
Oak Ridge National Laboratory, Oak Ridge, TN 37831-6115
bradymp@ornl.gov; Tel: (865) 574-5153; FAX (865) 241-0215

C.T. Liu
Oak Ridge National Laboratory, Oak Ridge, TN 37831-6115
liuct@ornl.gov ; Tel: (865) 574-4459; FAX (865) 574-7659

E. Andrew Payzant
Oak Ridge National Laboratory, Oak Ridge, TN 37831-6064
payzanta@ornl.gov; Tel: (865)574-6538; FAX (865) 574-3940

Peter F. Tortorelli
Oak Ridge National Laboratory, Oak Ridge, TN 37831-6156
tortorellipf@ornl.gov ; Tel: (865) 574-5119; FAX (865) 241-0215

Yukinori Yamamoto
Oak Ridge National Laboratory, Oak Ridge, TN 37831-6115
yamamotoy@ornl.gov ; Tel: (865) 576-7095; FAX (865) 574-7659

Larry Walker
Oak Ridge National Laboratory, Oak Ridge, TN 37831- 6064
walkerlr@ornl.gov; Tel: (865) 574-5339; FAX (865) 576-5413

ABSTRACT

FY2004 was a transition year with the completion of work devoted to the multi-phase Cr-base alloy development effort for aggressive high-temperature environments and the initiation of new projects, based on unique findings and understanding gained from this program. An effort was initiated for the development of intermetallic Laves-phase strengthened Fe-base alloys for improved elevated temperature strength in fossil energy system components such as superheater tubes and industrial gas turbines. Exploratory efforts were also initiated for proof of principle assessment of a novel synthesis approach to near-surface, complex ceramic phase structures of interest for functional applications by the control of oxidation reactions of multi-component/multi-phase metallic precursor alloys. Initial results from these efforts are presented.

INTRODUCTION

Efforts devoted to the development of multi-phase Cr-base alloys for aggressive high temperature environments will be completed in fiscal year (FY) 2004. Final results pertaining to the Cr_2Ta-reinforced Cr family of alloys [1,2] will be published in the open literature. For the

oxide dispersion ductilized Cr-base alloys also studied under this effort [3,4], industrial scale up and technology transfer activities will be pursued, in addition to the dissemination of results in open literature publications. The understanding of the manipulation of multi-phase microstructures gained under this program was transitioned to two new efforts during FY 2004. An effort was initiated for the development of intermetallic Laves-phase strengthened ferritic and austenitic alloys for improved elevated temperature strength in applications such as superheater tubes and industrial gas turbine components. Exploratory efforts were also initiated for the synthesis of functional surfaces by the control of oxidation (nitridation, carburization, etc.) reactions, based on phenomena observed during the oxidation of the multi-phase Cr_2Ta-reinforced Cr alloys. Preliminary results from these new projects will be presented in this report.

DISCUSSION OF CURRENT ACTIVITIES

Intermetallic Strengthened Austenitic and Ferritic Steels

High-temperature strength is a major issue for hot components in advanced fossil energy conversion and combustion systems. For example, the efficiency of boiler/steam turbine power plants is a strong function of steam temperature and pressure [5]. Coarsening of carbide dispersions currently limits Fe-base alloys to ~600-650°C in many critical applications. Nickel-base superalloys with elevated temperature strength above this range are available, but they are costly and may suffer from inadequate high-temperature corrosion resistance, particularly under sulfidation conditions due to the formation of low melting point Ni-S compounds. Multi-phase microstructures utilizing intermetallic phases for high-temperature strengthening and, depending upon the specific alloy system, a reservoir for protective-scale forming elements, offer a possible path to achieve a balance properties in Fe-base alloys sufficient to enable increased operating temperatures. A synergistic approach to improving elevated temperature strength utilizing solid solution, carbide, and intermetallic phase strengthening was therefore adopted (Fig. 1).

A initial series of alloys based on Fe-(10-20)Ni-20Cr atomic percent (at.%), with carbide, solid solution, and intermetallic forming alloying additions, was cast, forged, and heat treated to explore control of intermetallic precipitate phase equilibria and morphology to increase elevated temperature strength. (Full compositional and processing details are currently proprietary). Additions of Al in quantities potentially sufficient to promote Al_2O_3-base scale formation were also pursued. Preliminary results have indicated that the Al-modified alloys, in particular, show potentially attractive microstructures containing fine, uniform dispersions of carbide and intermetallic strengthening phases.

A typical microstructure is shown in Fig. 2a. Backscatter scanning electron microscopy (SEM) and electron probe microanalysis (EPMA) indicated that the microstructure consisted of submicron dispersions of an MC carbide phase (M = transition/refractory metal elements) and at least two intermetallic phase precipitates. Preliminary transmission electron microscopy (TEM) analysis (Fig. 2b) suggests that the intermetallic precipitates were C14 Laves phase, based on Fe_2Nb, and B2 NiAl-based. The C14 phase was present primarily as finely distributed 500 nm size range plates, although it was also observed as occasional, coarse (2 μm range) precipitates (fine white phase and coarse white phase regions, respectively, in Fig. 2a). The morphology of the B2 phase was roughly spherical 300 nm size range precipitates (fine dark phase in Fig. 2a).

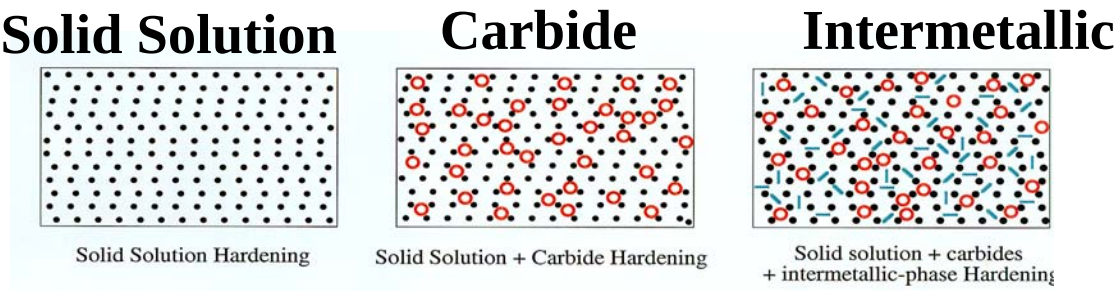

Fig. 1- Schematic cartoon of strengthening mechanisms.

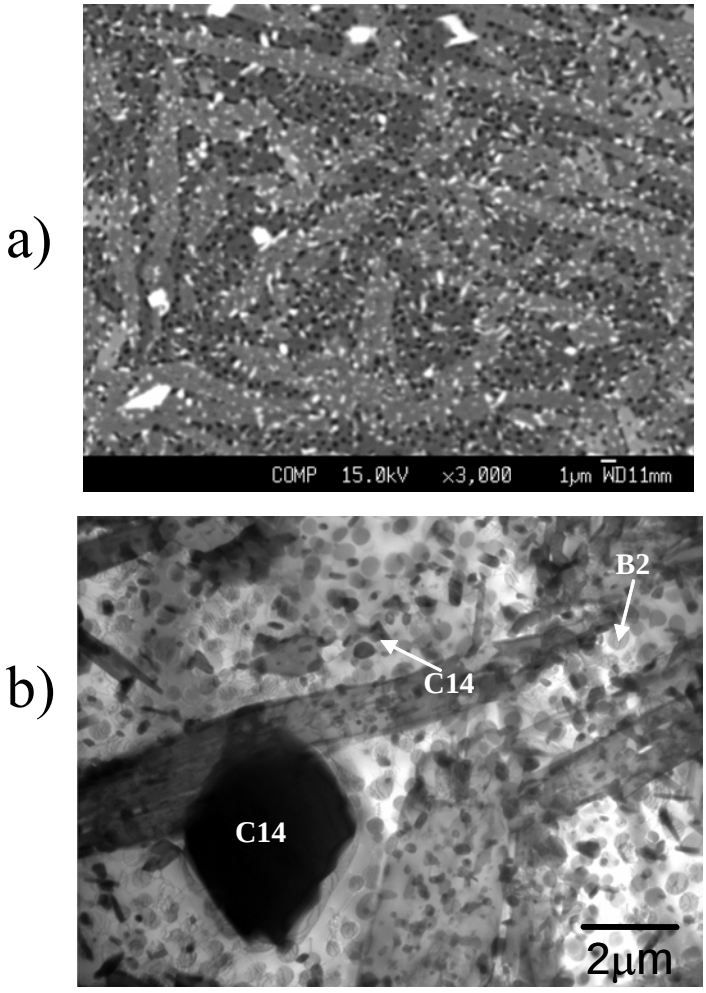

Fig. 2- Typical microstructures achieved for Al-modified Fe-20Cr-(10-20Ni) at.% base alloy.
a) Backscatter mode SEM b) Bright field TEM

Hardness measurements indicated an increase from the 250 Vicker's hardness range in the Al-free alloys to over 450 in the highest Al containing alloy, presumably due in part to the fine B2 precipitates.

Measurement of room and elevated temperature tensile properties are currently being pursued. Although this development effort is at a very early stage, the microstructures obtained thus far show definite promise for achieving improved elevated temperature strength. The C14 and B2

precipitates, in particular, are expected to be very stable to temperatures exceeding 700°C. Further, the observation of potentially attractive microstructures in the Al-modified alloys is particularly encouraging, as Al_2O_3-base scales offer superior environmental resistance compared to Cr_2O_3-base scales due to their lower growth rates and greater stability in H_2O-containing environments such as those encountered in advanced fossil energy steam plants.

Controlled Oxidation for Near Surface Functional Structures

Oxidation (nitridation, carburization) reactions are one of the most rapid, inexpensive, and technologically relevant methods of self constructing near-surface ceramic structures. Gaseous reactions of alloys can result in the formation of a myriad of ceramic phase arrangements, ranging from nanoscale clusters and dispersions to external layers, ranging from nanometers to tens and hundreds of microns thick. From a fundamental standpoint, many aspects regarding how the initial alloy composition and microstructure determine which, and how, the subsequent oxidation products are formed are not well understood. This is particularly true in ternary and higher order alloys under conditions where more than one alloy component can react, and, especially, when the alloy components are partitioned in a multi-phase microstructure. There are two ideal, yet technologically relevant and fundamentally interrelated, limiting cases: 1) the complete conversion of several or all of the reactive components in an alloy to form complex (ternary and higher order) ceramic phases, either as a dispersed internal phase or as an external layer, which is of interest as a method for the synthesis of functional materials for applications ranging from catalysts, sensors, and smart materials to wear and oxidation resistant surfaces, and, 2) the preferential oxidation of only one of the reactive components in an alloy to establish an external layer of a simple ceramic phase, i.e. selective oxidation phenomenon for the protection of materials in aggressive high-temperature environments. Initial efforts in FY 2004 were directed toward the first limiting case and the assessment of the potential of controlled oxidation to synthesize functional near-surface structures needed for a variety of applications in advanced fossil energy conversion and combustions systems. The origins of this work were the observations of unique internally nitrided structures that formed during the oxidation of Cr-Cr_2Ta alloys in air, in particular the preferential formation of ternary nitrides at Cr_2Ta precipitate sites [2].

Recent work at ORNL demonstrated that intermetallic phases show potential to be used as precursors to complex nitride and carbide phases by nitridation and carburization reactions [6-8]. A model intermetallic Cr_3Pt alloy yielded an external, single-phase scale of the complex perovskite phase Cr_3PtN on thermal nitridation. Further, internal nitridation of a two-phase Cr_3Pt dispersed Cr precursor alloy yielded dispersions of Cr_3PtN at Cr_3Pt sites, effectively utilizing the Cr_3Pt precipitates in the initial alloy microstructure as a template. The key issue to address in FY2004 was if such phenomena can be induced in systems of technological interest for the Fossil Energy Program.

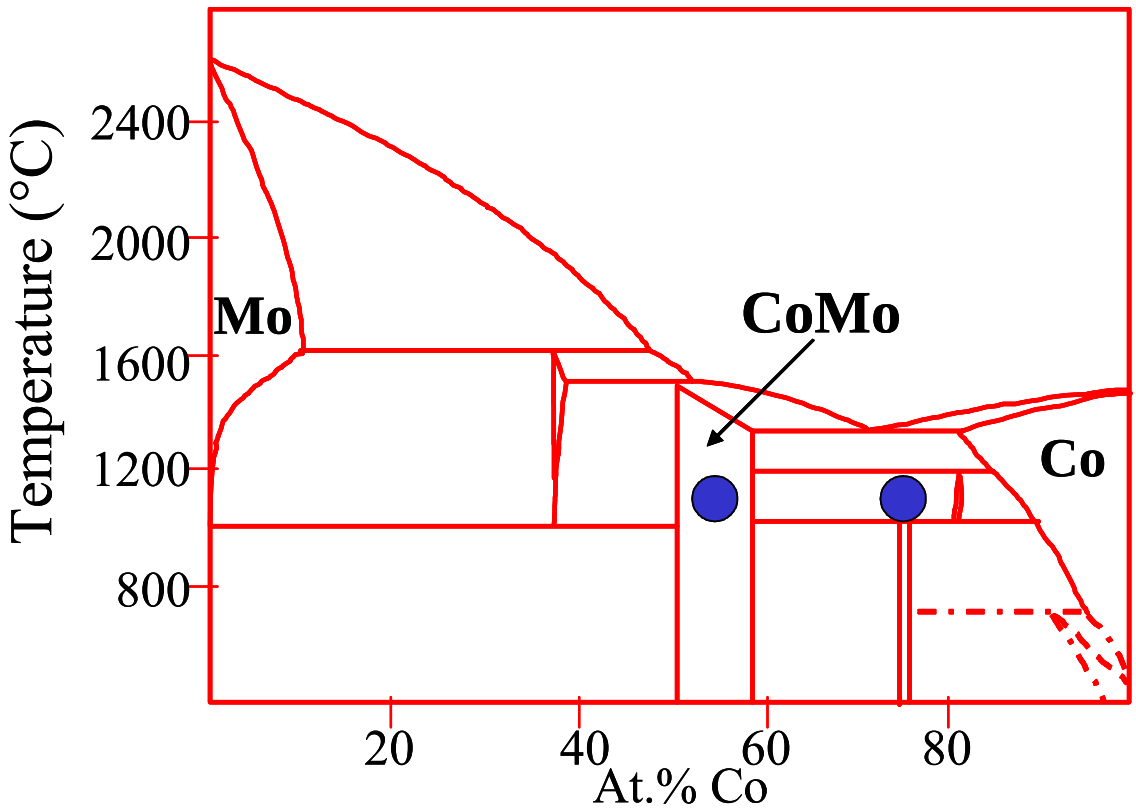

Fig. 3- Schematic Co-Mo phase diagram [after reference 16].

In particular, complex transition and refractory metal nitride and carbide phases are of increasing interest as catalysts for a variety of industrial processes, including hydrotreating to remove S, N, and O impurities from fossil fuels, ammonia synthesis, water gas shift reaction to produce hydrogen, and fuel cell catalysts [9-12]. These type phases are typically synthesized by gas reactions of complex oxide precursors or by molecular precursor or chemical synthesis [13-15] routes. The use of intermetallic precursors offers the potential to leverage a different set of precursor stoichiometries and structures, with the corresponding potential to form new complex carbide and nitride phases not attainable by currently used synthesis routes. It also offers the opportunity to leverage the initial metallic phase equilbria of the precursor alloy to control the morphology and structure of the phases that are formed; for example to synthesize a near-surface composite structure based on an initial two-phase alloy precursor microstructure. As a first step, a series of alloys based on the intermetallic CoMo phase were selected for study, in an attempt to form $Co_6Mo_6C_2$ and related complex carbide phases of interest for catalysis.

Figure 3 shows a schematic of the Co-Mo phase diagram [16]. A single-phase CoMo alloy, Co-45Mo, and a two phase Co(Mo) + CoMo alloy, Co-25Mo at.%, were selected for study. Coupons were cut from as arc-cast buttons and prepped to a 240 grit surface finish. Carburization was conducted at 1050°C in H_2-CH_4 mixtures (details of the processing are proprietary). A typical x-ray diffraction (XRD) pattern after carburization is shown in Fig. 4.

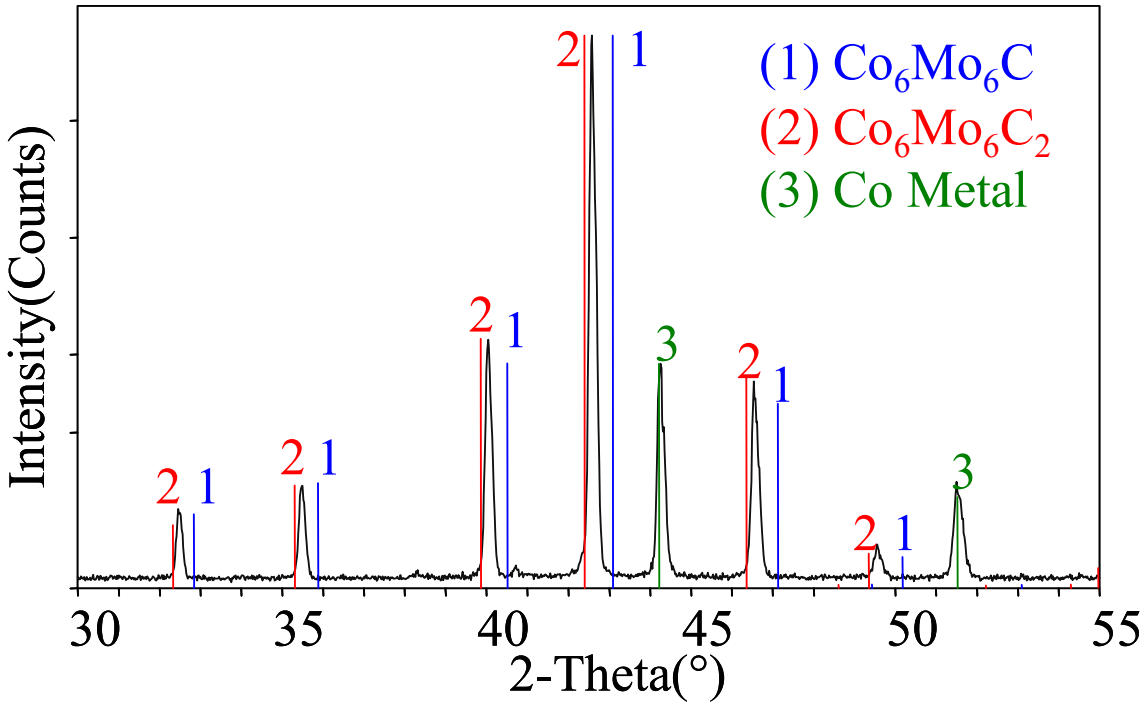

Fig. 4-Typical XRD data for carburized CoMo alloys

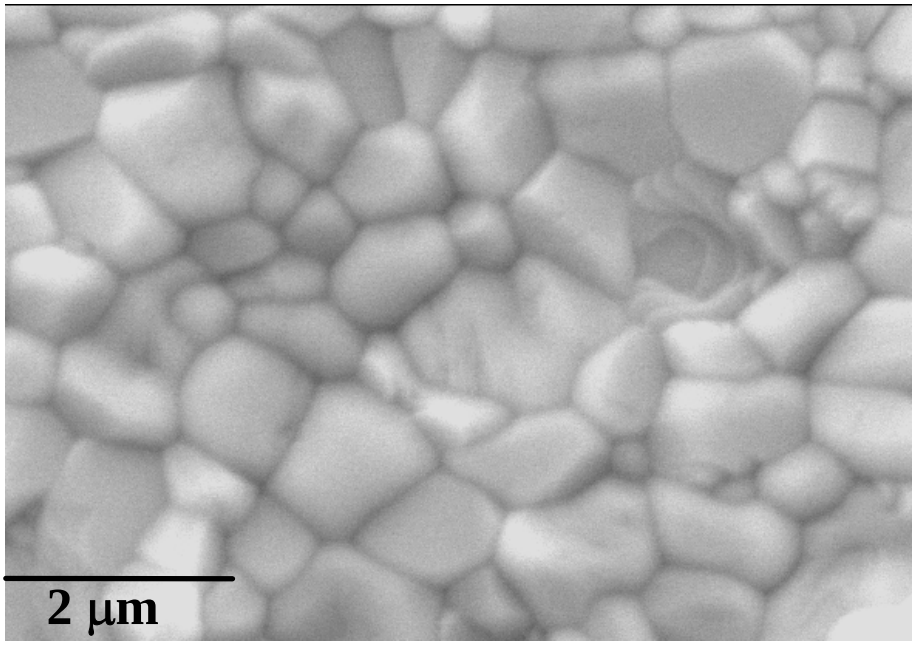

Fig. 5-Secondary mode surface SEM of Co-45Mo after carburization

Two phases were evident, slightly carbon-lean $Co_6Mo_6C_2$ and Co(Mo) metal. The relative amounts of the phases depended on the initial alloy composition, with Co-25Mo showing significant quantities of Co(Mo) metal, and Co-45Mo only trace levels. Surface SEM and EPMA analysis of the carburized coupons (Fig. 5 and 6) were consistent with the XRD data.

The surface of carburized Co-45Mo consisted of essentially single-phase Co-Mo carbide of average composition 45Mo-42Co-13C at.%, consistent with a slightly carbon-lean $Co_6Mo_6C_2$

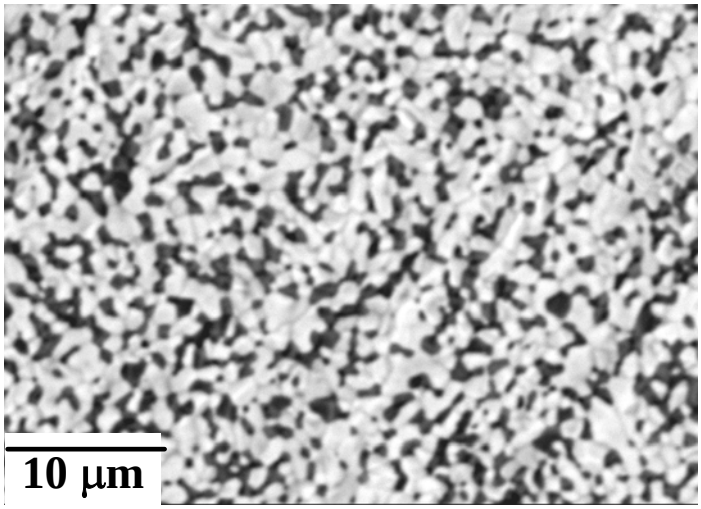

Fig. 6-Backscatter mode surface SEM of Co-25Mo after carburization.

(Fig. 5). A local composite surface structure of $Co_6Mo_6C_2$ and Co(Mo) solid solution metal was formed on Co-25Mo (Fig. 6). These results establish proof of principle for the synthesis of complex carbide phases of interest for catalysis by the carburization of intermetallic precursor alloys.

FUTURE WORK

For the intermetallic-strengthened steel effort, studies of precipitate phase equilibria and morphology as a function of composition and processing will be pursued. These will be correlated with mechanical property measurements, particularly elevated temperature tensile properties and creep behavior. An exploratory effort will also be pursued for multi-phase strengthened TiAl +Nb, W base alloys for applications above 800°C (industrial steam turbine blades and related components), including evaluation of alloying additions to promote protective Al_2O_3 scale formation.

For the controlled oxidation synthesis effort, further studies of carburization reactions in the Co-Mo and related systems will be pursued to gain insight into the relationships between the initial precursor alloy composition and structure, and the resultant carburized surface that is formed. Efforts to synthesize new phases in these systems will also be explored. Emphasis will also be placed on establishing collaborations to explore the catalytic properties of complex carbide structures synthesized from intermetallic precursors and their potential for technological impact.

REFERENCES

1. M.P. Brady, J.H. Zhu, C.T. Liu, P.F. Tortorelli, L.R. Walker, C.G. McKamey, J.L. Wright, C.A. Carmichael, D.J. Larson, M.K. Miller, and W.D. Porter, *Mate. High Temp.*, vol. 16, no. 4, pp. 189-193 (1999).
2. M.P. Brady, J.H. Zhu, C.T. Liu, P.F. Tortorelli, and L.R. Walker, *Intermetallics*, 8, 9-11, pp. 1111-1118 (2000).

3. D.M. Scruggs, 'Ductile Chromium Composition", U.S. Patent 3, 175, 279 (Mar. 30, 1965).
4. M. P. Brady, I.M. Anderson, M.L. Weaver, H.M. Meyer, L.R. Walker, M.K. Miller, D.J. Larson, I.G. Wright ,V.K. Sikka, A. Rar, G.M. Pharr, J.R. Keiser, and C.A. Walls, *Mater. Sci. Eng. A* 358 (1-2): 243-254 (2003)
5. R. Viswanathan and W. Bakker Journal Of Materials Engineering And Performance, 10 (1): 81-95 (2001)
6. M.P. Brady, S.K. Wrobel, T.A. Lograsso, E.A. Payzant, D.T. Hoelzer, J.A. Horton, and L.R. Walker, Chemistry of Materials 16 (10): 1984-1990 (2004).
7. M.P. Brady and P.F. Tortorelli, Intermetallics (in press).
8. M.P. Brady, D.T. Hoelzer, E.A. Payzant, P.F. Tortorelli, J.A. Horton, I.M. Anderson, L.R. Walker, S.K. Wrobel, Journal of Materials Research, Vol. 16, No. 10, 2784-2787 (2001).
9. S. Korlann, B. Diaz, M.E. Bussell, Chem Mater, 14, 4049-4058 (2002)
10. V. Schwartz V, S.T. Oyama, J.G.G., Chen Journal of Physical Chemistry B, 104 (37), 8800-8806 (2000).
11. J. Patt, D.J. Moon, C. Phillips, L. Thompson, Catalysis Letters, 65 (4): 193-195 (2000).
12. R. Kojima and K. Aika, Applied Catalysis A-General, 219 (1-2): 141-147 (2001).
13. S.H. Elder, L.H. Doerrer, F.J. DiSalvo, J.B. Parise, D. Giyomard, J.M. Tarascon, Chem. Mater., 4, 928 (1992).
14. R. Marchand, Y. Laurent, J. Guyader, P. L'Haridon, P. Verdier, J. Europ. Ceram. Soc., 8, 197 (1991)
15. K.S. and P.N. Kumta, Materials Science And Engineering B-Solid State Materials For Advanced Technology, 38 (1-2): 109-117 (1996).
16. ASM Binary Alloy Phase Diagrams Handbook Vol. 2, T.B. Massalaski et al, editors (1990).

ACKNOWLEDGEMENTS

This research was sponsored by the U.S. Department of Energy, Fossil Energy Advanced Research Materials (ARM) Program. Oak Ridge National Laboratory is managed by U.T.-Battelle, LLC for the U.S. Department of Energy. The authors thank B.L. Armstrong and J.H. Schneibel for reviewing this manuscript.

TESTING OF A VERY HIGH-TEMPERATURE HEAT EXCHANGER FOR IFCC POWER SYSTEMS

John P. Hurley, University of North Dakota Energy & Environmental Research Center
PO Box 9018, Grand Forks, ND 58202-9018
(701) 777-5159, jhurley@undeerc.org

Norman S. Bornstein, Metallurgical Consultant

ABSTRACT

Under funding from the U.S. Department of Energy, Xcel Energy Corporation, and the North Dakota Industrial Commission, the University of North Dakota Energy & Environmental Research Center has built and operated a coal-fired pilot-scale slagging furnace to test a high-temperature heat exchanger (HTHX) which could be the heart of an indirectly fired combined-cycle (IFCC) power plant. This type of system has the potential to reach an efficiency of 45% when firing coal and over 50% when a gas-fired duct burner is used to additionally heat the air entering the gas turbine. The high efficiency of an IFCC system makes it suitable for using oxygen-enriched combustion in order to make carbon sequestration more economical. It has the added benefit of minimizing water usage by dramatically reducing the amount of cooling and makeup water, since only half as much steam is produced as in a typical steam plant. Also, by staging combustion of the coal, the volume of flue gas would be dramatically reduced, shrinking the overall size and capital cost of the system.

The HTHX was designed and built by the United Technologies Research Center. It is composed of three 6-foot-long by 2½-inch-o.d. tubes of oxide dispersion-strengthened (ODS) alloys which were originally protected from the products of combustion by ceramic panels. It was used to produce process air at 1750°F and 150 psig over 2000 hours of testing with a variety of coals. For a short time, conditions of 2000°F and 100 psig were reached. In more recent tests, the bare alloy tubes were exposed directly to the products of combustion which increased heat exchange coefficients by five times, suggesting the HTHX cost would be only 1/10 as much as with the ceramic panels.

In the original HTHX, the three ODS alloy tubes were made from Ni–Cr MA754. Recently, the middle tube was removed and replaced with a tube made from Fe–Cr–Al MA956. Under the Advanced Research Materials Program, the MA754 alloy tube that was removed was analyzed by scanning electron microscopy to determine the state of the joints and exposed surfaces after 2300 hours of HTHX exposure to coal combustion conditions. The analyses show that although oxidation and corrosion of the materials were minimal, recrystallization had occurred in the tube joints that would likely compromise the mechanical properties of the joints. The recrystallization most likely occurred because of reactions with a residual glass lubricant used in the extrusion process, and the high temperatures and material used in the brazing process. It is suggested that the use of a lower-temperature, transient, liquid-phase bonding process may be more successful in creating joints without the recrystallization.

INTRODUCTION

To increase national energy self-sufficiency for the near future, power systems will be required to fire low-grade fuels more efficiently than is currently possible. The typical coal-fired steam cycle used at present is limited to a maximum steam temperature of 540°C and a conversion efficiency of 35%. Higher working-fluid temperatures are required to boost efficiency, exposing subsystems to very corrosive conditions. In order to initially evaluate the suitability of a new material for use in a fossil energy system and determine appropriate alterations in material composition or processing during the development stage, short-term tests of the corrosion resistance of the material and the corrosion mechanisms must be performed.

The University of North Dakota Energy & Environmental Research Center (EERC) is working with the Oak Ridge National Laboratory (ORNL) and the U.S. Department of Energy (DOE) National Energy Technology Laboratory to provide technical assistance to the Fossil Energy Materials Program investigating materials failure due to corrosion in

fossil energy systems. The main activities of the EERC are to assemble coal slag and ash samples for use in corrosion tests by materials researchers, assist in providing opportunities for realistic corrosion tests of advanced materials in pilot-scale fossil energy systems, and provide analytical support in determining corrosion mechanisms of the exposed materials.

This work serves DOE goals of advancing the efficiency and reducing the emissions of coal-fired power plants by providing inexpensive and rapid initial tests of the corrosion resistance of newly developed advanced materials. The information is most useful in the development stage so that the potential of the material for use in a fossil energy system can be quickly assessed and modifications can be made to the material or its processing in order to increase its corrosion resistance. Upon successful testing under this program, the materials developer will be able to produce a more corrosion-resistant material, recommend appropriate uses for the material in a fossil energy system, and choose appropriate long-term testing scenarios under other programs.

Under the DOE High-Performance Power System Program,[1,2] a pilot-scale solid-fuel combustion slagging furnace system (SFS) was designed and built at the EERC under an award to the United Technologies Research Center (UTRC). It was used to test the construction and operation of a high-temperature heat exchanger (HTHX) for possible use in an indirectly fired combined cycle (IFCC) power plant. The SFS and HTHX were operated under that program for over 2000 hours, routinely producing hot process air at 150 psi and 1750°F and, for a short time, at 100 psi and 2000°F. An IFCC using this type of heat exchanger has the potential to reach efficiencies of 45% when firing coal and over 50% when a gas-fired duct burner is used to additionally heat the process air entering the gas turbine.[3,4]

Because of its high efficiency, an IFCC system is the most appropriate power concept for employing oxygen-enriched combustion in order to make carbon sequestration more economical. It has the added benefit of minimizing water usage by dramatically reducing the amount of cooling and makeup water, since only half as much steam is produced as in a typical steam plant. By staging combustion of the coal in such an oxygen-blown system, the need for flue gas recirculation to manage the flame temperature could possibly be reduced, and the maximum amount of energy could be channeled to the gas turbine, raising overall plant efficiency. In addition, reducing the volume of flue gas would substantially reduce the required size of the baghouse or electrostatic precipitator, flue gas desulfurization system, and induced- and forced-draft fans, thereby reducing both capital and operating costs. It would also permit the most economical use of a condensing heat exchanger for reclaiming combustion water and thereby even further reducing the amount of outside water necessary for plant operation. In addition to oxygen-enriched firing, it could be used to fire blends of coal and biomass to reduce the rate of consumption of coal resources and net production of carbon dioxide.

EXPERIMENTAL EQUIPMENT AND PROCEDURES

The SFS is designed to heat the HTHX under flowing slag conditions so that it can produce process air at 1750°F and 150 psig. A schematic of the system is shown in Figure 1. The SFS is designed for a maximum furnace exit temperature of 2900°F but is typically run at 2750°F at the exit in order to maintain desired slag flow while extending the furnace lifetime. It has a nominal firing rate of 2.5 million Btu/h and a range of 2.0–3.0 million Btu/h using a single burner. The design is based on a bituminous coal (Illinois No. 6) and a nominal furnace residence time of 3.5 s. Resulting flue gas flow rates range from roughly 425 to 640 scfm, with a nominal value of 530 scfm based on 20% excess air. Firing a low-rank coal or cofiring with biomass will increase the flue gas volume, decreasing residence time to roughly 2.7 s. However, the high volatility of the low-rank fuels results in high combustion efficiency (>99%). The EERC oriented the furnace vertically (downfired) and based the burner design on a swirl burner currently used on two EERC pilot-scale pulverized coal-fired units that are fired at 600,000 Btu/h. The furnace dimensions are 47 in. inside diameter (i.d.) by roughly 18 ft in length. It is lined with three layers of refractory totaling 12 in. in thickness. The inner layer is composed of an alumina castable, developed by the EERC in cooperation with the Plibrico Company, that has been shown in laboratory and pilot-scale tests to be extremely resistant to slag corrosion.

A key design feature of the furnace is accessibility for installation and testing of a large HTHX test panel for testing material lifetimes and heat exchange coefficients. The HTHX is 1 × 6 ft in size. This size was based on manufacturing constraints identified by UTRC, which designed and built it. The HTHX is composed of three vertically oriented 2½-in.-diameter oxide-dispersion strengthened (ODS) alloy tubes. Process air to be heated by the HTHX panel is provided by

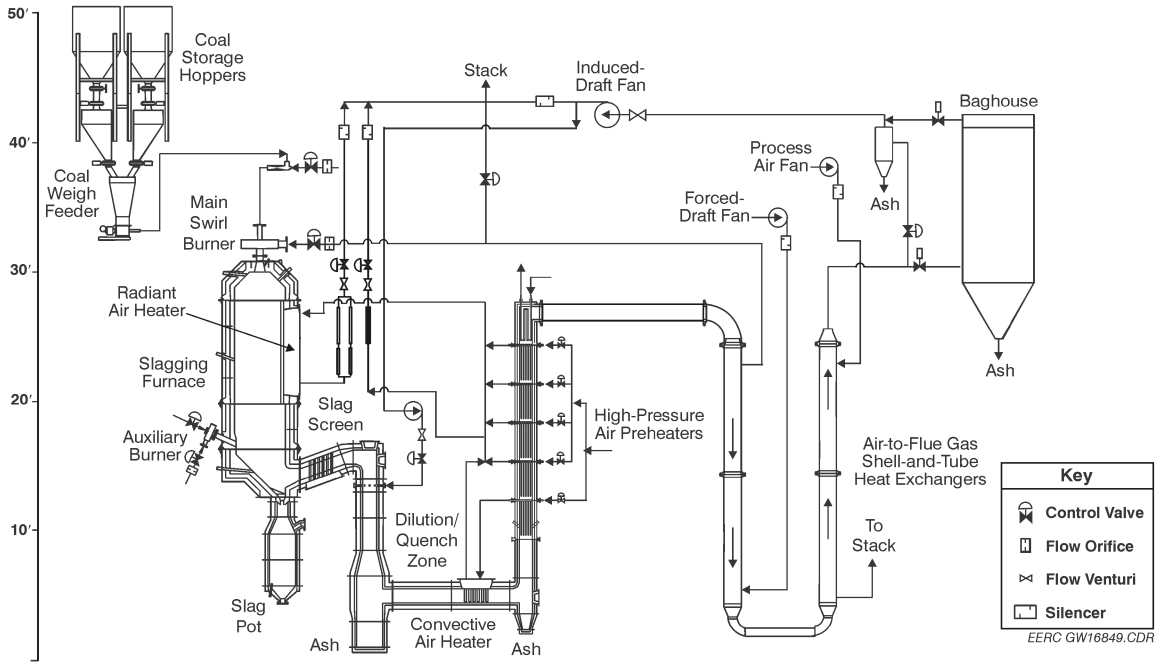

Figure 1. Schematic of the EERC high-temperature SFS.

an existing EERC air compressor system having a maximum delivery rate of 510 scfm and a maximum stable delivery pressure of 275 psig. It is heated from 1000°F to as much as 1800°F as it passes through. For a short time, air at 2000°F and 100 psi was produced. A tie-in to an existing nitrogen system was also installed as a backup to the existing air compressor system to prevent the panel from overheating in the event of a power outage. To protect the alloys from corrosion by the products of coal combustion, UTRC designed the HTHX to include panels of corrosion-resistant ceramic between the alloy heat exchanger tubes and the coal flame. The "tubes-in-a-box" design is shown in Figure 2. The alloy tubes were originally composed of MA754, a nickel and chromium ODS alloy. The elbow blocks and tube were transient liquid phase (TLP) brazed at Johnson Industries. The nickel-based braze contained 9.5% Cr, 3.0% Al, 4.9% Ti, 7.0% (Mo + W), 4.5% Si, and 0.7% B. The nominal melting point of the braze is about 1900°F (1040°C), and the TLP brazing process is usually completed within 36 hours. It was not known, until the analyses presented here, that the siliceous compound (a glass) used as a lubricant in the tube-manufacturing process was not completely removed.

After 2000 hours of pilot-scale testing, the ceramic panels were removed to expose the tubes directly to the products of coal combustion. After an additional 300 hours of testing in the bare-tube configuration, a tube of MA956, an iron, chromium, and aluminum ODS alloy, was substituted for the middle MA754 tube. ODS materials were chosen because the dispersed oxide particles (yttria) help to pin grain boundaries, reducing creep and stabilizing the protective oxide coatings.[5] Problems related to the use of ODS alloys are their relatively high cost, the current difficulty in joining them,[6] and the lack of data about their performance when exposed to the products of coal combustion at high temperature. To help resolve some of this lack of data, under the Advanced Research Materials Program, the MA754 alloy tube that was removed was analyzed by scanning electron microscopy (SEM) to determine the state of the joints and exposed surfaces after 2300 hours of HTHX exposure to natural gas and coal combustion conditions.

RESULTS AND DISCUSSION OF HTHX MA754 TUBE AND JOINT ANALYSES

To measure the corrosion of the HTHX, a section consisting of one main tube and two elbows was removed, and sections of the tube as well as the elbow/tube joint on the outlet side of the HTHX were analyzed by SEM. Figure 3 shows the tube and outlet elbow before being further sectioned in preparation for SEM analysis. Three coupons were cut from the main tube to look at fireside corrosion near the gas inlet, middle, and gas outlet sides of the tube. Figure 4 shows a

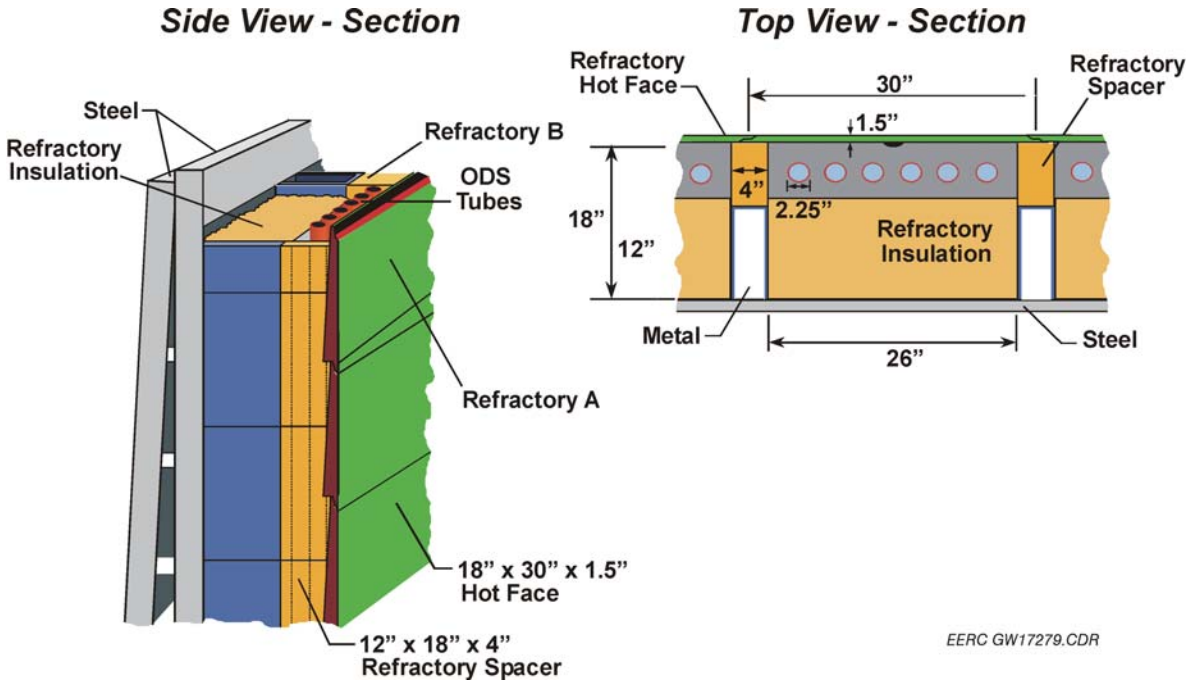

Figure 2. The original "tubes-in-a-box" heat exchanger design.

Figure 3. The central MA754 tube and one elbow removed from the HTHX.

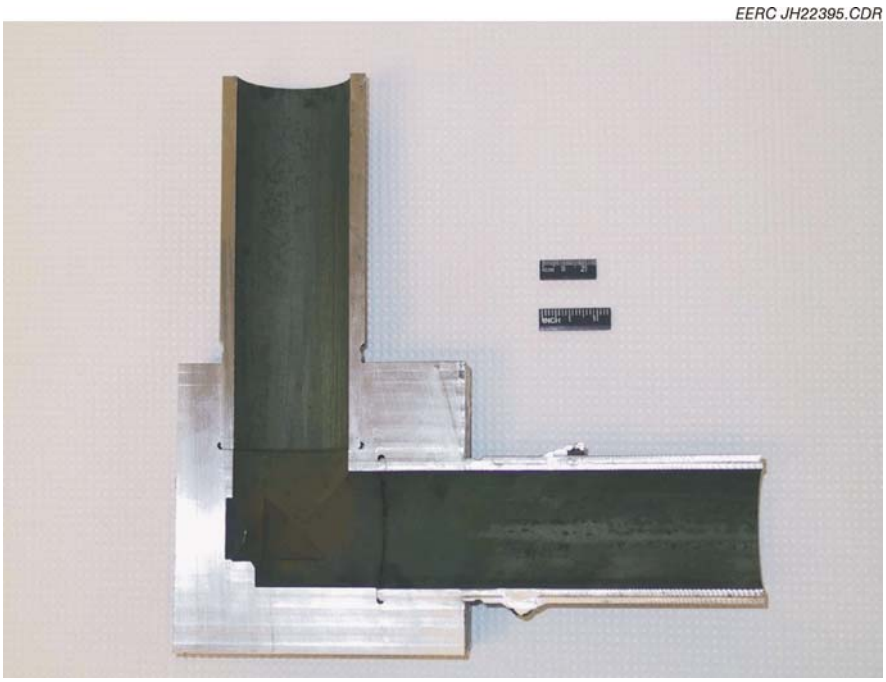

Figure 4. One half of the cross-sectioned MA754 elbow.

close-up of the cross-sectioned elbow. One-half of the elbow was sent to ORNL for further sectioning and strength testing of the joint between the pipe and the elbow. The EERC sectioned the other half of the elbow for SEM analyses of the joint. The SEM analyses were performed at the EERC under the direction of Dr. Norman S. Bornstein who is being funded under the ODS alloy development activities within the ARM program. Dr. Bornstein was the principal metallurgist on the UTRC team that designed and constructed the HTHX.

AS-RECEIVED MATERIAL

A section of unexposed MA754 pipe from the batch used in the construction of the heat exchanger was used as a baseline for comparison to the exposed material. The interior had a patchy green chromia layer. It formed during the manufacturing process when a high-temperature recrystallization treatment was used to develop the desired grain structure. The process consists of a heat treatment at 2400°F (1320°C) for 1 hour followed by air cooling to room temperature. Cross sections of the outer and inner surfaces of the unexposed alloy are shown in Figures 5 and 6, respectively. The nominal thickness of the friable surface oxide is about 13 μm, and the depth of the internally oxidized zone is about 30 μm. The composition of the matrix phase is consistent with substrate alloy chemistry. The oxide formed on the interior surface is quite tenacious (Figure 6a) and multiphased (Figure 6b). The nominal thickness of the outer siliceous-rich zone is about 8 μm; the chromia-rich inner layer is about 7 μm. The nominal composition of the outer siliceous-rich and chromia-rich inner layer is shown in Table 1. It is reasonable to assume that the internal and external scales formed during the high-temperature recrystallization treatment required to develop the desired grain structure. The siliceous contaminant is most likely remaining from the material applied to the surface during extrusion through a die as part of the mechanical alloying process. It is normally removed as part of processing. The nominal thickness of the internal oxide, approximately 7 μm, is consistent with the oxidation kinetics for chromia formation exposed 1 hour at 2400°F (1320°C).

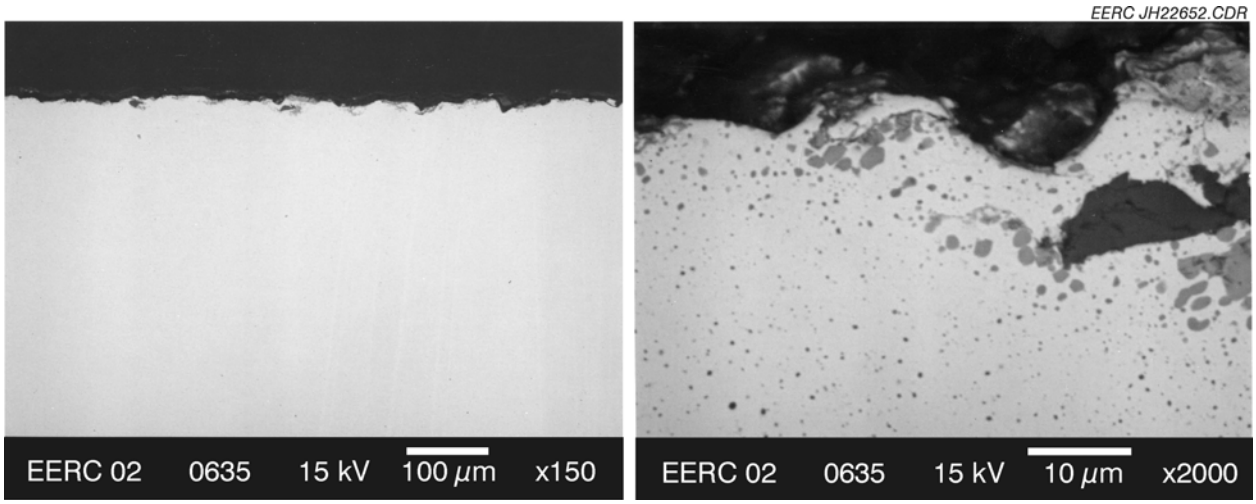

Figure 5. Outer surface of unexposed MA754 tube.

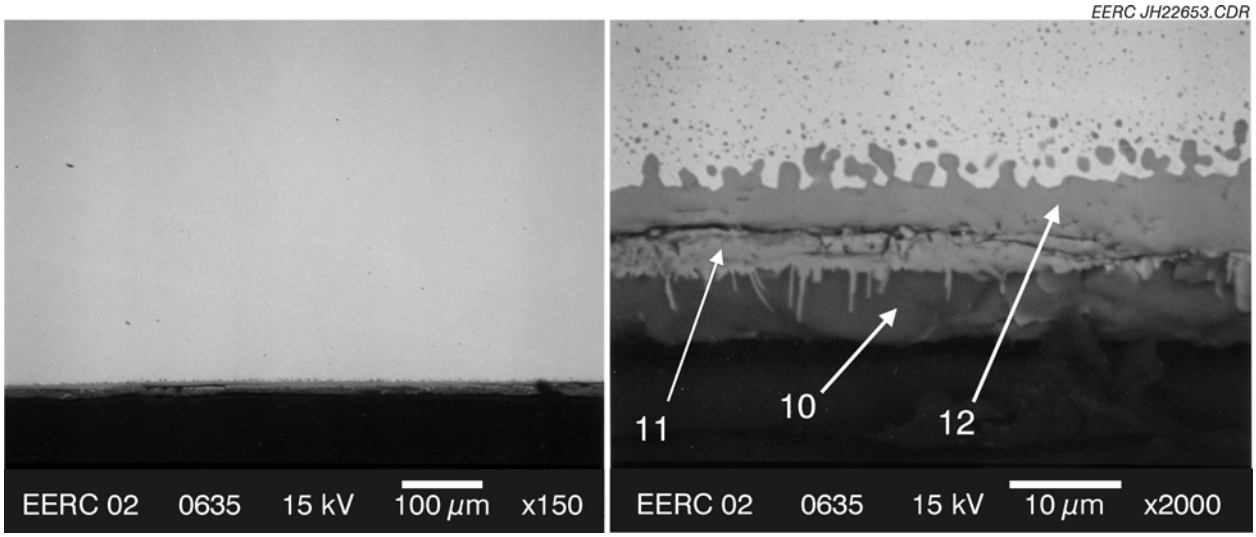

Figure 6. Inner surface of unexposed MA754 tube.

Table 1. Composition of Points Indicated in Figure 6, wt%

Point	10	11	12
Ni	13.8	2.2	1
Cr	2.7	87.8	89.1
Fe	0.5	0.3	0
Al	1.5	0.1	0.2
Ti	2.9	1.0	0.8
Y	0.6	0	0
O	12.7	7.8	7.9
Si	50.4	0.2	0.5

EXPOSED TUBE AT INLET

As shown in Figure 7, the oxide scale on the outer or flame side surface is nonuniform in composition. The compositions of the areas labeled 1 through 3 are listed in Table 2. The data show that foreign atoms indigenous to the ash and gases that contact the surface have been incorporated into the scale gases. Molten ash impacted the surface, and the elements calcium, magnesium, and phosphorus were observed within and on the chromia surface scale. The silica-rich inner scale varied in thickness from 18–85 µm and appeared quite tenacious. Fine precipitates moving into the alloy delineate the depth of diffusion of oxygen, which is very minimal.

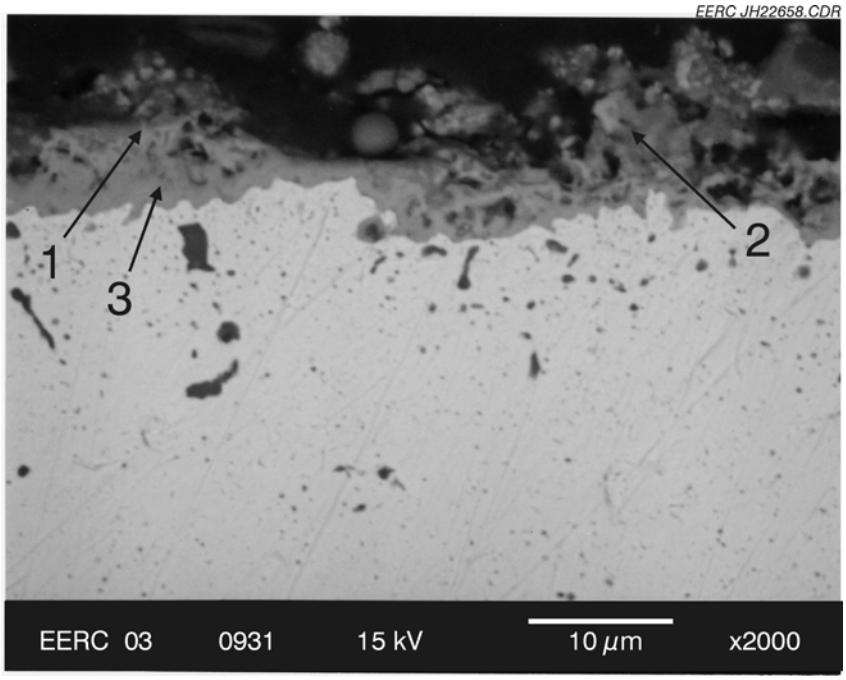

Figure 7. Outer surface of exposed MA754 tube.

Table 2. Composition of Points Indicated in Figure 7, wt%

Point	1	2	3
Ni	5.8	2.4	22.0
Cr	67.2	5.4	61.8
Fe	11.6	3.2	1.6
Al	0.9	2.5	2.6
Ti	3.2	11	4.3
Y	0.0	2.5	0.0
O	9.0	14.6	7.1
Si	0.5	7.7	0.2
Ca	0.0	33.8	0.0
Mg	0.0	2.3	0.0
P	0.0	11.8	0.0

The scale on the interior surface of the tube is relatively uniform and, as shown in Figure 8, about 18–85 µm thick and consists of silicates and chromia. Oxygen is diffusing into the substrate, but the depth of penetration is minimal.

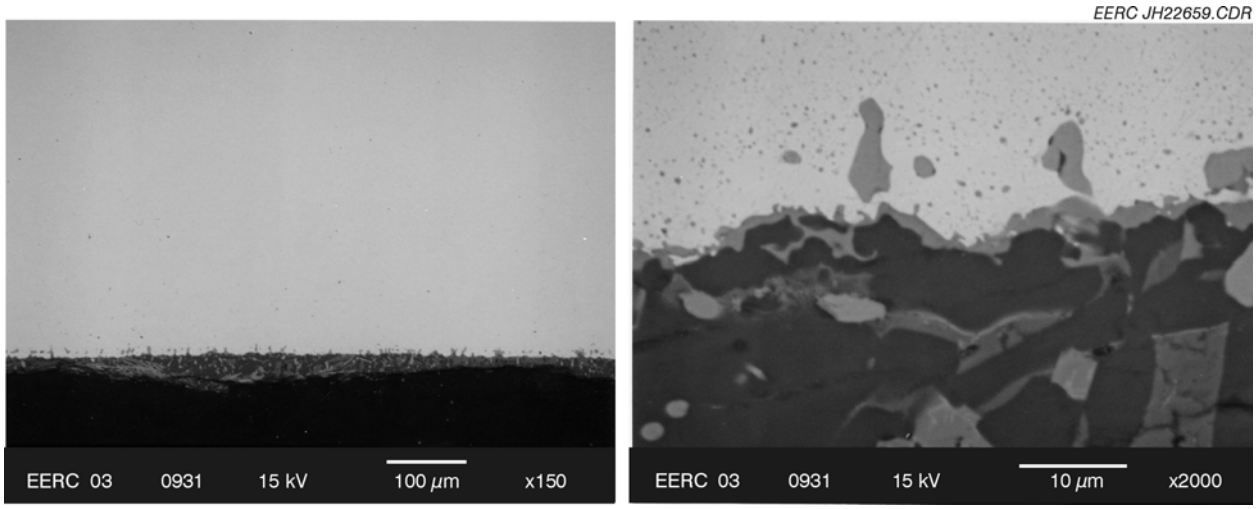

Figure 8. Inner surface of exposed MA754 tube.

ANALYSES OF THE OUTLET ELBOW

The MA754 tubing within the elbow at the outlet of the heat exchanger was exposed to temperatures of 1810°–1880°F during a typical test. The tube alloy structure consists of recrystallized grains outlined by oxide precipitates rich in the elements chromium, titanium, aluminum, yttrium, and silicon. The source of silicon is both the braze alloy and the glass initially present on the inner diameter of the tube. The changes in microstructure from the braze interface to the inner diameter of the tube are shown in Figures 9–12. The composition of the braze interface and the precipitates delineating the grain boundaries are shown in Tables 3 and 4. At the temperature range experienced within the elbow, the alloy is recrystallized. The zone just below the braze joint line in the tube appears to have a different morphology but is nevertheless recrystallized. The initial liquid associated with the braze alloy is most likely responsible for the recrystallization in this area. The source of silicon in the precipitates is most likely the braze alloy for the particles closest to the braze line and the siliceous lubricant for points closest to the inner diameter. A thorough examination of the behavior of the block was not performed. However, it is apparent that 1) the liquid braze did not significantly penetrate into the block and 2) the block did not exhibit any serious oxidation.

CONCLUSIONS

Although corrosion or oxidation of the tubes was not significant, the mechanical properties of the original MA754 tube are compromised because of recrystallization. There is little doubt that failure to remove the siliceous lubricant, necessary in the production of seamless tubing, may have significantly contributed to the demise of the alloy. However, there is no doubt that the initial brazing process promoted the recrystallization, an unwanted event. It is believed that a TLP bonding technique operating at a lower temperature than the braze process used in the original HTHX should alleviate the shortcomings of the braze process.

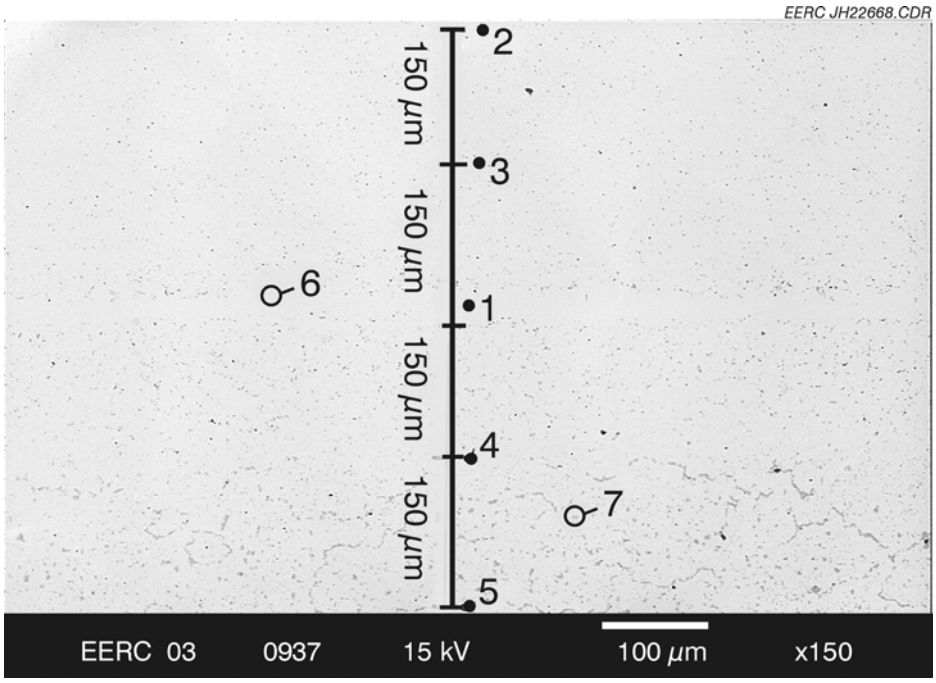

Figure 9. Outlet elbow 1810°F–1880°F braze interface. The interface is at the level of Point 1. Above is the elbow block, below is the tube.

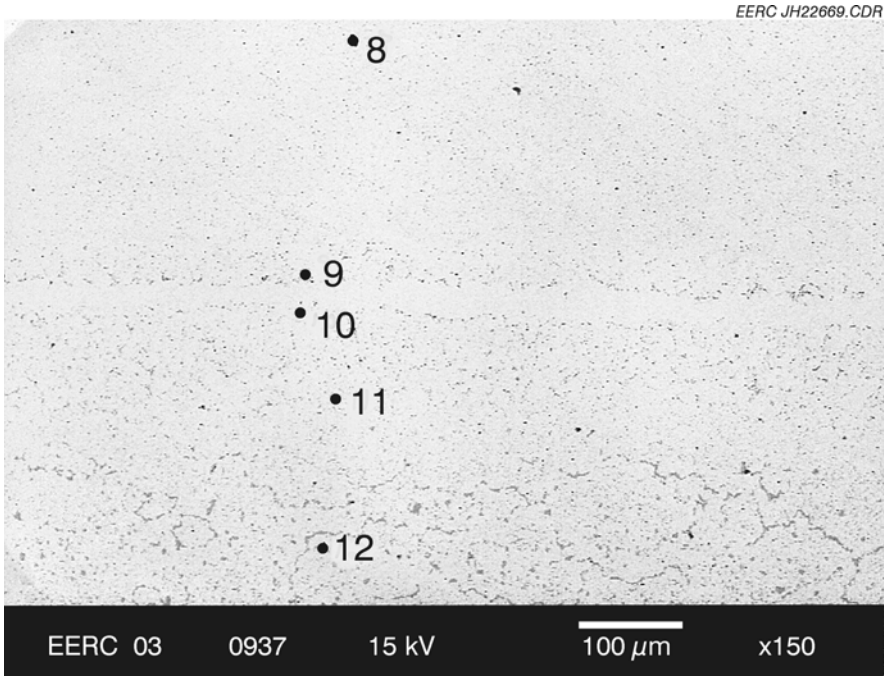

Figure 10. Outlet elbow Points 8–12. Same view as Figure 9, but analysis points chosen based on morphology.

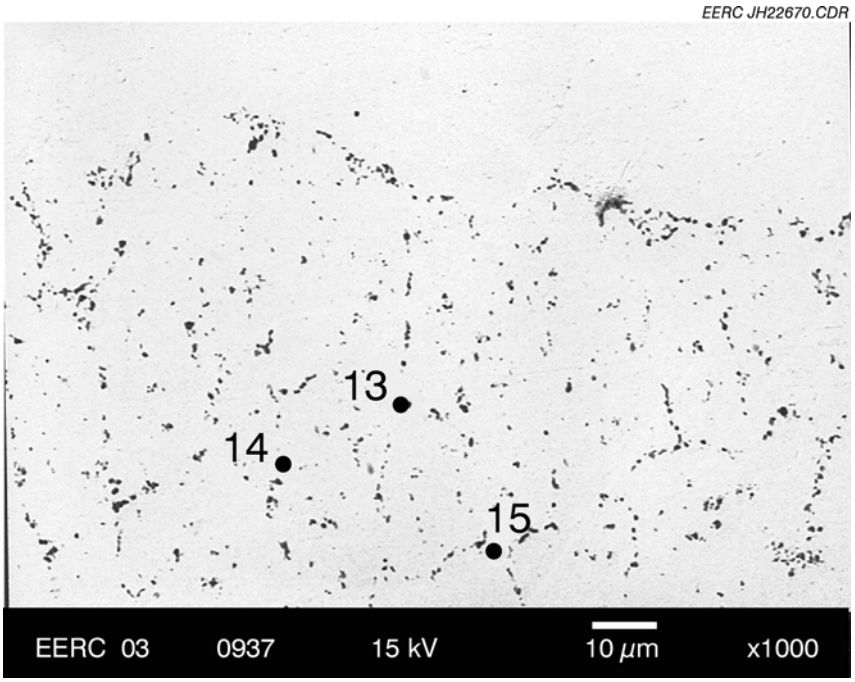

Figure 11. Points 13–15 outlet elbow. Higher-magnification view at the bottom of the braze line.

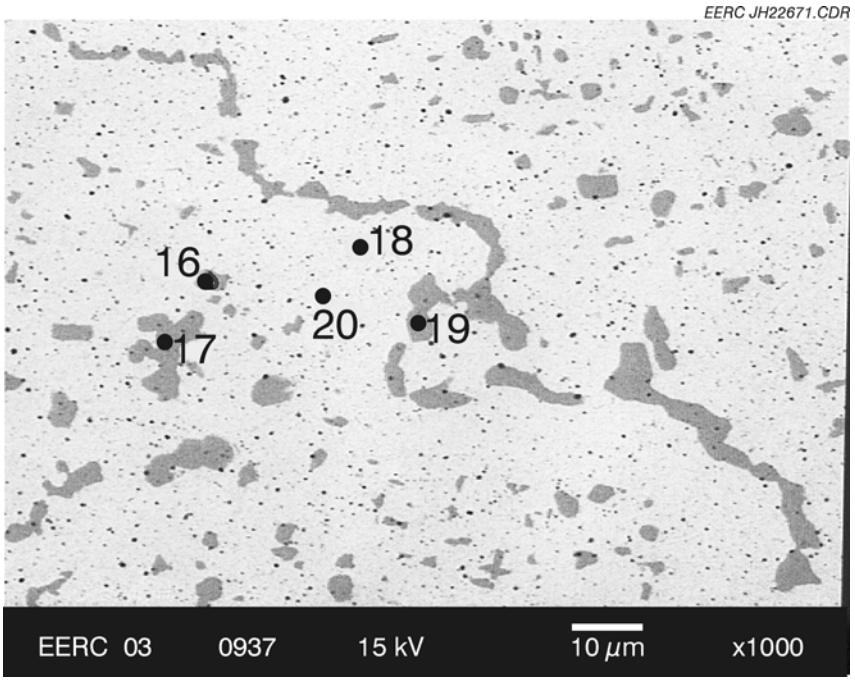

Figure 12. Outlet elbow Points 16–20, approximately one-half way between the inner radius of the tube and the braze line.

Table 3. Composition of Precipitate Points 1–12 in Figures 9 and 10, wt%

Point Number	1	2	3	4	5	6	7	8	9	10	11	12
Ni	72.8	77.9	74.1	70.2	70.3	16.7	7.7	70.2	73.4	72.1	70.9	70
Cr	25.1	20.5	21.8	26.1	27.1	9.4	88.7	21.7	24.2	25.9	26.6	27
Fe	0.3	0.2	0.2	0.3	0.3	0.1	0	0.1	0.2	0.3	0.4	0.2
Al	0.2	0.2	0.4	0.3	0.2	36.5	0.1	0.5	0.2	0.2	0.2	0.2
Ti	0.1	0.2	0.8	1.7	0.1	20.8	0.1	3.4	0.3	0	0.1	0.7
Y	<0.1	0.4	0.4	0.2	0.3	2.1	0.1	0.2	0	0	0.3	0.3
O	1.2	1.1	1.1	1	1.4	14.2	3	3.2	1.2	1.2	1.3	1.3
Si	0.1	0.1	0.1	0.1	0.1	0.1	0.1	0.2	0.2	0.2	0.2	0.1
Mg	0	0	0	0	0	0.1	0	0.2	0.1	0.1	0.1	0.1
Ca	0	0	0	0	0	0.1	0.1	0.1	0.1	0.1	0	0.1

Table 4. Composition of Points 13–24 in Figures 11 and 12, wt%

	Point Number											
Element	13	14	15	16	17	18	19	20	21	22	23	24
Ni	41.1	55.5	37	6.8	2.4	36.1	8.1	27.7	71.6	68.1	30.5	43.9
Cr	18.4	21	18	17.6	88.6	22.7	88.9	27.7	22.6	28.8	14.8	18.1
Fe	0.3	0.2	0.4	0	0	0.2	0	0.3	0.5	0.2	0.1	0.2
Al	16.4	4.1	25	43.8	0.2	26	0	0.1	2.5	0.2	28.2	29.3
Ti	2	11.9	9.5	13.2	0.1	7.5	0	0.1	0	0.1	13.3	0.2
Y	15.5	4.6	1.9	4.9	0.5	0.6	0	0	0.4	0.5	3.5	0
O	6.1	2.3	7.7	13.5	3	6.6	2.8	1.2	1.9	1.6	9.1	7.7
Si	0	0.1	0	0	0.1	0.3	0	0.1	0.3	0.1	0.3	0.2
Mg	0	0	0	0	0	0	0	0	0	0.1	0.1	0.1
Ca	0	0	0	0	0	0	0	0	0.1	0.1	0	0.1

REFERENCES

1. Klara, J.M. HiPPS: Beyond State-of-the-Art: Part I. *Power Eng.* **1993**, *Dec*, 37–39.
2. Klara, J.M. HiPPS Can Compete with Conventional PC Systems: Part II. *Power Eng.* **1994**, *Jan*, 33–36.
3. United Technologies Research Center. *Combustion 2000 Phase II Final Technical Report*; DE-AC22-95PC95144; 2001.
4. Robson, F.L.; Ruby, J.D.; Nawaz, M.; Seery, D.J.; Jones, M.L.; Hurley, J.P. Application of High-Performance Power Systems (HiPPS) in Vision 21 Power Plants. In *Proceedings of the 2002 American Power Conference*; Chicago, IL, 2002.
5. Quadakkers, W.J.; Holzbrecher, H.; Briefs, K.G.; Beske, H. Differences in Growth Mechanisms of Oxide Scales Formed on ODS and Conventional Wrought Alloys. *Oxidation of Metals* **1989**, *32* (1, 2), 67–88.
6. McKimpson, M.G.; O'Donnell, D. Joining ODS Materials for High-Temperature Applications. *JOM* **1994**, *July*, 49–51.

IMPROVED REFRACTORIES FOR SLAGGING GASIFIERS IN IGCC POWER SYSTEMS

James P. Bennett
U.S. Department of Energy Albany Research Center,
1450 Queen Ave., SW, Albany, OR 97321
E-mail: jbennett@alrc.doe.gov; Telephone: (541) 967-5983; Fax: (541) 967-5845

Kyei-Sing Kwong, Cynthia Powell Dogan and Richard E. Chinn
U.S. Department of Energy Albany Research Center, 1450 Queen Ave., SW, Albany, OR 97321

ABSTRACT

Most gasifiers are operated for refining, chemical production, and power generation. They are also considered a possible future source of H_2 for future power systems under consideration. A gasifier fulfils these roles by acting as a containment vessel to react carbon-containing raw materials with oxygen and water using fluidized-bed, moving-bed, or entrained-flow systems to produce CO and H_2, along with other gaseous by-products including CO_2, CH_4, SO_x, HS, and/or NO_x. The gasification process provides the opportunity to produce energy more efficiently and with less environmental impact than more conventional combustion processes. Because of these advantages, gasification is viewed as one of the key processes in the U.S. Department of Energy's vision of an advanced power system for the 21st Century. However, issues with both the reliability and the economics of gasifier operation will have to be resolved before gasification will be widely adopted by the power industry. Central to both enhanced reliability and economics is the development of materials with longer service lives in gasifier systems that can provide extended periods of continuous, trouble-free gasifier operation.

The focus of the Advanced Refractories for Gasification project at the Albany Research Center (ARC) is to develop improved refractory liner materials capable of withstanding the harsh, high-temperature environment created by the gasification reaction. Current generation refractory liners in slagging gasifiers are typically replaced every 3 to 18 months at costs ranging up to $1,000,000 or more, depending upon the size of the gasification vessel. Compounding materials and installation costs are the lost-opportunity costs for the time that the gasifier is off-line for refractory repair/exchange. The goal of this project is to develop new refractory materials or to extend the service life of refractory liner materials currently used to at least 3 years.

Post-mortem analyses of refractory brick removed from slagging commercial gasifiers and of laboratory produced refractory materials has indicated that slag corrosion and structural spalling are the primary causes of refractory failure. Historically, refractory materials with chrome oxide content as high as 90 pct have been found necessary to achieve the best refractory service life. To meet project goals, an improved high chrome oxide refractory material containing phosphate additions was developed at ARC, produced commercially, and is undergoing gasifier plant trials. Early laboratory tests on the high chrome oxide material suggested that phosphate additions could double the service life of currently available high-chromium oxide refractories, translating into a potential savings of millions of dollars in annual gasifier operating costs, as well a significant increase in gasifier on-line availability. The ARC is also researching the potential of no-chrome/low-chrome oxide refractory materials for use in gasifiers. Some of the driving forces for no-chrome/low-chrome oxide refractories include the high cost and manufacturing difficulties of chrome oxide refractories and the fact that they have not met the performance requirements of commercial gasifiers. Development of no/low chrome oxide refractories is taking place through an examination of historical research, through the evaluation of thermodynamics, and through the evaluation of phase diagram information. This work has been followed by cup tests in the laboratory to evaluate

slag/refractory interactions. Preliminary results of plant trials and the results of ARC efforts to develop no-chrome/low chrome refractory materials will be presented.

INTRODUCTION

Gasifiers are operated for refining, chemical production, and power generation, and are being considered as a possible source of H_2 for some future power systems. They act as a containment vessel to react carbon-containing raw materials with oxygen and water using fluidized-bed, moving-bed, or entrained-flow systems to produce CO and H_2, along with other gaseous by-products including CO_2, CH_4, SO_x, HS, and/or NO_x (1). Gasification provides the opportunity to produce energy more efficiently and with less environmental impact than more conventional combustion processes.

Ash originating from impurities in the carbon-containing raw materials (primarily coal, petroleum coke, or combinations of them) is considered one of the primary by-products of the gasification process, forming molten slag in the combustion chamber of slagging gasifiers. Amounts of slag exceeding 5 or more tons per hour can be generated in a slagging gasifier. The gasification chamber typically operates at temperatures between 1250º and 1550ºC, at pressures of 400 psi or higher, and is lined with refractory materials to contain the severe environment and to protect the outer steel shell from erosion, corrosion, and temperature. The ash from the carbon feedstock is liquefied into slag in the gasification chamber and can corrode, penetrate, and interact with the refractory liner at the elevated temperatures, severely limiting refractory service life and gasifier operation. Reactions can occur between refractory materials and slag oxides of Fe, Si, and/or V; or with H_2 and CO gasification products (2). Other slag components such as Ca and Al will play a role in slag fluidity and penetration. Refractory materials used as liner materials in a gasifier are typically dense firebrick composed of chromium oxide as the primary component, along with smaller quantities of other refractory oxides (typically aluminum and/or zirconium oxide).

Because of the severe environment in a slagging gasifier, the material challenges for a refractory liner are many, and include: elevated temperature; large and/or rapid changes in temperature; erosion by particulates; molten slag attack; variable slag composition resulting from the feed stock; attack by hot corrosive gases; alkali vapor attack; and variable oxidizing and/or reducing conditions (3-5). Refractory materials that can withstand these environments for long periods of time are necessary for a continuous, efficient, and reliable gasification process. The high chrome oxide material used today evolved through industrial efforts to develop an improved performance material, through plant trials conducted by industry, and through DOE and Electric Power Research Institute funded efforts traceable back to the 70's and 80's (3-11). This research and industrial experience indicated that only $Cr_2O_3 – Al_2O_3$, $Cr_2O_3 – Al_2O_3 – ZrO_2$, and $Cr_2O_3 – MgO$ compositions could withstand these conditions long enough to be economically feasible (3,12), although refractory materials with improved performance and lower material costs are desired. Bakker indicated that a minimum level of 75 pct Cr_2O_3 in a refractory material is necessary for sustained material performance in slagging gasifiers (13).

Failure of the refractory lining in a gasifier is expensive, both in terms of refractory replacement costs (up to $1,000,000 USD or higher, depending on gasifier size and the extent of rebuild required) and production down time. Re-lining a gasifier requires that the system be taken out of service, and under the best of circumstances takes about 10 days for a partial rebuild, longer for a complete rebuild. A rebuild involves cooldown (5-7 days) and teardown and repairs (3 days for a partial rebuild and 7-10 days or longer for a full rebuild - depending on the extent of repairs necessary). Some gasification facilities maintain a second gasifier for use while repairs are being made, reducing system downtime and increasing on-line service and availability of the gasification system. Even then, the time to switch gasifiers can vary from hours to days, depending on if the spare gasifier is in pre-heat mode and if it is available. Because of the long down times required for repair, gasifier operators would like to install

refractory linings with a reliable life of at least three years. The current generation refractory liners installed in gasifier systems have yet to meet this requirement, failing in as little as 3 months in high wear areas. Because of the short refractory service life and because of the importance of gasifiers in areas such as future power generation, the Albany Research Center of the U.S. Dept. of Energy (ARC) is researching hot face liners for integrated gasification combined cycle (IGCC) gasifiers. This paper discusses efforts to increase refractory service life on the hot face refractory walls of the gasifier through the use of an improved, chromium-oxide-based refractory containing phosphate additions and through the development of no-chrome/low-chrome oxide refractory liner materials. Improvements in refractory service life would lead to both enhanced gasifier reliability and economics, helping to give gasifier users extended periods of continuous, trouble-free gasifier operation.

CURRENT STATUS

CHROME BASED REFRACTORIES

A strategy was adopted by the Albany Research Center to develop new or improved high chrome-oxide refractory liner materials for the hot face of slagging gasifiers based on limiting refractory corrosion and on limiting slag penetration into a refractory material. This strategy was adopted after examining spent materials removed from slagging gasifier environments and determining their failure mechanisms. From the forensic analyses, it was noted that two primary causes of refractory failure occur; dissolution of the refractory in the molten slag and spalling of the refractory. These and other causes are shown in figure 1. Other gasifier issues that impact refractory wear, such as gasifier design, how a gasifier is operated, or factors involving refractory installation, were not evaluated in this study.

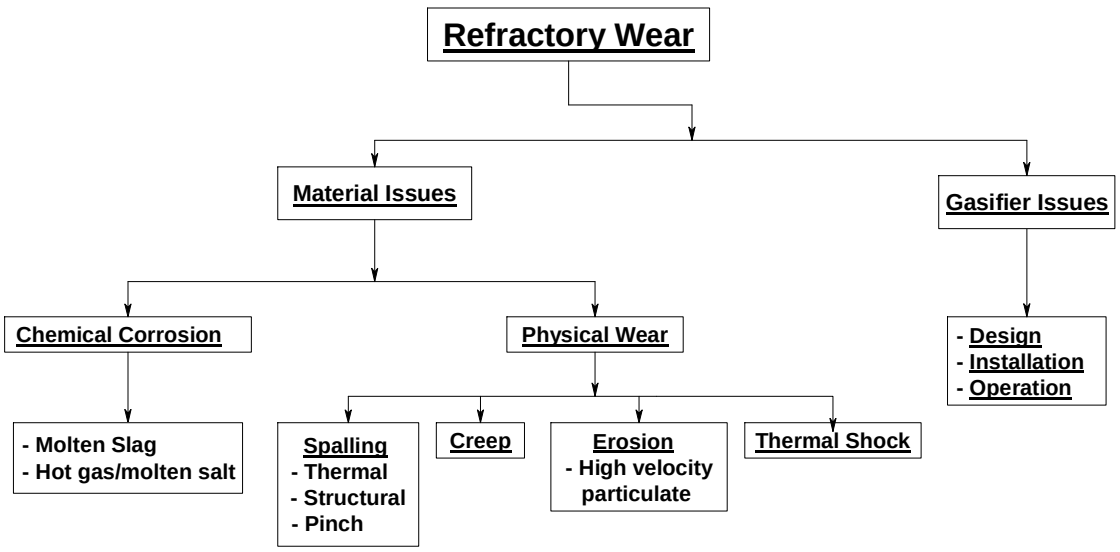

Figure 1 – Causes of refractory wear in a slagging gasifier.

Chemical corrosion as a refractory wear mechanism is caused by molten slag dissolution of the refractory as it flows down the refractory sidewall. During flow, a molten slag dissolves refractory material and releases some grains of refractory material into the slag as bond phases are removed. Both the dissolution and grain removal produce a gradual and predictable refractory wear. Spalling is caused by slag penetration and attack of the refractory hot face, leading to large "chunks" of the refractory material being removed as layers, and causing unpredictable and incremental refractory wear. Spalling starts with slag

that has penetrated the refractory surface, a process that is followed by small crack formation parallel to the hot face in or near the slag-penetrated/virgin refractory interface. These cracks link-up, a processes accelerated by sudden or large changes in gasifier operating temperature. Different expansion characteristics in the slag penetrated/non-penetrated layers, thermal cycling of the gasifier, stresses within the refractory and within the gasifier, and/or other possible factors contribute to spalling. Slag corrosion and spalling of a gasifier sidewall are shown in figure 2. Corrosion caused the gradual wearing away of refractory and is noted over all the gasifier sidewall, while the circled area indicates spalled material sliding down the gasifier hot face. Over time, the corrosion/spalling cycle repeats itself, leading to a rapid thinning of the gasifier sidewall.

Figure 2. Slagging gasifier refractory sidewall showing corrosive wear and spalling (circled material).

Analysis of the spent refractory failure mechanism was used to develop a phosphate containing high chrome oxide refractory material better able to withstand the severe service environment (14). Phosphate material additions were found to significantly reduce slag corrosion and slag penetration of the microstructure in laboratory tests, properties that should improve spalling resistance.

Under a cooperative research and development agreement with ANH Refractories, full-sized phosphate containing high chrome oxide refractory brick of several formulations were scaled-up by ANH using laboratory processes that simulated commercial production. These materials were tested at ARC. Test results indicated good material properties, so samples were produced commercially by ANH for field testing in a commercial gasifier. One of the test refractory materials produced by ANH is shown in figure 3a. Unfortunately, the commercial gasifier containing the test refractory materials was shut down after 17 days of service due to gasifier problems unrelated to the test materials. Because preliminary evaluation of the test samples indicated good service results, additional testing of these materials in a gasifier are scheduled. Photographs of the test material before removal from service are shown in figure 3b.

a.

b.

Figure 3. Phosphate containing high chrome oxide refractory materials for gasifier testing: a) as manufactured, and b) after 17 days of trial service.

NON-CHROME BASED REFRACTORIES

Refractory liner materials currently utilized in slagging gasification systems are composed of dense firebrick with a composition of Cr_2O_3 (60 to 95 wt pct) and a second (or third) refractory oxide (typically Al_2O_3, ZrO_2, or MgO). Experience has indicated that the high Cr_2O_3 content is necessary for the best refractory service life, with severe wear areas requiring a minimum of 75-wt pct Cr_2O_3. Refractory failure is typically by spalling and/or corrosive wear. Early attempts to develop non-chrome oxide refractories were hampered by a lack of understanding of the failure mechanisms in slagging gasifiers, by raw material purity issues, and by the superior performance of Cr_2O_3 refractories.

Several issues, however, exist with the Cr_2O_3 refractory materials currently used in slagging gasifiers that act as driving forces for new material development. These issues include the following: a) current high Cr_2O_3 containing refractories do not meet the performance requirements of gasifier users, b) perceived/real long term safety concerns associated with the use of Cr_2O_3 refractory materials, c) the high cost associated with refractory materials containing Cr_2O_3, d) the difficulty in sintering high chrome oxide materials, and e) possible long term domestic supply issues with high Cr_2O_3 refractories. Because of these issues, gasifier refractory research efforts at ARC are also centered on investigating and developing low-chrome/no-chrome oxide liner materials. These goals will be achieved by evaluating wear mechanisms of chrome oxide based refractories in gasifiers and by evaluating non-chrome or low-chrome high temperature refractory oxides with potential for use in combating these and other material specific wear mechanisms. A review of the literature, thermodynamic studies, and a review of phase diagram behavior will be used to identify potential non-chrome materials for laboratory testing.

The sequence of material testing is to evaluate small "cups" of materials first, which are used to study interactions between slag and refractory material at elevated temperatures. Scale-up testing to larger cup tests is next conducted to evaluate materials identified as having good refractory/slag interactions in the small sample studies. Cup tests are used to evaluate coarse grained microstructures and different matrix material for particle packing , densification, and the microstructure interaction with the gasifier slag. Samples that have encouraging properties from the larger cup tests will be scaled-up into full sized test brick for additional physical property testing and composition refinement. Physical property testing will include density, porosity, crushing strength, creep under load at elevated temperature, and slag resistance testing in the rotary slag test.

A review of historical research on non-chrome slagging gasifier refractories indicated problems with slag corrosion and/or reactions between the slag and refractory raw material as service limiting issues. Several

refractory compounds have been identified as potential liner materials for use in gasifiers. As mentioned earlier, material selection has been restricted through a combination of literature reviews, phase diagram research and by an evaluation of the thermodynamic interactions between slag, gas, and potential materials under gasifier operation conditions. It must be kept in mind that thermodynamic studies evaluate only potential refractory oxide/non oxides as hot-face liner materials. Data generated must be used with caution because it does not indicate reaction kinetics, only what material combinations are thermodynamically stable. Specific candidate material could appear unstable for use, but may be kinetically stable. Some of the specific oxide compounds identified as having potential as either aggregate or matrix materials meriting further evaluation include Al_2O_3, CaO, MgO, SiO_2, SrO_2, TiO_2, phosphates, and/or mixtures of them. The goal of this research is to form new or improved refractory compounds or controlled advanced microstructures that can provide longer service life than high chrome oxide refractories currently used in slagging gasifiers. Samples with low Cr_2O_3 content (less than 30 wt %) will be evaluated only after materials without chrome oxide have been considered.

Limited fabrication and testing of several compositions identified as having potential for use as a gasifier liner is underway. Samples have been manufactured in the laboratory or have been obtained from refractory manufacturers. Results of two types of slag tests (cup and rotary slag) are shown in figure 4. Some of the candidate material evaluated included MgO/Al_2O_3 spinel refractories and high Al_2O_3 refractory materials with/without SiC. Preliminary tests indicated that high wear occurred in refractory materials containing spinel materials and that reactions occurred between SiC containing refractories and the FeO in slag, producing metallic Fe and CO gas. Refinements are being made to the microstructure of these and other materials to control grain size and bond matrix materials with the goal of improving slag resistance.

a.

b.

Figure 4. Examples of gasifier slag resistance tests conducted on no-chrome materials by: a) cup tests, and b) rotary slag test results.

CONCLUSIONS

Slagging gasifier refractories currently used by industry contain high levels of chrome oxide and have not met the service requirements of industry. They fail by two primary mechanisms, slag attack that leads to

corrosion, and by spalling. The Albany Research Center has developed a high chrome oxide refractory containing phosphates that has been produced commercially and is being evaluated in a commercial gasifier. Preliminary testing of this material produced encouraging results, with additional field tests planned. Investigations to develop a non-chrome oxide refractory material are in the early research stages, with a number of compounds being considered. Early testing of slag resistance has indicated that the bond phase (intergranular material) and the interaction of grains with components in the slag is critical to developing a refractory material with superior performance.

REFERENCES

1. U. Mahgagaokar and A.B. Krewinghaus, "Coal Conversion Processes (Gasification)," Ch. in Kirk-Othmer Encyclopedia of Chemical Technology, ed by J. I. Kroschwitz and M. Howe-Grant, John Wiley & Sons, V. 6, 1992, pp 541-568.

2. W.A. Taber, "Refractories for Gasification," Refractories Applications and News, Vol. 8, No. 4, (July, Aug. 2003), pp. 18-22.

3. W.T. Bakker, Greenberg, M. Trondt, and U. Gerhardus, "Refractory Practice in Slagging Gasifiers," Amer. Ceram. Soc. Bulletin, Vol. 63, No. 7, 1984, pp 870-876.

4. J.A. Bonar, C.R. Kennedy, and R.B. Swaroop, "Coal-Ash Slag Attack and Corrosion of Refractories," Amer. Ceram. Soc. Bulletin, Vol. 59, No. 4, 1980, pp 473-478.

5. G. Sorell, M.J. Humphries, E. Bullock, and M. Van de Voorde, "Material Technology Constraints and Needs in Fossil Fuel Conversion and Upgrading Processes," Int. Metals Reviews, Vol. 31, No. 5, 1986, pp 216-242.

6. M.S. Crowley, "Refractory Problems in Coal Gasification Reactors," Amer. Ceram. Soc. Bulletin, Vol. 54, No. 12 (1975), pp 1072-74.

7. R.E. Dial, "Refractories for Coal Gasification and Liquefaction," Amer. Ceram. Soc. Bulletin, Vo. 54, No. 7 (1975), pp 640-43.

8. S. Greenberg, and R.B. Poeppel, "The Corrosion of Ceramic Refractories Exposed to a Synthetic Coal Slag by Means of the Rotating-Drum Technique," Research Report ANL/FE--85-9, research sponsored by USDOE/FE, 15pp.

9. S. Greenberg and R.B. Poeppel, "The Corrosion of Ceramic Refractories Exposed to Synthetic Coal Slags by Means of the Rotation-Cylinder Technique: Final Report," Research Report ANL/FE—85-15, research sponsored by USDOE/FE and EPRI, April 1986, 66 pp.

10. C.R. Kennedy and R.B. Poppel, "Corrosion Resistance of Refractories Exposed to Molten Acidic Coal-Ash Slags," Interceram, Vol. 27, No. 3 (1978), pp. 221-26.

11. C. R. Kennedy, et al, "Evaluation of Ceramic Refractories for Slagging Gasifiers: Summary of Progress to Date," research sponsored by USDOE, ANL report 78-61, Sept., 1978, 56 pp.

12. A.P. Starzacher, "Picrochromite Brick - A Qualified Material for Texaco Slagging Gasifiers," Radex-Rundschau, Vol. 1, 1988, pp. 491-501.

13. W.T. Bakker, "Refractories for Present and Future Electric Power Plants," Key Engineering Materials, Trans Tech Publications, (1993), Vol. 88, pp. 41-70.

14. Dogan, C.P., K.S. Kwong, J.P. Bennett, R.E. Chinn, and R. Krabbe, "A New Refractory for Slagging Coal Gasifiers," Proceeding of the 28th International Conference on Coal Utilization and Fuel Systems, 9-14 March, 2003, Clearwater, FL.

Commercial Process for the Production of Silicon Carbide Fibrils

Richard Nixdorf, Principal Investigator
ReMaxCo Technologies, Inc.
Oak Ridge, Tennessee

ABSTRACT

Single crystal silicon carbide fibrils have exhibited oxidation resistance to 1,600^{o}C. The high temperature properties of the fibrils will provide an advantage to the sponsoring Department of Energy Fossil Energy Program in the areas of heat exchangers and recuperative components in advanced coal-fire combustion plants. A manufacturing process for these fibrils with the potential for low cost and high volume fibril production is necessary. The initial phase of this development program demonstrated the feasibility of microwave-assisted fibril synthesis on a bench-scale. The second phase focused on the operation of a pilot-scale semi-continuous fibril growth furnace, which has been demonstrated. The current development phase objective is improving the pilot-scale phase semi-continuous silicon carbide fibril synthesis equipment to produce higher quality and some volume of production for customer testing. This Phase III semi-continuous microwave processing equipment has been designed and fabricated. Scanning electron microscopy of the silicon carbide fibril products will be presented, as evaluated at Oak Ridge National Laboratory during their fibril characterization. Areas where these silicon carbide fibrils may create new materials opportunities to facilitate increased coal combustion temperatures will be discussed, with an estimate of volume production silicon carbide fibril cost. The new synthesis equipment will have the capacity to provide test quantities of the high-temperature silicon carbide fibrils to parties concerned with the stability of components in advanced coal-fired combustion process.

INTRODUCTION

Silicon carbide (SiC) Fibrils have excellent high-temperature properties that make them attractive for use in a variety of high-temperature applications such as reinforcements in metals and ceramics (for example, Oak Ridge National Laboratory has verified the use of SiC Fibrils as reinforcements for aluminum oxide) and as a high-temperature filter media. Key properties of interest include an elastic modulus of 84 x 10^{6} psi (579 GPa), a tensile strength of 2,300 ksi (15.8 GPa) and exceptional oxidation, chemical and creep resistance at temperatures to 1600^{o} C (2910^{o} F).

The U.S. Department of Energy's Fossil Energy Advanced Research Materials Program envisions using SiC Fibrils as reinforcements in fiber-reinforced silicon carbide matrix composite heat-exchanger tubes, which would be fabricated using chemical vapor infiltration (CVI). Long Fibrils can be spun, wound and CVI coated for the high-temperature heat-exchanger tubes. In addition to this application, fibrils are being considered to solve some of the DOE Fossil Energy Program material challenges, which

include improving the creep strength of combustion-chamber refractory tiles, producing high-temperature media for filtering combustion gases and improving the toughness of refractory metals.

For other commercial applications, companies are looking at using SiC Fibrils in such applications as reinforcing CVI silicon carbide for heat management in silicon carbide computer circuit boards, replacing hazardous SiC whiskers with a nonrespirable product (SiC Fibrils are 5 to 10 micrometers in diameter, placing them safely above the 3.5 micrometer human respirable range) in ceramic based metal-cutting tools and using SiC fibrils as high-temperature filter media in diesel exhaust, chemical processing, and fossil energy-plant emissions control.

BACKGROUND

Companies have pursued the manufacture of SiC fibrils (VLS, or vapor-liquid-solid, whiskers) since 1965. Carborundum was the last to do so, and achieved a projected volume price of $2,000/lb, with little success at volume production. The major limitations of the previous 40 years of work on Fibril growth are the high temperatures required (1600^{o} to 1700°C, or 2910^{o} to 3090°F), the slow fibril growth rate (~0.17 mm/hr) and the large quantity of wasted expensive methyl trichlorosilane (MTS) gas (97%), which is very expensive [1]. The commercial process was also complicated by the processing of large quantities of hydrogen gas at high temperatures and the generation of corrosive hydrochloric acid by-products [2].

In 1999, ReMaxCo Technologies verified a novel microwave-based Vapor-Liquid-Solid reaction synthesis of silicon carbide Fibrils. Current work advances the proof-of-concept, microwave-based VLS process. In this process, the catalyst, only, is heated to the experimental temperature (1200 to 1300°C, or 2190 to 2370°F) by microwave energy, while a mixture of MTS and hydrogen are introduced into an aluminum oxide (Al_2O_3) boat. All previous processes have required heating the entire furnace chamber to these temperatures. The MTS is dissociated and the carbon and silicon components are dissolved into the catalyst. The catalyst saturates and precipitates silicon carbide onto the surface of the reaction boat. These proof-of-concept experiments yielded fibril growth rates of 0.75 mm/hr, which is an improvement of approximately 4.4 times faster than the previous graphite furnace runs [3]. Reaction gas utilization was increased from 3% to 90%.

The U.S. Department of Energy Fossil Energy Advanced Research Materials Program sponsored this research. The currently funded project continues the commercial process development to advance to an improved semi-continuous pilot-scale commercial reactor, which will yield sufficient quantities of Fibrils to allow evaluation of the Fibrils by Oak Ridge National Laboratory and commercial customer testing.

.

In the previous Phase II, a semi-continuous, microwave-heated, vacuum reactor was designed, fabricated and tested (Fig. 1). The major obstacles occurring during Phase II

were the non-uniform nature of the microwave field adversely affecting the performance of the reactor. There were also problems with uneven distribution of the reaction gases over the Fibril growth surface. Modifications have been made to the Phase II reactor to optimize Fibril production in the current Phase III work.

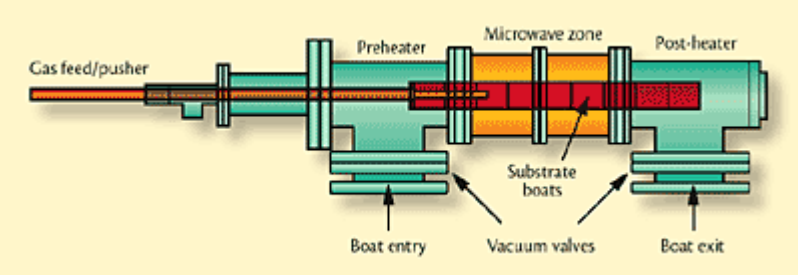

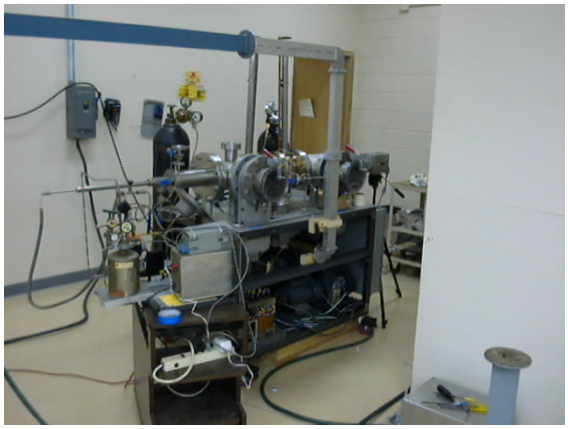

Figure 1. Phase II Fibril Synthesis Reactor

EXPERIMENTAL PROCEDURE FOR PHASE II

The boundary conditions for the experiments were determined by running a computer thermodynamic analysis on the raw materials reaction system. Cylindrical (7.6 cm diameter × 7.6 cm long) high-density aluminum-oxide reaction boats were coated on the inner surface with a catalyst and placed into the reactor under a light vacuum. The microwave reactor is evacuated to approximately 30 torr and flushed with nitrogen gas at a pressure of 150 torr. After the flush, the furnace is backfilled with hydrogen gas to a pressure of 150 torr and maintained at less than 180 torr throughout the microwave fibril-growth run. Ferrous silicon and iron powder catalysts (and several mixtures thereof) were tested. Fibril catalyst-seed paint is prepared using metallurgical grade –325 mesh ferrous silicon mixed in a dispersant paint from YZP Corp. in a 1:1 ratio.

A series of reaction boats were run (one at a time) through the reactor. Each boat is preheated using resistance heaters to a temperature between 850^{o} to 900°C (1560^{o} to 1650°F), and then moved to the microwave heated section where each of two 2-kW microwave sources is stabilized at 1.8 kW. The catalyst is heated to a temperature of 1200^{o} to 1300°C (2190^{o} to 2370°F), while introducing a mixture of MTS and hydrogen

into the catalyst-coated area of the boat. The MTS forms the carbon and silicon components, which dissolve into the catalyst to grow the Fibrils.

MTS reaction gas is generated by bubbling hydrogen through liquid MTS in a steel container. Replacing the steel container with a transparent, heated glass bubbler allowed the operator to view the hydrogen flow through MTS liquid and control the vapor pressure of the MTS gas. Hydrogen flow is passed through the MTS bubbler at a rate of 0.13 liters/min for a period of one to three hours.

Process optimization experiments were conducted after achieving consistent furnace operation to achieve fibril growth and define operating parameters. The reaction process in the aluminum oxide tube is shown in Figure 2. Ferrous silicon was replaced with iron particles, then a mixture of 50% ferrous silicon and 50% iron by weight. Fibrils produced using optimal operating parameters were analyzed at Oak ridge National Laboratory, and the results from these experiments were used to design the current Phase III microwave reactor. Experiments also were conducted to identify a less hazardous raw material gas than MTS. MTS liquid was replaced with a SP4000, a polysilymethylene CVD silicon carbide precursor. The SP4000 can be reacted in nitrogen gas rather than the more dangerous hydrogen required by the MTS liquid and gas and does not produce the hazardous hydrochloric acid by-product.

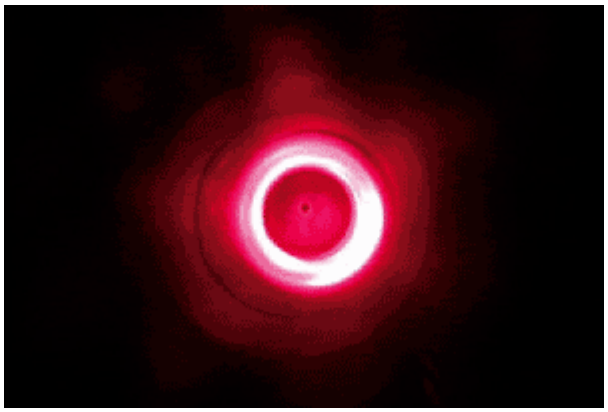

Figure 2. Microwave field reaction with catalyst for SiC Fibril growth

RESULTS

The only fibril growth in the initial microwave field experiments occurred after being in the microwave growth chamber for approximately three hours. Measured microwave intensity in the fibril growth area was measured at zero. Rebuilding the furnace to focus more of the microwave field in the fibril growth zone improved the fibril growth quality and time. However, the microwave energy in the growth field was still negligible. Figures

3 and 4 shows fibrils (2 to 5 μm in size) grown in this sequence. The fibril quality is good, but the fibril yield is very low.

Issues with the fibril reactor that need to be addressed, and that are being implemented in the current Phase III of this work include:

- Improving microwave field uniformity
- Using flat ceramic plates in place of cylindrical ceramic boats in which catalyst paint flakes off the top and sides
- Implementing a more accurate mass flow controller and a manifold-mixer for the reaction gas distribution because the current MTS gas feed mechanism had very little mass flow control and an irregular feed pattern to the fibril growth zone

One of the problems with scaling the Fibril development to a large-scale commercial process is the generation of significant quantities of hydrochloric acid in the off-gas stream. The acid destroys the vacuum system and the exhaust ducts. Silicon carbide fibrils made using the SP4000 in nitrogen produces no acid in the by-product gases. An unexpected advantage with the SP4000 is that Fibrils grew at a temperature of 850°C (1560°F) compared with required a temperature of 1200^{o} to 1300°C (2190^{o} to 2370°F) for the MTS reaction. Fibrils 5 to 15 μm in diameter grown in the SP4000 experiments are shown in Figures 5 and 6. Melt growth balls were observed with the fibrils indicating that they were true VLS Fibrils.

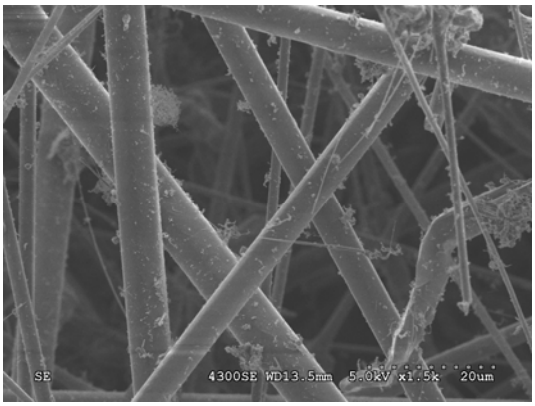

Figure 3. Microwave grown SiC Fibrils

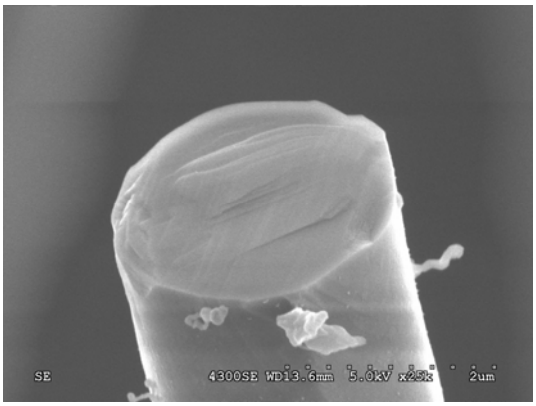

Figure 4. Evidence of single crystal product

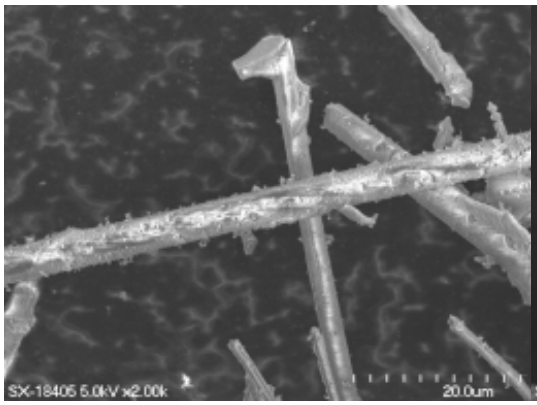

Figure 5. SP4000 Microwave Grown SiC Fibrils

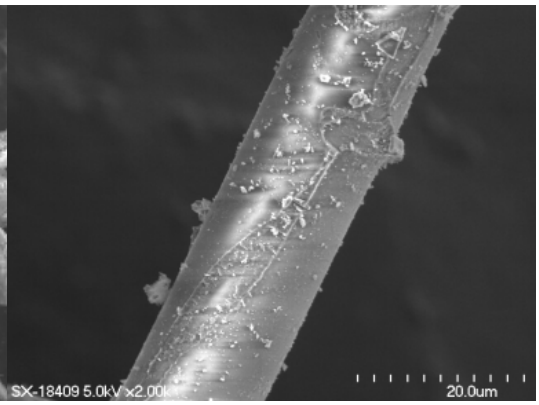

Figure 6. Surface roughness due to faster growth rate

CONCLUSIONS

Silicon carbide Fibrils can be produced at temperatures as low as 850°C (1560°F) compared with the 1700°C (3090°F) in previous graphite furnaces, and fibril growth rate has been increased by a factor of four over previous technologies. Microwaves play a major role in improving the fibril-growth process. The SP4000 silicon carbide precursor provides a reaction without hazardous off-gas products, with a projected future volume cost of $600/kilogram.

An added benefit to the development of this microwave process is the ability to also economically produce TiN, TiB_2 and TiC Fibrils.

It is feasible to scale up to a commercial volume process by overcoming the equipment engineering issues encountered in Phase II of this project, which include obtaining a uniform microwave field, good control and uniform distribution of reactant gases, and the use of flat ceramic reaction boats. These improvements will get the commercial process closer to the project goal of a Fibril price of $300/lb. With these improvements in place, 40 years of previous technology work can be significantly improved by the shift to microwave synthesis to accomplish lower energy consumption, higher growth rates, reduced reactant gas waste, lower cost raw materials and a consistent high-quality fibril product.

A new Phase III pilot-scale reactor is designed and fabricated, incorporating these improvements, which will be capable of producing 200 grams of fibrils per day. The reactor will be tested and then operated to supply sample quantities to various researchers in the Fossil Energy Materials Program. A production reactor capable of producing 50 kilograms of Fibrils per day will be designed, and will be built if a commercial demands evolve. A scale-up to production volume will cost approximately $3 million.

REFERENCES

1. P.D. Shaiek, et al., Scale-Up and Optimization of the VLS Growth Process for Beta-SiC Whiskers for the Period of April 1982 -September 1989, DARPA Final Report, DOE/OAR&TD Topical Report, LA-12119, Nov. 1991
2. R.W. Ohnsorg, W.E. Hollar Jr. and S.K. Lau, Engineering Scale Development of Vapor-Liquid-Solid (VLS) Process for the Production of Silicon Carbide Fibrils, Phase II Report, ORNL/Sub/90-SD861/02, April 1995
3. R.D. Nixdorf, Development of a Commercial Process for the Production of Silicon Carbide Fibrils, Phase I Final Report, ORNL/Sub/98-SU604/01, April 1999

ACKNOWLEDGEMENT

The author acknowledges the support of the U.S. DOE Fossil Energy through the Advanced Research Materials Program under the project direction of Dr. Roddie R. Judkins for funding this work. Gratitude is expressed to Oak Ridge National Laboratory's High Temperature Materials Laboratory for the electron microscopy work of Larry Allard and Larry Walker and to Microwave Materials Technology for microwave equipment engineering and fabrication.

For more information: Richard Nixdorf is president and CEO, ReMaxCo Technologies Inc., 1010 Commerce Park Dr., Suite 1, Oak Ridge, TN 37830; tele: 865-482-7552; fax: 865-482-7505; e-mail: nixdorfr@indceramicsolns.com

APPENDIX I

FINAL PROGRAM

FINAL PROGRAM
18TH ANNUAL CONFERENCE ON FOSSIL ENERGY MATERIALS
MARRIOTT HOTEL, KNOXVILLE, TENNESSEE
June 2 – 4, 2004

Wednesday, June 2

12:00 p.m. **Registration**

1:00 p.m. Welcome and Introductory Remarks, Roddie Judkins, Oak Ridge National Laboratory

1:10 p.m. Brief Update on DOE's Advanced Research Materials Program, Robert Romanosky U.S. Department of Energy, National Energy Technology Laboratory

Session I - Functional Materials

1:30 p.m. Introduction
Tim Armstrong, Oak Ridge National Laboratory

1a. Materials for Hydrogen-Separation Membranes

1:40 p.m. *Development of Inorganic Membranes for Hydrogen Separation*, Brian Bischoff, Oak Ridge National Laboratory

2:10 p.m. *Influence of Surface Coating on the Performance of V–Cu, V–Ti, and Ta Membranes for Hydrogen Separation*
Steve Paglieri, Los Alamos National Laboratory

2.40 p.m. *Economical Fabrication of Membrane Materials*
Tim Armstrong, Oak Ridge National Laboratory

3.10 p.m. Break

3:30 p.m. *Advances in Air Brazing for Use in Joining and Sealing High-Temperature Gas Separation Membranes*, Scott Weil, Pacific Northwest National Laboratory

1b. Advanced Gas-Separation Materials

4:00 p.m. *Advanced Processing of Metallic Powders*, Iver Anderson, Ames Laboratory

4.30 p.m. *Activated Carbon Composites for Air Separation*, Tim Burchell, Oak Ridge National Laboratory

5:00 p.m. Adjourn

6:00 p.m. **Reception and Poster Session**

Session II – POSTERS

2a. Alloys for Ultra-Supercritical Steam Applications

1. *Understanding Damage Mechanisms in Ferritic Steels*, Bob Swindeman, Oak Ridge National Laboratory

2. *High Creep-Strength Alloys*, Phil Maziasz, Oak Ridge National Laboratory

3. *Ultra-Supercritical Steam Corrosion*, G.R. Holcomb, Albany Research Center

4. *Formability of alloy IN740*, Gail Ludtka, Oak Ridge National Laboratory

SPONSORED BY THE UNITED STATES
DEPARTMENT OF ENERGY,
OFFICE OF FOSSIL ENERGY
NATIONAL ENERGY TECHNOLOGY LABORATORY

2b. Oxide Dispersion-Strengthened Alloys

5. *Improved ODS Alloy for Heat Exchanger Tubing,* Larry Brown, Edison Welding Institute

6. *ODS Alloy Development,* Ian Wright, Oak Ridge National Laboratory

7. *Optimization of ODS Alloy Properties,*Bimal Kad, University of California at San Diego

8. *Reduction in Defect Content in ODS Alloys* Andy Jones, University of Liverpool

2c. Corrosion Testing in Coal-Fired Environments

9. *USC Materials Plant Trails at the Niles Plantm* Denny McDonald, McDermott Corp

10. *In-Plant Corrosion Probe Tests,* Gregg Stanko, Foster Wheeler Development Corporation

11. *Fireside Corrosion of Alloys for USC Plants* Ken Natesan, Argonne National Laboratory

2d. Breakthroughs in Materials Performance and Reliability

12. *Novel Processing of Mo-Si-B Intermetallics for Improved Efficiency of Power Systems* Matt Kramer, Ames Laboratory

13. *Evaluation of the Intrinsic and Extrinsic Fracture Behavior of Iron Aluminides* B.R. Cooper, Bruce Kang, West Virginia University

14. *Study of Fatigue and Fracture Behavior of Cr-Based Alloys and Intermetallic Materials* Peter Liaw, University of Tennessee

Thursday, June 3

7:30 a.m. Continental Breakfast

Session III – Coatings and Protection of Materials

8:30 a.m. Introductory Remarks, Udaya Rao, U.S. Department of Energy, National Energy Technology Laboratory

8.45 a.m. *Investigation of Iron Aluminide Weld Overlays,* John DuPont, Lehigh University

9.15 a.m. *Coating Microstructure-Property Issues.* Richard Wright, Idaho National Engineering and Environmental Laboratory

9.45 a.m. *Extended Lifetime Metallic Coatings.* Bruce Pint, Oak Ridge National Laboratory

10.15 a.m. Break

10.45 a.m. *Aluminide Coatings for Power Generation Applications,* Ying Zhang, Tennessee Technology University

11.15 a.m. S*lurry-Based Mullite Coatings for Corrosion Resistance,* Beth Armstrong, Oak Ridge National Laboratory

11.45 a.m. Lunch

2:00 p.m. *Chemically Vapor-Deposited YSZ for Thermal and Environmental Barrier Coatings* Ted Besmann, Oak Ridge National Laboratory

2.30 p.m. *Modeling of Chemically Vapor-Deposited Zirconia for Thermal Barrier and Environmental Barrier Coatings*
Tom Starr, University of Louisville

3.00 p.m. *Development of Nondestructive Evaluation Methods for Ceramic Coatings*
Bill Ellingson, Argonne National Laboratory

3.30 p.m. Break

4.00 p.m. *Concepts for Smart, Protective High-Temperature Coatings*
Peter Tortorelli, Oak Ridge National Laboratory

4.30 p.m. *Corrosion Probes for Fireside Monitoring in Coal-Fired Boilers,* Bernie Covino, Albany Research Center

5.00 p.m. Adjourn

Friday, June 4

7:30 a.m. Continental Breakfast

Session IV - Breakthroughs in Materials Performance & Reliability

8:20 a.m. Introductory Remarks
Ian Wright
Oak Ridge National laboratory

8:30 a.m. *Locating Hydrogen with Neutrons--What's Possible, and What's Not,* Andrew Payzant, Oak Ridge National Laboratory

4a. Temperature Capabilities Beyond Current Alloys

9.00 a.m. Mo-Si Alloy Development
Joachim Schneibel, Oak Ridge National Laboratory

9.30 a.m. Progress in Controlled Oxidation for Functional and Protective Surfaces
Mike Brady, Oak Ridge National Laboratory

10:00 a.m. Break

4b. Materials for Increased Reliability in Combustion/Gasification Environments

10.30 a.m. *Testing of a Very High Temperature Heat Exchanger for IFCC Power Systems*
John Hurley, University of North Dakota, Energy and Environmental Research Center

11.00 a.m. *Improved Refractories for Slagging Gasifiers in IGCC Power Systems,* James Bennett, Albany Research Center

11.30 a.m. *Development of a Commercial Process for the Production of Silicon Carbide Fibrils*
Richard Nixdorf, ReMaxCo Technologies, Inc.

12.00 p.m. Closing Remarks
Robert Romanosky, U.S. Department of Energy, National Energy Technology Laboratory
Roddie Judkins, Oak Ridge National Laboratory

12.30 p.m. Adjourn

APPENDIX II

LIST OF ATTENDEES

Fossil Energy Materials Conference
Final Attendees List
Knoxville, Tennessee
June 2-4, 2004

a

Iver Anderson
Ames Laboratory
222 Metals Development
Ames, IA 50011
515-294-9791
515-294-8727
andersoni@ameslab.gov

Beth Armstrong
ORNL
P.O. Box 2008
Oak Ridge, TN 37831-6083
865-241-5862
865-574-6918
armstrongbl@ornl.gov

Tim Armstrong
ORNL
P.O. Box 2008
Oak Ridge, TN 37831-6186
865-574-7996
865-241-0112
armstrongt@ornl.gov

B

Fred Baker
ORNL
P.O. Box 2008
Oak Ridge, TN 37831-6087
865-241-1127
865-576-8424
bakerfs@ornl.gov

U. (Balu) Balachandran
Argonne National Laboratory
9700S. Cass Avenue
Building 212
Argonne, IL 60439
630-252-4250
630-252-3604
balu@anl.gov

James Bennett
Albany Research Center
US Department of Energy
1450 Queen Ave., SW
Albany, OR 97321
541-967-5983
541-967-5914
jbennett@alrc.doe.gov

Ron Bhada
New Mexico State University
1060 Frenger Mall, ECIII, 3rd Fl.
Room 336
PO 30001
Las Cruces, NM 88003
770-389-4836
505-646-5474
RONBHADA@aol.com

Brian Bischoff
ORNL
P.O. Box 4699
Oak Ridge, TN 37831-7271
865-241-3172
865-576-3502
bischoffbl@ornl.gov

Ralph Boroughs
TVA
1101 Market St., SP-5D
Chattanooga, TN 37401-2801
423-751-4644
423-751-6087
rdboroughs@tva.gov

Mike Brady
ORNL
P.O. Box 2008
Oak Ridge, TN 37831-6115
865-574-5153
865-241-0215
bradymp@ornl.gov

Fossil Energy Materials Conference
Final Attendees List
Knoxville, Tennessee
June 2-4, 2004

Tim Burchell
ORNL P.O. Box 2008
Oak Ridge, TN 37831-6088
865-576-8595
865-576-8424
burchelltd@ornl.gov

C

David Calabro
ExxonMobil Research and Engineering
1545 Route 22 East
Annandale, NJ 08801
908-730-3713
908-730-3198
dccalabro@exxonmobil.com

Kevin Cooley
ORNL
P.O. Box 2008
Oak Ridge, TN 37831-6063
865-574-4559
865-574-6918
cooleykm@ornl.gov

Bernie Covino
Albany Research Center
1450 Queen Ave., SW
Albany, OR 97321
541-967-5828
541-967-5914
Covino@alrc.doe.gov

D

Richard Dunst
NETL
626 Cochrans Mill Road
Pittsburgh, PA 15236-922-273C
412-386-6694
412-386-6685
dunst@netl.doe.gov

Mark E. Dupont
Westinghouse Savannah River Co.
Building 773-41A
Savannah River Site
Aiken, SC29808
803-725-0954
803-725-4129
Mark.dupont@srs.gov

E

William Ellingson
Argonne National Laboratory
9700 S. Cass Ave., Bldg. 212
Argonne, IL 60439
630-252-5068
630-252-4798
Ellingson@anl.gov

G

Nidia Gallego
ORNL
P.O. Box 2008
Oak Ridge, TN 37831-6087
865-241-9459
865-576-8424
gallegonc@ornl.gov

Thomas Gibbons
Consultant-ORNL
5005 Nicholas Creek Circle
Wilmington, NC 28409
910-798-1931
Snobbig50@msn.com

Fred Glaser
US DOE
1000 Independence AV, SW
FE-25 Germantown Bldg.
Washington, DC 20585-1290
301-903-2676
301-903-0243
Fred.glaser@hq.doe.gov

Fossil Energy Materials Conference
Final Attendees List
Knoxville, Tennessee
June 2-4, 2004

Steve Goodstine
ALSTOM Power Inc.
2000 Day Hill Road
Windsor, CT 06095
860-285-5686
860-285-4033
Stephen.1.goodstine@power.alstom.com

H

David A. Helmick, Ph.D.
GE Gas Turbines, LLC
300 Garlington Rd, GTTC 174D
Greenville, SC 29602
864-254-5325
864-254-4385
David.helmick@ps.ge.com

John Henry
ORNL
P.O. Box 2008
Oak Ridge, TN 37831-6063
865-241-1251
865-574-6918
henryjjjr@ornl.gov

Richard Higgins
CeraMem Corporation
12 Clematis Avenue
Waltham, MA 02453
781-899-4495 x23
781-899-6478
Higgins@ceramem.com

Lan Huang
University of Tennessee
Knoxville, TN 37996
865-974-0645
865-974-4115
Lhuang2@utk.edu

John Hurley
Energy & Environmental Research Center
P.O. Box 9018
Grand Forks, ND 58202-9018
701-777-5159
701-777-5181
jhurley@undeerc.org

J

Dr. Andy Jones
University of Liverpool Foresight Centre
1 Brownlow St.,
Liverpool
L69 3GL
UK
44 151 794 8026
44 151 794 8344
Andy.jones@liv.ac.uk

Roddie Judkins
ORNL
P.O. Box 2008
Oak Ridge, TN 37831-6084
865-574-4572
865-574-4357
judkinsrr@ornl.gov

K

Bimal Kad
University of California
409 University Center
MC0085 UCSD
LaJolla, CA 92093-0085
858-534-7059
858-534-6373
bkad@ucsd.edu

Fossil Energy Materials Conference
Final Attendees List
Knoxville, Tennessee
June 2-4, 2004

Bruce Kang
West Virginia University
353 ESB
Morgantown, WV 26506
304-293-3111
304-293-6689
Bruce.Kang@mail.wvu.edu

Glen Kirby
ORNL
P.O. Box 2008
Oak Ridge, TN 37831-6063
865-576-6545
865-574-6918
kirbygh@ornl.gov

Muneaki Kojima
J-Power
1101 17th Street NW Suite 802
Washington, DC 20036
202 429-8881
202-429-1660
mkojima@epdc.com

Matthew Kramer
Ames Laboratory
37 Wilhelm Hall
Ames, IA 50011-3020
515-294-0276
515-294-4291
mjkramer@ameslab.gov

L

K. J. Lee
Georgia Tech
771 Ferst Drive
Atlanta, GA 30332-0245
404-894-7399
404-894-7399
Kj.lee@mse.gatech.edu

Peter Liaw
University of Tennessee
434 Dougherty Hall
Knoxville, TN
865-974-5304
865-974-4115
pliaw@utk.edu

Chuck Love
Pall Corp
3669 State RT 281
Cortland, NY 13045
607-753-6041
607-753-1220
Chuck_love@pall.com

Zhaoping Lu
ORNL
P.O. Box 2008
Oak Ridge, TN 37831
luzp@ornl.gov

M

Mani Manivannan
West Virginia University
P. O. Box 6315 Hodges Hall
Morgantown, WV 26505
304-293-3422 x1429
304-293-5732
amanivan@wvu.edu

Arnold R. Marder
Lehigh University
Whitaker Lab
Bethlehem, PA 18015
610-758-4197
610-758-6407
Arm0@lehigh.edu

Fossil Energy Materials Conference
Final Attendees List
Knoxville, Tennessee
June 2-4, 2004

Richard Marinangeli
UOP LLC
P.O. Box 5016
Des Plaines, IL 60017-5016
847-391-3327
847-391-3724
Richard.marinangeli@uop.com

Phil Maziasz
ORNL
P.O. Box 2008
Oak Ridge, TN 37831-6115
865-574-5082
865-574-7659
maziaszpj@ornl.gov

G.B. Kirby Meacham
Meacham Company
18560 Parkland Dr.
Cleveland, OH 44122
216-752-9529
216-752-9599
gbkmeacham@cs.com

N

Ken Nalwasky
Praxair Surface Technologies
14442 Club Circle
Alpharetta, GA 30004
678-867-0800
678-867-0777
Kenneth_nalwasky@praxair.com

Ken Natesan
Argonne National Laboratory
212 Energy Technology Division
9700 South Cass Avenue
Argonne, IL 60439
630-252-5103
630-252-8681
natesan@anl.gov

Richard D. Nixdorf
ReMaxCo Technologies, Inc.
1010 Commerce Park Drive, Suite 1
Oak Ridge, TN 37830
865-482-7552
865-482-7505
nixdorfr@indceramicsolns.com

P

Stephen N. Paglieri
Los Alamos National Laboratory
P.O. Box 1663, MS C348
Los Alamos, NM 87545
505-667-0652
505-665-1687
Steve.paglieri@lanl.gov

Arvid Pasto
ORNL
P.O. Box 2008
Oak Ridge, TN 37831-6062
865-574-5123
865-574-4913
pastoae@ornl.gov

Dilo Paul
SAIC
626 Cochran Mill Road
Pittsburgh, PA 15236
412-386-6110
anton.d.paul@saic.com

Andrew Payzant
ORNL
P.O. Box 2008
Oak Ridge, TN 37831-6064
865-574-6538
865-574-3940
payzanta@ornl.gov

Fossil Energy Materials Conference
Final Attendees List
Knoxville, Tennessee
June 2-4, 2004

Bruce Pint
ORNL
P.O. Box 2008
Oak Ridge, TN 37831-6156
865-576-2897
865-241-0215
pintba@ornl.gov

Cynthia Powell
Albany Research Center
1450 Queen Ave. SW
Albany, OR 97321
541-967-5803
541-967-5914
powellc@alrc.doe.gov

R

Udaya Rao
NETL
MS 922-273C
626 Cochrans Mill Road
Pittsburgh, PA 15236-0940
412-386-4743
412-386-5917
rao@netl.doe.gov

Mary Rawlins
DOE-ORO
P.O. Box 2008
Oak Ridge, TN 37831-6269
865-576-4507
865-574-9275
rawlinsmh@ornl.gov

Richard Read
NETL
626 Cochrans Mill Road
P.O. Box 10940, MS 922-273C
Pittsburgh, PA 15236
412-386-5721
412-386-6685
read@netl.doe.gov

Weiju Ren
P.O. Box 2008
Oak Ridge, TN 37831-6155
865-576-6402
865-574-0641
renw@ornl.gov

Edward Robitz Jr.
Babcock & Wilcox
1562 Beeson St
Alliance, OH 44601
330-860-6636
330-860-6676
esrobitz@babcock.com

Robert Romanosky
NETL
3610 Collins Ferry Road
P.O. Box 880
Morgantown, WV 26507-0880
304-285-4271
304-285-4403
rroman@netl.doe.gov

S

Mike Santella
ORNL
P.O. Box 2008
Oak Ridge, TN 37831
865-574-4805
santellaml@ornl.gov

Joachim Schneibel
ORNL
P.O. Box 2008
Oak Ridge, TN 37831-6115
865-576-4644
865-574-7659
schneibeljh@ornl.gov

Fossil Energy Materials Conference
Final Attendees List
Knoxville, Tennessee
June 2-4, 2004

Naidu V. Seetala
Grambling State University
RWE Jones Drive, Carver Hall 81
Grambling, LA 71245
318-274-2574
318-274-3281
naidusv@gram.edu

John Shen
US Department of Energy
FE-24 GTN
1000 Independence Ave., SW
Washington, DC 20585-1290
301-903-4344
301-903-2238
john.shen@hq.doe.gov

John P. Shingledecker
ORNL
P.O. Box 2008
Oak Ridge, TN 37831-6155
865-574-4929
865-574-0641
shingledecjp@ornl.gov

Thomas Starr
University of Louisville
Chemical Engineering Department Ernst Hall
Louisville, KY 40292
502-852-1073
502-852-6355
Tom.starr@louisvill.edu

Karthik Subramanian
Savannah River National Laboratory
Bldg 773-A Rm. D1138
Aiken, SC 29808
803-725-8528
803-725-7369
Katrthik.subramanian@srs.gov

Bob Swindeman
ORNL
P.O. Box 2008
Oak Ridge, TN 37831-6155
865-574-5108
865-574-0641
swindemanrw@ornl.gov

T

Andrew Thom
Ames Laboratory
330 Spedding Hall
Iowa State University
Ames IA 50011-3020
515-294-4064
515-296-6166
ajthom@ameslab.gov

Paul Torgerson
Worldwide Energy, LLC
15 S. Excelsior avenue
Butte, MT 59701-1530
406-723-8110
406-723-8105
PaulTorgerson@wesofc.com

Peter Tortorelli
ORNL
P.O. Box 2008
Oak Ridge, TN 37831-6156
865-574-5119
865-241-0215
tortorellipf@ornl.gov

Terry Totemeier
INEEL
P.O. Box 1625 MS 2218
Idaho Falls, ID 83415
208-526-3074
208-526-4822
totetc@inel.gov

Fossil Energy Materials Conference
Final Attendees List
Knoxville, Tennessee
June 2-4, 2004

W

Richard Walters
Albany Research Center
1450 Queen Ave., SW
Albany, OR 97321
541-967-5873
541-967-5991
walters@alrc.doe.gov

Scott Weil
PNNL
902 Battelle Blvd
P.O. Box 999
Richland, WA 99352
509-375-6796
509-375-2186
Scott.weil@pnl.gov

Shiela Woodard
Pratt and Whitney
400 Main Street, MS 114-51
East Hartford, CT 06108
880-557-3336
880-755-1917
Shiela.woodard@pw.utc.com

Ian Wright
ORNL
P.O. Box 2008
Oak Ridge, TN 37831
865-574-4451
865-241-0215
wrightig@ornl.gov

Richard Wright
INEEL
P.O. Box 1525
MS 2218
Idaho Falls, ID 83415
208-526-6127
208-526-4822
RNW2@inel.gov

Z

Ying Zhang
Tennessee Technological University
115 W. 10th Street Box 5014
Cookeville, TN 38505
931-372-3265
931-372-6340
yzhang@tntech.edu

Jia Hong Zhu
Tennessee Technological University
115 W. 10th Street Box 5014
Cookeville, TN 38505
931-372-3186
931-372-6340
jzhu@tntech.edu

Jeff Zollar
ORNL
P.O. Box 2008
Oak Ridge, TN 37831-6084
865-574-5135
865-574-4357
zollarja@ornl.gov